The development of an *in-situ* UV ablation GC-*irms* technique for the analysis of oxygen isotopes in metamorphic minerals, and its application to polymetamorphic schists from Western Massachusetts, U.S.A.

by

Nicholas John Gardiner M.A.(Oxon) M.Sc.

Thesis submitted for the Degree of
Doctor of Philosophy
to the University of Oxford

Worcester College &
The Department of Earth Sciences
University of Oxford

Trinity Term
September 2000

SCIENCE LIBRARY
15 OCT 2001

THE DEVELOPMENT OF AN IN-SITU UV ABLATION GC-IRMS TECHNIQUE FOR THE ANALYSIS OF OXYGEN ISOTOPES IN METAMORPHIC MINERALS, AND ITS APPLICATION TO POLYMETAMORPHIC SCHISTS FROM WESTERN MASSACHUSETTS, U.S.A.

Thesis submitted for the degree of Doctor of Philosophy to the University of Oxford

by

Nicholas John Gardiner B.A. (Oxon) M.Sc.

Department of Earth Sciences & Worcester College

Trinity Term 2000

ABSTRACT

This thesis describes an attempt to develop a pioneering method for the analysis of oxygen isotopes in metamorphic rocks. This technique is then applied to a suite of metapelites from Massachusetts, U.S.A. with the aim of investigating metamorphic history.

The study of oxygen isotopes is a rapid and efficient way of deciphering the reaction history of a metamorphic rock, and they are particularly useful for quantifying the role of fluids during metamorphism. Technological advances have given the opportunity to develop a new laser fluorination facility capable of *in-situ* oxygen isotope analysis on the 100μm scale. The use of UV laser ablation coupled with helium carrier flow and isotope ratio mass spectrometry gives the potential for liberation, transfer and analysis of nanomoles of oxygen.

This analytical technique is developed herein, and applied to garnets from high alumina metapelites of the Hoosac Schist of Western Massachusetts. These large garnets contain concentric unconformity textures which are attributed to at least two metamorphic events. Core-rim zoning profiles from three Hoosac garnets has been accomplished.

Metamorphic modelling in the complex chemical system Na_2O-CaO-MnO-K_2O-FeO-MgO-Al_2O_3-SiO_2-H_2O has yielded P-T estimates for garnet cores of 520°C and 8.5 kbar, and rims at 590°C and 8-10kbar. Within this framework, a new approach enables calculation of oxygen isotope shifts with reaction progress in the presence of a non-equilibrium fluid. Fitted profiles from the Hoosac garnets imply prograde core growth during inflow of external low-$\delta^{18}O$ fluid, and calculations suggest a minimum time integrated fluid flux for the first garnet growth event of the order of 0.2 cm^3/cm^2, some four to five orders of magnitude less than other New England studies.

Extended Abstract

Oxygen comprises approximately one half of the Earth's crust by mass. Therefore processes which transfer matter from one phase to another are likely to involve the transfer of oxygen. Oxygen isotopes are stable, have well-defined equilibrium fractionations, and thus analysis of oxygen isotope ratios at an appropriate scale can potentially provide valuable information concerning mass transfer reactions in regionally metamorphosed rocks.

Following recent advances in analytical technology, a pioneering laser fluorination facility for the measurement of oxygen isotope ratios in metamorphic minerals has been constructed at Oxford. This employs UV laser light which is capable of *in-situ* ablation on the sub-millimetre scale without any margin effects which could lead to isotope fractionation. In order to quantitatively transfer and analyse the nanomoles of analyte gas liberated from the coupled ablation-fluorination reaction, the use of helium carrier-flow technology is matched to gas chromatography isotope-ratio mass spectrometry.

This, therefore, is a method which has the potential to offer true *in-situ* mineral analysis on the 100 μm scale, whilst still having an analytical precision capable of resolving the sub-per mil fractionations associated with medium-grade metamorphic reactions. Such a facility would provide a powerful tool for deciphering the reaction history of a metamorphic rock.

This study sets out to develop this new technique for the measurement of oxygen isotope ratios in metamorphic minerals. The chosen field area for the application of this method is a sequence of alumina-rich metapelites from Massachusetts, U.S.A. These Palaeozoic New England rocks lie within the zone of maximum overlap between Ordovician Taconian-affected and Siluro-Devonian Acadian-affected thrust slices. Thus

they are considered to have experienced at least two major episodes of metamorphism. Within this thesis is described an attempt to apply the coupled use of isotope analysis, detailed petrography and metamorphic modelling to unravel the complex metamorphic history of these rocks.

The Hoosac Schist of Western Massachusetts is a high-alumina metapelite, consisting largely of a muscovite, paragonite and quartz matrix, within which are found porphyroblasts of garnet, staurolite, biotite and kyanite (at appropriate grades). It displays compelling evidence for multiple generations of metamorphism: the most striking of which is the presence of large (2cm) garnets with distinct concentric unconformity structures, which separate inclusion-rich cores (and truncate a core fabric) from inclusion-poor rims. Garnets are particularly suitable minerals for this kind of study since they grow throughout much of the metamorphic history of the rock, and the intercrystalline diffusivities of the major cations, and of oxygen isotopes, is negligible within garnet. Thus they can preserve a record of the evolution of prevailing chemical conditions in the form of concentric zonation.

In this study, petrographic and geochemical analysis of the Hoosac Schist has proved the common existence of such garnet unconformities. This has also shown that the rocks record at least two phases of mineral growth. The first metamorphic episode comprised garnet core nucleation and growth. Inclusions in this core, principally chloritoid and rutile, define a sigmoidal fabric, suggesting garnet growth during a period of deformation. Accompanying this initial period of garnet growth were the white micas muscovite and paragonite, chlorite, chloritoid and quartz. Following at least one subsequent phase of deformation, giving rise to a pervasive crenulation cleavage, a second episode of metamorphism saw the growth of garnet rims, along with staurolite, biotite, kyanite, ilmenite and second generation white micas.

Examination of cation profiles from the Hoosac garnets show a core which records fairly constant growth conditions. Remarkably, the second, rim-producing episode of garnet growth appears to have commenced at similar metamorphic conditions to where the first event ceased; across the unconformity into the rim cation compositions merge smoothly. An additional feature is the absence of a correlated manganese spike with the textural break, which would otherwise imply a retrogressive episode separating the

two growth events.

These garnet textural breaks are similar to those found in garnets from both the Gassetts and Hoosac Schists of southern Vermont. The Vermont garnets have been the subject of two differing models to explain the origin of the unconformity textures. One model defines the textural break as a period of retrogression separating two prograde growth events; this requires the presence of external fluids to drive the hydration reaction. The second model describes the break as a prograde garnet resorption reaction. Recent work has shown that these models can be tested with the use of oxygen isotope analysis.

In this thesis the Oxford UV laser ablation facility is developed specifically to analyse the Hoosac Schist on scales far smaller than reported in the Vermont garnets. As described here, this development has been partially successful, with core-rim oxygen isotope ratio profiles measured in three Hoosac garnets. One small garnet sample evidences concentric zoning from 9.8‰ in the core to 10.6‰ at the rim over 1mm. This garnet is considered to be the result of the second metamorphic episode, and thus represents the result of a rim growth event. Two other garnet core-rim $\delta^{18}O$ profiles show a decrease in $\delta^{18}O$ from the inner core to the unconformity at the core-rim transition, and a recovery in $\delta^{18}O$ in the rim.

Metamorphic modelling allows reconstruction of the peak and pre-peak equilibrium conditions of the rock. Advances in modelling complex chemical systems coupled with refined internally-consistent thermodynamic datasets have given rise to the ability to calculate phase equilibria in the complex Na_2O-CaO-MnO-K_2O-FeO-MgO-Al_2O_3-SiO_2-H_2O (NCMnKFMASH) system. Two approaches to modelling are taken in this thesis.

Firstly, the coupling of equilibrium P-T phase diagrams with bulk rock compositional data allows the construction of P-T pseudosections. This enables the phase assemblage, phase composition (X) and phase modes (M) to be uniquely defined at each P and T point of interest. This can be extended to the reconstruction of the P-T-X-M conditions at points representing both the garnet core and garnet rim (initiation and cessation of garnet growth respectively). Garnet core conditions of 520°C and 8.5kbar have been calculated, and garnet rim conditions at 590°C and 8-10kbar.

Secondly, the Gibbs' method employs differential thermodynamics to allow the evolu-

tion of a system to be modelled, that is the changes in P-T-X-M conditions. Here, the use of a modified Gibbs' method augmented with oxygen isotope fractionation considerations is employed to facilitate calculation of oxygen isotope shifts with the progress of metamorphism.

Application of this to the P-T-X-M framework as defined by the equilibrium pseudosection modelling has allowed reconstruction of the garnet core-rim isotope profiles. This modelling confirms that closed-system garnet evolution yields an increase in $\delta^{18}O$ from core to rim. However, this does not fit the observed isotope profiles seen in the Hoosac garnet cores. In order to replicate these measured patterns, the continuous infiltration of a low-$\delta^{18}O$ external (non-equilibrium) fluid during core growth is required.

Fluid infiltration calculations as a result of this modelling have yielded a minimum time-integrated fluid flux of the order of 0.17 cm^3/cm^2 to explain these isotope shifts. This flux is four to five orders of magnitude less than other New England flux estimations, although different methods were used. One study, grounded in phase equilibria, used the difference between the CO_2-rich volatiles produced by dehydration reactions and the recorded equilibrium H_2O-rich fluids present during metamorphism to calculate time-integrated fluxes from southern Vermont of 10^4 - 10^5 cm^3/cm^2. Alternatively, oxygen isotope ratios measured in two populations of garnets from southern Vermont, one set close to the fluid source and one further away, used advection-diffusion models to yield a flux of 1.4×10^4 cm^3/cm^2.

Evolution of the Hoosac Schist is therefore defined as two episodes of metamorphism, giving rise to two periods of prograde garnet growth. The first metamorphic episode was responsible for initial garnet growth, and was accompanied by the infiltration of low-$\delta^{18}O$ non-equilibrium fluids during the entire episode of garnet core growth. After at least one period of deformation, garnet rims grew during the second metamorphic episode.

Acknowledgements

A thesis is never an individual effort, and there are a number of people I have to thank for its creation. Firstly my supervisors, Dave Waters and Ed Young. Dave has always been on hand to show incredible patience, and to help steer me through the mysteries of metamorphism and the vagaries of Thermocalc. His faith in the methods and processes were invaluable when I felt as though I were staggering through treacle. Ed Young ushered me into the world of laser microanalysis and fluid flow. He was always standing by with ideas (sometimes too many!), and also showed confidence in the analytical methods during times of adversity. I would also like to thank David Bell for being my department 'friend' when I needed one, and John Dewey for his boundless enthusiasm. Whilst in Massachusetts Jack Cheney is thanked for his insight into New England geology, and for his initial suggestion of the Hoosac as a study area.

The technicians at Earth Sciences are often the backbone of research. I am indebted to Norman Charnley for his magical ability to coax the old microprobe into life, and for help with the SEM, and for jollies to Yarnton. Steve Wyatt faithfully refilled and refilled endless LN_2 pots for me. Thanks to Phil Jackson and Jeremy Hyde for rock cutting, and to their ability to produce a mirror-like sheen from a Palaeozoic garnet. Richard McAvoy and Steve Baker are thanked for their imaging prowess, and thanks to both Steve Usher and May Chung for aid with computers, and Roy Goodwin.

I must thank all those, both in Earth Sciences, Worcester College, and beyond without whom my time back in Oxford would be undeniably poorer. Alison - pasta la vista baby! Dan for the gin moments, and, with Chris, the chance to lampoon the department through SEF! Those at Earth Sciences: Emily and Dave for spontaneous martinis; James - keep off the Dave's Insanity Sauce! Nick, Ana, Fiona, Rob. All the undergrads I vainly

tried to teach mapping in the rain! The Worcester crowd - Medwyn, Ian and Lavonne. Rob McD - thanks for the swisher sweets (finest cheroots for under a dollar) and the West Point tailgate experience. And those other friends - Dan (cheers for France!), David, Rachel, Steve, and Duncan.

NERC studentship GT4/96/228/E is gratefully acknowledged as is additional support from Worcester College, the Burdett-Coutts fund, and the University of Oxford.

Finally I must thank my long-suffering family who have been waiting patiently for me to get a 'proper job'. Dad and Mum - your support has been invaluable.

Abbreviations used in this thesis

Mineral abbreviations, after Kretz (1973) and Holland & Powell (1998)

Grt	garnet	Cld	chloritoid
Chl	chlorite	Ms	muscovite
Pg	paragonite	Mrg	margarite
Bt	biotite	St	staurolite
Ky	kyanite	Sil	sillimanite
Pl	plagioclase	Qtz	quartz
Rt	rutile	Ilm	ilmenite

Isotope abbreviations

‰	per mil	SMOW	Standard Mean Ocean Water
δ^{18}O	delta ^{18}O	Δ	big delta
^{18}O	oxygen 18	α_{x-y}	fractionation factor
D	diffusion coefficient	z	ionic porosity

Major thermodynamic variables

T	temperature	P	pressure
G	Gibbs free energy	$\overline{G}$	molar Gibbs free energy
V	volume	$\overline{V}$	molar volume
H	enthalpy	$\overline{H}$	molar enthalpy
S	entropy	$\overline{S}$	molar entropy
R	gas constant	C_p	heat capacity at constant pressure
X_j	mole fraction of component j	η_i	moles of component i
M^k	moles of phase k in the system	μ_j	chemical potential of component j
a_j	activity of component j	γ_j	activity coefficient for component j
f_j	fugacity of component j	Γ_j	fugacity coefficient for component j
ν_i	stoichiometric coefficient of component or phase i	K_{eq}	equilibrium constant
K_D	distribution coefficient	ξ	reaction progress

Contents

Short Abstract i

Extended Abstract ii

Acknowledgements vi

Abbreviations viii

Contents ix

1 Scope and Focus 1

1.1 Introduction 1

1.2 Ascribing parageneses to orogeneses 2

1.2.1 Garnets - the rock's natural recorder 5

1.2.2 The role of oxygen isotopes 6

1.2.3 The impetus behind the Oxford oxygen isotope microprobe 10

1.2.4 The application - high alumina pelites from Western Massachusetts 11

1.2.5 Modelling in NCMnKFMASH 11

1.3 Summarising the aims of the study 13

1.4 Fundamental isotope concepts 14

1.4.1 Terrestrial mass-fractionation 14

1.5 Stable isotope fractionation during metamorphism 15

1.5.1 Exchange reactions 16

1.5.2 Calculation of isotope fractionations and the increment method . . 17

1.6 Diffusion effects on the isotope profile 19

1.6.1 Diffusion calculations 21

1.7 Outline of this thesis 23

2 UV laser line - rationale and construction **25**

2.1 Oxygen isotope analysis 25

2.2 A brief history of oxygen isotope analysis 26

2.2.1 From nickel bomb to copper laser 26

2.2.2 Ablation with an UV laser 31

2.2.3 Isotope ratio monitoring mass spectrometry 33

2.3 The Oxford UV laser isotope line 35

2.3.1 The Ultra Violet source 36

2.3.2 The CO_2 laser source 38

2.3.3 The chamber and isotope line 39

2.3.4 Reactions within the chamber 39

2.3.5 The GC-irms system 41

2.3.6 The mass spectrometer and output 42

2.3.7 Analysis by microvolume and bellows 45

3 Development of the isotope line **46**

3.1 Introduction 46

3.2 Routine sample analytical technique 47

3.3 The Blank 49

3.4 Sample preparation 52

3.5 Standards 53

3.5.1 Gas standards and the link to SMOW 53

3.5.2 Mineral standards 54

3.6 Development 55

3.7 Construction of the line, test gas runs and the CO_2 laser 56

3.8 Ultra-Violet laser and BrF_5 57

3.8.1 UV, BrF_5 and macro-analysis using the microvolume 57

3.9 BrF_5 and the switch to F_2 58

3.9.1 Fluorine gas 60

3.9.2 Initial GC-*irms* analysis with UV and F_2 61

3.9.3 Explanation for the BrF_5 size-dependence problem 62

3.10 Routine standard analysis - fine-tuning the method 63

3.10.1 The bellows effect 63

3.10.2 USNM Garnet - implications for sample size and freezing times . . 66

3.10.3 The silica gel heating problem - and final corrections 68

3.11 Analysis of the Hoosac Schist 68

3.11.1 First analysis - sample 6a 68

3.11.2 Sample 6x - what we learnt 70

3.11.3 Sample 19a - a problem of shift or drift? 71

3.12 Postscript from sample R76 73

3.13 Conclusions 73

4 High-Alumina Schists of the Hoosac Formation 75

4.1 Introduction to the Hoosac Schist 75

4.2 The Appalachian orogen 77

4.3 The Hoosac Formation - its provenance and structural relations 78

4.3.1 Taconian and Acadian orogenic events 80

4.4 The High-Alumina Schists of the Hoosac Formation 85

4.4.1 Metamorphic history of the Hoosac Schist 88

4.4.2 Evidence for multiple generations of metamorphism 90

4.5 Field relationships 91

4.5.1 Locality 1 - Rowe quadrangle; the base of the garnet zone 93

4.5.2 Locality 3 - Cold River stream cutting; lower garnet zone 93

4.5.3 Locality 6 - Peru; staurolite zone 94

4.5.4 Locality 15 - French Hill; mid staurolite zone 96

4.5.5 Locality 32 - Bancroft Railroad cutting; mid kyanite zone 96

4.5.6 Locality 9 - MA 20 road cutting; upper kyanite zone 99

4.6 Why is there a range in garnet size? 101

4.7 Conclusions 101

4.8 Samples and sample collection 103

5 Petrography and Metamorphism of the High Alumina Hoosac Schist 105

5.1 Petrology of the Hoosac Schist 105

5.1.1 Sample P21 106

5.1.2 Sample S66 111

5.1.3 Sample R94 112

5.1.4 Sample R96 112

5.1.5 Sample P86 115

5.1.6 Sample 6 116

5.1.7 Sample R76 122

5.1.8 Sample 19 126

5.1.9 Sample P97 131

5.2 Plagioclase replacement of paragonite 136

5.3 Garnet unconformities 136

5.3.1 Titanium-bearing inclusions in the garnets 138

5.4 Metamorphism - synthesis 138

5.5 Comparison with work on adjacent, similar units 140

6 Mineral chemistry and thermobarometry **142**

6.1 Analytical methods 142

6.1.1 JEOL 840 Scanning Electron Microscope 143

6.1.2 Cambridge Instruments Microscan 9 electron microprobe 144

6.1.3 JEOL superprobe 144

6.2 Mineral Chemistry 145

6.2.1 Garnet 145

6.2.2 White Micas 151

6.2.3 Biotite 155

6.2.4 Chloritoid 157

6.2.5 Chlorite 157

6.2.6 Plagioclase feldspar 160

6.2.7 Staurolite 160

6.2.8 Summary of mineral analyses 160

6.3 Thermobarometry 161

6.3.1 Thermobarometry - principles and rationale 161

6.3.2 THERMOCALC thermobarometry 163

6.3.3 The effects of water activity 163

6.3.4 Thermobarometry - discussion 165

7 Oxygen isotope results from the Hoosac Schist 168

7.1 Introduction 168

7.2 Analytical errors 168

7.2.1 Counting statistics and theoretical precision 169

7.2.2 Standard data 170

7.2.3 Accuracy versus Precision 171

7.3 Sample 6a 172

7.3.1 Sample 6a - results 173

7.4 Sample 19a 178

7.4.1 Sample 19a - discussion 181

7.5 Sample R76 185

7.5.1 Sample R76 - results 186

7.5.2 Sample R76 - discussion 188

7.6 Conclusions 191

8 Metamorphic modelling 192

8.1 Why rock modelling? 193

8.1.1 Some basic principles - the Gibbs phase rule and Duhem's Theorem 194

8.1.2 Integral versus differential thermodynamics 196

8.1.3 Self-consistent thermodynamic dataset 196

8.1.4 Phase diagram calculation using THERMOCALC 197

8.1.5 Aims of modelling 198

8.2 Bulk Rock data for pseudosection calculation 200

8.2.1 Projection from paragonite 200

8.2.2 XRF analysis 200

8.2.3 Summary of bulk rock calculation 201

8.3 KFMASH 205

8.4 MnKFMASH 207

8.5 NCMnKFMASH 209

8.5.1 Prediction of conditions of garnet core formation 212

8.5.2 Garnet rim conditions - comparison between predicted and observed 216

8.5.3 Summary of THERMOCALC modelling 227

8.6 PTGRID - modelling isotope fractionation with reaction progress 230

8.6.1 Differential thermodynamics 230

8.7 PTGRID - application of the theory 233

8.7.1 Modelling results 235

8.7.2 Closed system 236

8.7.3 Fluid infiltration modelling 243

8.7.4 Calculation of Hoosac fluid fluxes 247

8.7.5 Validity of PTGRID modelling 250

9 Synthesis **252**

9.1 The Hoosac Schist - a summary 252

9.1.1 Garnet growth models 253

9.2 Fluid infiltration 256

9.2.1 The Hoosac fluid flux results in context 257

9.3 Comparison of this study with other New England Models 258

9.4 Conclusions 262

9.5 Further work 262

9.6 Epilogue 263

Bibliography **264**

Appendices **276**

A: All Development Data **278**

B: Hoosac Sample Analysis **293**

C: Garnet Standard Data **310**

D: X-Ray Fluorescence data **315**

E: Microprobe data **317**



Lenox, Massachusetts

Feel I'm goin' back to Massachusetts,
Something's telling me I must go home.
And the lights all went out in Massachusetts
The day I left her standing on her own.

Tried to hitch a ride to San Francisco,
Gotta do the things I wanna do.
And the lights all went out in Massachusetts
They brought me back to see my way with you.

Talk about the life in Massachusetts,
Speak about the people I have seen,
And the lights all went out in Massachusetts
And Massachusetts is one place I have seen.

I will remember Massachusetts...

(Barry, Maurice and Robin Gibb, 1967)

Chapter 1

Scope and Focus

1.1 Introduction

Understanding both the chemical and tectonic evolution of the Earth's crust is a major goal of metamorphic petrology. Examination of the rock record is the foundation of any metamorphic study, and traditionally has focused upon regionally metamorphosed terranes, and the use of both mineral assemblages, zoned minerals and thermodynamic formulation to infer pressure-temperature-time paths (P-T-t, *e.g.* Spear & Selverstone, 1983). Petrology has also found itself as the basis for interpretation of fluid-rock interaction history, using reaction-progress variables to infer the extent and nature of reaction (*e.g.* Ferry, 1984).

This thesis describes an exploration of a new technique for the analysis of oxygen isotopes on the sub-micron scale in metamorphic rocks. Results have been yielded from a number of samples from Western Massachusetts, U.S.A.

In addition, new P-T data from Western Massachusetts corresponding to both initial conditions of garnet growth, and to peak garnet rim conditions are presented. Using this pressure-temperature-composition-modal (P-T-X-M) framework, a technique to reconstruct the effect and nature of external fluids during metamorphism based on measured isotope profiles suggests garnet core growth during the infiltration of low-δ^{18}O fluids.

1.2 Ascribing parageneses to orogeneses

Rocks from the high-alumina schists of the Hoosac Formation, Western Massachusetts, USA, show compelling textural evidence for multiple metamorphic events. Minerals from the earlier event define a complex folded schistosity, over which later minerals have overgrown.

The most striking features are the abundance of large garnets, which are characterized by inclusion-rich cores separated from inclusion-poor rims by a distinct concentric unconformity. The tectonic history of these rocks implies that the multiple generations of minerals in these rocks record *either* Ordovician Taconian-related metamorphism overprinted by Siluro-Devonian Acadian metamorphism, *or* successive metamorphic events during the Acadian orogeny.

These features are very similar to those found in both the Gassetts and Hoosac Schists of Southern Vermont (the Hoosac Schist of Western Massachusetts has been correlated with both). Within these schists, the interpretation of polymetamorphism and linking of mineral growth with documented orogenic events has been hampered by ambiguous textural evidence for mineral replacements (Karabinos, 1985).

Two hypotheses have been put forward to explain the unconformities found within the Vermont garnets, in particular the documented presence of a manganese peak at the unconformity itself (see figure 1.1).

Karabinos (1984, 1985), working in the Hoosac Formation of Southern Vermont, explained the observed break as a period of garnet consumption during a retrogressive exhumation event separating two prograde growth periods. Initial garnet growth occurred by the forward progress of the reaction:

$$\text{Chl} + \text{Cld} + \text{Qtz} \rightarrow \text{Grt} + \text{H}_2\text{O}$$

Then, during a period of cooling the garnet resorption occurred, with this reaction essentially operating in reverse. The very presence of zoning anomalies such as the Mn peak implied that the rate of retrograde reactions could not keep up with the changing metamorphic conditions and the rate of diffusion in garnet. After this retrogressive

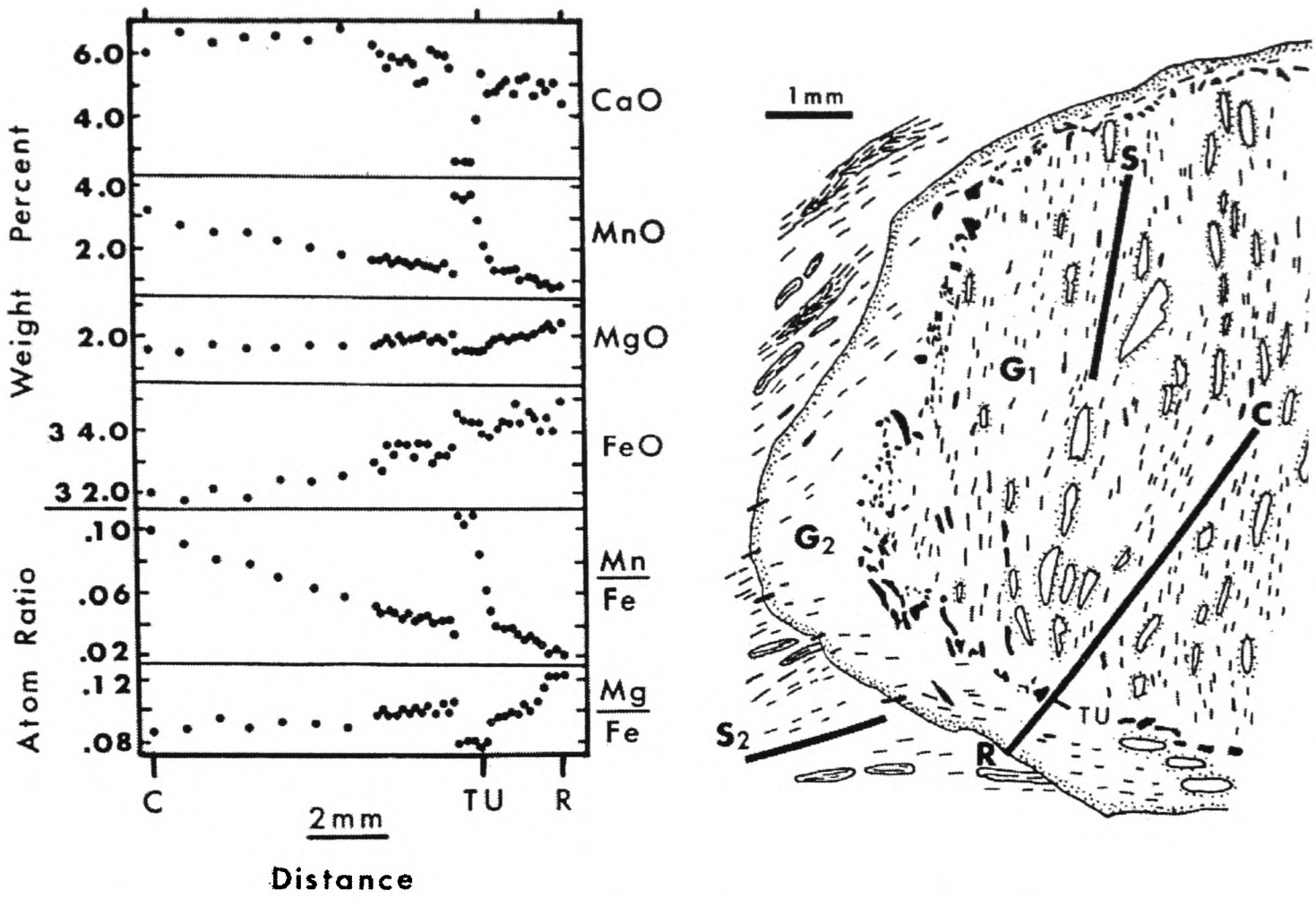


Figure 1.1: A sketch of a garnet from the Hoosac Formation, Southern Vermont (right) with core (C) - rim (R) garnet zoning profile (left). Early garnet growth (G1) is separated from later garnet growth (G2) by a textural unconformity (TU). The inner inclusion trail is assumed to represent the early schistosity S1, and the outer inclusion trail is conformable with the matrix crenulation cleavage S2. The opaque inclusions are ilmenite and magnetite, the elongate grains are white mica, chlorite and chloritoid. Taken from Karabinos (1984). The Mn spike at the textural unconformity is clearly seen.

period followed another period of garnet growth (representing the rim), this time accompanied by simultaneous staurolite growth at the expense of chloritoid and chlorite:

$$\text{Cld} + \text{Chl} + \text{Qtz} \rightarrow \text{Grt} + \text{St} + \text{H}_2\text{O}$$

In contrast, Thompson *et al.* (1977), working in the Gassetts Schist, proposed garnet core growth with staurolite by:

$$\text{Cld} + \text{Qtz} \rightarrow \text{St} + \text{Grt} + \text{H}_2\text{O}$$

Following complete consumption of chloritoid, staurolite and biotite grew at the ex-

pense of garnet and chlorite. This gave rise to the textural break and observed Mn anomalies as the result of a *prograde* reaction that consumed garnet:

$$Grt + Chl + Ms \rightarrow St + Bt$$

Garnet rims represent regrowth at the expense of staurolite, biotite and possibly chlorite.

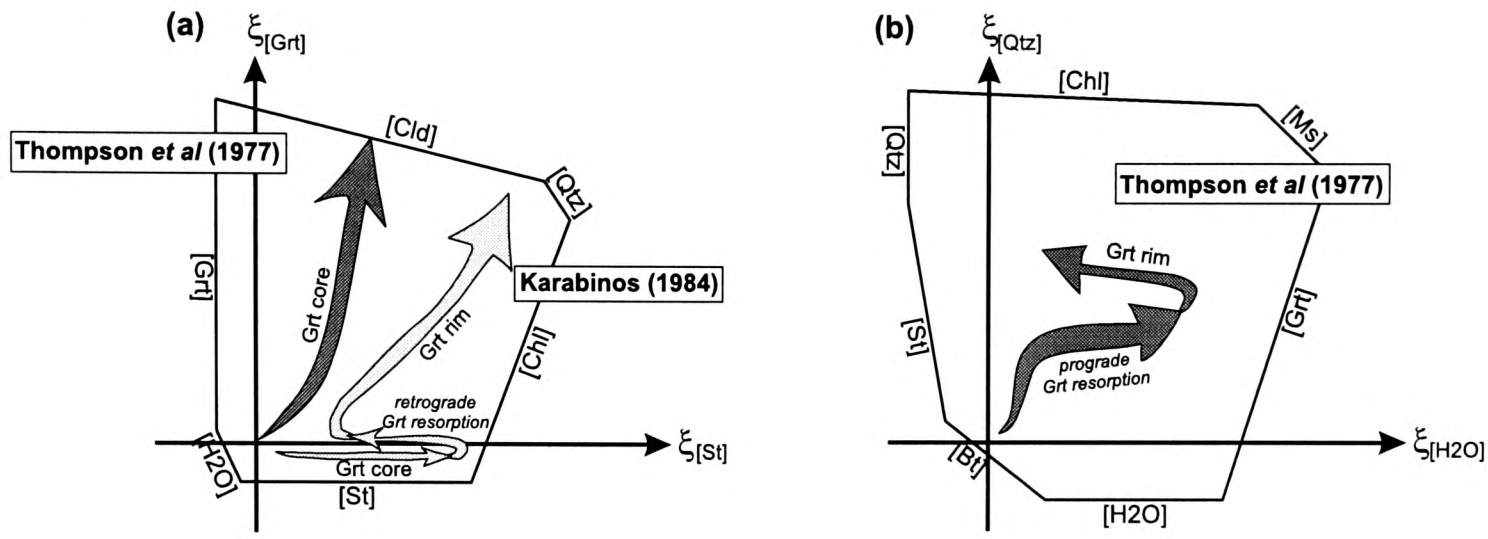


Figure 1.2: Schematic reaction polyhedra to illustrate the two hypotheses to explain the origin of garnet unconformities. Karabinos (1984) postulated an initial garnet growth phase in the absence of staurolite, followed by a period of retrogression, followed by prograde garnet growth with staurolite (a). Thompson *et al.* (1977) explained the unconformity as three separate prograde reactions, with the garnet core growing with staurolite (a), then a prograde garnet resorption event followed by garnet growth (seen in b). Reaction polyhedra are described fully in chapter 9; arrows represent progress of reactions towards phases being consumed and away from phases growing. The axes represent progress of phase-independent reactions.

The two models are summarized in figure 1.2; the essential difference between them is that in the Thompson *et al.* scenario, staurolite grew with the garnet *cores*, whereas in the Karabinos proposal staurolite grew with the garnet *rims*.

The schists studied by Karabinos (1984) are of lower grade than those described by Thompson *et al.* (1977), and there is no reason to believe that their reaction histories are identical. However, there is a fundamental geological implication in that the model of Karabinos requires infiltration of externally-derived fluid to help drive the garnet resorption reaction, whereas the Thompson *et al.* model proposes that the unconformities represent a dehydration reaction.

Young & Rumble (1993) showed that both these suggestions could be tested by the use of oxygen isotopes. Oxygen isotopes are sensitive indicators of minerals in equilibrium, and as such can potentially distinguish between parageneses. A paragenesis is defined as the condition of a mineral assemblage growing together in chemical (and therefore theoretically isotopic) equilibrium. In the case of the Karabinos versus Thompson models, oxygen isotope measurements of garnet and staurolite should show that staurolite is either in isotopic equilibrium with the garnet core (the Thompson scenario) or the garnet rim (as proposed by Karabinos). In addition, the influx of externally-derived fluids to drive the garnet resorption reaction potentially brings non-equilibrium fluid into the system. The crucial assumption here is that garnets preserve oxygen isotope zoning, just as they preserve major and trace element zoning.

1.2.1 Garnets - the rock's natural recorder

Garnets have traditionally been treated as a time-integrated record of the metamorphic evolution of a rock. They are robust minerals that grow and persist throughout much of the prograde history of a pelite. They can withstand high pressures without failing. Additionally, the inter-crystalline diffusivities of most cations, and of oxygen, is negligible at low and medium grades - therefore observed core-rim concentric zonation profiles can usually be assumed to be largely growth-related and relatively unmodified by later diffusion processes (*e.g.* Yardley, 1977). Indeed, the very existence of original growth zonation in garnets implies that the mineral has preserved a record of earlier metamorphic conditions.

Garnet zoning in major element, trace element (Spear & Kohn, 1996) and radiogenic isotope (Christensen *et al.*, 1989) has been recorded. Major cation zoning, which is sensitive to changes in P and T, is routinely used to infer pressure-temperature paths (*e.g.* Tracy *et al.*, 1976; Spear & Selverstone, 1983; Vance & Holland, 1993).

Such is the potential for garnets above all minerals to have recorded a major period of the metamorphic history of a rock, especially if that rock has undergone multiple orogenic and metamorphic cycles, that they have been the focus of study for workers attempting to link orogeneses and parageneses together - *i.e.* deducing which tectonic

event provided the driving force for which metamorphic event.

Geochronologic studies of elemental zoning in garnets have revealed both the timescales of garnet growth and their subsequent application to understanding tectonometamorphic processes. Christensen *et al.* (1989) used $^{87}Sr/^{86}Sr$ dating of Acadian garnets from Vermont to show that growth timescales of the order of some 10 Ma were recorded. Investigations into dating garnets and other minerals using Rb-Sr, U-Pb, Lu-Hf and Sm-Nd systematics have proved partially successful (Christensen *et al.*, 1989; Vance & O'Nions, 1990, 1992; Duchêne *et al.*, 1997). However, the problem with the dating approach includes the combined technological challenges of spatial resolution and age resolution: being able to measure on an appropriate length scale to resolve core-rim differences, and being able to analyse ages with sufficient accuracy to allow characterization of differing ages outside analytical error.

1.2.2 The role of oxygen isotopes

Oxygen comprises one half of the Earth's crust by mass, therefore processes that transfer matter from one phase to another during crustal evolution (such as a mass transfer reaction) must generally involve the transfer of oxygen. Measurement of oxygen isotopes thus potentially provides a powerful tool for deciphering reaction history, and hence they have been used to infer mechanisms of oxygen exchange amongst minerals and fluids during metamorphism (*e.g.* Rumble & Spear, 1983), and are highly effective tracers for monitoring fluid flow (*e.g.* Valley *et al.*, 1994).

Exchange of oxygen isotopes encrypts a sensitive record of the reaction history of metamorphic rocks. Understanding this record requires measurement of isotopic ratios at an appropriate scale together with the understanding of the mechanisms of material transfer involved: diffusion, recrystallization, mineral growth and fluid flow.

In summary, oxygen isotopes offer an elegant and efficient way to distinguish minerals in equilibrium.

Oxygen isotope analysis of garnets

In the light of recent advances in analytical techniques, notably both the use of laser heating to analyse refractory minerals such as garnet, and the ability to analyse at an increasingly fine spatial resolution, studies in the last ten years have shown the existence of oxygen isotope zonation within garnet porphyroblasts from regionally metamorphosed rocks (Chamberlain & Conrad, 1991, 1993; Young & Rumble, 1993; Kohn *et al.*, 1993).

Previous uncertainties as to whether measured heterogeneities in $^{18}O/^{16}O$ within minerals are the result of metamorphism have been removed with the application of these new techniques (Chamberlain & Conrad, 1991), and it is this unequivocal link between the progress of metamorphism and associated oxygen isotope fractionation that gives us a tool for deciphering metamorphic history, which is preserved as $\delta^{18}O$ zoning within garnet. Changes in $\delta^{18}O$ are sensitive to changes in temperature, reaction history and to fluid-rock interaction.

Three models have been described to explain stable isotope zoning in garnets. In addition to the paragenetic history, the differences between these models also have major implications for either the absence or presence of fluid - and in the latter scenario a profound disparity in timing of a fluid event. Calculated fluid fluxes vary over several orders of magnitude between the models, with implications for fluid infiltration upon crustal scale regional metamorphism.

Kohn *et al.* (1993) studied zoning in garnets from pelite and amphibolite samples and found small, systematic variations in $\delta^{18}O$ from core to rim in the pelitic garnets (as shown in figure 1.3), which was attributed to prograde garnet growth under closed-system conditions.

The requirement for matter conservation (as implied by closed system conditions) necessitates that as phase modal proportions change during the progress of net-transfer reactions along with changing P-T conditions during metamorphism, then the isotopic value of minerals will sympathetically alter (see Rumble, 1982, and later). Thus the change in $\delta^{18}O$ as the garnet grows merely reflects the changing nature of the rock as

a whole (a time-integrated record) - and the need to maintain closed-system isotopic equilibrium (*e.g.* Garlick & Epstein, 1967).

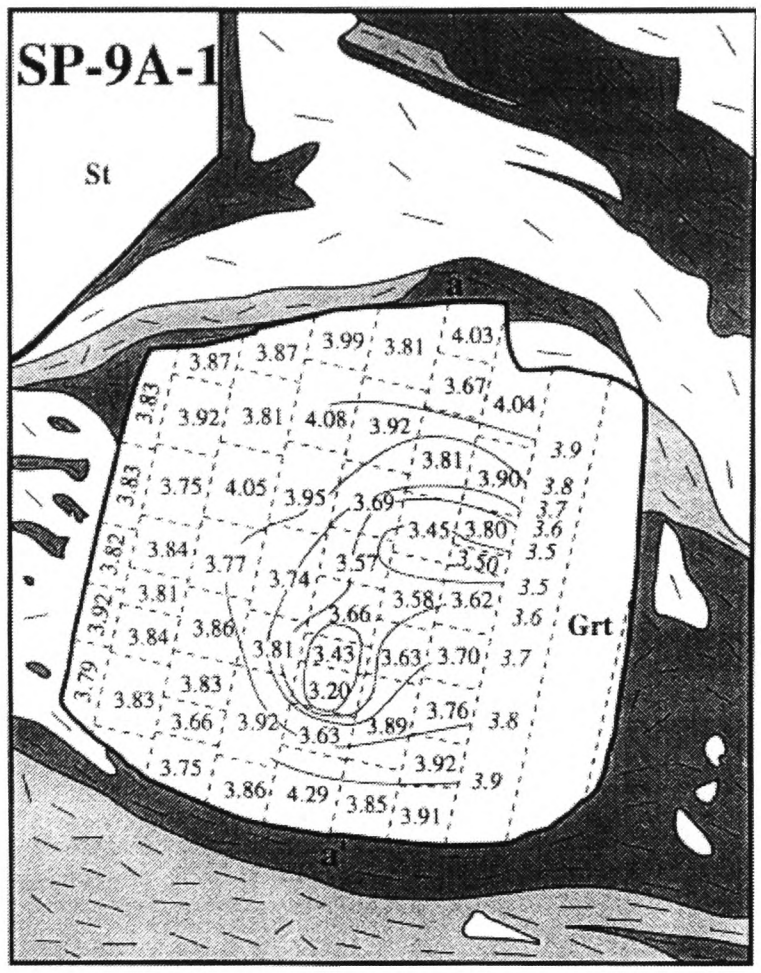


Figure 1.3: $\delta^{18}O$ zoning in a pelitic garnet as reported by Kohn *et al.* (1993). This study used the 'thin sawblade' technique where a garnet was sawn into millimetre-sized chips, and these analysed as mineral separates by IR heating.

Chamberlain & Conrad (1993) found concentric ^{18}O enrichment from core to rim in garnets from the Pinney Hollow Formation, Vermont, with a gradient of up to 3‰. This zoning was attributed to the infiltration of external fluids during the latter stages of garnet growth, in other words the zoning can be seen as a time-integrated record of fluid infiltration, and a calculation of the duration of flow could be easily yielded from an estimate for the time of rim growth that had equilibrated with the infiltrating fluid.

In contrast, Young & Rumble (1993)(figure 1.4) reported both *in-situ* and mineral chip IR analysis from the Gassetts Schist. $\delta^{18}O$ analysis of both garnet core and rim (either

side of the textural unconformity) showed a core value of 10.9‰ and a rim of 10.1‰ . They suggested that this concentric $\delta^{18}O$ zoning resulted from a two-stage process after initial garnet growth. Firstly an episode of garnet resorption to chlorite during which low-$\delta^{18}O$ fluid infiltration occurred. The chlorite thus produced acted as a reservoir for the fluid isotopic signature. Subsequently this resorption event was reversed, producing a garnet rim with the fluid isotopic signature. This was used as a test for determining which of the Karabinos (1984) and Thompson *et al.* (1977) models was more accurate.

The study of Young & Rumble, which included analysis of surrounding staurolite and quartz, suggested that oxygen isotope measurements of metamorphic minerals could potentially correlate which minerals grew together in equilibrium. Their study recognized the importance of examining whether punctuated fluid infiltration episodes were instrumental in the evolution of the Gassetts Schist.

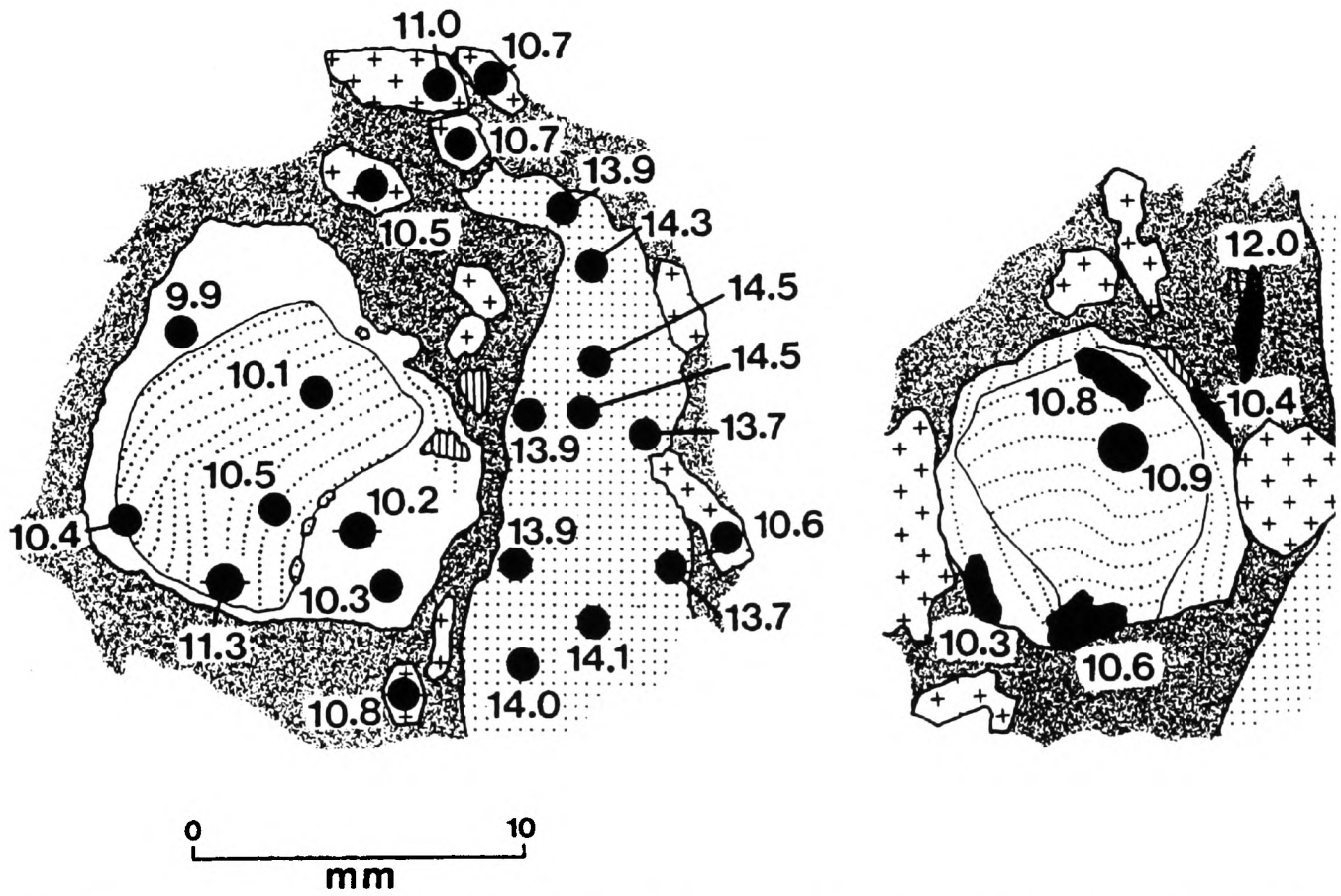


Figure 1.4: $\delta^{18}O$ analysis reported by Young & Rumble (1993). On the left are *in-situ* analysis; on the right localities of plucked mineral chips, both from a specimen of the Gassetts Schist. White = Grt, crosses = St, stippling = Qtz.

1.2.3 The impetus behind the Oxford oxygen isotope microprobe

In the light of these investigations it became apparent that further research demanded more accurate analysis on the sub-millimetre scale. With the development of UV laser ablation coupled with helium gas flow technology and GC-*irms* lay the potential for the development of a new facility offering true *in-situ* analysis on the 100μm scale.

Previous *in-situ* laser isotope analysis has been achieved with the use of an Infra-Red heating source. This approach yielded excellent precision ($\pm$ 0.1‰ Sharp, 1990, and others); however, spatial resolution was restricted due to edge effects arising from *in-situ* IR heating, manifesting in a partial melting halo around the laser pit, isotopic fractionation, and a minimum pit size of the order of 1mm to render these fractionation effects negligible. Ultra-violet ablation does not suffer from this edge-effect problem.

A different approach is secondary ionization mass spectrometry (SIMS), as used by the ion microprobe. This has very high spatial resolution, with a spot size of the order of 2-30μm . However, routine precision is of the order of $\pm$0.8 - 1‰ (Valley & Graham, 1991, 1996).

A fundamental goal of the development of the Oxford UV laser microprobe was to produce an analytical facility that can ablate sub-mm pits *in-situ* . Spatial resolution is limited by the instrument's ability to handle the analyte oxygen in a non-fractionating manner. The use of helium carrier-flow technology allows the transfer of the nanomoles of oxygen gas liberated from ablation of a 100μm scale pit, whilst maintaining isotopic fidelity. In addition, analytical precision is designed to be similar to a conventional infra-red heating technique, $\pm$0.2 - 0.4 ‰ .

Therefore, a new analytical facility at Oxford was instigated and developed, with the aim of producing an instrument that has the capability to:

- analyse oxygen isotopes with a high spatial resolution, on the 100μm scale *coupled with*
- analysis at a high precision - to have the ability to resolve the small $\delta^{18}O$ shifts associated with metamorphic reactions, *i.e.* sub 0.5‰

1.2.4 The application - high alumina pelites from Western Massachusetts

The suite of rocks selected for this study are high-alumina metapelites from the Hoosac Formation of Western Massachusetts. These pelites are ideal rocks for this type of investigation as they contain abundant garnets which have often grown over a large part of the P-T history of the rock; pelites also contain mineral assemblages with a range of diffusivities. The Hoosac Schists are partly correlated with the well-documented Gassetts Schist (*e.g.* Thompson *et al.*, 1977), and display a range in grade along strike; this gives the opportunity to investigate mechanisms of mass transfer operating under differing metamorphic conditions.

The Hoosac Formation is a Cambro-Ordovician nested thrust slice lying on the Eastern limb of the Berkshire Massif. It is exposed as a near-continuous belt, potentially exhibiting a near-continuous prograde metamorphic history (Cheney & Brady, 1992). It overlies Grenvillian basement, being sited within the zone of maximum overlap having been potentially affected by *both* Taconian and Acadian orogenic events.

The high-alumina schist is characterized by numerous sizeable garnet porphyroblasts (up to 2cm in diameter) in a quartz and micaceous matrix. These large garnets show a complex metamorphic history, having a distinct chemical and textural unconformity separating inclusion-rich cores from inclusion-poor rims. This is strong evidence for multiple phases of metamorphism.

This type of textural unconformity is similar to that reported by Karabinos (1984) and Thompson *et al.* (1977), and investigated by Young & Rumble (1993), who correlated it with an oxygen isotope unconformity. Vance & Holland (1993) also reported a similar change in cation ratios in their detailed study of two garnets from the Gassetts Schist, Vermont - but they concluded that these abrupt changes marked isograds within the prograde history of the garnet.

1.2.5 Modelling in NCMnKFMASH

The aims of metamorphic modelling are to reconstruct the pre-peak pressure-temperature-composition-modal (P-T-X-M) conditions of metamorphism. Modelling in the system

KFMASH (K_2O-FeO-MgO-Al_2O_3-SiO_2-H_2O) has proved a successful approach to reconstructing phase equilibria since introduced by Thompson (1957). However this system does have limitations: MnO and CaO are very important components in extending the stability of garnets to higher and lower P and T, and CaO and Na_2O are vital for modelling both paragonite and margarite white micas as well as plagioclase; excluding these components restricts modelling ability. Thus inclusion of these species is desirable in order to model as accurately as possible.

Recent advances in metamorphic modelling and thermodynamic dataset construction have given rise to the possibility of constructing equilibrium P-T projections for pelitic rocks including the full range of important chemical species (Spear & Cheney, 1989; Vance & Mahar, 1998; Walker, 1999).

In this thesis the complex pelite system Na_2O-CaO-MnO-K_2O-FeO-MgO-Al_2O_3-SiO_2-H_2O (NCMnKFMASH) is modelled. If bulk composition constraints are applied, *pseudosections* can be calculated for individual samples. These are usually P-T projections which graphically predict the equilibria that a particular bulk composition can 'see'. This procedure has been applied to the Hoosac Schist to define the initial and final P-T-X-M conditions of garnet growth in NCMnKFMASH.

The use of differential modelling, such as the Gibbs' method (Spear *et al.*, 1982; Spear, 1988) allows for evolution of thermodynamic variables and thus can track the progress of an evolving system when phases are growing or being consumed. Thermodynamic formalism has been developed to include oxygen isotope fractionations as a function of reaction progress (Young, 1993). This approach thus allows calculation of garnet isotope zoning, and includes the ability to model garnet growth in the presence of an externally infiltrating, non-equilibrium fluid.

1.3 Summarising the aims of the study

The aim of this thesis is to explore a new analytical method for the *in-situ* analysis of oxygen isotope ratios within metamorphic minerals. This technique is applied to high alumina schist samples from the Hoosac Formation, Western Massachusetts. These schists contain large garnets with concentric textural unconformities. Young & Rumble (1993) reported coincident oxygen isotope shifts with similar unconformity garnets from the Gassetts schist, Vermont. Analysis of core-rim oxygen isotope zonation has been performed on three Hoosac garnet samples.

Reconstruction of garnet growth P-T-X-M conditions is then effected using the equilibrium phase diagram modelling approach, this allows calculation of conditions of garnet core growth. Application of a differential thermodynamic approach for the prediction of oxygen isotope fractionation with progress of metamorphism is employed. The results from this are compared with observed isotope profiles in order to quantify the effect of fluid infiltration during metamorphism.

Therefore some of the questions to be addressed in this study are:

- can an analytical facility be developed to provide routine, accurate and reproducible *in-situ* analysis from garnets and other metamorphic minerals on the 100μm scale?
- can garnet profiles then be measured in the Hoosac garnets?
- do these profiles show a shift between the core and the rim?
- can these profiles be modelled, and what do they tell us about the role of fluids in the Hoosac rocks?

1.4 Fundamental isotope concepts

Oxygen isotopes ^{16}O,^{17}O and ^{18}O are all stable isotopes, *i.e.* they are unaffected by radioactive decay, and thus maintain a constant ratio $^{18}O/^{16}O$ (or $^{17}O/^{16}O$) unless affected by some process such as reaction (promoting isotope exchange), or diffusion.

The ratio $^{18}O/^{16}O$ is expressed in the delta notation, $\delta^{18}O_{SMOW}$, as defined by the ratio of the sample to a standard, and expressed in terms of per mil (‰), as summarised by the equation:

$$\delta^{18}O = \left(\frac{R_{\text{sample}}}{R_{\text{standard}}} - 1 \right) \times 10^3 \tag{1.1}$$

where R is the ratio of $^{18}O/^{16}O$. The standard used for oxygen isotope quotations is Standard Mean Ocean Water (SMOW), which has a $^{18}O/^{16}O$ ratio of $2.0052e^{-3}$.

The big delta notation (Δ_{x-y}) is used to describe the isotopic fractionation between two phases, and is also measured in ‰ :

$$\Delta_{x-y} = \delta^{18}O_x - \delta^{18}O_y \tag{1.2}$$

1.4.1 Terrestrial mass-fractionation

If measured $\delta^{18}O$ is plotted against $\delta^{17}O$, it is found that all terrestrial materials will lie upon a curve, termed the terrestrial mass fractionation curve (Santrock *et al.*, 1985), shown in figure 1.5. This can be defined as:

$$\ln\left(\frac{^{17}O}{^{16}O}\right)_{SMOW} = \alpha \cdot \ln\left(\frac{^{18}O}{^{16}O}\right)_{SMOW} + \ln K \tag{1.3}$$

where α = 0.516, and K = 0.04103 α × (1 - 0.011387). All known substances on Earth lie upon this terrestrial mass fractionation curve, and deviation from this is generally only observed in cosmogenic scenarios.

For the normal range of terrestrial isotope values encountered (*e.g.* $\delta^{18}O$ of -20 to +20 ‰), this terrestrial fractionation curve can be approximated to a straight line, summarized in equation 1.4:

$$\delta^{17}O_{\text{calculated}} = 0.516 \times \delta^{18}O_{\text{measured}} \tag{1.4}$$

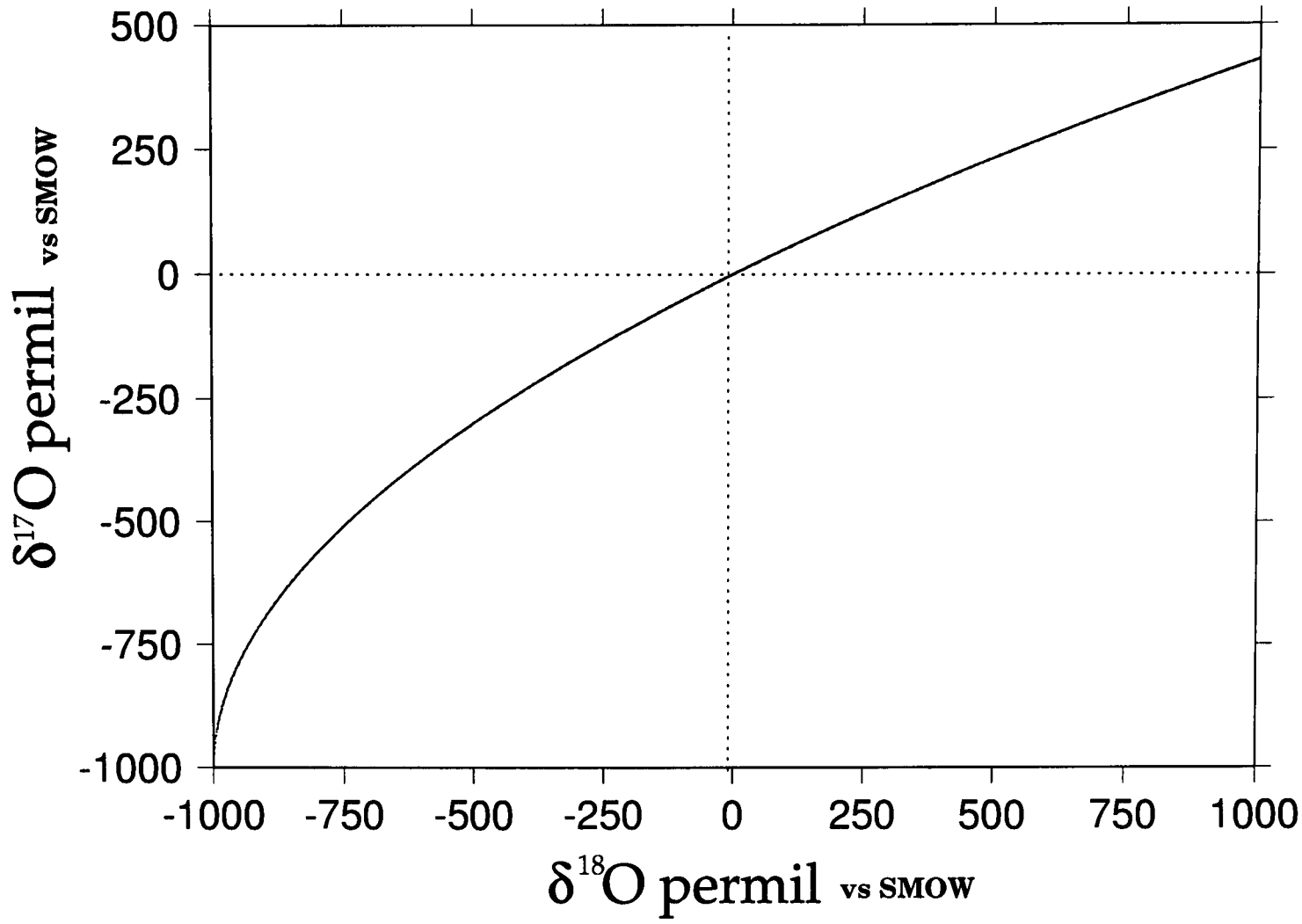


Figure 1.5: Terrestrial mass fractionation curve, as calculated from Santrock *et al.* (1985).

1.5 Stable isotope fractionation during metamorphism

There are two major effects that cause isotopic fractionation: kinetic and equilibrium. Kinetic isotope effects are associated with fast, incomplete, or unidirectional processes such as diffusion. Their effect relies upon the difference in mass between the isotopes, such that velocity differences arising from the kinetic energy equation ($KE = \frac{1}{2}Mv^2$) lead to isotopic fractionation whereby isotopically light species (^{16}O) diffuse out preferentially (O'Neil, 1986).

Equilibrium isotope effects are considered in terms of the effect of atomic mass on bond energy; substitution of a heavy isotope for a light isotope increases the binding energy, making the bond more stable. However, it must be pointed out that the free energy differences associated with isotope effects are three orders of magnitude less than typical bond energies or heats of chemical reactions. Such a low energy difference is not a driving force for chemical reactions, however it is considered reasonable that isotopic

exchange equilibrium should be obtained during reactions that achieve chemical equilibrium.

Considering a closed system, with the condition of chemical and isotopic equilibrium, it is possible to predict the $\delta^{18}O$ fractionation between two co-existing minerals growing together.

1.5.1 Exchange reactions

Exchange reactions govern the equilibrium partitioning of stable isotopes between two phases. A sample reaction between quartz and water is shown in equation 1.5, which details the exchange between ^{18}O and ^{16}O.

$$\frac{1}{2}Si^{18}O_2 + H_2^{16}O = \frac{1}{2}Si^{16}O_2 + H_2^{18}O \tag{1.5}$$

The equilibrium constant, K for this oxygen isotope exchange reaction is:

$$K = \frac{(X^2_{^{16}O,Qtz})^{1/2}(X_{^{18}O,water})}{(X^2_{^{18}O,Qtz})^{1/2}(X_{^{16}O,water})} \tag{1.6}$$

$X_{i,j}$ is the atomic fraction of ^{18}O or ^{16}O in the oxygen site of quartz or water, and the exponents of $(X^x_{i,j})^y$ are the multiplicities of the oxygen sites in the mineral formulas (x), and the stoichiometric coefficient (y). X is defined as:

$$X_{16,Qtz} = \left(\frac{^{16}O}{^{18}O + ^{16}O}\right)_{Qtz} \tag{1.7}$$

and similarly for water:

$$X_{16,water} = \left(\frac{^{16}O}{^{18}O + ^{16}O}\right)_{water} \tag{1.8}$$

Thus by substitution, one obtains:

$$K = \alpha = \frac{(^{18}O/^{16}O)_{water}}{(^{18}O/^{16}O)_{Qtz}} \tag{1.9}$$

Hence we can say during an exchange reaction, the partitioning of the isotopes between either mineral pairs or a mineral and a fluid species is described by the α notation:

$$\alpha_{x-y} = \frac{(^{18}O/^{16}O)_x}{(^{18}O/^{16}O)_y} \tag{1.10}$$

or, written in delta notation:

$$\alpha_{x-y} = \frac{1 + \delta_x/1000}{1 + \delta_y/1000} \tag{1.11}$$

Here x and y refer to a given mineral pair or fluid species. In order to obtain a useful approximation, the natural logarithm of both sides of equation 1.11 gives:

$$\ln\alpha = \ln(1 + \delta_x/1000) - \ln(1 + \delta_y/1000) \tag{1.12}$$

Since $\delta/1000$ is always less than 1.0, we can reduce this to the approximation:

$$\ln(1 + \delta_x/1000) \simeq \delta_x/1000 \tag{1.13}$$

and thus by substitution, obtain:

$$\Delta_{x-y} \equiv \delta_x - \delta_y \simeq 1000\ln\alpha_{x-y} \tag{1.14}$$

The accuracy of this approximation decreases as both the values of δ_x and δ_y increase above 10 (Friedman & O'Neil, 1977).

1.5.2 Calculation of isotope fractionations and the increment method

Since isotope fractionation between two phases, either mineral-mineral or mineral-water, is strongly temperature dependent, the equilibrium fractionation can be described as:

$$1000\ln\alpha_{Qtz-mineral} = A\frac{10^6}{T^2} + B\frac{10^3}{T} + C \tag{1.15}$$

Parameters A, B and C can be obtained either through theoretical calculation or through experimental observations. Richter & Hoernes (1988) used the *increment method* to yield an approximate oxygen isotope fractionation curve for all silicate minerals, in their attempt to standardize oxygen isotope thermometry curves. Zheng (Zheng, 1993a,b, 1999) attempted to improve upon the Richter & Hoernes increment method by use of the modified increment method. Although the Richter & Hoernes calculations are widely used, they do not include chloritoid, and so for this reason the Zheng parameters are used in this thesis. Results for parameters A, B and C are given in table 1.1. Equilibrium isotope fractionation factors between two minerals can thus be predicted at a given temperature using equation 1.15, where T is the temperature in Kelvin.

Experimental studies over a range of 1-20 kbar show no measurable dependence of α on pressure, P (Clayton *et al.*, 1975), and thus α can be considered independent of pressure. In fact, the negligible effect that isotopic substitution has upon the molar volume of a phase would suggest this.

Mineral	formula	*A*	*B*	*C*
chloritoid	$(Fe,Mg)_2Al_4Si_2O_{10}(OH)_4$	0.49	3.35	-1.40
biotite	$K_2Mg_{1.2-3.6}Fe_{4.8-2.4}Si_6Al_2(OH)_{20}$	0.64	3.99	-1.67
almandine	$Fe_3Al_2(SiO_4)_3$	0.72	4.26	-1.79
clinochlore	$Mg_{12}Si_8O_{20}(OH)_{16}$	0.51	3.43	-1.43
staurolite	$Fe_4^{2+}Al_{18}Si_8O_{46}(OH)_2$	0.39	2.90	-1.21
muscovite	$K_2Al_4Si_6Al_2(OH)_4O_{20}$	0.38	2.84	-1.18
paragonite	$Na_2Al_4Si_6Al_2(OH)_4O_{20}$	0.37	2.77	-1.15
margarite	$CaAl_4Si_6Al_2(OH)_4O_{20}$	0.38	2.84	-1.18
kyanite	Al_2SiO_5	0.32	2.52	-1.05
sillimanite	Al_2SiO_5	0.22	1.89	-0.78
albite	$NaAlSi_3O_8$	0.15	1.39	-0.57
orthoclase	$KAlSi_3O_8$	0.16	1.50	-0.62
water	H_2O	4.48	-4.77	1.71
quartz	SiO_2	0.00	0.00	0.00

Table 1.1: Isotope fractionation parameters for $10^3 \ln\alpha_{Qtz-mineral}$ (derived from Zheng, 1993a,b).

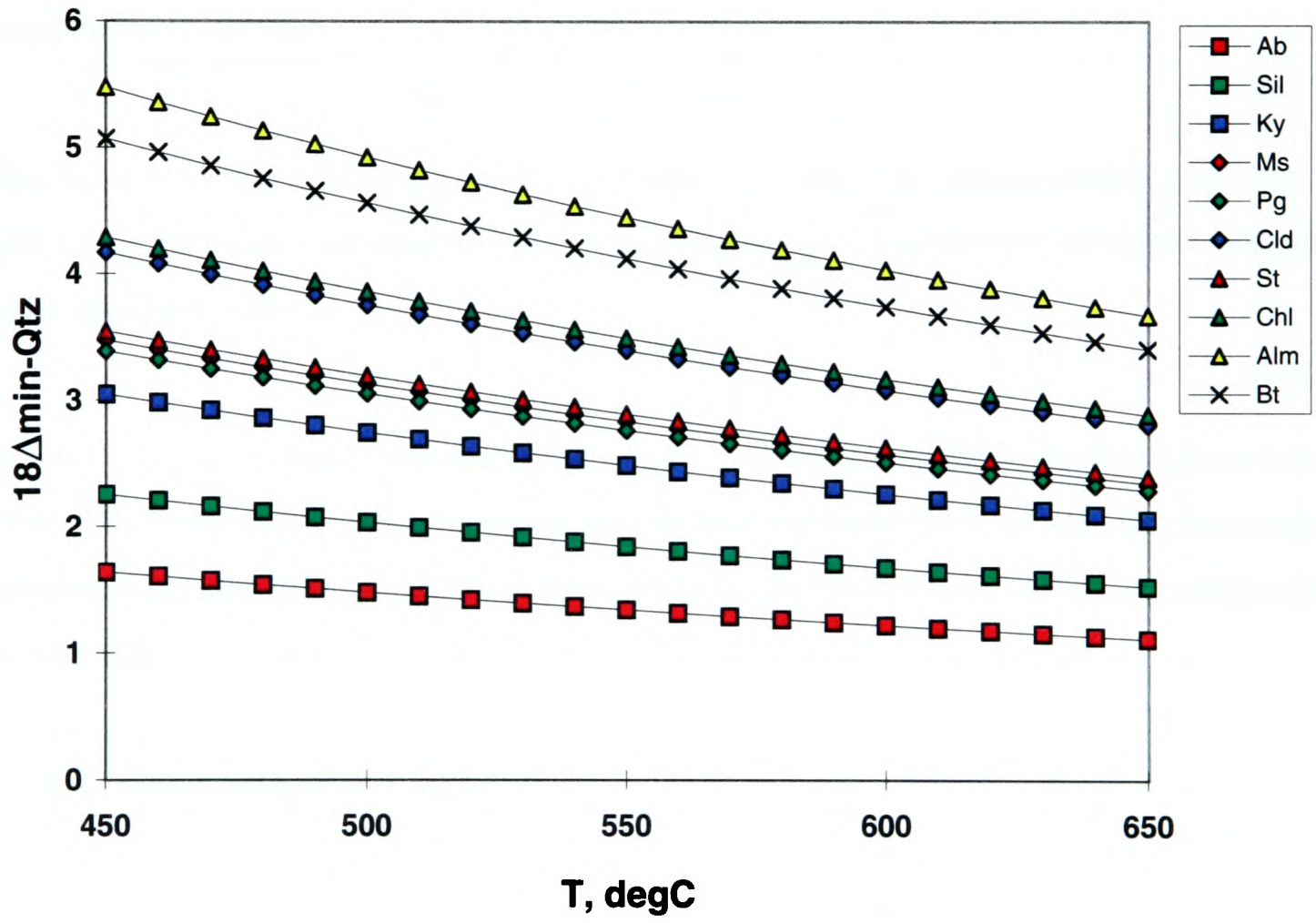


Figure 1.6: Calculated fractionation curves for quartz-mineral (per mil) using the increment method as described by Zheng (1993a,b).

1.6 Diffusion effects on the isotope profile

The descriptive property of a mineral in terms of volume self-diffusion is its chemical diffusivity, or diffusion coefficient (D, length^2/time), a temperature- and elemental- dependent variable. The characteristic time-length scale may be described by:

$$t = \frac{h^2}{D} \tag{1.16}$$

where t is the characteristic time and h is the length scale for diffusion.

Fortier & Giletti (1989) produced an empirical model for predicting the diffusion coefficient in silicates. This was based upon the calculated ionic porosity of the mineral structure, and assumed that the diffusion mechanism is identical for all the minerals considered. Using equation 1.17 they showed that, given the values $\alpha = -2$; $\beta = -3.4 \times 10^4 T$; $\gamma = -0.13$ and $\delta = 6.4 \times 10^2 T$, D for oxygen diffusion can be predicted at a specified temperature (Kelvin).

$$\log D = \alpha + \left(\frac{\beta}{T}\right) + z\left[\gamma + \left(\frac{\delta}{T}\right)\right] \tag{1.17}$$

The basis for the model relies upon a calculation for the total ionic porosity, z, at 24°C, and using this value irrespective of thermal expansion. Total ionic porosity is defined as in equation 1.18.

$$z = \left[1 - \frac{V_I}{V_C}\right] \times 100 \tag{1.18}$$

where V_C is the volume of the unit cell at 24°C, and is generally taken from Deer *et al.* (1992); V_I is the sum of the volumes of cations and anions in the unit cell. The ionic radii used in this calculation were taken from Shannon & Prewitt (1969), with the following conventions:

- O radius was set to 1.38 $\mathring{A}$
- all transition elements are assumed to be in the high spin state
- no changes in coordination nor ionic radii with temperature

Fortier & Giletti (1989) reported that micas proved to be the most difficult to model, due to their large interlayer spacings, and thus calculated ionic porosities for those interlayer spacings proved to be greater than bulk ionic porosities. Table 1.2 shows the calculated

ionic porosities for common minerals. The total ionic porosity for staurolite had to be calculated. Taking the unit cell to be $[R^{2+}]_2^4[R^{3+}]_9^6[Si]_4^4O_{24}H_4$, R^{3+} cations are taken as overwhelmingly Al; and R^{2+} dominated by Fe^{2+} (Deer *et al.*, 1992), z can be calculated as 26.7%.

Mineral	$V_I(Å^3)$	$V_C(Å^3)$	z(%)
almandine	1114.45	1532.81	27.3
staurolite†	542.58	740.33	26.7
muscovite	579.30	937.77	38.2
biotite	297.58	492.38	39.6
quartz	66.27	112.98	41.3
albite	371.93	665.32	44.1

Table 1.2: Calculated total ionic porosities (z) for various minerals, taken from Fortier & Giletti (1989), apart from† calculated from data provided in Deer *et al.* (1992) and Shannon & Prewitt (1969).

Figure 1.7 shows an Arrhenius plot of log D versus $10^3(1/T)$, where T is temperature in Kelvin, for common pelite minerals, over a temperature range of 400 - 800°C.

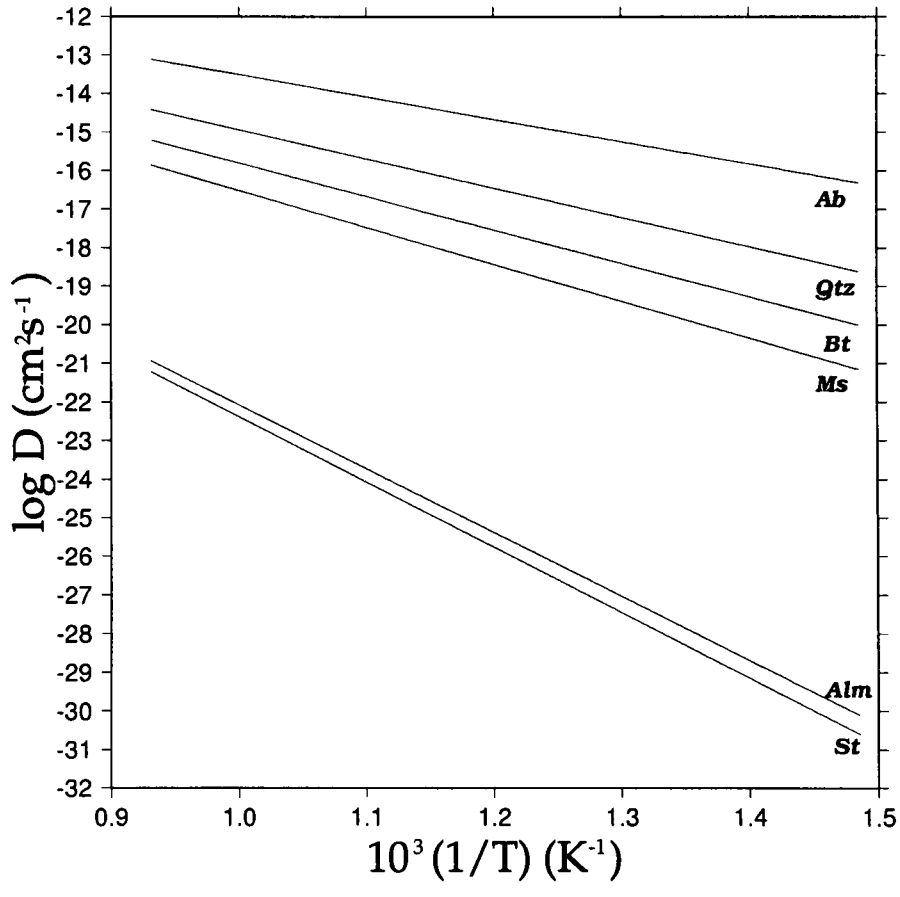


Figure 1.7: Plot of log D versus $10^3(1/T)$, calculated from Fortier & Giletti (1989).

1.6.1 Diffusion calculations

Diffusion is the migration of chemical species, driven by a chemical potential gradient, for which concentration gradients may be considered a proxy. The equations for diffusion are identical to those of heat flow, and the diffusion equivalent of Fourier's law is known as Fick's Law.

Diffusion is a vectorial process, and at any point in the medium, the flux of chemical species (J_i), can be described as a function of the gradient in concentration $\mathrm{d}C_i\ /\mathrm{d}x$, in one-dimension, as described by Fick's first law:

$$J_i = -D\left(\frac{\mathrm{d}C_i}{\mathrm{d}x}\right) \tag{1.19}$$

Fick's first law describes a steady-state position. However, this is rarely true in natural systems (which are usually dynamic), and so the second differential describes the change in concentration with time.

$$\frac{\mathrm{d}C_i}{\mathrm{d}t} = D\left(\frac{\mathrm{d}^2C_i}{\mathrm{d}x^2}\right) \tag{1.20}$$

which assumes that D is constant.

Diffusion exists as three types: surface diffusion, where the chemical species moves around on free surfaces; grain-boundary diffusion, where the species diffuses along a grain boundary between two mineral phases; and volume diffusion, through bulk material. Of these the latter is the most important to quantify when looking at isotope zoning within minerals, since oxygen self-diffusion, both as inter-mineral diffusion, and intra-mineral diffusion, may later modify existing $^{18}O/^{16}O$ isotope profiles.

The equation for diffusion in a sphere has an analytical solution (Crank, 1983):

$$\frac{C - C_1}{C_0 - C_1} = 1 + \frac{2a}{\pi r}\sum_{n=1}^{\infty}\frac{-1^n}{n}\sin\frac{n\pi r}{a}\mathrm{e}^{Dn^2\pi^2ta^2} \tag{1.21}$$

where C is concentration at point r below the surface (where a is thickness, and r=0 at surface; $r = a$ at core); C_1 and C_0 are initial uniform concentration and surface concentration respectively; t is time of interest and D is diffusivity.

This equation can be solved to model oxygen self-diffusion through a semi-infinite homogeneous medium. Figure 1.8 shows the results of oxygen diffusion through differing

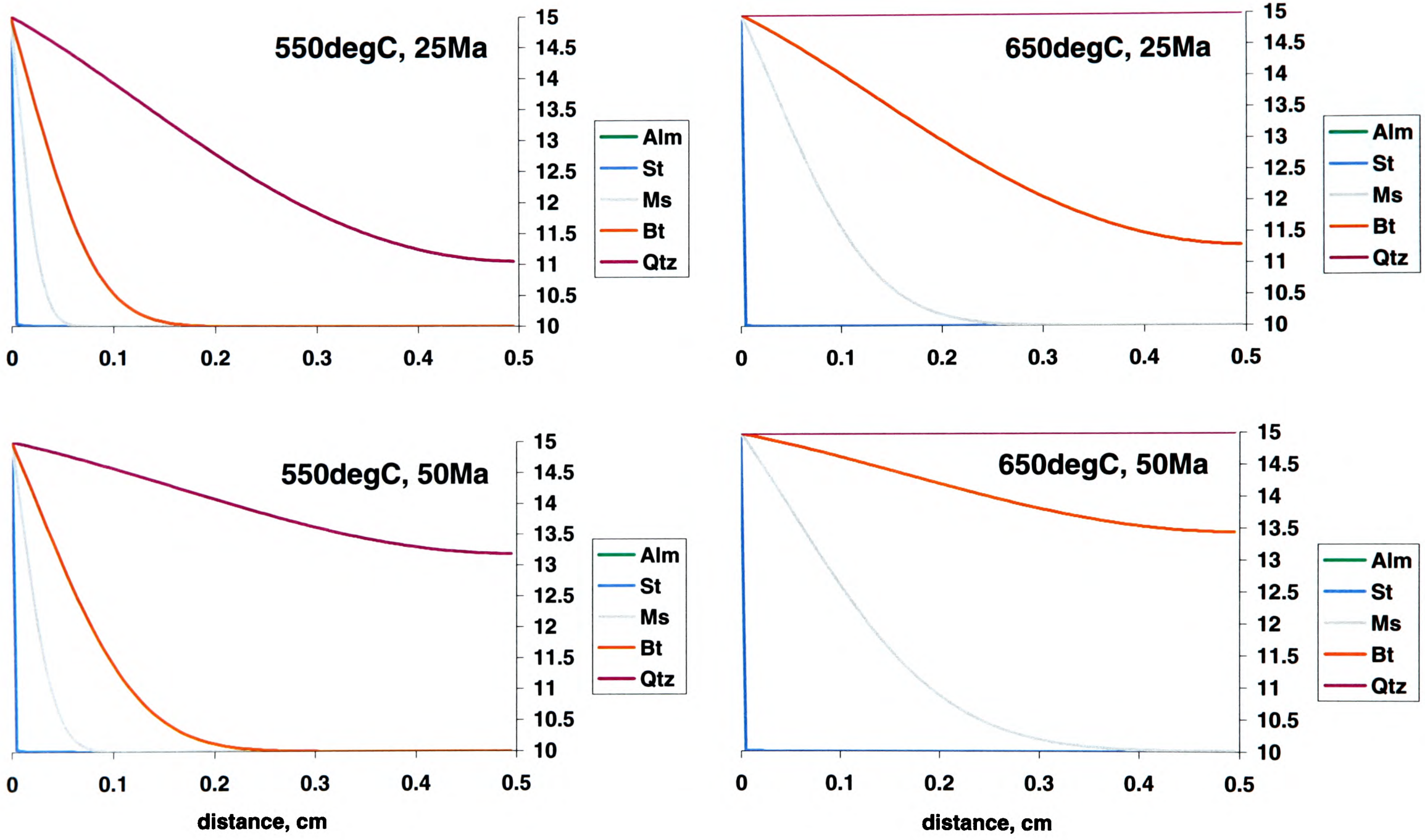


Figure 1.8: Modelled oxygen self-diffusion profiles for almandine, staurolite, muscovite, biotite and quartz, calculated at both 550°C and 650°C, and for 25Ma and 50Ma at each temperature. Table 1.3 details values of D used. The plots show the effect of oxygen diffusion on mineral $\delta^{18}O$, that at 0Ma were homogeneously 10‰, bounding an infinite reservoir at 15‰. The curves for almandine and staurolite essentially plot on top of each other. Vertical axis is $\delta^{18}O$ ‰; horizontal axis is distance from the edge of the mineral (where it bounds the reservoir) inwards in cm. Scale of laser microprobe observation is 100μm.

minerals after 25Ma and 50Ma at both 550°C and 650°C, using the value of D calculated at the appropriate temperature from the method described by Fortier & Giletti (1989), and detailed in table 1.3. The minerals were taken to be initially homogeneous with $\delta^{18}O = 10‰$, bounding an infinite reservoir with $\delta^{18}O = 15‰$. Such an infinite reservoir could be an approximate for a constant $\delta^{18}O$ fluid.

Mineral	550°C	650°C
almandine	2.335×10^{-26}	3.501×10^{-24}
staurolite	9.545×10^{-27}	1.607×10^{-24}
muscovite	2.677×10^{-19}	4.843×10^{-18}
biotite	2.160×10^{-18}	2.978×10^{-17}
quartz	2.725×10^{-17}	2.702×10^{-16}

Table 1.3: Values of D at 550°C and 650°C taken for the diffusion modelling in figure 1.8. Values calculated from Fortier & Giletti (1989).

This figure shows that for both garnet and staurolite, which effectively plot on top of each other, the oxygen isotope profile is essentially unmodified by self-diffusion; only the first few microns show any evidence for diffusive processes. Therefore we can be confident that any oxygen isotope profiles observed within these minerals have not been perturbed at a later stage by diffusive processes for minerals at least up to 650°C.

However for mica minerals, and especially quartz, oxygen diffusion occurs at a much faster rate. Considering that the scale of observation using the UV laser probe is 100-150μm, this underscores the value of analysis on this resolution; measurement using an Infra-Red laser would be unable to investigate isotopic differences on such a scale.

1.7 Outline of this thesis

This thesis is divided into three main parts, the design and development of the Oxford laser isotope facility, the geology and petrology of the high-alumina Hoosac Schist, and metamorphic modelling. The chapters are divided as such:

- **chapter 2** introduces oxygen isotope analysis and charts the history of development from the early 'bomb' methods in the 1950's; it also details the construction of the Oxford laser line

- **chapter 3** gives information as to the present analytical technique, standards used and sample preparation, and charts the development process from test gas runs to initial Hoosac sample analysis
- **chapter 4** introduces the Hoosac Schist within a regional context, with background geology, field observations and sample collection
- **chapter 5** gives a detailed qualitative assessment of the high-alumina Hoosac Schist with petrological and microstructural history
- **chapter 6** documents quantitative mineral data and attempted thermobarometry
- **chapter 7** reports oxygen isotope analysis from the Hoosac Schist
- **chapter 8** covers metamorphic modelling using THERMOCALC, detailing construction of NCMnKFMASH pseudosections to model garnet growth, and oxygen isotope fractionation calculations using PTGRID
- **chapter 9** provides a synthesis and gives final conclusions

The appendices contain all development (A), measured (B) and garnet standard data (C); X-ray fluorescence data (D) and microprobe analyses of minerals (E).

Chapter 2

UV laser line - rationale and construction

2.1 Oxygen isotope analysis

Since oxygen represents approximately one half of the Earth's crust by mass, processes which serve to transfer matter from one phase to another within the crust will generally transfer oxygen. This process will usually fractionate the isotopes of oxygen. The analysis of the stable isotopes of oxygen is therefore one of the most useful tools available for attempting to understand the mechanisms of mass transfer, in particular for this study those that occur within the mid-crust.

This chapter is presented in two parts: Firstly, the history of oxygen isotope analysis is described, from the original combustion (bomb) technique to modern-day ablation methods. This leads on to the reasons and motivation behind the initiation and development of the UV laser line at Oxford. The latter part of the chapter details the Oxford laser line, the technology involved and its construction. Information concerning both the development of the method for the analysis of metamorphic samples, and routine sample analysis methodology are dealt with in chapter 3.

2.2 A brief history of oxygen isotope analysis

Oxygen isotopes have been successfully measured for over forty years since the early days of mass spectrometry (*e.g.* Silverman, 1951). Investigations into the application of oxygen isotope analysis in metamorphic rocks really began in the 1960's (*e.g.* Garlick & Epstein, 1967). The drive to improve both spatial resolution and analytical precision has led to the introduction of microanalytical tools such as the ion microprobe and, latterly, laser-heating techniques.

2.2.1 From nickel bomb to copper laser

Traditional analysis of oxygen isotope ratios from silicate materials were made in heated reaction vessels. Ground-up mineral samples were placed in stainless steel, or nickel, bombs, which were evacuated, exposed to a fluorinating reagent, usually ClF_3 or BrF_5, and then sealed. The vessel was heated in a furnace for up to 18-20 hours at temperatures of 250 - 600 °C (*e.g.* Baertschi & Silverman, 1951; Clayton & Mayeda, 1963). The oxygen liberated from this reaction was then separated and collected by means of cryogenic clean-up within a vacuum line, usually made of glass, and then passed into the mass spectrometer. The oxygen was analysed as CO_2, and thus a conversion step from O_2 to CO_2 was required, usually by means of a hot graphite catalyst. CO_2 was chosen as the analyte as it was deemed less susceptible to adsorption onto the interior of the vacuum line and instrument than O_2, and hence promised much more in the way of isotopic fidelity.

This method proved very successful, and consequently changed little in over 30 years. However, it suffered from a number of drawbacks including lengthy analytical procedure, and the requirement for large mineral samples (a minimum of 5-15 mg of material) which meant that fine-scale analysis could not be considered. More limiting, however, was the inability to analyse some of the more refractory silicates, such as garnet, olivine or corundum, since the temperatures attained in the reaction did not allow for complete combustion of the mineral, thus leading to isotopic fractionation.

The introduction of the laser

Conventional oxygen isotope analysis was revolutionised when, after advances in the routine analysis of sulphur isotopes (*e.g.* Crowe *et al.*, 1990; Kelley & Fallick, 1990), a laser-heating method was developed by Sharp (1990).

The laser-heating technique for the microanalysis of oxygen isotopes in both silicates and oxides, as reported by Sharp, was a method which combined standard fluorination techniques with samples being heated directly by an Infra-Red (IR) laser (in Sharp's study a 20W CO_2 laser source). This allowed for the analysis of smaller quantities of material, and Sharp reported a resolution of less than 300μm in diameter with *in-situ* lasing, and less than 100μg for mineral separates. For IR fluorination, samples were placed in a nickel chamber (with a BaF_2 window, which is transparent to both IR and visible light, and is inert to fluorine), fluorinated with either BrF_5 or F_2, and then heated with the laser. The released and reacted gas was then transferred into a vacuum line as with the bomb method. Sharp reported both precision and accuracy of $\pm$ 0.1 ‰, equivalent to the conventional bomb technique. IR laser-heating allowed reaction times to be measured in seconds rather than hours, and using this method even the most refractory of ferromagnesian silicate minerals could be melted with ease (*e.g.* Mattey & Macpherson, 1993).

While routine, whole-grain analysis allowed rapid, high-precision measurement of some 100μg of sample, the application of this technique to the microanalysis of metamorphic analysis on the sub-millimetre scale was problematic. *In-situ* analysis of metamorphic minerals by IR laser is hampered by the nature of IR radiation during the ablation process. During IR heating, vibrational energy is taken up by the mineral lattice, resulting in heat dissipation and subsequent melting of the mineral adjacent to the ablated pit. Figure 2.1 details these 'edge effects' on oxides adjacent to an *in-situ* ablated pit. This edge effect also manifests itself as oxygen isotope fractionation, which has significant repercussions for the size of the ablated pit. In order to render the fractionation effect negligible, a minimum pit size of the order of 1mm in diameter or greater is necessary. Thus *in-situ* analysis using IR lasers are unable to achieve the desired spatial resolution for metamorphic investigations.

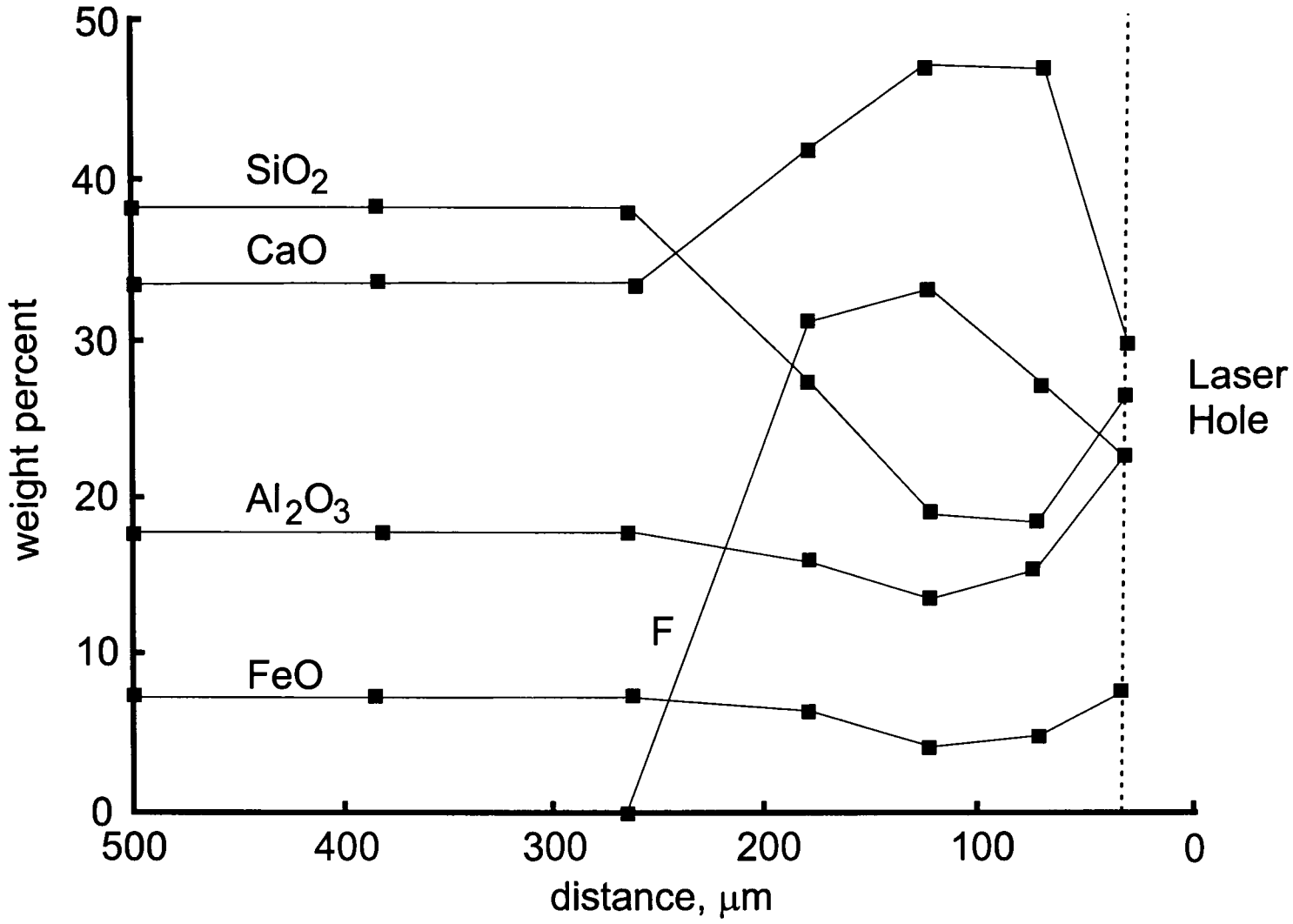


Figure 2.1: Figure showing a microprobe traverse adjacent to an IR laser pit. This clearly shows the chemical edge effects (after Chamberlain & Conrad, 1993).

However, Mattey & Macpherson (1993) described their successful analysis of silicate mineral *grains* with the use of a 60W Nd:YAG infra-red laser, using ClF_3 as a fluorinating agent, and CO_2 as the analyte. A Nd:YAG source had previously proved successful in the analysis of quartz and feldspar (*e.g.* Elsenheimer & Valley, 1992). Mattey & MacPherson claimed precision of $\pm$ 0.1‰ (1σ), with a sample size of 1000μg. However, when the sample was reduced to some 750μg or less, it was shown that light $\delta^{18}O$ values were systematically obtained, yielding a relationship between sample size and oxygen yield. The cause of this isotopic shift was found to lie in the conversion step of O_2 to CO_2; smaller samples meant lower analyte pressure thus encouraging the production of CO rather than CO_2. Mattey & MacPherson reported that fluorination yields were related to laser power, beam diameter, quantity of fluorinating agent and beam raster speed.

The results obtained by Mattey & MacPherson proved that focused high-power laser

heat sources provide a simple and rapid means of oxygen extraction from minerals, with negligible background oxygen and sufficient reaction temperatures to analyse even the most refractory of minerals. They concentrated on the analysis of single grains, due to the aforementioned analytical problems with *in-situ* measurements. However, the requirement for sub-millimetre *in-situ* analysis was still not fulfilled.

method	sample size	reference
Nickel bomb	5 - 15 mg	Baertschi & Silverman (1951); Clayton & Mayeda (1963)
IR (ND-YAG) grain separate	750 - 1000μg	Mattey & Macpherson (1993)
IR *in-situ* CO_2	300μg	Sharp (1990)
UV Excimer	100μg	Wiechert & Hoefs (1995)
UV GC-*irms*	1 - 10μg	Young *et al.* (1998b)

Table 2.1: Comparison of different methods of silicate analysis.

The Ultra Violet laser

Recent oxygen isotope studies in metamorphic rocks using Infra-Red laser technology have shown both isotope differences on a millimetre to sub-millimetre scale, and also isotopic shifts of the order of 1‰ or less (*e.g.* Chamberlain & Conrad, 1993; Young & Rumble, 1993; Kohn, 1993). The requirement to further improve both spatial resolution and analytical precision has driven the development of microprobe technology (see figure 2.2 for a comparison of microanalytical methods). In addition, the difficulties associated with extracting mineral chips on the sub-millimetre scale has lead to the requirement of true *in-situ* analysis on the sub-millimetre scale. Two predominant approaches lie with the ion microprobe and the ultra-violet laser-based microprobe.

Ion microprobe analysis (knows as secondary ion mass spectrometry, SIMS) is a technique where fast, heavy ions are focused to a fine spot onto the sample surface, which then eject secondary ions from the sample material. These are extracted and analysed. SIMS has an *in-situ* resolution on the order of 2 - 30μm, however it suffers from a reported $\delta^{18}O$ precision of the order of $\pm$0.8 - 1‰ (Valley & Graham, 1991, 1996; Graham *et al.*, 1996), although this can be bettered by effectively improving the counting statistics with systematic sets of sample analyses (Eiler *et al.*, 1995). The reason for the relatively large errors is that SIMS analysis requires complex matrix corrections, sometimes as much as 80‰ (*e.g.* Valley & Graham, 1996). This inherent error is not a problem

in low-temperature geological processes where isotope fractionations tend to be large (*e.g.* 10‰ and above); however the inability to resolve isotope differences of 0.5‰ or lower can be limiting to metamorphic studies.

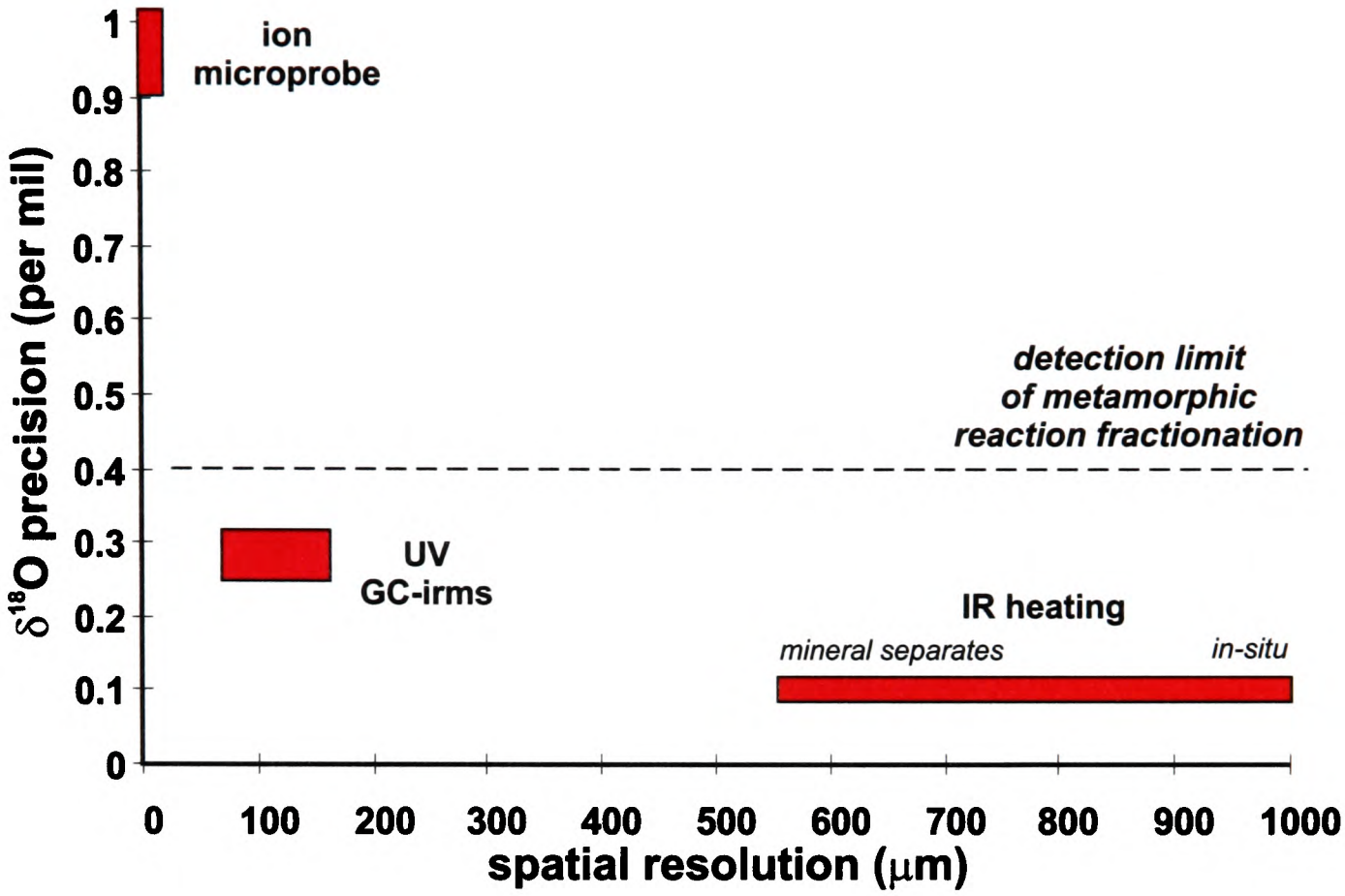


Figure 2.2: Comparison of oxygen isotope analytical methods, plotting spatial resolution versus reported precision (1σ). Also plotted is a line representing typical isotope fractionation for metamorphic reactions (from observations in this study). Any method has to lie under this line in order to be effective at resolving the isotope differences associated with high temperature mass-transfer reactions (after Sharp, 1990; Valley & Graham, 1991, 1996, this study).

Wiechert & Hoefs (1995) reported early results from the use of an Kr-F Excimer ultra-violet laser for *in-situ* analysis. The Excimer laser produces UV light at a wavelength (λ) of 248nm. They showed that the edge effects associated with ablation using either a CO_2 or Nd:YAG IR-source are not observed with the use of UV light. The lack of reaction halo is related to the nature of UV ablation: nanosecond pulses of short wavelength ultra-violet light excite the mineral lattice electronically (see section 2.2.2). Excess laser energy is thus dissipated as both kinetic and heat energy within the plasma plume that develops immediately above the mineral surface, rather than as heat energy into the mineral (as is the case with IR ablation). Hence UV light produces clean pits with

no trace of reaction haloes (figure 2.5), or zone of partial melting, adjacent to the pit. Wiechert & Hoefs analysed samples with sizes similar to that of the grains previously analysed with IR light (*e.g.* Mattey & Macpherson, 1993); but were limited by their inability to successfully handle analyte gas of a smaller volume.

2.2.2 Ablation with an UV laser

Fluorination by Ultra Violet laser ablation occurs within or adjacent to a plume of hot plasma generated above the target of the mineral whilst the laser pulse is active (Young *et al.*, 1998b). The characteristics of ablation by IR and UV lasers are very different (see figure 2.3 versus 2.4).

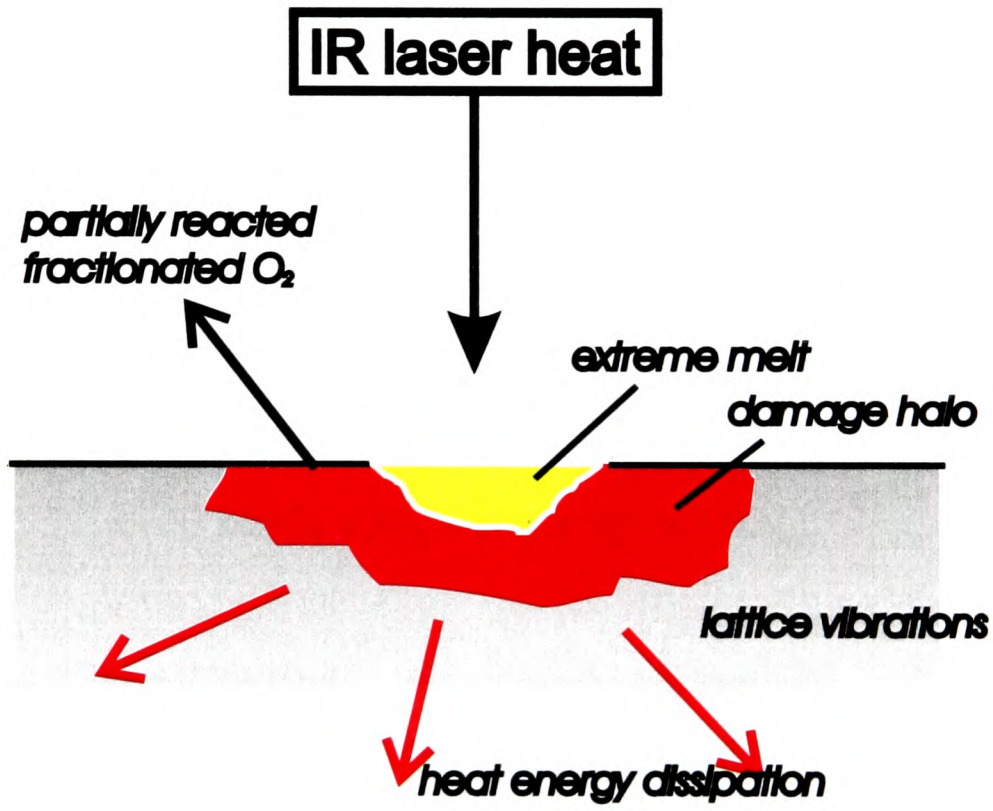


Figure 2.3: Schematic of a mineral being heated by an Infra-Red laser; photon energy is converted to vibration energy, heating and melting the surrounding material.

If a solid is heated with an Infra-Red laser (figure 2.3), most of the photon energy will be converted to vibration energy (*i.e.* phonons) of the crystal lattice (Wiechert & Hoefs, 1995). With increasing vibration, resultant melting of the radiated and surrounding material can occur.

The infra red fluorination process may be summarised by the following equation, where

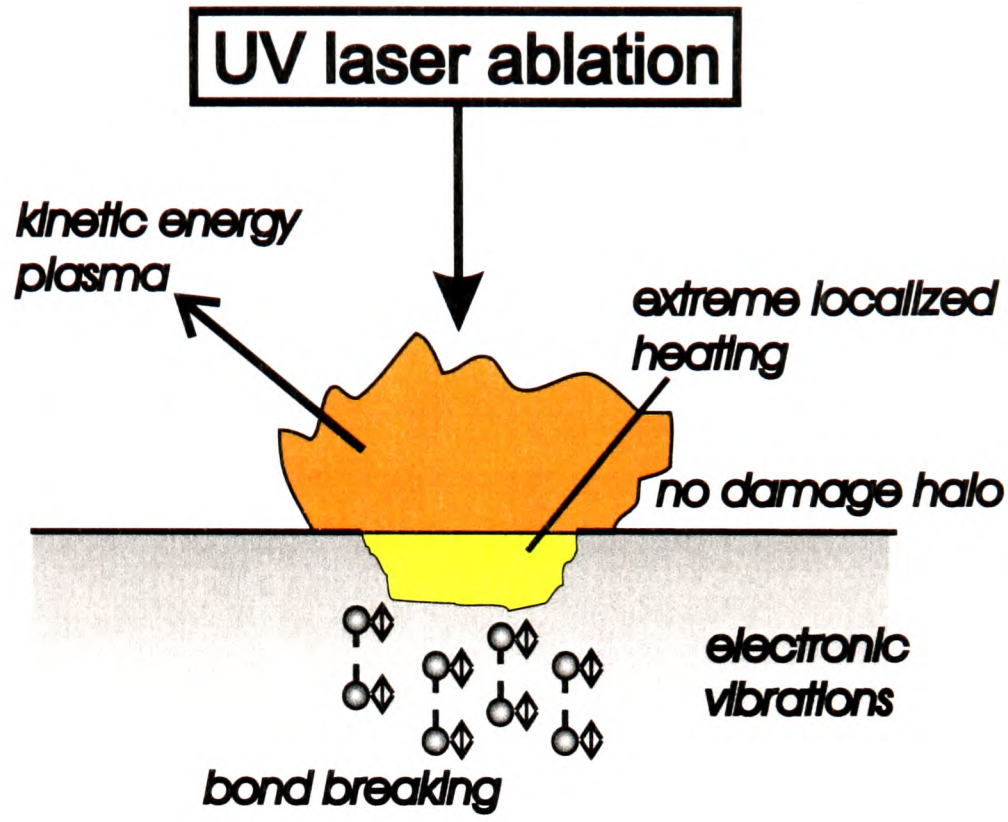


Figure 2.4: Schematic of a mineral being ablated by a UV laser; with each laser pulse, bonds are broken and a plasma forms immediately above the laser pit, containing vapourized material, where it reacts with the fluorine envelope.

M represents a divalent mineral cation.

$$MSiO_3 + 3F_2 = MF_2 + SiF_4 + 1.5O_2$$

However, using either a frequency-doubled copper-vapour laser (pulsing at a frequency of 4KHz), or a nanosecond pulsed excimer laser (20Hz), ablation effects are considerably different from ablation with CO_2 or Nd:YAG IR-source lasers.

UV laser ablation takes place only above a material-dependent energy density, or fluence, threshold (*c.f.* olivine, fig 5, Wiechert & Hoefs, 1995). At all energy densities a blue plasma forms perpendicular to the radiated area (figure 2.4). The size of the plasma depends both on the fluence of the laser and on the gas pressure of the fluorinating atmosphere (fluence of a laser is a function of both power and spot size - see figure 2.7 for the Oxford UV laser).

The coupled high power and fluence of UV lasers also gives rise to a different mechanism for the liberation of O_2, in which high-power nanosecond pulses quantitatively

vapourize the radiated material, subject to the criterion that the material-dependent threshold is exceeded. This is summarised below, which shows the material being excited to a vapour phase, or plasma, *with each laser pulse.*

$$MSiO_3 \rightarrow M^o + Si^o + 3^o$$

This state is maintained for a timescale measured in nanoseconds, after which the atoms will inevitably begin to condense together. During this condensation process, fluorides will be formed; however O_2 remains gaseous since fluorine is in excess, and due to its greater electronegativity, fluorine is the preferred anion for bonding:

$$M^o + Si^o + 3O^o + 6F_{2,excess} \rightarrow MF_2 + SiF_4 + 1.5O_2 + 3F_{2,excess}$$

The differences between IR and UV laser ablation are fundamental; absorption based on lattice vibration is restricted to infra-red, whereas absorption in UV is connected with the excitation of electronic transitions. For example, for radiation in the UV range (248nm for KrF excimer, 255nm for Cu-vapour), quartz is essentially transparent; photons will be deposited only at lattice defects, and point defects such as fluid inclusions. Thus it is found that UV ablation holes in quartz will show textures of mechanical fractures, and an oxygen yield for quartz ablated with UV is typically less than 30% (E.D. Young, pers. comm.).

2.2.3 Isotope ratio monitoring mass spectrometry

Ultra violet laser ablation provides a means for true *in-situ* liberation of oxygen in a quantitative manner from silicate minerals. However the minimum size of sample, and hence minimum spatial resolution, is determined by the need to maintain viscous laminar (non-fractionating) flow rather than fractionating molecular flow in the transfer of the analyte gas from the fluorination chamber via the vacuum line to the analytical instrument. The requirement to measure and transfer nanomoles of analyte gas (equivalent to micrograms of silicate) whilst maintaining isotopic fidelity has of necessity led to the development of new technology.

The nature of gas transfer flow within a constricting pipe is a function of sample pressure, diameter and length of vacuum tubing, as determined by the Poiseville equation (equation 2.1).

$$f = \frac{P_{out}^2 - P_{in}^2}{P_{out}} \cdot \frac{r^4}{16\eta L} \tag{2.1}$$

(where f is the flux; P_{in} and P_{out} are the input and output pressures respectively; r is the radius of the tubing, L is the length of tubing and η is the viscosity of the gas).

With conventional vacuum technology the need to maintain viscous flow has typically restricted the sample size to greater than 1×10^{-6} moles, or 1 mg (Rumble *et al.*, 1997). Static mass spectrometry, where the flight tube of the instrument becomes an intrinsic part of the vacuum line, is used for unreactive gases such as nitrogen; however O_2 suffers from chemical adsorption onto metal surfaces, and since it is preferable to use O_2 rather than CO_2 as the analyte (avoiding the need for a transformation step, and the size restrictions that this places upon the sample - as demonstrated by Mattey & Macpherson (1993) - as well as eliminating corrections for the different isotopes of carbon), this was not deemed an acceptable method.

Irm-MS (isotope ratio monitoring mass spectrometry) entrains the oxygen analyte gas in a stream of helium carrier gas (Young *et al.*, 1998a). This allows for the quantitative transfer of the analyte, avoiding the physical stipulations implied by the Poiseville equation. A method can therefore be developed utilizing this technology to combine small scale sampling with high precision mass spectrometry.

The original development of *irm*-MS occurred in the fields of biochemistry and organic chemistry, the term monitoring describing a time-dependence measurement, the analysis being a time-integrated calculation of the isotopic shifts observed as the gas is introduced into the instrument. Isotope ratios of compounds are determined by passing the sample through a gas chromatograph column prior to entry into the instrument, resolving and cleaning up the signals of the different isotopes. With the use of gas chromatography, ^{17}O can be successfully resolved and analysed, free from interference by NF, and other similar masses. Whilst measurement of this ratio is not critical for analysis of terrestrial samples (all sample originating from this planet should lie on the terrestrial fractionation line, with a $(^{17}O/^{16}O)/(^{18}O/^{16}O)$ ratio of approximately 0.5 - see figure 1.5), the requirement to distinguish and accurately measure $\delta^{17}O$ is important in

cosmogenic applications where non mass-dependent fractionations occur.

2.3 The Oxford UV laser isotope line

The Oxford laser line was developed to address the following points:

- rapid sampling, including analysis of refractory minerals - *laser ablation mass spectrometry accomplishes this*
- true *in-situ* sampling - *by using a UV laser, clean pits may be ablated without the risk of edge effects seen with in-situ IR heating*
- microanalysis on the 100 micron scale - *by having O_2 as the analyte there is no CO_2 conversion step necessary, and by using irm-MS technology nanomoles of oxygen can be analysed whilst maintaining isotope fidelity*
- a precision comparable to macro laser analysis - *of the order of ± 0.2 - 0.3‰*
- the analysis of $\delta^{17}O$ - *the use of gas chromatography resolves the isotopes of oxygen thus allowing accurate measurement of ^{17}O*

The Oxford laser line was designed to perform routine analysis of nanomoles of oxygen gas, corresponding to ablated pits as small as $100 \times 50 \mu m$, and $30 \mu m$ deep (see figure 2.5), with an analytical precision of at least ± 0.3 ‰, approaching that of conventional bomb isotopic analysis.

The analyte gas is oxygen, which removes the need for a conversion step to CO_2 (as with other systems), and potential isotopic fractionation effects associated with the transfer of this minute quantity of gas are solved with the application of GC-*irms* technology. The fluorinating agent used is F_2 gas, chosen after experiments showing a problem of an apparent dependence of sample size (in volt seconds, Vs) against $\delta^{18}O$ using BrF_5 (see chapter 3) (Rumble *et al.*, 1997; Young *et al.*, 1998b). Figure 2.6 shows a schematic of the complete isotope line, showing laser, vacuum line, GC system and mass spectrometer.

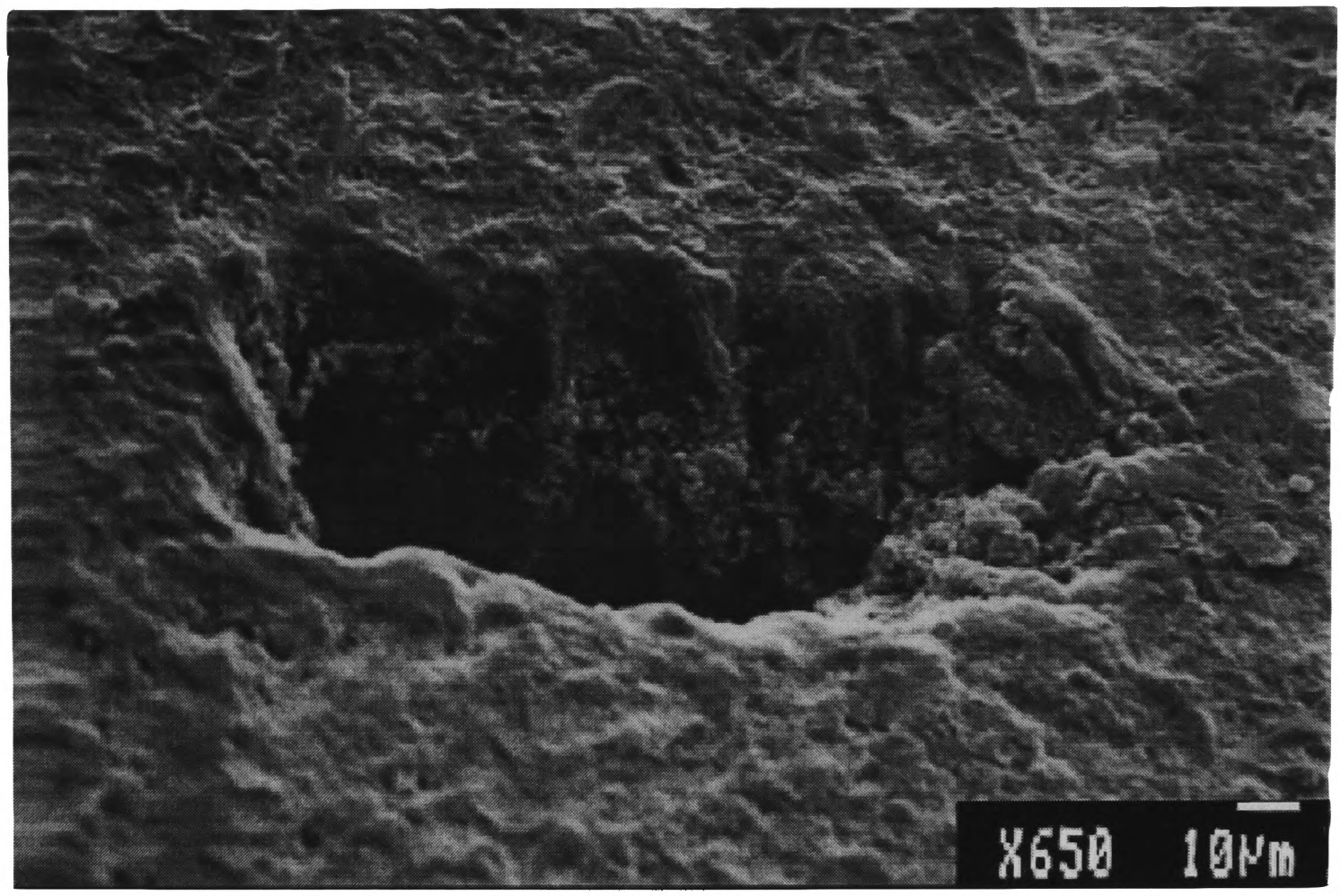


Figure 2.5: An SEM image of a UV-ablated laser hole in forsterite.

2.3.1 The Ultra Violet source

The UV laser source installed in the Oxford isotope laboratory is an Oxford Lasers LS-10 copper (Cu) vapour laser. Ultraviolet light (λ = 255nm) is generated by frequency-doubling the green (510.6nm) output from the Cu-vapour laser by focusing through a Betaphase Barium Borate (BBO) crystal, as described by Coutts & Brown (1995). The characteristics of generating UV light by this method from this laser source give a very high-pulse frequency (4kHz), but low pulse power laser beam, 450-600 mW, which, when focused to a spot size of approximately 25μm in diameter, can give a pulse fluence of 30 Jcm^{-2} (see figure 2.7). This compares with the typical output from a KrF Excimer laser which pulses at a maximum frequency of 100Hz (Rumble *et al.*, 1997). The contrast of high frequency, low pulse power (Cu-vapour) compared to low frequency, high pulse-power (Excimer) is significant; the former allows for comparatively gentle rastering of the sample - the Excimer cannot ablate gently, because the power in each pulse can move and crack samples. However, although the power within each laser pulse is much lower for the frequency-doubled laser source, ultimate delivered fluence

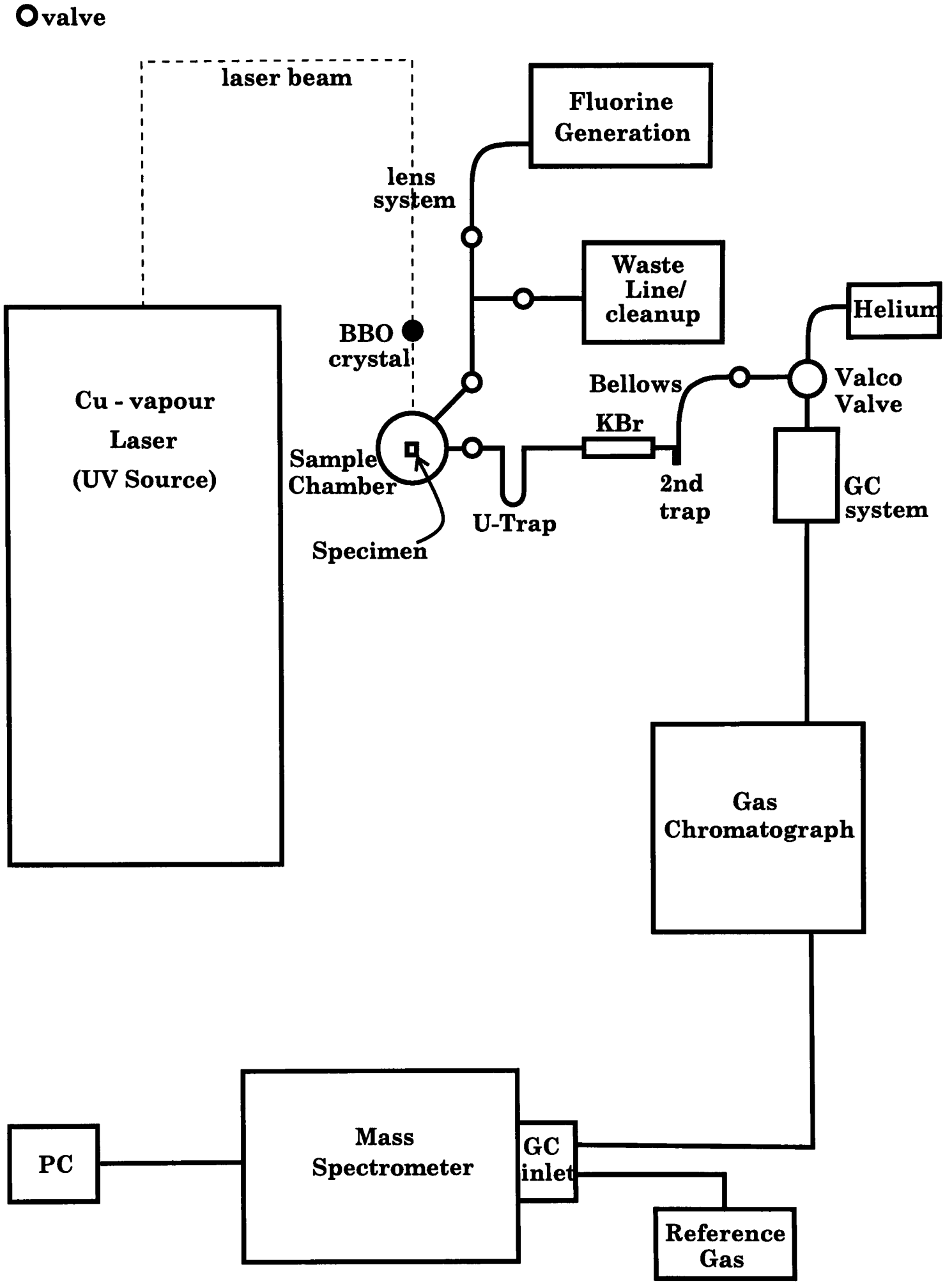


Figure 2.6: Schematic flowchart detailing the Oxford isotope line. The first silica gel loop is indicated as the 'Valco valve'. The second silica gel loop within the GC system (as detailed in figure 2.8) is shown as 'GC system'.

is much greater and samples can be ablated within a matter of seconds. Ablation using the Excimer laser would take a timescale of tens of seconds.

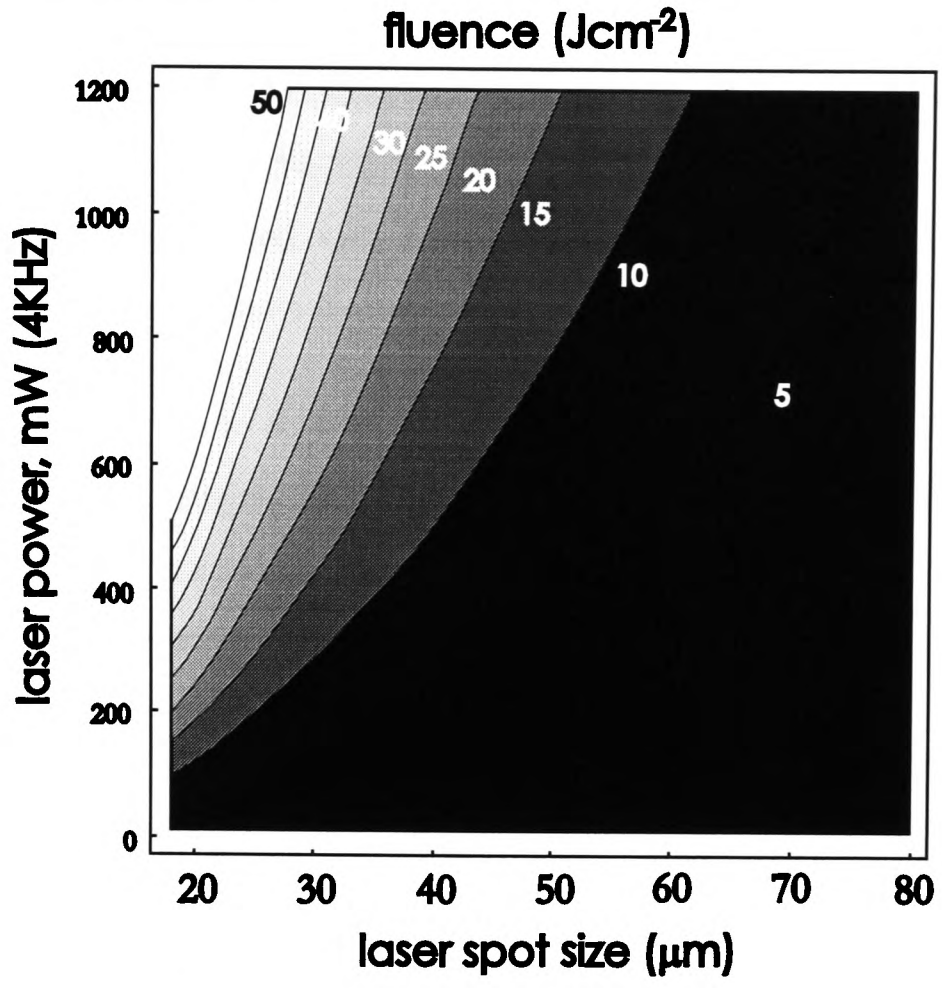


Figure 2.7: A chart of laser fluence as a function of laser power and spot size for the frequency-doubled Oxford Lasers LS-10. Courtesy of E.D. Young.

The beam is focused on the sample, with a co-axial video camera to allow for positioning of the laser spot. A chopper wheel may be used to strobe the beam to allow control over the depth of ablation. The sample chamber is mounted upon x- and y- axis stages, and pits are ablated by slowly moving the mineral relative to the laser beam.

2.3.2 The CO_2 laser source

A Merchantek IR laser, using CO_2 as a light source, is also available for analysis of mineral chips. A gold-coated holder can hold up to 10 samples at any one time. Generally the large quantity of analyte gas released through normal IR heating requires the use of microvolume for analysis, although development towards using small enough samples such that analysis via the GC system is possible, has been under study.

2.3.3 The chamber and isotope line

The sample chamber is machined from a single block of stainless steel; it has an internal volume of approximately 30 cm^3. The chamber has a window of MgF_2, which is transparent to both UV and visible light, is inert to fluorine, and is sealed by means of a Kal-rez O-ring (a pre-fluorinated, soft, Teflon-like material). A BaF_2 window, transparent to IR and visible light, is used for Infra-Red analysis.

The chamber has four exits to it, three of which are controlled by air-actuated valves, whilst a fourth exits to a high-pressure vacuum gauge to monitor the pressure in the chamber. The other three exits lead to the fluorine generator and waste trap; the sample line; and an input for helium gas, used to purge the chamber during sample changing.

The waste trap consists of two liquid-nitrogen traps, the second backing a high-conductance KBr trap for the passivation of excess fluorine. It also consists of a valved Kel-F tube which is used to condense bromine and other wastes.

The vacuum line is constructed from $\frac{1}{2}''$ diameter 316L stainless steel tubing, connected with Cajon S-VCR fittings and low dead-volume valves. It is evacuated by a turbomolecular pump, and both this and the roughing pump contain corrosive-grade Fomblin prefluorinated oil to allow for pumping of fluorine. A low vacuum Edwards rotary pump, also containing Fomblin oil, is available for waste-trap pumping.

2.3.4 Reactions within the chamber

The sample sits under high vacuum ($\sim 2\times10^{-7}$ torr) until fluorine is aliquoted into the chamber, F_2 quantity determined by pressure. Excess fluorine is sent to the waste trap and the high-conductance KBr trap to be converted into KF and bromine, which is trapped in a U-trap at liquid nitrogen temperatures.

Fluorine is generated by means of the method as described by Asprey (1976), whereby a potassium-nickel fluoride is heated to above 300°C to liberate greater than 99% pure fluorine gas as described by the progress of reaction 2.2 towards the right.

$$2[K_2NiF_6.KF]_{(s)} \rightleftharpoons 2K_3NiF_{6(s)} + F_{2(g)} \tag{2.2}$$

This reaction also has the advantage in that it reverses below 250°C, allowing excess fluorine to be resorbed. The Asprey method has an additional advantage over cylinder fluorine in that it is a purer source of fluorine (a cylinder is only around approximately 98% pure), and it is also safer to handle. The system installed in the Oxford Laboratory consists of a cylindrical chamber filled with 60 cm^3 K_2NiF_6.KF powder; the chamber temperature is controlled with an electronic thermostat.

Fluorination

Fluorination by UV laser ablation occurs within or adjacent to a transient plasma (ionized gas) that forms immediately above the mineral spot being ablated with each laser pulse. Inside this plasma temperatures may exceed 7000 K (Young *et al.*, 1998b), and laser energy is converted to both thermal and kinetic energy, the latter ejecting and propelling atoms into the plasma plume and creating a shockfront. Within the plasma, atoms (ejected from attack of the mineral by the laser) are excited to a neutral state, high energy level; on condensation of the plume (between laser pulses), mixing and reaction occurs between these atoms and the adjacent collapsing fluorine envelope. All atoms, except for oxygen, react with the fluorine (which is in excess) to produce various fluorides, whilst the oxygen condenses to form O_2. Thus complete, quantitative conversion of mineral oxygen to oxygen gas occurs. The following equations show an example reaction for this process for almandine:

$$Fe_3Al_2Si_3O_{12} + F_{2(excess)} \rightarrow 3Fe^\circ + 2Al^\circ + 3Si^\circ + 12O^\circ + 2F^\circ \qquad (2.3)$$

and then by condensation to:

$$3Fe^\circ + 2Al^\circ + 3Si^\circ + 12O^\circ + 2F^\circ \rightarrow 3FeF_3 + 2AlF_3 + 3SiF^{+4} + 6O_2 + F_2 \qquad (2.4)$$

Immediately after ablation of the mineral, the chamber is opened up to the isotope line (which is under high vacuum). Upon introduction of the gases into the sample line, condensable fluorides are trapped upon two liquid-nitrogen cold-traps, and any unreacted fluorine gas is passivated by passing over hot (100°C) KBr crystals; bromine produced in this reaction (2.5) is trapped by the cold-traps.

$$F_2 + 2KBr = 2KF + Br_2 \qquad (2.5)$$

The remaining oxygen and non-condensable gases are then transferred to the GC-*irms* system for entrainment in helium and subsequent direct injection into the source of the mass spectrometer. It is important that all excess fluorine has been passivated before the sample is transferred, since F_2 will attack the silica gel used to trap sample oxygen, releasing background oxygen held within the silica structure, and contaminating the sample.

2.3.5 The GC-irms system

The GC-*irms* (Gas Chromatography - isotope ratio monitoring spectrometry) system consists of a set of air-actuated switching valves to control the flow of helium through the second cryofocus trap (figure 2.8); a Shimadzu GC-R1A gas chromatograph and the Finnigan MAT GC II inlet consisting of an open split, a reference gas inlet and water-removal assembly.

The helium is first passed through water and oxygen traps, and a liquid nitrogen-temperature molecular sieve trap in liquid nitrogen to purge the carrier gas of detectable oxygen, before it enters the GC-*irms* system.

A VALCO switching valve sits between the isotope line and the GC-*irms* system, and forms a critical juncture between the vacuum and helium parts of the line. The liberated oxygen is trapped onto 2mm silica gel in the first silica gel loop at liquid nitrogen temperature.

After this trapping, the silica gel loop is isolated from the rest of the sample line, and the VALCO switching valve operated such that helium flows through the loop, which is allowed to thaw such that sample oxygen is liberated into the flowing helium (oxygen may start being released at temperatures as low as -150°C). This flowing helium, containing the entrained sample gas then flows into a system of fixed length fused silica capillary tubing acting as flow regulators, which forms the first part of the GC system.

This system of silica capillary tubing (as detailed in figure 2.8), consists of three air-actuated valves (A, B and C) which serve to act together to control the direction of helium flow through the *cryofocus trap*, whilst still maintaining a flow of helium through the rest of the GC system. The cryofocus trap consists of a length of 1/32" stainless steel

tubing filled with 150 - 250 μm silica gel, secured with nickel wool. There are two stages to the GC-system - the cryofocus stage and the injection stage.

In the **'cryofocus'** stage, valve A is closed, whilst valves B and C are open, allowing the helium from the first silica gel loop to pass through the cryofocus trap (at liquid nitrogen temperatures) where the oxygen is trapped. The remaining He exits through a vent.

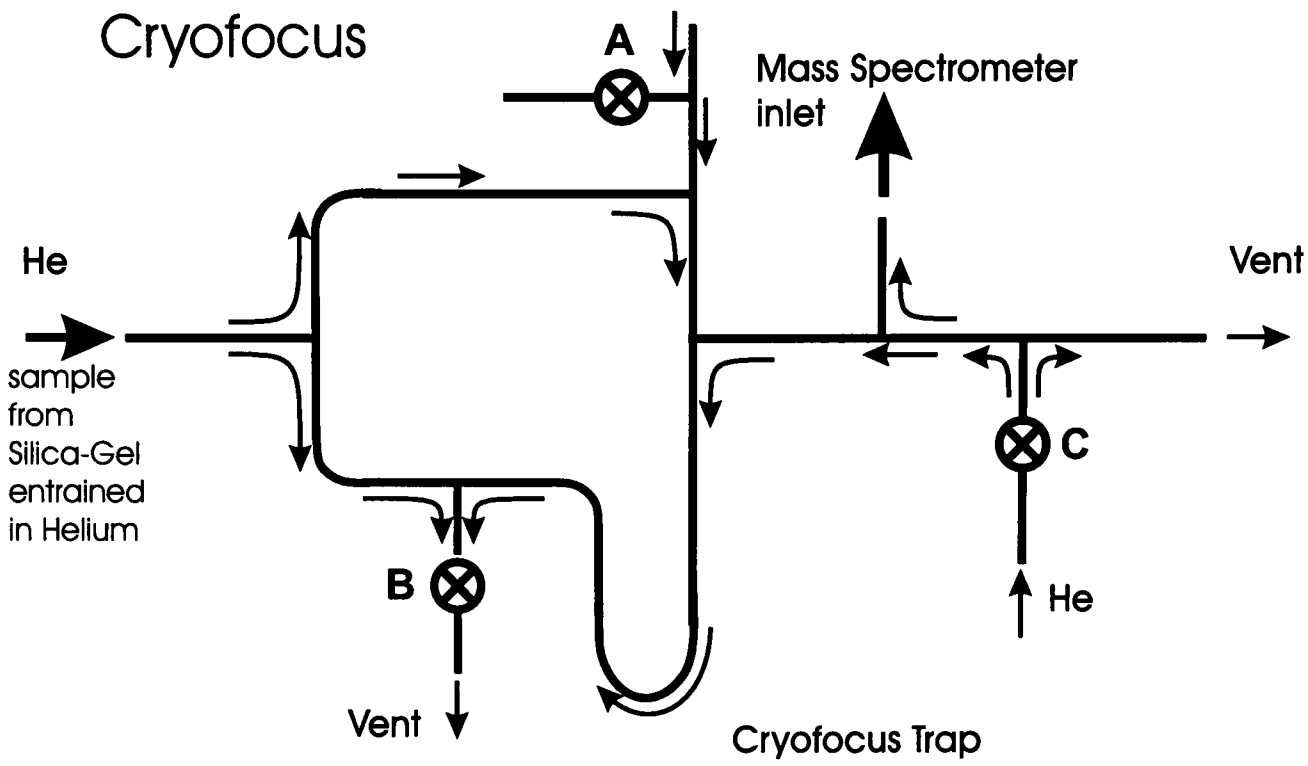
After a period of time trapping analyte gas upon the cryofocus loop, the VALCO valve is first operated to isolate the GC-system from the first silica gel loop (so that He flows straight into the GC-system and not through the first silica gel loop), and the air-actuated valves are simultaneously switched (A open, B and C closed) such that the flow of helium through the cryofocusing trap is now reversed. The trap is allowed to thaw, and release the oxygen into the helium. This is the **'injection'** stage. Oxygen is now carried into the mass spectrometer inlet via the Gas Chromatograph and GC II Interface.

The Gas Chromatograph consists of a GC separation column, of the porous layer open tubular (PLOT) type, 10m long, and 0.53mm internal diameter fused silica, filled with 5A molecular sieve. The GC column sits within an oven, operating at a temperature of 50°C.

The proprietary GC II interface system controls injection of sample and reference gases into the mass spectrometer, at the same time ensuring continuous flow of He into the instrument. Output of sample gas from the GC column undergoes water removal, by means of a Nafion ion-exchange membrane (perfluorinated sulphuric acid), and is then injected into an open split. This ensures continuous flow of He and GC effluent to the mass spectrometer and helps to smooth out any irregular pressure effects from the vacuum line. The open split and reference-gas inlets are switched by air-actuated valves controlled by computer.

2.3.6 The mass spectrometer and output

The instrument is a Finnigan MAT 252 gas-source mass spectrometer, utilizing a 90° magnetic sector and 10kV accelerating voltage. The ions are entered into the instrument, the sample arriving as oxygen gas (O_2) in helium. The gas passes over a filament where the



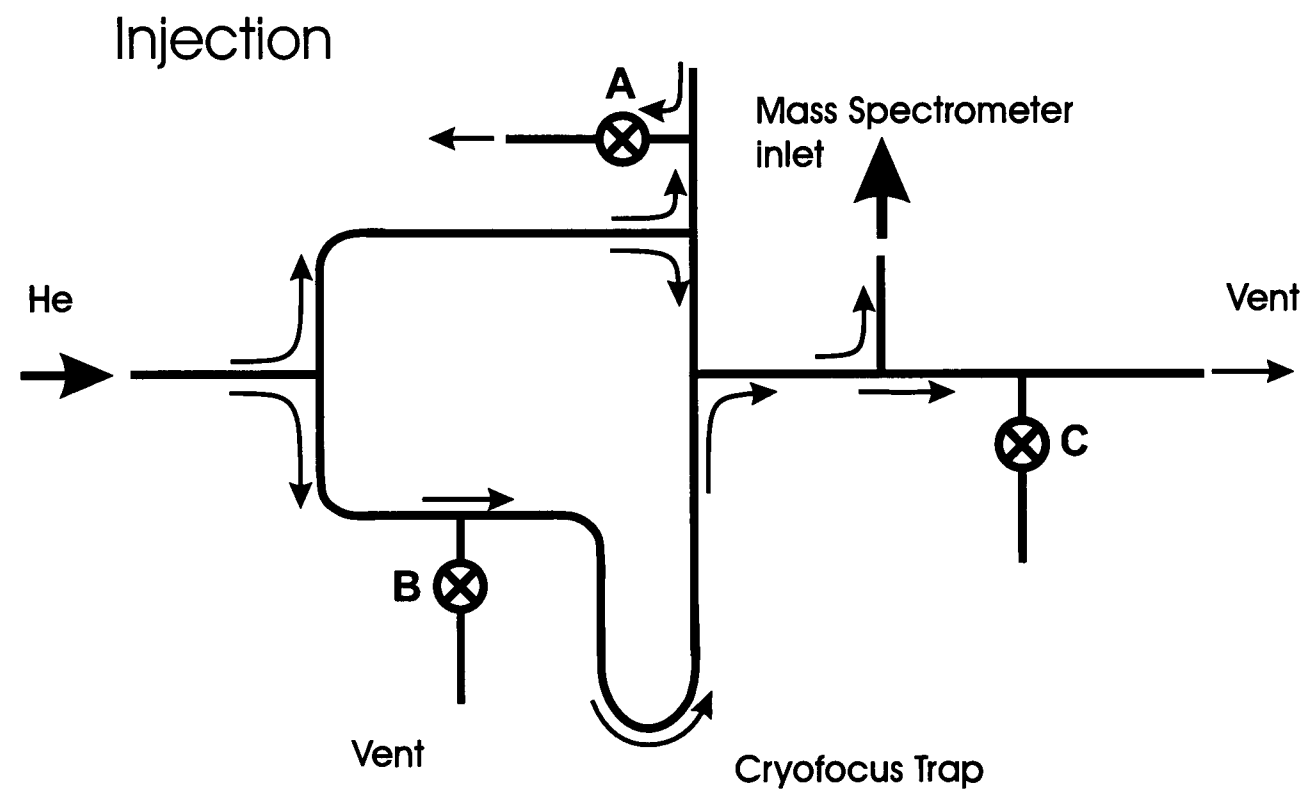


Figure 2.8: Detail of GC system. Arrows show direction of He flow, valves A, B and C as described in text. During the cryofocus stage, A is closed and B and C are open, such that oxygen is carried from the silica gel loop and trapped onto the cryofocus loop (at liquid nitrogen temperature). During the injection stage, A is open and B and C closed such that the flow of He through the cryofocus loop is reversed and oxygen from the now thawing loop is carried through into the GC column and mass spectrometer inlet.

oxygen is ionized to O^+, and accelerated by the 10kV potential, entering and exiting the magnetic field at 26.5° . This arrangement maximizes mass dispersion and increases analytical sensitivity. Three faraday cups allow for simultaneous measurement of 32I, 33I and 34I currents, representing $^{16}O^+$, $^{17}O^+$ and $^{18}O^+$ respectively. A time-integrated output allows calculation of $\delta^{18}O$ and $\delta^{17}O$ (figure 2.9). Analysis is calculated by integrating the area under the curve, providing a sample size measured in Volt Seconds, and comparing to the standard gas injection. Due to possible fractionation effects and the need to maintain linearity, the standard gas size should be as close to that of the sample as possible.

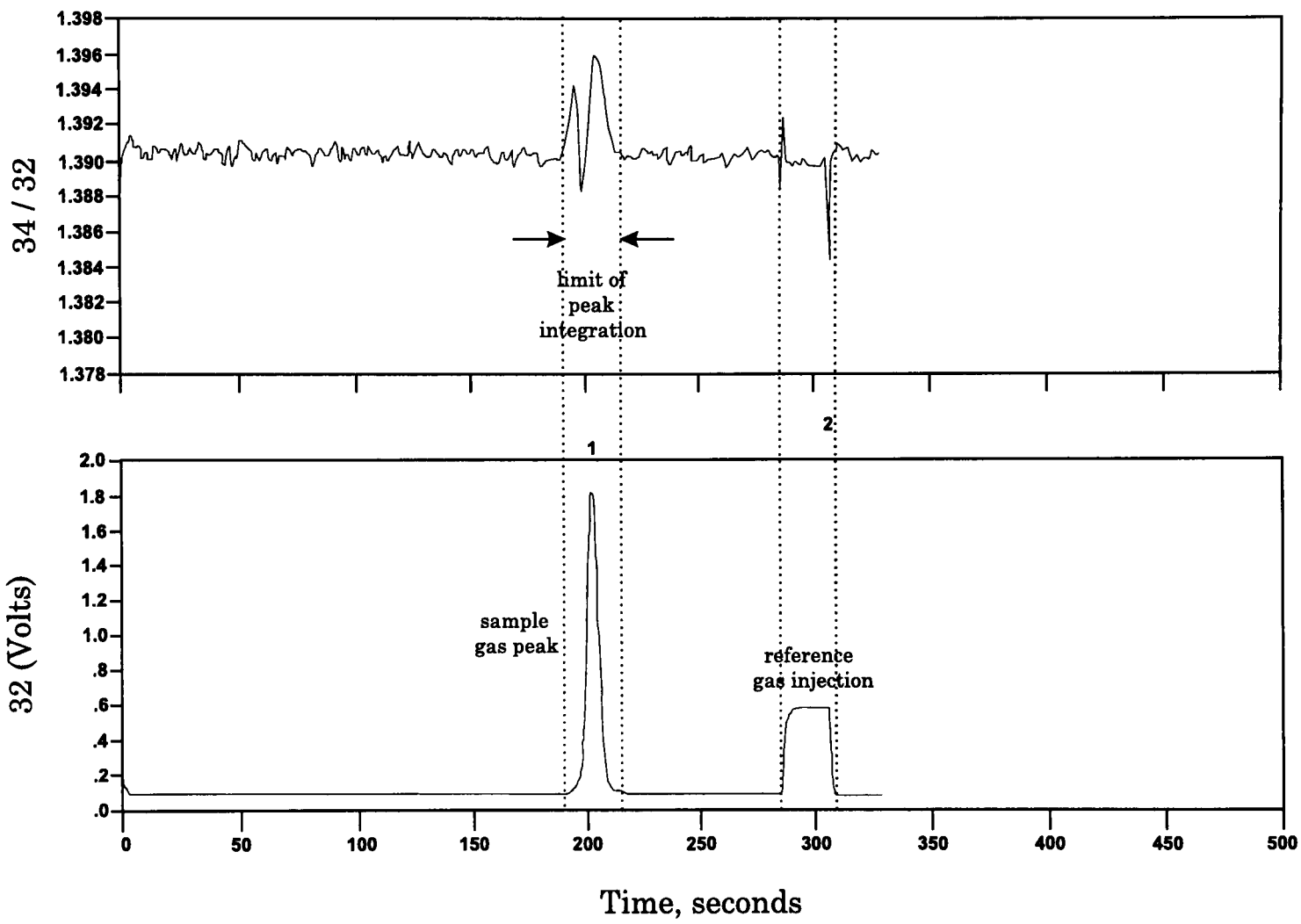


Figure 2.9: Typical analysis showing the measured 34/32 ratio ($\delta^{18}O$) trace (top) and the sample and reference peaks detected on the 32 cup. The dotted lines show the limits of integration to yield an area, and thus a result. This is an analysis of Garnet 6A, sample 5-23, area 10.464 Vs, uncorrected $\delta^{18}O$ 10.38 ‰ ; reference 7.28‰ .

2.3.7 Analysis by microvolume and bellows

Prior to later modification, the instrument also allowed larger samples to be run by use of the microvolume or mass spectrometer bellows. Instead of liberated oxygen being passed into the GC system, the gas was trapped either within the Finnigan MAT 252 microvolume inside the mass spectrometer (onto silica gel at liquid nitrogen temperature) or held in the mass spectrometer bellows, and then released into the mass spectrometer source, being measured against a reference gas also held in a bellows.

These methods have the advantage of allowing a mass scan to be performed upon the sample to check for impurities. However, for analysis the required sample size is some 5-20 times that of GC analysis (20 μmoles, and ablated pits of some 500 - 600μm are not uncommon. However, from October 1998 the line was rebuilt, and the option of microvolume runs was no longer available. The reason for this was to optimise the flow of gas for GC-*irms* analysis, by removing the dead-volume associated with the additional valve necessary to direct flow towards the microvoloume and bellows.

Chapter 3

Development of the isotope line

3.1 Introduction

The development and calibration of the Oxford laser fluorination line has the ultimate aim of performing *in-situ* oxygen isotope analyses in metamorphic silicate samples by UV-ablation and GC-*irms*. This chapter describes the major milestones in the evolution of the method, from the early standard runs through to initial results from Hoosac Schist samples. All development results are summarised in appendix A, and all Hoosac sample results are detailed in appendix B.

The overall development of the Oxford laser microprobe has been a team effort between myself, A.M. Jones and Dr E.D. Young, who have investigated palaeoclimate and non-terrestrial samples respectively; my role was in applying the technique to metamorphic samples, and in this chapter I outline my own contribution to the project, including the unique problems associated with UV fluorination of pelitic schists. All results detailed in this thesis (both within the chapters and the appendices) are my own (unless otherwise stated). In parallel with my own work has been the development of the method for the analysis of both meteorites (Young & Russell, 1998), and biogenic phosphate samples (Jones *et al.*, 1999).

It is important to regard every analysis presented here as an experiment in its own right. Currently, no other analytical facility is capable of *in-situ* oxygen isotope analysis at such

a high spatial resolution and with such a potentially high precision. Thus the data presented here both in the development section, and those later results yielded from the pelitic samples are unique. Included in this thesis are potentially the first ever analyses of garnet oxygen isotope zoning over 0.8‰ on the 100μm scale (observed within a 2mm garnet), as well as the first time this method has been applied to staurolite, and mica minerals. Chapter 7 details final isotope results for the purpose of the metamorphic investigation.

3.2 Routine sample analytical technique

What is described here represents the current optimal analytical technique for silicate samples (although due to the continual evolution of the analytical method parameters have varied over the course of the development process).

Sample mineral chips are prepared from the rock specimen, and are polished and cleaned. Degreasing is a necessity since fluorine will adversely react with any organic contamination on the surface of the sample (and, indeed, the surface of the chamber and line - see the later information on sample preparation). The sample chamber pressure is equalized with atmospheric pressure by bleeding helium into it; the sample is loaded, and then the chamber sealed and evacuated.

Vacuum pumping down to baseline (1.0×10^{6} torr) can take several days; the use of a heat lamp to warm the sample and chamber to about 60°C helps the sample de-gas and the system to pump down.

Prefluorination is required to purge any remaining contamination from both the sample surface, and from inside the chamber. Surface reactions are inevitable due to the presence of micro-cracks in the mineral sample which may harbour water, or any other reactive substance. By allowing the sample to sit in an atmosphere of fluorine at greater pressures than used for regular analysis, reaction between the fluorine and any contamination can occur. This leads to a reduction in the number of blank runs necessary to achieve blank stability. Usually allowing the sample to sit in fluorine for 4-5 hours is sufficient, perhaps with subsequent fluorinations after a few days.

Occasionally, a blank may be run where 15 millibar (mbar) F_2 is allowed to sit over the sample for 45 minutes or more, and then passed through the line and analysed as per normal. This appears to help accelerate the 'seasoning' of the line.

For analysis, the UV source is tuned by adjusting the angle of the BBO crystal relative to the laser beam to ensure optimal frequency doubling, to yield stable, optimal power. The chamber pressure (dynamic vacuum) must reach the normal baseline of the order of 1.0×10^{-6} torr with mechanical pumping, reducing to 3.0×10^{-7} torr with cryogenic pumping (when two liquid nitrogen traps on the line are chilled). The two traps are chilled with liquid nitrogen for each run, and then thawed and heated between runs, to effect line clean-up.

The chamber is closed off from the line and vacuum pump, and fluorine is bled in. Currently between 1 and 3 mbar F_2 is sufficient; the particular quantity is kept constant for all runs, both laser analyses and blanks. Figure 3.1 shows a flowchart detailing the normal analytical routine.

The chamber is then isolated, and the mineral ablated. A beam chopper (which strobes the laser) is used to avoid drilling too deep, the stage being rastered 4-5 times with respect to the laser beam to give a pit some $150\times80\mu$m in size, and 30μm deep.

After ablation, the chamber is immediately opened up to the isotope line, allowing the gases to migrate. Excess fluorine is passivated by the hot (100°C) KBr, and the two cryofocus traps condense any bromine produced, and any other condensable contaminants.

There are three stages of oxygen transfer; the first involves clean-up of the analyte by killing excess fluorine and trapping condensables; the second stage traps the analyte oxygen upon silica gel loop at liquid nitrogen temperature, and the third transfers the analyte from the (now) thawing silica gel onto the cryofocus loop with He-carrier flow. Normal times for these are 5, 10 and 10 minutes respectively, although various times have previously been used, and are reported in appendices A and B.

The oxygen is transferred to the first silica gel loop by opening the valve separating the two parts of the line. Once transfer is complete (after 10 minutes), this valve is closed

again to isolate the loop with all analyte oxygen trapped. The VALCO valve is then switched to allow helium to pass through the silica gel loop, which is then allowed to thaw, releasing the oxygen into the stream of flowing helium (10 minutes). The helium carries the oxygen into the GC-system, where analyte is trapped upon another silica gel loop cooled to liquid nitrogen temperatures (the cryofocus trap).

After this final trapping of sample gas, the software automation takes over, activating the two switching valves, which reverse the flow of helium through the cryofocus trap. At this point the silica gel loop is allowed to warm to room temperature naturally, releasing the oxygen into the flowing helium, which carries it through the gas chromatograph (GC) column, the GC interface, and eventually injects it directly into the source of the mass spectrometer. Since the cryofocus trap is of a much a smaller diameter than the silica gel loop, it thaws almost immediately, allowing a 'bundle' of oxygen into the helium rather than the slow release as effected by the larger silica gel loop.

The mass spectrometer is fully automated by a computer running the ISODAT program. An aliquot of reference gas is injected to follow the sample through the mass spectrometer, with which it is compared and the final result calculated.

3.3 The Blank

The quantity of sample analyte passed though the GC-*irms* system is of such a small size (tens of micromoles) that background oxygen can have a major effect upon analysis. Reaction of fluorine with mineral surfaces; reaction of fluorine with the surface of the line or with any minor contaminants contained therein; the impossibility of producing a perfect seal within the vacuum tubing connectors; the impossible goal of a perfect vacuum - these all play their part in the inevitable existence of background oxygen, which will be collected in the normal manner in addition to that released through mineral ablation. Because of this, complete quantification of this blank effect is a necessity, performed by repeated blank runs, which passes fluorine through the system in an identical manner to that during analysis. Blank values (both size and $\delta^{18}O$) evolve until they reach a steady state.

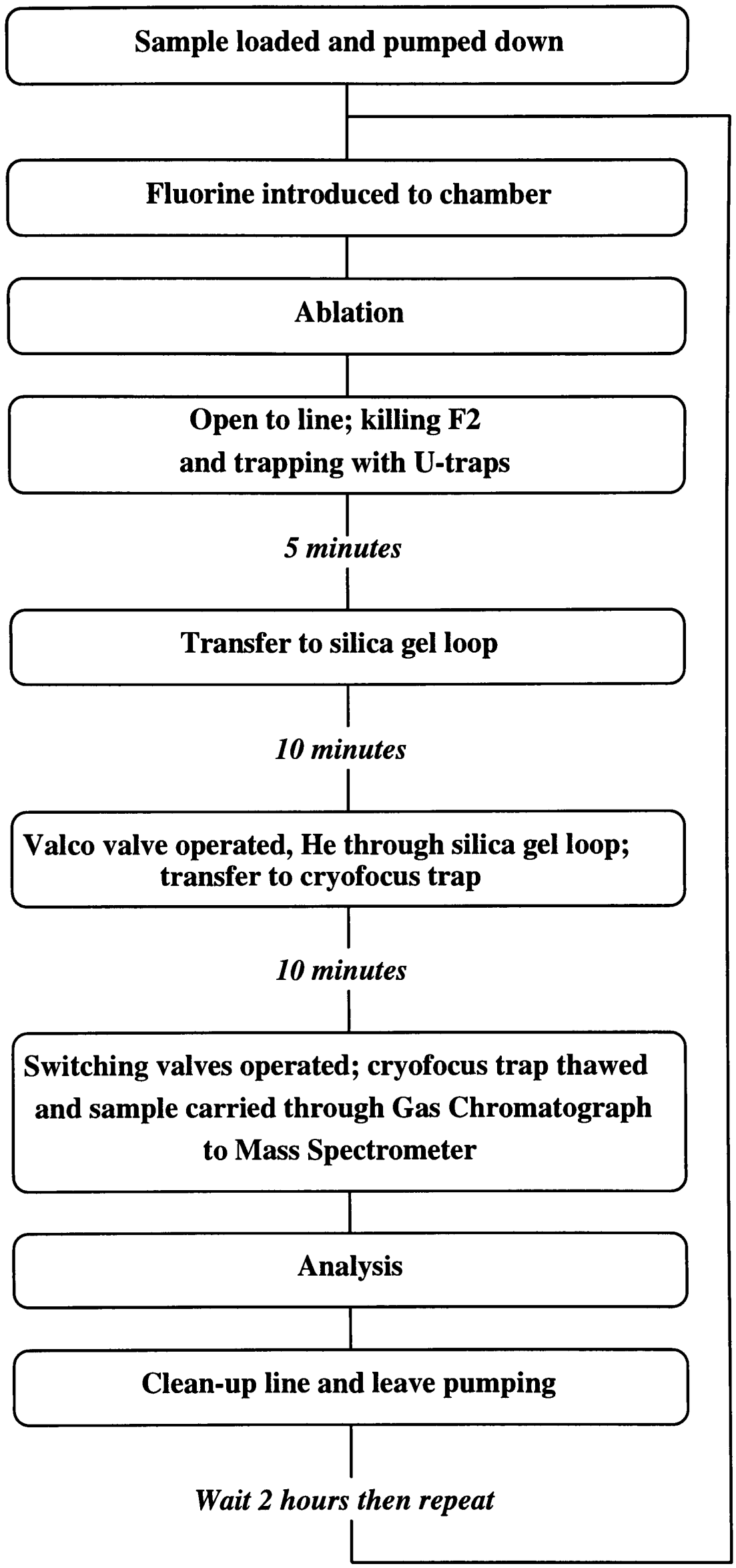


Figure 3.1: Flowchart detailing stages in typical sample analysis; for a blank run the ablation stage is skipped.

Blank sizes are proportional to fluorine quantity; if a greater quantity of F_2 (greater partial pressure of fluorine acting on the mineral surface) there will be a greater tendency to react. Table 3.1 shows some typical values for the blank under differing conditions.

F_2 mbar	Peak Area, Vs	$\delta^{18}O_{SMOW}$	$\delta^{17}O_{SMOW}$	comment
	0.57	4.1	0.4	cryofocus trap only
	0.55	5.0	6.1	silica gel loop + cryofocus trap only
	1.02	6.8	4.9	fluorine-free blank run, empty chamber
4.8	2.04	1.3	0.4	over empty chamber, heating bellows
4.8	1.73	1.5	0.2	over USNM augite, heating bellows
4.8	1.45	5.6	2.5	over USNM augite, not heating bellows
8.0	2.02	7.1	3.8	more fluorine
4.8	6.8	8.5	3.9	new backflush line
4.8	2.5	7.6	3.3	new cryofocus trap
26.0	3.30	6.6	4.2	more fluorine
8.0	2.896	10.31	4.65	over sample 6a
1.2	2.482	8.28	4.42	over sample 19a

Table 3.1: Typical blank values from varying conditions, in chronological order over several years of blank measurements.

Blanks as a fraction of total sample size can range from one tenth to perhaps up to a third of the size of the sample. This figure may be minimised by (a) running as large a sample as possible, although there is an upper ceiling limited by mass spectrometric sensitivity; and (b) performing repeated blank measurements until a steady-state is reached, and a reliable value for the blank determined. Latter-day experiments run over Hoosac schist samples typically give blanks of 2-3Vs, with analyses of 20Vs or greater, giving 10% blank effect.

Blanks are accounted for in the sample measurement by using a linear end-member mixing correction as shown in equations 3.1 and 3.2 (where x is the sample O_2 fraction).

$$\delta^{18}O_{\text{sample}} = \frac{\delta^{18}O_{\text{measured}} + (x-1)\delta^{18}O_{\text{blank}}}{x} \tag{3.1}$$

where

$$x = \frac{Area_{\text{measured}} - Area_{\text{blank}}}{Area_{\text{measured}}} \tag{3.2}$$

For silicate samples it is necessary to run blanks for several days after initial fluorination. It has been found that the blank value evolves during this period, either due to the conditioning of the sample with repeated runs, or an unquantified line 'seasoning'

effect. Several subsequent fluorinations may also be required during the blank analysis period.

The other controlling factor in blank evolution is heating the metal bellows on the isotope line. The bellows are necessary to allow the isotope line to flex as the sample chamber is being moved (relative to the laser beam). However, metal bellows suffer from having a large surface area. During prefluorination of the sample, that part of the isotope line containing the KBr trap and bellows has to be left isolated (since it is impossible to pump when the chamber is closed). Despite the KBr trap temperature being routinely reduced to 50°C during prefluorination to limit any contamination, bromine emitted from the hot KBr trap can adsorb onto the large surface area provided by the bellows. This can be cleaned up by heating the bellows above 200°C, with associated heating of the two U-traps. However, it has been observed that this clean-up procedure has a marked effect upon both the size and value of the subsequent four to five blank measurements, by pushing it both large (size) and light ($\delta^{18}O$) (see 3.10.1). Because of this phenomena, the bellows are only heated every few days when it is suspected that contaminants have built up.

3.4 Sample preparation

Samples were sectioned into thin section-sized chips (15×30mm), about 10mm thick. These chips were then machine-polished, using 5μm diamond dust. Such polishing allows mineral textural relations and inclusions to be observed. Polishing is, however, not only important for observational considerations: a smooth surface has less surface area and therefore both less blank and less potential areas for adsorption of liberated oxygen. It also potentially provides a superior surface for the purposes of ablation.

Inspection with microscopy under reflected light allowed selection of specimens for analysis on the basis of the textural relations between minerals. Additional mapping using backscattered imaging on a scanning electron microscope (SEM) showed not only textural relations but also potential sources of contamination such as mineral inclusions.

Selected areas of specimens were then cut down to produce a thin (2-5mm) chip with

parallel sides using a slow-velocity circular saw, and further chipped down to extract the desired area. The samples were then cleaned by ultrasounding twice in distilled water (for 30 minutes each time), and left to dry thoroughly in a vacuum oven at over 100°C for several days to purge any water left in cracks. These were then loaded directly into the sample chamber.

Isotope standards were prepared by chipping off an appropriate sample, hand-polishing with 3μm diamond-dust and cleaning in an analogous way to the samples. Since these standards are considered isotopically homogeneous they do not require mapping. Both samples and standards were stored in a vacuum dessecator to ensure they are kept moisture free.

3.5 Standards

The isotope line was calibrated using a number of known standards. A standard is a sample, either gas, or mineral, that has an isotopic value verified by an external laboratory. Analyzing standards represents both a means to initially develop the method by adjusting various parameters associated with the analytical procedure, and a monitor of both short- and long-term analytical fluctuations. The Oxford isotope line was designed to yield a real isotopic value without the need for correction. The direct measurement of O_2 means no conversion step to CO_2 is required.

3.5.1 Gas standards and the link to SMOW

All $\delta^{18}O$ and $\delta^{17}O$ values are reported relative to standard mean ocean water (SMOW). Two primary standards were used; initial calibration was undertaken by use of sealed vials of Panama oxygen gas, a standard gas that had been reliably analysed at the Geophysical Laboratory, Washington DC, USA. The $^{18}O/^{16}O$ of the Panama gas was determined by conventional dual-inlet mass spectrometry, after quantitative reaction with hot graphite to form CO_2 followed by comparison with the Geophysical Laboratory reference gas. The Panama gas has a value of 48‰ vs SMOW. The other primary standard was oxygen from air that has a nominal value of 23.5 $\pm$ 0.3‰ vs SMOW (Craig, 1972).

Mineral	Source	Smithsonian ref.	accepted $\delta^{18}O_{SMOW}$ range, ‰	Reference
UWG-2 Almandine	New York, USA		5.8	Valley *et al.* (1995)
USNM Almandine	New York, USA	107144	6.1	Rumble *et al.* (1997)
USNM Forsterite	Arizona, USA	136718	5.2 - 5.8	Rumble *et al.* (1997)
USNM Augite	New Zealand	133866	5.9 - 6.0	E.D. Young, pers. comm.
USNM Schorl	Finland	R11871-1	9.0 - 9.2	Rumble *et al.* (1997)

Table 3.2: Silicate standards used for UV analysis. The UWG-2 and USNM Almandine are both samples of the Gore Mountain garnet.

One tank of pure O_2 gas (grade 5) was used as secondary standard. The $^{18}O/^{16}O$ of this was determined in Oxford by measurement against the Panama gas. This secondary standard was used as the Oxford reference gas.

Calibration of $\delta^{17}O$ was performed by an iterative comparison between models of mass-dependent fractionation and measured $^{17}O/^{16}O$ of geological samples.

3.5.2 Mineral standards

Mineral standards are chosen on several criteria: firstly, they must be as free from inclusions as possible; secondly, and perhaps the most important, is that they must be homogeneous with respect to $\delta^{18}O$. A potential pitfall with isotopic observations at a resolution at least one order of magnitude smaller than conventional laser isotope analysis is that one may observe heterogeneity on a scale that has not been distinguished before. The only other instrument capable of a spatial resolution on the 100μm scale is the ion microprobe (indeed they work on scales down to 10μm). The Ion Microprobe facility at Edinburgh University, UK, also uses the Gore Mountain Garnet standard, and while their precision is of the order of $\pm$0.8 - 1‰ (Valley & Graham, 1991, 1996) they claim homogeneity on the 20μm scale (C.M. Graham, pers. comm.). Table 3.2 details standard minerals used for calibration of analysis with the UV laser and accepted $\delta^{18}O$ values. Errors are fully discussed in chapter 7.

Gore Mountain Garnet

Special mention must be made of the Gore Mountain Almandine. There are two standards of Gore Mountain Garnet, a locality within the Adirondack Mountains, New York state, USA. The USNM almandine, from the Smithsonian Collection (No. 107144), Washington, DC, USA; and a specimen from the University of Wisconsin (UWG-2), as reported in Valley *et al.* (1995). The USNM almandine has a value of 5.8-6.1‰ depending on the laboratory. The Wisconsin garnet standard (UWG-2) was prepared from a single large porphyroblast, homogeneous on the millimetre scale prior to cutting. The $\delta^{18}O$ has been determined in seven laboratories with either the IR laser probe or bomb method, the laboratory average given as 5.78‰ (Valley *et al.*, 1995).

3.6 Development

The Oxford laser line has been constructed to allow analysis with two different lasers. The Ultra-Violet laser is the principal analytical tool, used for *in-situ* ablation of most silicate minerals for micro-analysis by GC-*irms* (although it has also been used for macro analysis, taking the analyte via the microvolume). Initial development also used the CO_2 laser (IR source) for heating of larger mineral chips to test the viability of the isotope line. Whilst appendix A details all results, only those pertinent to the development process will be discussed here.

Development can be broadly divided into 5 sections:

- test-gas runs to assess the viability of the GC-*irms* system to quantitatively transfer and analyse the gas - this was largely completed prior to my arrival
- using BrF_5 as the fluorinating agent and the CO_2 laser for analysis of mineral chips (especially quartz) - this tests the viability of the chamber and isotope line, designed to replicate those IR-heating systems already proved successful - this is not detailed here but proved moderately successful
- BrF_5 and the UV laser for mineral *in-situ* analysis, taking the sample to either the microvolume or GC-system - allows assessment of the ability of the UV laser to

ablate mineral specimen, and testing of the carrier-flow system

- with F_2 as the fluorinating agent and the UV-GC-*irms* system for *in-situ* analysis on the sub-millimetre scale - using fluorine gas after problems with BrF_5 ; leading up to the initial analysis of schist samples
- analysis of Hoosac Schist samples - and complications introduced by large specimens containing multiple minerals

The chronological development is described below.

3.7 Construction of the line, test gas runs and the CO_2 laser

Purchase and construction began in early 1995, and the line was largely built upon my arrival in 1996. My role in development had been preceded by a year of test-gas analysis to check the viability of sample transfer via the GC-*irms* system. Test-gases (oxygen of a known isotopic composition) were bled into the first silica gel loop, and then transferred to the mass spectrometer. The results of these experiments proved that transfer was possible with no fractionation effects, and as such subsequent development generally focused upon the ablation and gas transfer and clean-up processes, occurring in the chamber and isotope line, as possible sources of error and fractionation.

The infra-red source was used to analyse separated sample chips, to replicate other infra-red heating isotope lines (*e.g.* Sharp, 1990), and heat up mineral chips within a fluorinating atmosphere. The liberated gas was passed through to either the bellows of the mass spectrometer, or more usually, to the microvolume for smaller quantities of gas. Initial analysis of a quartz standard yielded $\delta^{18}O$ =11.68‰ ±0.6 (1σ); this was 0.7‰ heavy. Later attempts to heat small enough sample chips in order to utilize the GC-*irms* system have met with mixed success (a reported accuracy of ±5‰ ; A.M. Jones pers. comm.).

3.8 Ultra-Violet laser and BrF_5

Initial investigations with the UV laser, using BrF_5 as a fluorinating reagent, drilled large enough pits to produce sufficient gas quantity to analyse via the microvolume. This allowed assessment of the efficiency of UV lasing without the added uncertainty of passing a sample through the GC-*irms* system.

The Ultra-Violet laser proved to be extremely efficient in its ability to ablate samples. The inherent power and high pulse frequency of the copper-vapour laser meant that sufficient gas for a GC run could be produced by ablating for a matter of seconds. In fact, due to the high fluence, there was a concern that the laser would drill too deeply into the mineral causing the plume to visibly die (beyond circa 50μm deep), potentially leading to inefficient fluorination and thus isotopic fractionation. To prevent this occurring either the speed of rastering could be increased, or a beam chopper could be employed, which consists of a rotating (12Hz) disc with apertures that strobe the beam and effectively reduce laser fluence. The latter approach proved more successful, as it gave greater control over the ablation process without sacrificing spatial resolution, and, with practice, neat, shallow pits could be created in 2-5 rasters (see figure in chapter 2).

3.8.1 UV, BrF_5 and macro-analysis using the microvolume

A specimen of Gore Mountain almandine was prepared and loaded. The sample was prefluorinated with 44.1 mbar BrF_5 overnight. Table 3.3 details $\delta^{18}O$ results. Analytical mean excluding the first runs of each day is $\delta^{18}O = 6.61 \pm 1.3$ (1σ, n=16). This represents an accuracy, or $^{18}\Delta$ between the measured and accepted value of +0.5-0.6‰ .

These and other results (obtained by co-workers) proved that the UV laser was inherently capable of coupled ablation-fluorination, at least on a macro scale, although it should not be forgotten that even using the microvolume represents a reduction in sample gas size of at least one order of magnitude over previously reported analytical techniques.

Run	BrF_5, mbar	V_{32}	$\delta^{18}O_{SMOW}$	comment
2-46†	24.2	1.351	10.652	chopper
2-47	15.0	2.043	8.130	
2-48	15.0	2.300	9.468	no chopper, deep
2-49	15.6	3.500	6.769	chopper
2-50	15.3	5.000	6.553	chopper
2-51†	15.0	3.960	7.527	
2-52	55.8	1.500	4.982	no chopper
2-53	56.8	2.191	5.090	
2-54	73.7	1.350	4.759	no chopper
2-55	35.3	2.700	5.565	
2-56	23.7	3.960	5.834	
2-57†	23.7	4.020	4.742	
2-58	25.8	2.864	5.940	deep hole
2-60	23.2	2.807	7.042	
2-62†	24.0	4.306	9.384	
2-63	25.7	5.070	6.954	chopper
2-64	50.0	2.373	7.480	
2-65	28.1	3.263	10.767	10% chopper
2-66	62.5	1.829	7.964	
2-67	70.1	1.274	6.779	no chopper, pc-square
2-68	74.8	0.680	7.075	
2-69	69.8	1.939	6.178	
2-70	73.7	1.800	6.996	

Table 3.3: Gore Mountain almandine analysed with UV, BrF_5 and the microvolume; †= first run of the day.

3.9 BrF_5 and the switch to F_2

In the light of the relative success of garnet UV macroanalysis with BrF_5, investigations began to concentrate upon passing the sample through the GC-*irms* system, however early experiments produced rather unexpected results.

GC-*irms* analysis with BrF_5 on several mineral samples gave wildly varying results - with the concern that analyses were purely random. However, when the size of sample (in volt seconds) was plotted against *corrected* $\delta^{18}O$ (see figure 3.2 for almandine, schorl and forsterite results), a curious trend was observed - an apparent linear relationship between the peak area of the sample gas and the corrected $\delta^{18}O$. Further investigations confirmed that this was a real phenomenon (A.M. Jones, pers. comm.).

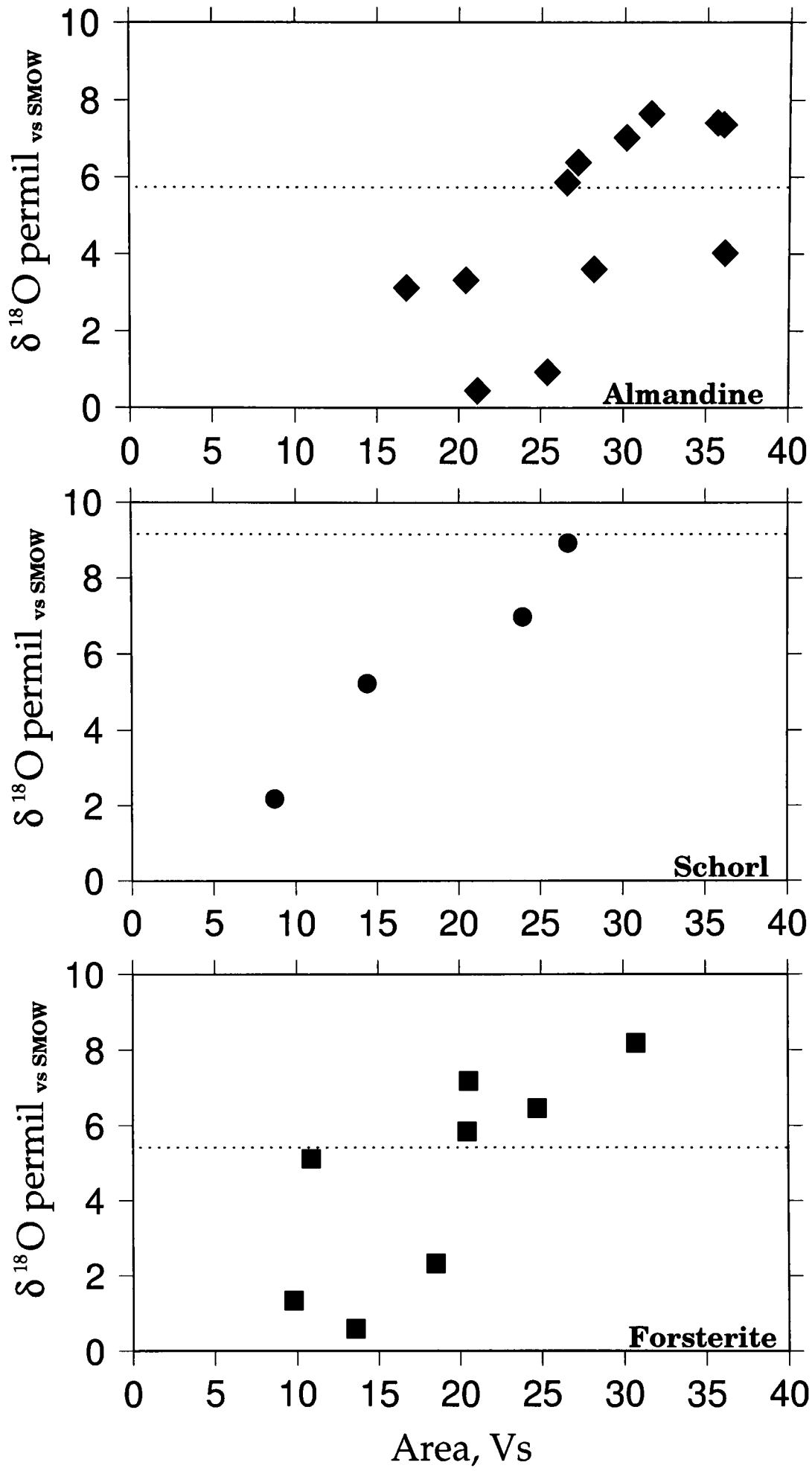


Figure 3.2: Size-dependence of GC-*irms* analysis using BrF_5 . Corrected $\delta^{18}O$ data are shown for USNM almandine, schorl and forsterite; dotted lines show accepted $\delta^{18}O$. (Schorl and forsterite collected by A.M. Jones and E.D. Young - presented here for comparison).

Since test gas runs had proved the viability of the GC-*irms* system in quantitative gas transfer, attention focused upon the ablation process. It was this unpredictable size dependence that lead to concern about the viability of BrF_5 as an effective fluorinating agent, and this fuelled the switch to fluorine gas.

3.9.1 Fluorine gas

Bromine pentafluoride (BrF_5) was initially chosen for use as a fluorinating reagent for several reasons:

- BrF_5 has been proven as an effective fluorinating agent on both conventional bomb isotope lines (*e.g.* Clayton & Mayeda, 1963), and infra-red laser isotope lines (Sharp, 1990; Chamberlain & Conrad, 1993; Young & Rumble, 1993)
- BrF_5 is easier to handle, being condensable under liquid nitrogen temperatures, and thus simpler to clean-up and potentially easier to separate during cryogenic clean-up
- BrF_5, while still a hazardous chemical, is considered a safer reagent than F_2 gas
- F_2 requires either a fluorine tank, which is only perhaps 98% pure F_2, or a complex fluorine generation system; pure BrF_5, on the other hand, can be dispensed directly from the cylinder, although with the Oxford line it was double-distilled via two Kel-F tubes prior to use

However, due to the BrF_5 size-dependence problem, a switch to fluorine became inevitable. A fluorine generator was installed, where fluorine was produced as per the method described by Asprey (1976). Above 300°C fluorine is generated; below this it is resorbed, allowing any excess fluorine to be passively resorbed overnight. After installation, blank testing proceeded, and mass scans performed on the results to check for impurities.

3.9.2 Initial GC-*irms* analysis with UV and F_2

Early F_2 analyses were extremely promising, with no visible size-dependence that characterized BrF_5 analysis. Indeed, sample size appeared to have no bearing upon $\delta^{18}O$. Figure 3.3 plots corrected almandine and forsterite $\delta^{18}O$ analysis collected by myself, A.M. Jones and E.D. Young (as summarized in Young *et al.*, 1998b). This shows no apparant dependence on corrected $\delta^{18}O$ with sample size.

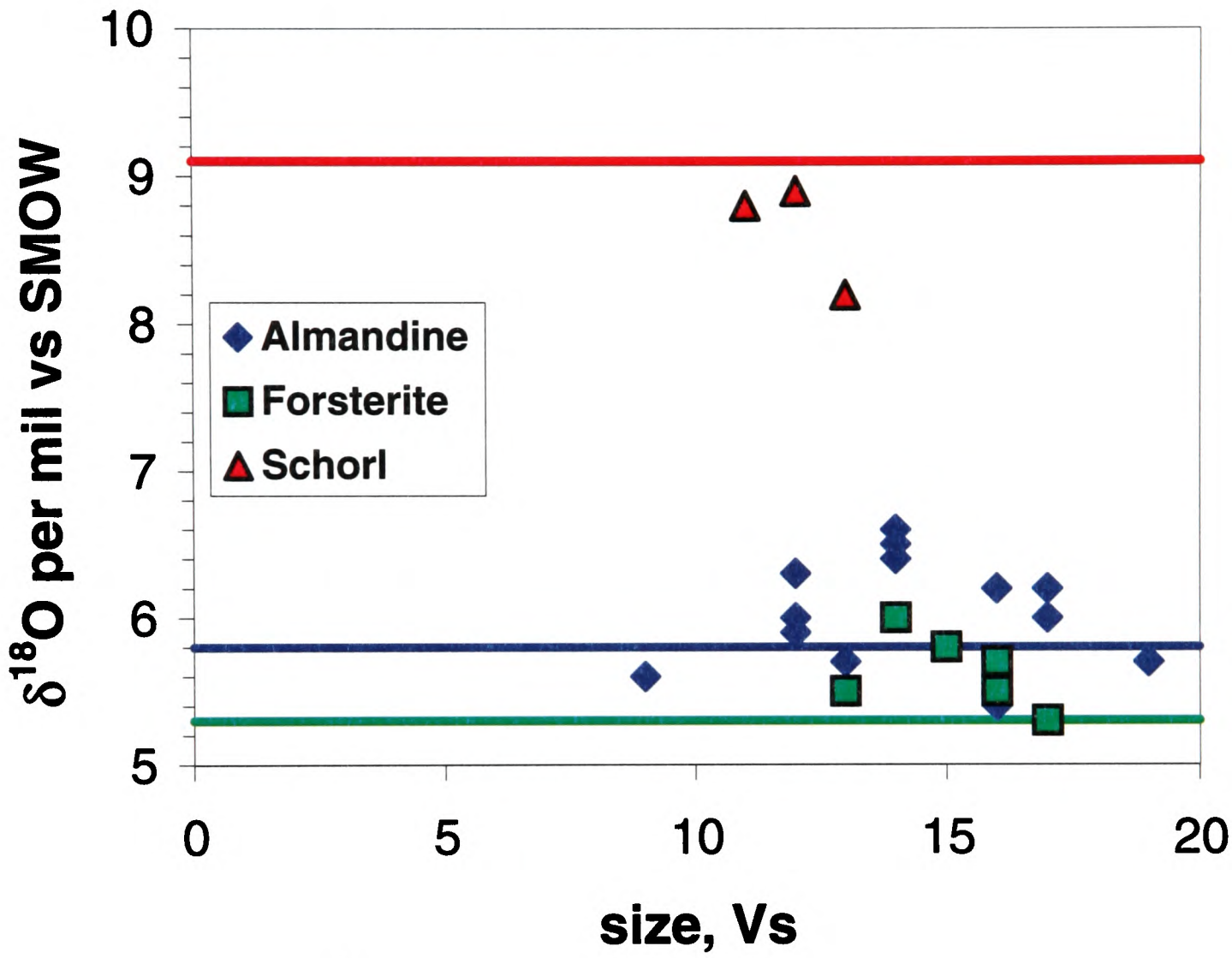


Figure 3.3: Plot of corrected $\delta^{18}O$ analysis of almandine, forsterite and schorl using F_2 and GC-*irms*; data collected by myself, A.M. Jones and E.D. Young and reported in Young *et al.* (1998b). The size-dependence observed with BrF_5 analysis is not evident here. Horizontal lines give expected values of almandine (5.8), forsterite (5.3) and schorl (9.1).

A summary of collected data for USNM almandine, USNM schorl and USNM forsterite is shown in table 3.4; this also shows the total of collected data by myself, A.M.Jones and E.D.Young.

These data points were the first indication that the entire system as an analytical tool was

Sample	corrected $\delta^{18}O_{mean}$	precision $\pm$ (1σ)	Accuracy per mil
almandine	6.2	0.5	+0.1 → +0.4
schorl	7.9	0.4	- 1.1 → -1.3
forsterite	6.4	0.9	+0.6 → +1.2
almandine	6.1	0.3	+0.0 → +0.3
forsterite	5.6	0.3	-0.2 → +0.4

Table 3.4: Summary of collected data for almandine, schorl and forsterite. Top shows my data, bottom shows combined data collected by myself, A.M.Jones and E.D.Young, and published in Young *et al.* (1998b).

inherently viable; the adoption of fluorine gas as the fluorinating reagent was perhaps the most important developmental step taken. Subsequent analytical problems proved to be due more to minor parameters such as freezing times, reagent quantity and line conditioning, but none had the fundamental impact that switching to fluorine gas did. It paved the way for the later successful analysis, and proved that the Oxford laser isotope facility could give real, reproducible results, certainly from standard minerals.

3.9.3 Explanation for the BrF_5 size-dependence problem

Debate as to the cause of the problems associated with BrF_5 fluorination has focused upon the period during and immediately after ablation. Since fluorination occurs in or adjacent to the plume of hot plasma forming immediately above the target mineral, the few nanoseconds during which the laser pulse is active are potentially critical to how quantitative fluorination is. A plasma generated during ablation in an atmosphere of BrF_5 is much smaller and less bright than that with fluorine gas (from observations during analysis). Young *et al.* (1998b) presented a theory to explain this phenomena, where shockfronts forming within the BrF_5 envelope create something approaching a vacuum between the fluorinating reagent and the plasma forming from the mineral, impeding mixing of BrF_5 and plasma, and hindering fluorination. In contrast, fluorine gas is predicted to mix readily, coming closer to complete reaction.

The more sample gas present, the less proportionally would be the effect of inefficient fluorination. In addition, light ^{16}O atoms would, due to kinetic effects, possibly be more likely to fluorinate, explaining why with smaller quantities of gas a lighter $\delta^{18}O$ is

measured.

3.10 Routine standard analysis - fine-tuning the method

During the two months from September-October 1998, an augite, garnet and finally a sample of Hoosac Schist (sample 6a) were analysed using the GC-*irms* method. The line had been rebuilt, removing the option to use the microvolume, shortening the path-length that the gas has to migrate down, and with less 'dead volume' due to the removal of a valve.

The analysis of the USNM augite, and the garnet after it, proved to be something of a watershed in understanding the line. During these two months the following were achieved:

- changing the length of the transfer tubing that allows the helium and sample gas to flow into the GC-system - this had a significant effect on blank reduction
- changing the silica gel crystals in both the silica gel and cryofocus loops, reducing blanks to a more manageable level
- better quantification of the effect of the blank
- better understanding of how a sample needs to evolve and be treated to give more reliable results
- quantifying the effect of heating the transfer bellows
- showing that samples previously thought too large to sample were, if treated correctly, capable of producing consistent, reliable data

3.10.1 The bellows effect

As is normal practice, blanks were run over a sample of augite until they had settled. The line bellows were being heated between runs up to 200°C for 5 minutes whilst pumping - a practice used with success for phosphate analysis to help purge the line

of the greater contaminants ablation of such samples can liberate. They were then left to cool completely before the next sample was run (generally 1 - $1\frac{1}{2}$ hours between runs was not unusual), since reaction between warm steel surfaces and both oxygen and fluorine will promote both fractionation (in the case of the former), or reaction producing a thin, but reactive, layer of FeF_2 on the inside of the line.

However, these blanks, although small, were unusually light (some 2-3‰). During subsequent analysis of augite the corrected $\delta^{18}O$ drifted down towards 3.5‰ ; this drift was only arrested by ceasing to heat the bellows between runs (see table 3.5). Therefore, at this juncture, the cause of the consistently light results was thought to be an effect generated by the practice of heating the bellows.

Run No	F_2 , mbar	Area, Vs	$\delta^{18}O_{SMOW}$	laser, mV	
4-191	4.6	12.177	5.04	18.6	
4-192	4.6	11.121	4.73	15.3	
4-193	4.5	11.604	6.56	16.3	
4-194	4.4	10.744	5.33	15.8	
4-195	5.0	25.041	4.31	16.9	
4-197†	4.8	10.095	5.12	14.9	
4-198	4.8	15.493	3.98	15.7	
4-199	5.6	14.220	4.28	15.1	
4-200	4.6	10.297	3.46	14.8	
4-201	6.2	7.847	4.97	15.5	not heating bellows
4-202	4.2	12.684	6.01	14.5	not heating bellows

Table 3.5: Corrected GC-*irms* $\delta^{18}O$ for the USNM Augite, showing lightwards drift.

Investigations into the bellows effect followed; figure 3.4 charts the evolution of the settled blank $\delta^{18}O$ run over the augite sample over a few days, from loading. During the bellows heating the blank stays around 2‰ ; however, there is a sudden jump when the transfer bellows were not heated between runs (up to 6-8‰), and another slight jump when a new transfer tube from the switching valves to the GC oven was fitted. Heating the transfer bellows has a profound effect on the analysis via the blank correction, and maybe a similar effect on the sample data.

This practice of heating the bellows between runs was stopped as it was thought to be the cause behind the light standard analyses; but the very fact that such an effect occurs does imply that there is a certain degree of contamination, and this will inevitably build

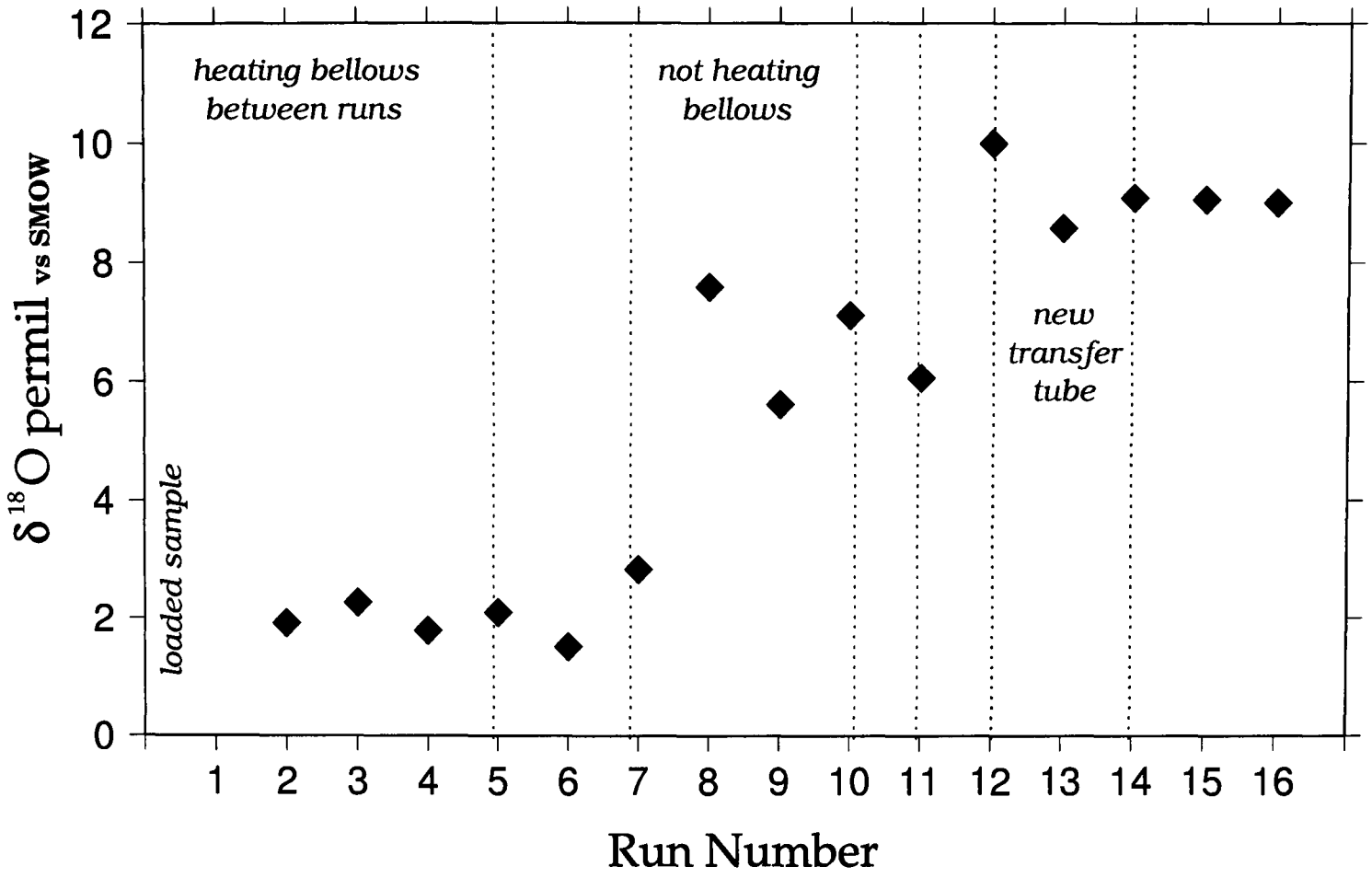


Figure 3.4: Evolution of the blank $\delta^{18}O$ over USNM Augite; dotted line represents a new day. The effects of not heating the bellows between runs, and of replacing the transfer tube are clearly seen.

up over the analytical period. Whether this is, in fact, a bad thing, or whether this is part of the phenomenon known as 'conditioning' the line is unclear.

With the concern over contamination still pertinent, the practice of heating the bellows at the beginning of each day, or every other day, started. The effect of this on the blank was remarkable; the blank values would go very light (often into the negative per mil territory), and size would increase, from circa 2Vs up to 20Vs. Often four blank runs or more would be necessary to bring it back down to a normal value.

It has since been felt that as the line may need to be 'conditioned' over a period of several days after first loading a new sample, bellows heating is not a necessary routine. However, since garnet standard values were still in the 4-5‰ range, and as bellows heating was not considered the sole problem in causing light values, there was another factor.

3.10.2 USNM Garnet - implications for sample size and freezing times

Up to now routine analysis used 10 minute times for all stages of gas transfer. However, it was noticed that although the results still suffered from being too light (eventually overcome by ceasing the practice of heating the silica gel loop upon release, see section 3.10.3), heavier numbers could be achieved when the quantity of sample gas was small. This size-dependence, echoing the one that dogged BrF_5 analysis, although operating to push values heavier rather than lighter at smaller sample areas, is plotted up along for 10, 15 and 20 minute intermediate transfer times to the silica gel loop (see figure 3.5).

For 10-minute freeze times, if the sample area was smaller than 12Vs, then heavier $\delta^{18}O$ values were realized. These values settled out to be 1.5-2‰ light at larger sample sizes. For 15 and 20-minute freeze times the fractionation was not observed, implying that 10 minutes was not long enough to collect all the sample gas upon the silica gel loop.

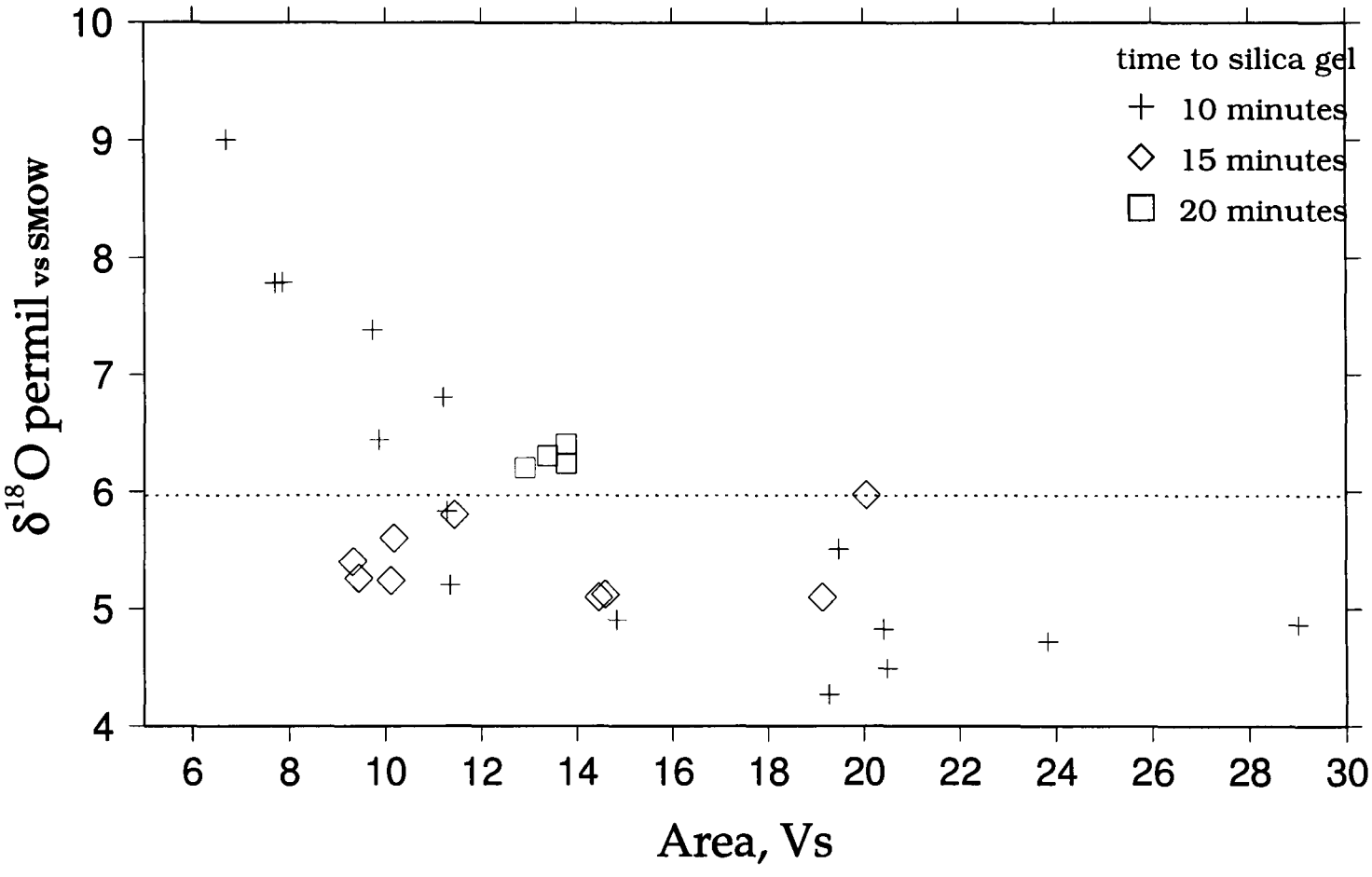


Figure 3.5: Size relation of corrected $\delta^{18}O$ for USNM almandine when freezing for 10, 15 and 20 minutes to the silica gel loop.

This size-dependence was also observed later on with a sample of USNM almandine loaded alongside sample 6x (section 3.11.2), when the light fractionation problem had been sorted out (see later), and real, viable standard values were obtained (figure 3.6).

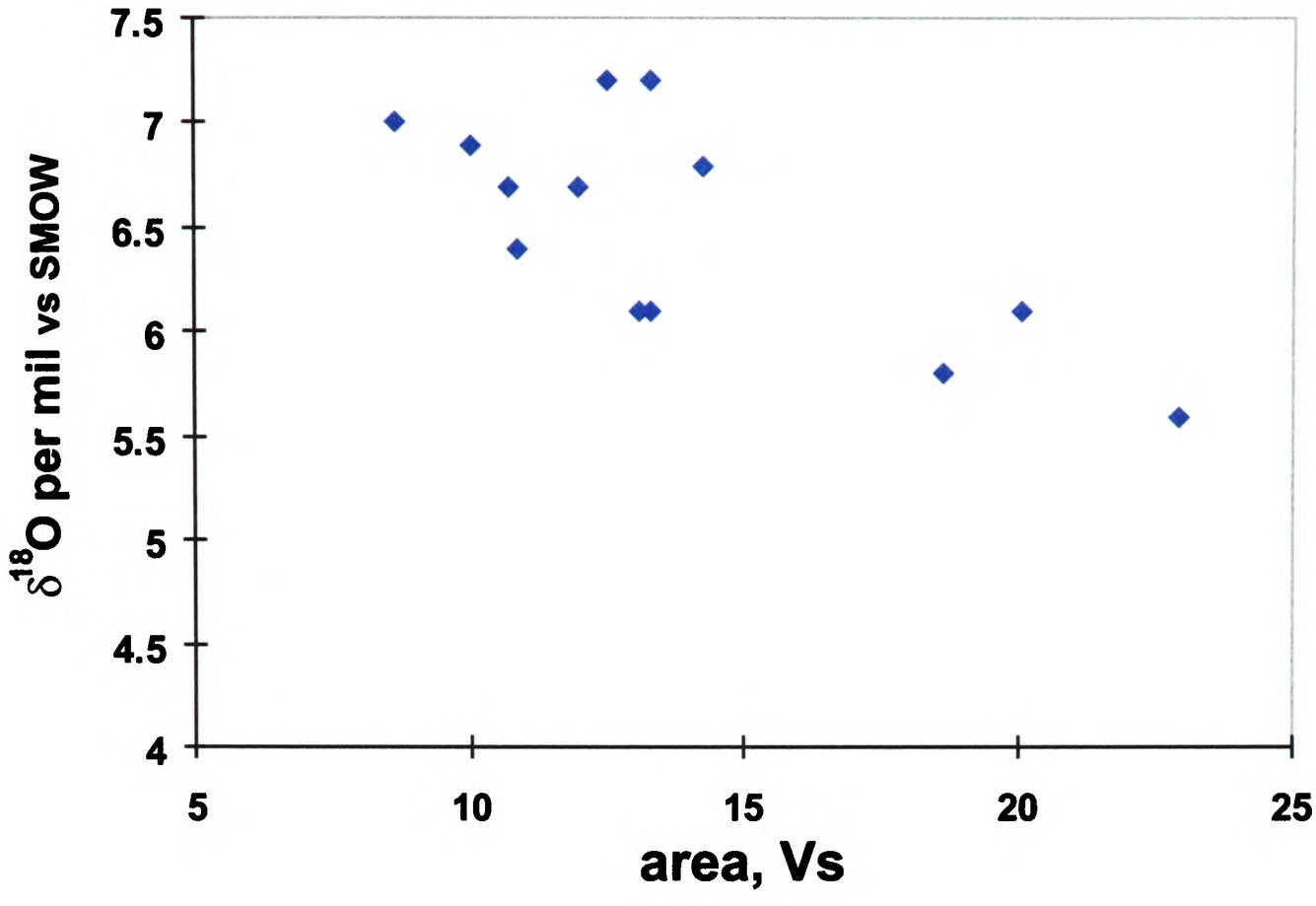


Figure 3.6: Size relation of corrected $\delta^{18}O$ for almandine loaded with sample 6x.

The size-$\delta^{18}O$ relationship must be explained by how quantitative migration of gas to the silica gel loop is. With longer freezing times the gas has more time to migrate across from the chamber and line to the silica gel loop. For larger quantities of gas there is a greater back-pressure forcing the gas through into the silica gel loop vacuum, and the 'missing' gas is proportionately less.

Why this problem was not observed before may lie with the age of the line and silica gel; after several years of analyses the interior of the line may become more 'sticky' after repeated attack by bromine, with the result that oxygen is more likely to adsorb onto it, and take a longer time to migrate down. The other factor is that the quantity of fluorine used for these experiments (5-8mbar) is less than before, and this may contribute to a lower back-pressure that forces gas to migrate down the line when the valve is opened (the silica gel loop is at high-vacuum baseline when exposed to the rest of the line).

3.10.3 The silica gel heating problem - and final corrections

Despite taking account of the bellows heating effect and fine-tuning the parameters for freezing times and sample size, standard analysis would settle down to a value some 1.5-2‰ lighter than expected.

The cause of this was found to lie in the practice of heating the silica gel loop during release of oxygen analyte into the helium for transfer to the cryofocus loop. Figure 3.7 shows blank corrected USNM almandine analysis both while still heating the silica gel on release, and after stopping this practice and allowing the loop to thaw naturally. The plot shows two consecutive days of analysis, the first day shows a typical decline in $\delta^{18}O$ over the day towards 5‰ and lighter. But when, the next day, the silica gel is not heated the garnet analyses are stable and correct. Also, ceasing to heat the silica gel loop has an effect on the value of the blank (rising towards 10‰), and it should be noted that the jump in garnet analysis is real, and not due to correcting with a different blank value, otherwise even lighter values would be obtained.

Once the practice of heating the silica gel loop had stopped, real, reproducible, correct values were obtained from the garnet standard.

3.11 Analysis of the Hoosac Schist

The culmination of the development effort was to analyse samples of the Hoosac Schist. Results are fully detailed in chapter 7. Samples 6a, 19a and R76 were chosen.

3.11.1 First analysis - sample 6a

Sample 6a was loaded, along with a small sample of USNM almandine. 6a is a specimen from the staurolite zone, broken away from the edge of a larger garnet, and contains a number of small (2mm) garnets, a couple of staurolite grains, a largely mica matrix, and a quartz vein to the edge of the sample.

This introduction of two samples contained a number of uncertainties:

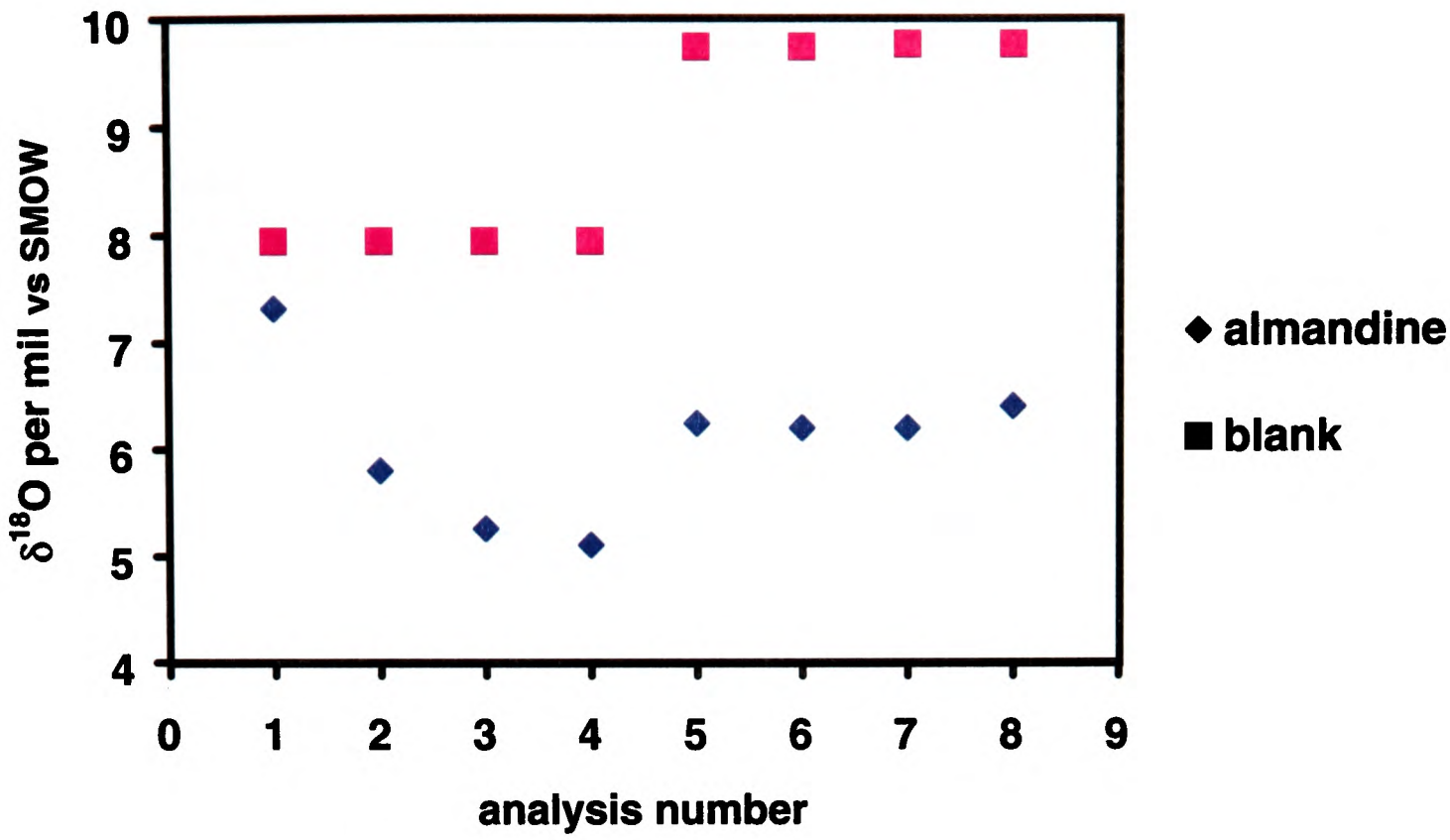


Figure 3.7: Plot showing the effect of heating and then not heating the Silica Gel loop on analyte release upon both blank and corrected almandine $\delta^{18}O$.

- the sample of schist was much larger than a usual sample size (1.2×0.8cm)
- two minerals were being loaded simultaneously
- the schist contained a number of minerals such as the micas and some feldspar which are potentially highly reactive within a fluorine atmosphere, and some of which were weathered

All of these factors could have an adverse effect on the blank, rendering microsampling analysis futile if blank values shift continuously.

Although it took a few days of daily blank analysis and nightly fluorinations, eventually the blank stabilized, with a size of 2.5-3.0 Vs, and $\delta^{18}O$ between 10.0 and 10.5‰. This blank size was small enough to allow easy categorization of the blank effect, and thus allow analyses to be fairly robust even if there were slight blank $\delta^{18}O$ fluctuations.

The time of gas transfer to the first silica gel loop was reduced from 20 to 15 minutes, which still allowed complete, quantitative transfer of analyte from line to silica gel (figure 3.5). Successful garnet analysis proceeded on both standard and sample, and most

of the garnet zoning profile was built up during this period (see chapter 7 for full results).

However, laser maintenance required firing into the mineral in the absence of fluorine, and this had an extremely adverse effect, upsetting the blank value. Even after 3 days of blank runs and bad standard analyses it still had not steadied, and as laboratory time was limited, analyses proceeded, which were corrected using a correction factor. This was based upon an idealised blank used to correct the standard value, and then the $^{18}\Delta$ between this and the proper value applied to the sample analysis. This was proved successful since a couple of 6a garnet analysis yielded a $\delta^{18}O$ that matched earlier results.

The idealized blank was taken as 2.9 Vs, $\delta^{18}O = 10.5‰$ (the average for the previous 8 normal blank values was 2.81Vs, 10.37‰). Then the system was calibrated with an almandine analysis, which was found to be +0.4‰ heavy after correction with the theoretical blank. Analysis of the Hoosac sample was thus undertaken using recalculation with the theoretical blank and then subtracting 0.4‰ . The first few 6a sample analysis using this correction were taken from areas of the garnet where the $\delta^{18}O$ was measured prior to maintenance: these yielded similar results, and so the correction was deemed viable, and used for the last few mineral analyses.

3.11.2 Sample 6x - what we learnt

In February-April 1999 both sample 6x and 19a were analysed. Sample 6x and a specimen of USNM almandine were loaded. A heat-lamp was used to warm the sample and chamber to some 60°C while pumping for several hours. This practice was introduced as a way to help pump down to baseline more speedily, and reduce the number of blank runs necessary. The heat lamp technique promotes release of adsorbed material by direct (radiation) heating.

Blanks were run until steady and then the standard garnet run, as is normal practice, to season the line. However, the value of the garnet standard did decline from initial heavy values, but it never reached 5.9-6.0‰ , instead settling in to between 6.8-7.1‰ . This was odd since good data had just been gained from another chip of the same standard; the difference here was that a sample of schist was also loaded.

To see if the problem lay with the standard, the sample or the line, sample 6x was removed leaving just the USNM standard. Analysis proceeded, and this time yielded correct results for the standard. This pointed towards the presence of the sample 6x as a direct factor hindering the standard settling in. Indeed, when sample 6x was reloaded, the problem returned, with the USNM garnet steadfastly sticking to 7.0-7.2‰ . This was puzzling. The experiment also showed that a sample can potentially be re-analysed after it had been exposed to fluorine and then air. Due to this problem, sample 6x was abandoned and 19a loaded instead.

3.11.3 Sample 19a - a problem of shift or drift?

Sample 19a showed a similar problem trying to settle the standard value down to its proper value; the lightest $\delta^{18}O$ reached was 6.4‰ , and no amount of running the standard could shift its value down further. As such, results from 19a analysis were corrected in line with the $^{18}\Delta$ calculated from standard analysis.

Analyses were performed with only 1-1.5 mbar F_2 ; this has an appreciable effect on the blank size by minimizing its area. A real isotopic zoning pattern was being revealed from the large (1×1.5 cm) garnet, with an apparent 10.5‰ at the rim, declining to 9.9-10.0‰ and then rising again at the core to 10.6‰ .

However, after a number of days of analysis it was observed that the isotope values appeared to have shifted downwards. At localities on the garnet where early analyses gave 10.5‰ , now 9.9-10.0‰ were given; where analysis once gave 10.0‰ , now 9.6‰ was yielded. A consistent shift of the order of -0.5‰ seemed to have occurred (documented in chapter 7). Figure 7.11 shows the zoning patterns before and after the determined shift (chapter 7).

Standard almandine values also had declined; they had evolved to 6.7-6.8‰ (and used for correcting 19a analyses down), but then appeared to shift to 6.2-6.3‰ , which is more the correct value. Perhaps, then, the line was still showing the effects of being seasoned, and it was just taking an extended period of time to complete the process. The only problem with this is that the standard value was very steady at 6.7‰ , and there seemed to be a sudden jump in the analyses.

No definite explanation has yet been found to account for this sudden shift in values. One theory concerns the observation that some of the micas started to split away from the garnet due to the force of the laser. It has already been noticed that the laser is capable of moving and rotating samples, and as these micas are fragile there is the chance that the power imparted during ablation can crack and move them. Figure 3.8 shows a schematic of where the cracks occurred. Cracking open would reveal fresh mineral surfaces, or even weathered minerals such as micas which would prove highly reactive to fluorine. These cracks could provide a fresh surface for oxygen adsorption. However, previous observations suggest that the effect of a fresh surface is to shift analyses to heavier rather than lighter $\delta^{18}O$ values. This is based on the fact that for a new sample, analysis are heavy during first running-in, or seasoning of the line or sample. However, there may be other factors than just fresh mineral surface leading to this effect.

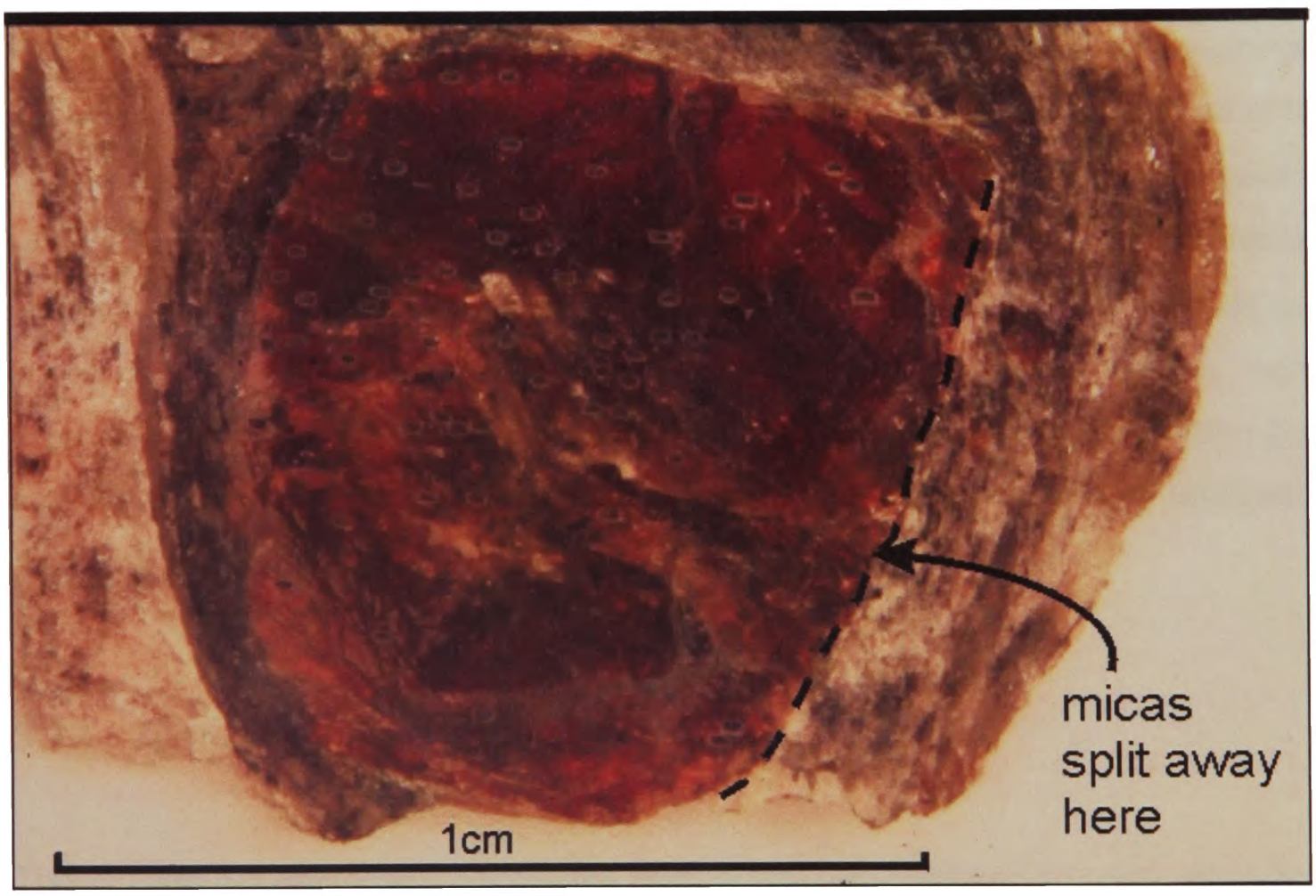


Figure 3.8: Photograph of sample 19a showing where the micas split away.

It has to be noted that such a shift is not reported to be observed when analysing other silicate (*i.e.* meteorite) samples (E.D. Young, pers. comm.). This adds credence to the theory that the cause of this shift lies with the actual sample material, not the isotope

line. It is unfortunate that time did not allow sample 6a to be analysed for a similar length of time to see if that also showed a comparable effect.

3.12 Postscript from sample R76

R76 is a sample from the staurolite zone, and was a quartered garnet sample to reduce surface area. In addition, micas were removed from around the edge to prevent any potential problem as observed with sample 19. Analysis proceeded using 4mb of F_2 and transferring for 5/10/10 minutes.

During analysis of sample R76 a drift similar to that observed with sample 19 was also noticed, but this drift was arrested by the practice of fluorinating the sample with 15mb for 1hour at the start of the day, and then running the fluorine gas *through* the isotope line and analysing as normal (although killing the fluorine for 10 minutes instead of 5). This initially produced a huge peak of 25Vs, and a $\delta^{18}O = 6‰$, but the blanks quickly settled back down, and subsequent sample garnet analysis was restored to previously late 10‰ values. It would appear that not only does a large quantity of fluorine gas sitting over the sample reacts with any oxygen (and this being oxygen of 6‰, light compared to the sample), but the running through of this gas through the isotope line also benefits for subsequent blanks, and was used as a technique for initially stabilizing the blank value.

3.13 Conclusions

This chapter has attempted to condense several years of development work into a few pages. Mixed analytical success has been gained, especially with routine standard analysis. However, despite this work, problems still remain with the analysis of pelitic schists. Pelite samples appear to be more difficult to analyse routinely than some other samples, especially meteorites. This could in part be the nature of the material, with highly reactive (in the presence of fluorine) minerals such as sheet silicates and plagioclase present, and the effect that weathering has had on the analysed samples. Despite

this, it is still possible, with care, to acquire acceptable analysis from pelites.

The important points to bear in mind are:

- the importance of steadying the blank, performing blank runs for several days allowing it to settle before commencing analysis
- using the standard as a monitor of line condition; to see when it has settled in to a constant $\delta^{18}O$ after loading (maybe up to a week), and to watch for a drift after an extended period of analysis
- looking after the isotope line - every few days perhaps heating the bellows and traps to clean-up, although this means 4-5 blank runs to steady the blank value
- keeping sample size to at least 20Vs, otherwise there is a size-dependent fractionation

The method for pelite analysis is not robust; however with care and patience analysis can be gained. The results from sample 19a, however, may point to a problem with long-term drift when working on one sample for an extended period of time. This may result in a 'window of opportunity': after the blank has been characterised, and the line has been seasoned (with appropriate standard analysis), but before any long-term drift manifests itself.

Summarizing the rapidity of the method, after loading it usually took between three to four days to steady the blank, and then at least another four to five days to allow the standard to settle in, before sample analysis could commence.

Chapter 4

High-Alumina Schists of the Hoosac Formation

The first part of this thesis is directed towards the development of the Oxford UV laser microprobe for the *in-situ* oxygen isotope microanalysis of metamorphic rocks. This second part is concerned with the application of this pioneering analytical technique to samples of the high-alumina schists of the Hoosac Formation, Western Massachusetts, USA.

This chapter introduces the Hoosac Schist: its context within regional New England geology; the relationship between the high-alumina (garnet-bearing) schist to the surrounding rocks; and the nature of the high-alumina schist at outcrop scale. Qualitative petrology and petrography is discussed in chapter 5, with mineral chemistry and attempted thermobarometric calculations covered in chapter 6.

4.1 Introduction to the Hoosac Schist

The Hoosac Schist is the high-alumina unit of the Hoosac Formation, principally defined as garnet-bearing, but also containing other Al-rich minerals such as chloritoid, staurolite and aluminosilicates. The Hoosac Formation lies within the New England Acadian metamorphic belt, extending from the Connecticut border northwards into southern

Vermont. The geology of this area has been comprehensively mapped by the United States Geological Survey (USGS), culminating in the Massachusetts Geological Map of Zen *et al.* (1983), and associated cross sections. The Hoosac Schist outcrop runs obliquely to the regional metamorphic isograds, and thus is considered to offer a complete sequence from garnet-chlorite through staurolite to at least kyanite-biotite zone.

The high alumina Hoosac Schist was chosen as a subject based on the following criteria:

- it is considered to represent a continuous prograde sequence from garnet to at least kyanite zone, the metamorphic grade increasing from north to south over some 60km (although a sillimanite isograd has been mapped in the south, bulk composition differences may indicate that the sillimanite grade rocks belong to a different formation; J.T. Cheney, pers. comm.)
- it is well documented within a regional geological context; however as a subject matter in its own right little published work exists
- garnets within the Hoosac Schist show similar textural unconformities to those described in both the Hoosac (Karabinos, 1984, 1985), and Gassetts (Thompson *et al.*, 1977) Schists of Southern Vermont - with which these rocks have been correlated; in addition, the metamorphic history is considered to be extremely similar to that of the Gassetts Schist (J.T. Cheney pers. comm.)
- the correlated Gassetts Schist has already proved to be a suitable study material for oxygen isotope work (Chamberlain & Conrad, 1991, 1993; Young & Rumble, 1993)

Both textural and chemical evidence from the Hoosac Schist indicate at least two metamorphic events. Those minerals that grew under the older *diastrophic* (*i.e.* mountain building) event record a complex, folded schistosity, with local crenulation cleavage, characterized by intergrown paragonite and phengitic muscovite, with chloritoid and chlorite. A later metamorphic episode is shown by undeformed porphyroblasts of phengitic muscovite (with paragonite rims), staurolite, chlorite, chloritoid, biotite and kyanite (depending on grade) all of which overgrew the deformed schistosity (see chapter 5).

Of particular interest are the large garnets, up to 2cm in diameter in some cases, which are characterized by a textural unconformity separating an inclusion-rich core (with sigmoidal inclusion trails) from an inclusion-poor rim; these appear similar to those features seen in Gassetts Schist garnets and equivalents (Rosenfield, 1968; Thompson *et al.*, 1977; Karabinos, 1984).

4.2 The Appalachian orogen

New England geology is dominated by the effects of the Palaeozoic Appalachian orogenic event, part of the Caledonian-Appalachian orogen. The structural and metamorphic history of the rocks found within the Hoosac Formation is shaped by the effects of the Taconian and Acadian metamorphic events that occurred during this orogen.

The Caledonian-Appalachian orogen dominated what is now the North Atlantic during the Palaeozoic, encompassing the collision between two major continental blocks: Laurentia and Gondwana-Baltica. The closure of the Iapetus ocean between these blocks formed the three segments of the main orogen: the Scandanavian and the British Isles' Caledonides, and the Appalachians of eastern North America (see figure 4.1). The Appalachians were formed by the collision between Laurentia and North Western Gondwana during the mid-Palaeozoic.

During the Ordovician and Permian, Appalachian deformation was relatively continuous, but has been sub-divided into two main events on the basis of temporal breaks. The Taconic orogen relates to deformation episodes in the mid-Ordovician, and can be plausibly related in the northern Appalachians to the attempted subduction of the Laurentian craton beneath an Ordovician island arc (however since there is no evidence for the existence of Ordovician island arcs in the central and southern Appalachians, there is a lack of explanation as to what caused the Taconian deformation for some two-thirds of the Appalachians).

After post-tectonic erosion the Appalachians were covered by a shallow sea; deposited upon the Ordovician Taconic-affected rocks is an unconformable Siluro-Devonian succession that starts with clastic deposits and is succeeded by a bank of carbonate rocks.

During and subsequent to this depositional period the Acadian orogeny occurred, which continued into the mid-Devonian (Windley, 1995).

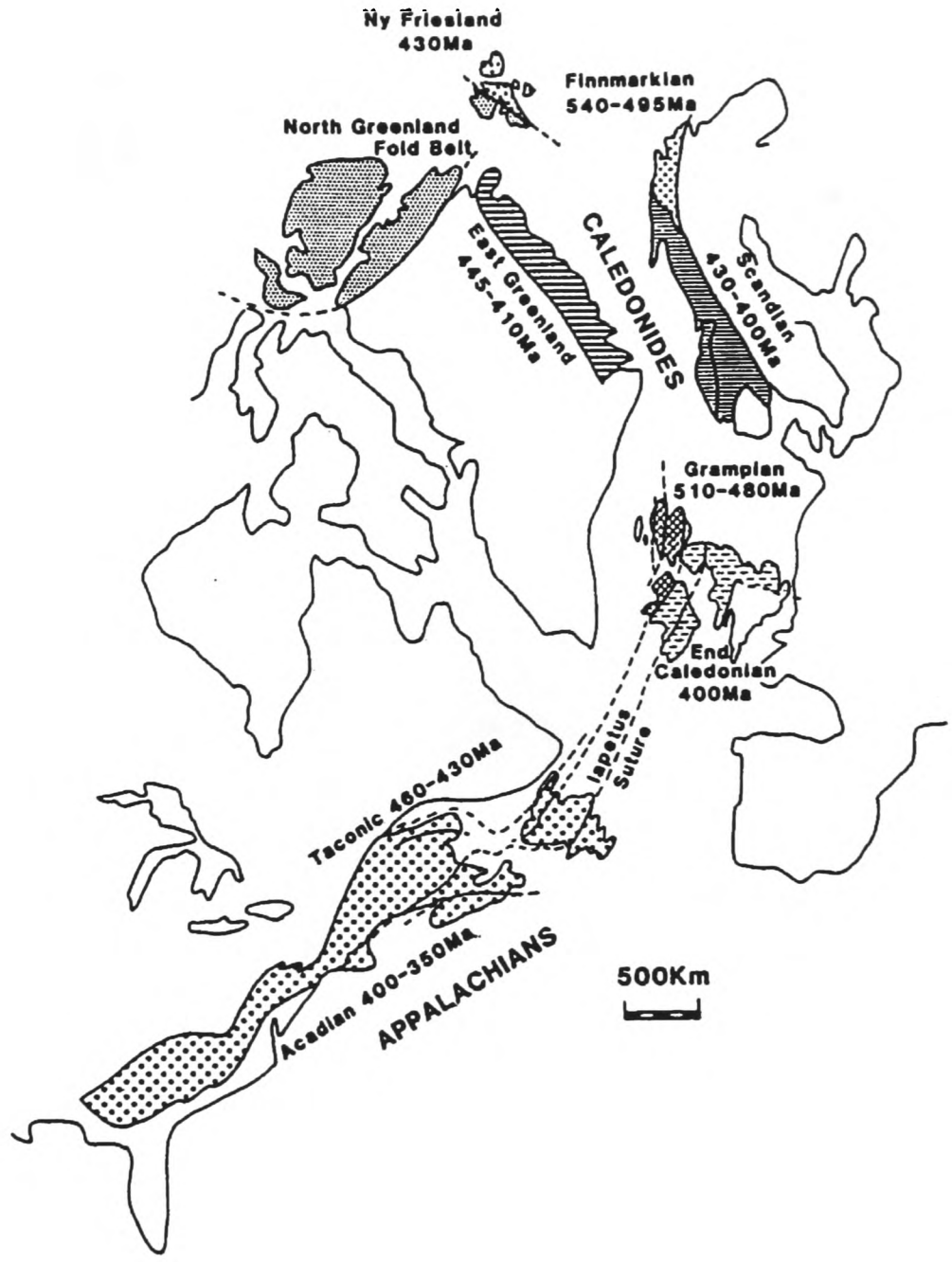


Figure 4.1: Map of the Caledonian-Appalachian orogen showing regions with distinctive deformational events. Taken from Windley (1995).

4.3 The Hoosac Formation - its provenance and structural relations

The Hoosac Formation is part of a multiply deformed and metamorphosed, Taconian-Acadian orogenic terrane, sited on the eastern limb of the Berkshire anticlinorium, New

England, USA (figure 4.2). It is one of a series of nested thrust slices consisting of a mid-Proterozoic (1Ga, *Grenvillian*) basement of metamorphosed sedimentary, granitic and volcanic gneisses, unconformably overlain by the Cambrian Dalton formation.

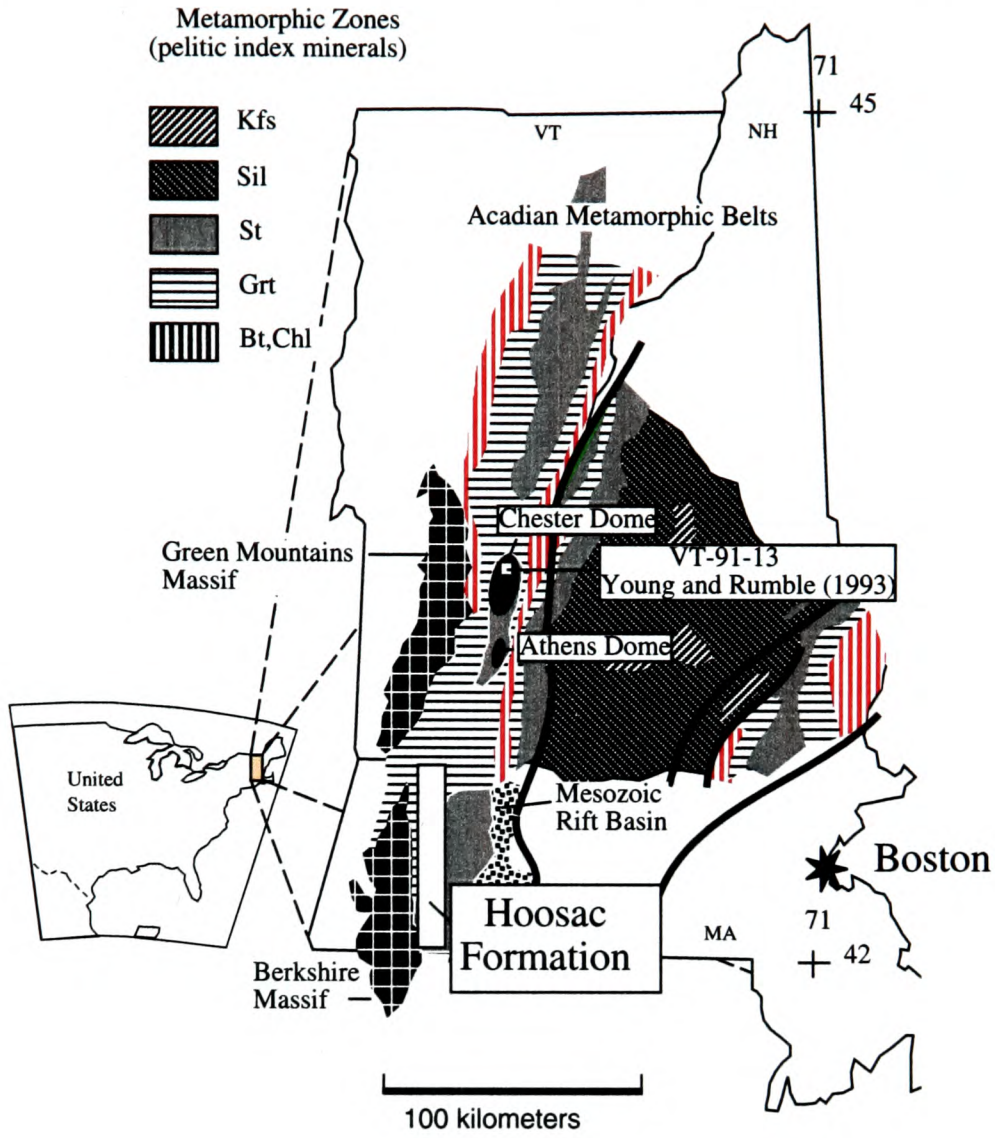


Figure 4.2: Generalized metamorphic setting of the Hoosac Formation. The location of the Young & Rumble (1993) study is also shown, from which this figure is modified.

Older Taconian orogenic-related folding that affected the Proterozoic-middle Devonian rocks was subsequently re-folded during the Acadian event to create the antiform of the Berkshire massif. The Berkshire massif and its eastern cover sequence have traditionally been sub-divided into three litho-tectonic assemblages: the Taconic-Berkshire zone; the Rowe-Hawley zone; and the Bronson Hill zone. Figures 4.3 and 4.4 summarize the stratigraphy of the Berkshire Massif.

The Taconic-Berkshire zone, within which is sited the Hoosac Formation, is an allochthon of Grenvillian basement gneisses. Figure 4.5 shows a generalized near east-west cross-section across the Berkshire Massif. To the west lie autochthonous basal clastic rocks

that unconformably rest on basement; these are succeeded by Cambrian-Lower Ordovician carbonate bank deposits (the Stockbridge and Dalton Formations). This miogeoclinal sequence is itself overlain by allochthonous Cambrian-Mid Ordovician clastic sediments and minor volcanics of the Taconic allochthonous thrust slices, which include the Hoosac Formation. These Taconic allochthons are thought by Stanley & Ratcliffe (1985) to have been transported from the east of the continental basement, being the eastern facies of the autochthonous section. The Hoosac Formation, considered by Stanley & Ratcliffe as the source of the Taconic allochthons, is thus a 'western' facies, equivalent to some of the autochthonous section, but remaining east of the Berkshire Massif (compare with the autochthonous rocks found west of the Berkshire Massif).

As a nested thrust slice, the Hoosac Formation is separated from the Berkshire massif by the Middlefield thrust (becoming the Hoosac summit thrust in the North Adams quadrangle), and from the Cambro-Ordovician rocks to the east by the Whitcomb summit thrust (both Taconian in age). The Whitcomb summit thrust carries the Rowe-Hawley zone over the root zone of the Taconic allochthons (Stanley & Hatch, 1988), and it separates the Hoosac Formation to the west (deposited on Grenville basement) from the Rowe, Moretown and Hawley Formations to the east, which were deposited on oceanic crust (Hall & Robinson, 1982).

4.3.1 Taconian and Acadian orogenic events

Both the Taconian and Acadian orogenic events are considered to have affected the Hoosac Formation. Although the intensity, and associated schistosity, of Acadian deformation diminishes towards the west, Acadian fabrics overprint Taconian (western) fabrics at least as far as the western edge of the Rowe-Hawley zone (see figure 4.6). The Hoosac rocks reside within this zone of *maximum overlap* of both the Taconian and Acadian orogenies, and thus have been significantly affected by both events, giving rise to both a complex structure and a complex fabric. The combined Taconian-Acadian history potentially records up to five stages of folding and multiple pulses of metamorphism; post-Taconic rocks record at least three generations of folds (Acadian-related), and the dominant schistosity is parallel to sub-parallel to Taconian-age schistosity (Cheney & Brady, 1992).

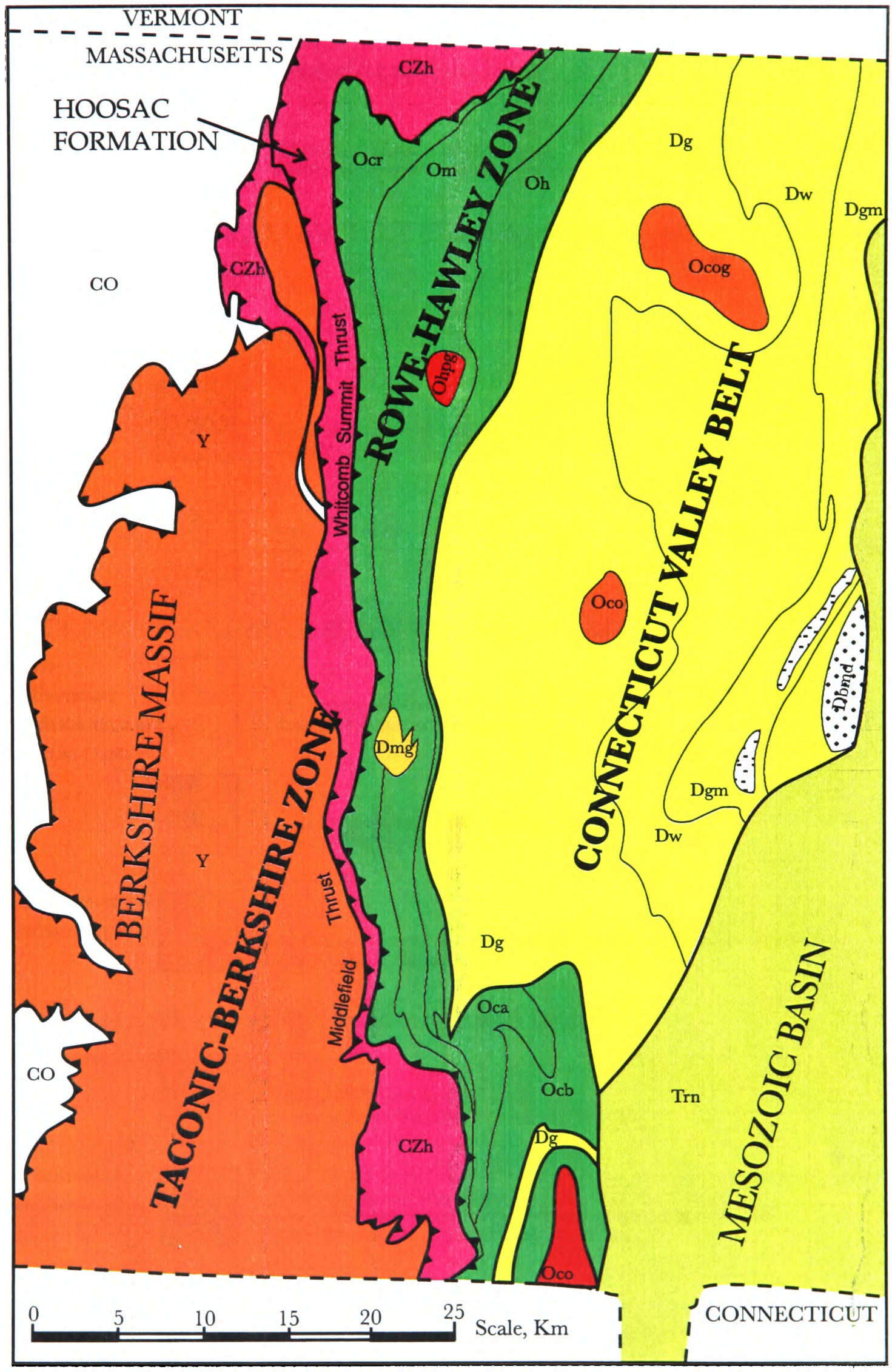


Figure 4.3: Map of the Berkshire Massif showing generalized geology, after Cheney & Brady (1992) and Zen *et al.* (1983). See figure 4.4 for key.

KEY TO MAP OF THE BERKSHIRE MASSIF

(After Zen etal, 1983)

MESOZOIC BASIN (Triassic and Jurassic)

Sedimentary/ Metamorphic — Trn

New Haven Arkose (Upper Triassic);
locally conglomeratic arkose interbedded with shaley siltstone

CONNECTICUT VALLEY BELT (Silurian and Devonian)

Intrusive — Dmg

Middlefield Granite (Devonian);
biotite-muscovite granite

Dbmd

Belchertown Complex (Devonian);
primary igneous orthopyroxene-augite quartz mozodiorite

Sedimentary/ Metamorphic — Dgm, Dw, Dg

Dgm - Gile Mountain Formation (L. Dev); schist with interlayered quartzite
Dw - Waits River Formation (L. Dev); dark grey, granofels and amphibolite schist
Dg - Goshen Formation (L. Dev); micaceous quartzite

TACONIC-BERKSHIRE ZONE (Ordovician and Older)

Auto-chthonous Sedimentary/ Metamorphic — CO

Stockbridge and Dalton Formations (Lower Ordovician to Proterozoic Z);
dolomite marble overlaying quartzite

CZh

Hoosac Formation (Lower Cambrian and Proterozoic Z);
muscovite-biotite schist or gneiss

Sedimentary/ Metamorphic — Y

Proterozic Y Sedimentary/Metamorphic rocks in the Berkshire Highlands;
plagioclase-quartz gneisses

ROWE-HAWLEY ZONE (Ordovician and Older)

Intrusive — Ohpg

Gneiss at Hallockville Pond (Ordovician);
grey microcline-plagioclase-quartz biotite gneiss

Sedimentary/ Metamorphic — Oh, Om, OCr

Oh - Hawley Formation (M. Ord); amphibolite, greenstone, gneiss and granofels
Oca/Ocb/Occ - Cobble Mountain Fm (M. Ord); mica schists
Om - Moretown Formation (M. Ord or older); granofels and schist
Ocr - Rowe Schist (L. Ord and Camb); schist

Oco

BRONSON HILL ZONE - Collinsville Formation (Mid Ordovician or older);
plagioclase gneiss with minor amphibole

Figure 4.4: Key to figure 4.3

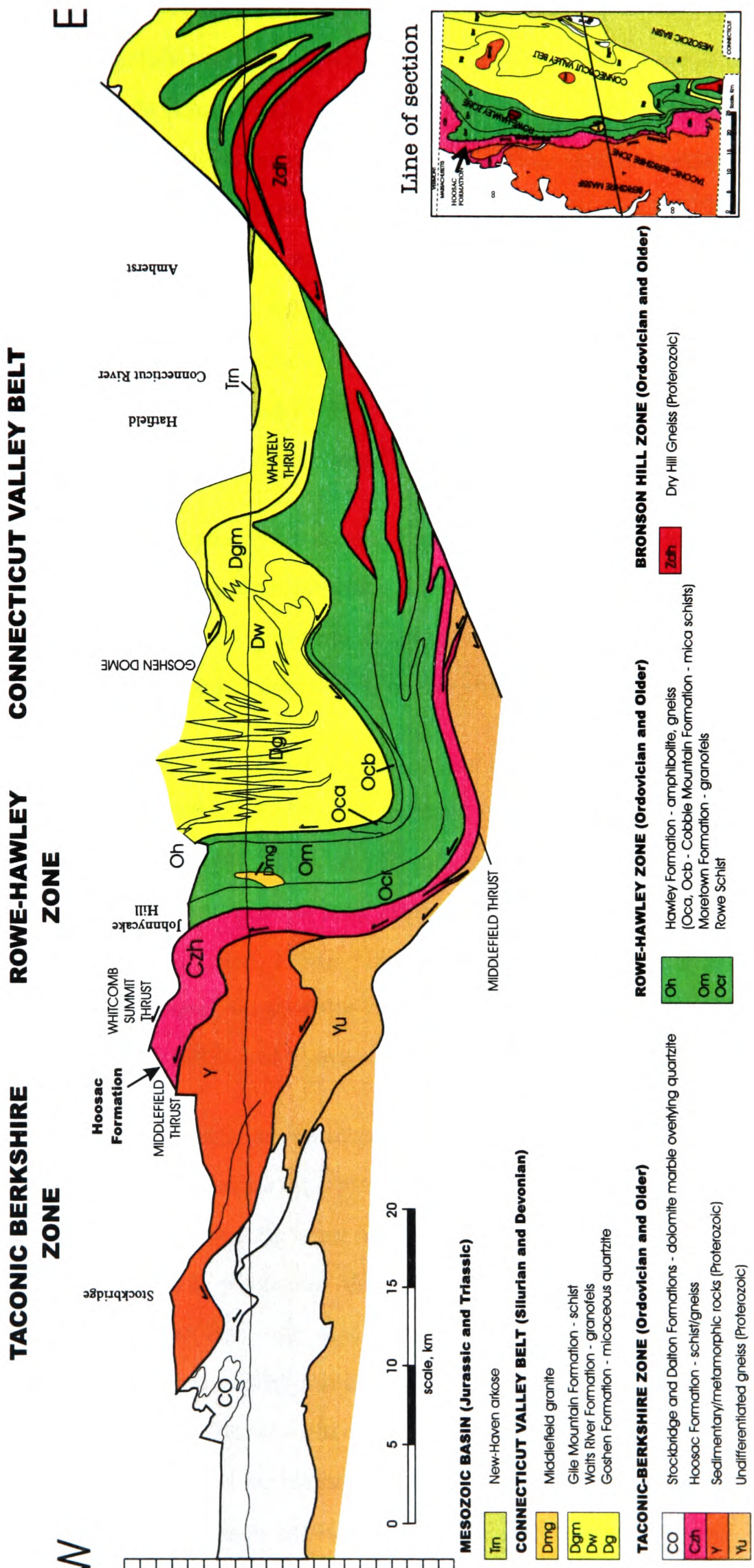


Figure 4.5: Simplified East-West cross-section across the Berkshire Massif; modified from Zen *et al.* (1983)

Taconian metamorphism has been dated at 450 Ma (Tucker & Robinson, 1990; Armstrong *et al.*, 1992), while the later Acadian metamorphic event has either yielded varying ages of 395-375 Ma (Laird *et al.*, 1984; Christensen *et al.*, 1989; Armstrong *et al.*, 1992), representing either a single event of uncertain age, or successive metamorphic episodes within the Acadian orogeny (Rosenfield, 1968; Thompson *et al.*, 1977; Laird & Ablee, 1981; Karabinos, 1984). The Taconian metamorphism is therefore of late Ordovician in age, and only affected rocks of Ordovician and older, such as those found in the Taconic-Berkshire and Rowe-Hawley zones. The Acadian, on the other hand, is of early-mid Devonian, and thus also affected rocks of Silurian and Devonian in age, such as those formations found within the Connecticut Valley Belt.

Despite these measured ages, there is considerable uncertainty concerning both the age and extent of polymetamorphism affecting the Hoosac rocks. Considering that multiple paragenesis has occurred, the problem is one of unravelling the orogenic history, and linking the observed metamorphic events to the known (and dated) orogenic events.

The western extent of Acadian fabric development and mineral growth is difficult to ascertain, as is the separation of Acadian-dominant versus Taconian-dominant metamorphism (Cheney & Brady, 1992). The uncertainty in the timing of metamorphism is due to conflicting age dates, ambiguous rock fabrics and the complex metamorphic history of the area (Karabinos & Laird, 1988). The Acadian-dominant boundary appears to lie within the Berkshire Massif, west of the Whitcomb summit thrust (see geochronological studies by Sutter *et al.* (1985) and Hames *et al.* (1991)).

Figure 4.6 shows a schematic metamorphic map for the eastern limb of the Berkshire massif. The large-scale metamorphic map of Massachusetts was compiled by Zen *et al.* (1983); while individual isograds were mapped by a succession of students at Amherst College, Massachusetts, in particular the St+Bt and Ky+Bt isograds (Cheney & Brady, 1992). It is apparent from this map that the isograds are off-set along both the Taconic-Acadian line and across the Whitcomb Summit thrust, giving rise to a pattern with a north-south Grt+Chl zone (the so-called *barren core*) of the Rowe, Moretown and Hawley formations, which is flanked by higher-grade rocks of the Hoosac and Goshen Formations. These off-sets have been explained either by post-metamorphic faulting, which could account for the apparent juxtaposition of differing metamorphic grades, or by the

effect of the spessartine and grossular components of garnet on the Grt+Chl → St+Bt isograd.

In the latter scenario, as proposed by Cheney *et al.* (1980), the effect of the spessartine and grossular components of garnet upon the AFM discontinuous reaction Grt+Chl = St+Bt promotes stabilization of the Grt+Chl join. Essentially, rocks containing MnO+CaO-rich garnet (and the near-rim analytical sum MnO+CaO is generally higher in barren core garnets relative to garnets from the flanking Goshen and Hoosac Formations) should push the co-existence of staurolite with biotite to higher temperatures (since the addition of MnO and/or CaO causes the AFM discontinuous reaction to become a continuous one). Thus within the Goshen and Hoosac formations the St+Bt isograd should occur at lower temperatures (*ergo* lower grades) than the barren core.

4.4 The High-Alumina Schists of the Hoosac Formation

The Hoosac Formation has been sub-divided into at least ten stratigraphic units (outlined from oldest to youngest in table 4.1). The predominant unit is a medium-grained muscovite-quartz-albite, schist or granofels with a variety of accessory minerals (chloritoid, chlorite, kyanite, sillimanite, staurolite, garnet, biotite) depending both upon bulk composition and metamorphic grade. It is continuous with the Lower Cambrian Hoosac Formation of Vermont (Hatch *et al.*, 1968; Norton, 1976). The entire Hoosac stratigraphic succession within Massachusetts extends as a continuous sequence from Vermont in the north (where it is 6km thick), through to Connecticut in the south (3km thick), and thins to a minimum of circa 1km in the Becket quadrangle.

The focus of this study are the coarse-grained, garnet-rich, and, at appropriate grades staurolite- and kyanite-rich, high-alumina pelitic schists found within the Hoosac Formation. These schists are characterized by medium to large garnets in a quartz and muscovite-rich matrix. Norton (1976) described two near-continuous mappable garnet-bearing high-alumina schist units that extend north-south from the Vermont border to near Connecticut, at a width rarely exceeding 300 metres; these two units were mapped extending northwards until the top of the Cheshire USGS 7.5×15 minute quadrangle, where the stratigraphically-lower (western) schist was documented to thin out. How-

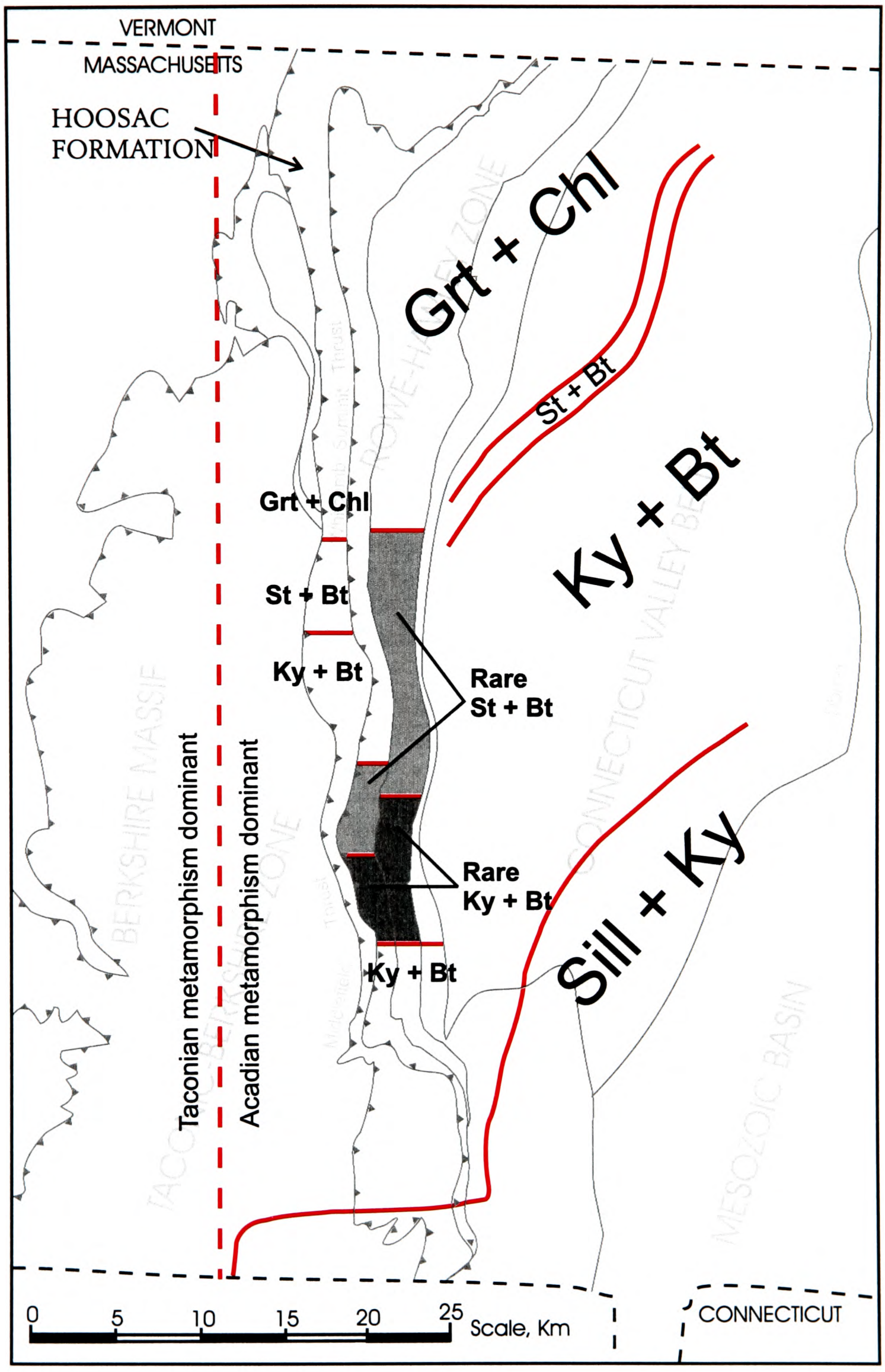


Figure 4.6: Metamorphic isograd map of the eastern limb of the Berkshire massif, after Cheney & Brady (1992).

Unit	Description	thickness m
Unit 1	**schistose quartz-gneiss-pebble metaconglomerate with a quartz-plagioclase-muscovite-chlorite schist matrix** only outcrops in the Cheshire quadrangle	0⇒ 160
Unit 2	**quartz-plagioclase-muscovite-biotite-(garnet) schist** forms the lowermost outcropped unit from the southern edge of the Cheshire quadrangle, rare quartz-rich lenses occur	0⇒ 35
Unit 3	**quartz-muscovite-garnet-(biotite-chlorite-staurolite-kyanite schist** coarse-grained, rusty-weathered; can be traced nearly continuously along the entire eastern edge of the Berkshire massif; thickness varies from 65m, through 50m in the Cheshire quadrangle west of the Precambrian rocks to zero in the northeastern corner of the Cheshire quadrangle; outcrops have a highly corrugated surface, due to weathering effects of the numerous quartz lenses; garnet porphyroblasts as much as 2.5cm in diameter; bedding obscure; chloritoid and paragonite are locally abundant -the latter found only south of the kyanite isograd; this unit is less aluminous to the north and west in Massachusetts, but is very aluminous near the Vermont border; west of the Precambrian terrane in the Cheshire quadrangle typically a dark-brown to black-weathering graphitic, quartz-albite-muscovite-garnet-biotite schist	0⇒ 65
Unit 4	**quartz-plagioclase-muscovite-biotite-(garnet) schist** slightly rusty-weathering, poorly-bedded, medium-grained - transitional between units 3& 5	0⇒ 35
Unit 5	**quartz-muscovite-garnet-biotite-kyanite-staurolite-schist** coarse-grained	0⇒ 65
Unit 6	**quartz-plagioclase-muscovite fine to medium-grained schist and minor gneiss** with accessories including chlorite, biotite, garnet, staurolite, kyanite and sillimanite, depending on bulk composition and grade; makes up most of the Hoosac Formation; east of the Precambrian terrane; overlies units 3 or 5	350⇒ 3500
Unit 7	**calcareous quartz-muscovite schist** only found in the Cheshire quadrangle; discontinuous	0⇒ 65
Unit 8	**quartz-plagioclase-muscovite-biotite schist** overlies unit 7 where it is present; similar to unit 6	350⇒ 3500
Unit 9	**quartz-plagioclase-garnet-muscovite-biotite schist** with staurolite and kyanite; garnet porphyroblasts as large as 1cm, kyanite, staurolite up to 5mm; coarse-grained, massively-bedded, extends from Becket southward to Chester, south of which it is absent due to thrust faults or facies changes; commonly interbedded with a schist similar to unit 8	0⇒ 65
Unit 10	**graphitic, quartz-plagioclase-muscovite-biotite-garnet schist** with impure quartzite; overlies unit 9	

Table 4.1: Units of the Hoosac Formation, listed in ascending stratigraphy (oldest to youngest). The oldest is thrust upon Proterozoic basement rocks to the west, and thus this table shows ascending stratigraphy from west to east. Modified from Norton (1976).

ever, exposure in the Berkshire hills is very poor, and it is quite likely that there are more than two of these high-alumina units, which may or may not be continuous. Outcrop observations (section 4.5) indicate that the thickness of the garnet-bearing schist is of the order of 100 metres, grading in quite sharply from the Ms+Qtz+Ab bearing granitic schist surrounding it.

These two stratigraphically disparate bands, as recorded, have been potentially correlated with other New England pelitic schists; the stratigraphically higher band has been considered equivalent to the high-alumina compositions within the Rowe Formation (the Hoosac Formation in Vermont, *e.g.* Karabinos (1984); Ratcliffe *et al.* (1988)), whilst the stratigraphically lower big-garnet schist has been correlated with the Gassetts schist, Vermont (Thompson *et al.*, 1977, and others).

4.4.1 Metamorphic history of the Hoosac Schist

There is great difficulty in constraining the timing of many of the fundamental metamorphic events in the evolution of the Hoosac Schist. This is especially true in differentiating between the effects of the Taconian and Acadian orogenic events.

Figure 4.7 summarizes the metamorphic zones and mapped isograds for the Hoosac Formation, including the Pg+Qtz=Ky+Ms+Pl isograd. The mineral assemblages of the high-alumina schists are generally consistent with the AFM mineral assemblage diagrams (see map). They have been sub-divided into three zones (Cheney & Brady, 1992):

- **Zone I:** the garnet zone can itself be sub-divided into 3 prograde *sub-zones*: (Ia) Chl+Grt+Cld; (Ib) St+Chl+Grt+extra components; (Ic) St+Chl+Grt (although assemblage Ic rocks have yet to be observed, J.T. Cheney pers. comm.)
- **Zone II:** the traditional staurolite zone is defined on the basis of St+Bt compatibility (St-in for Al-poor rocks Grt+Chl=St+Bt)
- **Zone III:** the Kyanite zone, which can also be divided into 2 subzones; although there is an overlap due to the stabilizing effect of Ca in feldspar; (IIIa) Ky+Bt+Pg; (IIIb) Ky+Bt+Pl

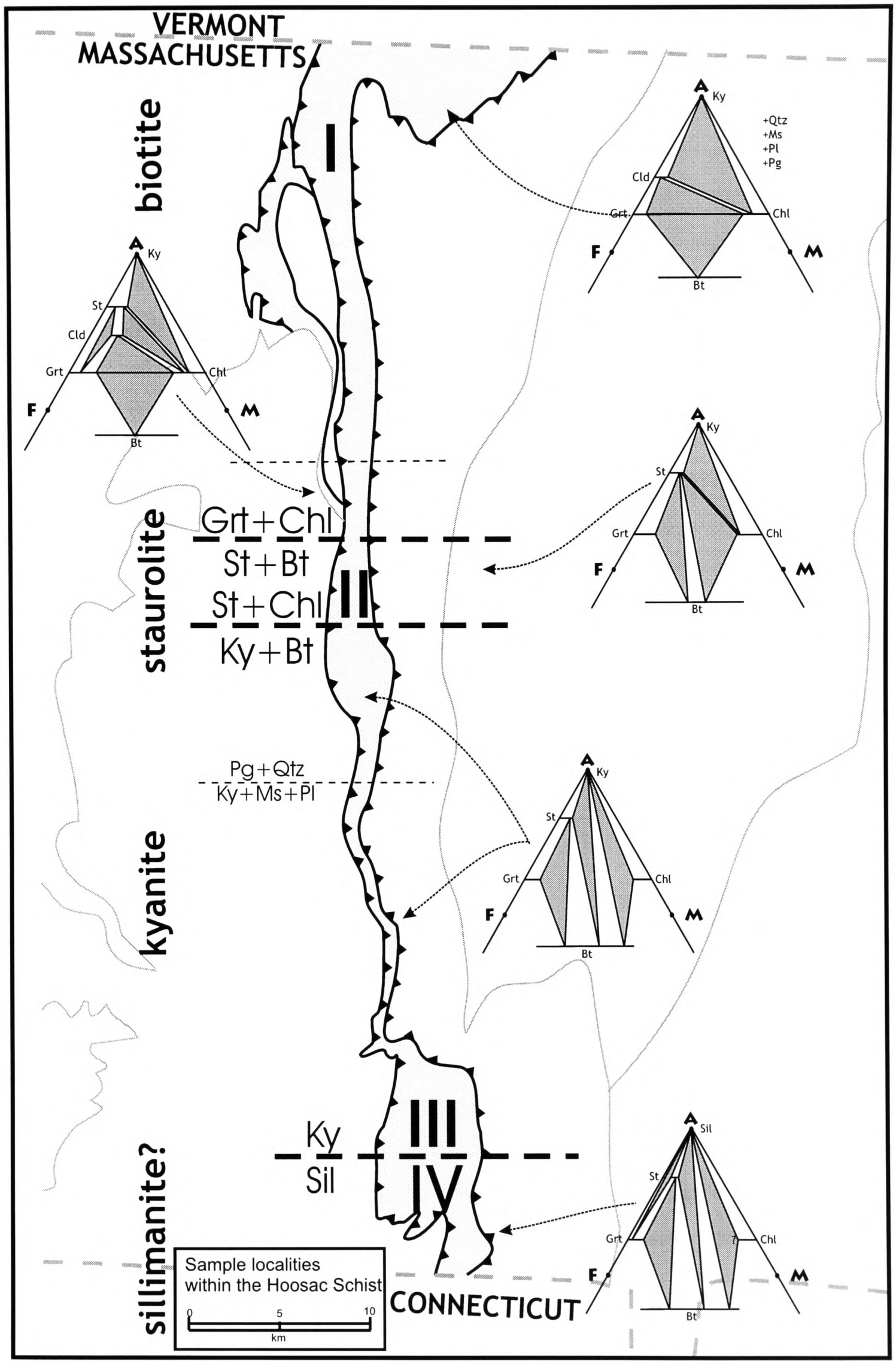


Figure 4.7: Metamorphic map for the Hoosac Formation showing metamorphic zones and schematic AFM projections (after Cheney & Brady, 1992).

4.4.2 Evidence for multiple generations of metamorphism

Later generation 'megacrysts' of muscovite and other, largely undeformed porphyroblasts of muscovite, staurolite, kyanite, biotite, chlorite and chloritoid, appear to reflect a prograde metamorphic history that has been superimposed upon a pre-existing (possibly Taconian) fabric. This original fabric is largely defined by intergrown fine-grained laths of muscovite and paragonite. Garnet zone rocks have chloritoid and chlorite present locally, while those in the staurolite and kyanite zones have fabrics predominately defined by white micas, with rare staurolite and kyanite. Primary plagioclase is absent until the mid kyanite zone, however, plagioclase has locally replaced paragonite.

The other major evidence for an earlier metamorphic event superseded by a later event of a similar grade is the existence of garnets with striking unconformity textures (they can be observed in hand-specimen), with inclusion-free rims separated from inclusion-rich cores. These Hoosac garnets show very similar features to those described by Karabinos (1984) in a specimen from Vermont: 2 stages of garnet growth separated by a retrogressive resorption event was required to explain the chemical zoning accompanying the overgrowth of later rims. Multiple sizes of garnet porphyroblasts occur in many of these Hoosac rocks; in Vermont, the smaller garnets have similar chemical compositions to the rims of the larger garnets, and some of the larger garnets appear to have formed from the coalescence of several smaller garnets.

Petrological examination of the high-alumina big-garnet Hoosac Schist has revealed at least two stages of metamorphic growth, and possibly three stages of deformation. Garnets grew with an original D1 event, perhaps related to Taconian metamorphism. A second deformation event imposed a pervasive crenulation cleavage on the matrix. Then later, over this fabric, porphyroblasts of staurolite, kyanite and biotite (where applicable) grew, pre- or during a shearing event. This secondary metamorphic event could well be related to Acadian metamorphism, although the exact relationship of this and whether the crenulation cleavage event (D2) is late Taconian or early Acadian is unclear. See chapter 5 for a full petrographic description.

4.5 Field relationships

Although garnets are the characteristic feature of the high-alumina schist, their size and distribution varies spatially both across and along strike. This study concentrates on the large garnet schist, containing garnets of some 10mm in diameter. Field observations show that this large garnet schist is only a minor constituent of the high-alumina schist.

The outcrops of the Hoosac Schist lie within the Berkshire Hills, Western Massachusetts. These are thickly covered in dense forest, and thus outcrops are occasional at best, and are often heavily weathered. The Hoosac Schists tends to make a positive topography against the surrounding rock, being found on top of hills such as French Hill and Garnet Hill.

Outcrop-scale observations have been made to understand the nature of the large garnet schist and its relationship to surrounding units. Originally mapped as two continuous units by the USGS (Norton, 1976), the actual number of units, and the spatial continuity up through the grades, is impossible to determine owing to the vegetation cover.

Traverses and outcrop mapping have been completed at the following localities (see figure 4.8):

- **locality 1:** lowermost garnet zone
- **locality 3:** the Cold River stream cutting in the North Adams quadrangle; two different lithologies containing small and large garnets respectively
- **locality 6:** at Peru in the staurolite zone
- **locality 15:** French Hill, south of Peru
- **locality 32:** the Bancroft railroad cutting which affords 150m of across-strike exposure
- a road cutting at **locality 9**, the southern-most limit of the studied rocks, upper kyanite zone

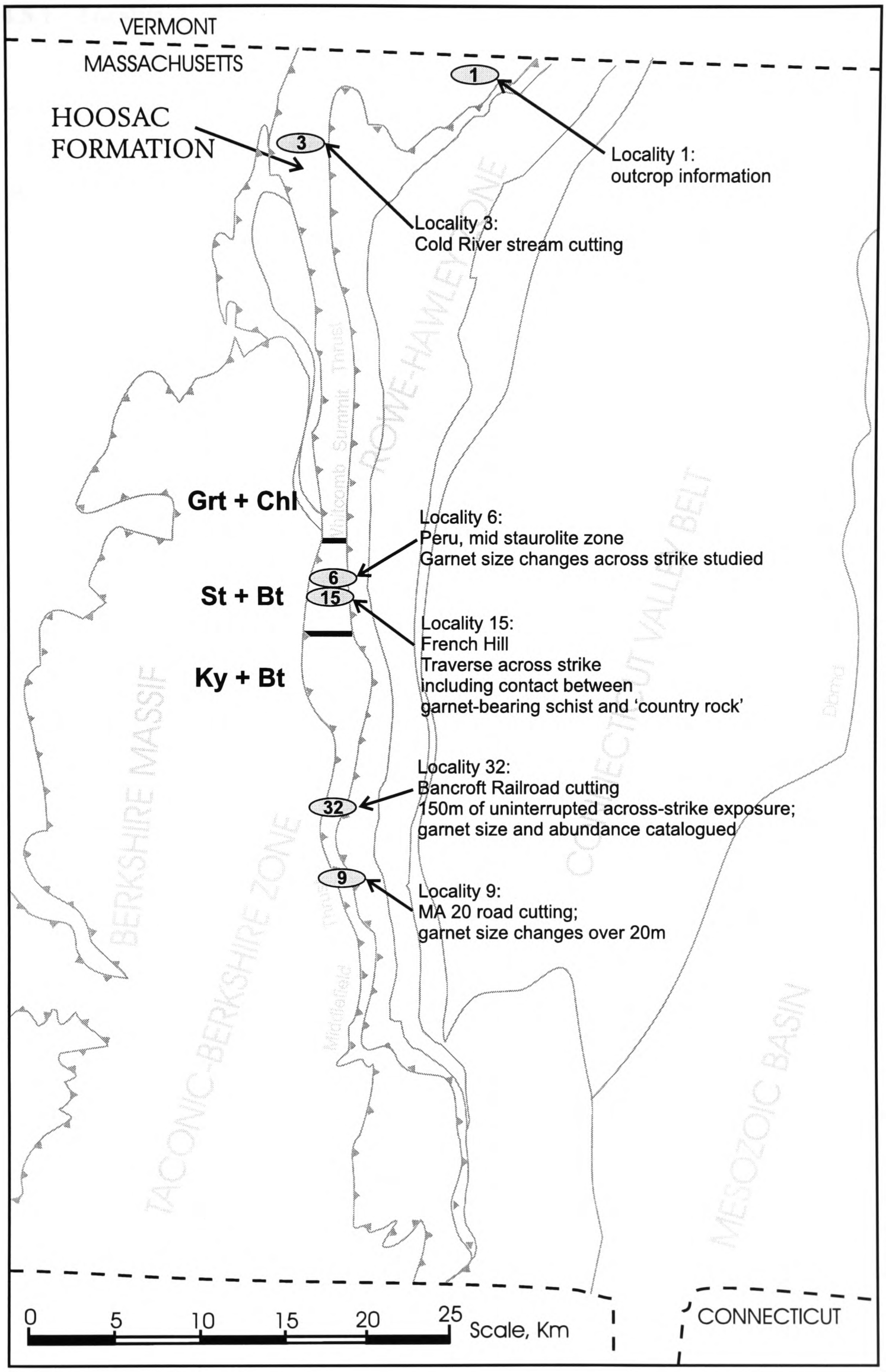


Figure 4.8: Map showing field localities as described in the text.

4.5.1 Locality 1 - Rowe quadrangle; the base of the garnet zone

Locality 1 is where sample P21 was collected, and represents the lowest grade studied here, sited at the base of the garnet zone near the Vermont border. Here outcrop strongly deformed and later folded Ms+Pg+Qtz+Grt+Cld+Chl schist. Already at this low grade, garnets locally reach over 10mm in diameter, but their size varies on the 10cm scale. Additionally, the outcrops contain dark green layers rich in chloritoid on the 5-10cm scale (see figure 4.9).



Figure 4.9: Locality 1, showing the chloritoid-rich bands, from which sample P21 was taken.

4.5.2 Locality 3 - Cold River stream cutting; lower garnet zone

An exposure in the Cold River stream cutting shows two units. Both are dipping 15° E, striking 150° , of thickness 0.5-1m, and appear to be in stratigraphic contact. The major textural difference between the units lies in the size of the garnets. The upper unit has large garnets (6mm plus). The lower unit has smaller garnets (less than 4mm). Mineralogically, the large garnet-bearing rock is biotite-absent, whilst the small garnet rock contains biotite; these mineralogical and garnet size differences can perhaps be explained as the result of differing bulk composition, with the smaller garnets lying in a less aluminous rock (see discussion in section 4.6). Further up grade these differing

compositions manifest themselves in different generations of biotite (J.T. Cheney, pers. comm.).

4.5.3 Locality 6 - Peru; staurolite zone

The samples from Peru show some of the most striking outcrops, in terms of garnet sizes and of the corrugated surfaces, consisting of garnet and quartz ribbons (see figure 4.10). A traverse across strike (roughly E-W) is shown as an outcrop map that yields information on the garnet size distributions (figure 4.11).

The map and associated garnet size distribution plot shows that exposure of garnet-bearing schist is seen over a 120m wide (across strike) map, although there is at least 40m without exposure. From this, the large, 10-15cm garnets appear to only occur over some 30m. The remaining garnet-bearing rock has garnets of 6-8mm or less in diameter.



Figure 4.10: A photograph showing large garnets (10-15mm diameter) from Peru.

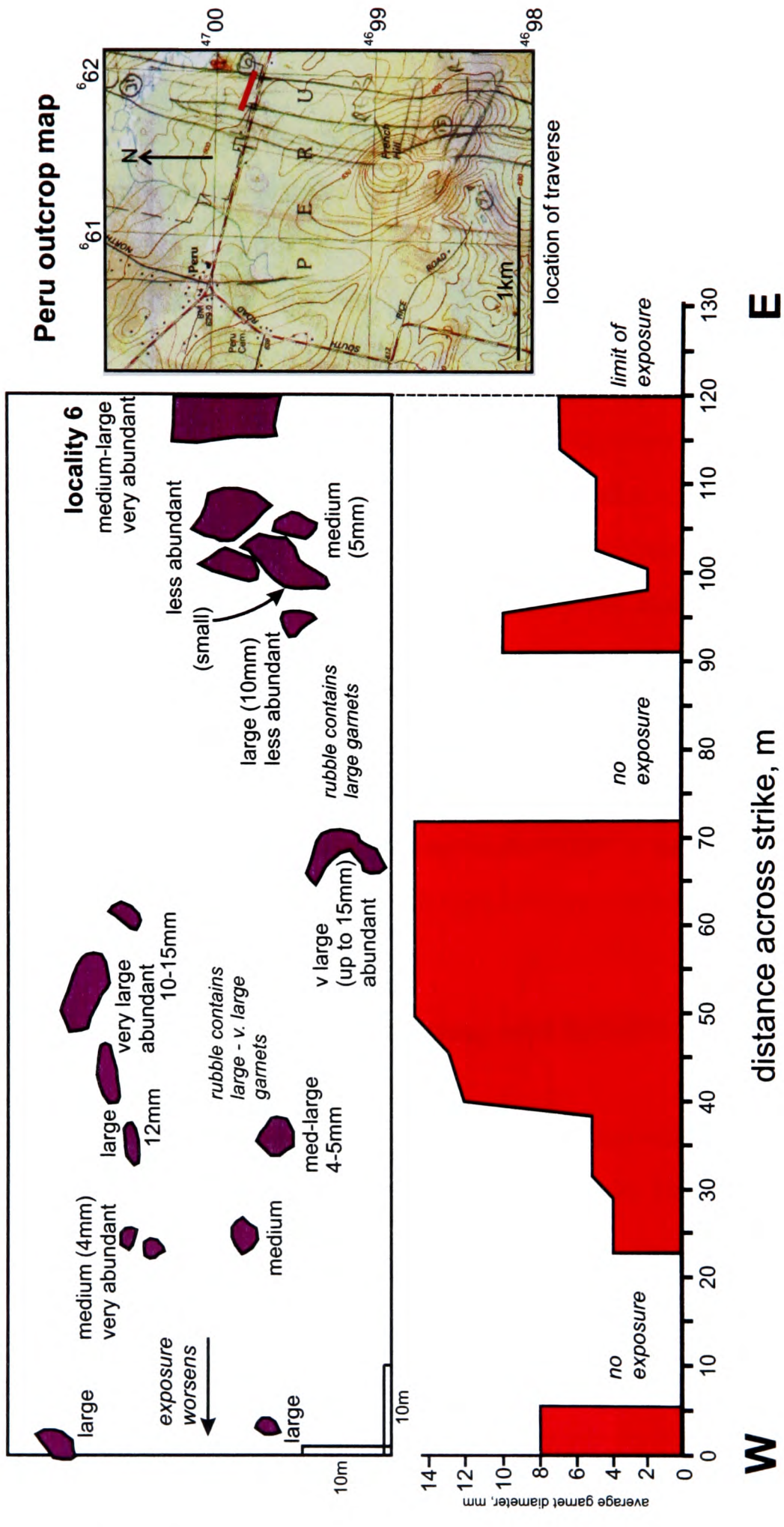


Figure 4.11: Peru outcrop map from locality 6 and a plot of average garnet size versus distance across strike.

4.5.4 Locality 15 - French Hill; mid staurolite zone

French Hill (locality 15) lies c.1km south of Peru, within the staurolite zone, and a traverse across strike on the southern flank was mapped out. This section contains two garnet-bearing high-alumina units, and thus in addition to detailing garnet size changes, and also gives the opportunity to investigate the relationship between the garnet-bearing schist and the surrounding Ms+Qtz+Ab schist.

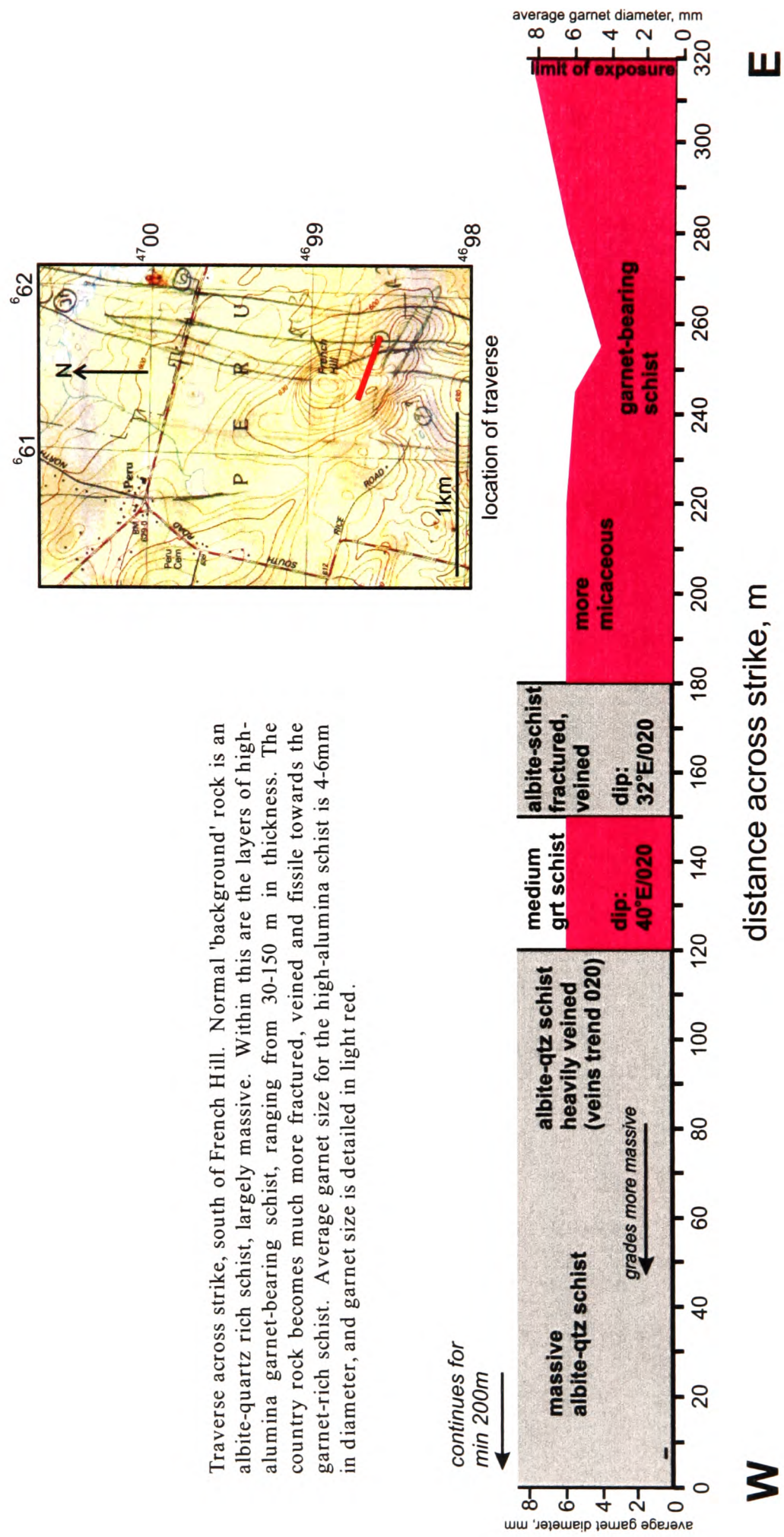
Figure 4.12 summarizes the traverse, detailing the change in garnet sizes. As noted by Norton (1976) there are two mappable units, with varying sizes of garnets; the units have a width of 30m (stratigraphically lower) and at least 140m wide (stratigraphically higher - this width determination is limited by exposure). Within these garnet-bearing schists the average garnet diameter is of the order of 6mm, and only at the eastern extremity do garnets exceed 10mm in size.

The Ms+Qtz+Ab schistose 'country rock' grades very sharply into the garnet-bearing units, over a distance of a metre. Adjacent to the high-alumina schist, this rock is heavily fractured and veined, the veins trending along strike (020°); further away from the contact with the garnet schist, the Ms+Qtz+Ab rock becomes much more massive.

4.5.5 Locality 32 - Bancroft Railroad cutting; mid kyanite zone

The railway cutting at Bancroft affords the opportunity for near-uninterrupted exposure across 150m of strike. Bancroft sits within the mid-kyanite zone. This traverse is detailed in figure 4.13.

Garnet-bearing units are interspersed with rocks containing no garnets at all. At the eastern end the contact with the host Ms+Qtz+Ab rock is observed as a seemingly sudden break with no garnets, however the sizes of the garnets in the rock leading to this break diminish and they become more sparse. Average garnet diameter is of the order of 4-5mm, and only for a distance of 5-10m do garnets sized on average 8mm and over outcrop.



Traverse across strike, south of French Hill. Normal 'background' rock is an albite-quartz rich schist, largely massive. Within this are the layers of high-alumina garnet-bearing schist, ranging from 30-150 m in thickness. The country rock becomes much more fractured, veined and fissile towards the garnet-rich schist. Average garnet size for the high-alumina schist is 4-6mm in diameter, and garnet size is detailed in light red.

Figure 4.12: Details from French Hill with plot of average garnet size versus distance across strike.

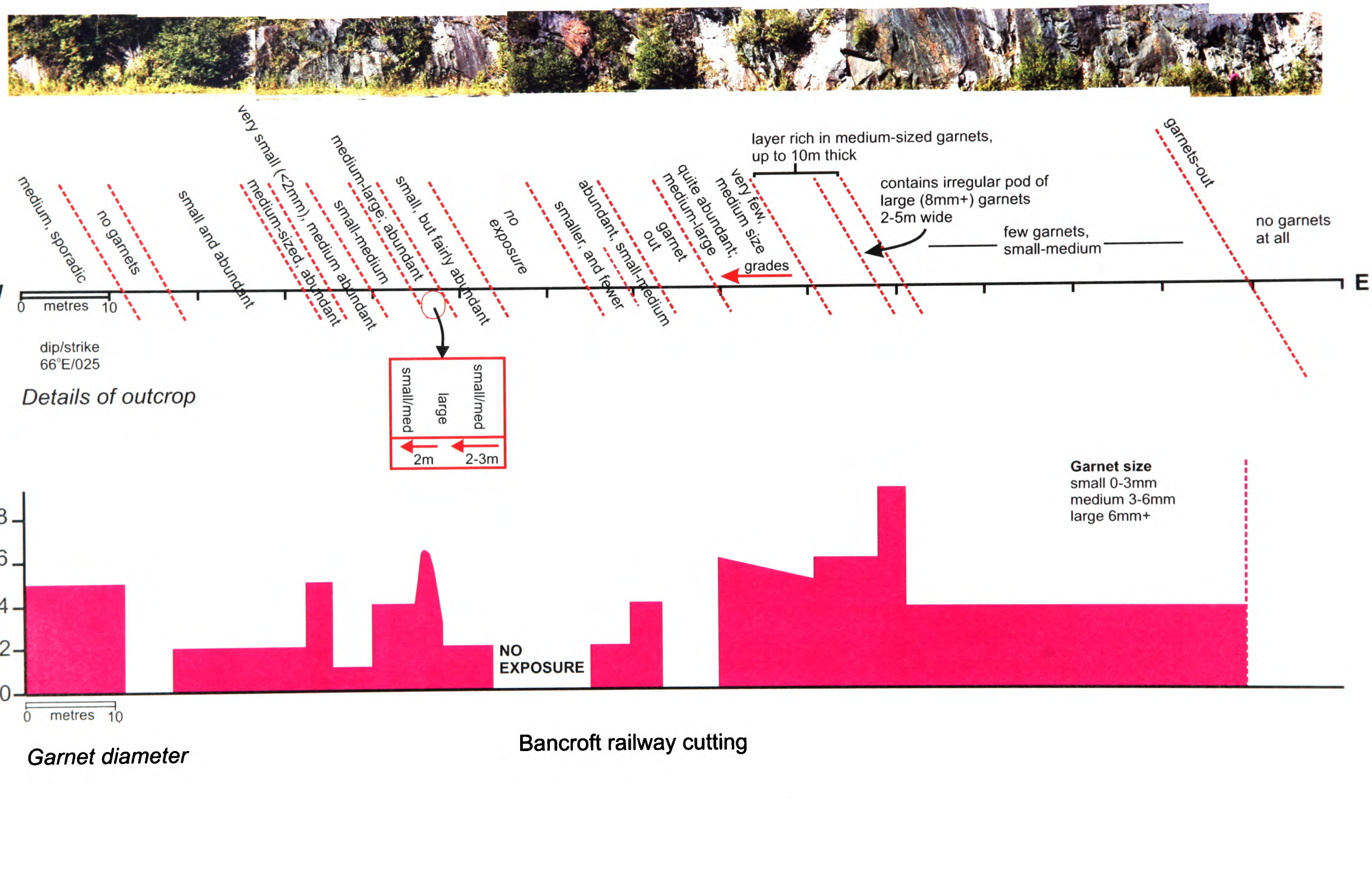


Figure 4.13: Details from the Bancroft Railroad cutting, with plot of average

Locality 32a - Bancroft stream cutting

50 metres south of the Bancroft Railroad cutting is a stream section which gives the opportunity to observe the large garnet schist in detail on the decimetre scale; a photograph of this is shown in figure 4.14.



Figure 4.14: Detail of garnets outcropping by the stream 50m south of the Bancroft Railroad cutting; hammer is 20cm long.

4.5.6 Locality 9 - MA 20 road cutting; upper kyanite zone

Locality 9 is the highest-grade sampling area in this study, and here outcrop kyanite and staurolite-rich schists, which also contain biotite. Figure 4.15 shows how the size of garnets vary locally, over a distance of 15-20 metres. Again, very large garnets (here up to 12mm in diameter) are only seen in a minor unit of 1m in thickness; the grade into this bed from both sides is very sudden over a metre scale.



Figure 4.15: Detail of locality 9, showing the change in garnet size.

4.6 Why is there a range in garnet size?

The information gathered from the field indicates that the high-alumina Hoosac Schist contains a variety of sizes of garnets, and that the large garnet-bearing schist is only a minor constituent of this. The explanation for two adjacent rocks, which have experienced near-identical metamorphic conditions, having differing sized garnets almost certainly lies in differences in bulk rock composition.

Presented here are two scenarios: either the two bulk rock compositions (representing the large and the small garnet-bearing schist respectively) fall within two different phase volumes and thus two different reactions produce garnets; or the two bulk rock compositions fall in the same phase volume, and the same reaction may be responsible for garnet growth in both rocks.

In the first scenario (see figure 4.16a) there are two different bulk rock compositions, one more aluminous and plotting within the Grt+Chl+Cld phase triangle, and one less aluminous and plotting within the Grt+Chl+Bt phase triangle. Garnets are formed by two different reactions, the garnets in the more aluminous rock growing with chloritoid and chlorite, garnets in the less aluminous rock growing with biotite and chlorite. This potentially explains the observations at locality 3.

In the alternative proposal, (figure 4.16b) the two different bulk rock compositions lie within the same phase triangle of Grt+Chl+Cld. The same reaction is thus responsible for garnet growth in both rocks, but as one bulk is more Fe-rich than the other, garnet nucleates and grows in one rock prior to the other, thus in the Fe-rich rock bigger and more numerous garnets grow. There is thus potentially a correlation between size and mode percent garnet. Investigations at Bancroft, and Peru, however, fail to make any definite link between garnet size and abundance.

4.7 Conclusions

The Hoosac Schist lies within a folded thrust belt, striking roughly north-south with an increase in grade from garnet in the north to kyanite in the south, strike lying obliquely

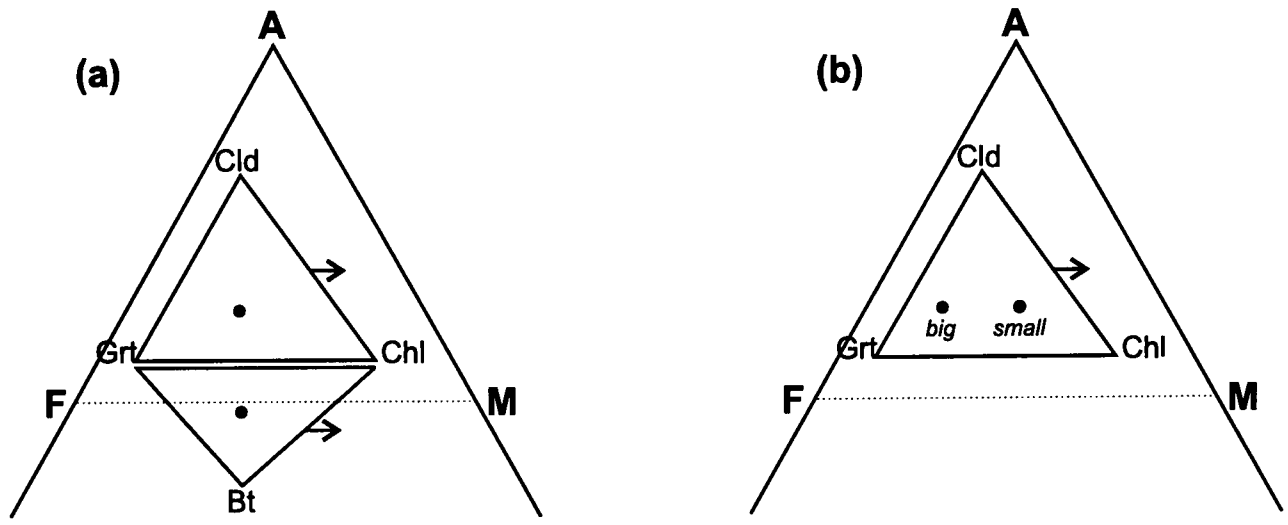


Figure 4.16: AFM diagrams illustrating two possible scenarios to achieve two different sizes of garnets based on differing bulk rock compositions. Dots represent plotted bulk rock compositions. See text for details.

to the regional isograds. The high-alumina member of the Hoosac Schist manifests itself as garnet-bearing units, containing staurolite and kyanite at appropriate grades, lying within dominantly Ms+Qtz+Ab country rock. The contact with this country rock is abrupt. These units are of 10-150m in width, and although they were mapped as two continuous bands, the exact number of high-alumina layers is uncertain. Field observations indicate that the large garnet schist is only a minor constituent of the garnet-bearing high-alumina schist. Within these schists, the garnet size varies considerably; in places, the large (10mm) garnet schist is only 5-10m wide, surrounded by schist of medium-sized garnets (4-6mm).

The big-garnet Hoosac Schist is notable for the absence of any primary plagioclase at low grades, at least up until the kyanite zone, and for the abundance of white micas (muscovite, paragonite, and minor margarite) and large garnets.

4.8 Samples and sample collection

This study focuses on a range of samples from along the grades. Some samples were provided by Dr. John T. Cheney, Amherst College, Massachusetts, USA, while others have been collected from the field. A range of samples from across the range of metamorphic zones has been studied, and those samples provided by Dr.Cheney are correlated in table 4.2, while figure 4.17 shows the location of collected samples.

Sample ID	Cheney ref.	location	grade
1	P21	Rowe	lowermost garnet
2	P37	Rowe Formation	lower garnet
3	S66	Cold River, North Adams	lower garnet
R94	R94		upper garnet
4		Notchview Reservation	upper garnet
R96	R96		upper garnet
P86	P86		upper garnet
22			topmost garnet
31			lowermost staurolite
6		Peru	mid staurolite
15		French Hill	mid staurolite
R76	R76		upper staurolite
30		Garnet Hill	lowermost kyanite
18			lower kyanite
19			lower kyanite
32		Bancroft railway cutting	mid kyanite
P97	P97		upper kyanite
9		MA20 road cutting, Becket quad	upper kyanite

Table 4.2: Full list of samples referred to in the text, with appropriate correlation to samples collected by J.T. Cheney and referenced in (Cheney & Brady, 1992). Listed in increasing grade, from garnet to kyanite zones.

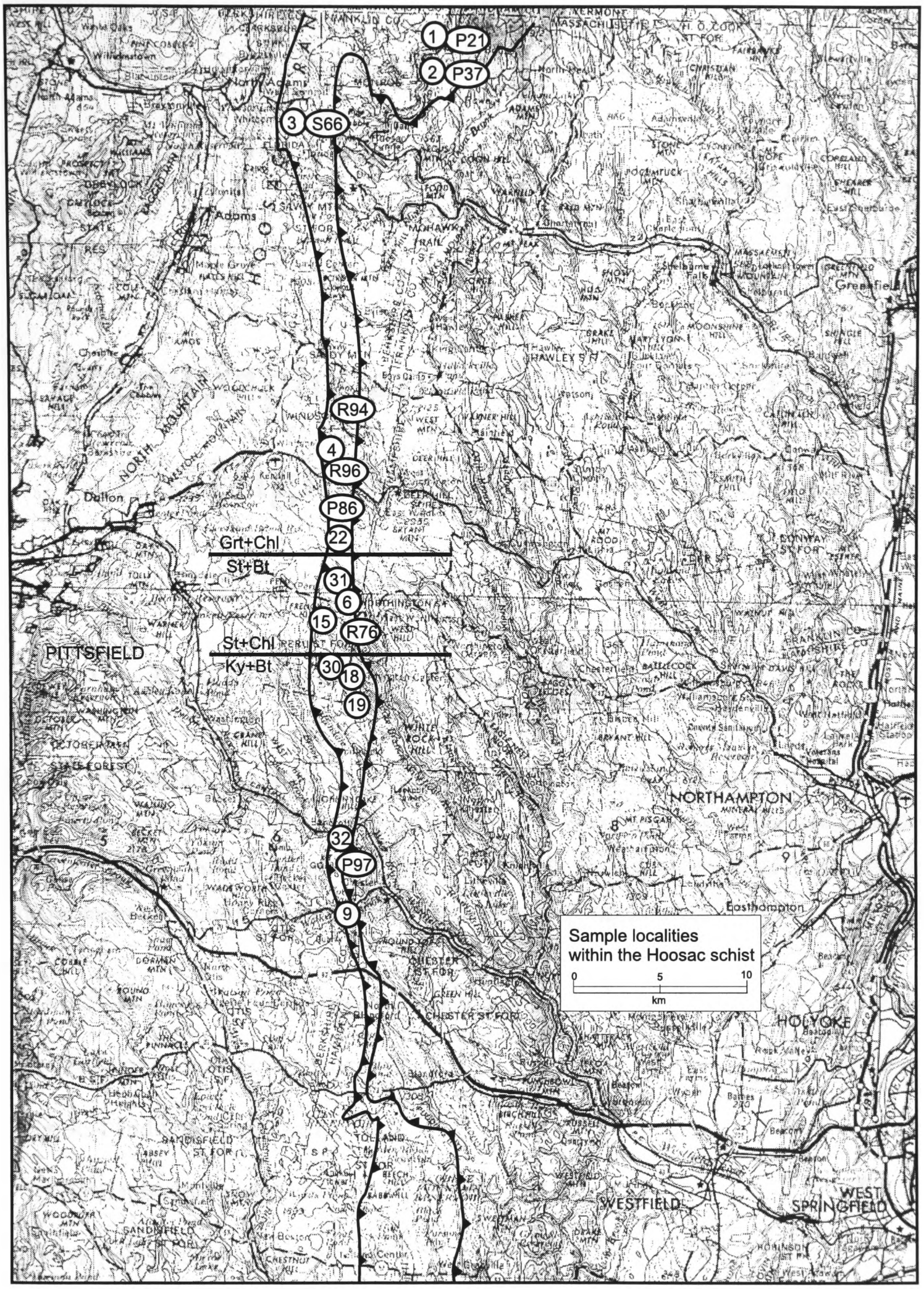


Figure 4.17: Map showing big garnet Hoosac Schist sample locations.

Chapter 5

Petrography and Metamorphism of the High Alumina Hoosac Schist

5.1 Petrology of the Hoosac Schist

This chapter details the petrology and metamorphic history of the big-garnet high alumina Hoosac Schist. Mineral chemistry is covered in chapter 6. In order to understand the metamorphic history, a number of samples have been selected for study from across the range of metamorphic grades (refer to locality map, figure 4.17):

- P21, from locality 1, the lowest grade studied
- S66, lower-mid garnet zone
- R94 and R96, upper garnet zone
- P86, top-most garnet zone
- sample 6, lower staurolite zone
- R76, upper staurolite zone, from near locality 15 (French Hill)
- sample 19, lower kyanite zone
- P97, middle kyanite zone and the highest grade studied

The high alumina Hoosac Schist is essentially a garnet-white mica-quartz schist. White micas include both muscovite and paragonite, and in some cases minor margarite. Primary plagioclase occurs only in higher (mid kyanite and above) grades. Chloritoid is common in the lowest grades, while chlorite is observed as a frequent later phase. Biotite typically occurs only in the highest (kyanite) grade rocks. No aluminosilicates are observed prior to the appearance of kyanite at high grade.

What follows is a complete petrological description of the range of big-garnet Hoosac Schist samples, increasing in grade from lower garnet to mid-upper kyanite.

5.1.1 Sample P21

Sample P21 (locality 1) is the lowest garnet grade sample described here, outcropping close to the Vermont border. The striking feature of these rocks is that even at low grades the garnets are already coarse-grained (1-2cm). These large garnets are sited within a heterogeneous matrix divided between domains of dominantly white mica interrupted by quartz-rich domains, which show evidence of strain. The separation between mica and quartz is marked by a distinct dark boundary.

There is evidence for at least two generations of white mica. The first generation defines a strong fabric (S1), which has in places developed into a strong crenulation cleavage (S2). This crenulation cleavage has locally evolved into a continuous mica fabric, especially near the garnets, while it turns into a discrete spaced foliation near the quartz-rich domains. In addition, it wraps around garnet. Scanning electron microscopy reveals these first generation white micas to be intimate intergrowths of muscovite and paragonite (figure 5.1).

The later generation of white mica post-dates the S2 crenulation cleavage, directly overgrowing the earlier folded, crenulated white micas, as seen in figure 5.2. This later generation of white mica is larger (up to 1mm), and tends to have a muscovite core, with a narrow discontinuous rim of paragonite (figure 5.3).

There is abundant chloritoid, occurring within the micas as chloritoid-rich bands, on scales from 0.5 to 10cm. The chloritoid is aligned with the earlier strong fabric S1 and

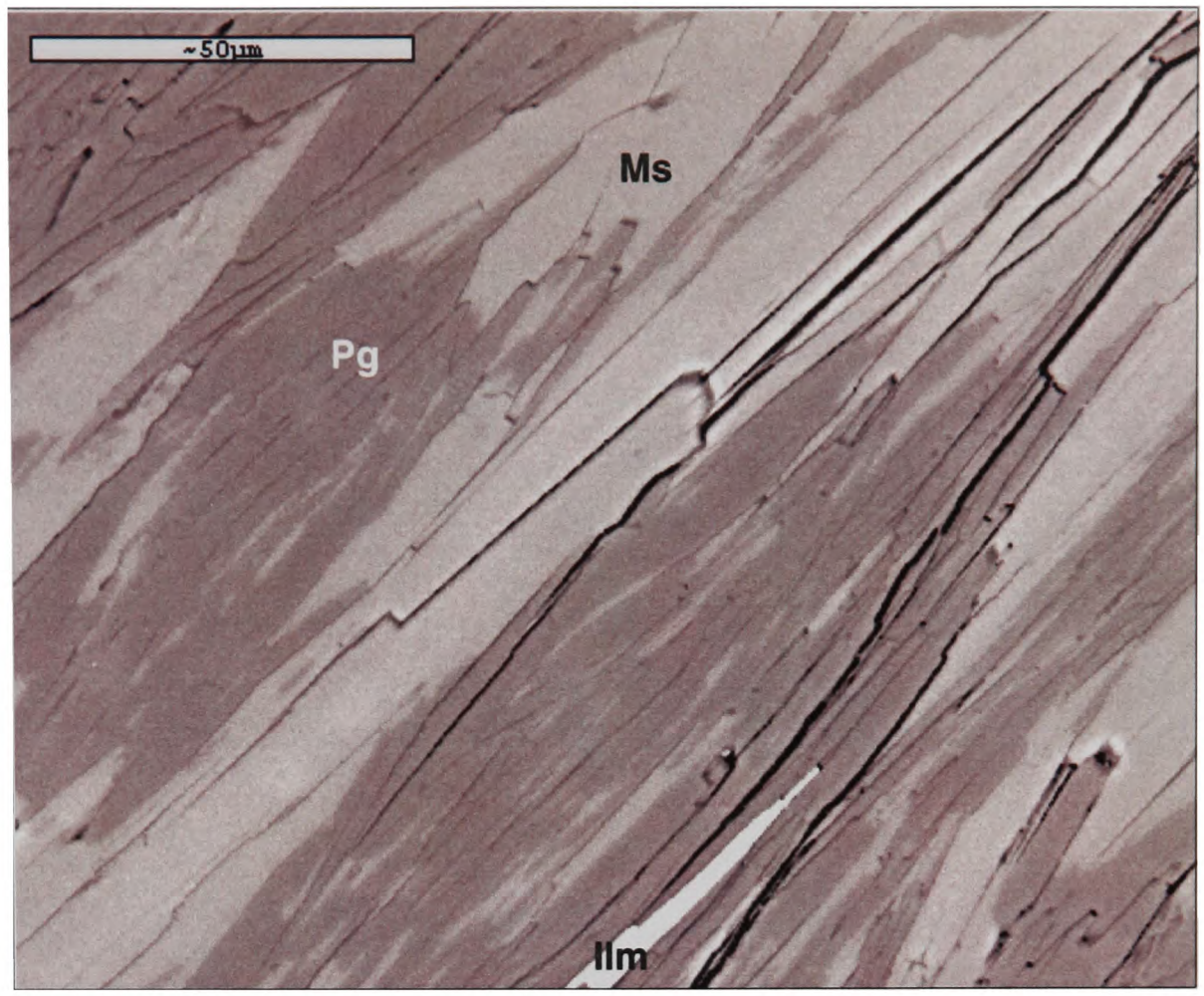


Figure 5.1: Backscattered SEM image from sample P21 showing first-generation matrix muscovite-paragonite intergrowth defining S1 (running NE-SW). Also shown is ilmenite at a small angle to the S1 fabric.

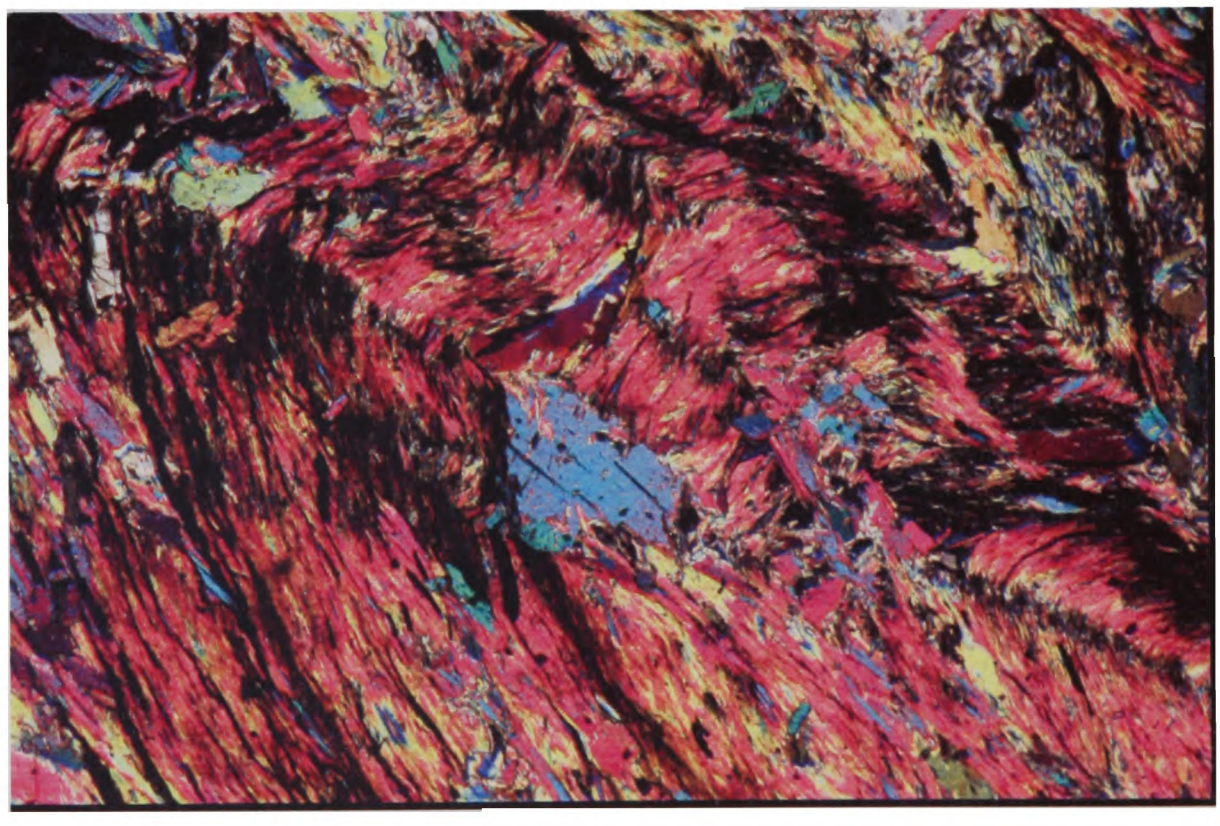


Figure 5.2: Photomicrograph from P21 showing second generation white mica overgrowing earlier white mica, which shows both S1 alignment, and S2 crenulation running NW-SE. XPL, field of view 2.4×3.6mm.

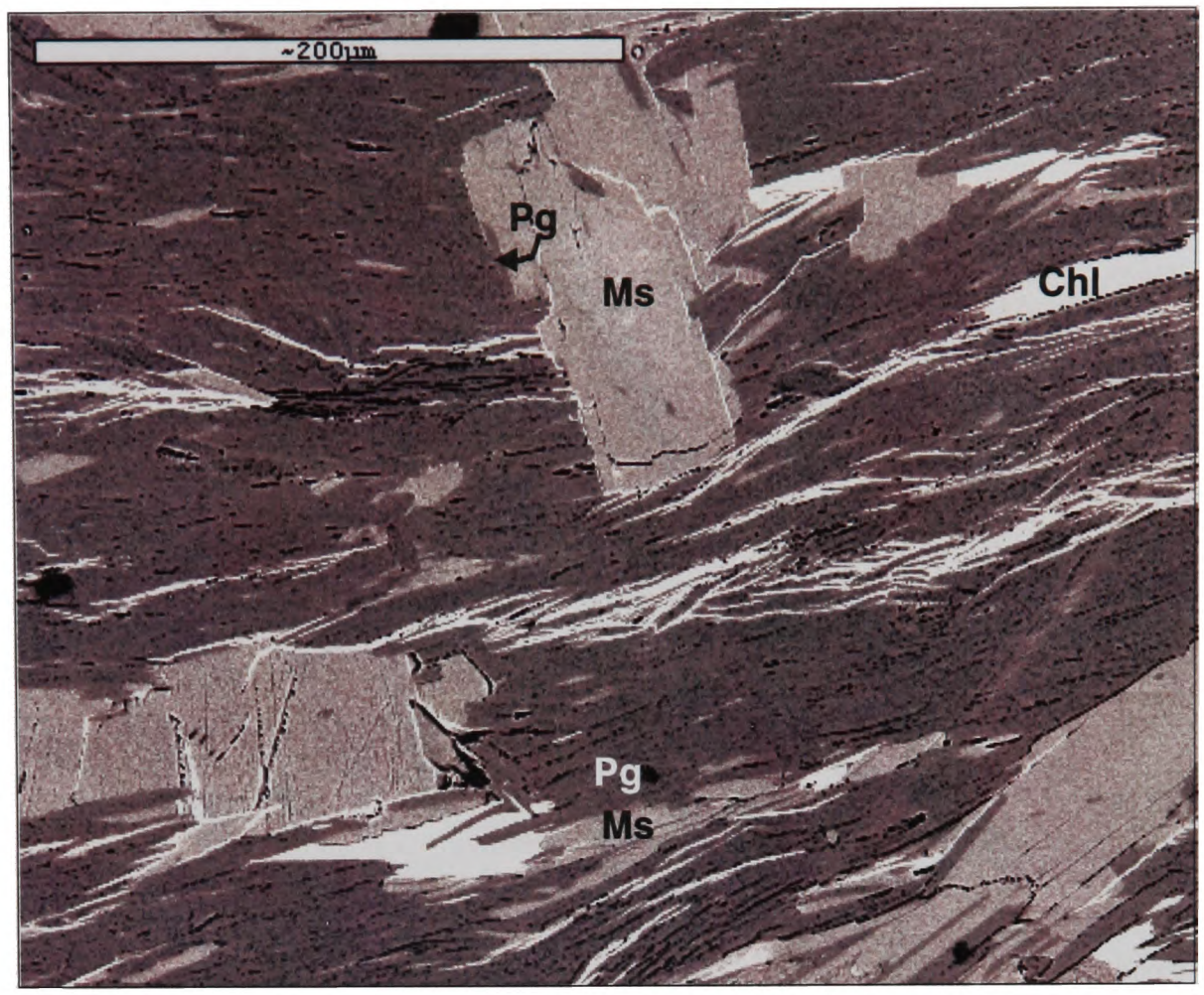


Figure 5.3: Backscattered SEM image from sample P21 detailing cross-cutting second generation muscovite with discontinuous paragonite rims. 1^{st} generation chlorite is also pictured.

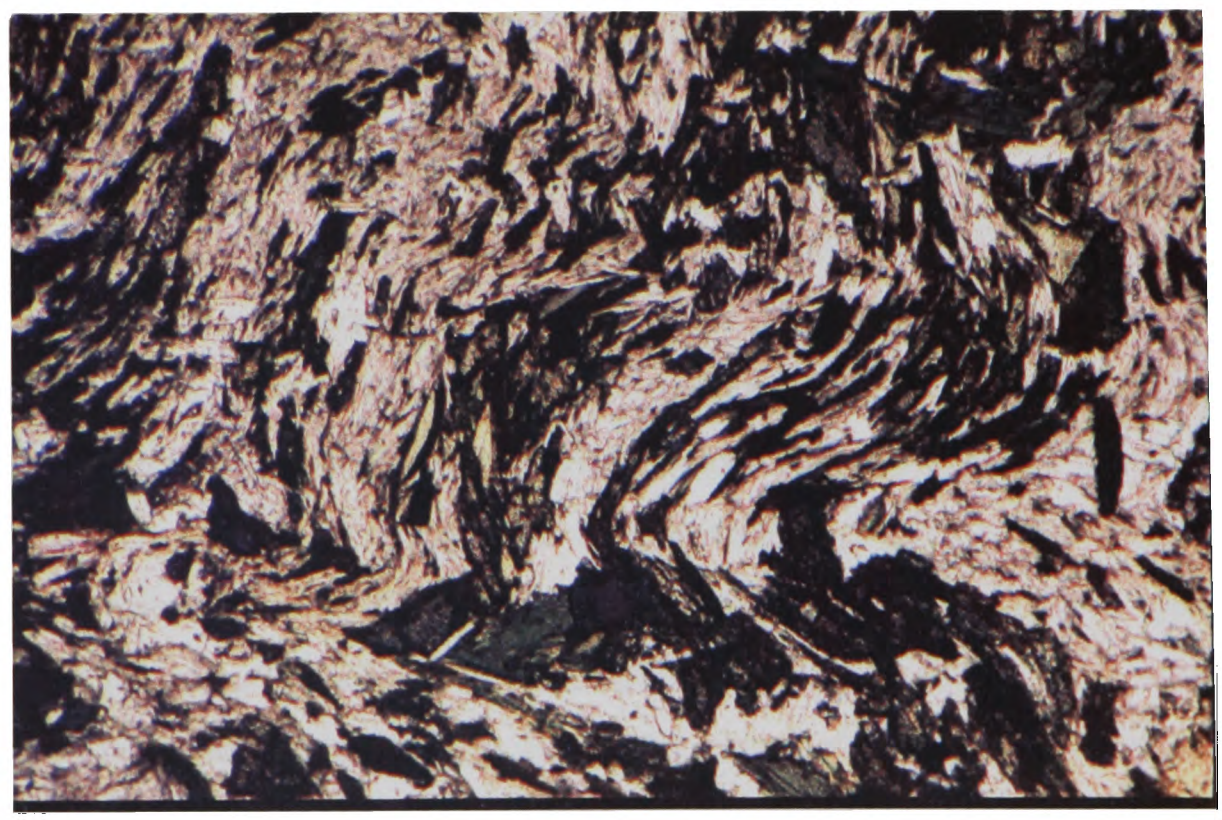


Figure 5.4: Photomicrograph from P21 showing chloritoid (green) folded in with the earlier white mica crenulation (S2). PPL, field of view 2.4×3.6mm.

has been crenulated with S2, as seen in figure 5.4. The earlier fabric S1 can be seen in places to pass through into the garnet, as demonstrated by chloritoid in figure 5.5. The abundant chloritoid inclusions (with rutile) define a garnet core fabric which exhibits a curvature, demonstrating garnet growth and rotation during D1 deformation. Rutile is



Figure 5.5: Photomicrograph from P21 showing chloritoid-defined S1 passing through into the rim of the garnet. In addition, the matrix shows evidence for S2 crenulation. PPL, field of view 3.6mm.

the major Ti-bearing phase in the garnet core, whereas ilmenite is the major Ti-bearing phase in the garnet rim and the matrix, where it is found imperfectly aligned to the earlier fabric S1, at small angles to it. Other garnet inclusions are largely white mica and quartz, with some apatite. Figure 5.6 shows a schematic garnet inclusion pattern from P21. The illustrated garnet lies within a white mica-rich domain and as such chloritoid is a minor inclusion; other P21 garnets contain abundant chloritoid inclusions. Matrix chlorite is present but also overgrows both S1 and S2, being of the same generation as the later white mica. There is no evidence for an earlier generation of chlorite, although this cannot be ruled out completely. Figure 5.7 summarizes the microstructural history. Assemblage: Ms+Pg+Qtz+Cld+Grt+Chl+Ilm+Ap.

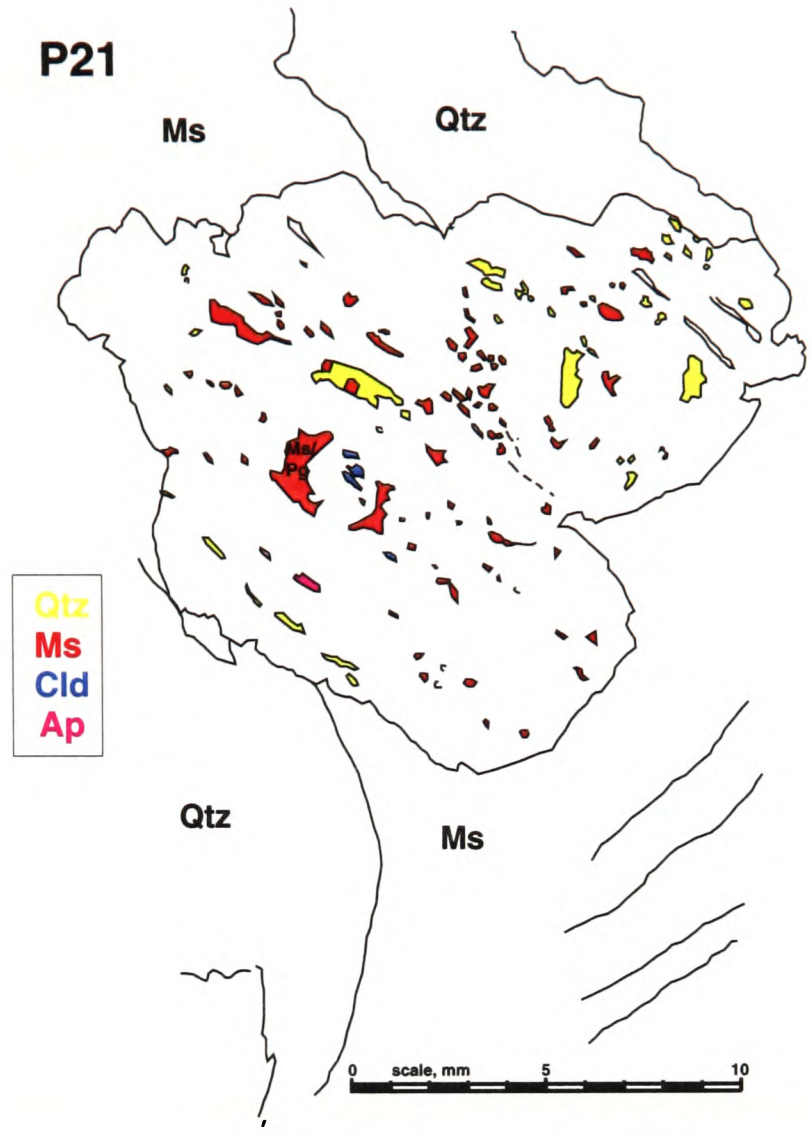


Figure 5.6: Schematic P21 garnet inclusion pattern.

P21	D1, M1	D2	M2
Grt	S1 rotation		
Ms, Pg	S1	S2 crenulation	
Cld	S1	S2 crenulation	
Chl	no evidence for early Chl		

Figure 5.7: Schematic microstructural history of sample P21. D and M refer to a deformational and metamorphic event respectively, and S refers to a fabric.

5.1.2 Sample S66

Sample S66 outcrops south of P21, in the lower-mid garnet zone. Here, the S2 schistosity is dominant, forming a very strong matrix foliation with ribbons of quartz separating micaceous zones. This fabric wraps the garnets, giving rise to marked pressure shadows filled with chlorite and feldspar (syn-post D2, perhaps D3 shearing). Figure 5.8 details a quartz string wrapping around a garnet, with pressure shadows.

The micaceous domains contain recrystallized white mica; chloritoid appears to be pre-tectonic and is almost aligned to S2, but has slightly undulose extinction, and very fine lamellar twinning. Ilmenite is stable in the matrix with chloritoid. There is much re-crystallization, and a lot of chlorite, occurring as chlorite-rich bands, which appear to be post-S2.

Garnet cores show curved trails of fine chloritoid and rutile, which extend to the rim. At the very latest garnets grew and rotated in early D2, otherwise they are all pre-D2. Assemblage: Ms+Pg+Qtz+Grt+Cld+Chl+Ilm.



Figure 5.8: Photomicrograph from sample S66, showing aligned quartz string and white micas wrapping around garnet, giving rise to pressure shadows. XPL, field of view 6×9mm.

5.1.3 Sample R94

From the mid-upper garnet zone, R94 is notable for the appearance of late-stage plagioclase, which texturally replaces paragonite. This plagioclase replacement is probably associated with late-stage fluid influx (as discussed in section 5.2) and is texturally later than garnet growth. Plagioclase also appears in the garnet crack system, again a later phenomenon.

Early white mica defines an S1 schistosity which is largely obscured by a pervasive S2 irregularly folded crenulation. A later generation of white mica grows across this. S2 wraps around the garnets, giving rise to pressure shadows filled with quartz and later plagioclase (draping caused by S3 shearing). Some garnets show a marked textural unconformity, separating cores from rims. The cores of these garnets preserve an early (original, S1) fabric defined by chloritoid and rutile needles. At the unconformity, there is a transition between rutile and ilmenite. The rims of these garnets do not contain any chloritoid inclusions, just white micas and quartz, suggesting garnet growth after complete consumption of matrix chloritoid. However, in other garnets with an absence of a textual unconformity, chloritoid inclusions are seen right up to the rims (figure 5.9). The inclusion fabric is distinctly curved in the core region, suggesting garnet rotation during growth, but is more linear in the rim, truncating the curvature in the core (although the core and rim fabrics are similar in style). Figure 5.10 shows the garnet inclusion patterns in sample R94. This details a complex inclusion pattern with a core largely consisting of chloritoid inclusions, and some white mica and quartz inclusions towards the rim of the garnet.

There is now fairly abundant chlorite, especially adjacent to quartzose layers (in the same orientation), as well as growing locally in the older fabric. This is probably later chlorite. Assemblage: Ms+Qtz+Pl+Grt+Cld+Chl.

5.1.4 Sample R96

R96 is a slightly higher grade than R94, still within the middle-upper garnet zone. Garnet inclusions show a broadly sigmoidal pattern defined by quartz, chloritoid and rutile

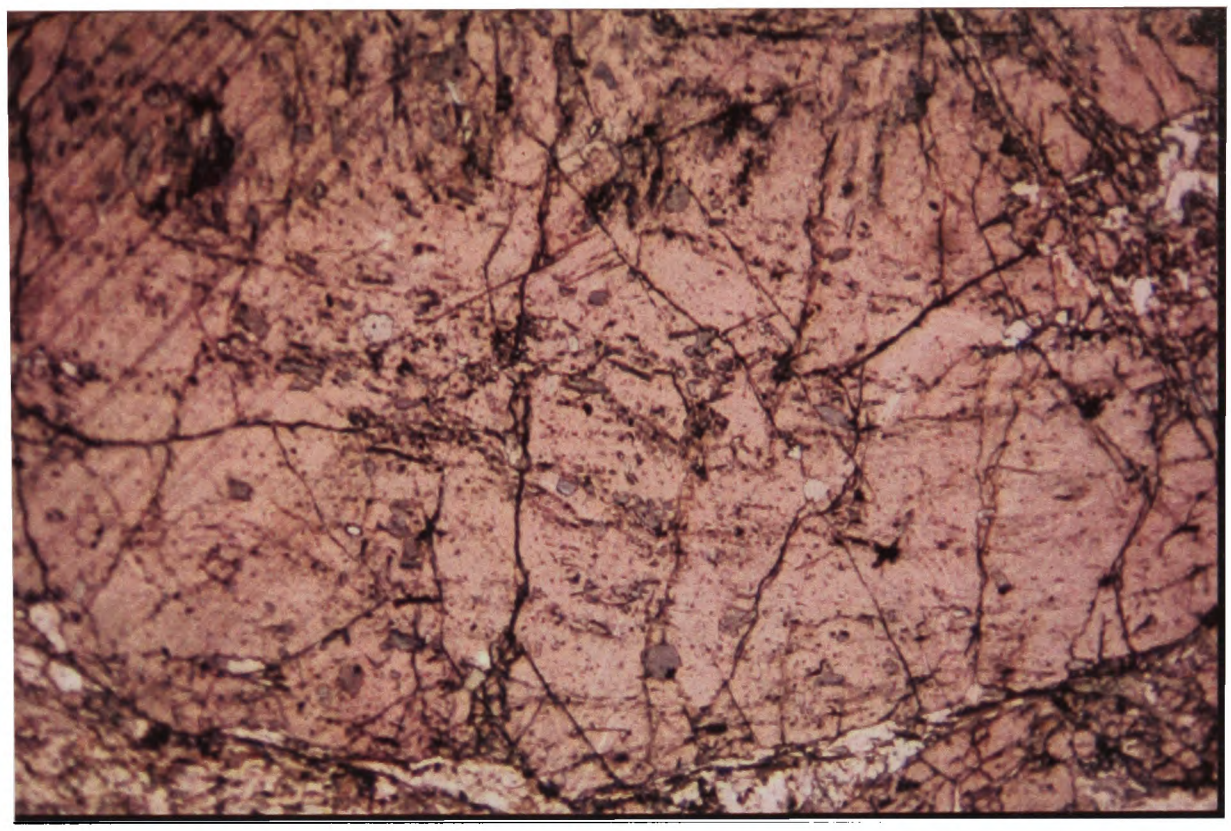


Figure 5.9: Photomicrograph from sample R94, showing S1 inclusion trails defined by chloritoid and rutile running through right to the rim. PPL, field of view 6×9mm.

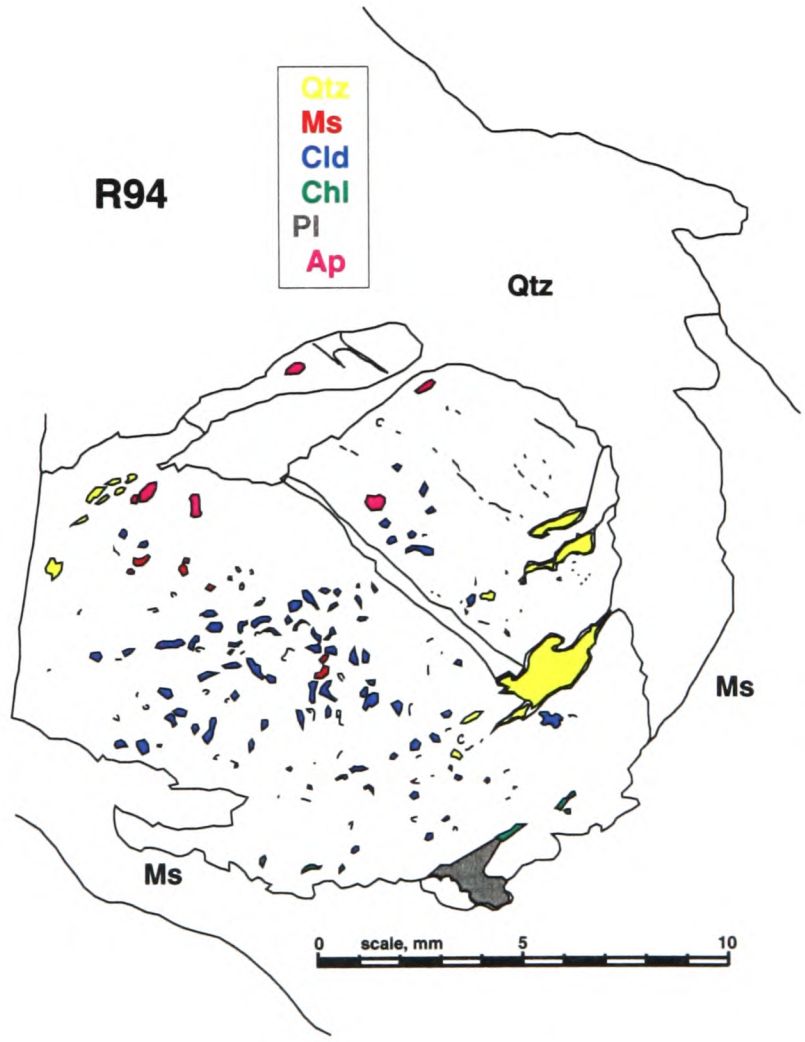


Figure 5.10: Schematic R94 garnet inclusion pattern.

(S1, which can be observed going through into the matrix). Occasionally, near the rim of the garnets, the rutile (changing to ilmenite) trails can be seen to flex back to the opposite direction just before the edge, as seen in figure 5.11. The garnet is wrapped by S2 (S3?) in the matrix, giving rise to quartz pressure shadows. S1 can be traced going from the garnet into the matrix where the garnet is embayed, however the texture is quickly caught up in and folded into S2; therefore this garnet is pre-D2. However, again some garnets show a distinct rim, often separated from the core by quartz trails and a truncation of the core fabric. Other garnet inclusions include white micas, of which some appear original, but others appear as very fine-grained pseudomorphs, probably originally chloritoid; there are also quartz and some chlorite inclusions towards the rim.

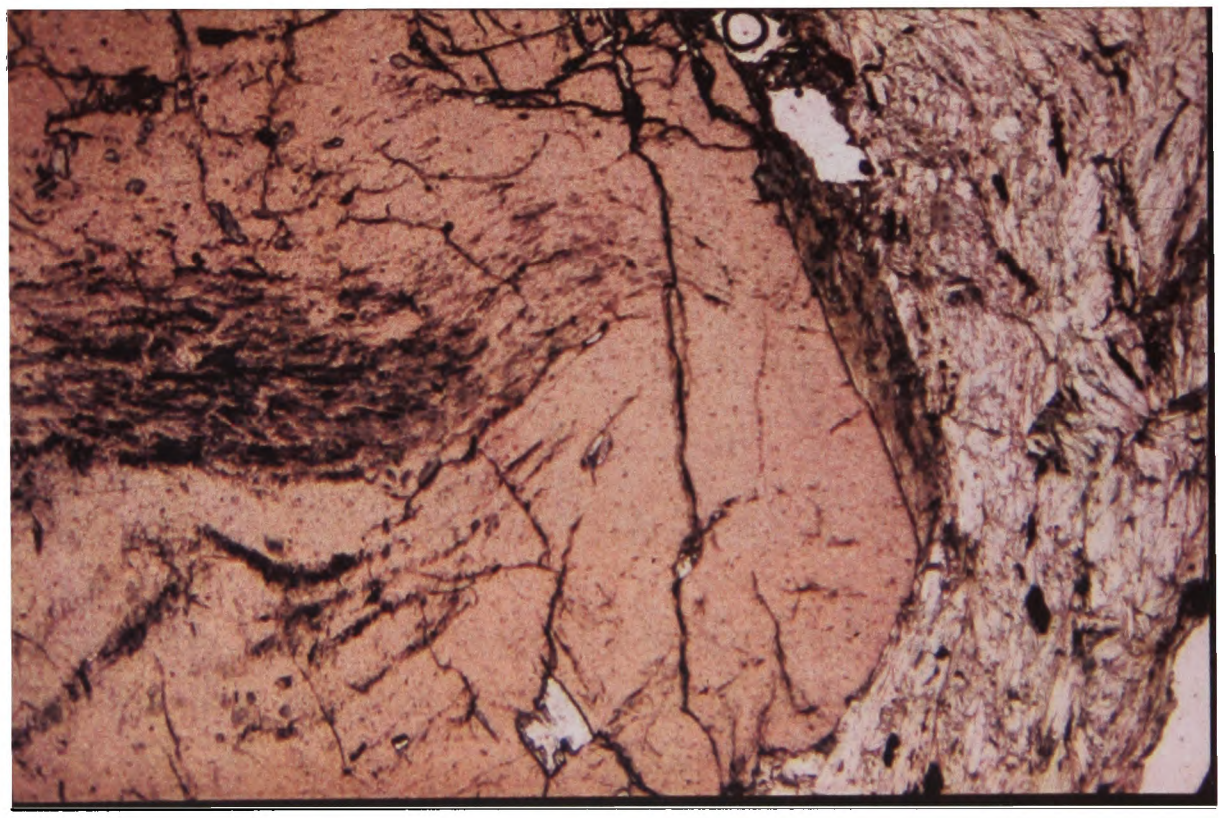


Figure 5.11: Photomicrograph from R96 showing rutile inclusions defining S1 trails that flex back towards the rim of the garnet. PPL, field of view 6×9mm.

White micas are coarser than at lower grades, being less finely felted. Again, at least two generations of white mica can be distinguished: an early generation folded by D2 crenulation, and a later cross-cutting generation. However, there is no primary paragonite present; it has all been replaced by later plagioclase that picks up the texture of the first generation paragonite-muscovite intergrowth, and all simultaneously goes into extinction (see figure 5.12). There is abundant late chlorite; however there is

no unambiguously early chlorite, some may be present folded in with the early generation of white micas. Matrix chloritoid is now absent. There is an abundance of quartz, mostly showing undulose extinction, but occasionally appearing to have recrystallized, with a reduction in grain size. There is also some minor margarite. Assemblage: Ms+Qtz+Pl+Grt+Chl+(Cld).

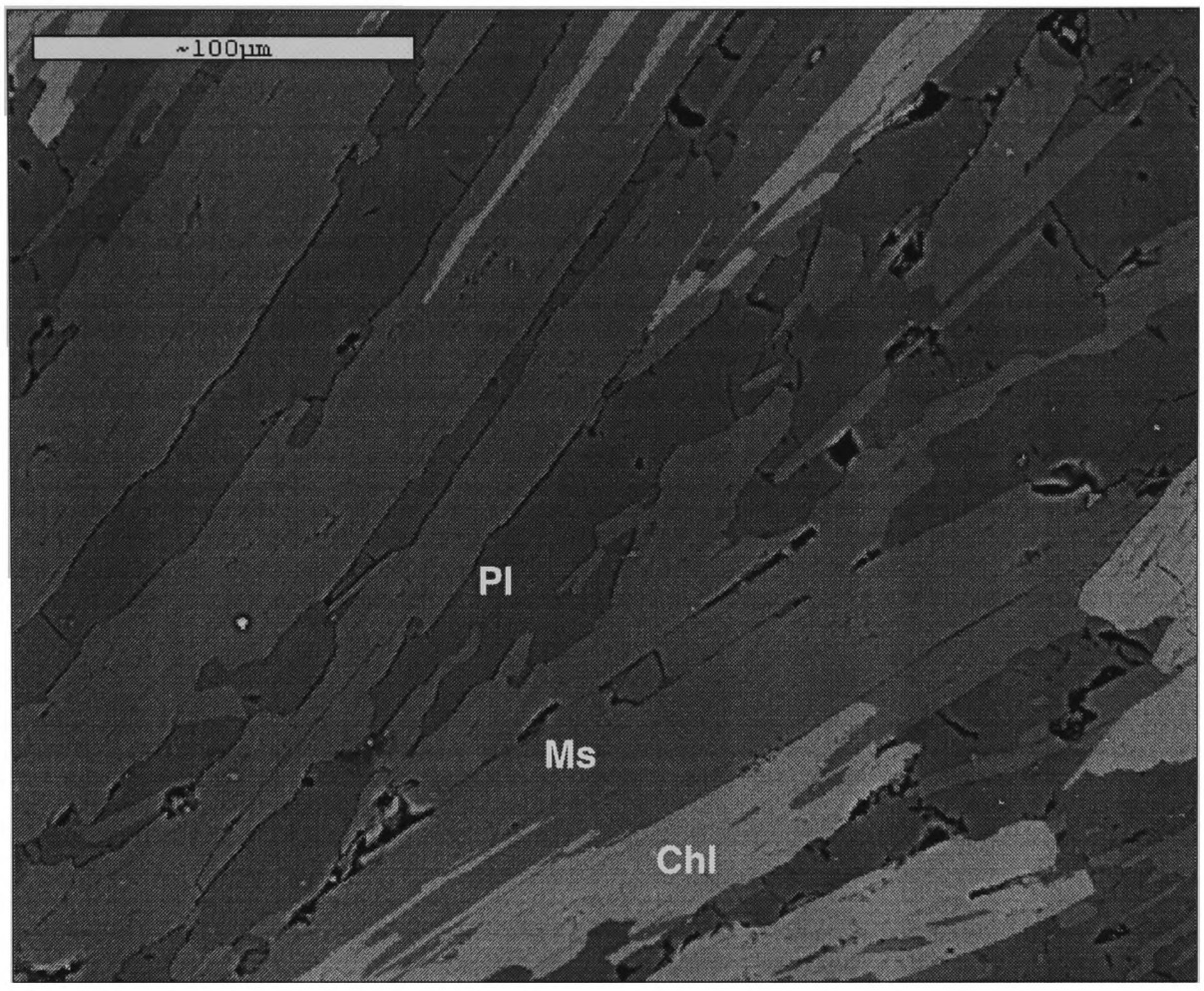


Figure 5.12: Backscattered SEM image of matrix muscovite, plagioclase and chlorite from sample R96; this shows plagioclase replacement of paragonite, picking up the first generation muscovite-paragonite texture (compare with figure 5.1).

5.1.5 Sample P86

In the highest garnet grade sample studied, garnets are wrapped by a lenticular streaky fabric (an intense S2 fabric). There is abundant matrix chloritoid and chlorite; the chlorite is mostly late, partially replacing chloritoid, and not aligned with the mica fabric. The garnet inclusion patterns in the samples studied (principally chloritoid and rutile) define a helicitic (partial crenulation) fabric, however this is possibly not associated with D2, since the matrix S2 wraps around the garnet, and thus inclusion of S2 in garnet core region would require unfeasibly rapid garnet growth. In some garnets, chloritoid in-

clusion trails can be observed right up to the rim of the garnet, defined in some cases by a chloritoid crystal that emerges from the garnet into the stream of S2, as seen in figure 5.13.

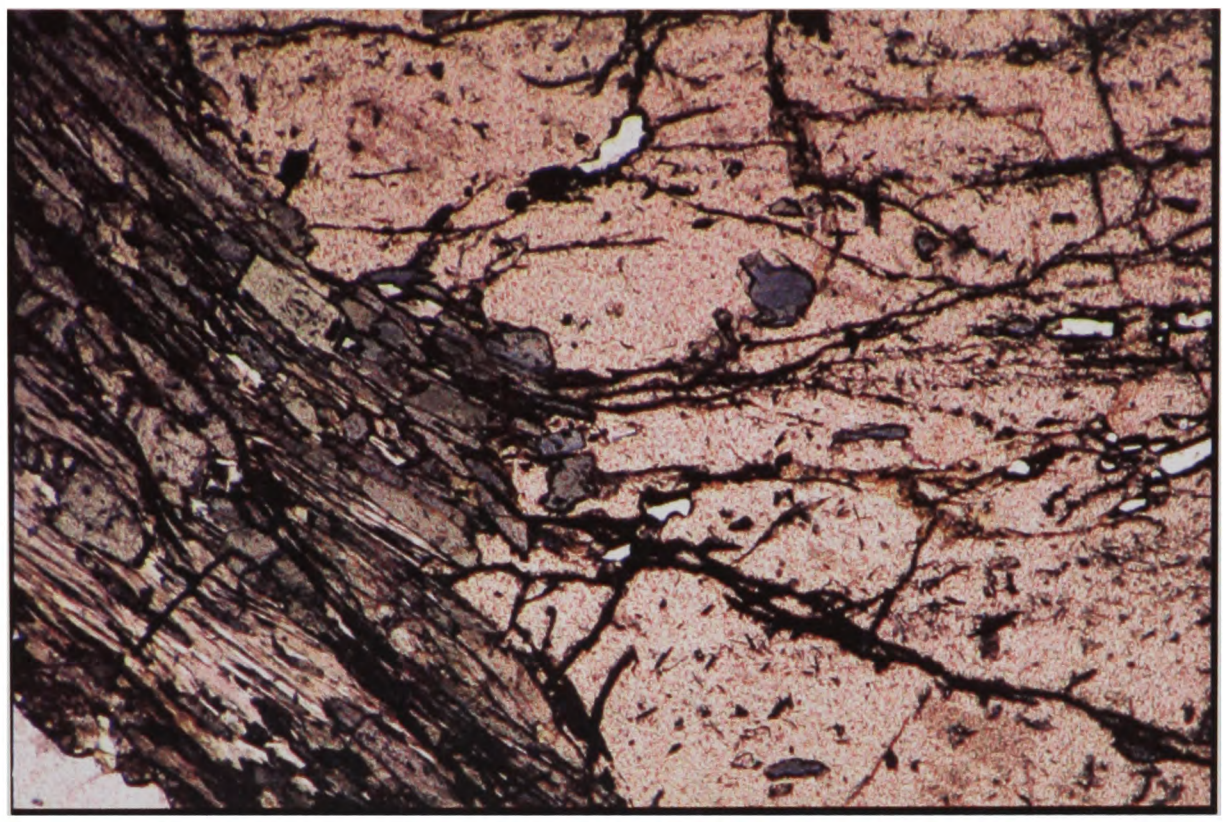


Figure 5.13: Photomicrograph from sample P86 detailing chloritoid inclusions in the garnet (defining S1), emerging from the porphyroblast and being taken up in S2. PPL, field of view 2.4×3.6mm.

5.1.6 Sample 6

Sample 6, from the Peru locality in the mid-staurolite zone, shows evidence of substantial late-stage retrogression; the most striking features of this being the abundant chlorite, especially rimming the garnets, and the break-down of staurolites to ragged relics surrounded by ponds of fine-grained sericite.

The external fabric is marked by lenticular quartz ribbons, characteristic of the S2 crenulation cleavage. At least two, possibly three generations of white micas are observed (figure 5.14). The first manifests itself as fine, well-brushed felted white mica, usually found in relic patches with a curved fabric. The second is coarser but also well aligned with flats parallel to S2 (including some orientated ilmenite). The third (later) is found as cross-cutting flakes.

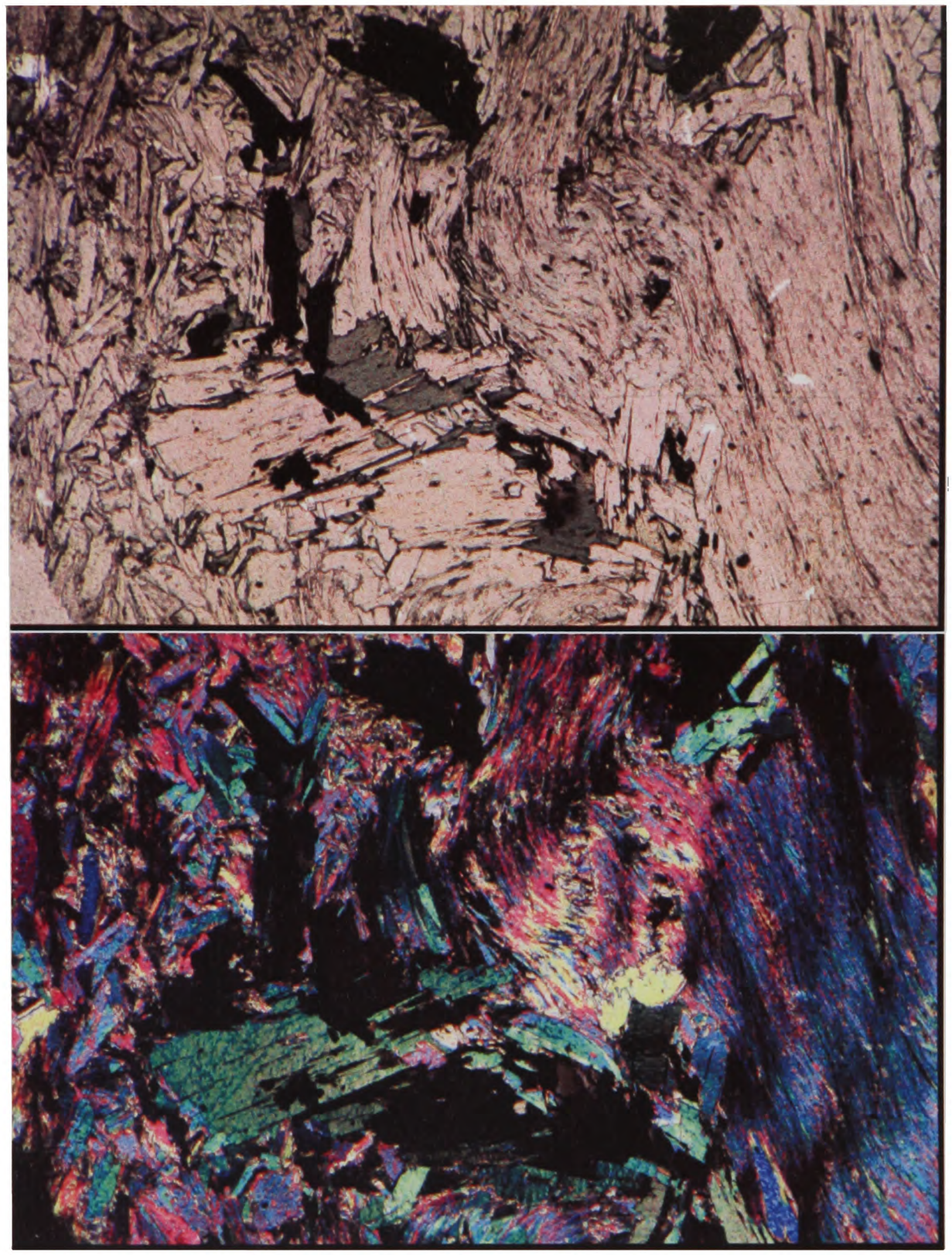


Figure 5.14: Photomicrograph from sample 6 showing 3 generations of white micas. The first generation are the finely felted white micas to the right of the image, which show S1 and S2 crenulation. A potential second generation, still showing S1 and S2 fabric is the coarser white mica to the left. In the centre a third generation lath overgrows the two earlier generations; this has been later partially altered to chlorite. PPL (top) and XPL (bottom), field of view 2.4×3.6mm.

All staurolites have been partially or totally pseudomorphed by a fine-grained intergrowth of mainly white mica and quartz, texturally known as 'shimmer aggregate'. In figure 5.17, the staurolite can be seen to cross-cut the crenulation cleavage (implying staurolite is post-S2), although in places the fabric appears to wrap *around* staurolite; this may be a D3 shearing event giving rise to a D3 fabric. There is occasional late retrograde chloritoid from staurolite breakdown, figure 5.18 shows small twinned chloritoid crystals after staurolite. The retrograde conditions after staurolite are Cld+Chl+Ms, associated with the chlorite rims on the garnets.

Some garnets have inclusion patterns of chloritoid right to the rim; in places it appears to progress into the matrix with the sericite after staurolite: again, chloritoid and staurolite appear to be related. Additionally, these chloritoid inclusions appear to coexist with ilmenite. The inclusion fabric in these garnets is entirely pre-D2 (again probably D1); S2 and S3 wrap around the garnets. Other garnets show a textural break with chloritoid, chlorite and rutile inclusions in the cores, and ilmenite, white mica and quartz inclusions in the rims. The fabric in these garnet cores is probably S1, however the rims truncate this fabric and therefore represent later garnet growth. Figure 5.15 shows schematic microstructural history. Assemblage:Ms+Pg+Qtz+Grt+St+Chl.

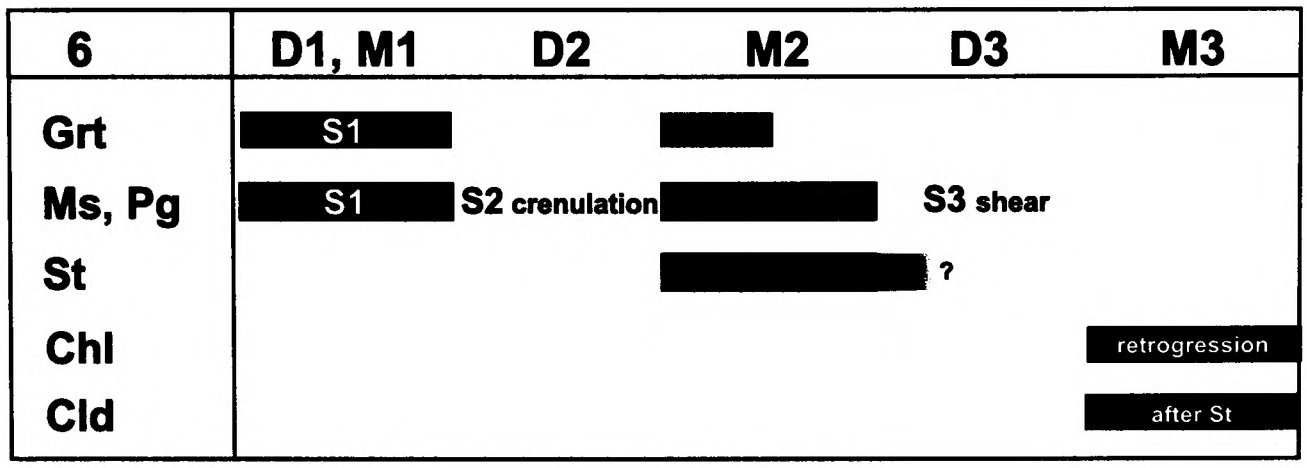


Figure 5.15: Schematic microstructural history of sample 6.

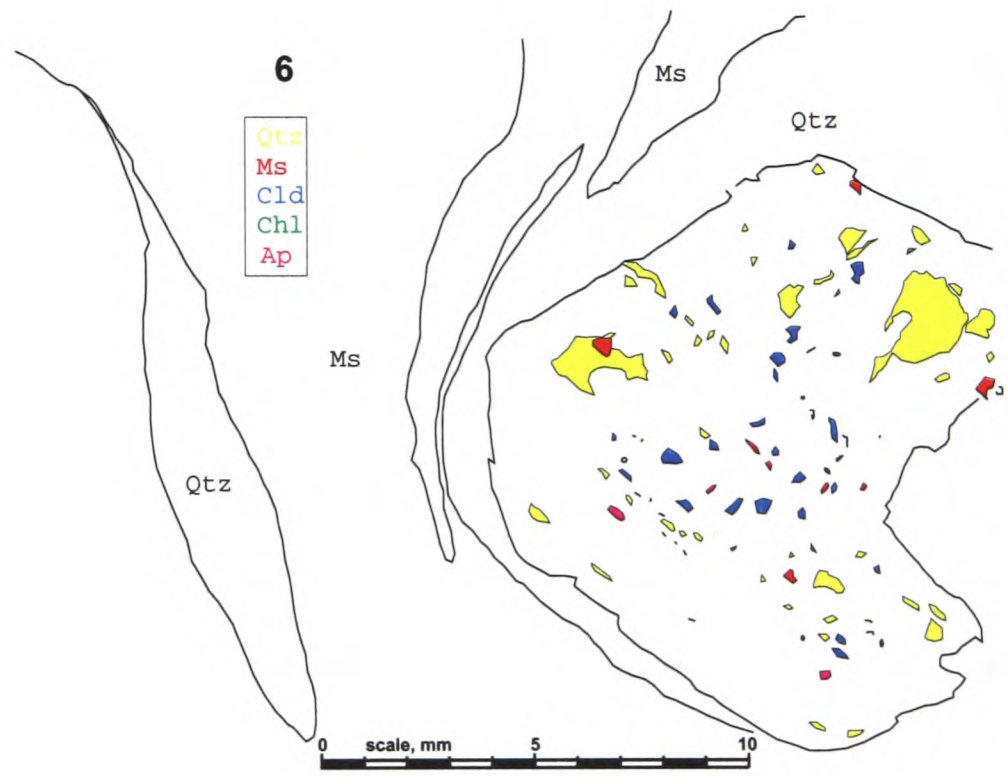


Figure 5.16: Sample 6 schematic garnet inclusion patterns.

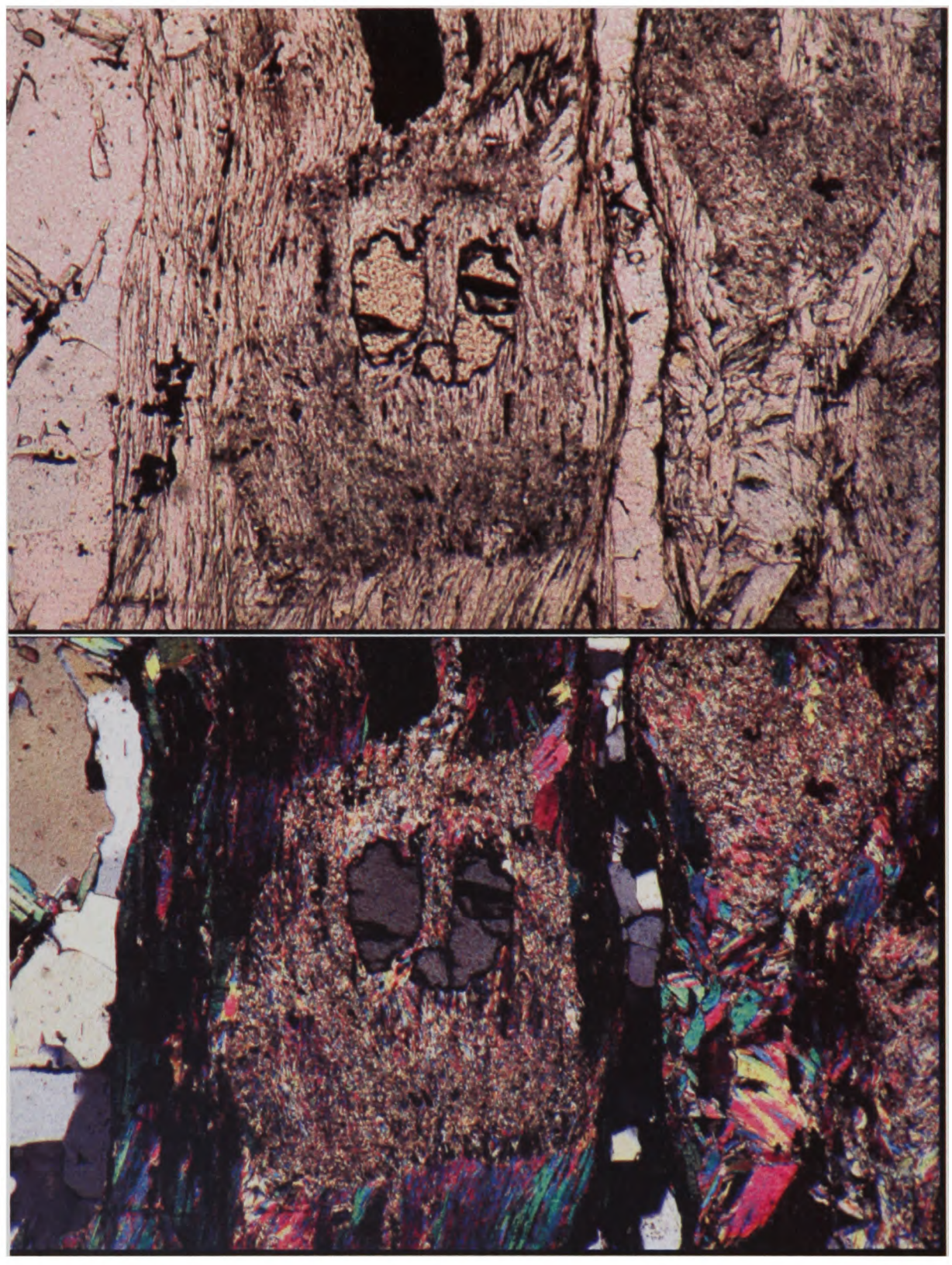


Figure 5.17: Photomicrograph from sample 6 showing a staurolite relic surrounded by sericite overgrowing early white mica (S2, aligned with the quartz ribbon). PPL (top) and XPL (bottom), field of view 2.4×3.6mm.

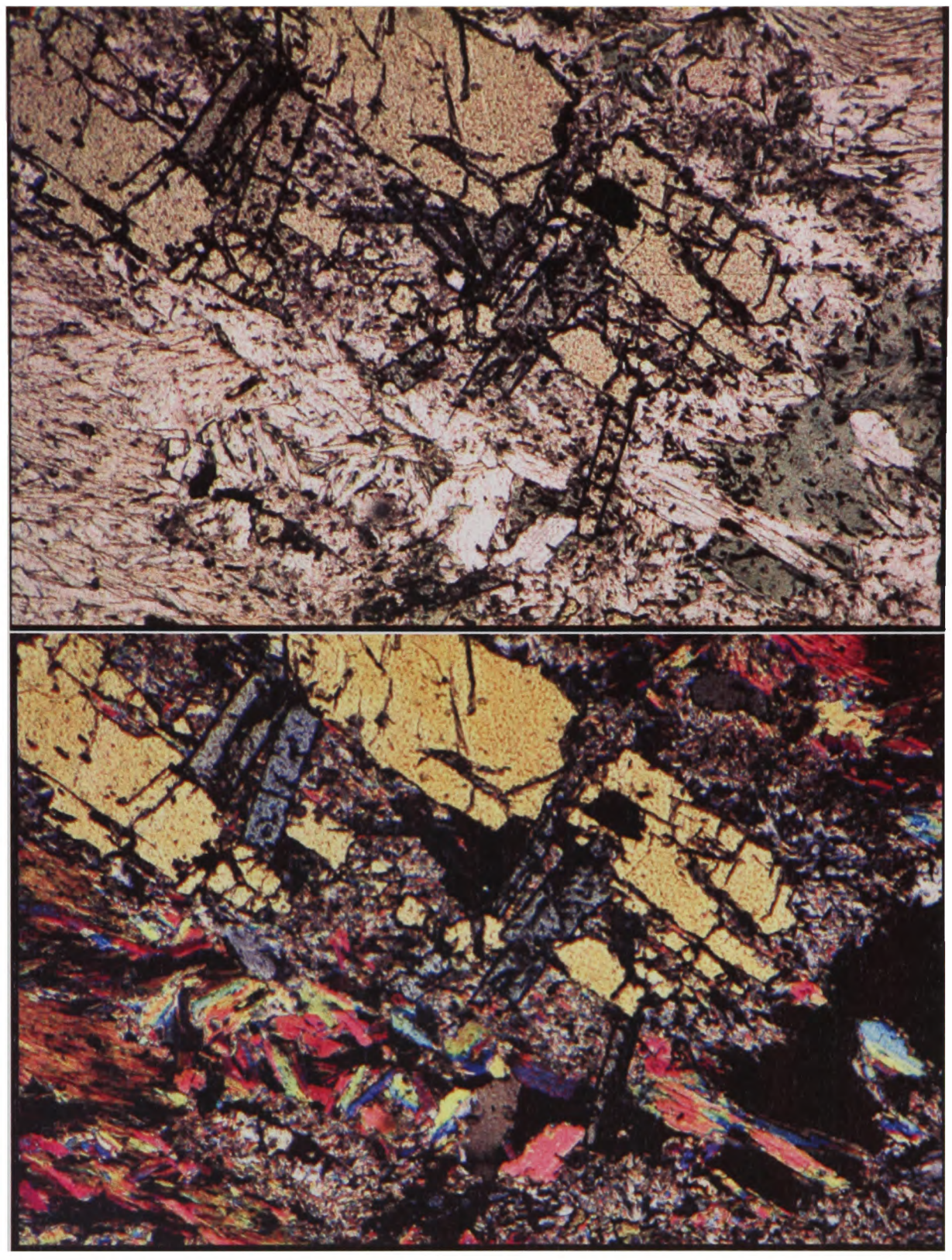


Figure 5.18: Photomicrograph from sample 6 showing staurolite breakdown associated with twinned chloritoid and muscovite. PPL (top) and XPL (bottom), field of view 2.4×3.6mm.

5.1.7 Sample R76

R76 is of a slightly higher grade than sample 6, and here marks the first appearance of biotite. The matrix contains a white mica-defined crenulation cleavage parallel with, and more intense adjacent to, quartz strings (S2). The S2 crenulation cleavage has therefore developed parallel to the quartz-mica banding. This in turn has been flattened and sheared (D3 shearing event giving rise to S3 fabric) around the garnet porphyroblasts (figure 5.19).

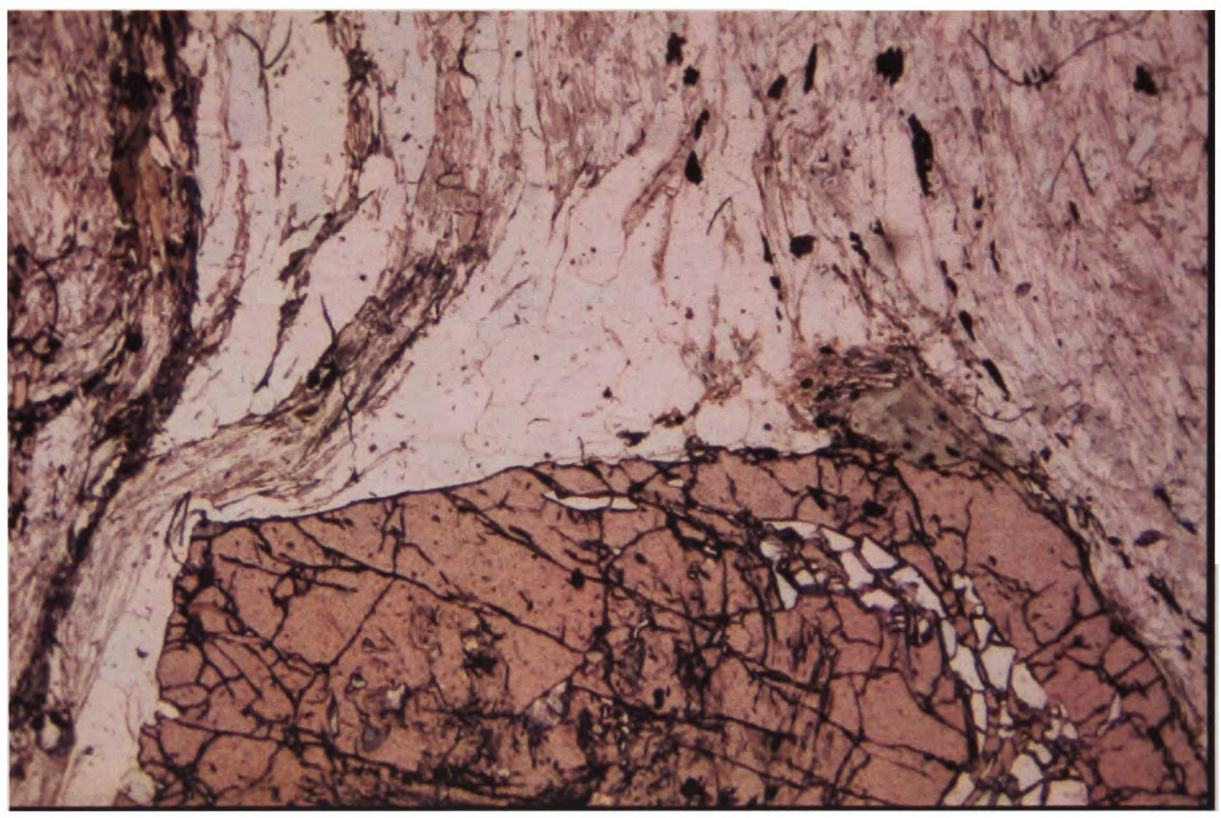


Figure 5.19: Photomicrograph from R76 showing S3 draping around garnet, with quartz-filled pressure shadow. A textural unconformity manifests itself as a garnet overgrowth separated by quartz to the right of the porphyroblast. PPL, field of view 6×9mm.

Staurolites are smaller than in sample 6 (1mm compared to 2-4mm), and appear as cross-cutting porphyroblasts within the white-mica matrix (figure 5.20). Minor biotite is present adjacent to the quartz-rich zones. Both staurolite and biotite are post-S2 but before the last period of shearing (S3), since some mica drapes around them. Additionally, late second generation white micas appear to be pre-S3. Later chlorite cross-cuts the matrix, and is related to the retrogressive event, which post-dates everything. There is also minor plagioclase derived from the retrogression.

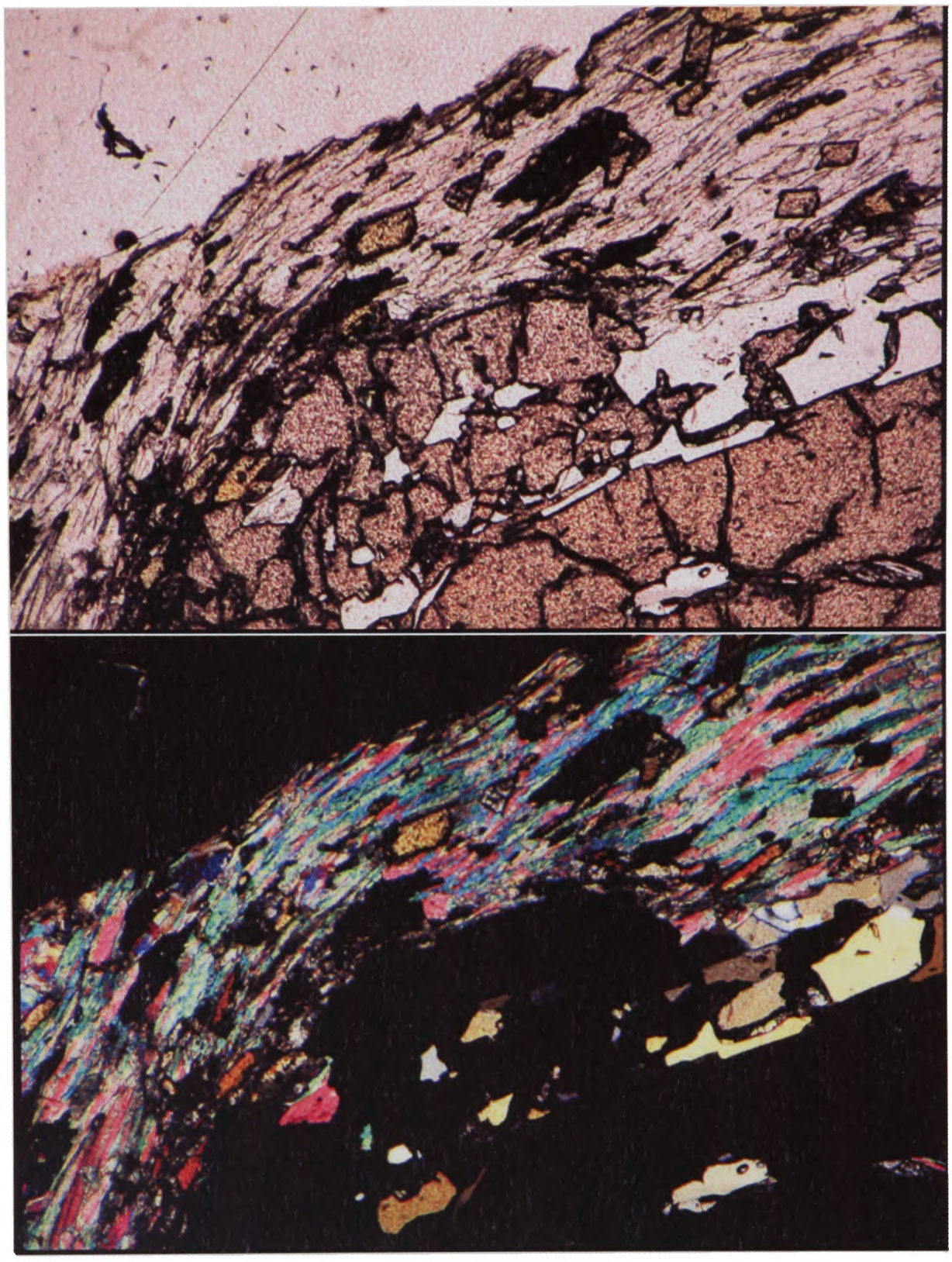


Figure 5.20: Photomicrograph from sample R76 showing S3 draping round the edge of the garnet. Small staurolite crystals are visible, cutting across the white mica matrix. PPL (top) and XPL (bottom), field of view 2.4×3.6mm.

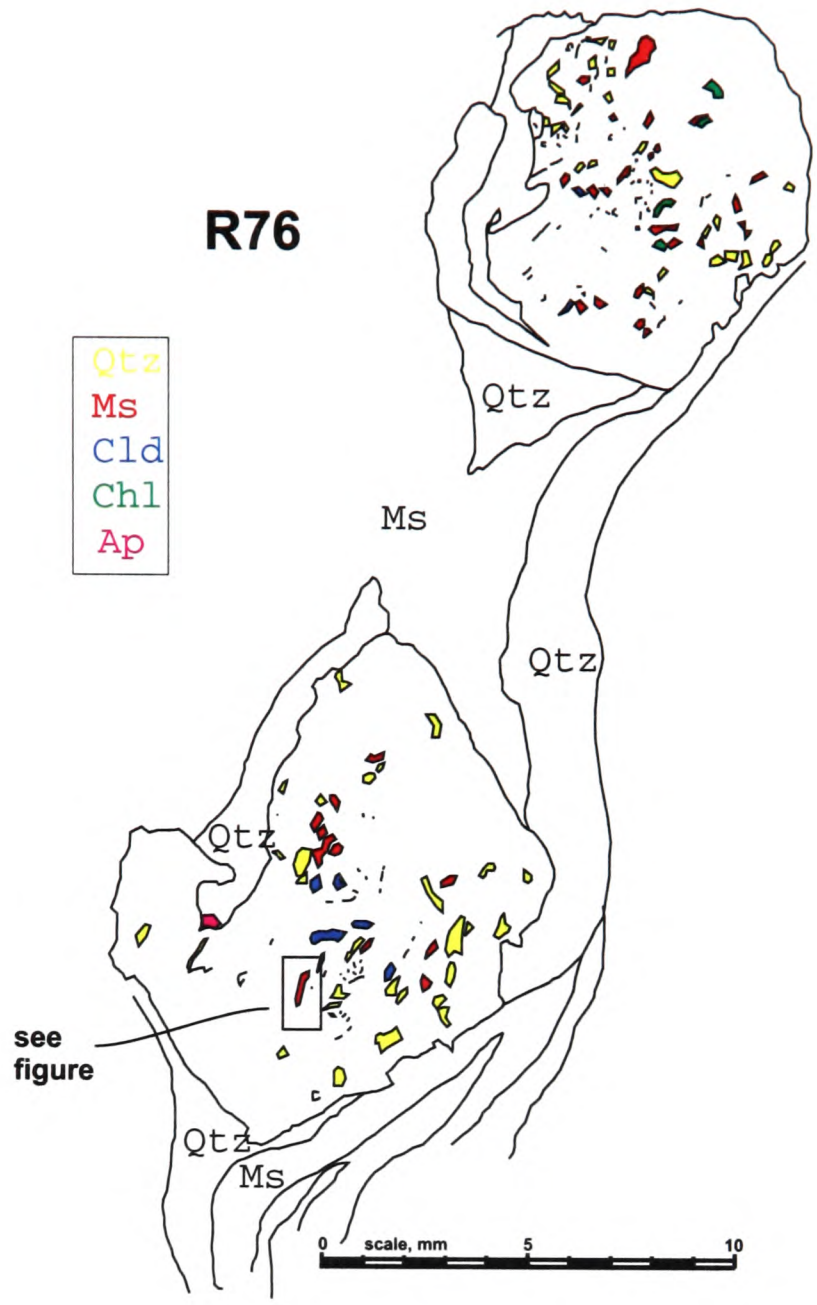


Figure 5.21: Schematic sample R76 garnet inclusion patterns.

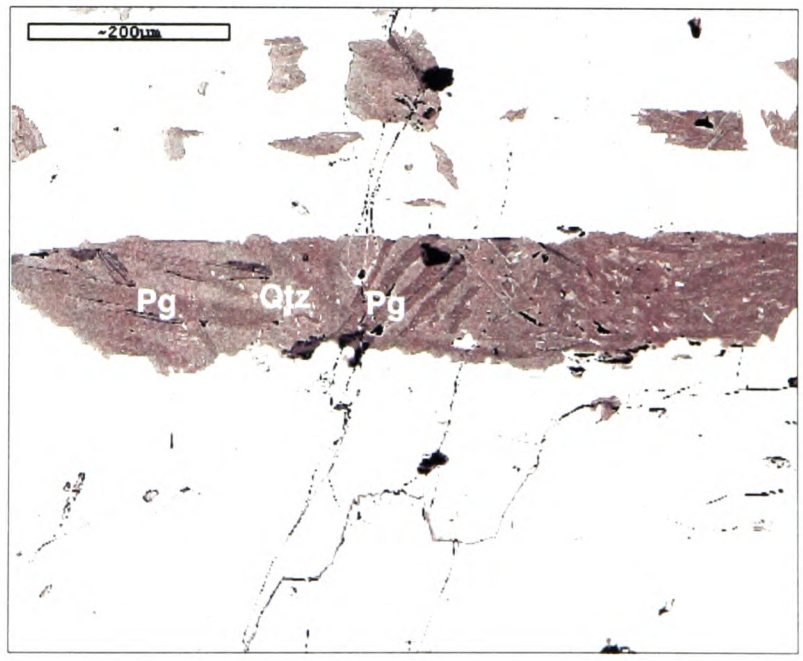


Figure 5.22: Detail of a composite Pg+Qtz garnet inclusion from R76.

Garnet inclusions include chloritoid, quartz and white mica, but no biotite or staurolite is observed as inclusions. In places the chloritoid inclusions are replaced by composite inclusions of a paragonite-quartz pseudomorph (see figure 5.22). Again some garnets have a distinct unconformity separating chloritoid and rutile-rich cores from white mica, quartz and ilmenite-rich rims. This unconformity is clearly seen in the backscattered image of R76 in figure 7.17. Figure 5.23 summarizes the microstructural history.

Assemblage: Ms+Pg+Qtz+Bt+Grt+St+Chl.

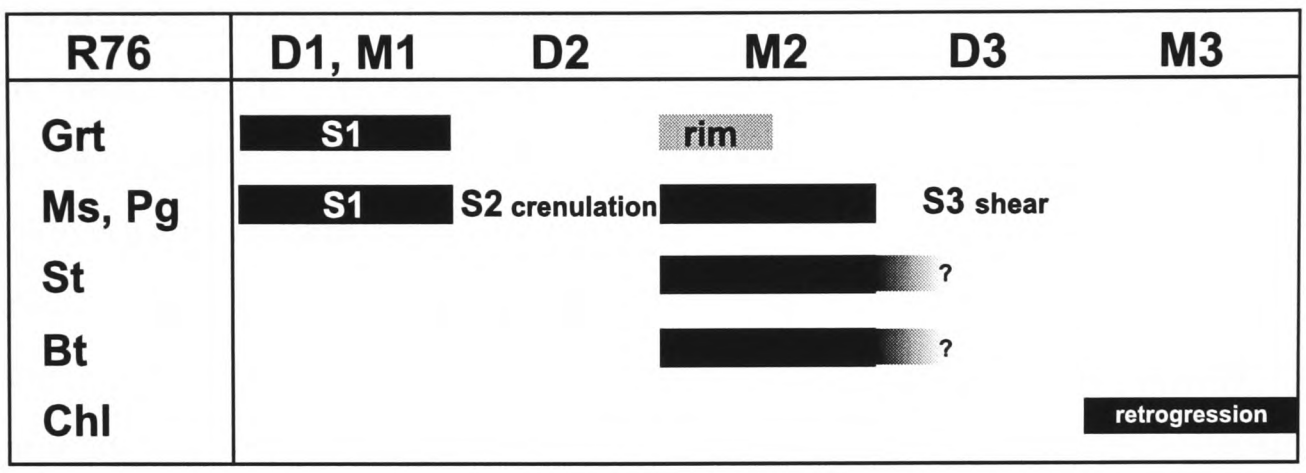


Figure 5.23: Schematic microstructural history of sample R76.

5.1.8 Sample 19

Sample 19 lies at the base of the kyanite zone. White micas define an S2 crenulation that is draped over garnet porphyroblasts by a later D3 shearing episode, giving rise to quartz-filled pressure shadows (S1 is obscured at this grade). The earlier generation of white micas is associated with quartz ribbons, while the later micas cross-cut the earlier (S2) fabric.

Large kyanite porphyroblasts (2-3mm long) have overgrown the early white mica generation fabric, but are generally pre-D3, although some growth into D3 may have occurred (see figure 5.28). Kyanite is also observed to overgrow staurolite and biotite. Staurolite crystals, 2-3mm, show faint, sub-linear inclusion trails of white mica that are sub-angular to the early matrix white mica fabric (figure 5.24), suggesting later rotation (D3, shear event?). The staurolite is also associated with biotite. Biotite may evidence two generations, with sparse biotite folded in with the earlier white mica, and later biotite cross-cutting S2, as seen in figure 5.25.

Large garnets contain inclusions of white mica and chloritoid, which define a fabric (probably S1) which, in some of the porphyroblasts, continues to the rim, but in others is arrested by a rim fabric which contains no chloritoid. Figure 5.27 shows an electron microprobe map of a garnet rom sample 19 for Ti, showing rutile-defined core inclusion trails. These exhibit an S1 sigmoidal fabric, which is truncated by the ilmenite-defined rim fabric. Other garnet inclusions are quartz and chlorite. Also associated with the garnet is plagioclase replacing white mica, associated with staurolite and kyanite. Biotite has late-stage chloritization at the rims. See figure 5.26 for a petrogenetic summary of sample 19.

Assemblage: Ms+Pl+Qtz+Bt+Grt+St+Ky+Bt+Chl.

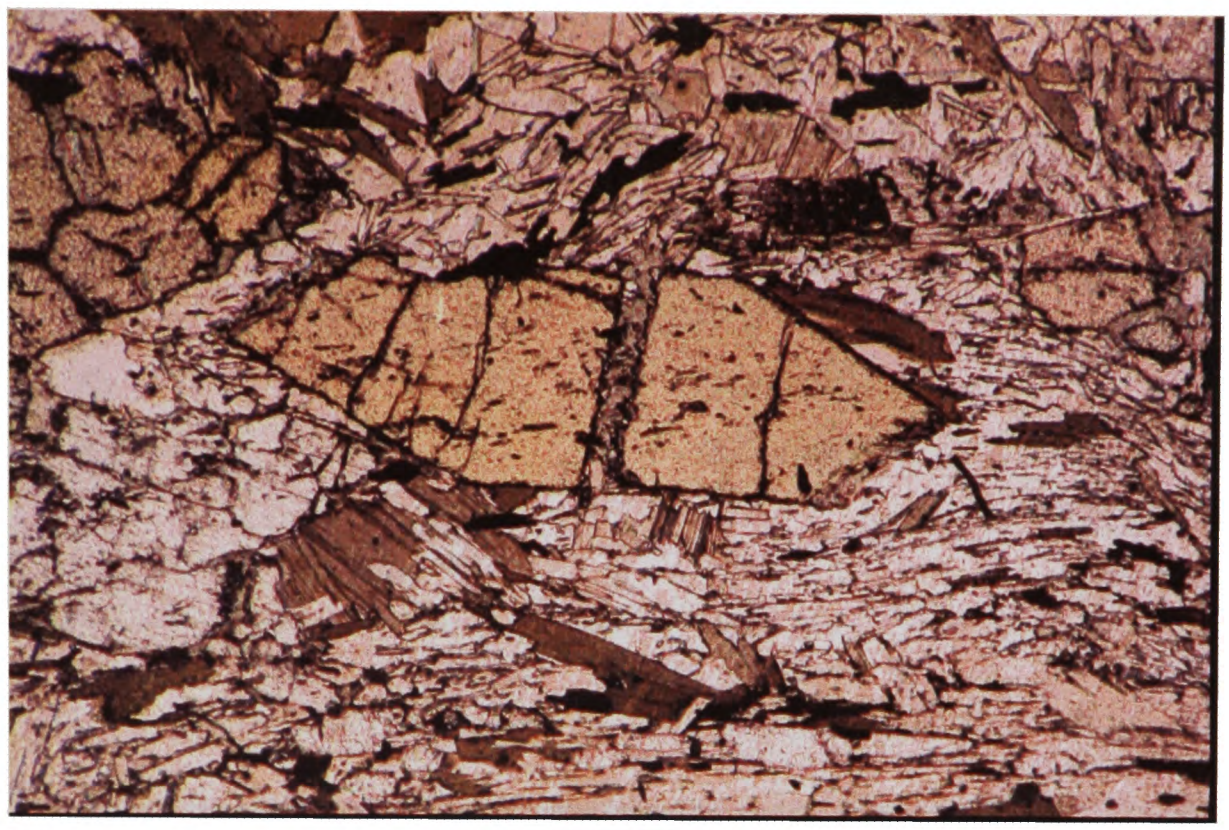


Figure 5.24: Photomicrograph from sample 19 showing staurolite associated with biotite. Inclusion trails are clearly visible in the staurolite. PPL, field of view 2.4×3.6mm.



Figure 5.25: Photomicrograph from sample 19, showing plagioclase intergrowth with muscovite, and biotite overgrowing both. XPL, field of view 2.4×3.6mm.

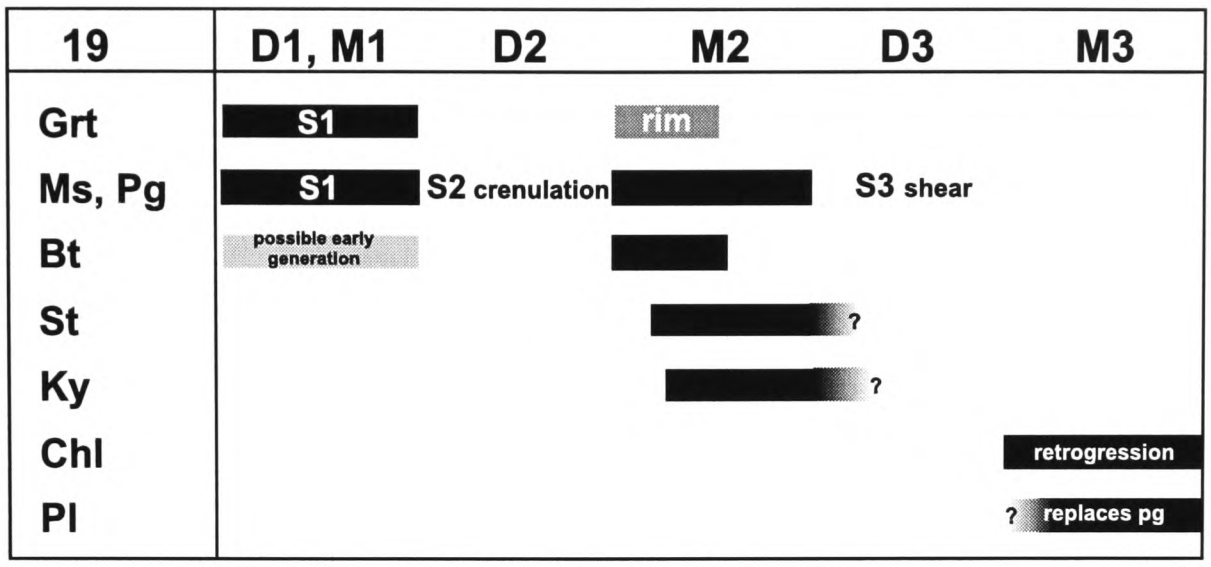


Figure 5.26: Schematic microstructural history of sample 19.

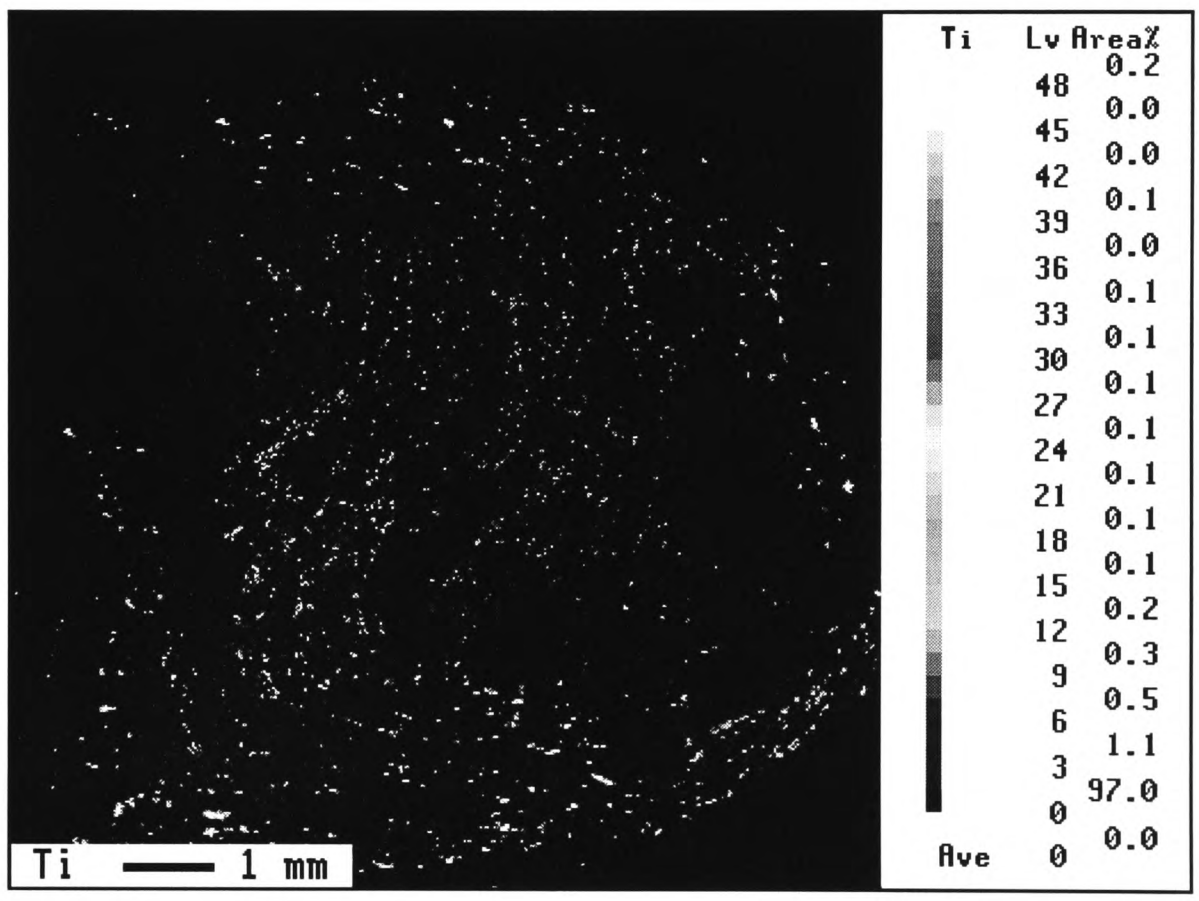


Figure 5.27: Qualitative electron microprobe map detailing Ti in sample 19. In the core of the garnet, Ti-bearing inclusions are exclusively rutile. These define a sigmoidal inclusion pattern, which is truncated by the rim of the garnet, within which the Ti-bearing inclusions are exclusively ilmenite.

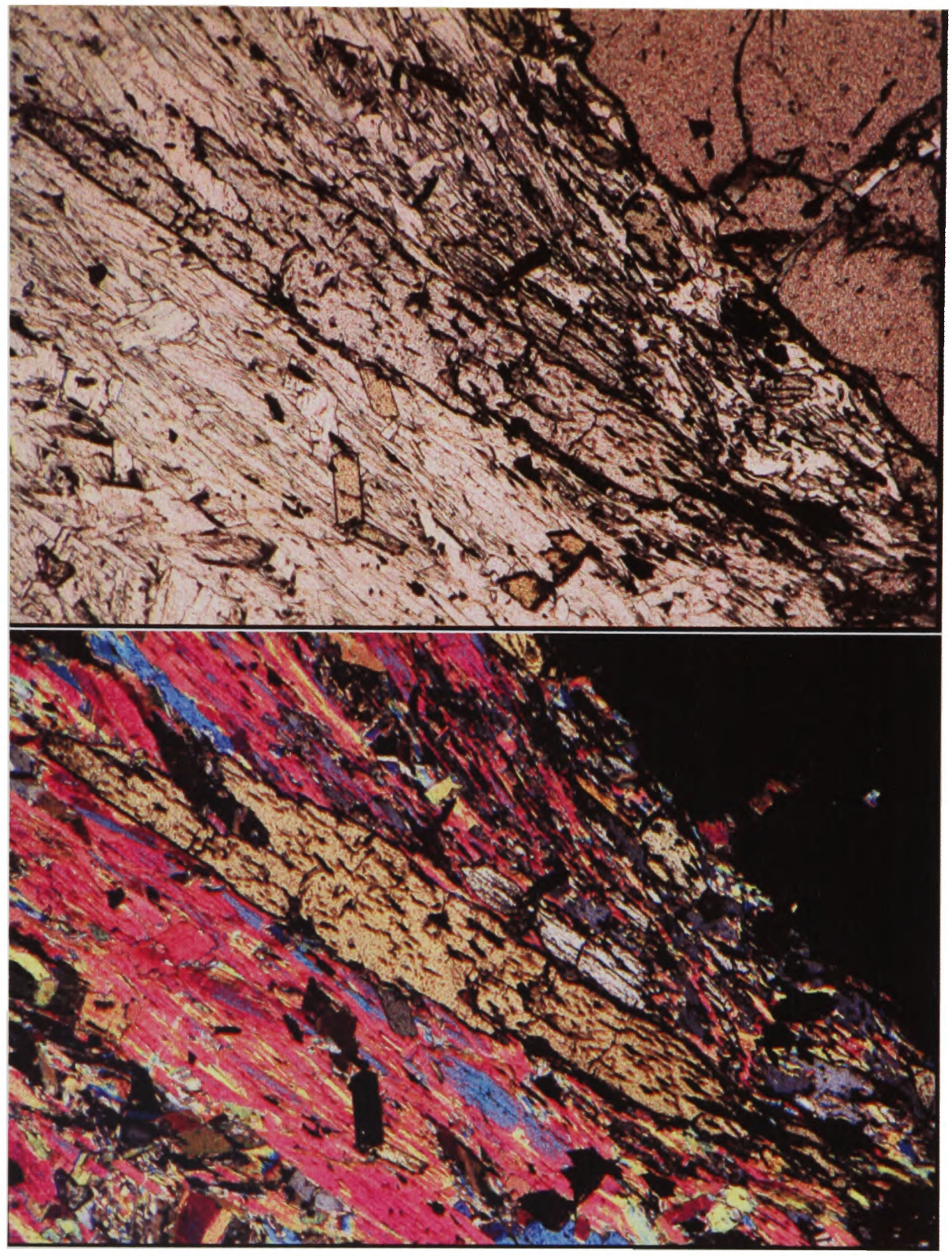


Figure 5.28: Photomicrograph from sample 19 showing a large kyanite crystal with inclusion trails overgrowing the early generation white mica. Small staurolite crystals also cross-cutting S2 fabric are visible. PPL (top) and XPL (bottom), field of view 2.4×3.6mm.

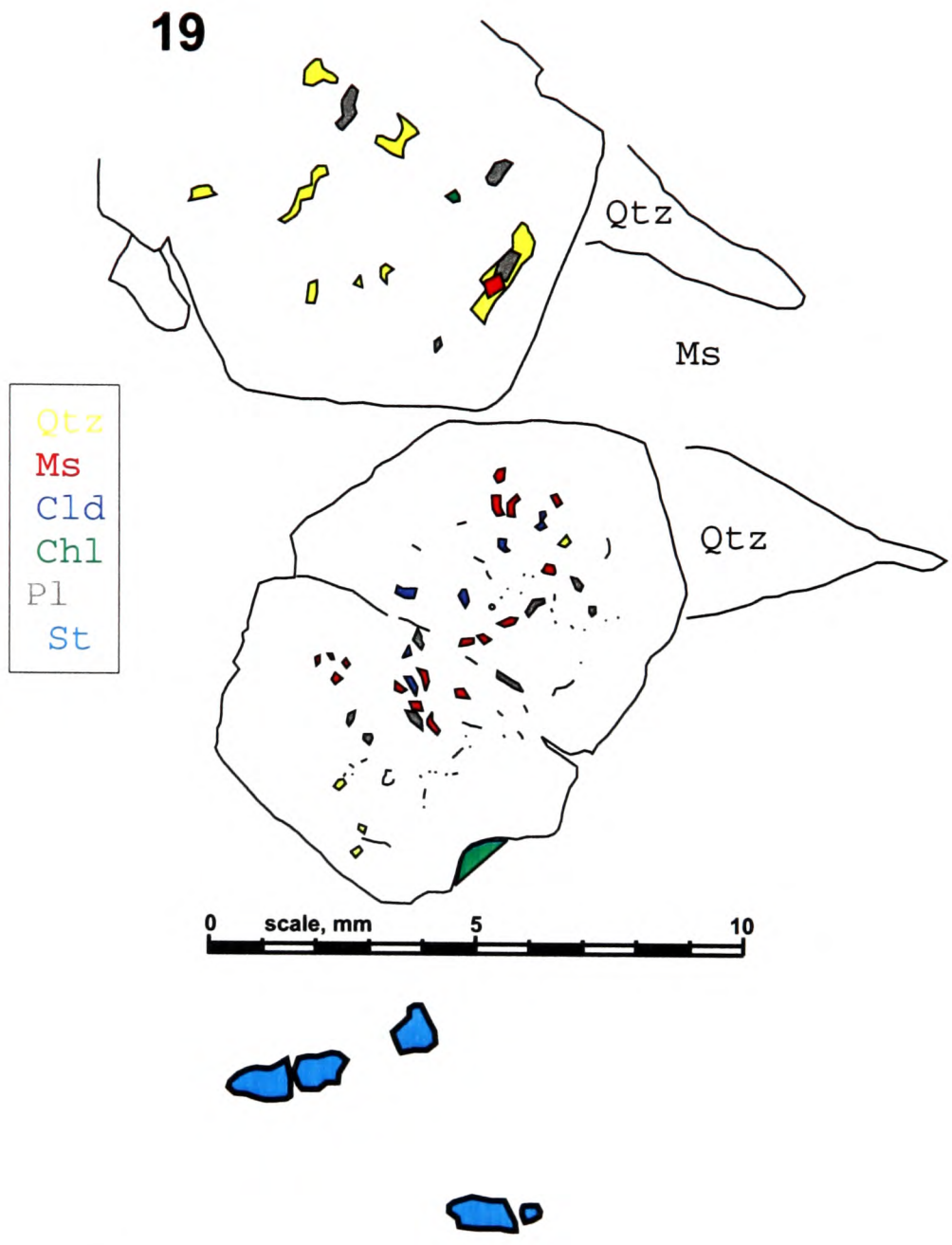


Figure 5.29: Schematic sample 19 garnet inclusion patterns.

5.1.9 Sample P97

P97 is the highest grade studied, and shows features pointing to a different bulk composition from the other samples, not least the presence of strongly graphitic bands on scales from 1mm upwards. There is a much greater abundance of biotite, staurolite and kyanite. In addition, the timing of garnet growth with respect to the deformation may imply that garnet grew at a different stage relative to lower grade samples.

The matrix is defined by aligned muscovite defining an S2 fabric which has been slightly folded; this is associated with quartz ribbons. Later muscovites cross-cut this early fabric. There is abundant graphite, which defines clear inclusion trails that show garnet and staurolite overgrew isoclinal graphitic folds. These graphite trails are folded in with the earlier generation white micas (S2), and picked up by the staurolites, many of which have not subsequently been rotated as evidenced by the concordance of graphite inclusions with the outside fabric (figure 5.30). The inclusions in the garnet also mirror the matrix foliation, and go right to the rim, where they meet up with the matrix fabric. There is some slight draping of micas around the garnet (S3), with quartz and plagioclase strain shadows; however this draping is not nearly so marked as in samples R76 and 19.

Therefore, garnet has grown at a different stage with regard to the deformation compared to crystals in lower zones (post S2 instead of pre-S2). Additionally, garnet and staurolite appear to have grown together (figure 5.31). Other inclusions include chloritoid, white mica, biotite and chlorite (figure 5.34).

The staurolites are large (up to 7mm in places), and are found in the white mica domains as well as occasionally intergrown with the garnets. Staurolite also appears as an inclusion in the garnets, and is associated with a second generation of biotite, in places overgrowing and enclosing biotite. There is an early generation of biotite folded in with the white mica, affected by S2. Biotite also partially rims the garnets, and is associated with kyanite (figure 5.32). Figure 5.33 summarises the microstructural history. Assemblage: Ms+Qtz+Pl+Grt+St+Bt+Ky.



Figure 5.30: Photomicrograph from P97 showing staurolite overgrowing graphitic folds, defining S2. PPL (top) and XPL (bottom). Lack of staurolite rotation is exhibited by the concordance of inclusion trails with the matrix fabric. Field of view2.4×3.6mm.

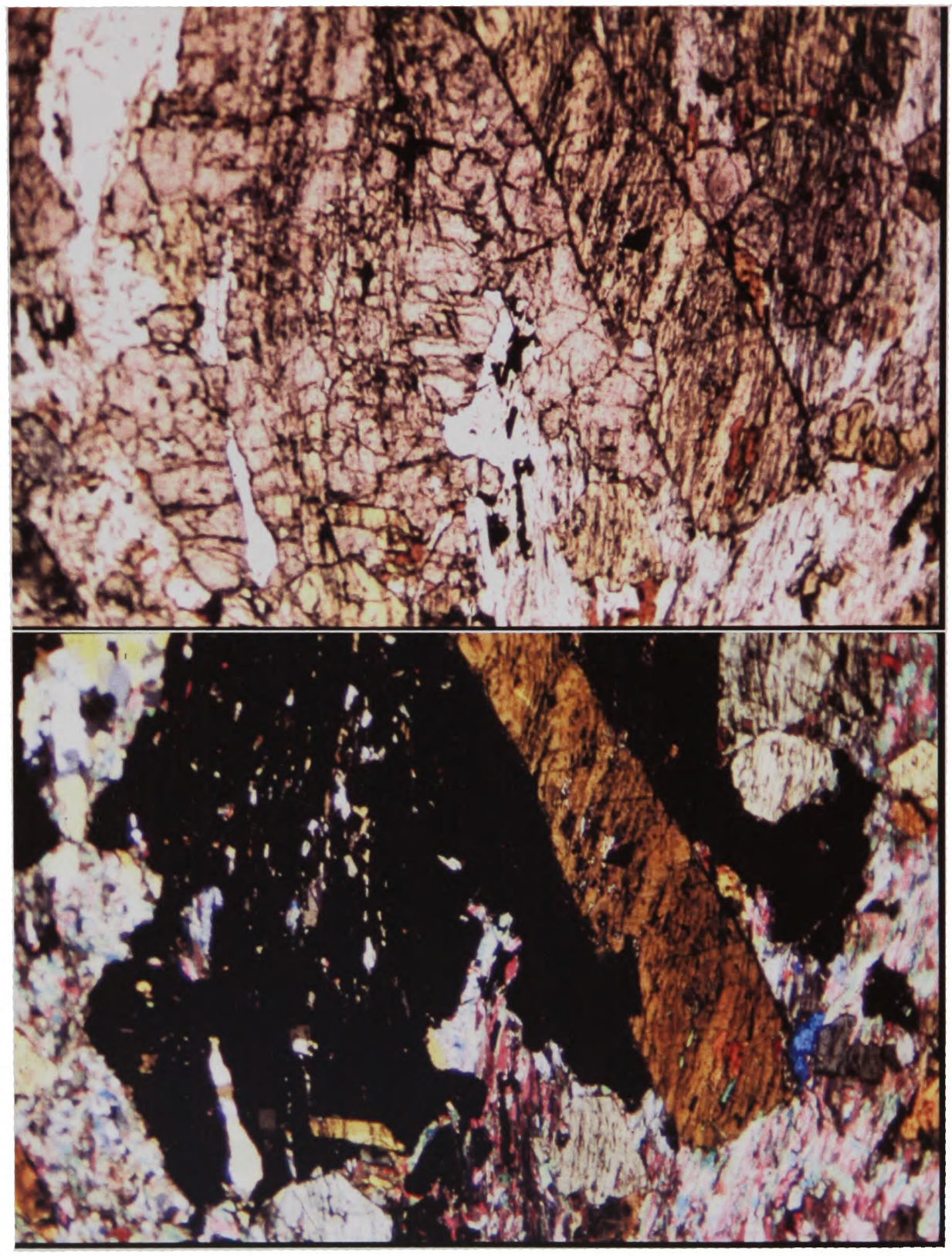


Figure 5.31: Photomicrograph from P97 showing garnet and staurolite intergrowths, both evidencing graphitic inclusion patterns that define S2. PPL (top) and XPL (bottom), field of view 6×9mm.



Figure 5.32: Photomicrograph from P97 showing kyanite and biotite association. PPL, field of view 2.4×3.6mm.

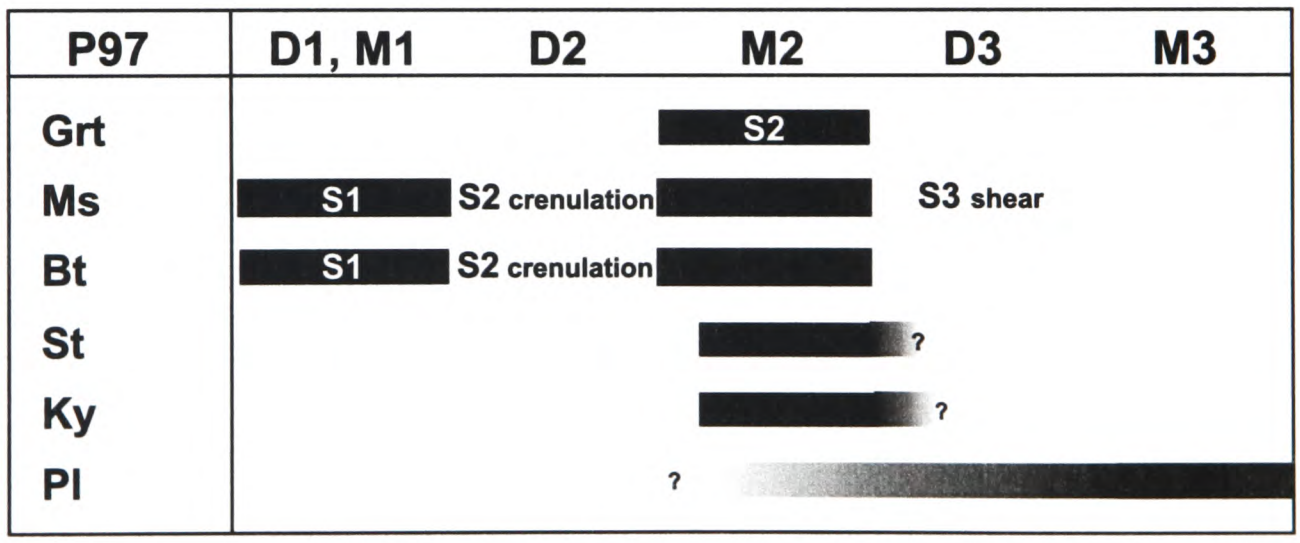


Figure 5.33: Schematic microstructural history of sample P97.

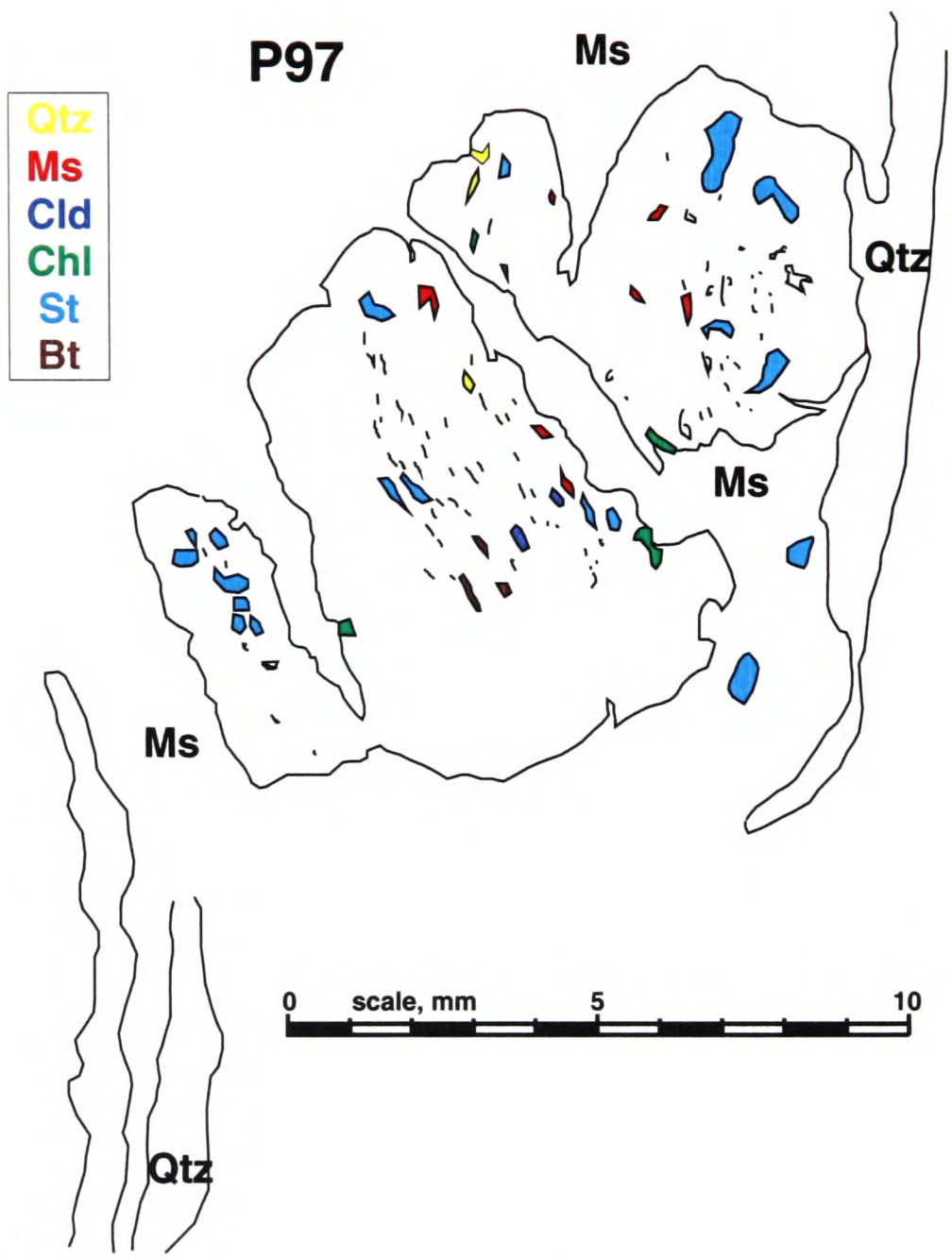


Figure 5.34: Sample P97 garnet inclusion patterns.

5.2 Plagioclase replacement of paragonite

Plagioclase only appears as a primary phase in mid kyanite grade rocks and higher, above the plagioclase isograd; at lower grades than this most Na is contained within paragonitic white micas, and Ca in apatite, garnet and some minor margarite. However, some lower grade rocks (*e.g.* R94, R96, 19) show evidence for late-stage paragonite replacement by albitic plagioclase.

Wintsch (1975) studied the effect of temperature, pressure, and activity of H_2O on mineral solution equilibria within the system $KAlSi_3O_8$-$NaAlSi_3O_6$-Al_2SiO_5-SiO_2-H_2O-HCl, in order to evaluate metamorphic phase equilibria in terms of the co-existing fluid (see activity diagram in figure 5.35).

Within a closed system, the chemical potentials of the components in both solids and fluids are buffered by the mineral assemblage - they can only be altered by a change in T or P. In thermodynamically closed systems, by definition, the ratio of any two components cannot be altered. However, in thermodynamically open systems, components may be exchanged with the surroundings; the chemical potentials may be fixed by processes outside the system, such as the influx of a non-equilibrium fluid.

Therefore, this plagioclase replacement of paragonite may be evidence of external (*i.e.* non-equilibrium) fluid infiltration during late-stage metamorphism.

5.3 Garnet unconformities

Large garnets from the Hoosac Schist have abundant inclusions. Inclusion patterns give information about the pre-existing rock fabric over which the garnet grew, and also give an idea about early equilibrium conditions and mineral stability. Chloritoid inclusions are present in the cores of all garnets, despite the absence of matrix chloritoid from mid-garnet zone upwards. This reflects a garnet core that grew within a chloritoid-rich matrix. The chloritoid inclusions define a sigmoidal S1 fabric, suggesting garnet rotation with D1 during growth. In some garnets this fabric extends right to the rim, where it is truncated by a S2 matrix fabric. However in most samples the garnets exhibit a distinct

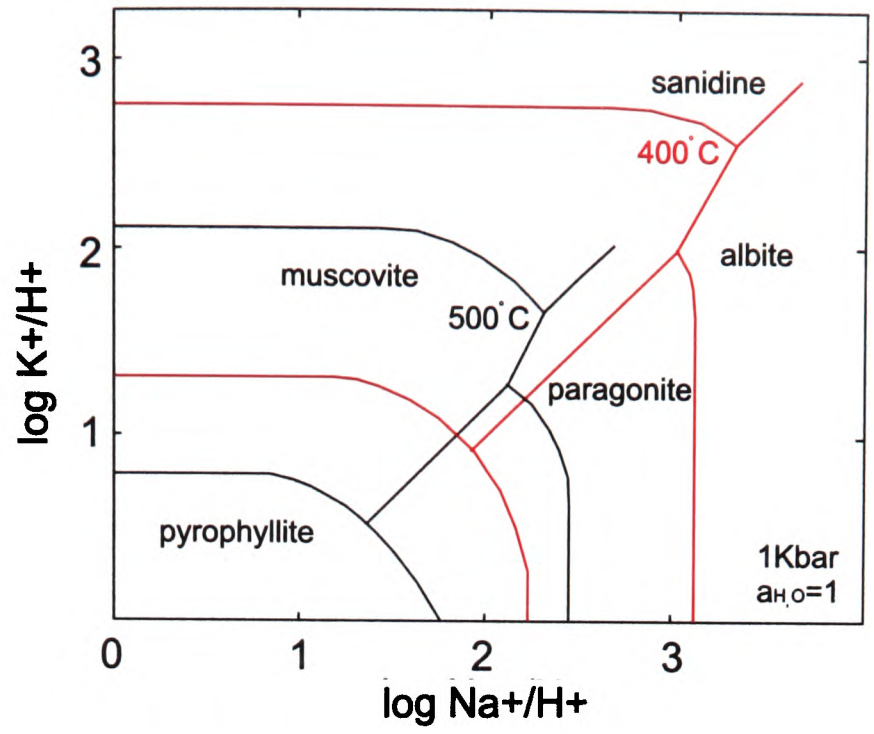


Figure 5.35: Activity diagram of $\log(Na^+/H^+)$ versus $\log(K^+/H^+)$ showing the stability fields of pyrophyllite, paragonite, muscovite, albite and sanidine with excess quartz as a function of fluid composition at 1kbar pressure, 400°C and 500°C, and at a_{H2O}=1. After Wintsch (1975).

rim, separated from the core by a concentric textural break. Within this rim, chloritoid is absent as an inclusion; additionally, the rims truncate the sigmoidal core inclusion fabric. Rim inclusions include white micas and quartz, suggesting a later garnet growth event within a chloritoid absent-matrix *i.e.* chloritoid had been entirely consumed.

Not all garnets show an unconformity defining a distinct rim; those that do not tend to have chloritoid inclusions right to the edge. It can be supposed that the cores of the unconformity garnets grew in the same garnet-forming reactions as the unconformity-absent garnets, since they show the same inclusion and fabric evidence.

Staurolite is absent as a garnet inclusion (except in the highest-grade sample P97), as is biotite. This does not presume that staurolite was absent as a matrix phase during the garnet rim growth.

The fact that the cores of the garnets generally contain a greater concentration of inclusions than the rims implies that the cores grew faster than the rims (Vance & Holland, 1993).

5.3.1 Titanium-bearing inclusions in the garnets

A common feature to all the Hoosac unconformity garnets is the pattern of the titanium-bearing mineral inclusions. In the cores of the garnet, the Ti-bearing inclusions are exclusively rutile; in the rims (as defined by the textural unconformity), and in the matrix it is ilmenite that is the exclusive Ti mineral phase. Figure 5.36 details a close-up of R76 showing the rutile-ilmenite transition at the unconformity. Rutile defines the original S1 fabric. At the textural unconformity this original fabric is truncated. In some cases it is possible to see a Ti-bearing phase straddle the unconformity, being rutile on the core side and ilmenite on the rim side.

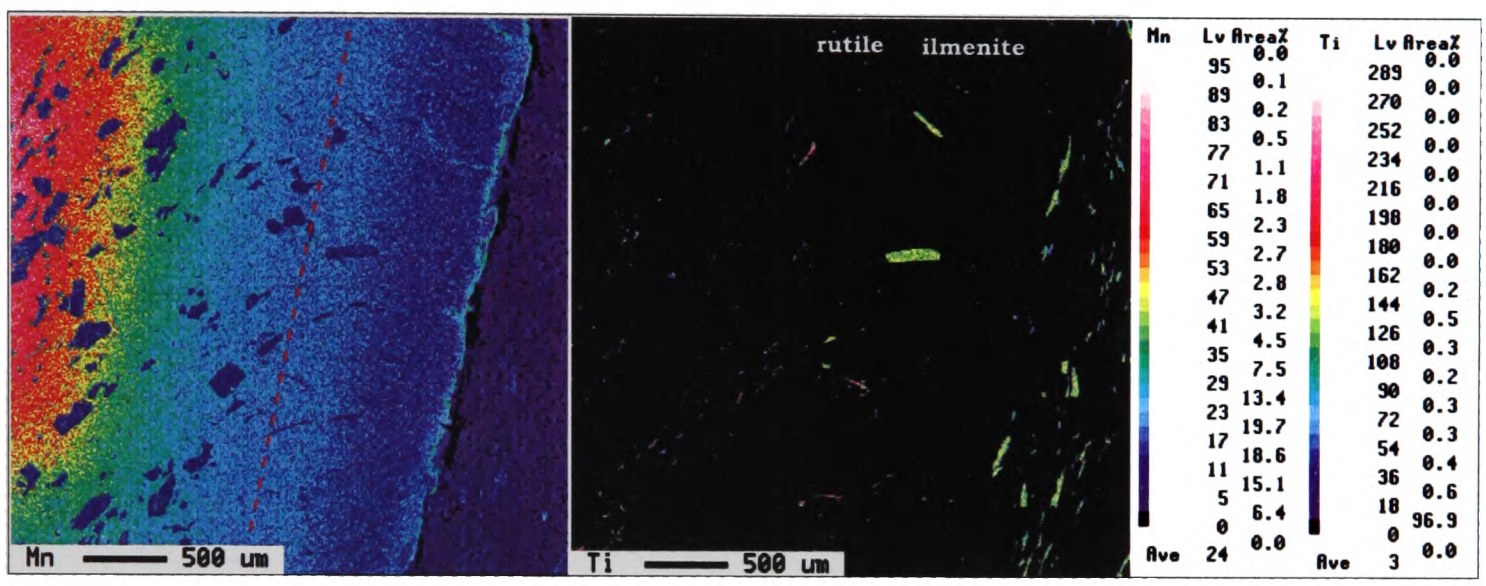


Figure 5.36: Qualitative electron microprobe map detailing Mn and Ti cations in a piece of R76 garnet. Dotted line shows position of textural unconformity. Rutile appears as small needles, ilmenite as much larger grains.

Although rutile (TiO_2) and ilmenite ($FeTiO_3$) are not strictly polymorphs, they are the dominant Ti-bearing minerals, and as such this transition from one to another is a monitor of mineral growth under differing P-T conditions, with rutile being a higher-pressure Ti-bearing phase than ilmenite.

5.4 Metamorphism - synthesis

Table 5.1 shows a summary of the major metamorphic features of the Hoosac Schist samples, with the exception of P97. Sample P97 shows features that are unique, especially

relating to the timing of garnet growth.

Event	Details
M1	Growth of chlorite, chloritoid, white micas (paragonite + muscovite) and quartz. Within this matrix garnet cores initiate and grow, with rutile.
D1	Fine mica fabric locally preserved outside garnet (S1). Local folds inside garnet demonstrate growth and rotation during D1 deformation. Growth of garnet encloses chloritoid, chlorite, quartz and white mica as inclusions. Rutile stable during the growth of garnet core, defines S1 fabric.
D2	Crenulation cleavage, at higher grade get white mica recrystallization along it (S2); Qtz ribbons - lenticular.
M2	Second generation white micas overgrow S2 crenulation cleavage. Growth of staurolite, biotite and kyanite (where appropriate) - cross-cutting porphyroblasts. Potential later garnet rim growth on some porphyroblasts with ilmenite stable.
D3	Shear bands & other features associated with flattening and shear (S3) - *e.g.* draping round garnets and locally around staurolite.
M3	Retrogression event(s): Sericite and chloritoid after staurolite. Late plagioclase replacing paragonite with fluid event. Late generation chlorite. Lower grade rocks get Chl+Pl association; in strain shadows maybe between S2 + S2b events.

Table 5.1: Summary of microstructural events for the big garnet Hoosac Schist.

Rutile, chloritoid and other inclusions in the cores of garnets define an earlier fabric (S1, *e.g.* figure 5.27), although there are hints of an S0 with the graphitic bands, and, in sample P37 (lower garnet zone), concentrations of accessory minerals defining narrow heavy-mineral bands, the origin of which is most probably sedimentary.

M1 growth includes chlorite, chloritoid, white micas, quartz and garnet cores. Reflecting D1 deformation, the S1 fabric is defined by white micas, chloritoid in low grades and possibly biotite in high grades. The S1 trace within the garnets is sigmoidal and reflects garnet core growth during D1; in some specimens this inclusion fabric can be seen to reach the rim of the garnet. Associated with garnet core growth are chloritoid and white micas, seen as inclusions.

During D2 deformation event, the S1 fabric has developed into a crenulation cleavage that becomes more intense with increasing grade (S2).

Overgrowing this are the second generation white micas, and staurolite and kyanite where appropriate (M2). Garnet rim growth probably occurred during this event. During the later stage of M2, and certainly after, a shearing episode (D3) drapes white micas around the garnets (causing pressure shadows of quartz and in some cases plagioclase).

Plagioclase as a primary phase is only observed in P97, above the Pg=Pl isograd; its presence in lower grade specimens is due to later fluid effects transforming paragonite to plagioclase. This is probably associated with the retrogression episode (chloritization in many places, breakdown of staurolite to chloritoid), which post-dates everything.

In essence: garnet cores grew in a matrix of chloritoid, white micas and quartz during D1 deformation. Rutile was stable. Garnet rims grew in a matrix of white micas and quartz, with ilmenite stable, possibly during or after D2. Staurolite, biotite and kyanite are post-D2.

5.5 Comparison with work on adjacent, similar units

Rosenfield (1968) commented on garnets from the Pinney Hollow Formation, Vermont, and what he termed 'tectonometamorphic angular unconformities'. Here, garnet has an inner zone which has its enclosed relict schistosity truncated against a sharp boundary with an outer zone, the latter having different colour and inclusion assemblage. He concluded that the outer zone must have grown under altered metamorphic conditions after a rotation of the inner zone (unrecorded in the garnet) but before the development of evidence for D1 in the outer zone.

By studying foliation inflexion or intersection axes (FIAs) in garnets from Siluro-Devonian rocks in south eastern Vermont, Bell *et al.* (1998) concluded that up to four sets of FIAs are observed, and thus four periods of garnet porphyroblast growth occurred, although no single garnet recorded all four stages of growth.

A similar study of FIA orientation in garnets from the Devonian Littleton Formation schists in the Bolton Syncline, Connecticut, revealed three generations of growth that all pre-dated development of the syncline (Hickey & Bell, 1999), while staurolite was

deemed to have grown during and perhaps after folding (Bell *et al.*, 1997).

Considering the contrasting models of the Hoosac Formation from southern Vermont (Karabinos, 1984, 1985) versus the evolution of the Gassetts Schist, also from southern Vermont (Thompson *et al.*, 1977; Vance & Holland, 1993), the observations presented here suggest that the high-alumina Hoosac Schist from Western Massachusetts shows a similar metamorphic history to those garnets studied by Karabinos. However the rocks studied here are lacking direct evidence of simultaneous garnet rim and staurolite growth, since no inclusions of staurolite within the garnet rim have been documented.

Chapter 6

Mineral chemistry and thermobarometry

This chapter focuses on the more quantitative aspects of the high-alumina Hoosac Schist. Mineral chemistry and associated thermobarometry for P-T estimation calculations is covered.

6.1 Analytical methods

Major mineral chemistry was determined in six of the samples selected for petrological study: P21, R96, 6, R76, 19 and P97.

All samples were mounted as 30μm thick polished sections and then carbon-coated. Measured element apparent weight percentages were subject to a ZAF correction (atomic number, specimen absorption, fluorescence) to adjust for differences between the matrix of the unknown and the standards used for calibration. Three different analytical tools were used.

6.1.1 JEOL 840 Scanning Electron Microscope

Mineral chemistry was analysed using a JEOL 840 Scanning Electron Microscope at the Department of Earth Sciences, Unicersity of Oxford. This utilizes an energy dispersive detector (EDS) running Oxford Instruments' ISIS software. The JEOL instrument was calibrated for probe currents of 1×10^{-9}A (1nA) and 6×10^{-9}A (6nA) with an accelerating voltage of 20kV. A cobalt standard was used for calibration.

In addition to EDS analysis, the JEOL was used for compositional imaging. Backscattered electrons (BSE), which are primary electrons emitted as a result of elastic collisions between the probe electron beam and specimen, are detected and processed to give an image. BSE image intensity is a function of the mean atomic number of the specimen; the higher the mean atomic number, the brighter the signal. It is thus of paramount use in distinguishing between minerals that appear near-identical under transmitted light, but have different compositions and therefore different mean atomic numbers (for example muscovite and paragonite).

For normal mineral analysis the JEOL 840 was calibrated for a probe current of 6nA. However, during routine analyses of both white mica and plagioclase at this current anomalously low Na and K analyses were observed. An investigation revealed significant Na and K depletion over three consecutive analysis on the same spot in a paragonite from P21 (see table 6.1). This 'alkali loss' can be attributed to Na and K ejection due to interaction with the electron beam. Thus over time, proportionally less alkalis remain and the counts decrease.

There are three approaches to dealing with this problem:

1. by defocusing the beam total energy and thus counts are unaffected, but flux is reduced, and so is spatial resolution - *this is easily achieved with a conventional electron microprobe but is not applicable with a scanning electron microscope*
2. rastering the beam over an area of the specimen - *perfectly feasible with an SEM*
3. by reducing the beam current less damage is effected but this has the consequence of proportionally lower count rate, and also lower totals

Approach (2) is possible with an SEM, however beam rastering sacrifices spatial resolution, and therefore for determining fine-scale compositional variation approach (3) is preferable. All muscovite, paragonite and plagioclase have been analysed at the lower beam current of 1nA.

Run No	1	2	3
Na counts	41587	36276	31309
K counts	18114	17113	17401

Table 6.1: Na and K net counts from three immediately consecutive paragonite SEM analyses on the same spot from sample P21 at a probe current of 6nA. This shows significant Na depletion.

The other concern is silicon underestimation by EDS analysis. The way the JEOL 840 is presently configured, silicon counts appear to be low. Consider figure 6.5, showing Fe+Mg plotted against Si for all Hoosac muscovites. When Fe+Mg = 0, Si should equal 6.0, but with analysed muscovites the trend appears to intercept y=0 at approximately Si=5.75. A similar pattern is observed with paragonite and biotite.

6.1.2 Cambridge Instruments Microscan 9 electron microprobe

Garnet traverses were completed using a Cambridge Instruments Microscan 9 electron microprobe also at the Department of Earth Sciences, University of Oxford. The Microscan 9 employs 2 wavelength dispersive spectrometers (WDS) for quantitative analysis with a beam spot of some 0.5 - 1.0 μm. For major elements the beam current was 35 - 40 nA, with an accelerating voltage of 20kV. Calibration was undertaken using mineral standards.

6.1.3 JEOL superprobe

For qualitative mineral mapping of major cations, a JEOL JXA 8800RL microprobe was employed at Material Sciences, University of Oxford. The superprobe employs 4 wavelength dispersive spectrometers. Accelerating voltage was 20kV, and probe current 80nA. Spot size is normally 0.5μm but was defocused slightly for step-scanning.

6.2 Mineral Chemistry

6.2.1 Garnet

Garnet zoning - models

Since the advent of the electron microprobe technique in the early 1960's, giving workers the ability to quantitatively perform a chemical analysis on a sub 10 micron spot, concentric garnet zonation of the major cations Fe, Mg, Ca and Mn has been recognized. Early workers attempted to explain the observed patterns; the bell-shaped Mn profile has been attributed to a fractionation process, with garnet preferentially taking up Mn from the matrix as it grows (Harte & Henley, 1966); therefore, there would be progressively less Mn able to partition into the garnet. Hollister (1966) and Atherton (1968) quantified this with a simple Rayleigh fractionation process, modelling the depletion of Mn in the rock with a constant K_D (distribution coefficient) between rock matrix and growing garnet. There were, however, two major drawbacks with this approach: K_D is likely to be temperature-dependent, and most garnets do not grow within an isothermal regime; additionally, K_D may also be dependent on both mineralogical compositions and proportions, especially those adjacent to the growing garnet - this adds further complications.

The reaction partitioning model (Kretz, 1973; Trczienski, 1977) proposed that minerals grew with a surface composition controlled by multivariant equilibria with one or more reactant minerals. When material is crystallized and incorporated as garnet during these reactions, it loses communication with the reacting matrix. The effect of this is to shift the effective bulk composition of the rock away from the composition of the garnet interior; each subsequent layer of garnet will be controlled by a slightly more evolved effective bulk composition than the last, this composition being controlled by K_D for the multivariant equilibria responsible for garnet formation.

Both the simple Rayleigh fractionation and the reaction partitioning models describe the same process of preferential fractionation of certain elements into the garnet, but the latter is generally believed to be closer to the actual behaviour of the system (Tracy,

1982). Heterogeneous equilibrium between reactive mineral compositions is assumed for the above models. This appears to hold true for Fe, Mg and Mn in garnets. However, it has been suggested that on a hand-specimen scale Ca does not equilibrate during garnet growth due to its relatively slow diffusion rate (Chernoff & Carlson, 1997); this has implications both for interpretation of Ca zoning profiles and for geobarometry.

Garnet results

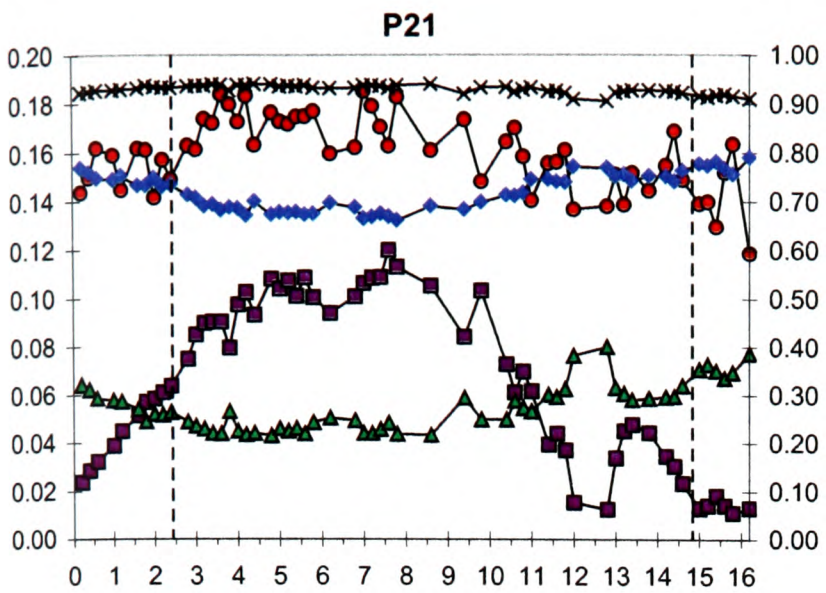
Electron microprobe traverses have been completed on a range of garnet samples from across the range of grades, and are shown in figures 6.1 and 6.2. These plot mole fractions of components, X_{Sps} (Mn), X_{Pyp} (Mg), X_{Grs} (Ca), X_{Alm} (Fe) as well as X_{Fe} (Fe/Fe+Mg) against rim-rim distance in millimetres. X_{Sps} represents Mn/(Mn+Mg+Ca+Fe) in cations per formula unit (12 O). No correction is made for Fe^{3+}, all Fe is taken as Fe^{2+}.

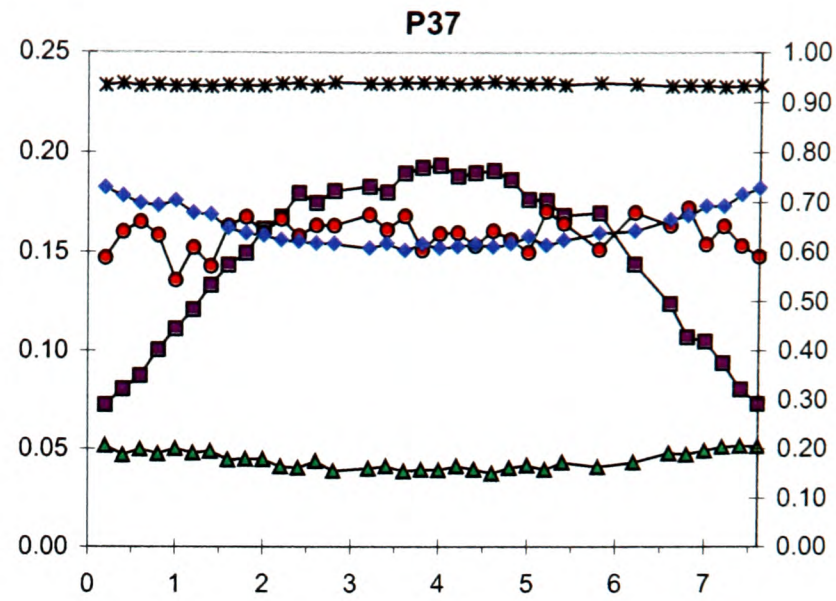
Normal rim-rim garnet zoning profiles have a number of characteristic features, as shown schematically in figure 6.3a. Mn usually exhibits a bell-shaped profile, generally going to zero at the rims. Ca also decreases from the core to the rim. Conversely, both Fe and Mg increase towards the rim. Such garnet zoning is indicative of changes in P-T-X relations. Additionally, X_{Fe} (Fe/Fe+Mg) normally shows a slight decline from core to rim, as the garnet gets more Mg-rich; such a feature is a good indicator of increasing temperature during garnet growth (Spear, 1993).

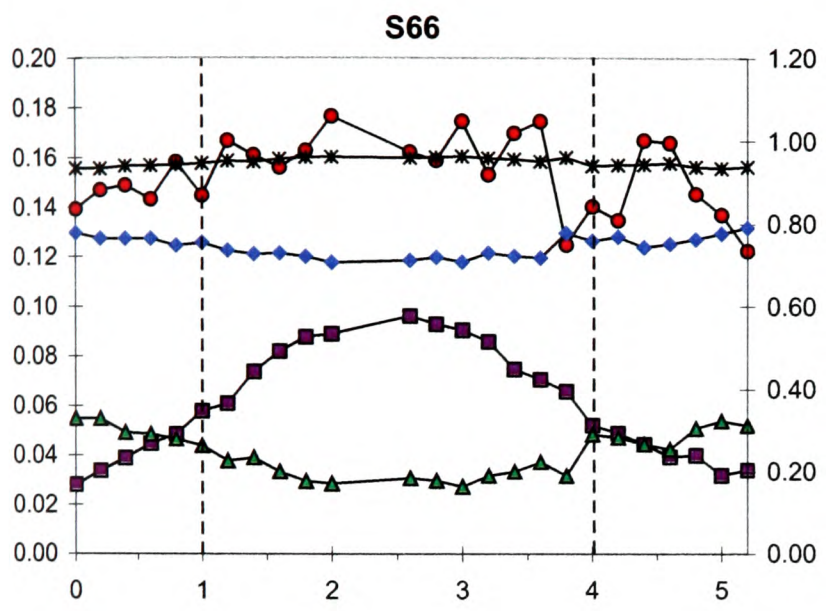
Two main processes can operate to alter this original growth zoning (both shown in figure 6.3b). Near-rim reversals occur due to two possible factors: Cation exchange between the garnet rim and adjacent minerals usually leads to Mg decrease and Fe increase (as graphically illustrated by Tracy *et al.* (1976), with Fe-Mg exchange between garnet and biotite). Alternatively, garnet resorption has the effect of releasing and concentrating Mn in the rim of the garnet.

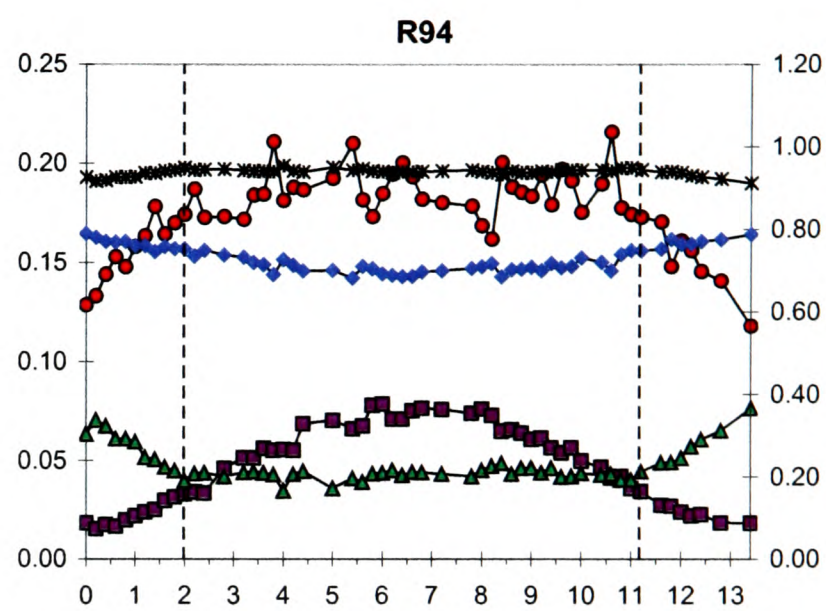
Partial homogenization after garnet growth due to cation self-diffusion is manifested as flattening of the growth profiles. Since diffusion is a temperature-activated process this is most marked in higher grade rocks (Yardley, 1977).

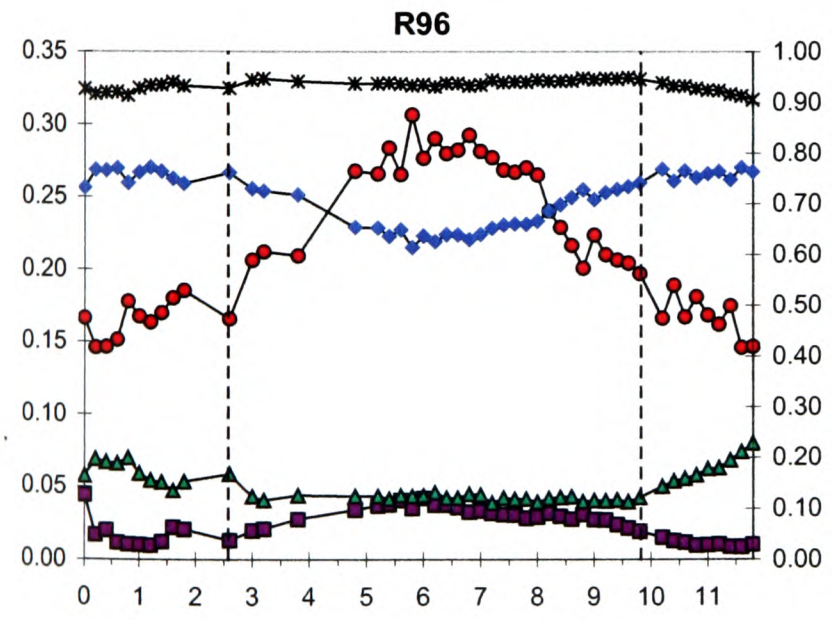
The majority of Hoosac garnets show normal zoning profiles, generally appearing un-

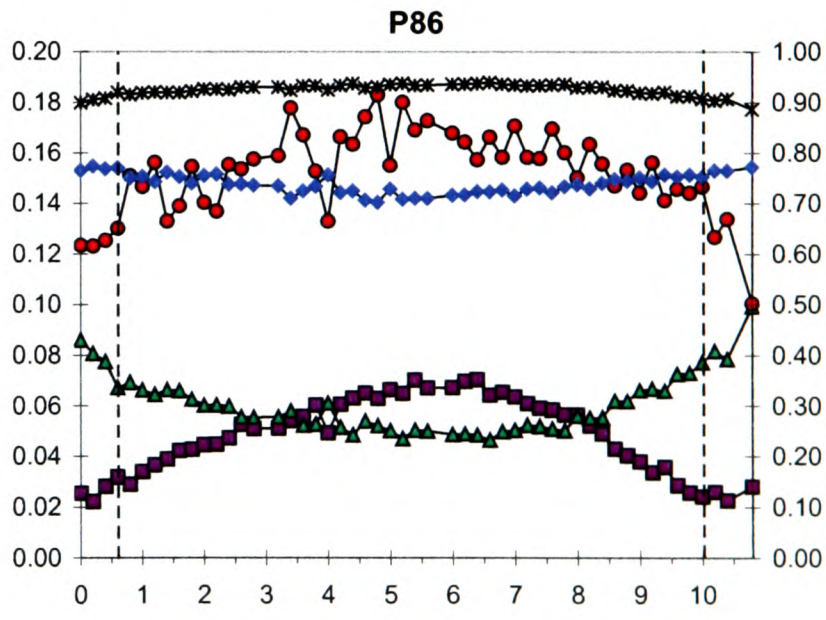


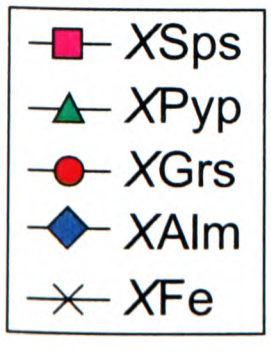












P21
P37
S66
R94
R96
P86 Grt+Chl
6 St+Bt
R76 St+Chl
19 Ky+Bt
P97

Figure 6.1:

Garnet zoning profiles from the Hoosac Schist, increasing from lower to higher garnet zone.

The left-hand axes represent X_{Sps}, X_{Pyp} and X_{Grs}; the right-hand axes represent X_{Alm} and X_{Fe}, and the bottom axes are rim-rim distance in mm. Dotted lines represent textural unconformities separating cores from rims.

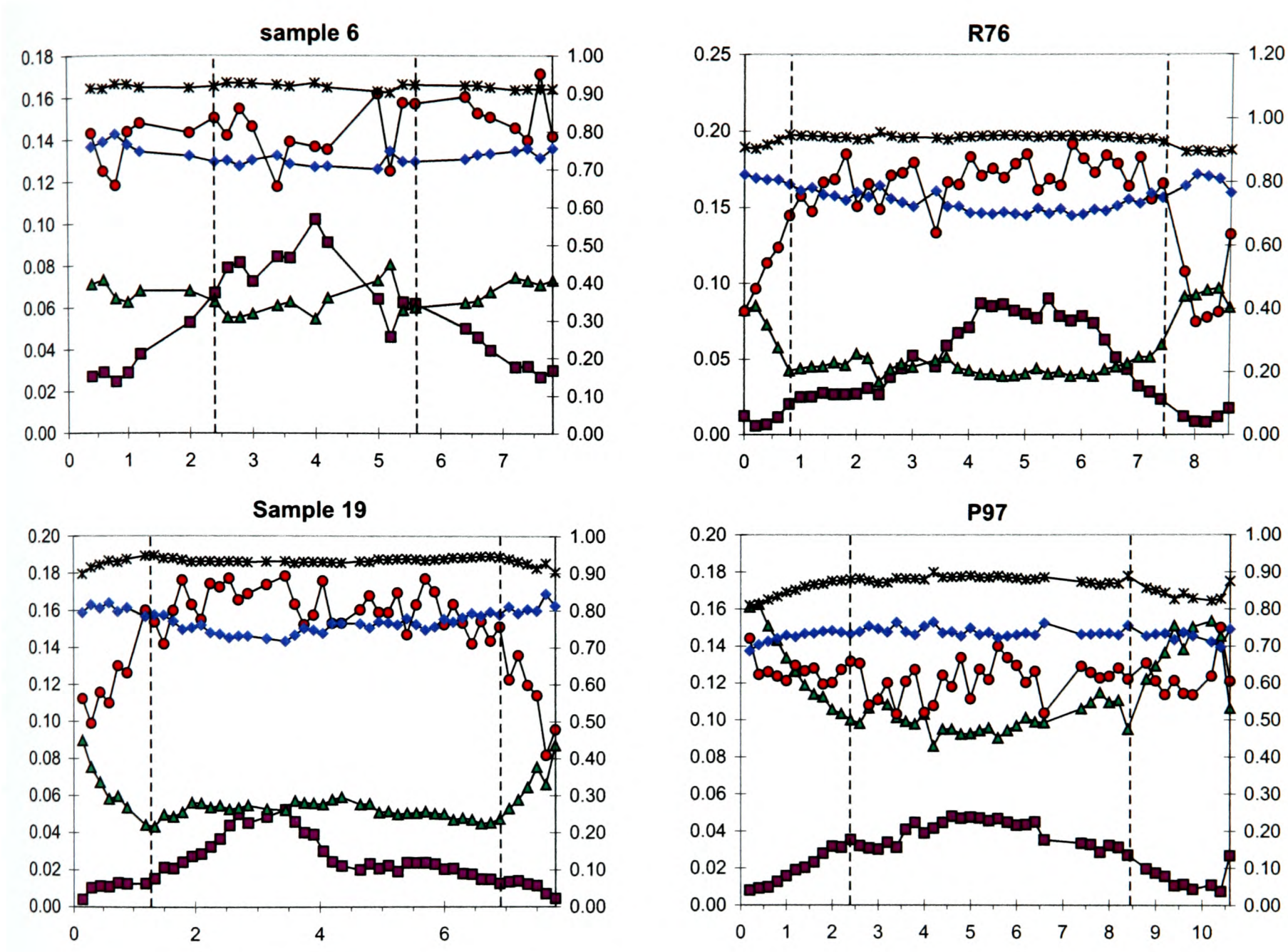


Figure 6.2:

Garnet rim-rim zoning profiles from the Hoosac Schist, increasing from staurolite to kyanite zone.

The left-hand axes represent X_{Sps}, X_{Pyp} and X_{Grs}; the right-hand axes represent X_{Alm} and X_{Fe}, and the bottom axes are rim-rim distance in mm. Dotted lines represent textural unconformities separating cores from rims.

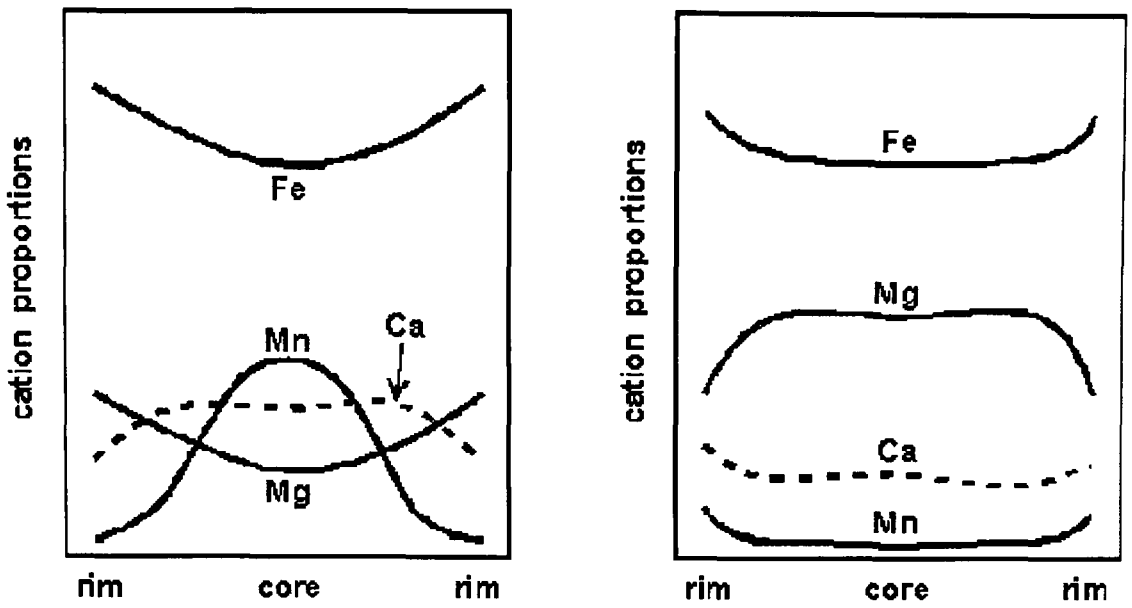


Figure 6.3: Schematic garnet zoning profiles a (left) shows 'normal' garnet zoning, with Mn and Ca decreasing, and Fe and Mg increasing from core to rim. b (right) shows the effect of both diffusion, cation exchange and retrogression. Partial homogenisation by diffusion manifests itself as a flattening of the growth profiles. The rims are affected by both cation exchange (enriching Fe) and partial resorption of the garnet, with Mn enrichment. See text for details.

modified by later diffusion. There is only minor evidence for later cation self-diffusion, however it is notable that even in the highest grade sample shown here, P97, there is no large-scale diffusion evident.

Mn rarely drops to zero at the rim, and although in some samples there is evidence for slight Mn-enrichment at the rim, thus implying slight garnet regression (*e.g.* samples R94, R96, P86, 6, R76 and P97), other profiles systematically drop towards the rim but never reach the baseline - this could be due to an abundance of Mn in the bulk rock. Typically, the mole fraction of spessartine, X_{Sps}, shows a maximum of 0.08 - 0.12 in the core, diminishing to 0.02 at the rim, although some samples, *e.g.* R96, show a lower Mn content, with a maximum of 0.04, while P37 reaches 0.20 in the core. These most likely reflect local differences in Mn concentrations. In addition, P21 shows evidence for two grains coalescing together, and this is confirmed by textural evidence.

The mole fraction of pyrope, X_{Pyp}, shows a uniform core content of 0.04 - 0.06, rising to 0.06 - 0.08 at the rim. Grossular, X_{Grs}, typically has values of 0.15 - 0.20. An interesting feature of all of the grossular profiles is that they do not show a smooth decline, but have a spiky appearance; this may be related to the relatively slow diffusion rate of Ca.

Garnet unconformities

The garnet zoning profiles in figures 6.1 and 6.2 show the location of the core-rim unconformity (as marked by a dotted line). Examination of these profiles with regard to the textural break and the implication of two different garnet growth episodes leads to a number of conclusions.

Firstly, spessartine profiles (X_{Sps}) show no major evidence for a spike at these unconformities. This is in contrast to those large unconformity Mn-peaks as reported in the Gassetts Schist (*e.g.* see profiles in Young & Rumble, 1993). The presence of a Mn spike is usually attributed to a period of garnet resorption separating the two garnet growth events. Instead, most Hoosac garnet profiles show a gradual decrease in X_{Sps} from core to outer rim, with a slight inflection across the textural break. This possibly implies that the rim had a different growth rate to the core, a conclusion which is supported by the relative lack of garnet rim inclusions compared to the cores, implying slower growth for the rims (Vance & Holland, 1993).

X_{Pyp} shows a jump across the unconformity into the rim. This is most apparent with samples R94, R76, 19 and P97, and is correlated with a decrease in X_{Fe}. However, X_{Alm} shows little change across the core-rim transition, generally becoming slightly enriched (except in sample P97). X_{Grs} in some samples shows a marked decrease into the rim; this is most obvious in samples R94, R96, P86, R76 and 19. Conversely, P97 actually shows an *increase* in X_{Grs} from core to rim, which may be related to the presence of original plagioclase in this sample buffering the calcium content of the garnet. Grossular content in garnet is strongly pressure-dependent, with X_{Grs} enrichment with increasing P.

There is evidence for different P-T conditions for core and rim as suggested by the shift in X_{Fe}. Across the core-rim transition, the implied increase in X_{Mg} may suggest higher temperatures for the rims (*e.g.* Spear, 1993). Additionally, the transition from rutile to ilmenite and the rapid decrease in X_{Grs} both indicate lower pressures for rim growth compared to core growth. There is, however, no evidence for a garnet resorption event separating core and rim growth episodes.

Generally, garnet cores show remarkably flat profiles for X_{Pyp} X_{Alm} and X_{Grs}, implying

fairly constant conditions for garnet core growth. In addition, across the unconformity there is not much of a jump in any of the four cation traces. This may indicate that the second stage of garnet growth picked up at fairly similar conditions to where the first one ceased.

6.2.2 White Micas

The dominant sheet silicate minerals found in the Hoosac Schist are the white micas muscovite and paragonite, and their chemistry is plotted below to illustrate the important cation substitutions that can take place. Occasional margarite has been observed in some of the samples, but the most important Ca-bearing mineral is garnet, with plagioclase in higher grades, and minor apatite.

Muscovite

Table 6.2 shows that ideal muscovite has 3 Si per 11 O, equivalent to 6 Si per 22 O. The Tschermak substitution operating in reverse, $Si^{iv}(Fe,Mg)^{vi}=Al^{iv}Al^{vi}$, leads towards the celadonite end-members, known as the *phengites*, and celadonites ideally have 8 Si per 22 O. This substitution is akin to the Tschermak substitution that operates in biotites except that muscovites move to less Al-rich compositions rather than more. By plotting Fe, Mg and octahedral Al (Al^{vi}) against Si cations per formula unit (p.f.u., 22 O), as shown in figure 6.4, the phengite content of the muscovites can be ascertained, although with the caveat of Si-underestimation. This shows that Hoosac muscovites contain between 6 and 6.35 Si p.f.u. This Si enrichment from ideal muscovite of 6 Si p.f.u. is due to phengite content. As Si is enriched, so Al^{vi} decreases while Mg increases, reflecting substitution of Mg+Fe for octahedral Al. The positive correlation between Si and Mg implies muscovite is moving towards Mg-Al celadonite. Fe does not show much of a correlation, perhaps because Fe^{3+} can substitute for Al on octahedral sites.

The phengite content of muscovite should increase with increasing pressure, and decrease with increasing temperature (Guidotti & Sassi, 1976); figure 6.5 plots phengite content (Fe+Mg) of muscovites against Si cations p.f.u. as a function of sample, and

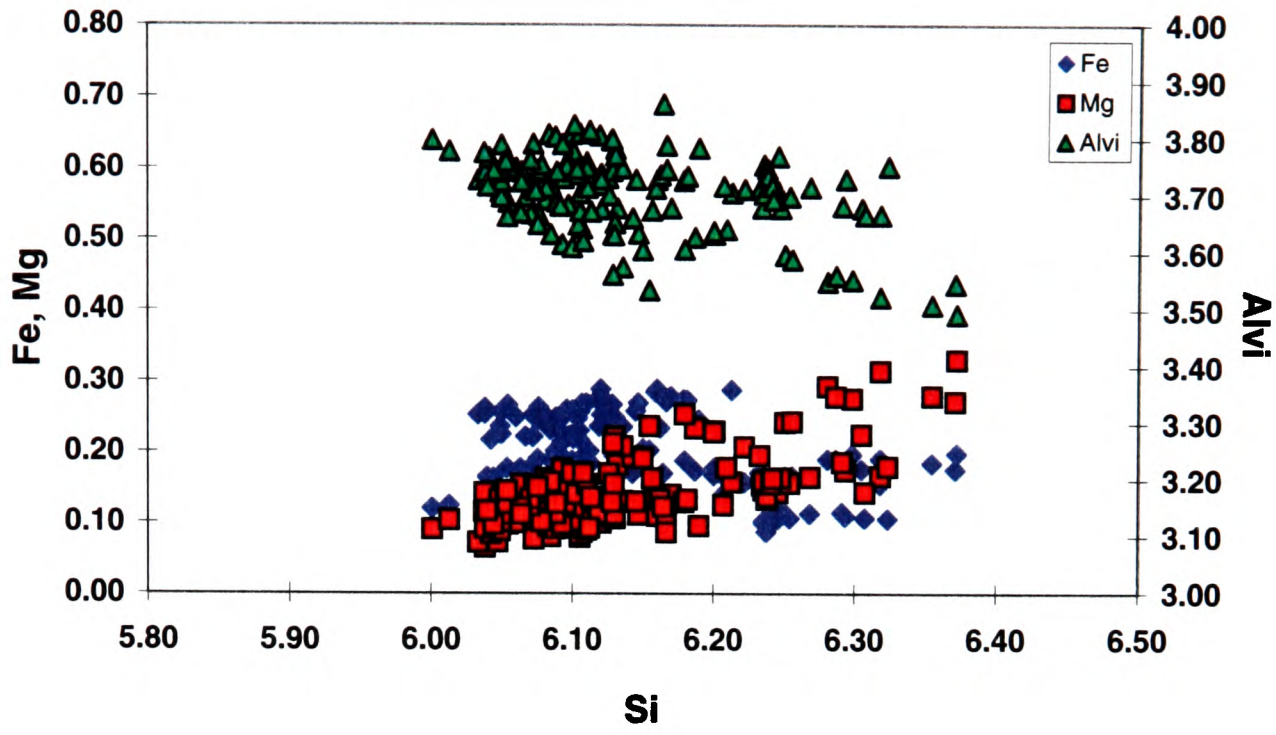


Figure 6.4: Hoosac muscovites, plotting Si cations p.f.u. versus Fe, Mg and Al^{vi} (octahedral aluminium).

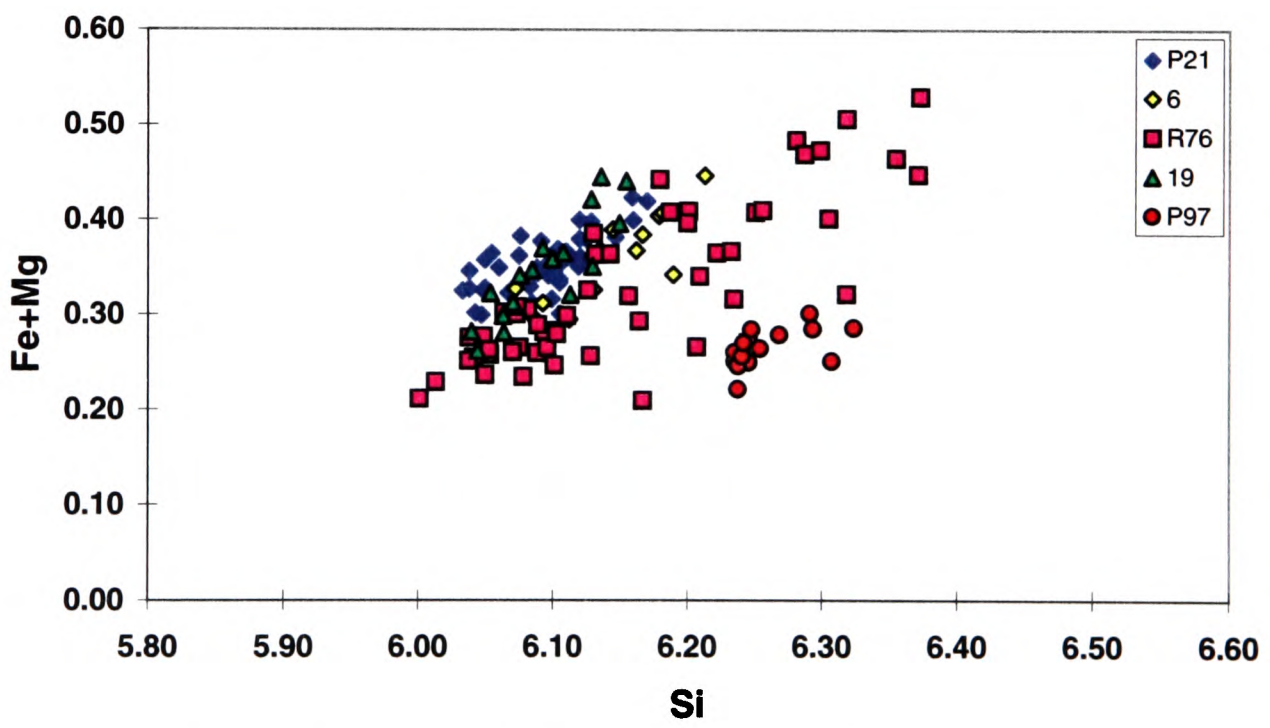


Figure 6.5: Phengite content (Fe+Mg) in muscovites as a function of metamorphic grade. Metamorphic grade increases from P21 (garnet zone) to P97 (kyanite zone).

muscovite	$KAl_2(AlSi_3)O_{10}(OH)_2$
paragonite	$NaAl_2(AlSi_3)O_{10}(OH)_2$
margarite	$CaAl_2(Al_2Si_2)O_{10}(OH)_2$
Mg-Al celadonite	$K(Mg,Al)(Si_4)O_{10}(OH)_2$
Fe-Al celadonite	$K(Fe,Al)(Si_4)O_{10}(OH)_2$

Table 6.2: White mica end-member compositions, for 11 oxygens per formula unit.

thus grade. Curiously there is not an agreement with this model, with a rather cluttered grouping, although within some samples there is a positive correlation.

Figure 6.6 plots Si cations versus X_{Mg} for muscovites as a function of sample. Clearly, X_{Mg} increases with increasing grade, although there is some overlap and R76 in particular has a higher X_{Mg} than would be expected.

The paragonite content (Na) of muscovites is temperature-dependent, since the muscovite-paragonite solvus closes with increasing temperature, allowing a greater degree of solid solution (Guidotti, 1984). Figure 6.8 shows a pseudobinary diagram between Ms and Pg. This shows closure of the miscibility gap between the two mica end-members with increasing temperature. The paragonite-plagioclase transition is also shown, and this is probably responsible for the plagioclase-in isograd within the kyanite zone. Transformation of paragonite to plagioclase releases surplus Al which is taken up by growing aluminous phases such as staurolite and kyanite.

Figure 6.7 plots Si versus Na cations p.f.u. for each sample. However not much correlation is observed. Phengites commonly show inverse correlation between Na and Si; this is evident here, especially in R76.

Paragonite

Primary paragonite occurs with muscovite in lower grade samples. Figure 6.9 plots Si versus Fe, Mg and Al^{vi} cations per formula unit (22 O). There is very little or no Mg and not much Fe in the Hoosac paragonites, reflecting the negligible Tschermak substitution experienced by paragonites. Thus Si content varies between 5.85 and 6.10 Si per 22 O, although this reflects Si underestimation and should perhaps be between 6.00 and 6.25.

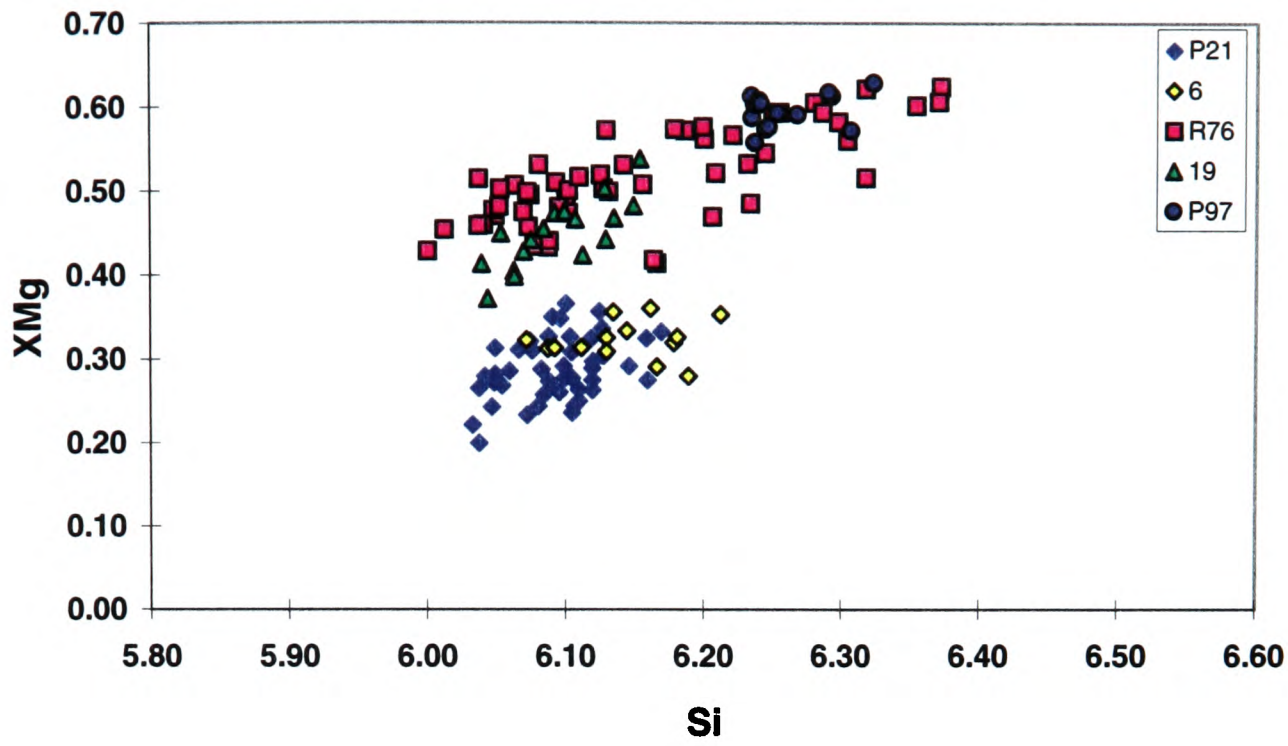


Figure 6.6: Hoosac muscovites: plot of Si versus X_{Mg} (Mg/Fe+Mg) by sample. Metamorphic grade increases from P21 (garnet zone) to P97 (kyanite zone).

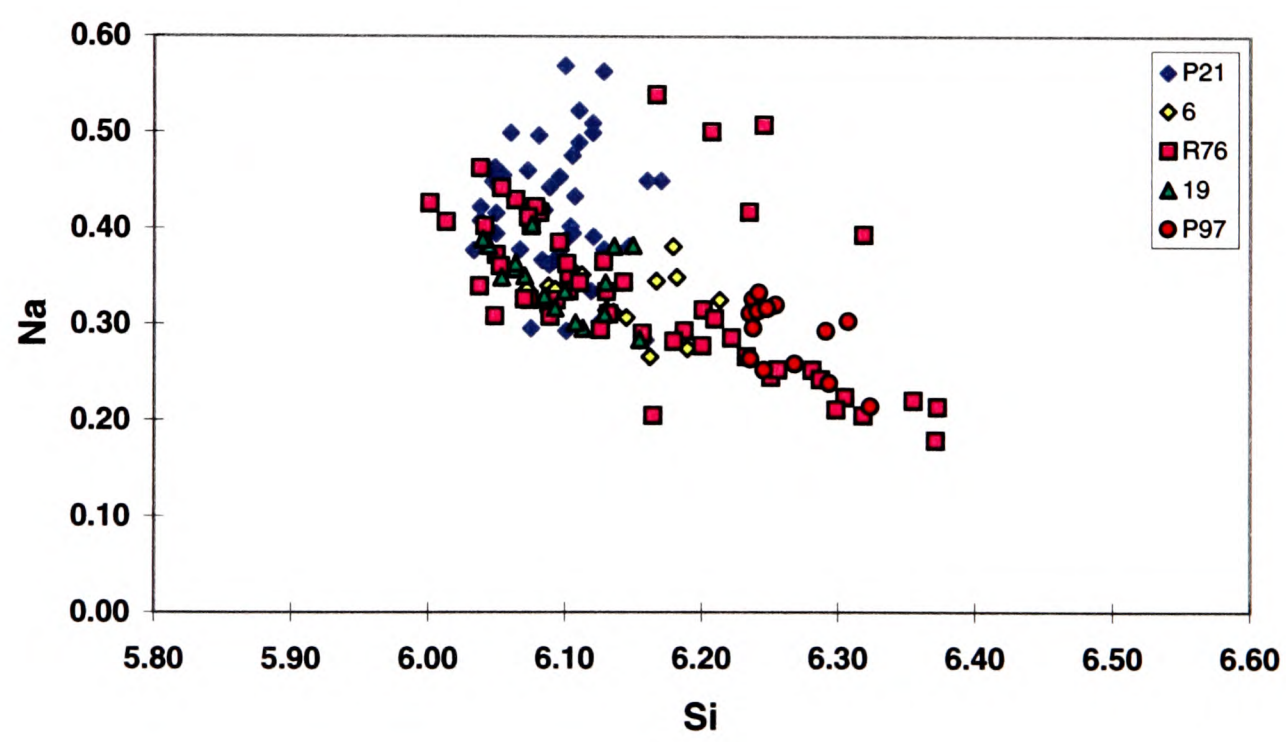


Figure 6.7: Paragonite content (Na) in muscovite as a function of metamorphic grade. Metamorphic grade increases from P21 (garnet zone) to R76 (staurolite zone).

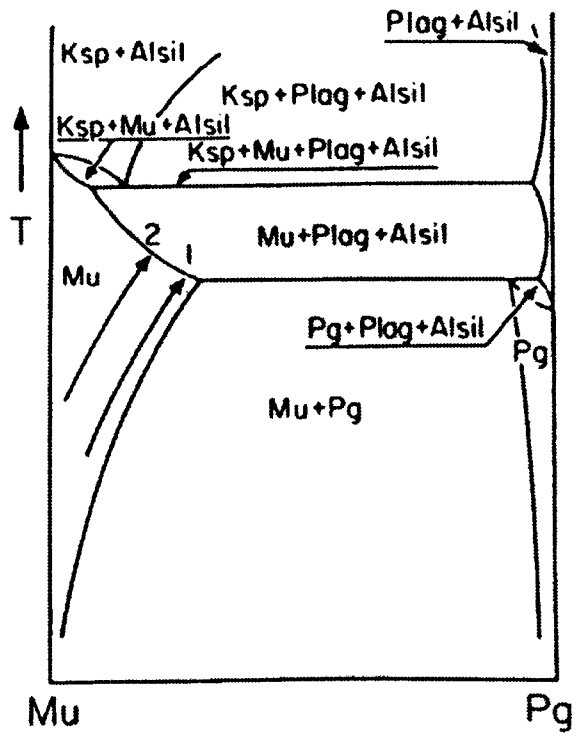


Figure 6.8: Schematic pseudobinary diagram between muscovite (Mu) and paragonite (Pg). From Guidotti (1984).

The margarite content (Ca) in paragonite decreases with metamorphic grade, from 0.10 in P21 to 0.02 in R76 (figure 6.10). Calcium is taken up by garnet and apatite, and plagioclase in higher grades.

6.2.3 Biotite

Biotite occurs only in the higher grade samples R76, 19 and P97. Figure 6.11 plots Si cations per formula unit (22 O) against Ti, X_{Mg}, Al^{vi} (octahedral aluminium) and Fe for all Hoosac biotites. Ideal phlogopite-annite endmembers have Si_6Al_2 for 22O p.f.u. (table 6.3), and the Hoosac biotites exhibit Si between 5.4 - 5.6 , reflecting the Tschermak substitution $Al^{iv}Al^{vi}$=$Si^{iv}(Fe,Mg)^{vi}$ towards eastonite (the Tschermak substitution in biotites operates in reverse to that in white micas, moving the biotite to a more Al-rich and Si-poor composition).

Sample 19 is notably poorer in Si with a spread of 5.40 - 5.45 cations p.f.u. compared to R76 (5.45 - 5.55) and P97 (5.40 - 5.55). Ti composition is in general 0.2 cations p.f.u. These are fairly Ti-rich rocks with abundant rutile and ilmenite inclusions in the garnets, and ilmenite in the matrix, and although Ti substitution for Al increases with temperature

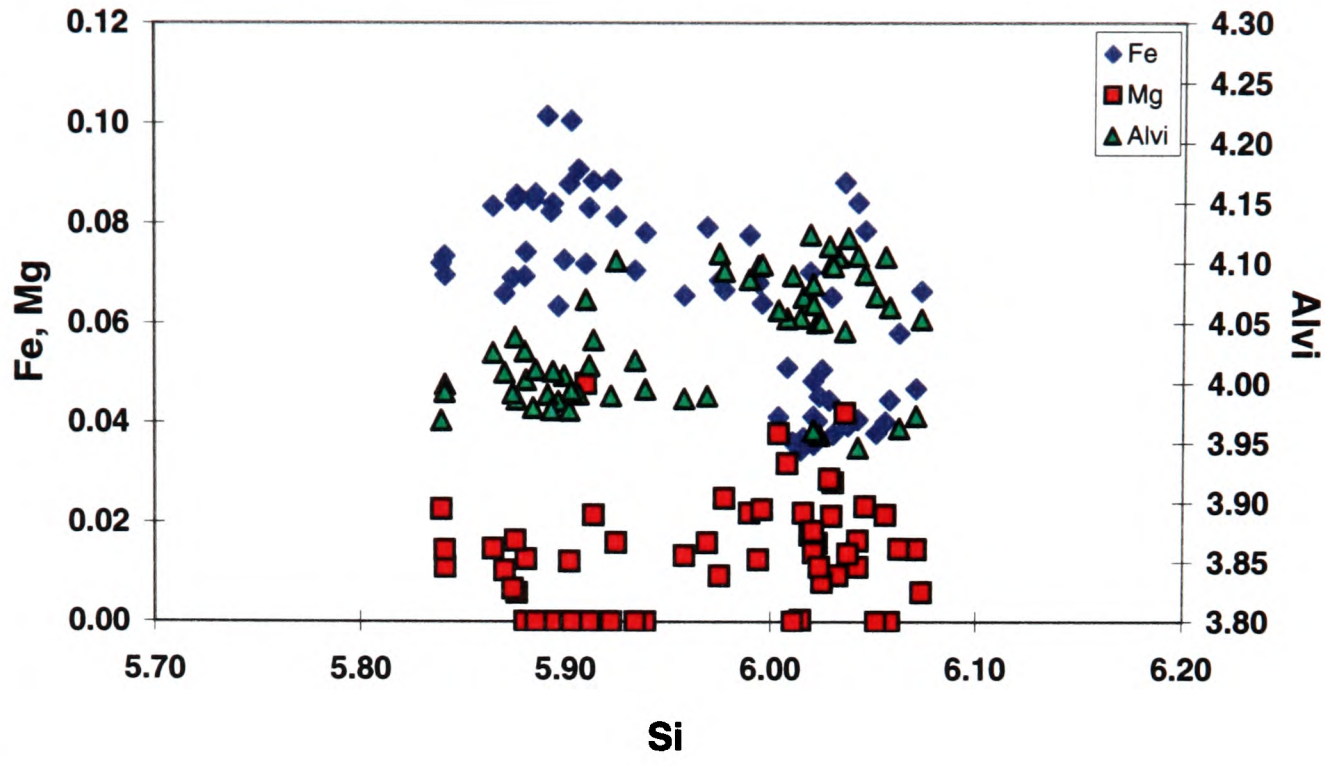


Figure 6.9: Hoosac paragonites, Fe, Mg and octahedral Al (Al^{vi} versus Si p.f.u. (22 O)).

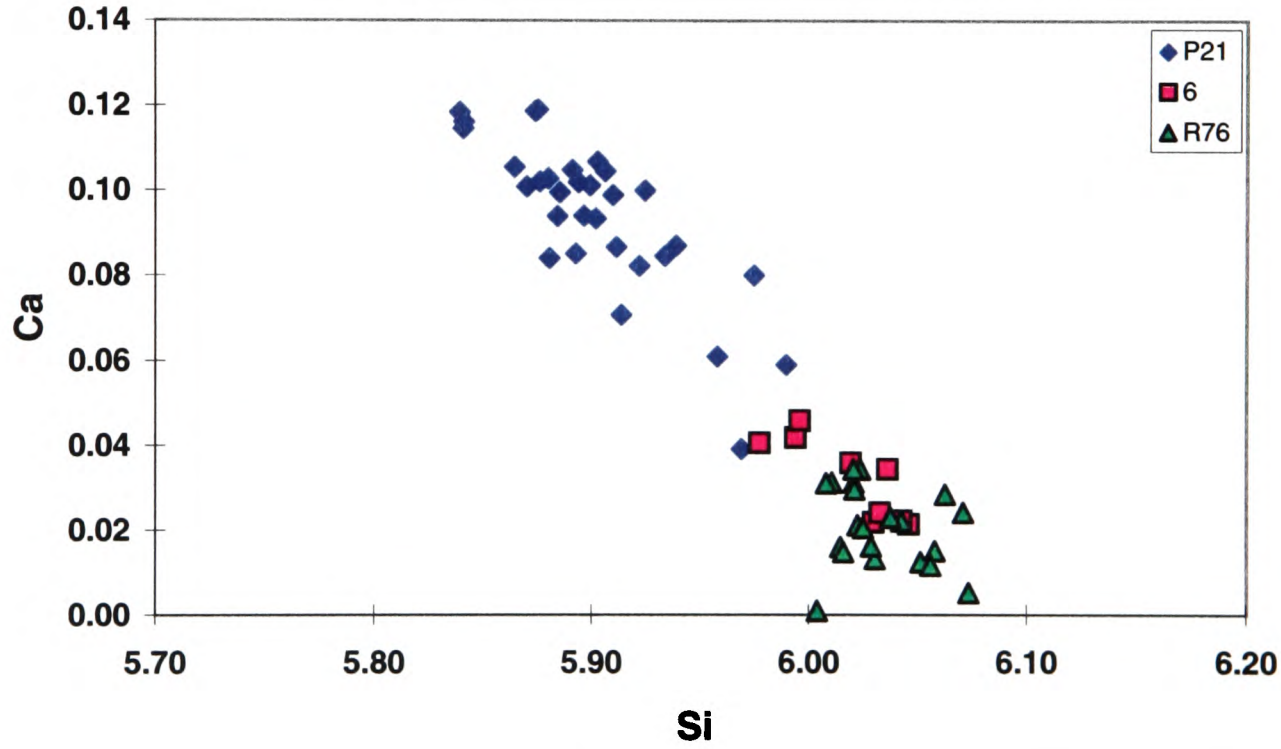


Figure 6.10: Margarite content in paragonite as a function of metamorphic grade. Metamorphic grade increases from P21 (garnet zone) to P97 (kyanite zone).

(and has therefore been used as a monitor of metamorphic grade, Guidotti *et al.* (1977)), there is very little change in biotite Ti content between these three samples.

phlogopite	$K_2Mg_6(Al_2Si_6)O_{20}(OH)_4$
annite	$K_2Fe_6(Al_2Si_6)O_{20}(OH)_4$
eastonite	$K_2(Mg_4Al_2)(Al_4Si_4)O_{20}(OH)_4$

Table 6.3: Biotite end-member compositions, for 22 oxygens per formula unit.

Fe shows two distinct clusters, one of between 1.9 - 2.1 p.f.u. representing P97 analyses, and the other representing R76 and 19 of between 2.3 - 2.5. Fe content is often a monitor of bulk rock composition, and again this implies P97 has a different bulk composition to either R76 or 19. X_{Mg} is plotted against Si by sample in figure 6.12, and P97 has a higher X_{Mg} than either R76 or 19 (which have about the same, 0.5). In addition, there is a potential positive correlation between Si and X_{Mg} for P97. Overall, X_{Mg} increases with increasing grade.

6.2.4 Chloritoid

Of the probed samples only P21 contains matrix chloritoid. Chloritoid can be thought of as an Fe-Mg end-member series, with the formula $(Fe,Mg)_2Al_4Si_2O_{10}(OH)_4$. P21 chloritoids are Fe-rich with an X_{Mg} of 0.15.

6.2.5 Chlorite

Chlorite is present in all rocks analysed, generally as late, retrogressive chlorite, often replacing biotite. The range of chlorites are plotted in figure 6.13. Si cations p.f.u. (22 O) vary from 3.95 - 4.30. X_{Mg} is largely in the range 0.3 - 0.6. Octahedral Al cations (the Tschermak content of the muscovites, Al^{vi}/Si) have values from 0.4 - 0.7. Fe varies from 0.6 - 1.1, and there appears to be a negative correlation between Si and Fe.

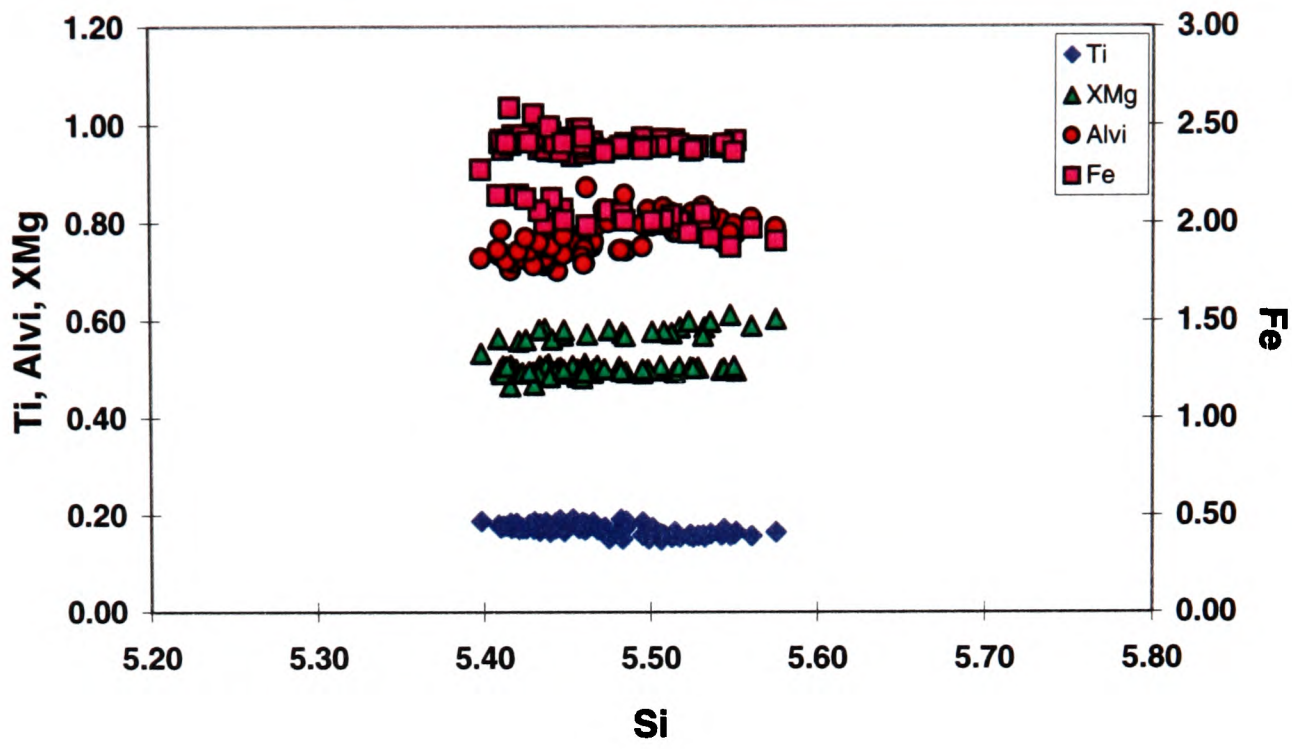


Figure 6.11: Hoosac biotites, plotting Ti, octahedral Al (Al^{vi}), X_{Mg} and Fe versus Si cations p.f.u. (22O).

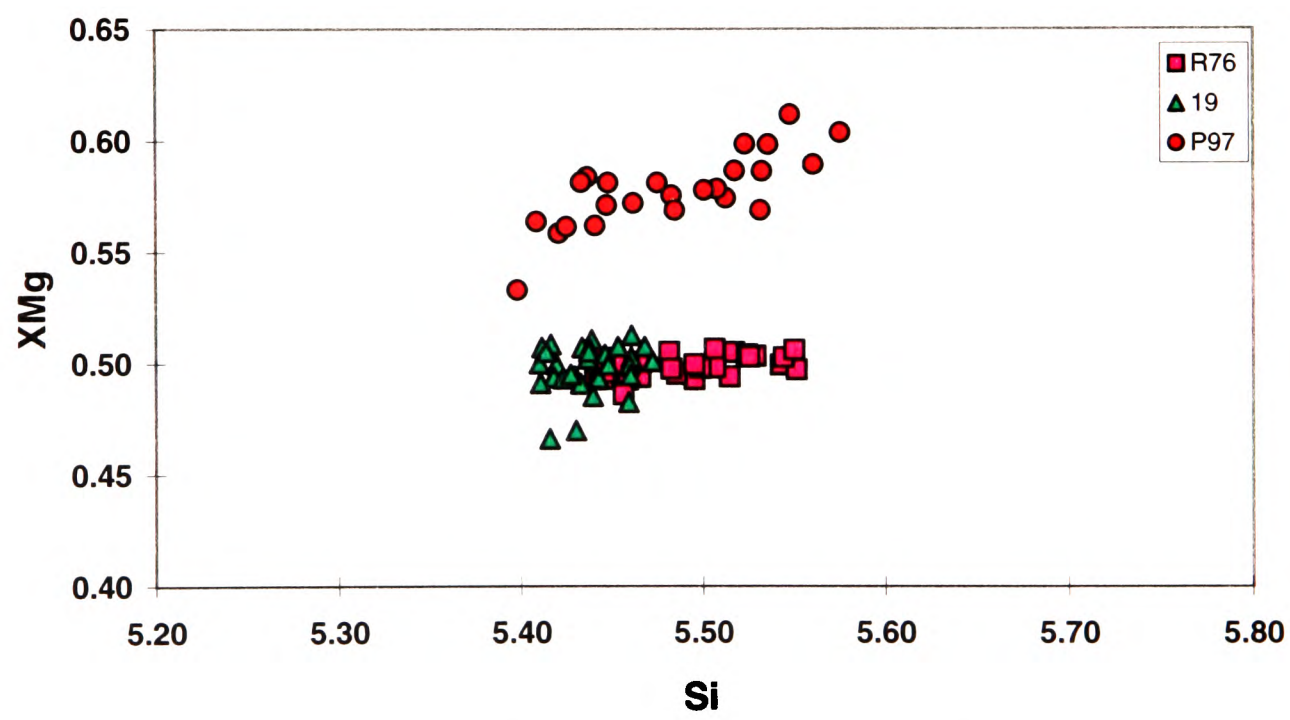


Figure 6.12: Hoosac biotites, detailing X_{Mg} by metamorphic grade. Metamorphic grade increases from R76 (staurolite zone) to P97 (kyanite zone).

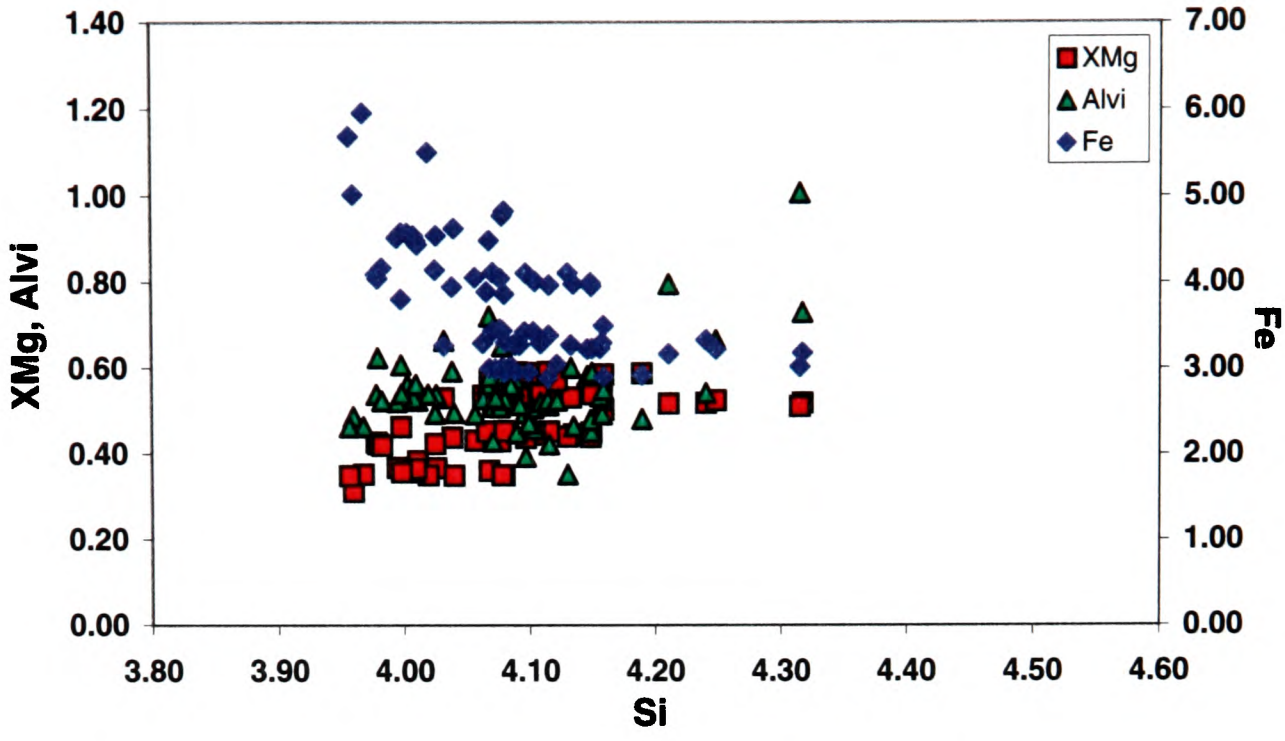


Figure 6.13: Hoosac chlorites, plotting X_{Mg}, Al^{vi} and Fe versus Si p.f.u. (22 O).

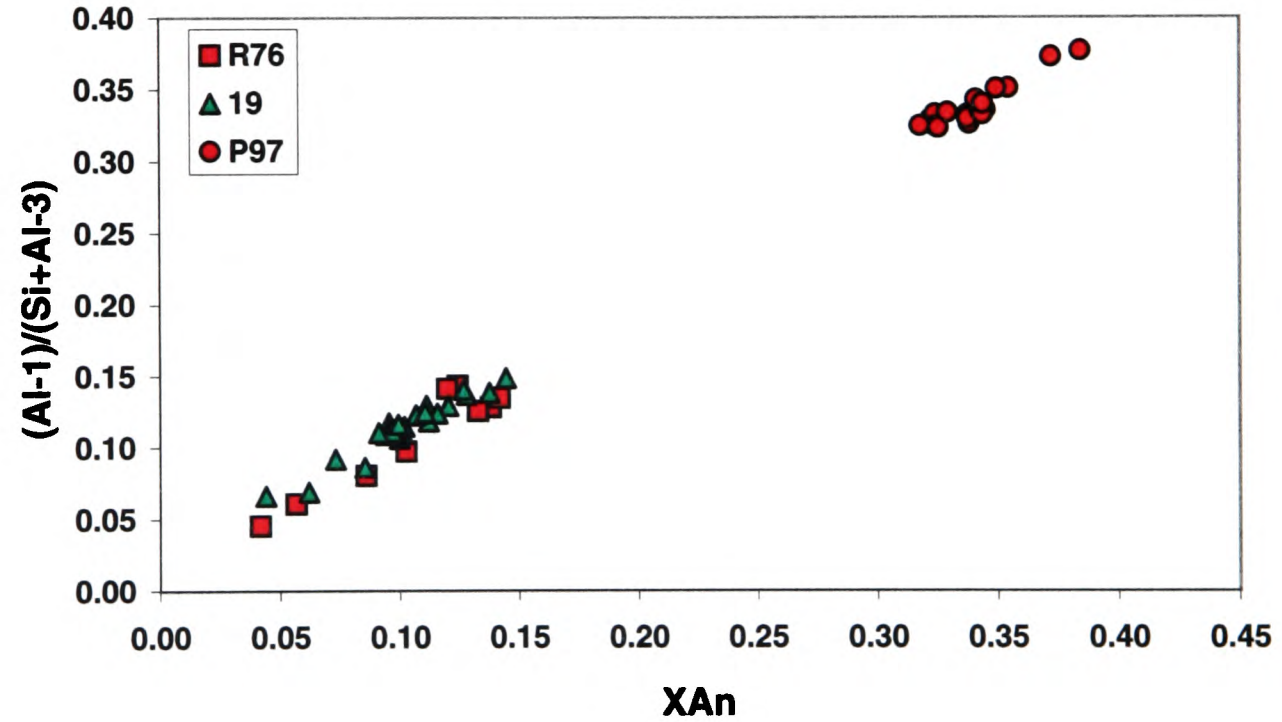


Figure 6.14: Hoosac plagioclases, plotting X_{An} versus (Al-1)/(Si+Al-3); all values are cations p.f.u. (8 O).

6.2.6 Plagioclase feldspar

Plagioclase feldspars are plotted in figure 6.14. Primary feldspar is present only in higher-grade rocks; plagioclase present in lower grades is due to post-peak alteration from paragonite. Only feldspar analysis from samples R76, 19 and P97 are shown here. Feldspars from R76 and 19 show similar X_{An} of 0.05 - 0.13 (essentially albite), whilst those from P97 are distinctly more Na-rich, with X_{An} of around 0.35 (andesine).

Since the plagioclase in R76 and 19 has formed by the late-stage replacement of paragonite, it reflects the Na content of paragonite, and is therefore very sodic. Sample P97 contains primary plagioclase, being found up-grade of the plagioclase-in isograd, and thus is much more Ca-rich, reflecting prevailing near-equilibrium conditions.

6.2.7 Staurolite

A plot of X_{Mg} versus sample is shown in figure 6.15. This shows a slight enrichment in Mg with increasing grade.

6.2.8 Summary of mineral analyses

A summary of mineral data by grade is shown in figure 6.15. Hoosac garnets exhibit normal growth zoning, with minimal evidence for later diffusive effects. Muscovites are slightly phengitic, the phengite content roughly increasing with grade, except in the case of P97. Paragonites show minimal Tschermak substitution, but they show a marked decrease in margarite content with metamorphic grade.

Biotites, being found only in the three highest grade samples probed, show evidence for slight eastonite content, away from ideal biotite end-members. They also show a distinctly different Fe content for P97, reflecting a different bulk composition. Mg/Fe ratios of muscovite and biotite increase with increasing grade.

Feldspars reveal a difference between the primary, Ca-rich plagioclase as found in P97, and the replacement plagioclase after paragonite in R76 and 19, being much more sodic

in composition.

P97 consistently seems out of step with the other rocks studied, perhaps reflecting a real bulk compositional difference. It is certainly much more graphitic.

6.3 Thermobarometry

In order to model the growth of garnet in the Hoosac samples, it is necessary to estimate the peak metamorphic pressures and temperatures of garnet formation. Thermobarometric calculations have been performed for a number of samples using the average PT approach of THERMOCALC (Powell & Holland, 1994). The Hoosac rocks do not contain many ideal phases for conventional thermobarometry, and best estimates were given by use of THERMOCALC in average PT mode.

6.3.1 Thermobarometry - principles and rationale

All geothermometers and geobarometers rely upon the condition of *chemical equilibrium*. Equation 6.1 details the fundamental relationships between pressure, temperature and mineral composition, and free energy (ΔG), enthalpy (ΔH), entropy (ΔS), volume (ΔV) and heat capacity (ΔC_P) (Spear, 1993). All terms are at steady state conditions: 298K and 1 bar.

$$\Delta G = 0 = \Delta H^{298,1} + \int_{298}^{T} \Delta C_P \mathrm{d}T + \int_{1}^{P} \Delta V \mathrm{d}P - T\left(\Delta S^{298,1} + \frac{\int_{298}^{T} \Delta C_P}{T}\mathrm{d}T\right) + RT\ln K_{eq} \tag{6.1}$$

This can be simplified to equation 6.2, giving ΔH and ΔS at the P and T of interest.

$$\Delta G = 0 = \Delta H^{\circ} - T\Delta S^{\circ} + \int \Delta V \mathrm{d}P + RT\ln K_{eq} \tag{6.2}$$

Taking the temperature and pressure derivatives of the free energy:

$$\left(\frac{\partial P}{\partial T}\right)_{\ln K_{eq}} = (-RT\ln K_{eq} + \Delta S\Delta V) = \frac{\Delta H}{T\Delta V} \tag{6.3}$$

we can define a curve in PT space, with slope $(-RT\ln K_{eq} + \Delta S)/\Delta V$. We can then define the equilibrium constant, K_{eq} of a reaction:

$$K_{eq} = \prod_{i=1}^{m} (a_i^{\nu_i}) \tag{6.4}$$

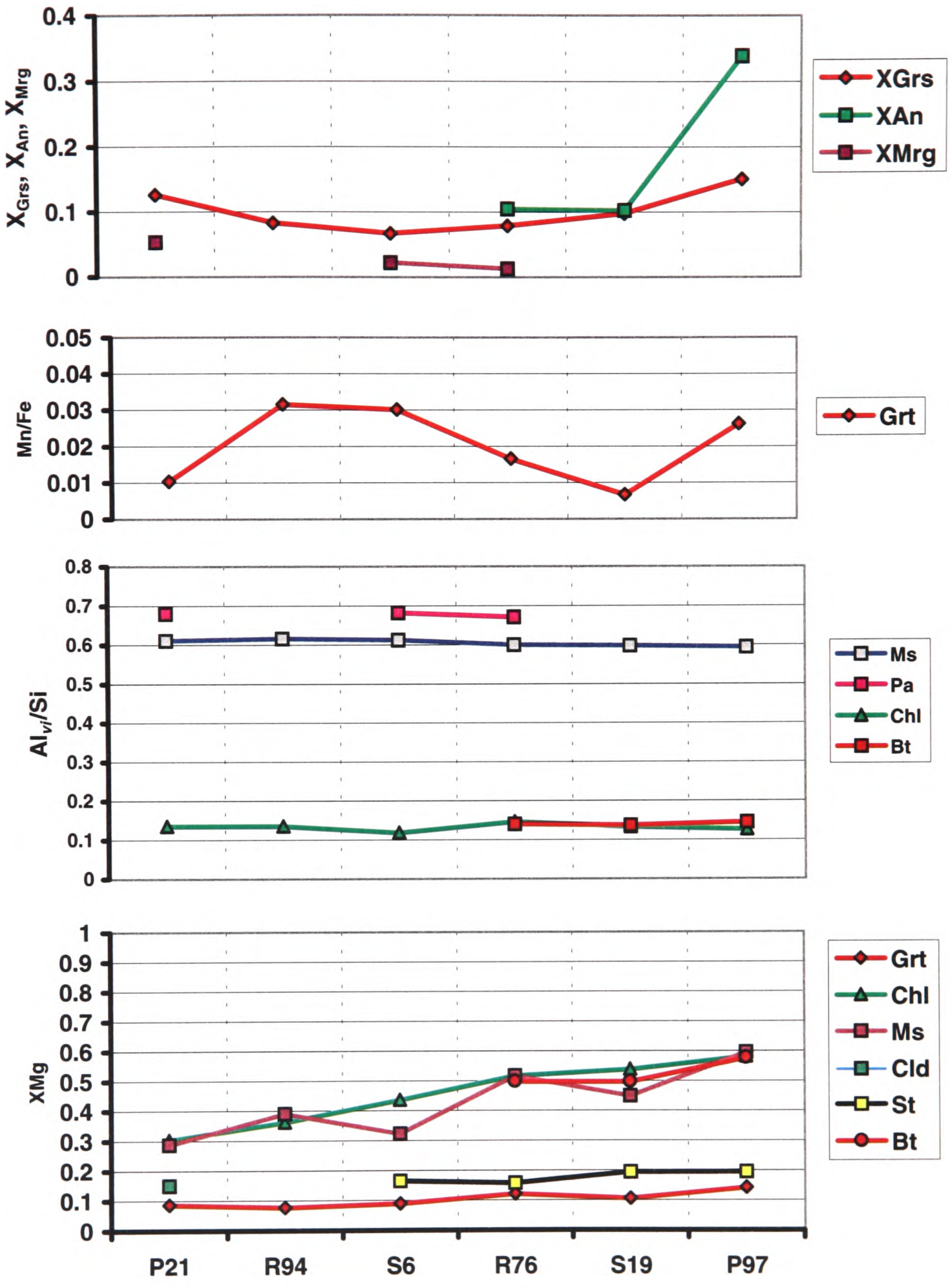


Figure 6.15: A summary of X_{Mg}, Al_{vi}/Si, Mn/Fe, X^{Grt}_{Grs}, X^{Pl}_{An} and X^{Pg}_{Mrg} by grade (P21, garnet → P97, kyanite).

where m is the number of components in the reaction, a_i is the activity of component i, and ν_i is the stoichiometric coefficient.

From coexisting mineral composition data a line of constant K_{eq} can be drawn in PT space, and the sample inferred to have equilibrated somewhere along this line. If two or more lines intersect then they should intersect at a unique temperature and pressure.

Since these principles require the condition of equilibrium, in order to obtain meaningful PT estimates, mineral analyses must be chosen carefully to represent as best those phases in equilibrium. These analyses are then converted to end-member activities using the program AX and the dataset of Holland & Powell (1998).

6.3.2 THERMOCALC thermobarometry

The program THERMOCALC uses a self-consistent thermodynamic dataset to calculate an independent set of reactions from a given set of phase components (Holland & Powell, 1998, and references therein). Although the thermodynamic principles employed are the same as for conventional thermobarometry, THERMOCALC differs in that it calculates all possible independent reactions between the mineral end-members involved. A least-squares method is then employed to obtain an optimal P-T from this set of reactions, which includes uncertainties and correlations on the activities and enthalpies of formation of the endmembers - essentially a procedure to vary the position of the reactions in P-T space in proportion to their uncertainties and correlations so that they intersect at one point: the average PT. The displacements of any one reaction cannot be made independently of the other reactions because they are all linked and correlated through their shared end-members. In this way THERMOCALC attempts to obtain superior accuracy for pressure-temperature estimation than could be calculated from conventional thermobarometry by using a greater range of thermodynamic data.

6.3.3 The effects of water activity

THERMOCALC allows the user to specify a water activity by approximately modelling an H_2O-CO_2 binary mixture equating X_{H_2O} with a_{H_2O}. Due to the presence of C-bearing

species, many rocks will have $a_{H_2O} < 1$. Table 6.4 shows the effect of varying water activity on average P-T results from sample 19, and these results are plotted in figure 6.16.

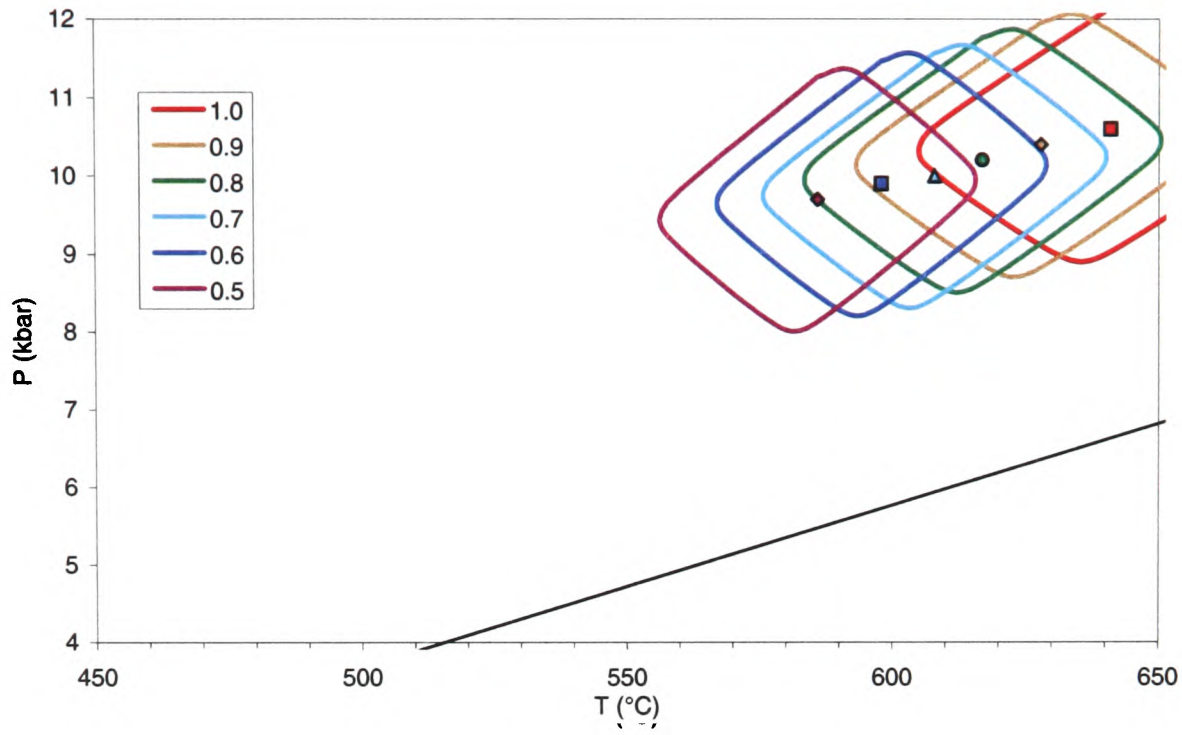


Figure 6.16: Graph plotting P-T results from THERMOCALC for sample 19 with different water activities. Ky=Sil curve provided for reference. Error ellipses are 2σ.

X_{H_2O}	T°C	sd (T)	P kbar	sd (P)	corr	fit
1.0	641	28	10.6	1.3	0.268	1.39
0.9	628	27	10.4	1.3	0.258	1.39
0.8	617	26	10.2	1.3	0.253	1.39
0.7	608	25	10.0	1.3	0.252	1.39
0.6	598	24	9.9	1.3	0.255	1.40
0.5	586	23	9.7	1.3	0.258	1.41

Table 6.4: P-T results for sample 19 showing the effect of varying water activity, approximated as X_{H_2O}.

The calculated temperatures span 65°C and 0.9 kbar, and there is little deterioration in the quality of the least-squares fit ('fit' value). For the purposes of both P-T estimation and metamorphic modelling (chapter 8), a value of $H_2O = 0.75$ was chosen for all Hoosac samples.

THERMOCALC P-T results

Table 6.5 details THERMOCALC average P-T results from five of the Hoosac samples. These are plotted up in figure 6.17, and given an uncertainty ellipse calculated as described by Powell & Holland (1988, 1994). All samples yielded a result, except sample 6, which did not contain sufficient phase components to produce a sufficient set of independent reactions to estimate PT.

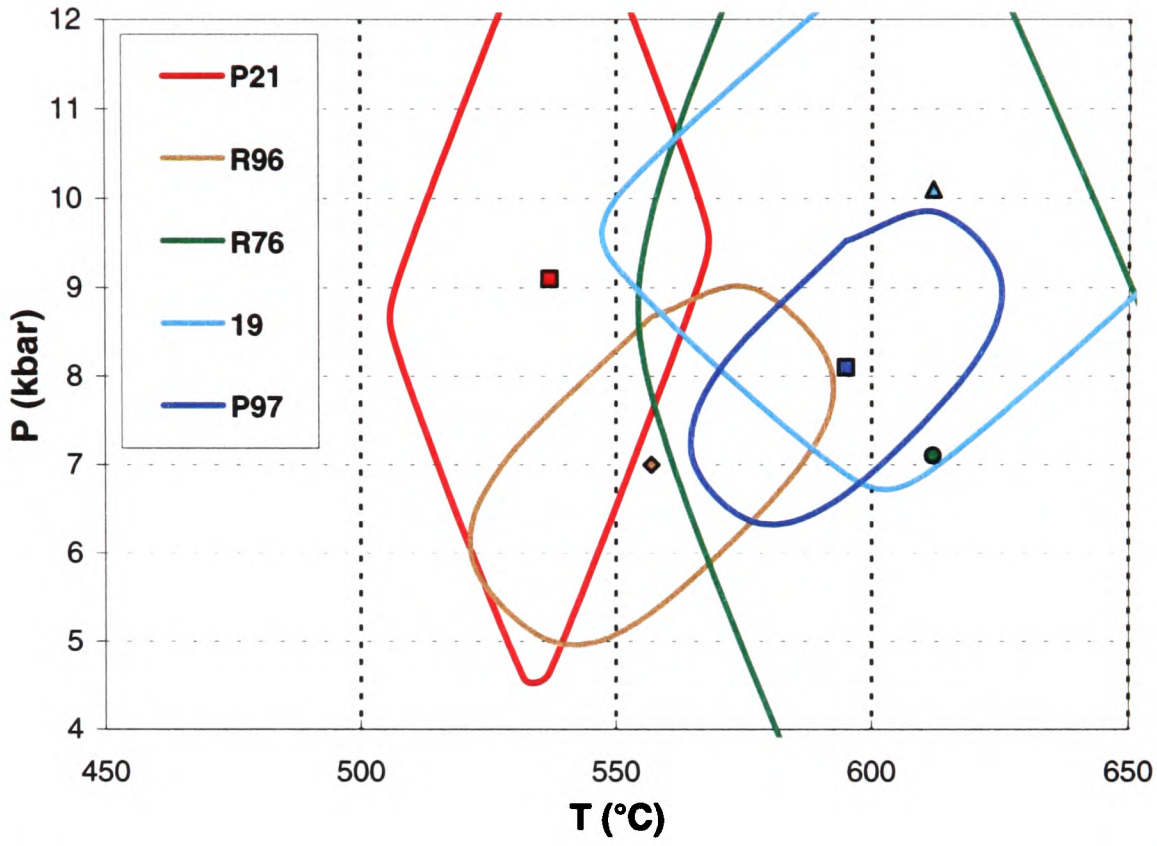


Figure 6.17: Average P-T results calculated from THERMOCALC, increasing in grade from P21 to P97. Error ellipses are calculated as per Powell & Holland (1988) and are 2σ.

6.3.4 Thermobarometry - discussion

The results gained from THERMOCALC show a broad increase in average PT from garnet grade (P21 and R96) through staurolite (R76) to kyanite (19). Sample P97, potentially the highest grade of all shows an anomalous PT value within the range of results shown here.

The two important cations for thermometry in garnets are Fe and Mg; Mn is only found in quantity in garnet, and Ca in the Hoosac rocks is either present in garnet or as a

Sample		P21	R96	R76	19	P97
Activities		500°C 8.5kbar	550°C 8kbar	550°C 8kbar	600°C 10kbar	600°C 8kbar
Garnet	py	0.00104	0.00117	0.0026	0.00160	0.0036
	gr	0.0024	0.0042	0.00055	0.00122	0.0047
	alm	0.41	0.35	0.43	0.44	0.29
Ms	ms	0.70	0.47	0.63	0.72	0.69
	pa	-	0.510	-	0.75	0.80
	cel	0.012	0.069	0.039	0.019	0.021
Pg	pa	-	0.81	-	-	-
	ma	0.099	-	0.022	-	-
Bt	phl	-	-	0.062	0.060	0.082
	ann	-	-	0.051	0.050	0.030
	east	-	-	0.046	0.051	0.066
Cld	mctd	0.17	-	-	-	-
	fctd	0.50	-	-	-	-
St	mst	-	-	0.00067	0.0015	0.0015
	fst	-	-	0.50	0.42	0.41
Chl	clin	0.0023	0.001	-	-	-
	daph	0.122	0.026	-	-	-
	ames	0.0055	0.0206	-	-	-
Pl	an	-	0.36	-	0.15	0.49
	ab	-	0.76	-	0.90	0.66
Other		Qtz H2O	Qtz H2O	Ky Qtz H2O	Ky Qtz H2O	Ky Qtz H2O
Results	a_{H_2O}	0.75	0.75	0.75	0.75	0.75
	T°C	**537**	**557**	**610**	**612**	**595**
	s.d.(T)	12	31	23	25	13
	P kbar	**9.1**	**7.0**	**7.4**	**10.1**	**8.3**
	s.d.(P)	1.8	0.8	2.9	1.3	0.7
	correl	0.172	0.549	-0.361	0.251	0.581
	sigfit	1.11	0.67	0.14	1.39	0.63
	No. rxns	6	5	7	8	8

Table 6.5: Summary of average PT results from THERMOCALC.

margarite component in paragonite. Given that garnet cation self-diffusion is so slow as to lock up garnet peak conditions (*i.e.* those conditions at the point when garnet ceased to grow), it is not unrealistic to predict that any PT estimation may actually predict the limit of garnet growth, since Fe-Mg bearing phases in the matrix (chloritoid, biotite, staurolite and chlorite in appropriate rocks) may not be able to exchange with anything.

The errors given by THERMOCALC for the Hoosac rocks reflect a problem with the lack of useful minerals in high-alumina rocks for precise thermobarometry. The use of pseudosection calculation gives a much better control on peak metamorphic conditions than thermobarometry in these rocks. This is covered in chapter 8.

Chapter 7

Oxygen isotope results from the Hoosac Schist

7.1 Introduction

Oxygen isotope results collected from three big-garnet Hoosac Schist samples by UV-ablation, GC-*irms* are presented here. These results have been collected within the framework of development; routine analysis of pelite samples has consistently proved problematic compared to meteoritic samples, and many of the problems encountered appear to be sample-specific. Despite the problems, isotope results have been attained and are presented here. Only blank-corrected $\delta^{18}O$ are dealt with in this chapter; appendix B contains all uncorrected, raw data collected from the Hoosac samples, while chapter 3 details development and problems with Hoosac sample analysis.

7.2 Analytical errors

Analytical errors are derived from three main sources: (a) from inherent instrumental drift; (b) from the analytical procedure, including contamination from sample chamber and line, the nature of ablation, and the gas clean-up and transfer process; and (c) from the blank correction.

Analyses of nine aliquots of reference gas sequentially injected into the mass spectrometer (a *stability* test), show an instrumental precision of ±0.1‰ . This is the baseline error of the Finnigan MAT 252 with the GC inlet.

Additionally, user errors concerning the cleanliness of the line, the nature of laser ablation and the nature of gas transfer all add to uncertainty. On top of this is the uncertainty derived from the blank correction, which includes both the analytical error implicit in the blank measurement, and the operator's assessment of when the blank has reached stability, and what blank value to use in recalculation.

Given the uncertainties detailed above, as well as observed reproducibility in natural samples it is believed an overall precision of between ±0.2 - 0.3‰ (1σ) is achievable.

7.2.1 Counting statistics and theoretical precision

Measurement of $^{18}O/^{16}O$ by GC-*irms* amounts to measuring ion currents, and therefore the maximum precision obtainable is limited by the reproducibility of ion current detection. Repeated measurements of the reference gases have shown that uncertainties in oxygen isotope analysis by the Oxford GC-*irms* system are approximately double those imparted by current fluctuations known as shot noise (Young *et al.*, 1998a). Such fluctuations are inherent in the statistics of counting discrete charges over a fixed time interval and are calculable.

Uncertainties are expressed in the delta notation, such:

$$\delta^{17}O = ({}^{17}R^{x}/{}^{17}R^{std} - 1) \cdot 10^{3} \tag{7.1}$$

$$\delta^{18}O = ({}^{18}R^{x}/{}^{18}R^{std} - 1) \cdot 10^{3} \tag{7.2}$$

Here, ${}^{17}R^{x}$ and ${}^{17}R^{std}$ are $^{17}O/^{16}O$ for the unknown and the standard respectively. ^{17}R and ^{18}R are represented by the ratios of ion currents for m/z corresponding to the O_2 isotopomers $^{16}O^{16}O$, $^{18}O^{16}O$, $^{16}O^{18}O$, $^{17}O^{16}O$, $^{16}O^{17}O$ and $^{17}O^{17}O$. The three currents of interest are ${}^{32}I$, ${}^{33}I$ and ${}^{34}I$. Ratios of ${}^{33}I$ and ${}^{34}I$ relative to ${}^{32}I$ are written as ${}^{33}R_i$ and ${}^{34}R_i$, and their relation to the isotope ratios of oxygen is straightforward if there are no interferences from other species:

$${}^{33}R_i = 2^{17}R \tag{7.3}$$

$$^{34}R_i = 2^{18}R +^{17} R^2 \tag{7.4}$$

Expressions for uncertainties in measured δ values in terms of the total number of oxygen molecules admitted to the source are:

$$\sigma^2_{\delta^{17}\mathrm{O}} = \left(\frac{2 \times 10^6(1 +^{33} R_i)(1 +^{33} R_i +^{34} R_i)}{^{33}R_i x_g \epsilon M}\right) \tag{7.5}$$

$$\sigma^2_{\delta^{18}\mathrm{O}} = \left(\frac{2 \times 10^6(1 +^{34} R_i)(1 +^{33} R_i +^{34} R_i)^{34}R_i}{\left(^{34}R_i - \frac{^{33}R^2}{4}\right)^2 x_g \epsilon M}\right) \tag{7.6}$$

where x_g is the fraction of sample gas that enters the source of the mass spectrometer, ϵ is the ionization efficiency of the source expressed as ions per molecule, and M is the total number of oxygen molecules comprising the sample.

Values of 0.00414 and 0.00075 for $^{33}R_i$ and $^{34}R_i$ respectively, are suitable for most geological samples (Nier, 1950). The Oxford laboratory has a value of ϵ for O_2 entrained in He of 4.2×10^{-4}, and the fraction of sample entering the source via the open split is 0.33 (Young *et al.*, 1998a). Substitution of these values, and incorporation of Avogadro's number gives:

$$\sigma^2_{\delta^{17}\mathrm{O}} = \frac{0.03199}{n_{\mathrm{O}_2}} \tag{7.7}$$

$$\sigma^2_{\delta^{18}\mathrm{O}} = \frac{0.00581}{n_{\mathrm{O}_2}} \tag{7.8}$$

where n_{O_2} is the amount of sample O_2 in nanomoles.

Figure 7.1 shows the expected real-world precision (2σ) in δ^{18}O and δ^{17}O given by equation 7.7 and 7.8 as a function of the amount of silicate mineral analyzed. This gives a minimum volume of silicate analyzed to a 2σ precision of $\pm$ 0.2‰ to be a pit measuring 191 nanograms giving 2.4 nanomoles O_2. These calculations suggest that GC-*irms* analysis of O_2 should, in the absence of other analytical influences, enable high-precision oxygen itotope analysis of silicates with a minimum resolution of 40μm, smaller than the 100-150μm pits analysed in this thesis.

7.2.2 Standard data

Repeated analyses of USNM Almandine give the best indication of the achieveable precision of the Oxford laser line when analyzing garnet. Since it has been found that the

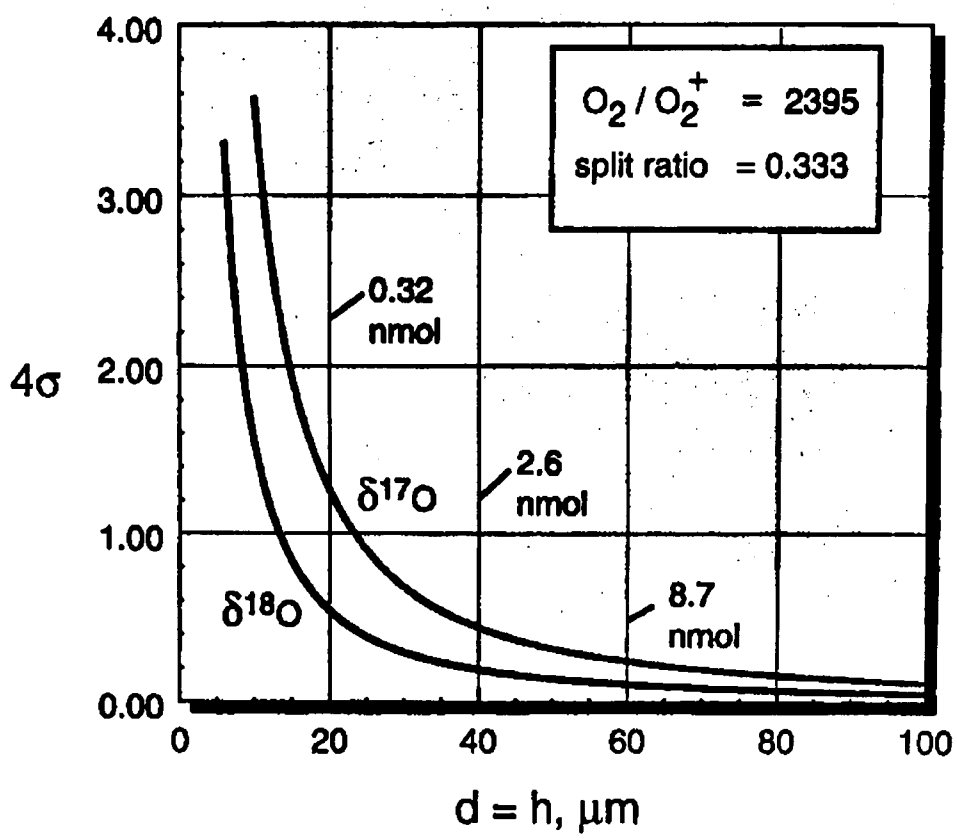


Figure 7.1: Estimated precision for $\delta^{18}O$ and $\delta^{17}O$ as a function of silicate sample size. σ represents the shot noise, and 4σ corresponds to a realizable 2σ. d is the diameter of a cylinder of silicate, and h is the height of the cylinder in μm. After Young *et al.* (1998a).

accuracy of the line depends on the nature of the samples loaded (*i.e.* loading a sample of USNM Almandine with a large specimen of Hoosac schist gives a worse accuracy than loading the standard alone), blocks of analytical data have been defined depending on what the standard garnet was loaded with. Appendix C contains all relevant standard data, and figure 7.2 shows corrected $\delta^{18}O$ results from USNM Almandine loaded with samples 6, 19a and r76. Inspection of these show that a precision of ± 0.2 (1σ) is achieveable. Therefore all result plots within this thesis have 1σ error bars of ± 0.2.

7.2.3 Accuracy versus Precision

The accuracy of an isotope line refers to the difference between the average standard value analysed on that insturument compared with the accepted international value of the standard. The isotope line is consistently heavy by 0.8-1.0‰ , as can be seen in figure 7.2.

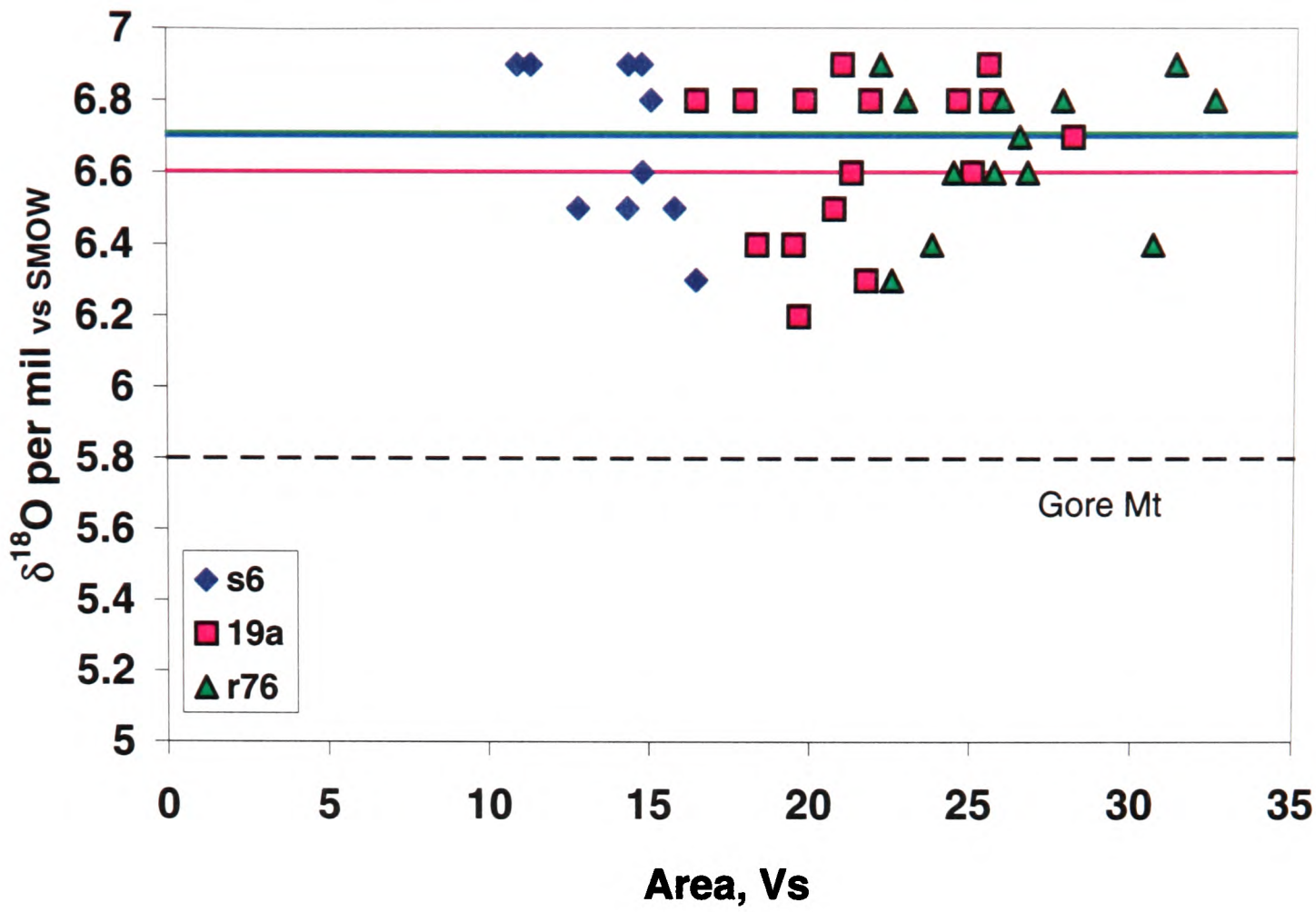


Figure 7.2: Corrected USNM $\delta^{18}O$ analyses loaded with samples 6, 19a and r76, with an achieveable precision of ± 0.2 (1σ). Horizontal lines give the mean for samples 6 (6.7‰), 19a (6.6 ‰) and r76 (6.7‰). This contrasts with the accepted value of 5.8‰ (Valley *et al.*, 1995).

7.3 Sample 6a

Sample 6a is from locality 6, within the staurolite zone, and consists of a small (2mm diameter) garnet set within a matrix of white mica, quartz and chlorite, with some minor garnets and a staurolite. It was chipped off from the edge of a large garnet along a quartz vein, and thus may reflect a rim growth event. 6a is the first pelite sample to have had successful *in-situ* oxygen isotope mapping, and includes perhaps the highest-resolution oxygen isotope zonation yet observed in garnet.

Petrologically, it is characterized by extensive retrograde features including abundant later chlorite and partially broken-down staurolites pseudomorphed by a fine-grained groundmass consisting largely of muscovite and quartz (a 'shimmer-aggregate' texture - see chapter 5). Isotope investigations concentrated on mapping out zonation within the small garnet (here termed 'garnet A'), but some staurolite, chlorite and muscovite

analyses were also collected.

7.3.1 Sample 6a - results

Complete isotope results from sample 6a are shown in figure 7.3. These results are summarised in figure 7.4, while figure 7.5 details analytical localities as referred to in table 7.1.

Analysis no.	Mineral	Corrected $\delta^{18}O$ ‰ SMOW
5-23	garnet A	10.3
5-24	garnet A	10.5
5-25	garnet A	10.5
5-26	garnet A	9.8
5-27	garnet A	10.3
5-30	garnet A	10.0
5-31	garnet A	10.1
5-32	garnet A	10.4
5-33	garnet A	10.2
5-34	garnet A	10.5
5-35	garnet A	10.6
5-36	garnet A	10.6
5-38	garnet	10.6
5-39	garnet	10.4
5-40	garnet	10.7
5-42	garnet A	10.4
5-62	staurolite	9.9
5-63	garnet A	10.6
5-64	staurolite	9.9
5-65	sericite (largely muscovite)	10.2
5-66	chlorite	8.1

Table 7.1: Summary of corrected $\delta^{18}O$ results from sample 6a.

Garnet A - results

Oxygen isotope analyses from garnet A in sample 6a can be plotted as a normalized distance versus $\delta^{18}O$ plot, constructed by normalizing the distance of the isotope analysis from the centre of the garnet to the radial distance 2mm, as shown in figure 7.6. Error bars are ± 0.2‰ (1σ).

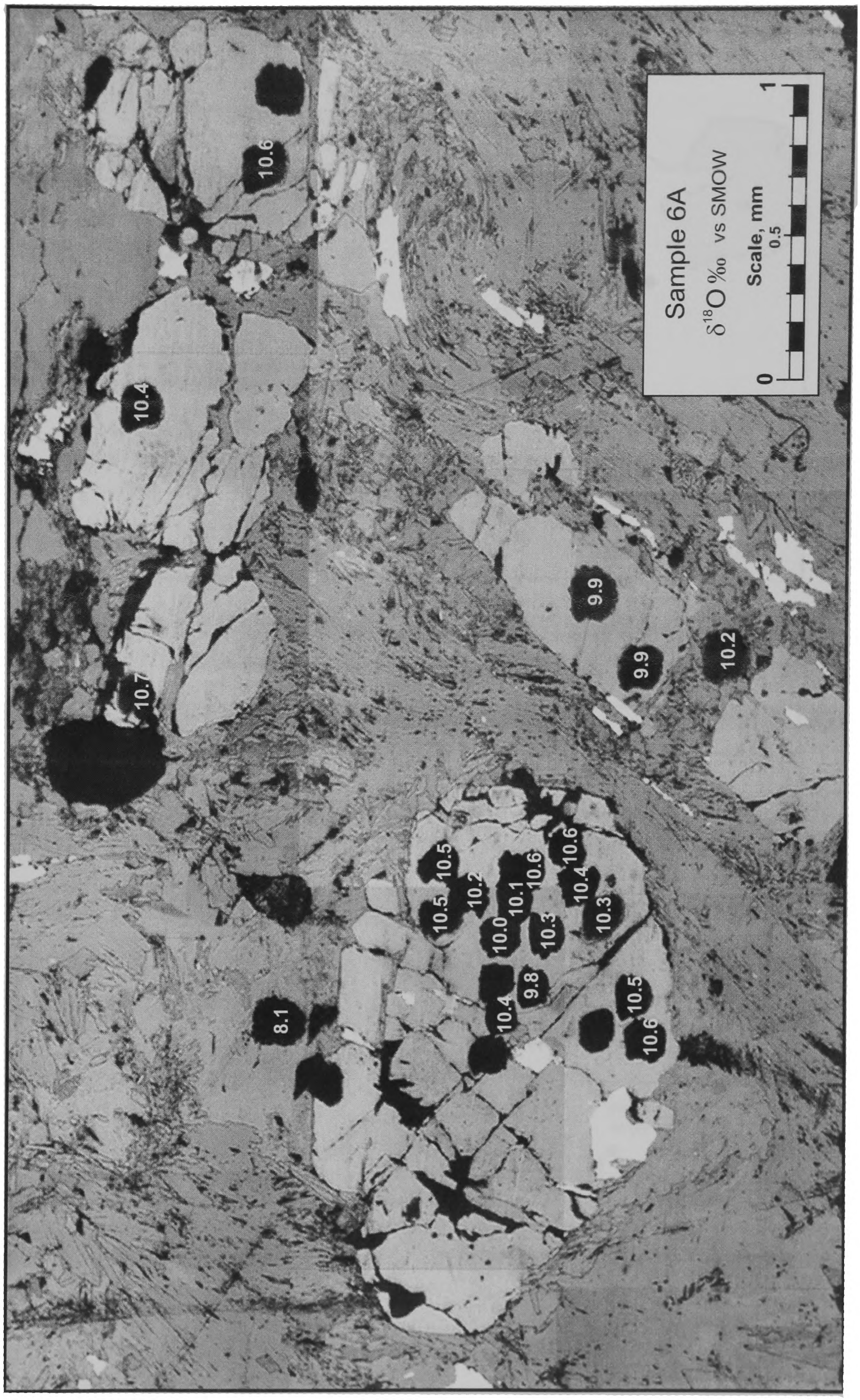


Figure 7.3: Corrected $\delta^{18}O$ results from sample 6a.

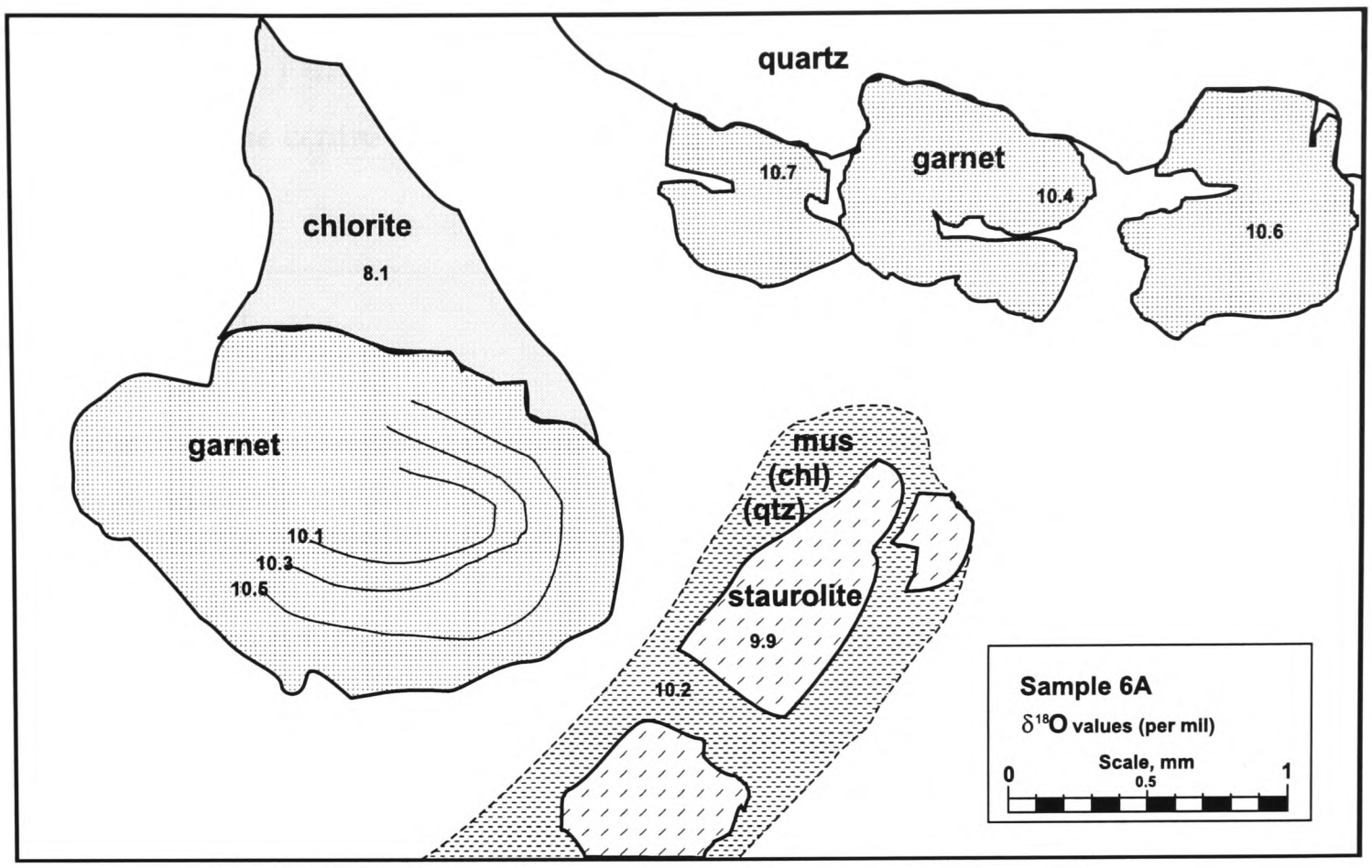


Figure 7.4: Summary of δ^{18}O results from sample 6a, per mil vs SMOW.

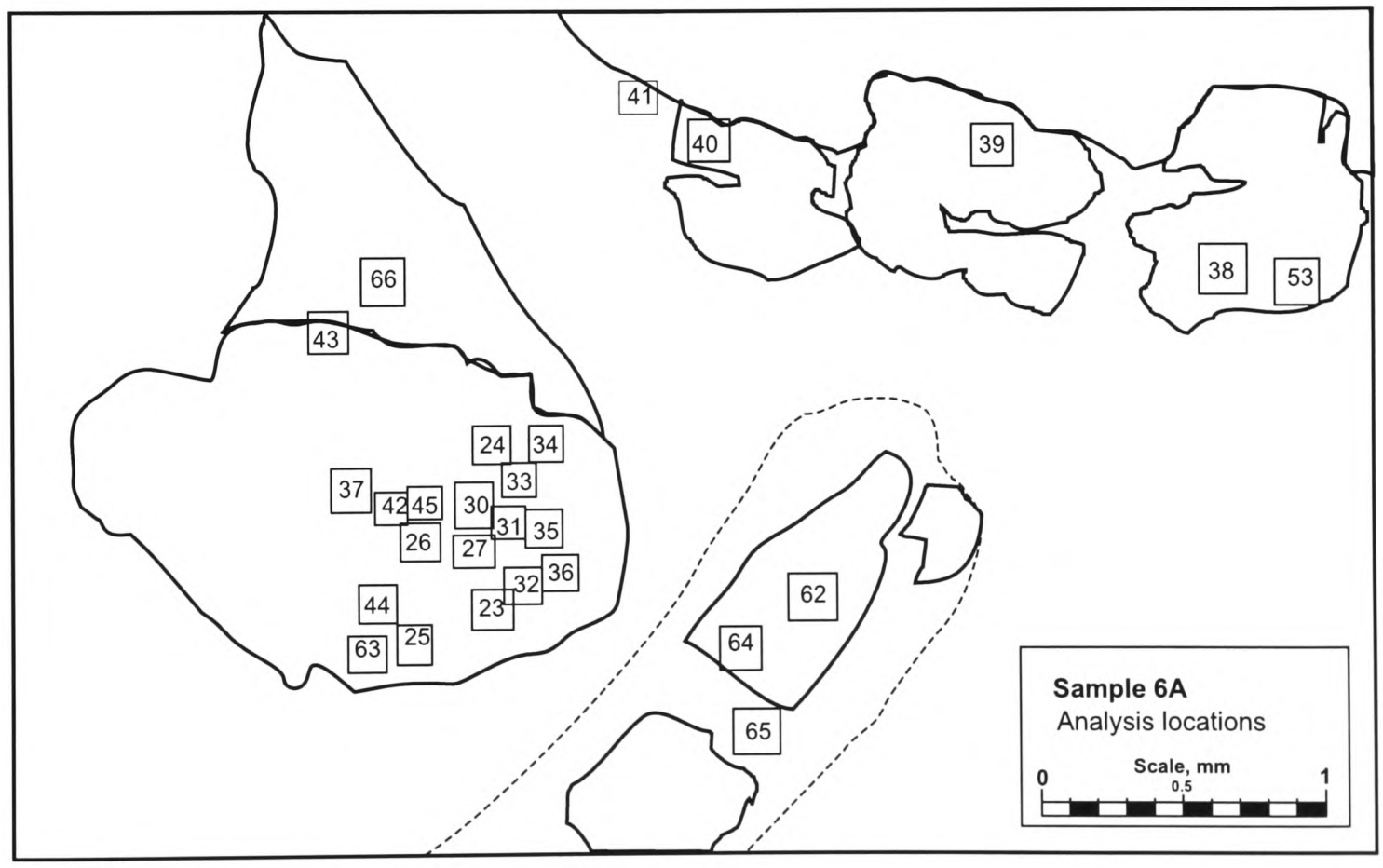


Figure 7.5: Location of δ^{18}O analyses from sample 6a; analysis numbers should be prefixed by '5-'; *e.g.* 65 is sample no. 5-65.

These results show consistent, concentric oxygen isotope zonation, with $\delta^{18}O$ increasing from core (9.8‰) to rim (10.6‰), over a range of 0.8 - 1.0‰. Note that the heavy $\delta^{18}O$ value at the centre of the garnet (10.4‰) contains part of an inclusion, and thus is discounted.

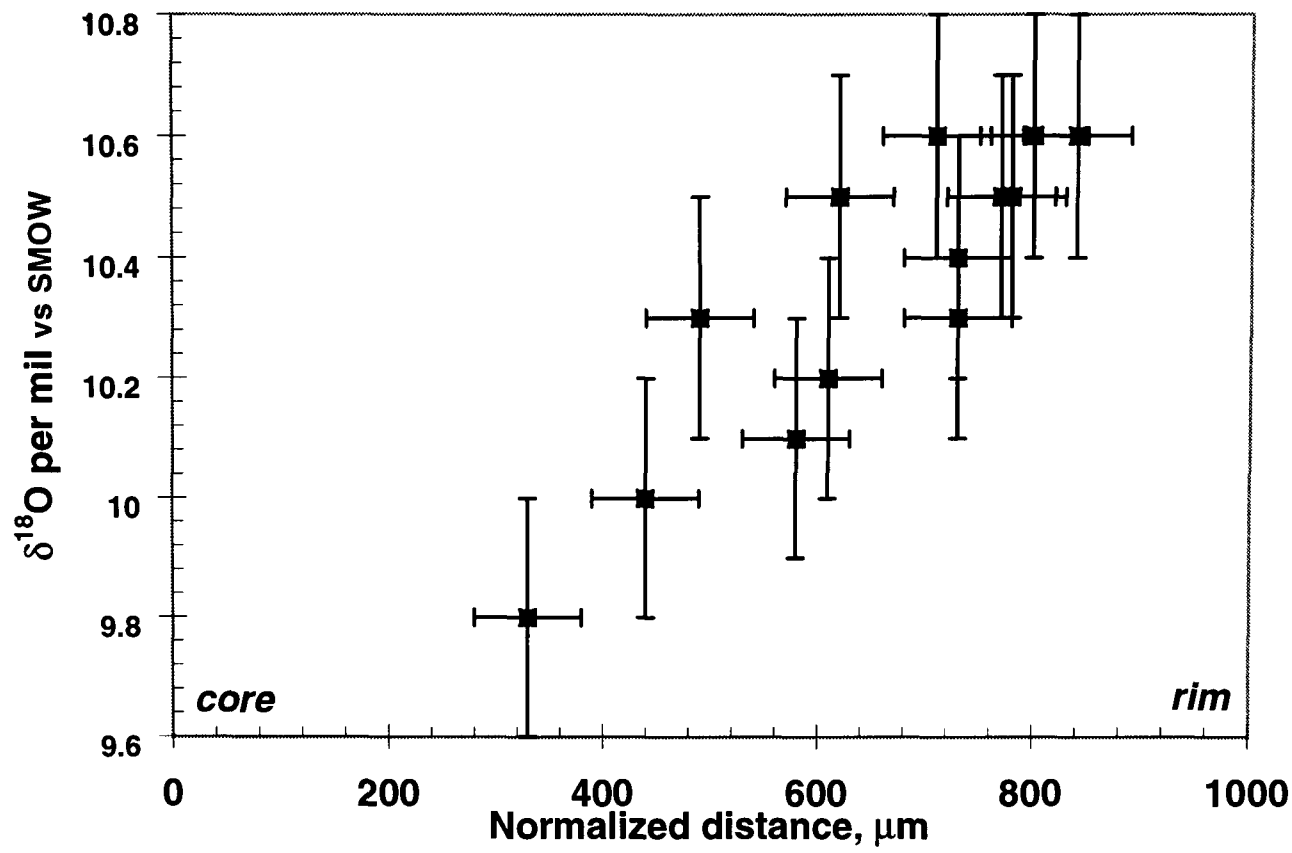


Figure 7.6: Normalized $\delta^{18}O$ zoning pattern for garnet A in sample 6a. Garnet A has a maximum diameter of 2mm; this plot was calculated by ratioing core-analysis : core-rim distance for every point, and then normalizing to a average radius of 1mm. Error bars are ±0.2‰ (1σ).

Both the textural (the absence of a textural break) and chemical evidence imply that garnet A probably grew in a single uninterrupted prograde growth event. Core-rim elemental profiles of the four major cations (Fe, Mg, Ca and Mn) are shown in figures 7.7 and 7.8. When the isotope results are compared to Ca zoning (Mn is at too small concentrations), the evolution of $\delta^{18}O$ with the growth history of the garnet can be seen. Calcium decreasing from core to rim has been attributed to normal prograde growth zoning of garnet (Tracy *et al.*, 1976). Mn is slightly enriched at the rim implying some later garnet breakdown. The low core values of X_{Sps} and the high values of X_{Pyp} compared to other probed large garnets from sample 6 reinforce the idea that garnet A represents the result of a later growth event.

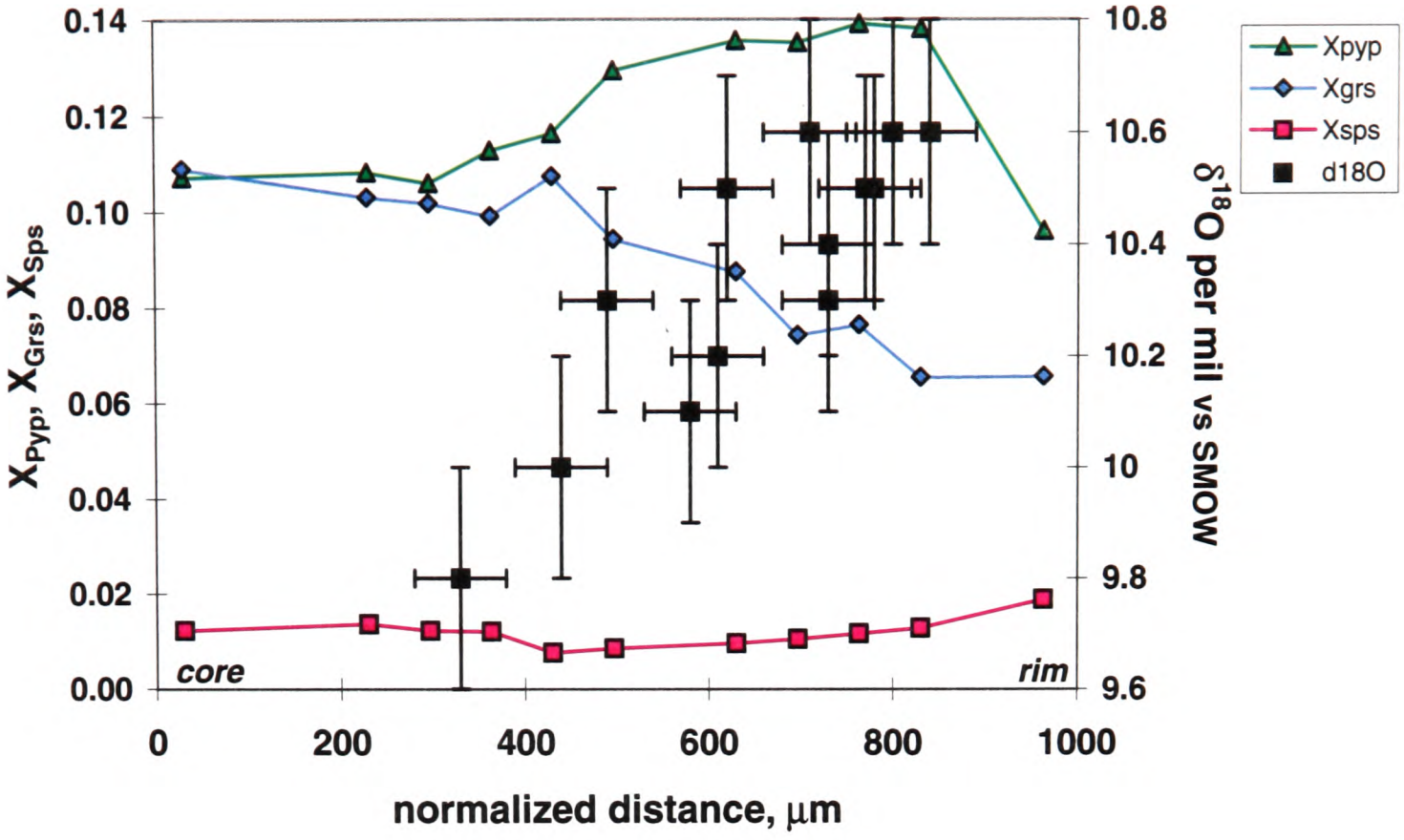


Figure 7.7: Core-rim Mg, Ca and Mn profile (X_{Pyp}, X_{Grs} and X_{Sps} respectively) across 6a, plotted alongside $\delta^{18}O$.

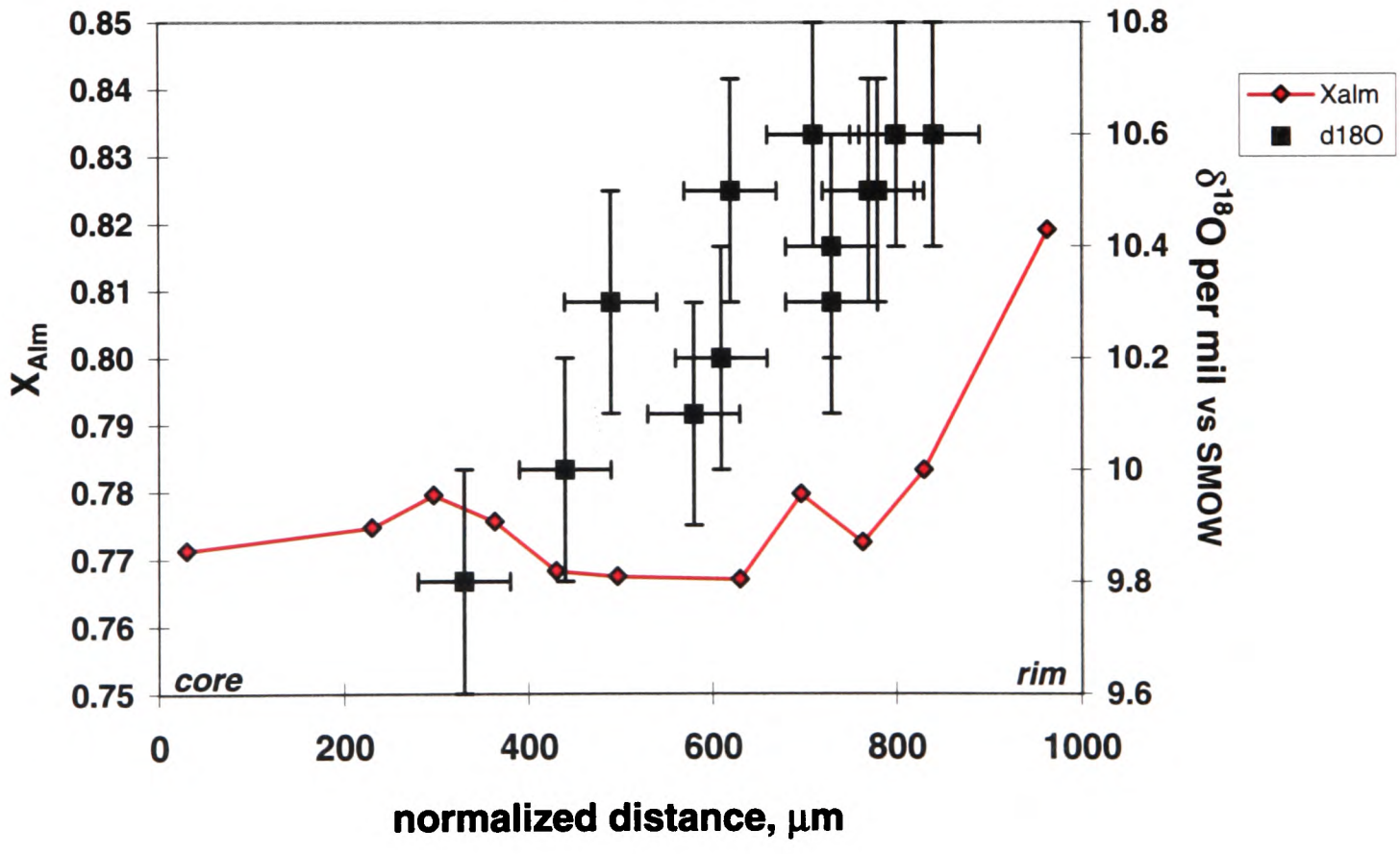


Figure 7.8: Core-rim Fe (X_{Alm}) profile across 6a, plotted alongside $\delta^{18}O$.

7.4 Sample 19a

Oxygen isotope analysis on a large (8mm diameter) garnet taken from sample 19a (lower kyanite zone) were collected. Figure 7.9 is a map of sample 19a showing corrected $\delta^{18}O$, while figure 7.10 details analytical localities (as referred to in data summary table 7.3).

Data collection was performed on the garnet complete with the mica-rich matrix still surrounding it. During the course of analysis, 19a was the first sample to exhibit the phenomena of downward-drifting $\delta^{18}O$. This shift was initially blamed on the surrounding micas splitting away from the garnet, exposing fresh mineral surface. This theory, however, was later discounted. Work on meteorite samples showed a similar downward-drifting effect, and proved that by blanketing the sample in fluorine for an hour and then passing the gases through the line as per a normal run, the drift can be corrected. This remedy was later successfully tried with garnet sample R76, and its ability to arrest and reverse the shift points to the cause being a surface effect. It may be that the outfall of fluorides onto the sample surface (which build up with increasing numbers of runs) provides a surface onto which heavier oxygen can preferentially adsorb; the blanketing fluorine cures the shift by attacking these fluorides, and releasing this oxygen.

Whatever the exact cause, this drift manifested itself as an apparent shift with time. Adjacent analyses made within a day or two of each other were generally within 0.1-0.2‰, thus reinforcing confidence in the analytical technique. However, after approximately a week of sample analysis, when returning to a domain on the garnet that was previously analysed, a lightwards-shift of approximately 0.5-0.8‰ was observed. Where (for example) analysis had consistently yielded 10.5 and 10.6‰, after this shift 9.8 and 9.8‰ were measured respectively. Table 7.2 compares some adjacent analysis made before and after the shift.

Early analysis no.	Corrected $\delta^{18}O$ ‰ SMOW	Late analysis no.	Corrected $\delta^{18}O$ ‰ SMOW	Shift
5-301	10.7	5-325	10.1	-0.6
5-298	10.5	5-330	9.8	-0.7
5-312	10.6	5-331	9.8	-0.8
5-296	10.3	6-4	9.8	-0.5

Table 7.2: Comparison of analysis from adjacent points on sample 19a, before and after the shift.

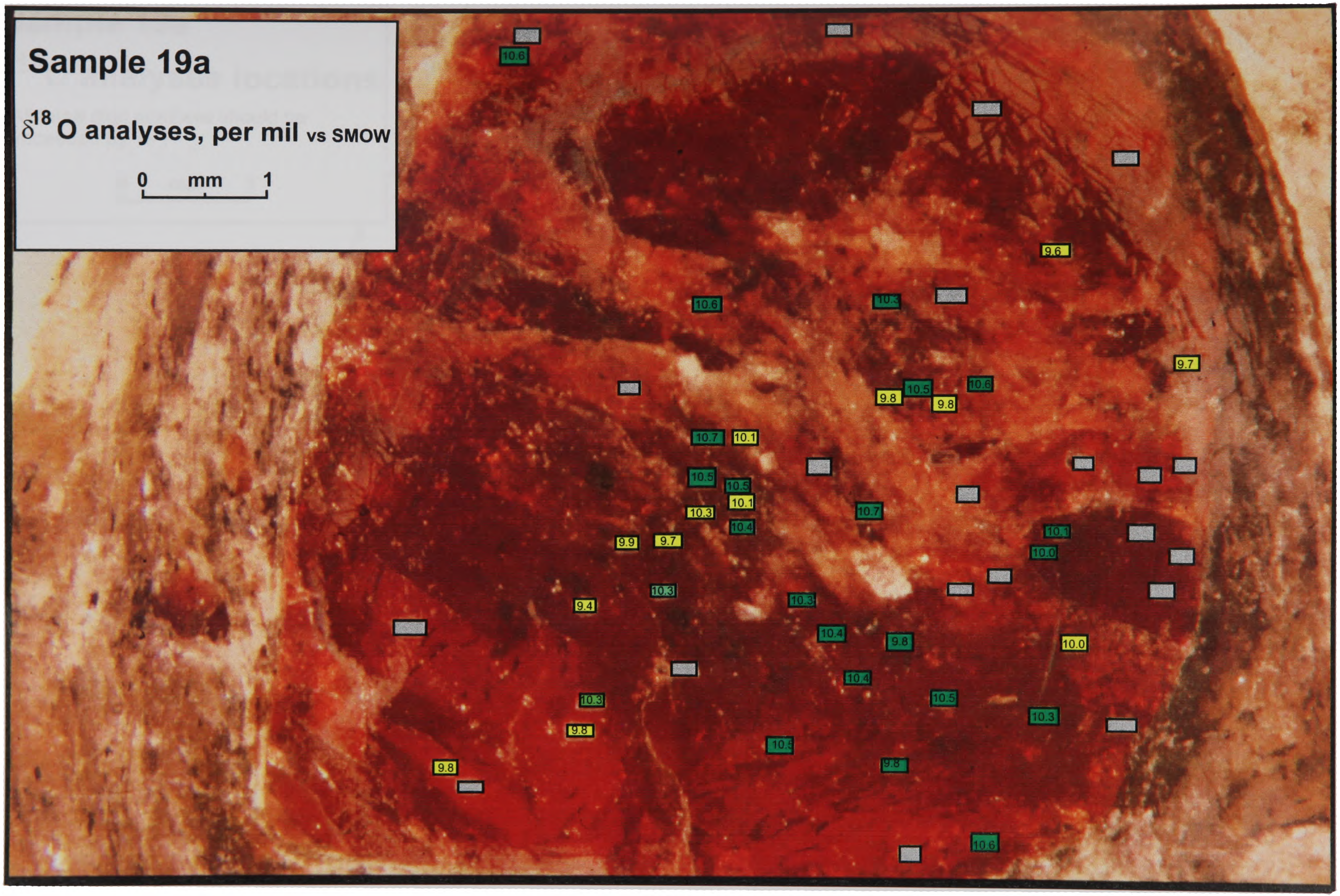


Figure 7.7: $\delta^{18}O$ analyses from sample 19a. The green analyses represent 'early' values, and the yellow 'later' values - see text. Grey represents a discounted analysis.

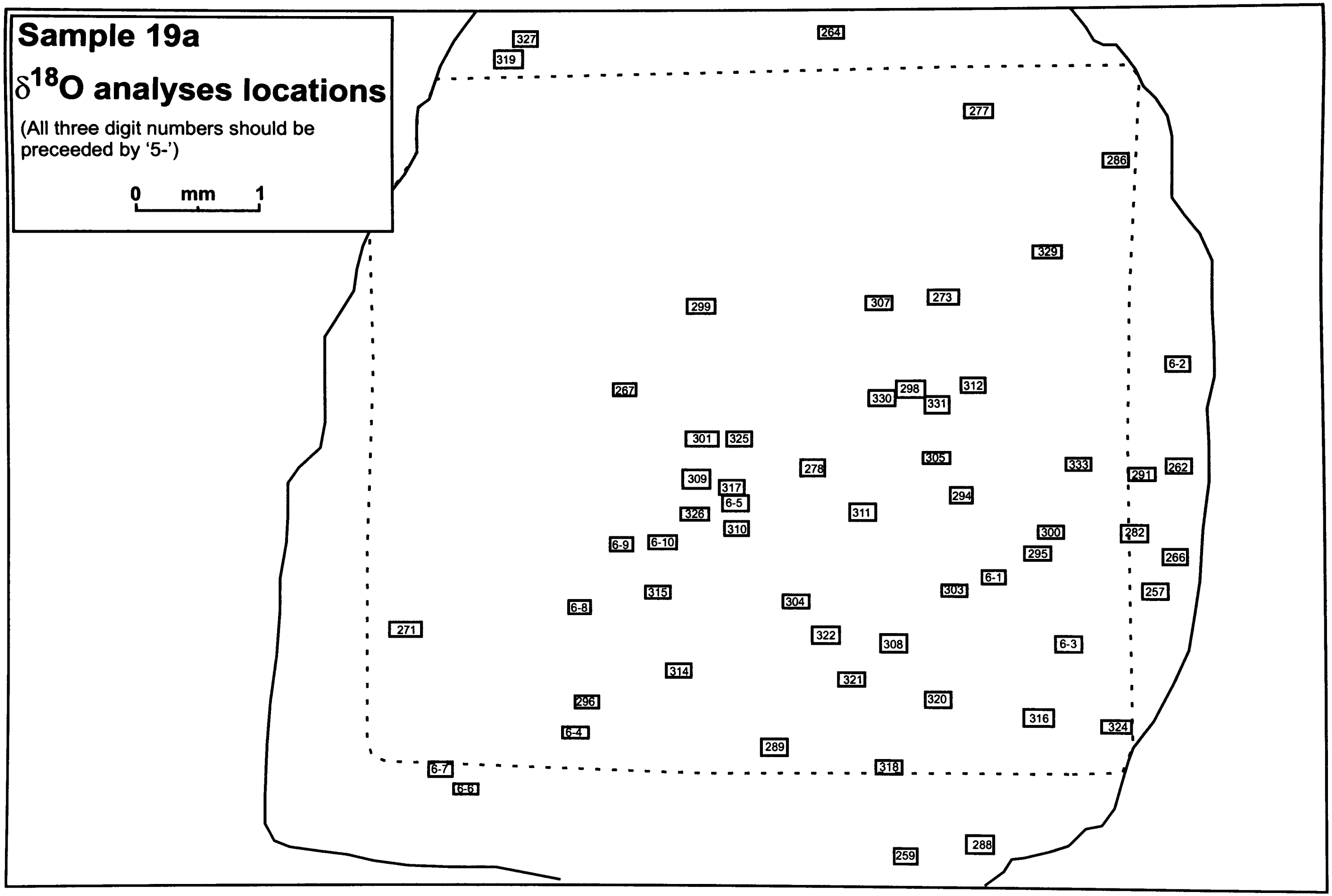


Figure 7.8: Locations of laser analyses in sample 19a. Dotted line shows approximate position of textural break.

In order to understand collected data in the light of this observed isotopic shift, the dataset has been divided into 'early' and 'late' results, *i.e.* those results recorded before and after an arbitrary point chosen when the shift was first considered to be observed (although this effect is most probably a gradual shift with time). If the results are plotted on a normalized core-rim diagram (figure 7.11), then this isotope shift is more obvious; a third-order polynomial curve has been fitted to each dataset as a guide. Table 7.3 summarizes corrected $\delta^{18}O$ for sample 19a.

'Early'		**'Late'**	
analysis no.	Corrected $\delta^{18}O$ ‰ SMOW	analysis no.	Corrected $\delta^{18}O$ ‰ SMOW
5-288	10.6	5-325	10.1
5-289	10.5	5-326	10.3
5-291	10.0	5-329	9.6
5-295	10.0	5-330	9.8
5-296	10.3	5-331	9.8
5-298	10.5	6-2	9.7
5-299	10.6	6-3	10.0
5-300	10.1	6-4	9.8
5-301	10.7	6-5	10.1
5-304	10.3	6-7	9.8
5-307	10.3	6-8	9.4
5-308	9.8	6-9	9.9
5-309	10.5	6-10	9.7
5-310	10.4		
5-311	10.7		
5-312	10.6		
5-315	10.3		
5-316	10.3		
5-317	10.5		
5-318	9.8		
5-319	10.6		
5-320	10.5		
5-322	10.4		

Table 7.3: Summary of both 'early' and 'late' corrected $\delta^{18}O$ analyses from garnet sample 19a.

7.4.1 Sample 19a - discussion

Taking the earlier curve as being the more accurate of the two (these results are assumed to be unaffected by the drift) both core and rim have values of 10.5-10.7‰ , dropping to

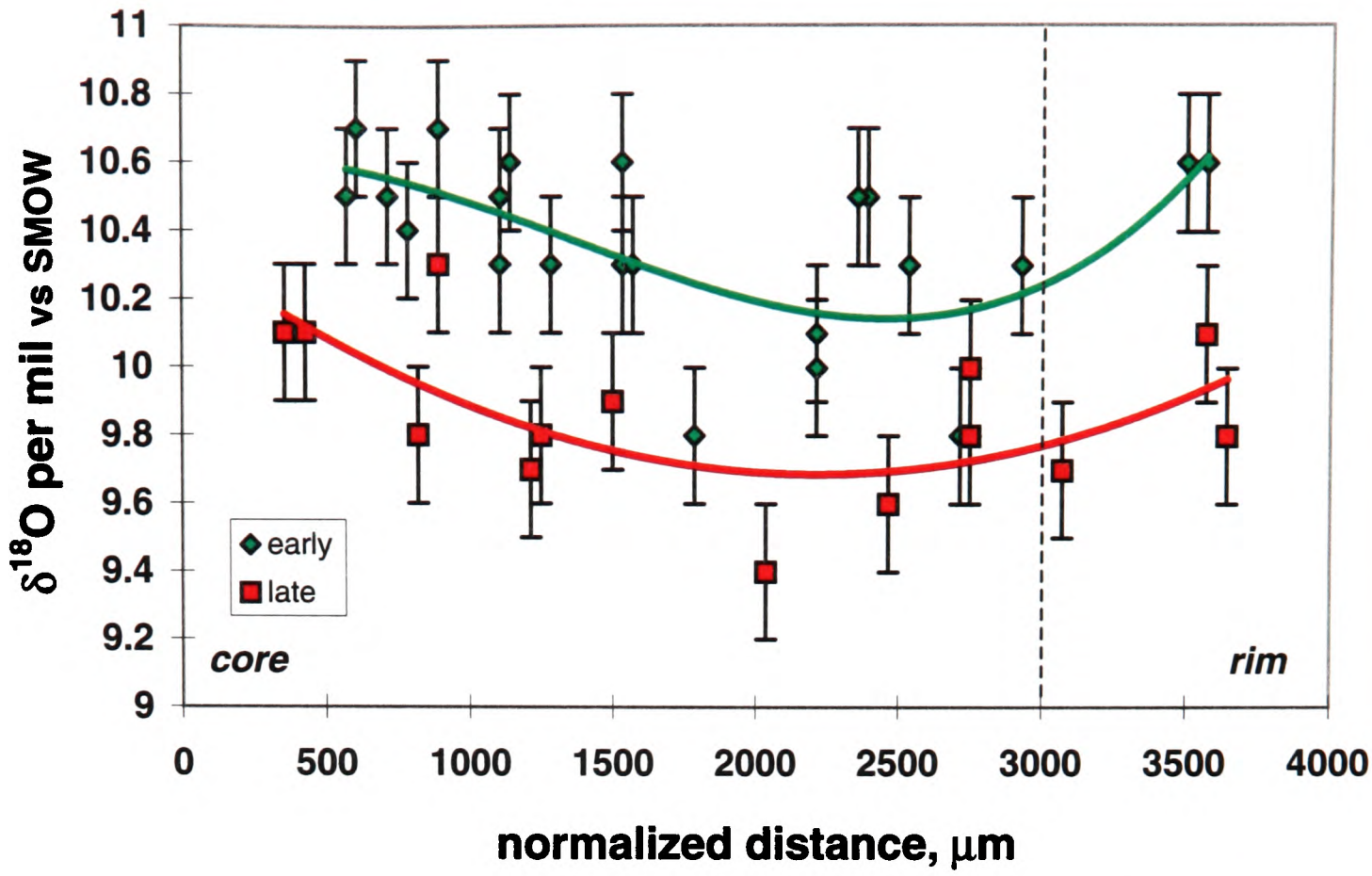


Figure 7.11: Garnet core-rim normalized diagram from sample 19a, showing the 'early' and 'late' (post-shift) datasets; a 3rd order polynomial has been plotted for each set. Error bars are ±0.2‰ (1σ). Dotted line shows unconformity.

9.8-10.2‰ some 2.0 - 3.5mm from the core. Figures 7.12 and 7.13 show the four major cation core-rim profiles. Manganese in particular shows apparently uninterrupted garnet growth, with a X_{Sps} decrease steadily from core to rim. Calcium also decreases, while Mg and Fe show an increase, *i.e.* normal garnet growth patterns.

Figure 7.14 shows an electron microprobe map of X_{Mg} in 19a. (X_{Mg} = Mg/Mg+Fe). This shows a distinct concentric dip in X_{Mg} between 200-400μm from the centre, which may correlate with the lower $\delta^{18}O$ region. Figure 7.15 shows electron microprobe maps of the four major cations.

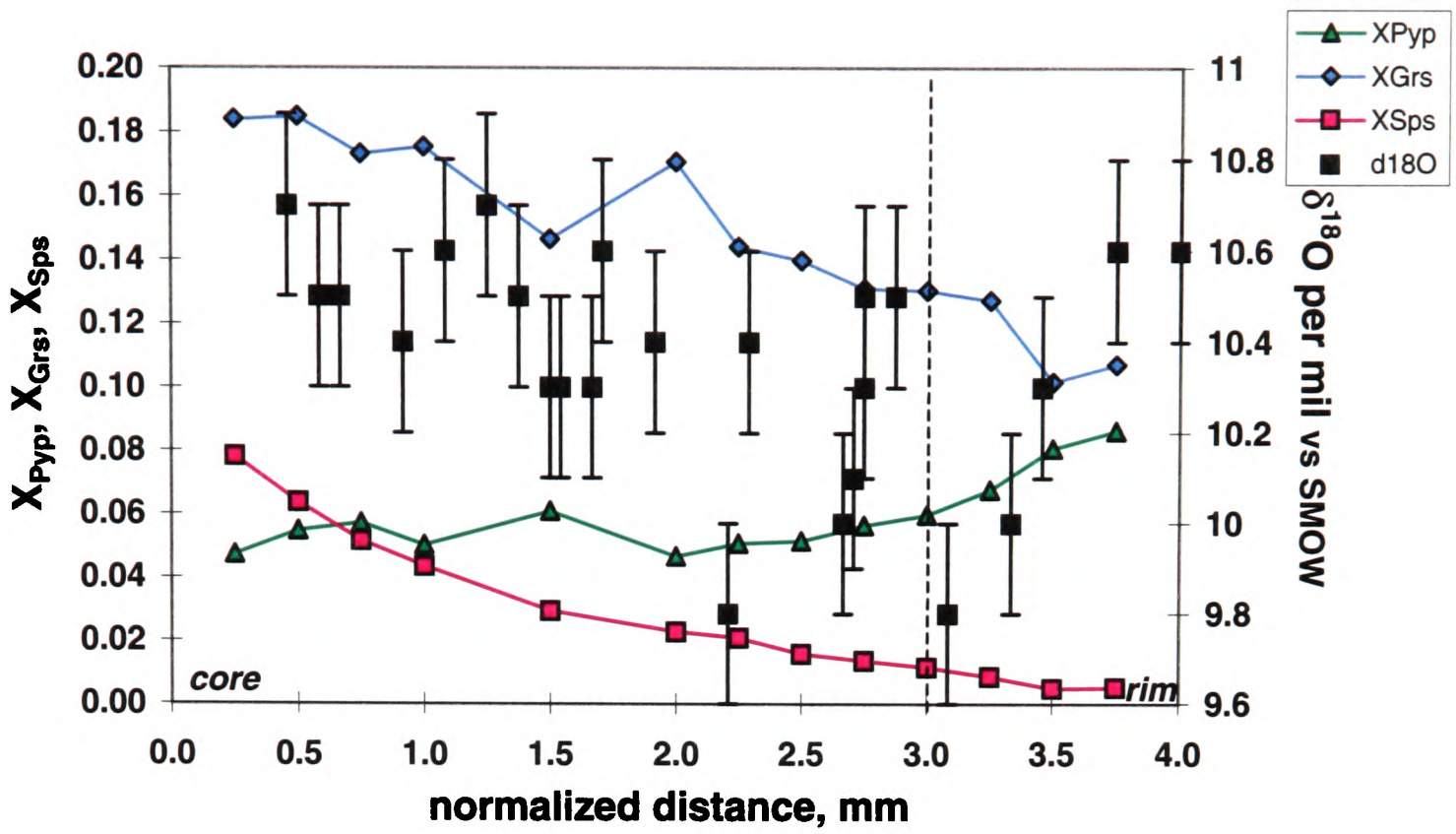


Figure 7.12: Sample 19: core-rim Mg, Ca and Mn profiles (X_{Pyp}, X_{Grs} and X_{Sps} respectively), plotted alongside $\delta^{18}O$.

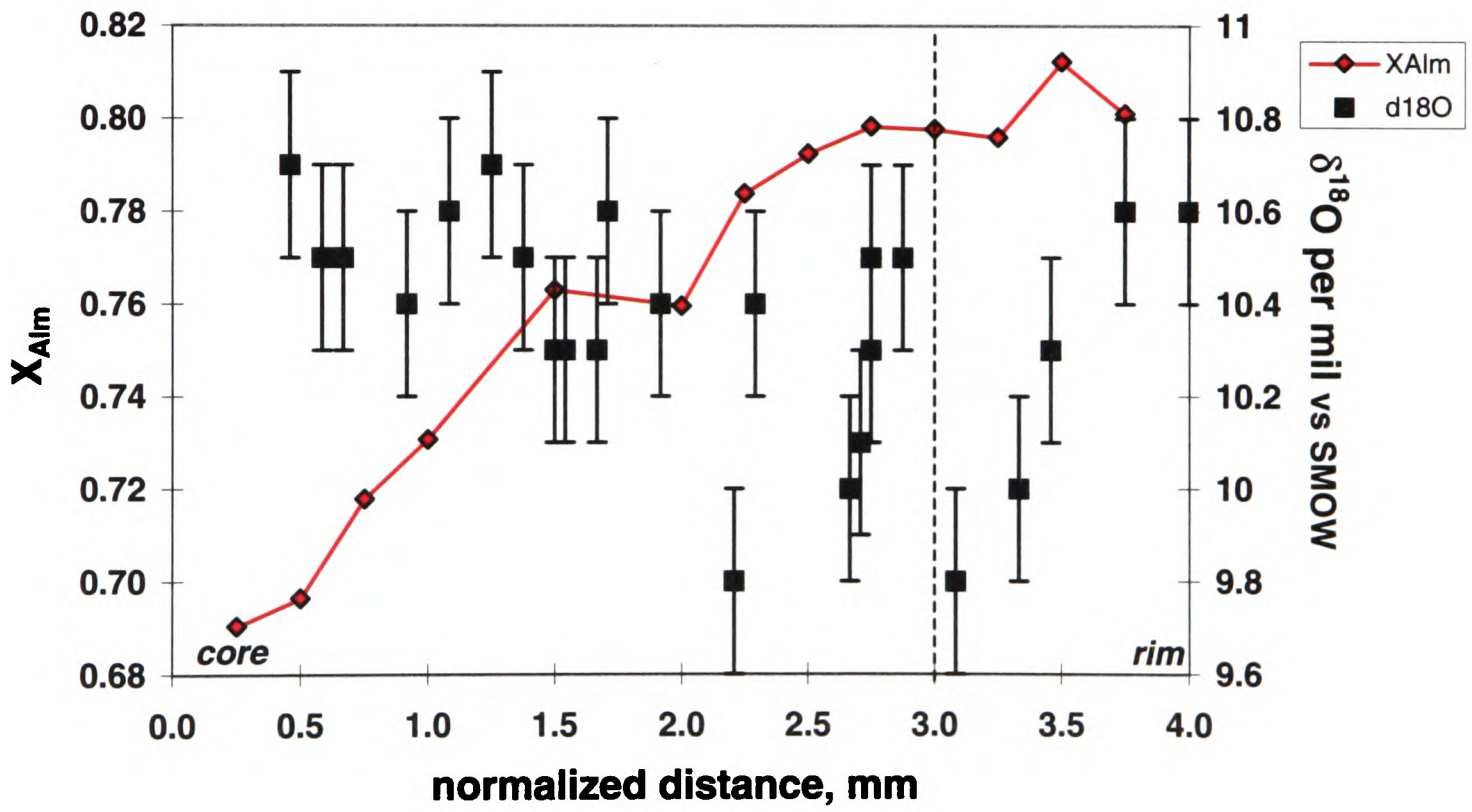


Figure 7.13: Sample 19: core-rim Fe profile (X_{Alm}), plotted alongside $\delta^{18}O$.

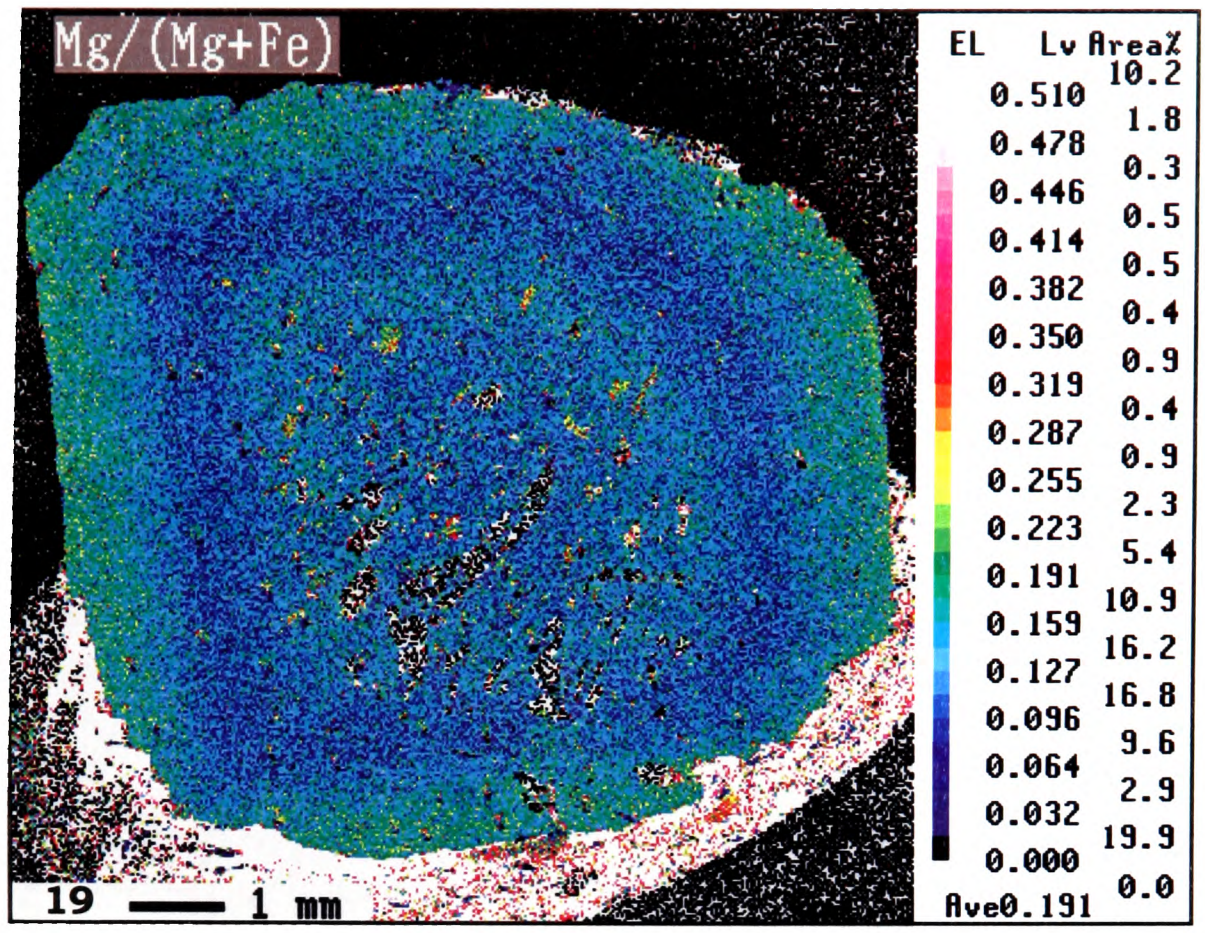


Figure 7.14: Electron microprobe map showing X_{Mg} in sample 19a; X_{Mg} = Mg/(Mg+Fe).

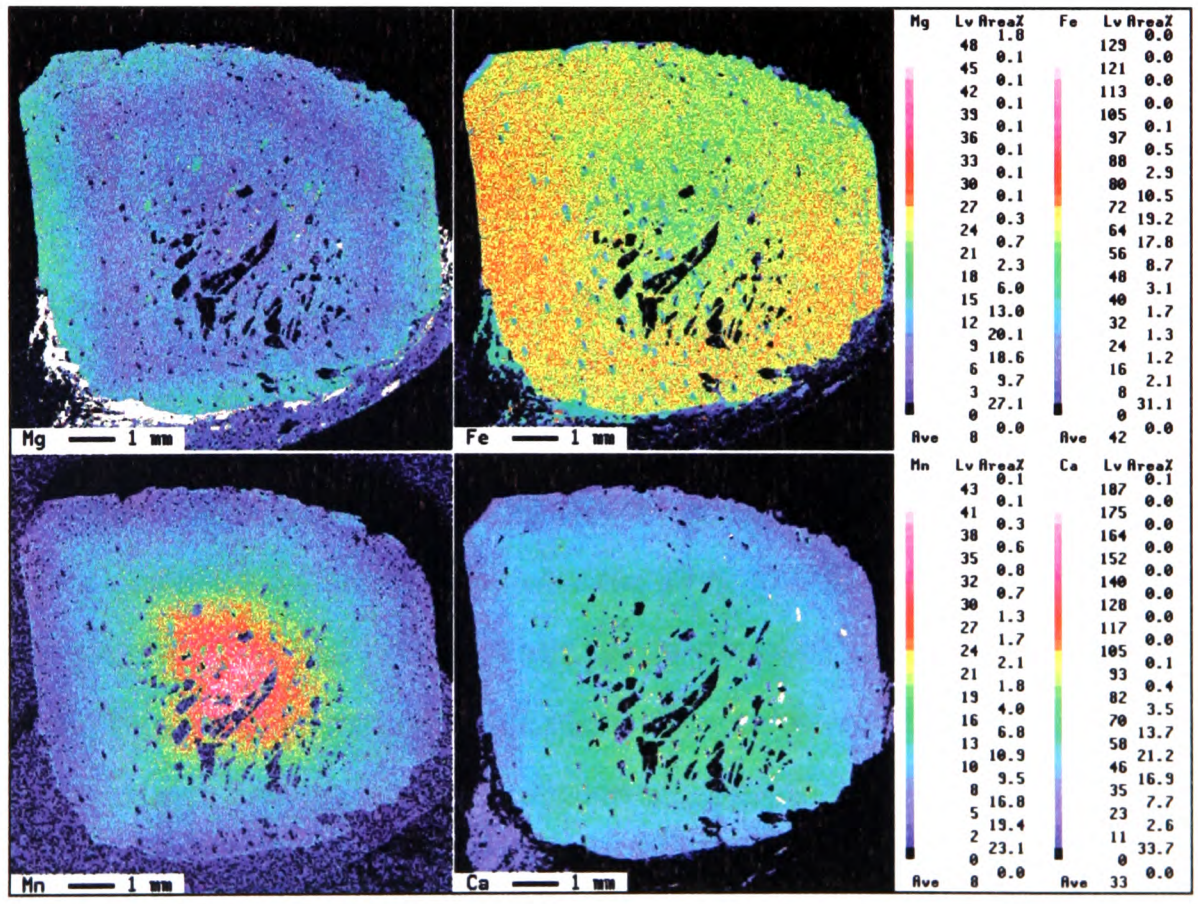


Figure 7.15: Electron microprobe maps showing cation distributions in sample 19a.

7.5 Sample R76

R76 is from the upper staurolite zone, and electron microprobe maps (figure 7.16) show the garnet has striking Mn zonation, and a distinct rim. Inspection proved the rim is relatively inclusion-free compared to the core, which is riddled with chloritoid and quartz inclusions. Additionally, this rim break also coincides with the change in Ti-bearing inclusion phase from rutile (core) to ilmenite (rim).

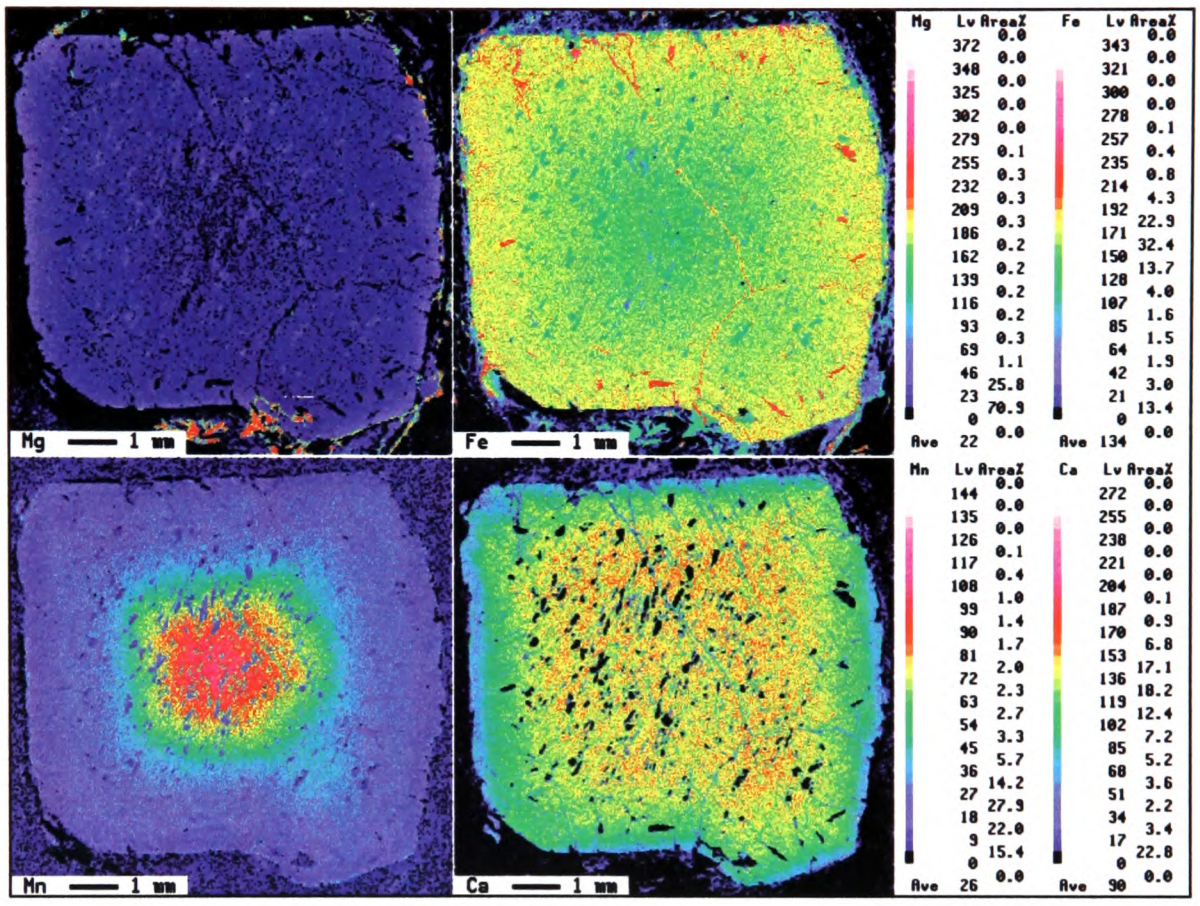


Figure 7.16: Electron microprobe maps showing cation distributions in sample R76.

In order to reduce both surface area and remove potential contamination from the surrounding mica (after experience with sample 19a), the garnet was chipped from the matrix and quartered. Additionally, a sample of the matrix containing abundant staurolite was removed and separately analysed. The location of the chipped samples of garnet and staurolite-bearing matrix is shown in figure 7.17.

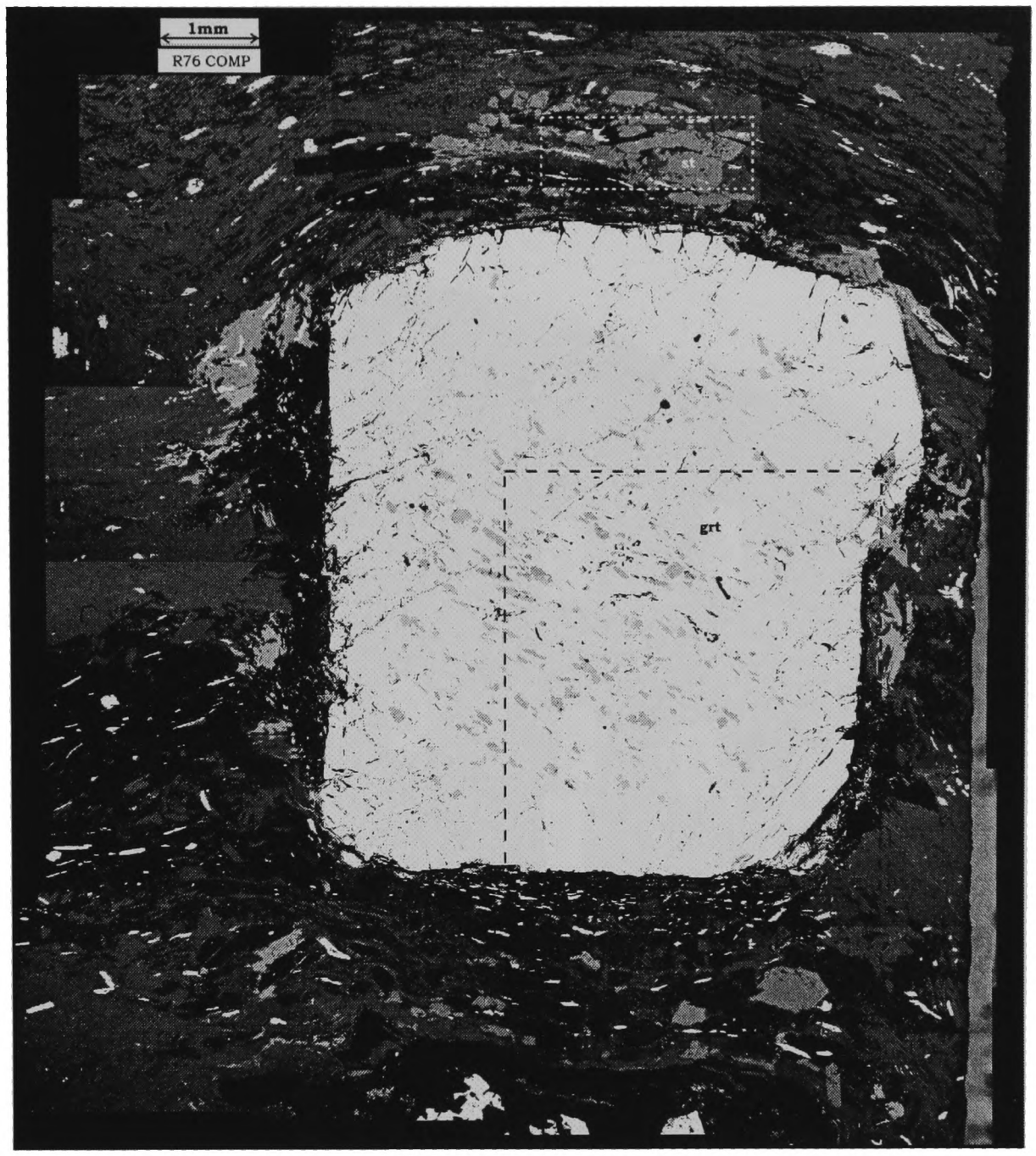


Figure 7.17: Backscattered electron image of R76 showing the location of garnet and staurolite samples taken for analysis, shown by dotted lines. Scale bar is 1mm long. Core inclusion patterns can be clearly observed.

7.5.1 Sample R76 - results

Figure 7.18 summarizes garnet isotope results, whilst figure 7.19 shows the analytical localities. A summary of the corrected data is detailed in table 7.4.

A normalized core-rim profile is shown in figure 7.20. Garnet $\delta^{18}O$ results show both core and rim have consistent $\delta^{18}O$ of approximately 11.0‰ . However, the pattern of $\delta^{18}O$ in the outer part of the core, *i.e.* before the textural break, gave anomalous results, with some areas consistently yielding lighter (10.6 - 10.7‰), whilst others consistently giving 11.0‰ (seemingly unchanged from either core or rim values).

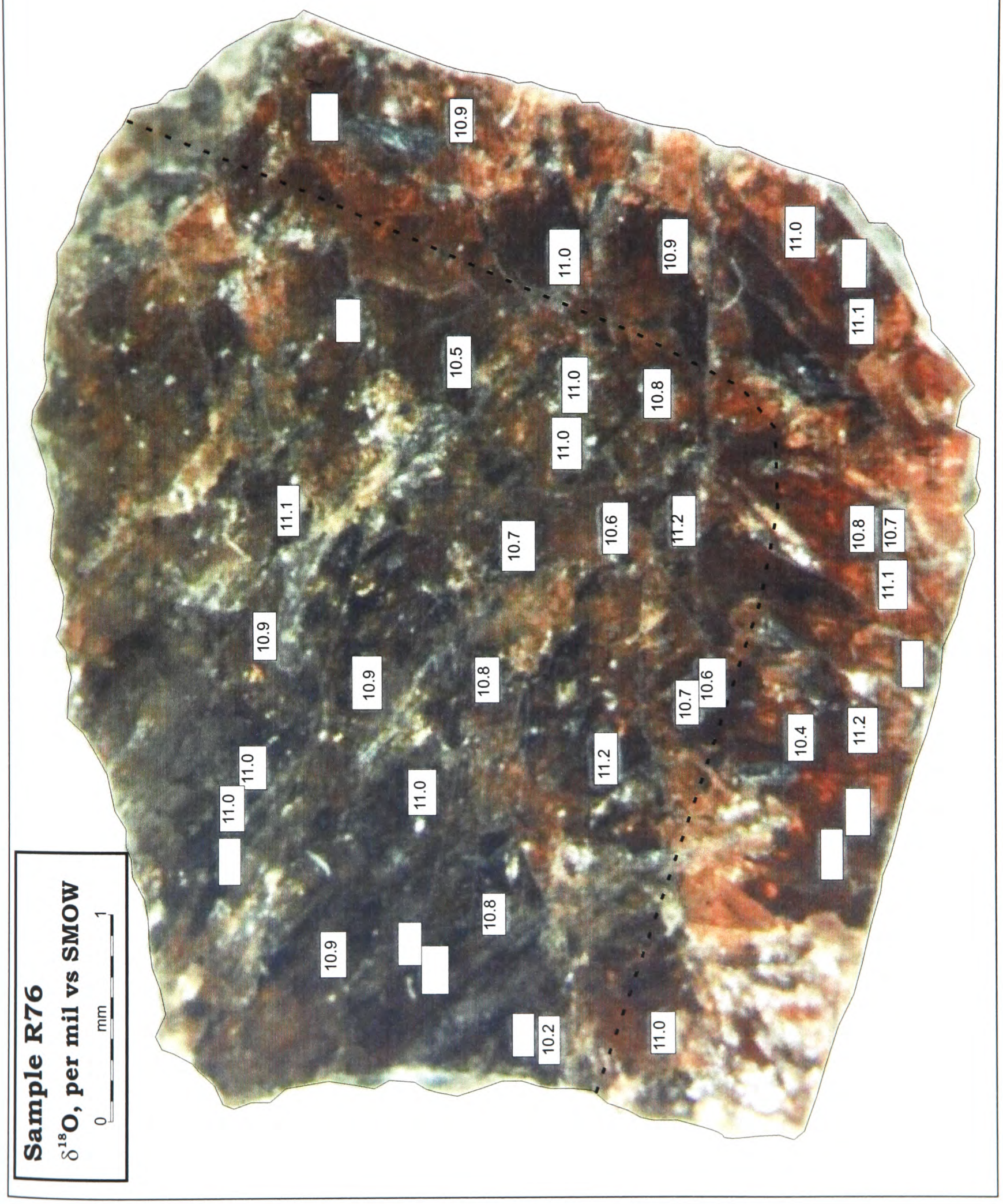


Figure 7.16: $\delta^{18}O$ results from sample R76.

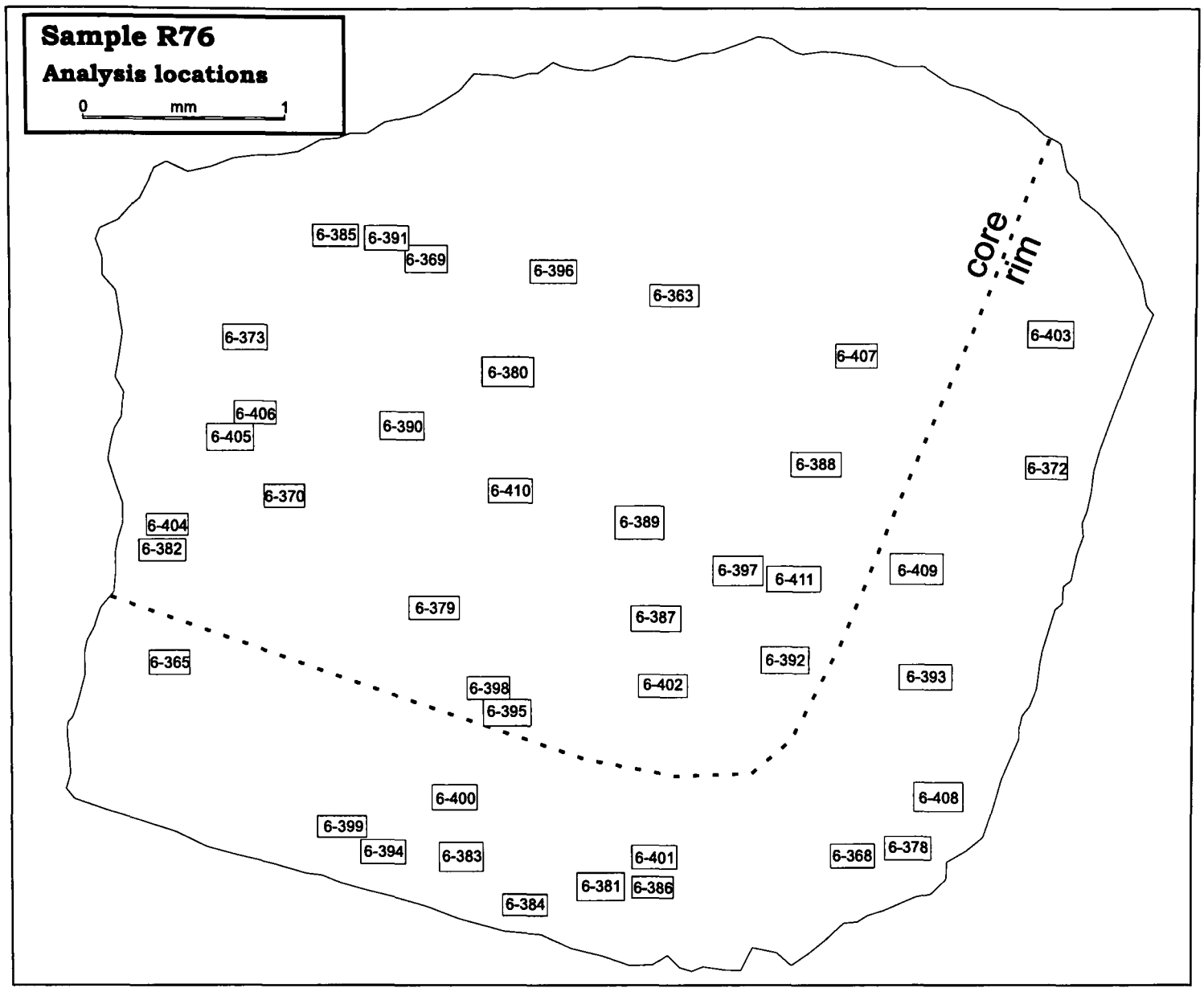


Figure 7.19: Analytical localities in sample R76 garnet; core is top left, rim is bottom and right.

Additionally, the five staurolite analyses gave a mean $\delta^{18}O$ of 10.5‰ , and one white mica analysis yielded 10.4‰ .

7.5.2 Sample R76 - discussion

Figures 7.21 and 7.22 show major cation core-rim profiles. Again, this is evidence for a normal zoning pattern. Data from R76 garnet show a core and rim with consistent (and more or less identical) analyses, in the region of $\delta^{18}O$ =10.8 - 11.0‰ ; however they also show a variable outer core region, exhibiting results ranging from 10.2 - 11.2‰ . Within this region, some areas appear to be consistently heavier (11‰) than others. There is no definite isotope shift across the textural unconformity.

Analysis no.	Corrected δ^{18}O ‰ SMOW	Analysis no.	Correctedδ^{18}O ‰ SMOW
6-363	11.1	6-390	11.0
6-365	11.0	6-391	11.0
6-368	11.1	6-392	10.8
6-369	11.0	6-393	10.9
6-370	10.8	6-395	10.6
6-372	10.9	6-396	10.9
6-373	10.9	6-397	11.0
6-379	11.2	6-398	10.7
6-380	10.9	6-400	10.4
6-381	11.1	6-401	10.8
6-382	10.2	6-402	11.2
6-383	11.2	6-408	11.0
6-386	10.7	6-409	11.0
6-387	10.6	6-410	10.8
6-388	10.5	6-411	11.0
6-389	10.7		

Table 7.4: Summary of corrected δ^{18}O analyses from sample R76 garnet (δ^{18}O vs SMOW).

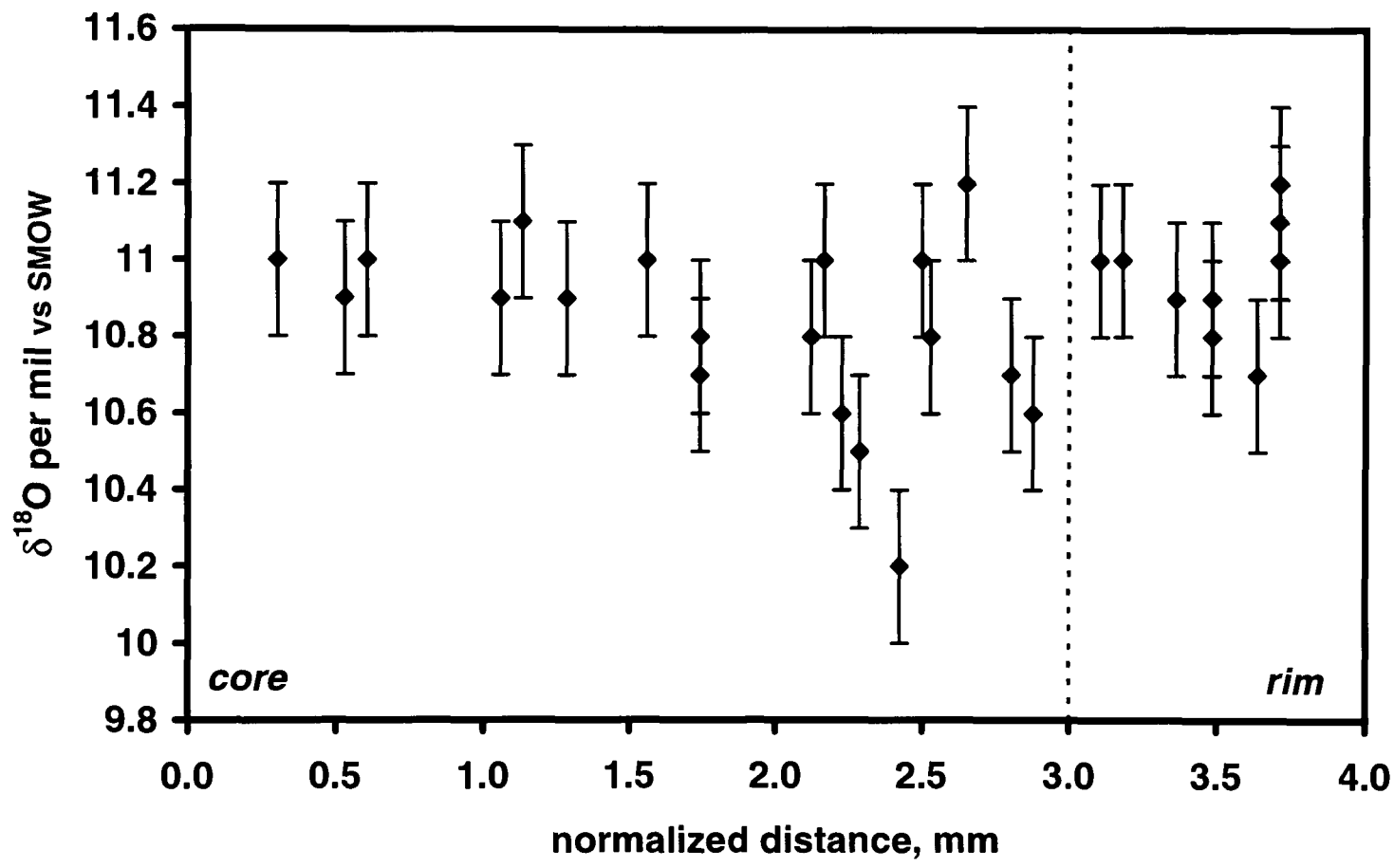


Figure 7.20: Normalized core-rim profile of garnet R76. The dotted line represents the textural break and the transition from rutile to ilmenite as the Ti-bearing inclusion phase. Error bars are ±0.2‰ (1σ).

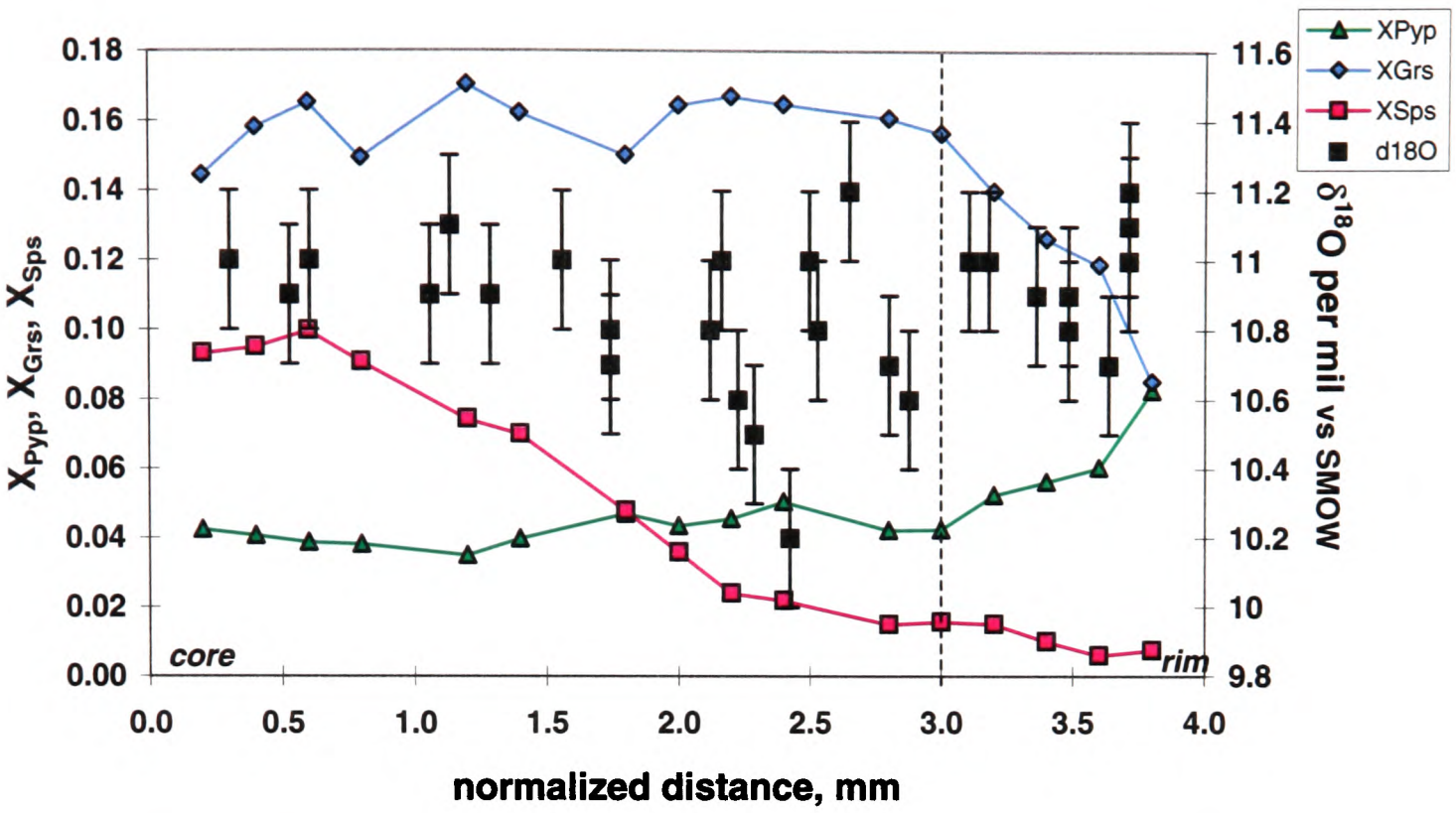


Figure 7.21: Sample R76: core-rim Mg, Ca and Mn profiles (X_{Pyp}, X_{Grs} and X_{Sps} respectively), plotted alongside $\delta^{18}O$.

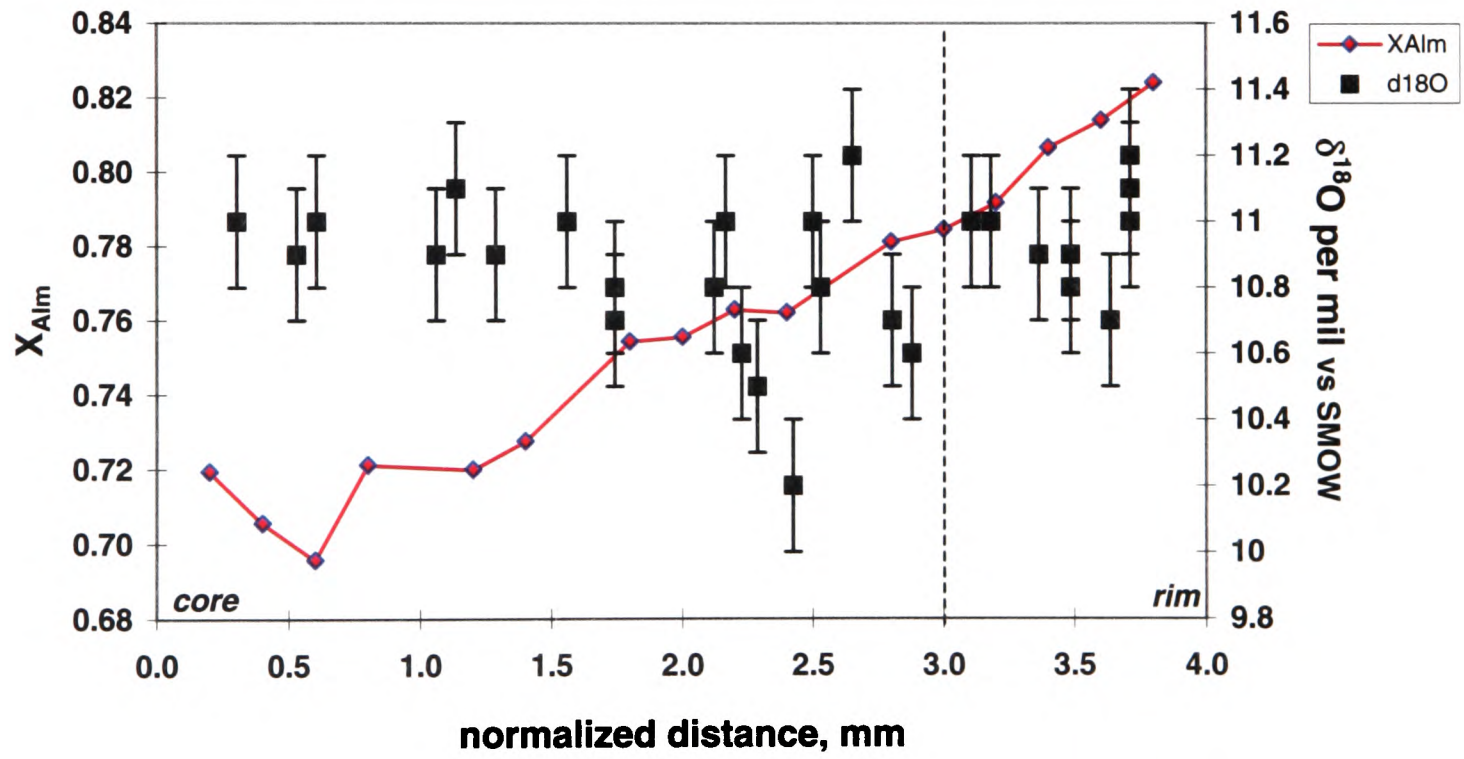


Figure 7.22: Sample R76: core-rim Fe (X_{Alm}) profile, plotted alongside $\delta^{18}O$.

Mineral	Analysis no.	Corrected δ^{18}O ‰ SMOW
Staurolite	6-421†	10.5
	6-423	10.5
	6-425	10.7
	6-426	10.3
	6-428	10.6
Mean St		**10.5**
White mica	6-427	10.4

Table 7.5: Corrected staurolite and white mica analysis from sample R76.

7.6 Conclusions

UV ablation GC-*irms* oxygen isotope analysis of garnets and other metamorphic minerals from pelitic schists is possible, but difficult. Presented here are three profiles gained from three different grade samples from the same suite of rocks. Only one, sample 6a, has a well-defined isotope zoning profile; the other two are more obscured.

For sample 19a, taking the 'early' data, the garnet profile appears to show a zone of lighter δ^{18}O which may coincide with the growth of staurolite, and may also coincide with the dip in X_{Mg}.

Sample R76 shows a core and rim with consistent (and more or less identical) analyses, however it also shows a variable outer core region, where some areas appear to be consistently heavier (11‰) than others.

Chapter 8

Metamorphic modelling

Reconstruction of conditions of metamorphism is a fundamental goal of any metamorphic study. Modelling of both peak and pre-peak conditions allows calculation of evolving prograde phase equilibria. This chapter deals with deploying an approach to calculate phase relations and calculate prograde reaction histories for the Hoosac garnets.

Modelling pre-peak metamorphic conditions requires the use of equilibrium thermodynamics to calculate P-T-X-M conditions, where P, T and X are the *intensive* variables pressure, temperature and composition respectively, and M is the *extensive* variable mode or moles of phases present. Here, a technique is introduced and applied to the Hoosac rocks to determine starting and finishing conditions of garnet growth. This provides a P-T-X-M framework within which an attempt to use a differential thermodynamic approach augmented with oxygen isotope mass-balance equations is made. This allows modelling of oxygen isotope fractionation with reaction progress, and thus an attempt is made to predict oxygen isotope zonation within the Hoosac garnets.

8.1 Why rock modelling?

Information about the prograde P-T history of metamorphic rocks is essential in order to understand reaction history. There are three approaches that can be taken:

1. The coupled use of conventional thermometry and barometry with microstructural information has proved useful for estimating peak metamorphic temperatures and pressures. In addition, the use of inclusion suites in zoned minerals such as garnets has been used to predict pre-peak metamorphic conditions and thus P-T paths (*e.g.* St-Onge, 1987). However, the Hoosac Schist does not possess ideal minerals for thermobarometric calculations. Biotite comes in late, and thus for much of the prograde history the useful garnet-biotite exchange thermometer cannot be employed. Additionally, the high alumina content prevents early appearance of primary plagioclase, thus eliminating the range of useful feldspar-based barometers.

2. The Gibbs method (Spear *et al.*, 1982; Spear & Selverstone, 1983; Spear, 1988) has been used for studying garnet growth from garnet cation zoning. Zoned minerals, such as garnet, maintain disequilibrium between the cores of the mineral and the matrix. Given a set of thermodynamic data for all phases of interest, the Gibbs method allows calculation of P-T-X-M relations for measured garnet compositions from the core to the rim, with the proviso that the reacting garnet rim maintained equilibrium with the matrix phases. The Gibbs method also allows for modelling bulk composition fractionation. Growth of refractory minerals such as garnet 'lock-up' system components as they grow, thus fractionating the effective bulk composition.

3. The third approach is the construction of phase diagrams by calculating equilibrium conditions at each P-T point of interest. This allows equilibrium phase relations to be predicted, and with the addition of bulk composition data, allows phase assemblage and compositions to be modelled. A potential drawback with this approach is the inability to model a fractionating system easily, since absolute conditions are determined at each point in P and T.

8.1.1 Some basic principles - the Gibbs phase rule and Duhem's Theorem

A chemical system such as an evolving metamorphic rock consists of phases, which in turn are made up of phase components and system components. Phases are chemically homogeneous substances, such as water and minerals. Phase components are the chemical species necessary to describe the chemical variability of a phase, and system components are the chemical species necessary to describe the chemical variability of the system as a whole. For example, garnet is a phase; grossular, pyrope, almandine and spessartine are the phase components of aluminosilicate garnet (*i.e.* garnet solid solution as distinct from garnet phase); and FeO, MgO, CaO, MnO, Al_2O_3 and SiO_2 are the system components necessary to describe garnet within a system (although in a given system it is the smallest number of system components needed to define the compositions of all the phases that is significant).

The following thermodynamic treatment is adapted from Spear (1993), chapter 8. For a system, the thermodynamic variables are pressure (P), temperature (T) and composition (X, mole fraction) for each phase component of each phase in the assemblage. If npc^k is the number of phase components in each phase k and there are nph total phases in the system, there are $npct$ phase components in the system, defined as:

$$npct = \sum_{k=1}^{nph} npc^k \tag{8.1}$$

The total number of variables in the system is thus $npct$ + 2, with the inclusion of P and T. The number of linearly independent reactions that can be written among a set of phase components in an assemblage can be thought of as: *number of independent reactions = total number of phase components - number of system components*, or:

$$nrx = npct - nsc \tag{8.2}$$

Each of these nrx reactions acts as a constraint on the phase equilibria of a heterogeneous system. Furthermore, there is a stoichiometric constraint for each phase k, because the mole fractions of the phase components j in each phase are not all independent:

$$1 = \sum_{j=1}^{npc} X_j \tag{8.3}$$

There is one equation of this form for each phase in the assemblage, leading to the total number of constraints of:

$$nrx + nph = npct - nsc + nph \tag{8.4}$$

The number of degrees of freedom in the system is calculated as the difference between the number of variables and the number of constraints:

$$\text{variance} = npct + 2 - (npct - nsc + nph) = nsc + 2 - nph \tag{8.5}$$

This is known as the *Gibbs phase rule* and is also written as P + F = C + 2, where P = nph, C = nsc and F is the variance, or number of degrees of freedom.

The phase rule only applies to *intensive variables* T, P and X_j, or alternatively T, P and μ_j, where μ_j is the chemical potential of phase component j. However, in metamorphic studies the bulk composition of the rock plays a vital role when considering the stability of phases. Bulk composition is an *extensive variable*, in that it depends on the amount of matter in the system. In order to incorporate bulk composition data into the analysis of phase equilibria, mass balance equations need to be incorporated. The new variables in the system are M^k, the moles of phase k in the rock of which there are nph (one for each phase), and η_i, the moles of system component i in the rock, of which there are nsc (one for each phase component). There are now nsc new equations with nph unknowns (the η_i's are known if bulk composition is fixed), and the variance can be calculated by adding the variables and subtracting the constraints:

$$\begin{aligned} \textbf{variance} &= \textbf{2 + npct + nph - (nrx + nph + nsc)} \\ &= \textbf{2 + npct + nph - (npct - nsc + nph + nsc)} \\ &= \textbf{2} \end{aligned}$$

This states the number of degrees of freedom for a system for which the bulk composition is fixed is 2, which is *Duhem's Theorem*. Therefore, **specification of any two independent variables completely determines the state of the system including the composition of all minerals and their modal abundance**. This is used in phase diagram modelling with compositional information, and is crucial when considering large chemical systems with many variables.

8.1.2 Integral versus differential thermodynamics

There are two main approaches in the calculation of mineral equilibria involving solid solutions. An *integrated* thermodynamic approach involves the solution of simultaneous non-linear equations at each point of interest (Powell & Holland, 1990; Powell *et al.*, 1998), as described by the following equation:

$$\Delta G = 0 = \Delta H^{\circ} - T\Delta S^{\circ} + \int \Delta V \mathrm{d}P + RT\ln K_{eq} \tag{8.6}$$

The integrated approach calculates *absolute* values of P, T, X and M, and is therefore best used to predict equilibrium phase relations of rocks - with the requirement of both an internally-consistent thermodynamic dataset and activity-composition (a-X) models for all non-pure phases.

On the other hand, a *differential* approach takes a starting position and evolves away from it (Spear *et al.*, 1982; Spear, 1988; Spear & Cheney, 1989). The differential approach can be described by the following equation:

$$\Delta G = 0 = (-\Delta S + RT\ln K_{eq})\mathrm{d}T + \Delta V \mathrm{d}P \tag{8.7}$$

The differential approach will calculate *changes* in P, T, X and M, and is best used to predict the evolution of a mineral species, such as tracking the growth of a garnet in changing P-T conditions, and predicting zonation. In addition, enthalpy (H) is no longer involved in the calculation, thus removing the variable with the largest uncertainties.

An important point to make is the assumption of equilibrium when using a thermodynamic approach. Conventional thermodynamics takes no account of kinetic factors, assuming all reactions occur instantaneously, completely, and with no overstepping. However, real rocks tend to be in various stages of disequilibrium - as evidenced by the very existence of zoned minerals.

8.1.3 Self-consistent thermodynamic dataset

Thermodynamic theory is not practice without the addition of a set of thermodynamic data. Thermodynamics provides a fundamental tool for quantifying phase relationships, and the only limitation on the accuracy of calculated phase equilibria is that im-

posed by our knowledge of the thermodynamic parameters describing the state functions of each phase, component, or species.

A self-consistent thermodynamic dataset is one which relates thermodynamic properties - enthalpy, entropy, molar volumes, heat capacity, thermal expansion - between a set of phases within the system of interest. Efforts have been to compile cohesive thermodynamic databases that are internally consistent. This kind of dataset is achieved by extracting information from calometric and phase equilibria experiments and natural mineral partitioning, and then using a least-squares approach to calculate enthalpies of formation, which allows the simultaneous generation of all thermodynamic data for the system considered (Powell & Holland, 1985).

The two most commonly used datasets are those compiled by T.J.B. Holland and R. Powell (Powell & Holland, 1985; Holland & Powell, 1985; Powell & Holland, 1988; Holland & Powell, 1990, 1998), and that devised by R. Berman (Berman, 1988).

8.1.4 Phase diagram calculation using THERMOCALC

THERMOCALC is a program written to use the integrated thermodynamic approach to model phase relations using the dataset of Holland & Powell (1998). It calculates mineral equilibria using an input datafile that describes activity relations for multi component phases. Activity-composition (a-X) relationship models are detailed in Holland & Powell (1998).

THERMOCALC calculates phase diagrams by simultaneously solving sets of non-linear equations. These equations, for the purpose of calculating P-T projections, are calculated and solved for each equilibrium point at the P and T of interest, and are the equilibrium relationships for an independent set of reactions between the end-members of the phases in equilibrium. The user supplies values for the number of variables, and the variance, and the program solves for the remainder. This is the method described by Powell *et al.* (1998).

Phase diagram calculation for an individual rock of specified bulk composition is called a *pseudosection* (Powell & Holland, 1990). Here, the addition of the extensive variables

allows Duhem's Theorem to be applied, such that the assemblage, phase composition and phase modes are uniquely defined at each P and T of interest (or, indeed, any two independent variables).

Phases referred to are abbreviated according to Kretz (1983), and detailed in table 8.1.

garnet	Grt	$(Fe,Mg,Mn,Ca)_3Al_2Si_3O_{12}$
chloritoid	Cld	$(Fe,Mg,Mn)Al_2SiO_5(OH)_2$
chlorite	Chl	$(Fe,Mg,Mn)_4(Fe,Mg,Mn,Al)_2Si_2(Si,Al)_2O_{10}(OH)_8$
muscovite	Ms	$(K,Ca,Na)(Fe,Mg,Al)_2Si_2(Si,Al)_2O_{10}(OH)_2$
paragonite	Pg	$(K,Ca,Na)Al_2Si_2(Si,Al)_2O_{10}(OH)_2$
margarite	Mrg	$(Ca,Na)Al_2Si_2(Si,Al)_2O_{10}(OH)_2$
biotite	Bt	$K(Fe,Mg,Mn)(Fe,Mg,Mn,Al)_2Si_2(Si,Al)_2O_{10}(OH)_2$
staurolite	St	$(Fe,Mg,Mn)_4Al_{18}Si_{7.5}O_{48}H_4$
kyanite	Ky	Al_2SiO_5
sillimanite	Sil	Al_2SiO_5
plagioclase	Pl	$(Ca,Na)Si_2(Al,Si)_2O_8$
quartz	Qtz	SiO_2
rutile	Rt	TiO_2
ilmenite	Ilm	$FeTiO_3$

Table 8.1: Mineral abbreviations and formulæ, taken from Kretz (1983).

8.1.5 Aims of modelling

The chemical system should match the real rock as closely as possible. Too simple a system will not include important phases, and here the complex system Na_2O-CaO-MnO-K_2O-FeO-MgO-Al_2O_3-SiO_2-H_2O (NCMnKFMASH) is modelled. The system is expanded from KFMASH to include Mn with MnKFMASH, and finally into the full system with the addition of Na and Ca.

Previous studies have gradually increased in system complexity in the last ten years. Studies of phase relations in KFMASH resulted in the petrogenetic grids of Spear & Cheney (1989) and Powell & Holland (1990), the former using the thermodynamic dataset of Berman (1988), and the latter the dataset of Holland & Powell (1990).

The importance of Mn on extending the stability of garnet, despite usually being present in such small proportions, led to the inclusion of MnO into the various models. Symmes & Ferry (1992) investigated the incorporation of Mn into the NKFMASH system, and

studied the effect on garnet. Droop & Harte (1995) attempted to categorize the effect of MnO on KFMASH phase relations in Grt+St+Cld+Bt+Chl assemblages, and then to construct petrogenetic grids. Mahar *et al.* (1997) used THERMOCALC to investigate mineral stability in metapelites in the KMnFMASH system.

The incorporation of both Na and Ca is a vital step, not only for taking into account the effect of Ca on garnet stability, but also to be able to model plagioclase feldspar, and the white micas paragonite and margarite. Worley & Powell (1998) used the system NCKFMASH to model plagioclase phase relations. However, the full system NCMnKFMASH has been used to study garnet growth in the Gassetts Schist (Vance & Holland, 1993), and has been employed to infer P-T paths from pseudosection calculations from the Zanskar Himalaya, India (Vance & Mahar, 1998). More recently, Walker (1999) used NCMnKFMASH to calculate phase relations in the Zanskar Himalaya, using pseudosections to predict conditions of garnet growth. This is the approach used here. The Hoosac Schist is highly aluminous: here an attempt to correctly predict the sequence of mineral growth observed in petrological study is made.

The additional components TiO_2 and Fe_2O_3 are not treated here. Most Ti is present in accessory minerals - either rutile or ilmenite, and thus is not included here for reasons of unnecessary complexity. Fe^{3+} is present in minor amounts in certain phases, however it cannot be distinguished from Fe^{2+} by conventional microprobe analysis.

This study uses THERMOCALC version 2.75 to build up to the construction of pseudosections for the three Hoosac samples selected for isotope study. Calculation of initial and final conditions of garnet growth is made. This allows determination of two points on the prograde path in P-T space. Comparison between predicted and observed peak conditions is made to monitor the accuracy of THERMOCALC prediction.

Both the incorporation of Mn and the extension into CNMnKFMASH required modification of the existing data scripts. This was accomplished by Walker (1999), and D. J. Waters (pers. comm.), and involved the incorporation of Mn, Ca and Na into the garnet, chlorite, biotite, staurolite and chloritoid mixing models where appropriate, as well as the addition of paragonite and plagioclase.

8.2 Bulk Rock data for pseudosection calculation

Bulk rock data are required for pseudosection calculation, and provide information regarding the available chemical species and their abundance. There are two principal means of obtaining this information: either through a direct bulk-rock chemical analysis (*e.g.* by X-Ray Fluorescence, XRF) or by coupled point-counting and mineral analysis.

The direct measurement approach gives a precise analysis of the material presented, however this may not necessarily be an accurate analysis for the purposes of modelling phase relations, as evidenced below.

8.2.1 Projection from paragonite

The majority of Hoosac samples contain paragonite rather than albite as the primary Na-bearing phase. This has to be taken into account when projecting with muscovite on an AFM or AKF diagram, calculating the Al coordinate as Al_2O_3-$3K_2O$-$3Na_2O$ instead of Al_2O-$3K_2O$-Na_2O for Ab + Ms projection.

Figure 8.1 shows sample R76 bulk rock composition, as measured by XRF analysis, projected from both Ab+Ms and Pg+Ms on a standard AKF diagram. AKF diagrams plot Al_2O_3 (minus K and Na) versus K_2O versus FeO+MgO+MnO. Since paragonite contains more Al than albite, the projected bulk rock composition is pushed *below* the Grt+Chl tie-line, thus predicting early formation of biotite rather than the more aluminous phases such as chloritoid and staurolite.

8.2.2 XRF analysis

Analysis of 19 samples of the Hoosac Schist was completed by X-Ray Fluorescence at the Open University, UK, and full results are given in appendix C. Figure 8.2 shows all results plotted on an AKF diagram, projected from muscovite and paragonite. Petrological examination of the Hoosac rocks shows that on the basis of garnet inclusions, early garnet-forming conditions were Grt+Chl+Cld not Grt+Chl+Bt, *i.e.* the bulk rock projected from muscovite must plot on the Al-rich side of the Grt+Chl tie-line on an

AFM diagram (plotting on the Al-rich side). On an AKF, this tie-line is represented by the line joining Ms+Chl. The XRF analyses plot on the Al-poor side of this, and therefore early formation of biotite and not chloritoid is predicted. However this is not observed in the petrology.

These observations conclude that XRF bulk-rock analysis of Hoosac rocks does not correctly predict the sequence of mineral formation observed, *i.e.* it is not aluminous enough. This is probably due to the scale of XRF sampling coupled with the heterogeneous nature of the Hoosac rocks. The actual rock matrix 'seen' by a growing garnet is very localized, and is probably more specific than the rock volume selected and homogenized for XRF analysis.

A more suitable way of bulk rock measurement is to calculate an effective bulk rock composition by using localized mineral modes and mineral analyses on a scale appropriate to a growing garnet, for example point counting a microprobe slide containing a garnet. Although modal estimation has an implicit low precision, and there is the question over the effect of minerals with variable or zoned compositions, nevertheless this approach produces a bulk composition that better reproduces the observed phase relationships.

8.2.3 Summary of bulk rock calculation

Modal analysis was performed on a number of slides from each sample of interest to estimate the volume percent of all the major phases. These volumes were then converted to moles and combined with mineral compositional data. Table 8.2 summarizes measured volume percent in Hoosac samples.

Sample	Ms	Pg	Grt	Bt	St	Ky	Chl
Molar vol	141	132	115	151	447	44	210
6	47.8	27.8	7.8	0.0	8.9	0.0	7.8
R76	47.2	27.0	9.0	2.2	7.9	2.2	4.5
19	48.8	26.2	9.5	3.6	4.8	4.8	2.4

Table 8.2: Volume percent modes for bulk rock calculation.

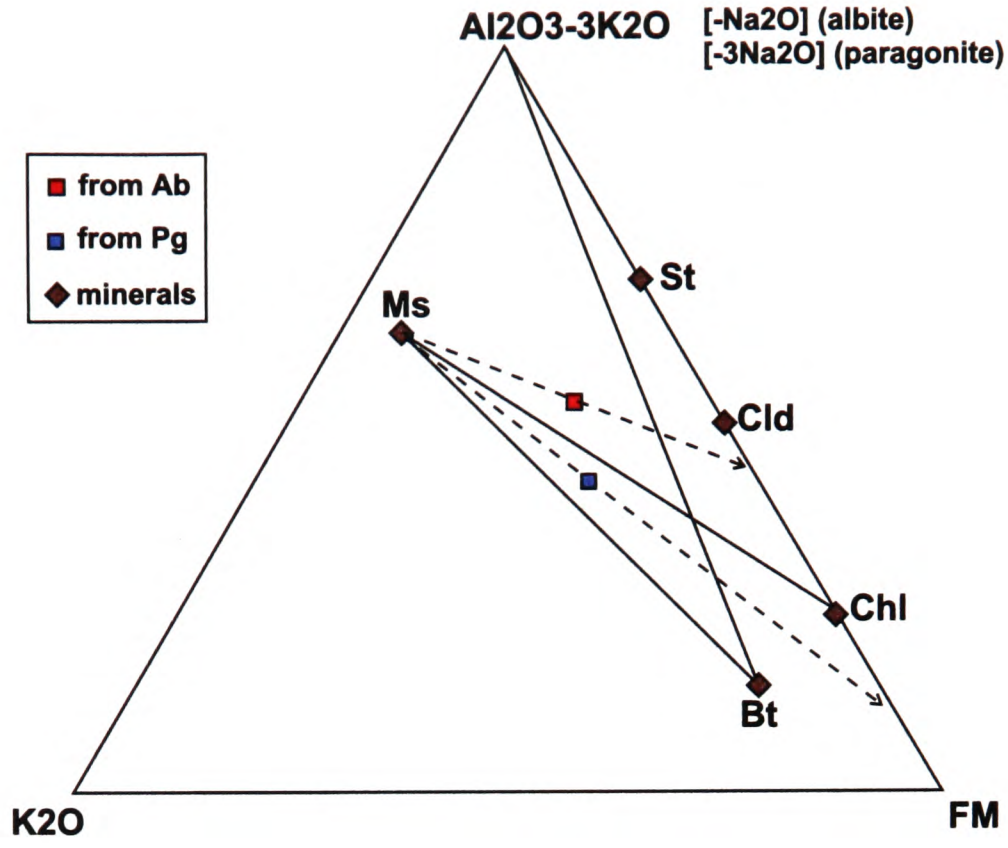


Figure 8.1: AKF diagram showing the effect of plotting R76 XRF bulk rock analysis from both albite and paragonite.

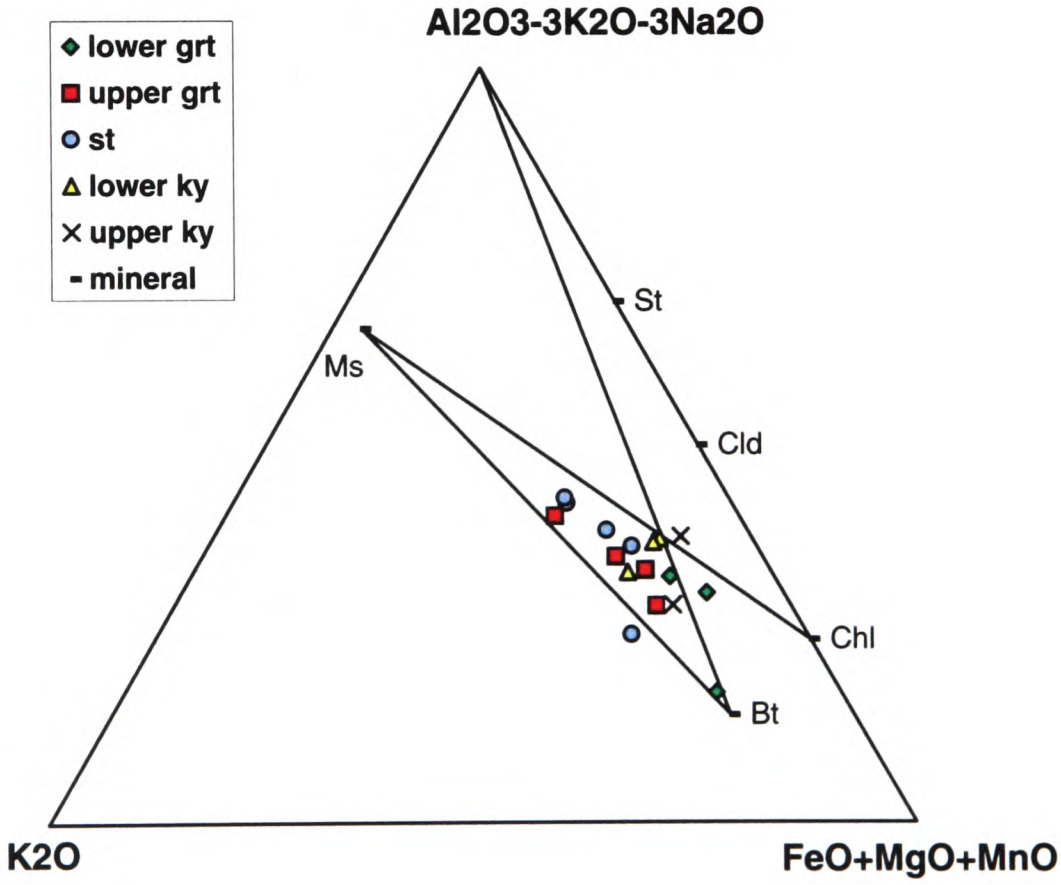


Figure 8.2: All XRF bulk rock analysis plotted on an AKF diagram projected from paragonite+muscovite. Schematic tie-lines are also shown.

For example, in the case of sample 6, with aluminium-bearing phases Ms+Pg+Grt+St+Chl the total bulk molar aluminium is calculated by:

$$(M^{Ms} \times cations^{Ms}_{Al}) + (M^{Pg} \times cations^{Pg}_{Al}) + (M^{Grt} \times cations^{Grt}_{Al}) + (M^{St} \times cations^{St}_{Al}) + (M^{Chl} \times cations^{Chl}_{Al})$$

This figure is then divided by 2 to get bulk moles Al_2O_3 in line with Al stoichiometry.

Calculation of garnet cation concentrations

Average garnet composition is required for the bulk rock calculation. Garnet shows concentric zoning in the four major cations (FeO, MgO, CaO and MnO). Plotting mole fraction versus normalized radius cubed effectively plots concentration against normalized volume (approximating garnet to a sphere). Figure 8.3 shows plots for sample 6, R76 and 19. The best estimate is thus to use the concentration of Fe, Mg and Ca half-way along, when normalized distance is 0.5 (marked on the plots).

However, the estimate for bulk molar manganese needs to be given special consideration, given the effect MnO has on mineral stability despite being in small concentrations (Mahar *et al.*, 1997). MnO cannot be estimated in the same way at the other element oxides as it concentrates in the cores of the garnets, and decreases to almost zero at the rims. The procedure for estimating Mn concentration in the bulk rock is detailed in section 8.5.1.

In addition, in order to model garnet-absent equilibria an effective bulk composition without garnet needs to be calculated. Table 8.3 summarizes calculated bulk rock data for all three samples both with and without garnet for use in THERMOCALC modelling.

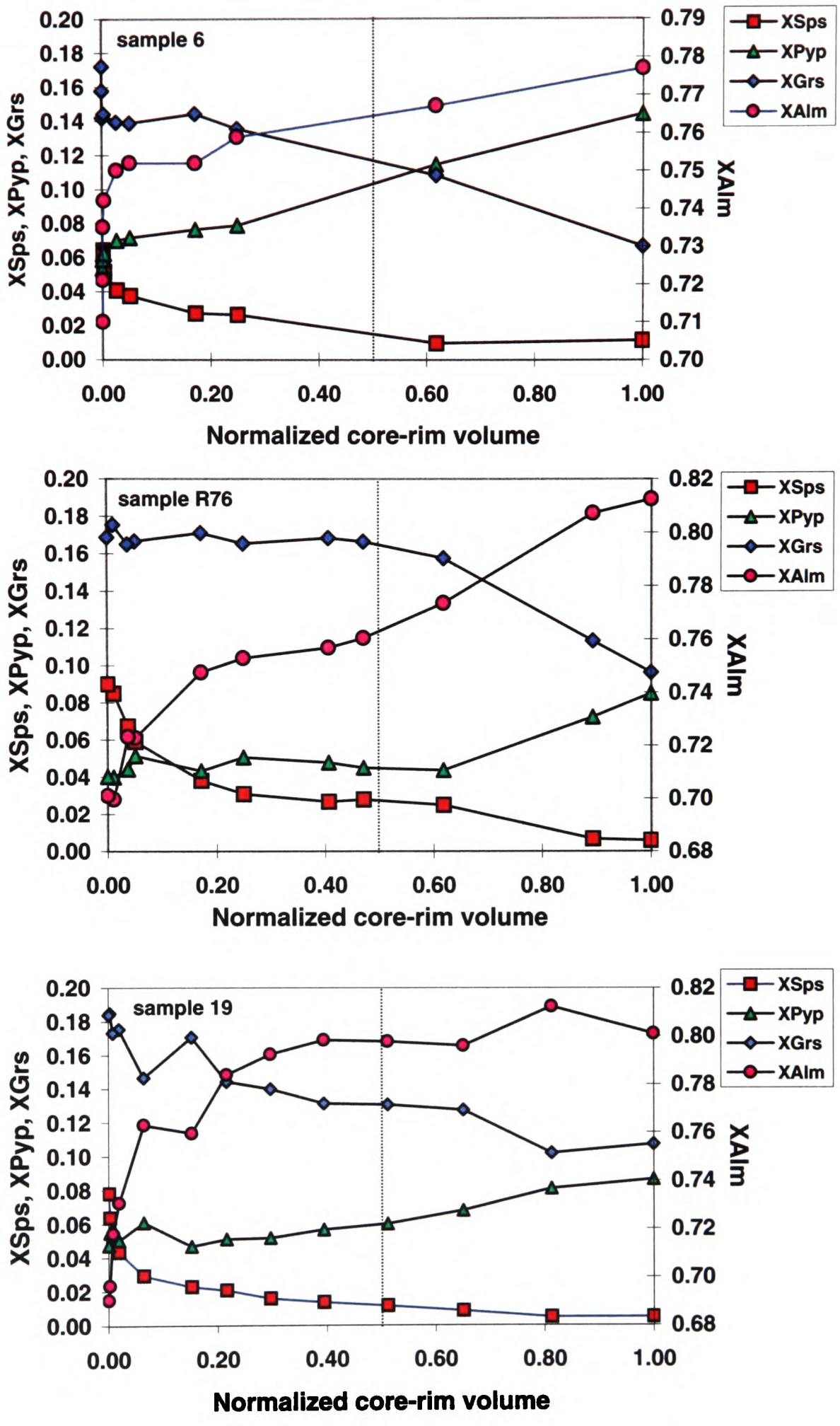


Figure 8.3: Plot of garnet cation concentrations versus core-rim radius cubed, approximating to core-rim volume. Samples 6 (top), R76 (centre) and 19 (bottom). Dotted line shows half-way point where estimates for Fe, Mg and Ca are taken. Mn is treated in a different way (see text).

Sample		Al_2O_3	CaO	MgO	FeO	K_2O	Na_2O	MnO
6	with Grt	58.34	1.72	6.27	18.68	10.20	4.54	0.30
	w/o Grt	64.84	0.45	6.03	11.07	12.18	5.42	0.01
	XRF	*53.61*	*0.99*	*9.43*	*19.55*	*10.49*	*5.72*	*0.22*
R76	with Grt	57.10	2.33	5.92	17.93	8.93	6.71	0.16
	w/o Grt	64.92	0.43	6.32	9.05	11.00	8.27	0.01
	XRF	*58.12*	*1.02*	*6.98*	*15.71*	*11.34*	*6.65*	*0.19*
19	with Grt	58.69	2.25	5.67	16.87	10.61	5.76	0.13
	w/o Grt	66.24	0.44	5.91	7.31	13.03	7.07	0.01
	XRF	*48.67*	*3.10*	*8.56*	*24.11*	*10.89*	*4.33*	*0.35*

Table 8.3: Summary of bulk rock data for THERMOCALC pseudosection. XRF results are included for comparison.

8.3 KFMASH

The system KFMASH (K_2O-FeO-MgO-Al_2O_3-SiO_2-H_2O) is traditionally employed when modelling pelites (Thompson, 1957; Spear & Cheney, 1989; Powell & Holland, 1990) as it allows for the main substitutions to be modelled ($FeMg_{-1}$; (Fe,Mg)$SiAl_{-1}Al_{-1}$). For the purpose of Hoosac Schist modelling nine phases are considered: chlorite, chloritoid, biotite, garnet, staurolite, aluminosilicate, muscovite, quartz and H_2O. Figure 8.4 shows a P-T projection for the KFMASH system, taking Qtz, Ms and H_2O in excess. This illustrates all possible univariant equilibria in the KFMASH system, and predicts two invariant points, [Bt] and [Cld].

The petrogenetic grid is constrained by the Gibbs phase rule. However, the addition of compositional data allows calculation of a pseudosection, obeying Duhem's Theorem. Taking a typical Hoosac bulk rock composition, a P-T pseudosection can be constructed in KFMASH, as shown in figure 8.5. The topology of the pseudosection is constrained by the curves calculated in the P-T projection, but graphically describes what reactions the rock can 'see' given the compositional data. Here the restriction on the extent of KFMASH univariant equilibria seen is evident, and the garnet-in isograd at moderate pressures (6-10kbar) plots between 560-580°C.

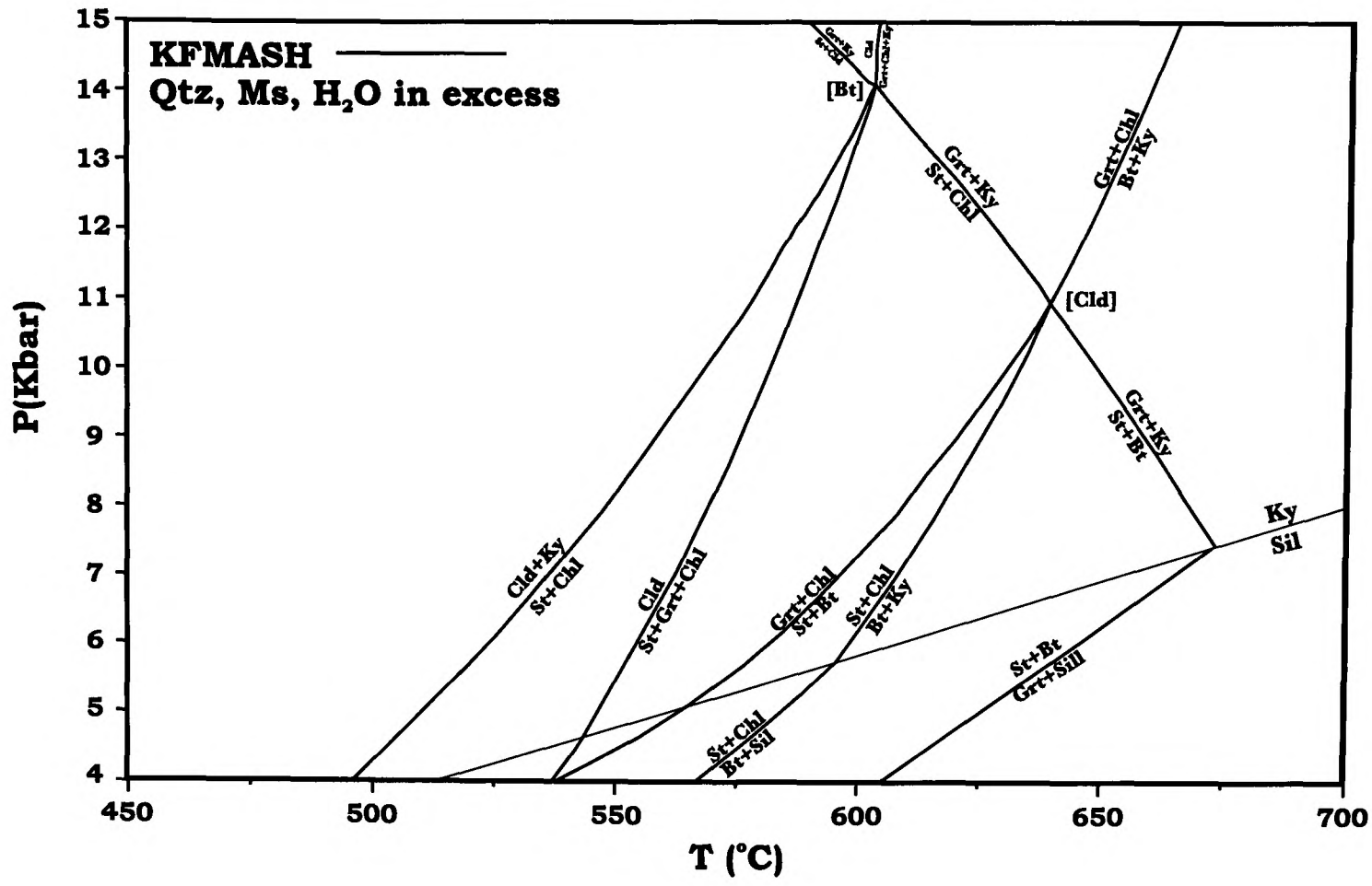


Figure 8.4: P-T projection in the KFMASH system (+Qtz+Ms+H_2O).

Figure 8.5: P-T pseudosection in the KFMASH system for a typical bulk Hoosac composition. Quartz, muscovite and water in excess (+Qtz+Ms+H_2O).

8.4 MnKFMASH

Although the simple system KFMASH can be extremely useful in calculating a sequence of isograds, models in this system predict that garnet should only be observed in rocks of a narrow range of Fe-rich pelites at high P-T (Mahar *et al.*, 1997). However, the near-ubiquitous presence of garnet in medium- to high-grade pelites is attributed to the stabilizing effect of MnO; studies have shown that Mn has a strong effect on pelite phase relations (Symmes & Ferry, 1992; Mahar *et al.*, 1997); Mn partitions strongly into garnet relative to other minerals. Symmes & Ferry (1992) included Mn into the NKFMASH system through $MnFe_{-1}$ and $MnMg_{-1}$ substitutions; their results showed that, for MnO contents of 0.1 - 0.5%, garnet-bearing assemblages could be stabilized over a wide range of P and T. Thus Mn has to be incorporated into the Hoosac model to correctly predict garnet growth.

Figure 8.6 shows a P-T projection for both the KFMASH and MnKFMASH systems. Addition of MnO increases the number of system components to seven, however the total number of phases is unchanged. This increases the variance of the system. The KFMASH grid is shown to illustrate how the petrogenetic grid for a chemical system is related to grids of subsystems. The MnKFMASH univariant curves [Bt] and [Cld] emanate from the KFMASH invariant points [Bt] and [Cld].

A P-T pseudosection in the system MnKFMASH is shown in figure 8.7; this is based on the same bulk rock composition data as figure 8.5, but with the addition of MnO. Comparison of the two shows garnet has now been stabilized down to 550-560°C at medium pressures. The effect of the increased variance on the topology of the pseudosection is to produce extra fields; fields containing three stable phases (a trivariant field) can no longer juxtapose each other; instead there is a field with four stable phases (divariant field) lying between them, taking the place of the KFMASH univariant curves.

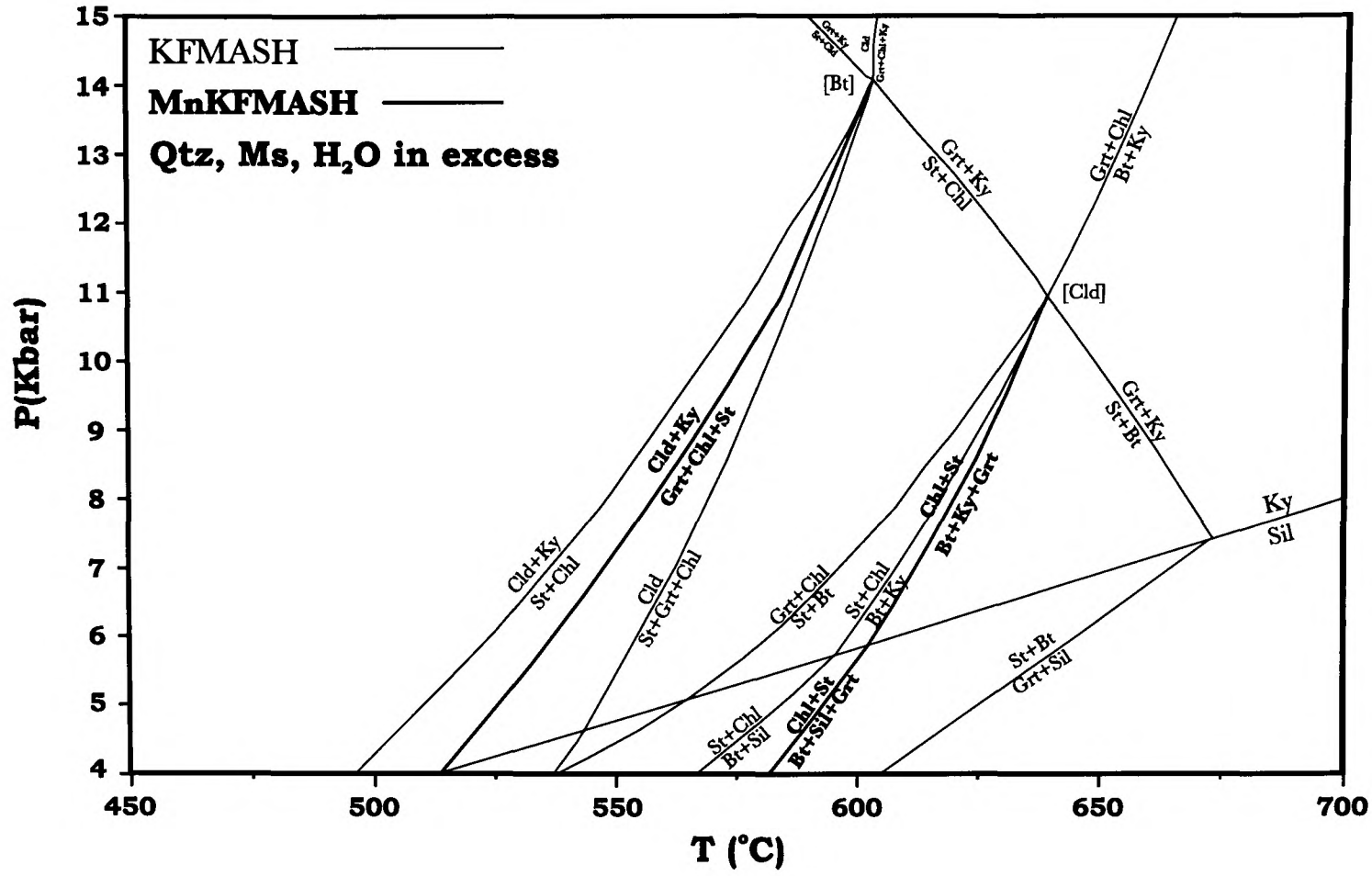


Figure 8.6: P-T projection in the KFMASH and MnKFMASH systems (+Qtz+Ms+H_2O).

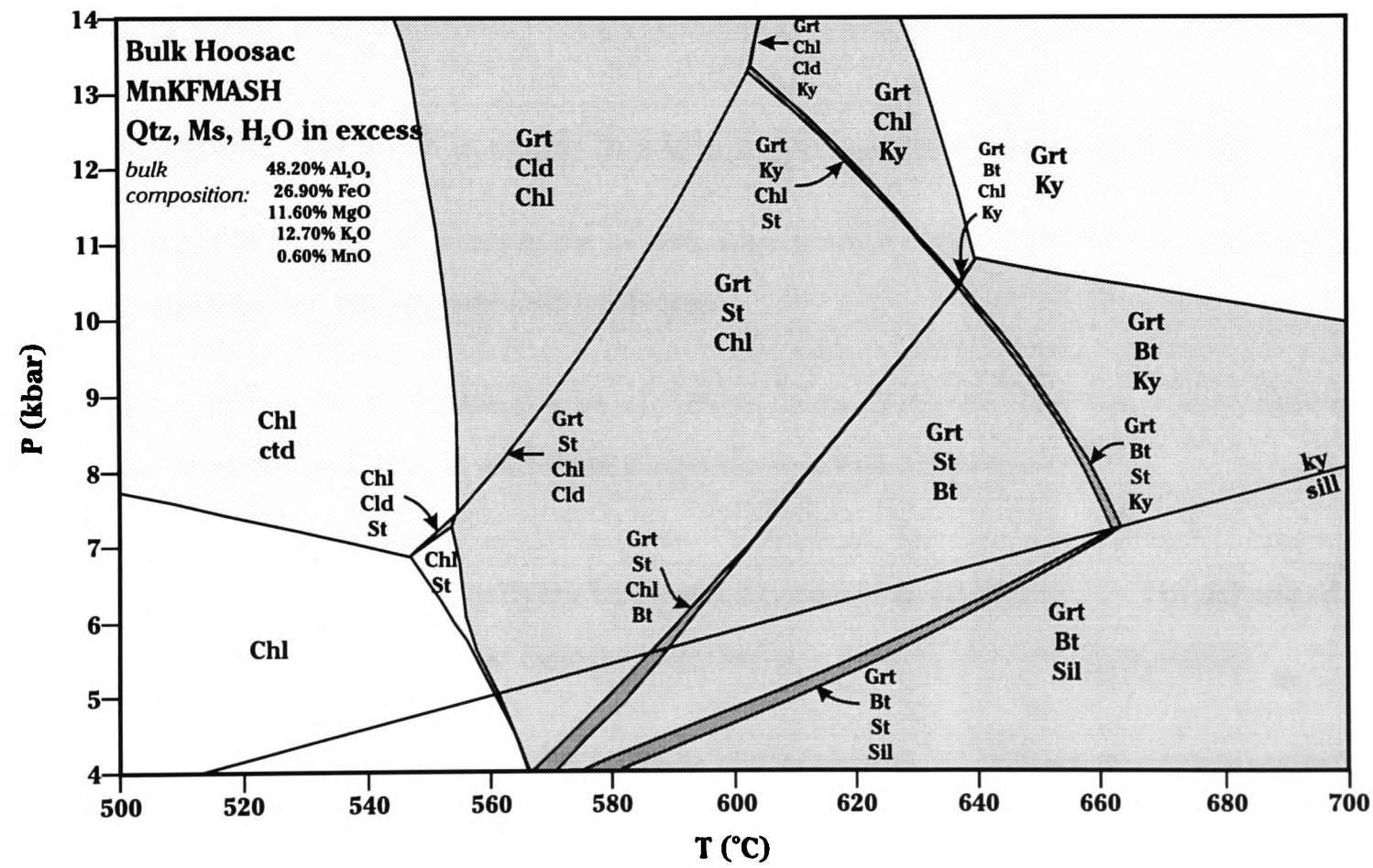


Figure 8.7: P-T pseudosection in the MnKFMASH system for the same typical bulk Hoosac composition as used in figure 8.5, with MnO added. Quartz, muscovite and water in excess (+Qtz+Ms+H_2O).

8.5 NCMnKFMASH

While KFMASH and MnKFMASH adequately model the behaviour of many pelitic rocks, some important natural phase equilibria are not treated. In the case of the Hoosac rocks, the presence of major phases such as paragonite, margarite and plagioclase, as well as the partitioning of Ca into garnet, requires the extension of the MnKFMASH system to include CaO and Na_2O (Vance & Holland, 1993; Worley & Powell, 1998; Walker, 1999).

The addition of CaO and Na_2O increases the number of system components to nine. In NCMnKFMASH, ten phases are predicted to co-exist along each univariant equilibrium (which is more than is commonly observed in natural assemblages). Commonly-observed assemblages have high phase-rule variance (3 or 4). With such a high variance the ordinary phase diagram approach is not constraining enough, thus the use of pseudosection calculation is vital, where the addition of composition data allows employment of Duhem's Theorem. A number of constraints have been applied to the modelling based on observations made on the natural rocks:

- paragonite was taken in excess in addition to muscovite, quartz and water
- margarite is rare as a separate phase, and occurs, and is modelled, as a phase component of paragonite solid solution
- the appearance of plagioclase as a primary phase is restricted only to mid-kyanite grade rocks and above, and thus plagioclase is not considered

The effects of varying water activity has been discussed in section 6.3.3. For all calculations a_{H_2O} is taken as 0.75, fluid being modelled as a binary H_2O - CO_2 solution.

The pseudosection approach can be used to constrain the conditions of garnet growth. Strictly, a zoned garnet is fractionating from the system as it grows, such that the equilibrium pseudosection for the total bulk composition only applies to garnet-free assemblages (or at the very initial point of garnet nucleation and growth). This is because the growth of garnet (or indeed any refractory zoned phase) changes the effective bulk composition of the rock.

Thus in principle:

- a pseudosection constructed for the total bulk composition can be used to determine conditions at the start of garnet growth (*i.e.* the core composition).
- a pseudosection constructed for a fractionated bulk composition from which garnet has been removed (section 8.2) can be used to assess phase relations and P-T conditions in equilibrium with the garnet rims

This potentially gives two critical points on the P-T evolution of a rock. However, the second fractionated pseudosection can be difficult to achieve due to the major differences between real minerals and THERMOCALC-modelled minerals. In particular, THERMOCALC partitions more Fe into muscovite than is observed; there are also discrepancies between the Al content of chlorite and biotite.

Using calculated bulk rock data (section 8.2), pseudosections were calculated for samples 6, R76 and 19. Pseudosections calculated from both garnet-included and garnet-absent bulk rock compositions for sample 6 are shown in figures 8.8 and 8.9. Outlined in red are the Grt=0 isopleths, equivalent to Grt-in conditions up temperature.

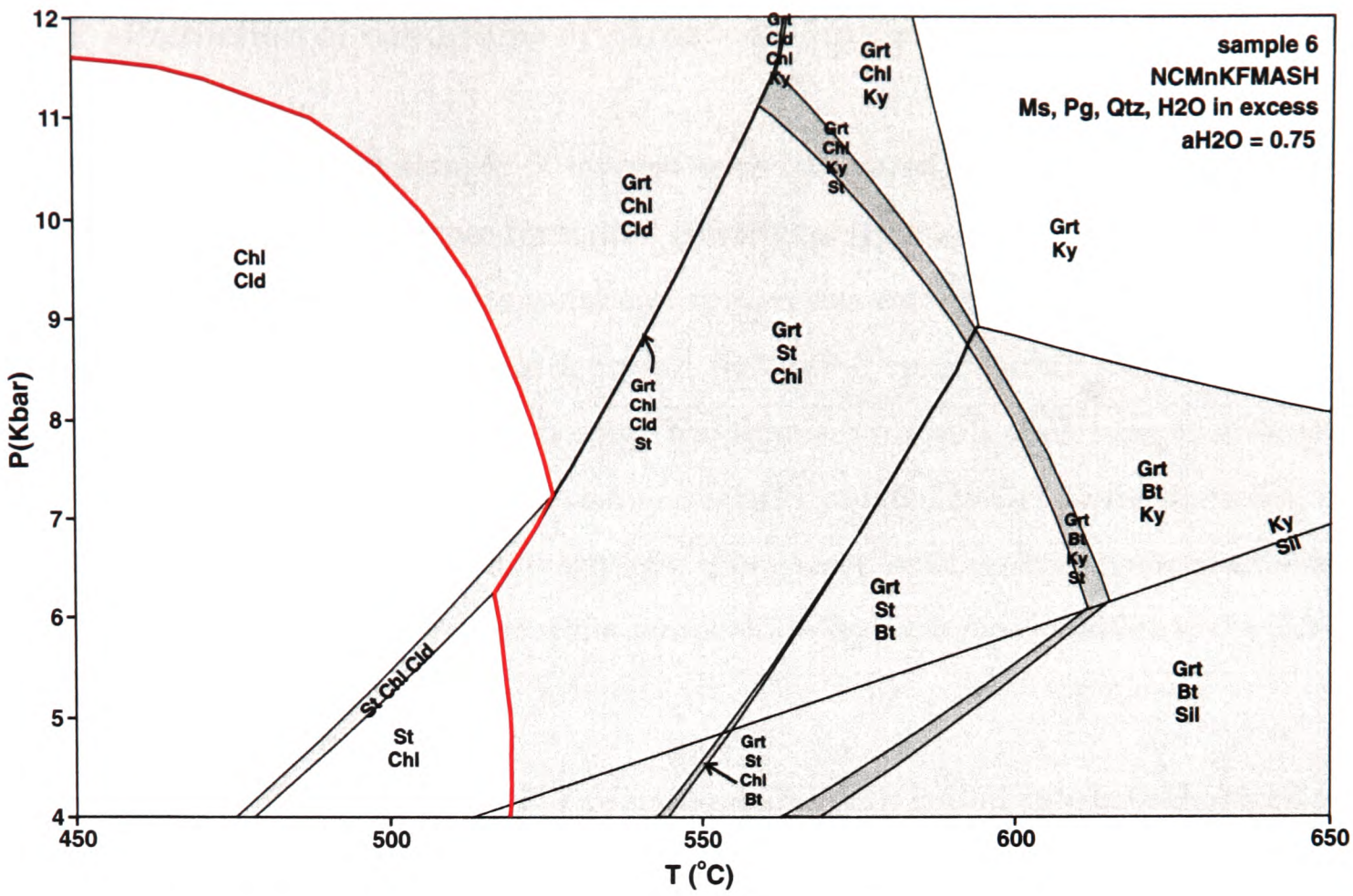


Figure 8.8: P-T pseudosection in the NCMnKFMASH system for sample 6 bulk (+Qtz+Ms+Pg+H_2O). Red line marks Grt=0 isopleth, effectively garnet-in.

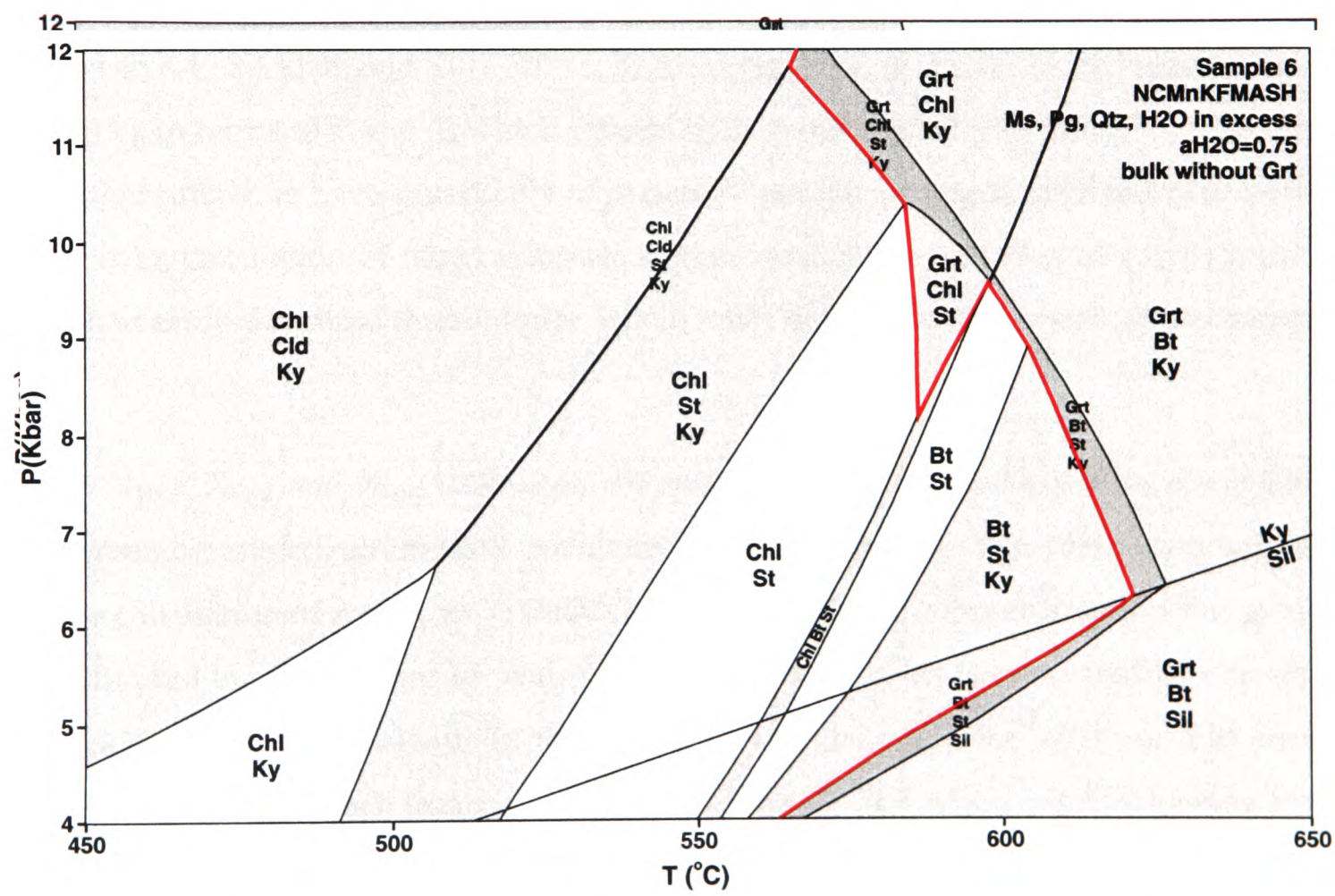


Figure 8.9: P-T pseudosection in the NCMnKFMASH system for modified sample 6 bulk with garnet removed (+Qtz+Ms+Pg+H_2O). Red line marks Grt=0 isopleth.

8.5.1 Prediction of conditions of garnet core formation

Pseudosections for each sample of interest were calculated using unfractionated bulk composition data. Garnet core formation conditions were located by calculating end-member isopleths of pyrope, grossular and spessartine, corresponding to the measured garnet core concentrations. These define an area in P-T space within which the garnet initiated growth. However, at this stage the estimate for bulk-rock composition was fine-tuned. Since the X_{Sps} isopleths run essentially parallel to Grt mode isopleths, reflecting the fact that Mn partitions strongly into garnet, bulk manganese was adjusted such that the measured core spessartine composition lay as close as possible to the Grt=0 isopleth.

Figures 8.10, 8.11 and 8.12 show P-T pseudosections with garnet core conditions calculated. The accompanying tables show the phases present, with their compositions and modal abundancies at the initial point of garnet growth.

Garnets grew within a Cld+Chl+Qtz+Ms+Pg matrix, as evidenced by their inclusion suites. Modelled garnet core conditions concur with this observation, and start to grow between 8.4 - 8.6 kbar, and 510 - 520°C. There is remarkable similarity between the three samples in terms of P and T, which reflects their geographical proximity; they lie close together and thus have potentially experienced similar prograde metamorphic paths. However, calculation of mineral modes suggest that at the initiation of garnet growth R76 had more chloritoid than chlorite, which is not the case for either sample 6 or sample 19.

Only X_{Pyp}, X_{Grs} and X_{Sps} have been defined since THERMOCALC takes these three end-member mole fractions and calculates X_{Alm} by difference. The other point to make is the calculation of modes in THERMOCALC. In order to convert to moles the modes are divided by the number of oxides per formula unit. This is calculated by counting moles of system components in the formula, with the exception of those that are in excess (SiO_2, H_2O), such that for paragonite, $0.5\ Na_2O + 1.5\ Al_2O_3 = 2$. Converting from moles into volume percent requires multiplying moles of phase with the molar volume of phase.

Sample 6

Plotting isopleths of $X_{Pyp} = 0.05$, $X_{Grs} = 0.14$ and $X_{Sps} = 0.10$ predicts that the garnet core formed within an assemblage of Chl+Cld+Ms+Pg+Qtz at T=519°C and P=8.6 kbar.

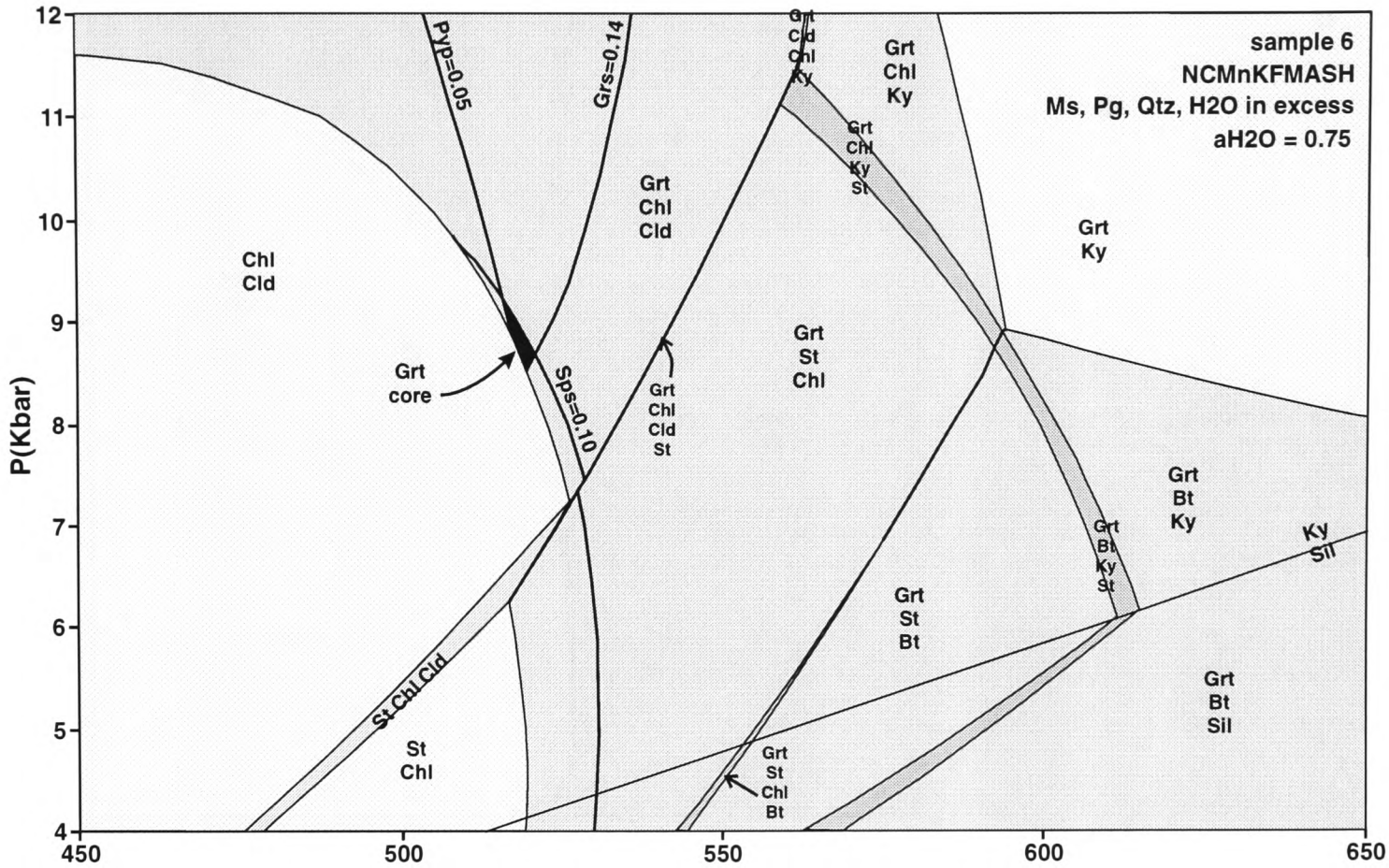


Figure 8.10: P-T pseudosection in the NCMnKFMASH system for sample 6 bulk, with plotted isopleths of pyrope, grossular and spessartine (+Qtz+Ms+Pg+H_2O).

	Grt	Ms	Pg	Cld	Chl	
Si	3.00	3.19	3.00	1.00	2.39	+Qtz
Ti	0.00	0.00	0.00	0.00	0.00	+H_2O (0.75)
Al	2.00	2.62	3.00	2.00	3.22	+CO_2 (0.25)
Fe	2.10	0.16	0.00	0.79	2.82	
Mn	0.32	0.00	0.00	0.02	0.03	P=8.60kbar
Mg	0.15	0.03	0.00	0.18	1.54	T=519.1°C
Ca	0.43	0.00	0.16	0.00	0.00	
Na	0.00	0.05	0.75	0.00	0.00	
K	0.00	0.95	0.09	0.00	0.00	
Total	8.00	7.00	7.00	4.00	10.00	
X_{Mg}	0.07	0.14	0.00	0.19	0.36	
Mode	0.00	0.411	0.230	0.213	0.146	
vol%	0.00	51.0	26.8	13.1	9.0	

Table 8.4: Sample 6: a summary of calculated conditions of garnet core formation.

Sample R76

Plotting isopleths of $X_{Pyp} = 0.04$, $X_{Grs} = 0.15$ and $X_{Sps} = 0.09$ predicts that the garnet core formed within an assemblage of Chl+Cld+Ms+Pg+Qtz at T=514°C and P=8.5 kbar.

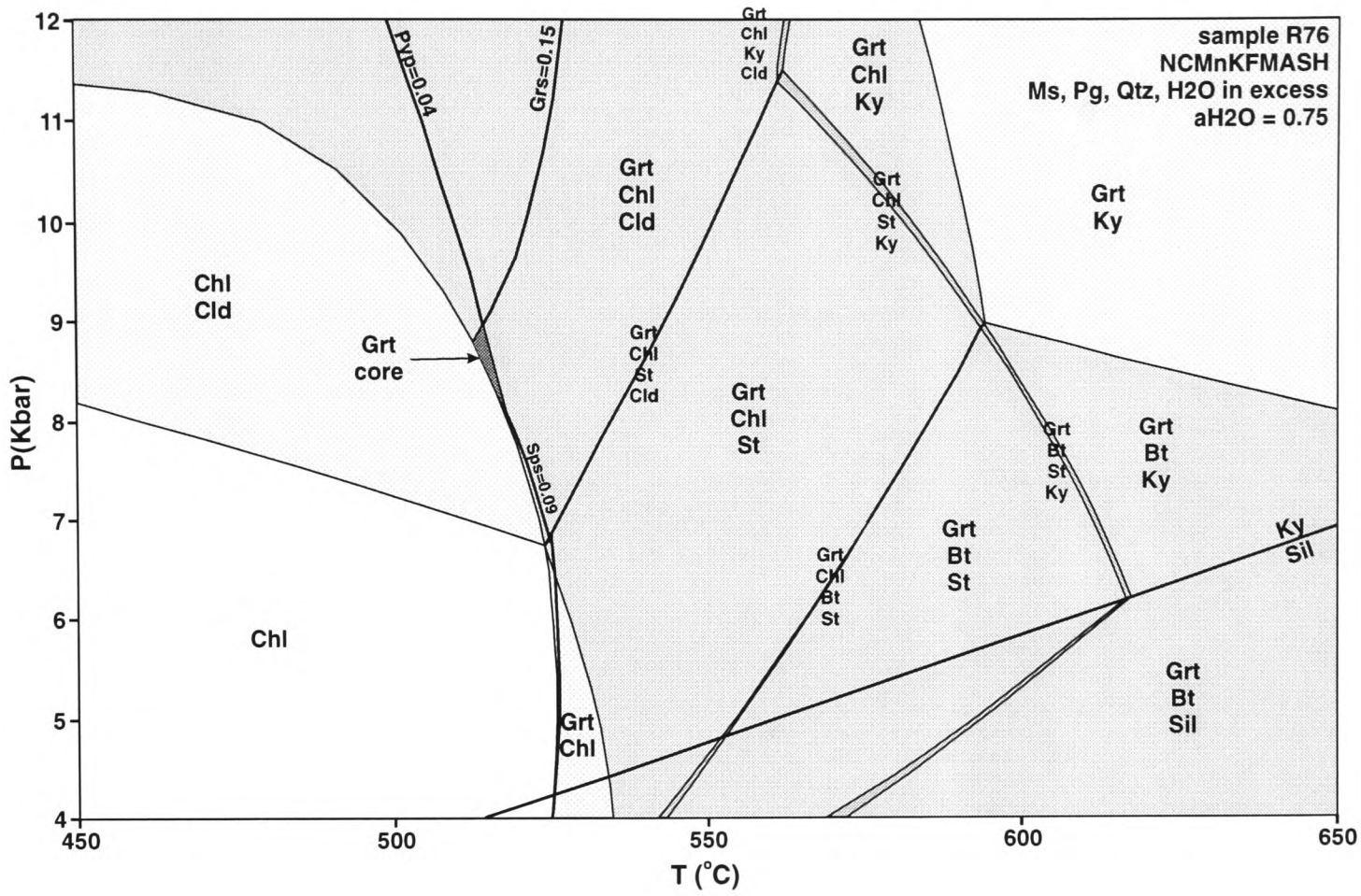


Figure 8.11: P-T pseudosection in the NCMnKFMASH system for sample R76 bulk, with plotted isopleths of pyrope, grossular and spessartine (+Qtz+Ms+Pg+H_2O).

	Grt	Ms	Pg	Cld	Chl	
Si	3.00	3.20	3.00	1.00	2.36	+Qtz
Ti	0.00	0.00	0.00	0.00	0.00	+H_2O (0.75)
Al	2.00	2.60	3.00	2.00	3.28	+CO_2 (0.25)
Fe	2.21	0.18	0.00	0.84	3.09	
Mn	0.27	0.00	0.00	0.02	0.03	P=8.50kbar
Mg	0.12	0.02	0.00	0.14	1.24	T=514.9°C
Ca	0.41	0.00	0.14	0.00	0.00	
Na	0.00	0.06	0.77	0.00	0.00	
K	0.00	0.94	0.09	0.00	0.00	
Total	8.00	7.00	7.00	4.00	10.00	
X_{Mg}	0.05	0.11	0.00	0.15	0.29	
Mode	0.00	0.352	0.350	0.042	0.256	
vol%	0.00	42.5	39.6	2.5	15.3	

Table 8.5: Sample R76: a summary of calculated conditions of garnet core formation.

Sample 19

Plotting isopleths of X_{Pyp} = 0.045, X_{Grs} = 0.17 and X_{Sps} = 0.07 predicts that the garnet core formed within an assemblage of Chl+Cld+Ms+Pg+Qtz at T=519°C and P=8.4 kbar.

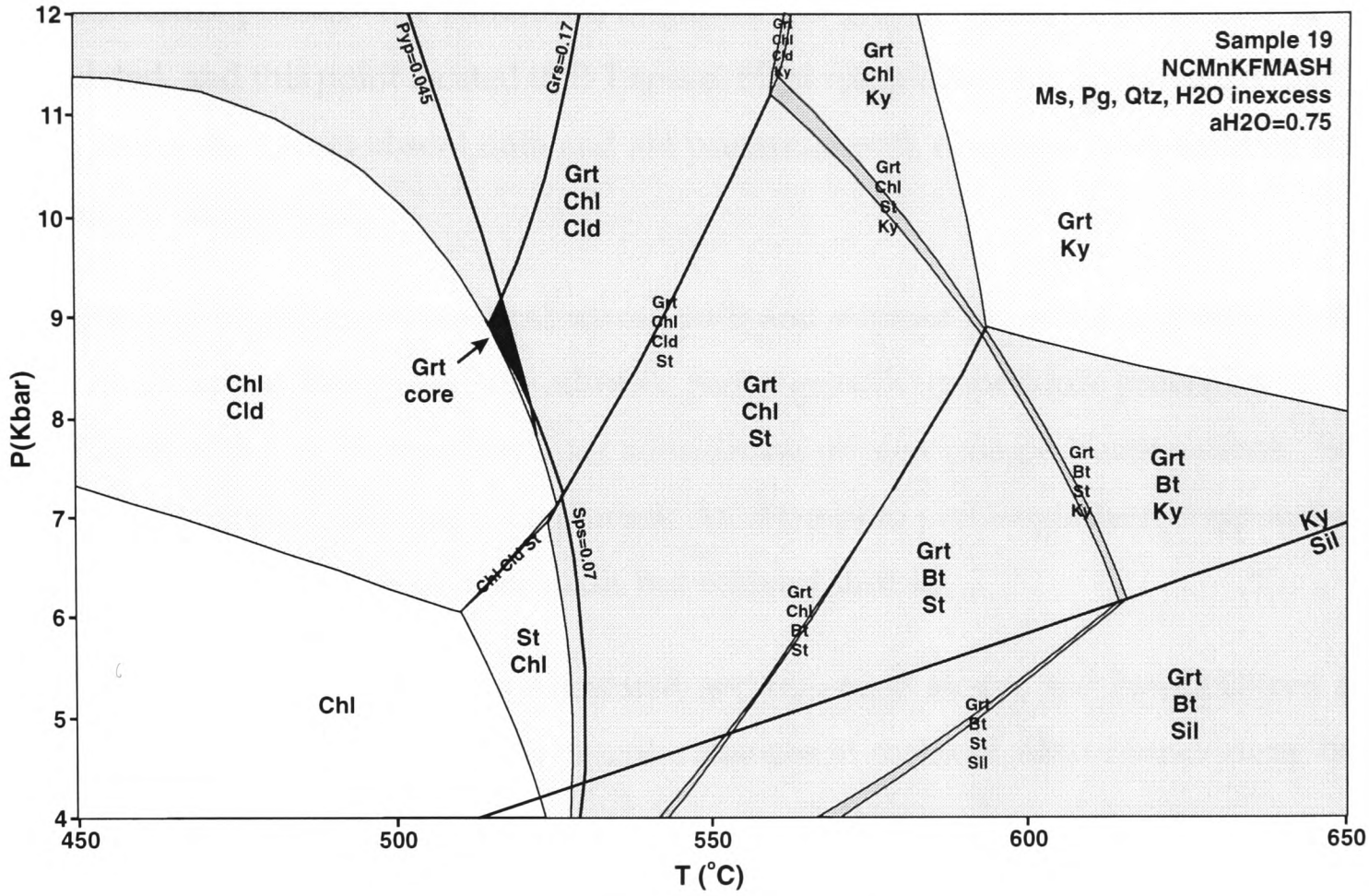


Figure 8.12: P-T pseudosection in the NCMnKFMASH system for sample 19 bulk, with plotted isopleths of pyrope, grossular and spessartine (+Qtz+Ms+Pg+H_2O).

	Grt	Ms	Pg	Cld	Chl	
Si	3.00	3.19	3.00	1.00	2.36	+Qtz
Ti	0.00	0.00	0.00	0.00	0.00	+H_2O (0.75)
Al	2.00	2.61	3.00	2.00	3.27	+CO_2 (0.25)
Fe	2.22	0.17	0.00	0.83	3.00	
Mn	0.22	0.00	0.00	0.01	0.02	P=8.40kbar
Mg	0.13	0.02	0.00	0.16	1.34	T=519.1°C
Ca	0.43	0.00	0.16	0.00	0.00	
Na	0.00	0.06	0.75	0.00	0.00	
K	0.00	0.94	0.09	0.00	0.00	
Total	8.00	7.00	7.00	4.00	10.00	
X_{Mg}	0.06	0.12	0.00	0.16	0.31	
Mode	0.00	0.423	0.299	0.070	0.207	
vol%	0.00	50.3	33.3	4.2	12.2	

Table 8.6: Sample 19: a summary of calculated conditions of garnet core formation.

8.5.2 Garnet rim conditions - comparison between predicted and observed

Using a pseudosection calculated with the fractionated bulk rock composition (*i.e.* taking out garnet), it is possible to locate equilibrium phase assemblages corresponding to observed matrix phases. The conditions of garnet rim growth should then be able to be calculated, and this point located in P-T space. Final compositions and modes are calculated using the garnet-absent data and are presented with observed compositions and modes for comparison.

Comparison of pseudosections calculated with and without the effect of garnet in the bulk rock composition potentially allows a garnet growth temperature procession to be estimated, which is of importance for considering oxygen isotope fractionations. For this, a fairly isobaric line has been plotted. An attempt to plot isopleths corresponding to garnet rim concentrations was made, but without success.

The accompanying tables show calculated and observed modes and compositions of phases. Also shown are figures to describe changes in moles of AFM phases along the plotted P-T line.

Examination of the microstructural history of the Hoosac Schist reveals at least two episodes of metamorphism. It is important to remember that in the following P-T pseudosections, THERMOCALC has enabled the calculation of two snapshots in the P-T evolution of the Hoosac Schist, the garnet core and rim conditions respectively. There is, however, no implication that the plotted P-T procession represents a P-T path for these rocks, indeed the very presence of two stages of metamorphism separated by a deformation event implies that there were probably at least two P-T paths along which the Hoosac rocks evolved. However, since oxygen isotope fractionations are strongly temperature-dependent the plotted P-T procession is used for the purposes of garnet isotope profile modelling later in this chapter. This is considered valid due to the near pressure-independence of oxygen isotope fractionations (Clayton *et al.*, 1975). Interestingly, garnet cation profiles imply that renewed garnet growth (rim) compositions merge smoothly with the core.

Sample 6 peak conditions

Sample 6 AFM matrix phases are Chl+St; there is no biotite or kyanite. The predicted peak conditions are therefore Chl+St, Grt=0, and can be located on the fractionated pseudosection, as shown in figure 8.15. This calculates a peak P-T of 8.6kbar, 586°C, with compositional and modal conditions summarized in table 8.7.

When this peak P-T is plotted on the non-fractionated pseudosection (figure 8.14), it lies within the Grt+St+Chl field. A schematic P-T procession can be drawn, which is nearly isobaric, and cuts from Grt+Chl+Cld through Grt+Chl+Cld+St to the Grt+Chl+St field.

Figure 8.13 shows calculated versus observed peak volume percent (normalized excluding quartz). THERMOCALC modelling calculates more staurolite than is observed, but otherwise there is similarity between the two.

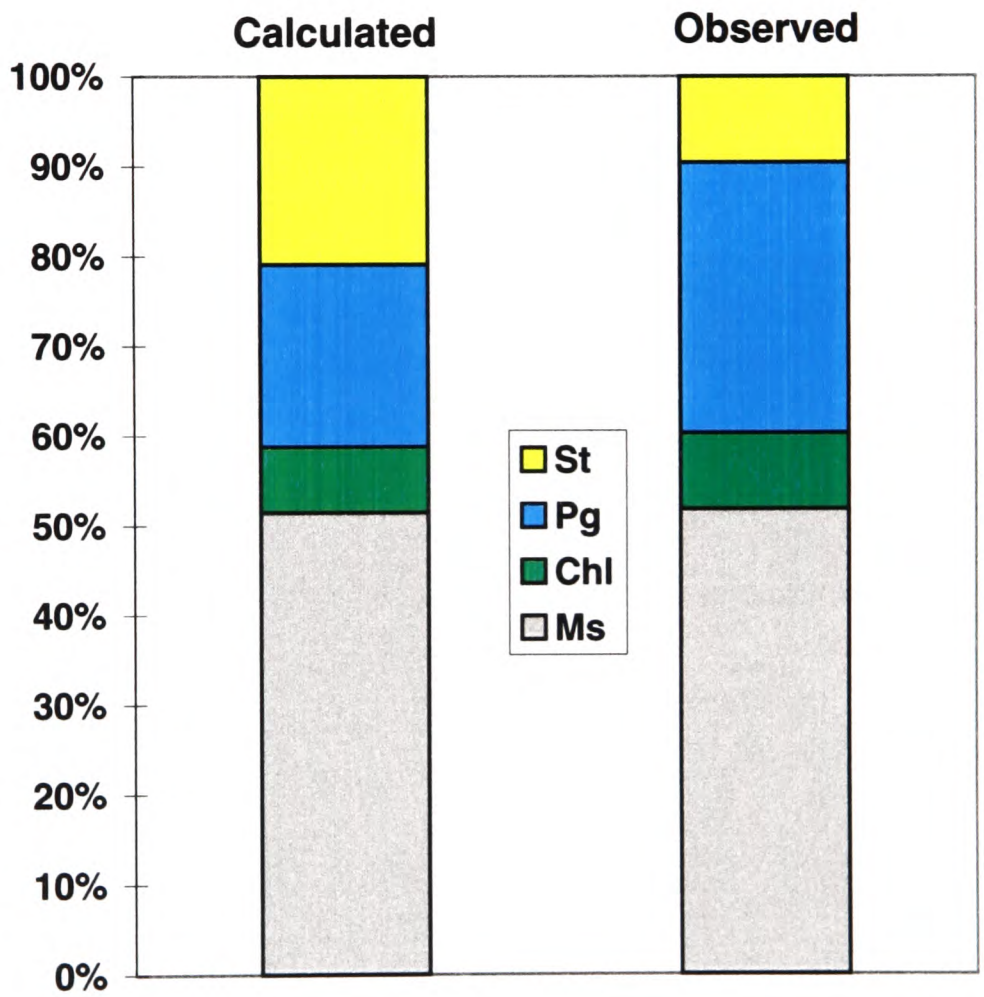


Figure 8.13: Sample 6: A plot showing calculated versus observed mineral volume percent.

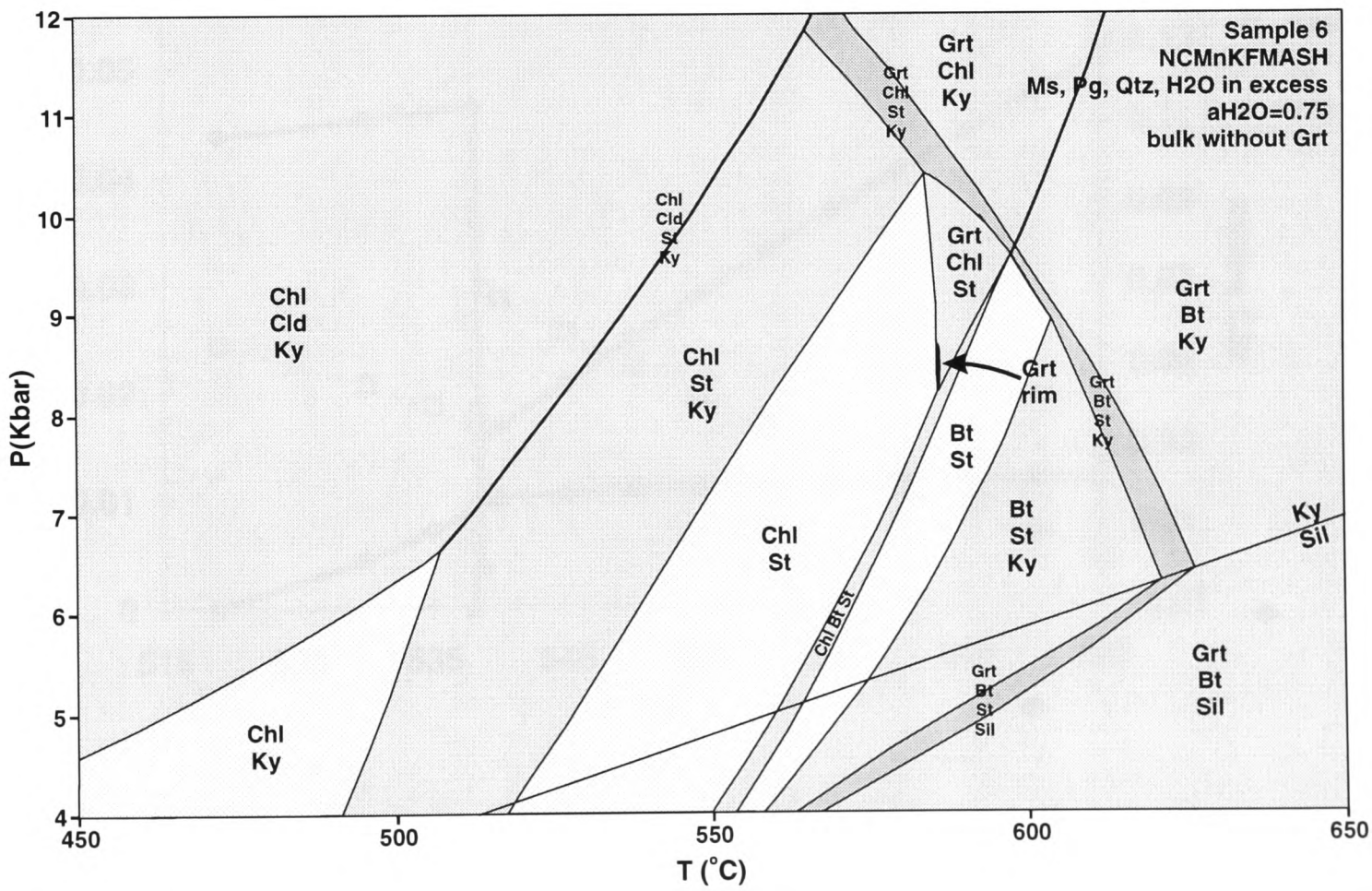


Figure 8.14: P-T pseudosection in the NCMnKFMASH system for unfractionated sample 6 bulk data. Dotted line shows P-T procession (+Qtz+Ms+Pg+H_2O).

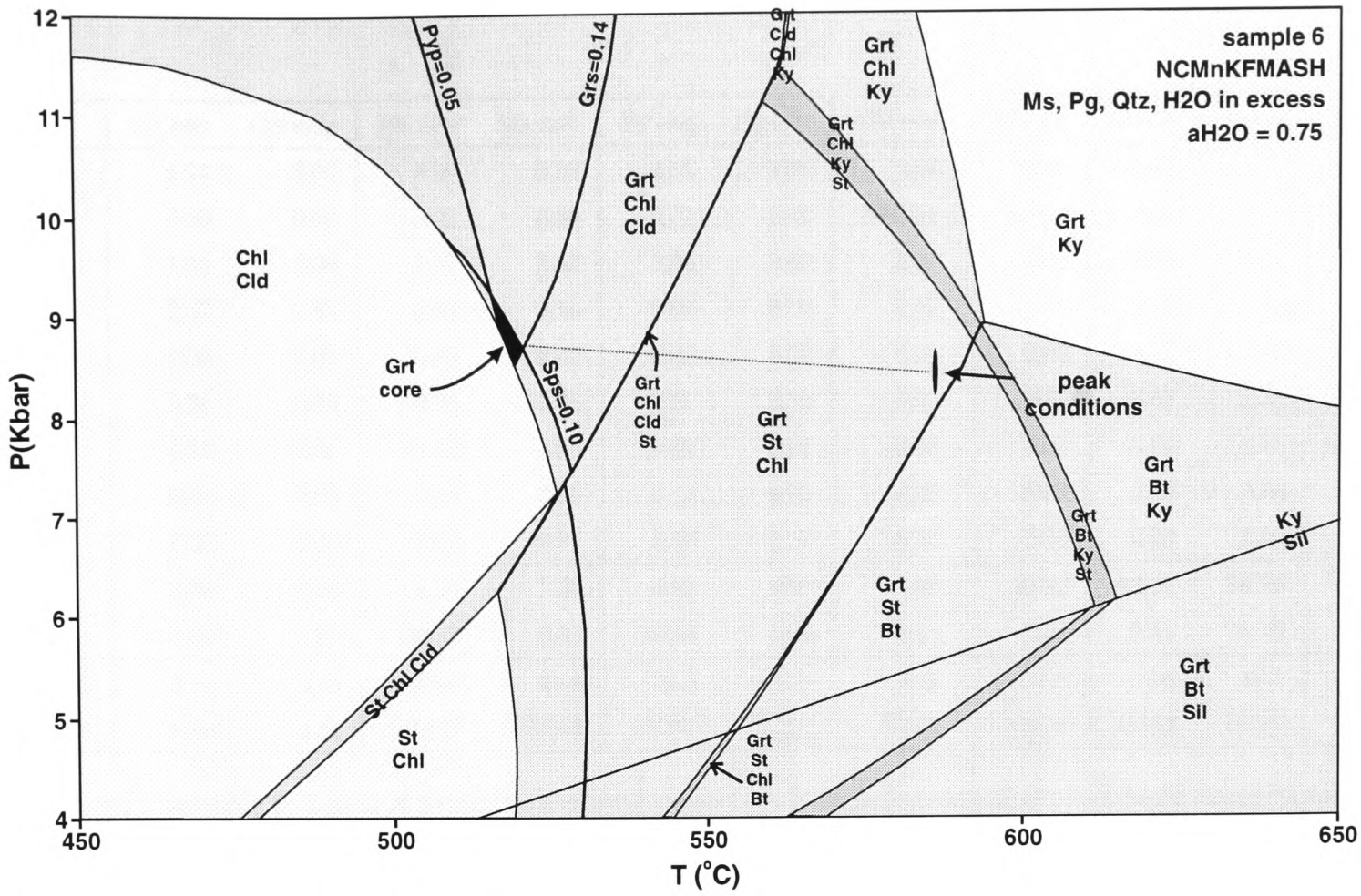


Figure 8.15: P-T pseudosection in the NCMnKFMASH system for fractionated sample 6 bulk data (+Qtz+Ms+Pg+H_2O).

	Grt obs	Grt calc	Ms obs	Ms calc	Pg obs	Pg calc	Chl obs	Chl calc	St obs	St calc	
Si	2.94	3.00	3.07	3.19	3.01	3.00	2.04	2.69	3.83	3.75	+Qtz
Ti	0.00	0.00	0.02	0.00	0.01	0.00	0.01	0.00	0.04	0.00	+H_2O (0.75)
Al	1.99	2.00	2.81	2.62	3.04	3.00	2.20	2.62	8.84	9.00	+CO_2 (0.25)
Fe	2.57	2.32	0.12	0.14	0.04	0.00	2.02	1.91	1.59	1.63	
Mn	0.08	0.05	0.00	0.00	0.00	0.00	0.00	0.00	0.00	0.00	P=8.60kbar
Mg	0.26	0.58	0.06	0.06	0.01	0.00	1.57	2.77	0.31	0.36	T=586.3kbar
Ca	0.21	0.06	0.00	0.00	0.01	0.05	0.00	0.00	0.00	0.00	
Na	0.01	0.00	0.16	0.09	0.64	0.85	0.02	0.00	0.00	0.00	
K	0.00	0.00	0.70	0.91	0.07	0.10	0.00	0.00	0.00	0.00	
Total	8.06	8.00	6.94	7.00	6.83	7.00	7.86	10.00	14.61	14.75	
X_{Mg}	0.09	0.20	0.33	0.33	0.30	0.00	0.44	0.59	0.16	0.18	
Vol %	n/a	n/a	51.8	61.0	30.1	22.6	8.5	4.3	9.6	12.1	
Mode	n/a	n/a	0.429	0.514	0.266	0.203	0.142	0.073	0.163	0.209	

Table 8.7: Sample 6: a summary of calculated peak conditions versus observed peak conditions.

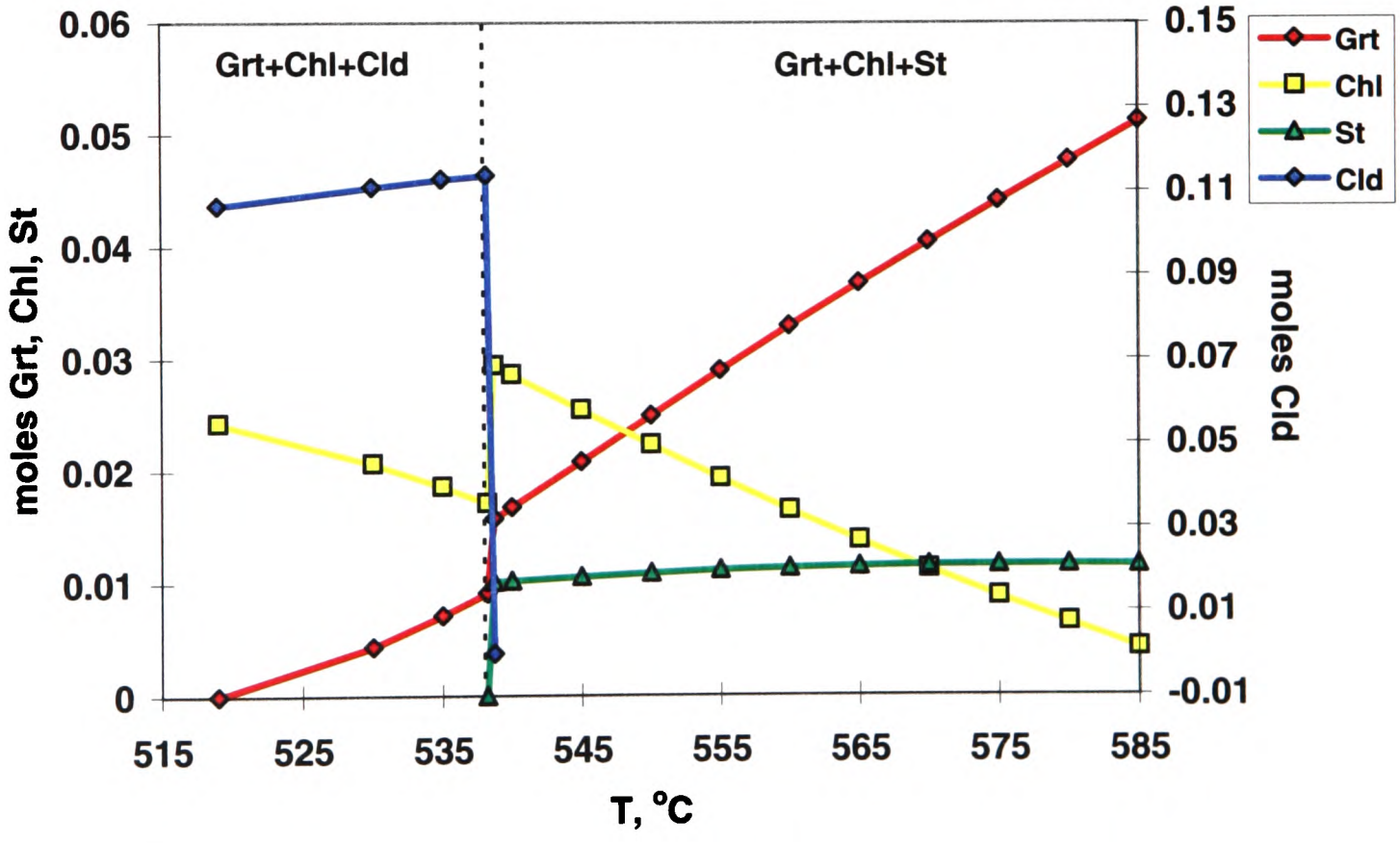


Figure 8.16: A plot showing changes in moles of phases along the plotted P-T procession of sample 6, at P=8.6 kbar.

Sample R76 peak conditions

Sample R76 AFM matrix phases are Chl+St+Bt; there is very minor kyanite. Phase diagram modelling only predicts co-existence of chlorite and biotite along a small trivariant field. This is not compatible with matrix observations, and as such peak conditions are chosen where St+Bt co-exist, and where Grt=0. This occurs in a well-constrained point, marked in figure 8.19. Peak conditions are calculated at 8.6kbar, 604°C . When this peak P-T is plotted on the non-fractionated pseudosection (figure 8.18), it lies just within the Grt+Ky field. A P-T procession has been drawn, however this fails to cut through any biotite-bearing fields in the non-fractionated pseudosection.

Figure 8.17 shows calculated versus observed peak volume percent. The problem of Chl and Bt only being stable together over a very small P-T area is apparent here, with more biotite being predicted and no chlorite compared to observations. It is possible the chlorite here is largely retrograde, otherwise there is a remarkable correlation between calculated and observed.

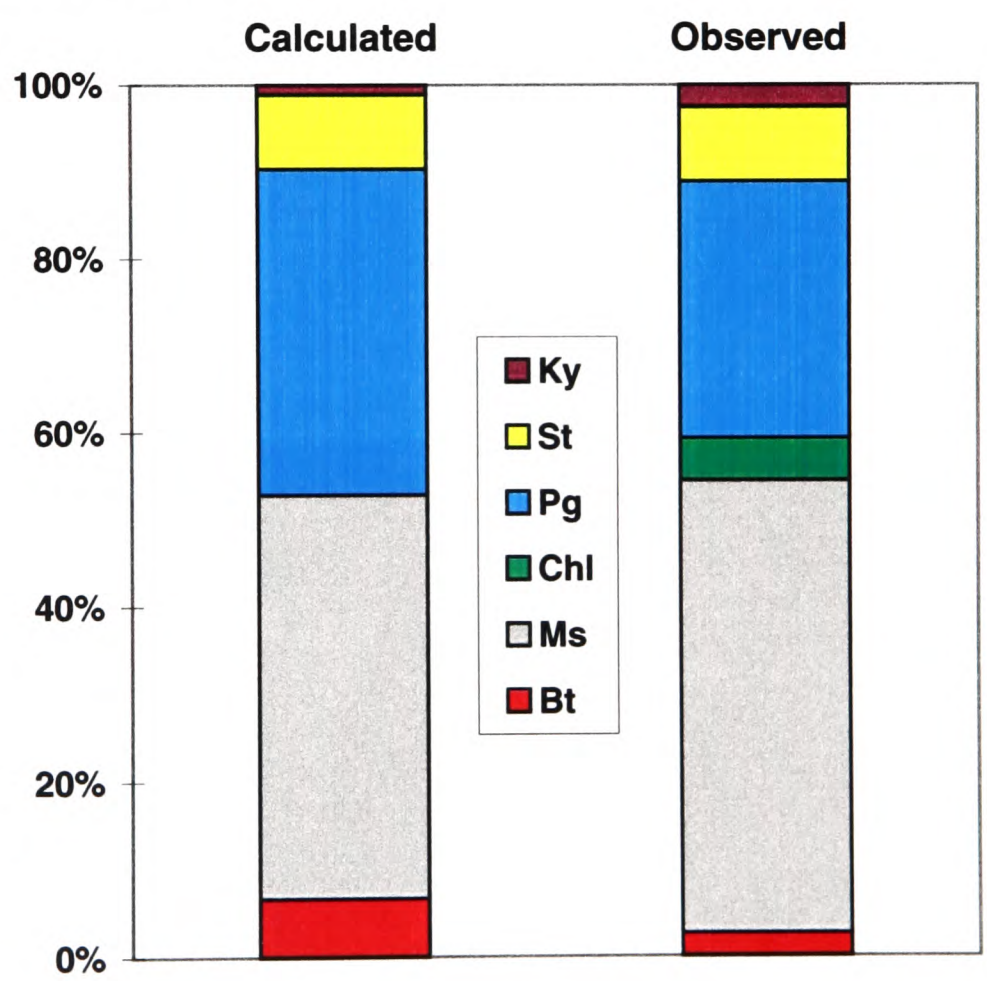


Figure 8.17: Sample R76: A plot showing calculated versus observed mineral volume percent.

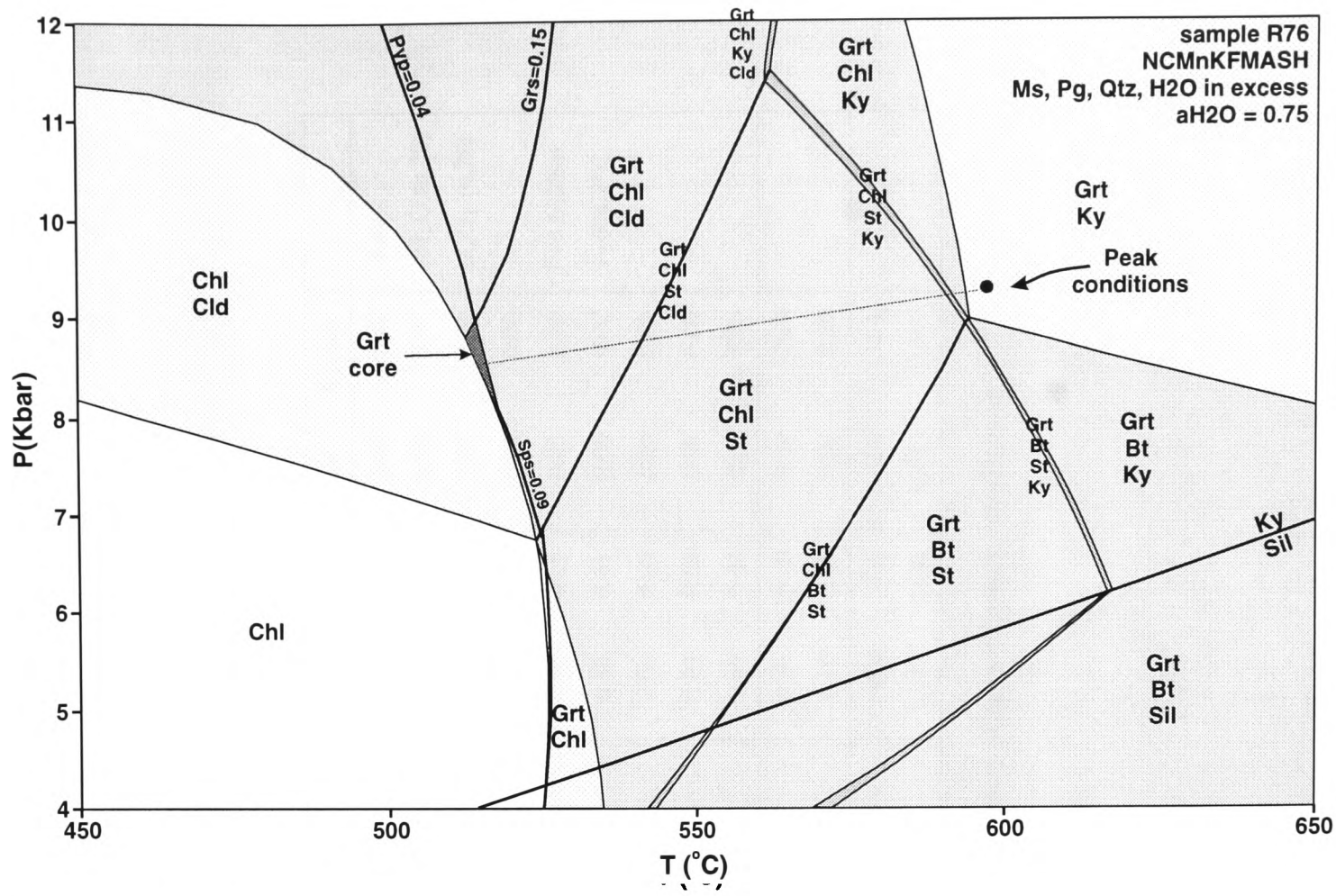


Figure 8.18: P-T pseudosection in the NCMnKFMASH system for unfractionated sample R76 bulk data. Dotted line shows P-T procession (+Qtz+Ms+Pg+H_2O).

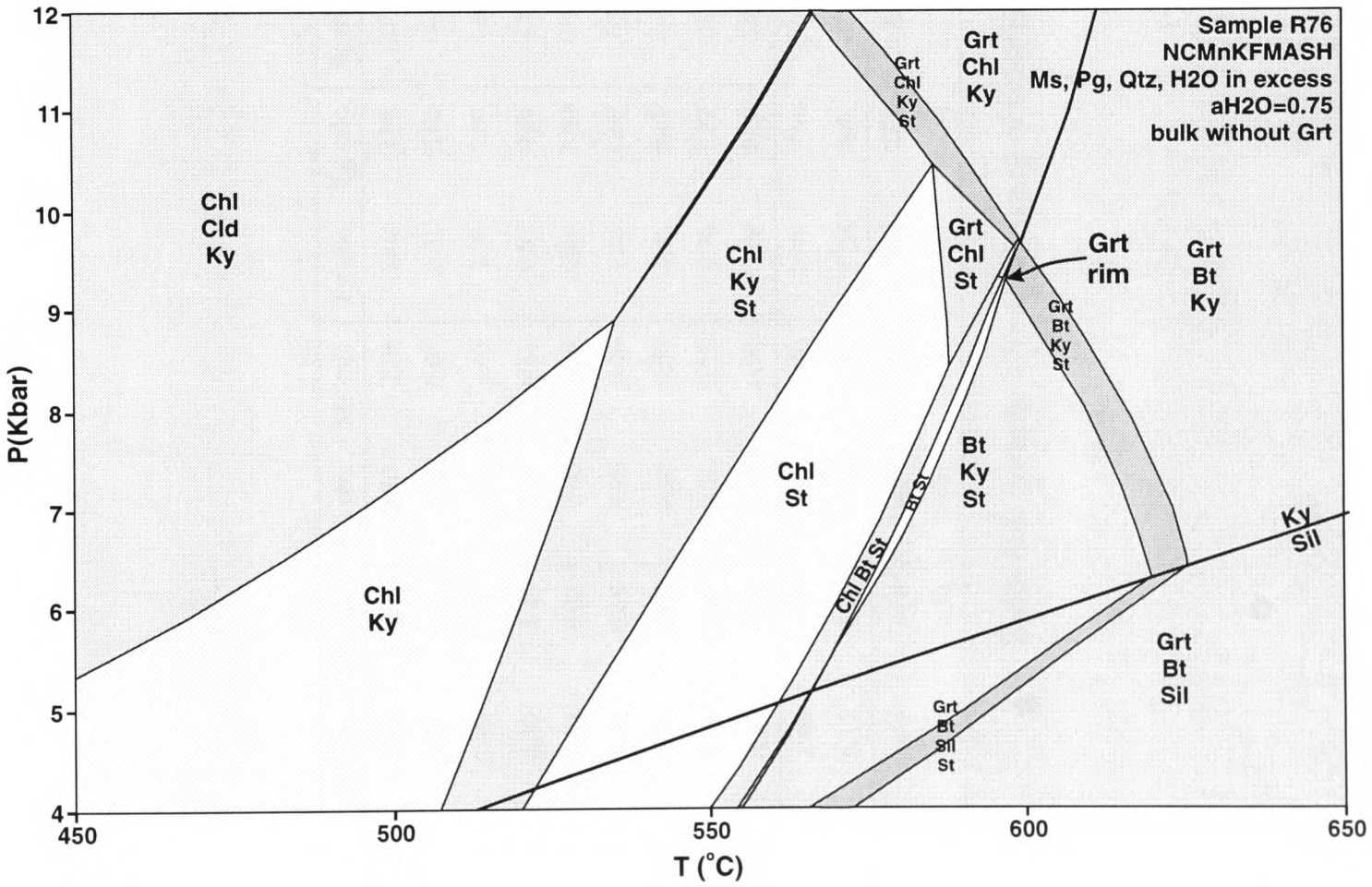


Figure 8.19: P-T pseudosection in the NCMnKFMASH system for fractionated sample R76 bulk data (+Qtz+Ms+Pg+H_2O).

	Grt obs	Grt calc	Ms obs	Ms calc	Pg obs	Pg calc	Bt obs	Bt calc	Chl obs	Chl calc	St obs	Stcalc	Ky obs	Ky calc	
Si	2.94	3.00	3.10	3.19	3.02	3.00	2.76	2.74	2.08	-	3.94	4.00	1.00	1.00	+Qtz
Ti	0.00	0.00	0.02	0.00	0.01	0.00	0.08	0.00	0.01	-	0.06	0.00	0.00	0.00	+H_2O (0.75)
Al	1.99	2.00	2.76	2.63	2.99	3.00	1.64	1.51	2.22	-	8.73	9.00	2.00	2.00	+CO_2 (0.25)
Fe	2.50	2.24	0.08	0.13	0.02	0.00	1.20	1.13	1.67	-	1.59	1.59	0.00	0.00	
Mn	0.04	0.07	0.00	0.00	0.00	0.00	0.00	0.00	0.00	-	0.01	0.01	0.00	0.00	P=8.60kbar
Mg	0.35	0.66	0.08	0.06	0.01	0.00	1.20	1.61	1.79	-	0.30	0.41	0.00	0.00	T=604.2°C
Ca	0.23	0.03	0.00	0.00	0.01	0.03	0.00	0.00	0.00	-	0.00	0.00	0.00	0.00	
Na	0.01	0.00	0.18	0.10	0.76	0.87	0.05	0.00	0.01	-	0.02	0.00	0.00	0.00	
K	0.00	0.00	0.71	0.90	0.09	0.10	0.86	1.00	0.03	-	0.01	0.00	0.00	0.00	
Total	8.06	8.00	6.92	7.00	6.91	7.00	7.79	8.00	4.90	-	14.66	15.00	0.00	0.00	
X_{Mg}	0.12	0.23	0.50	0.32	0.33	0.00	0.50	0.59	0.52	-	0.16	0.21	0.00	0.00	
Vol %	n/a	n/a	51.9	46.2	29.0	37.5	2.5	6.6	4.9	-	8.0	8.6	2.5	1.1	
Mode	n/a	n/a	0.434	0.392	0.264	0.340	0.039	0.104	0.082	-	0.147	0.149	0.033	0.015	

Table 8.8: Sample R76: a summary of calculated peak conditions versus observed peak conditions.

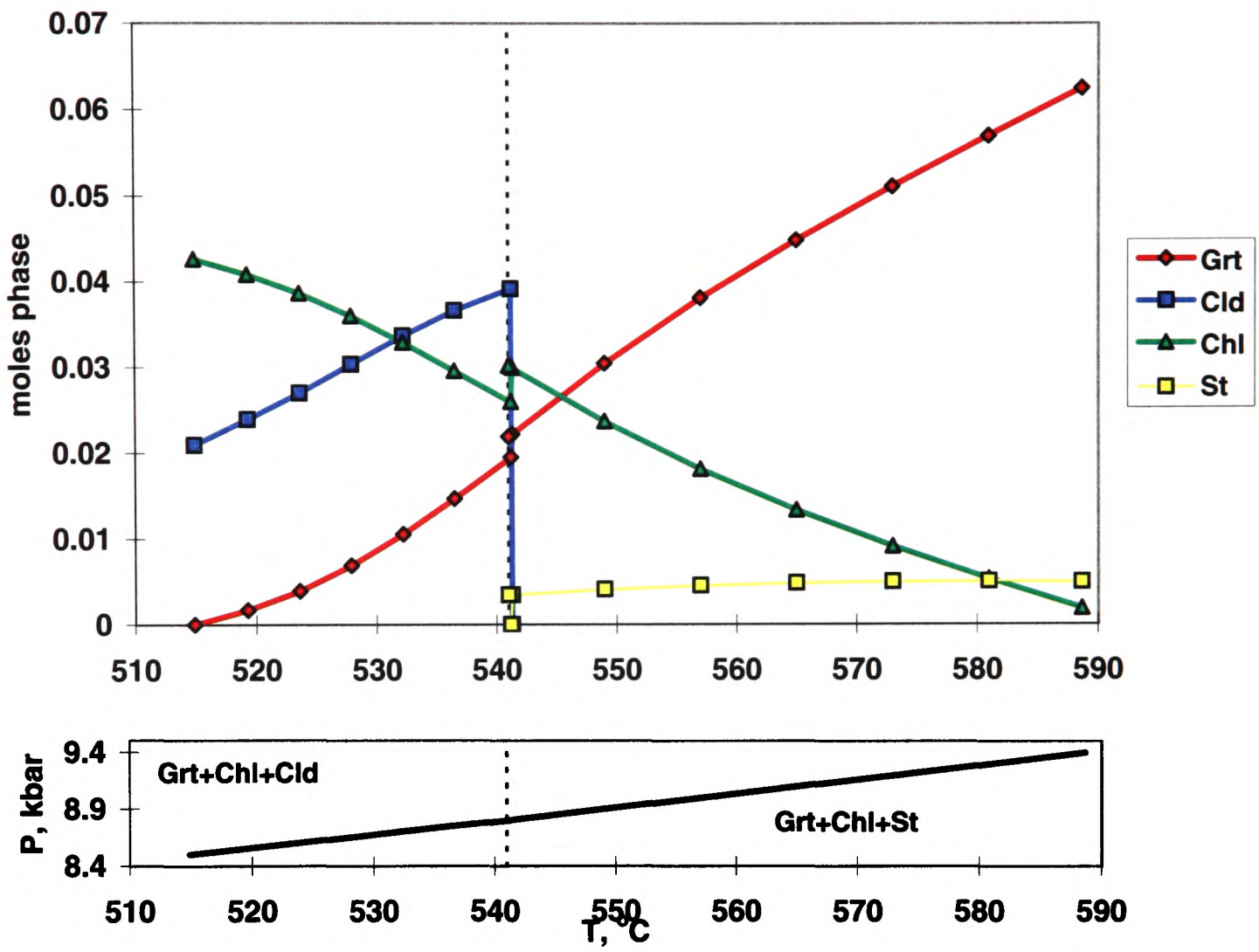


Figure 8.20: A plot showing changes in moles of phases along the plotted P-T procession of sample R76.

Sample 19 peak conditions

Sample 19 AFM matrix phases are St+Bt+Ky. On the fractionated pseudosection peak conditions are calculated at Bt+Ky+St, Grt=0 (figure 8.23). Peak conditions are calculated at 8.6kbar, 598°C.

On the non-fractionated pseudosection (figure 8.22), this P-T point lies within Grt+Bt+Ky. A near-isobaric P-T procession has been plotted, which runs through Grt+Chl+Cld - Grt+Chl+Cld+St - Grt+Chl+St - Grt+Chl+Bt+St - Grt+Bt+St - Grt+Bt+St+Ky - Grt+Bt+Ky.

Figure 8.21 shows calculated versus observed peak volume percent. Again, there is the problem of not predicting chlorite as a stable phase, however again much chlorite may well be retrograde. There is still a good correlation between calculated and observed modes.

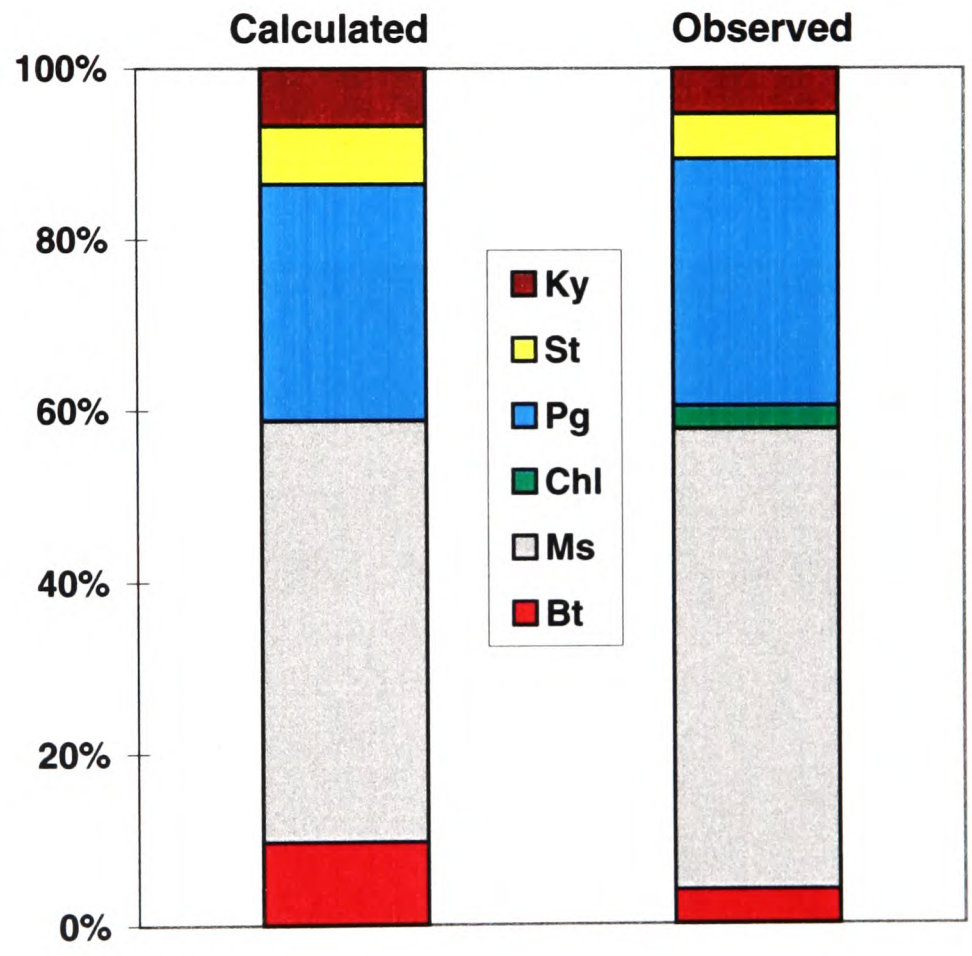


Figure 8.21: Sample 19: A plot showing calculated versus observed mineral percent volume.

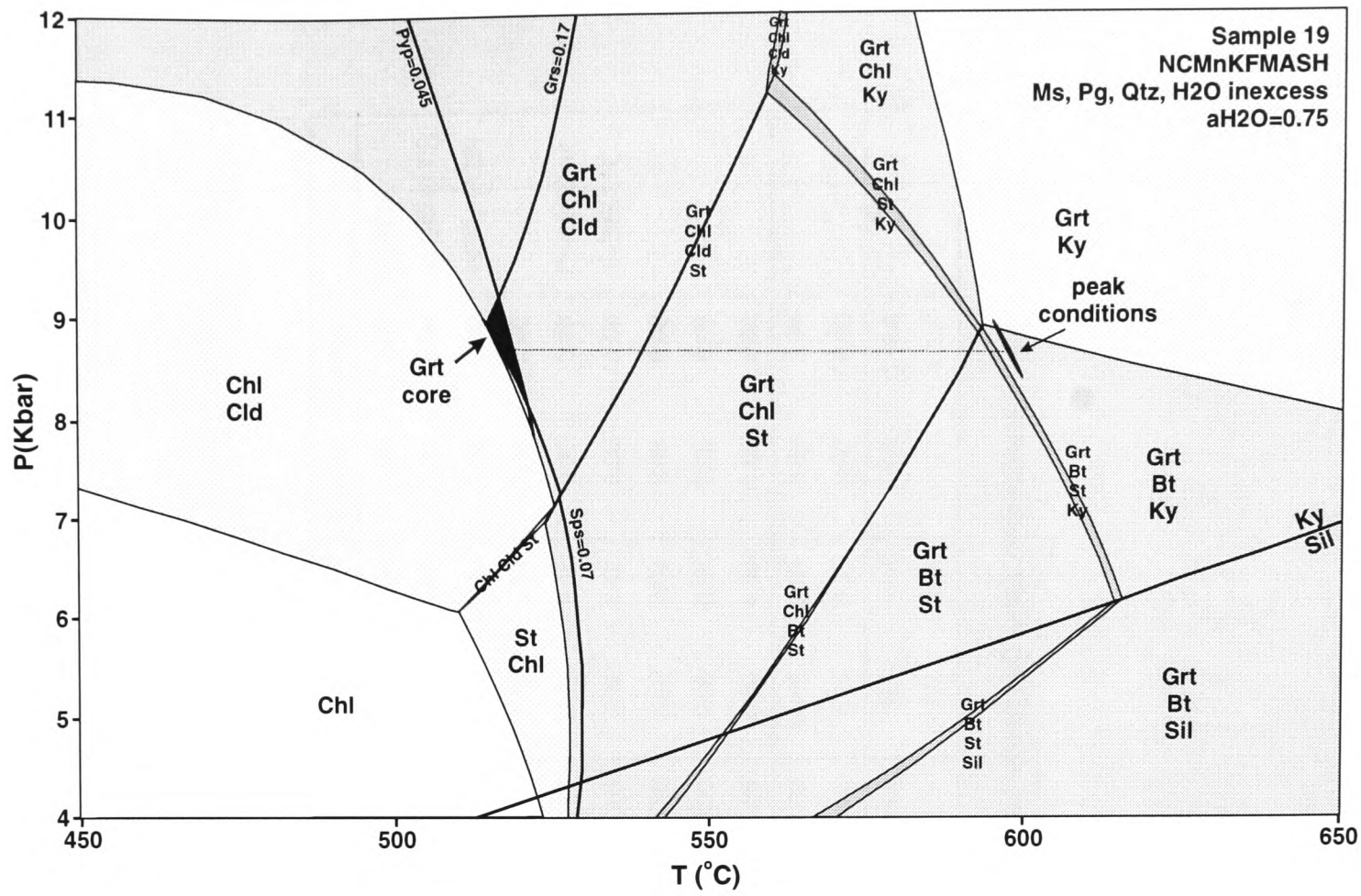


Figure 8.22: P-T pseudosection in the NCMnKFMASH system for unfractionated sample 19 bulk data. Dotted line shows P-T procession (+Qtz+Ms+Pg+H_2O).

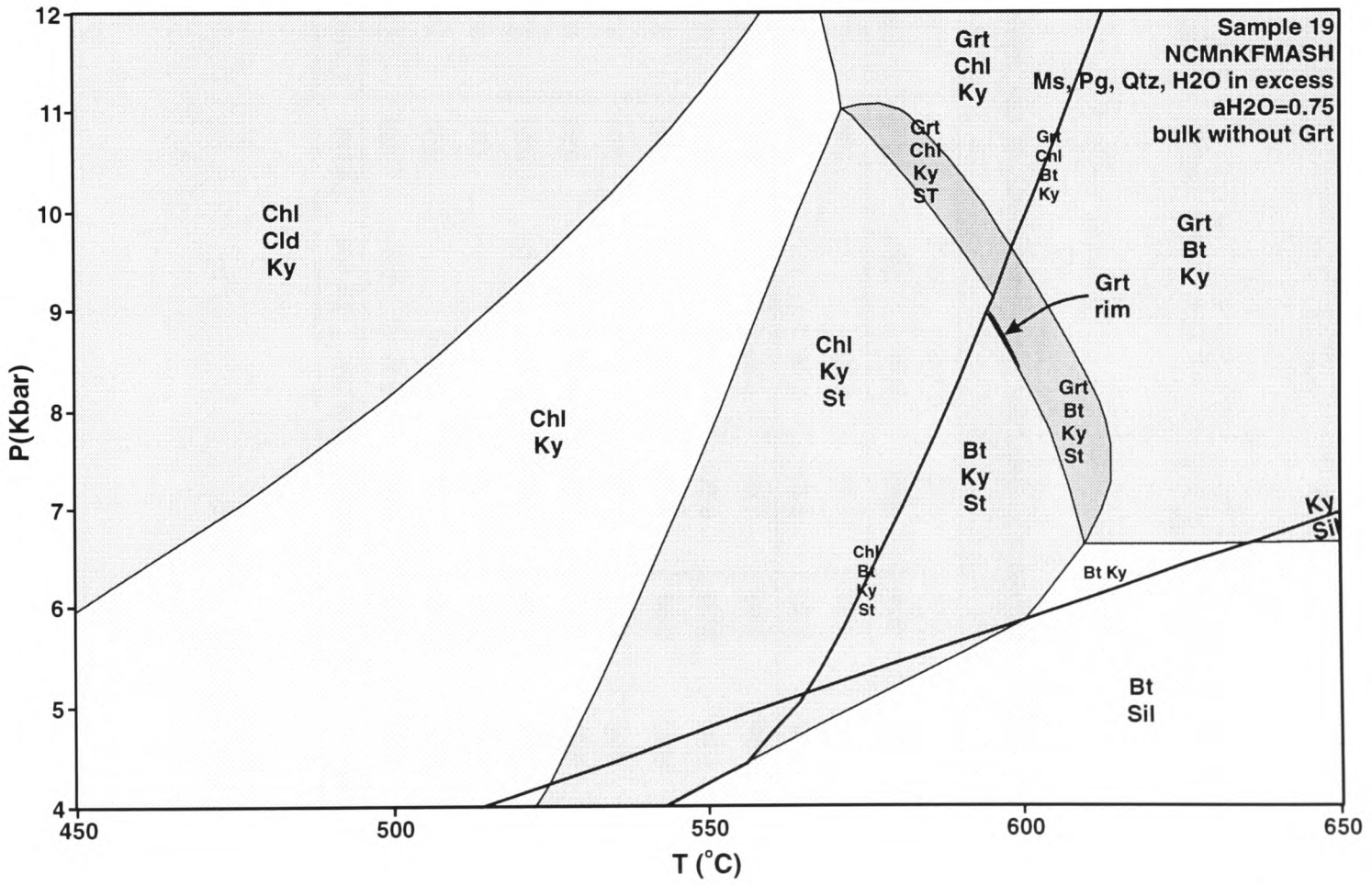


Figure 8.23: P-T pseudosection in the NCMnKFMASH system for fractionated sample 19 bulk data (+Qtz+Ms+Pg+H_2O).

	Grt obs	Grt calc	Ms obs	Ms calc	Pg obs	Pg calc	Chl obs	Chl calc	Bt obs	Bt calc	St obs	St calc	Ky obs	Ky calc	
Si	2.95	3.00	3.04	3.19	-	3.00	2.05	-	2.72	2.75	3.78	4.00	1.00	1.00	+Qtz
Ti	0.00	0.00	0.03	0.00	-	0.00	0.00	-	0.09	0.00	0.06	0.00	0.00	0.00	+H_2O (0.75)
Al	2.00	2.00	2.79	2.63	-	3.00	2.24	-	1.65	1.50	8.83	9.00	2.00	2.00	+CO_2 (0.25)
Fe	2.48	2.18	0.09	0.12	-	0.00	1.69	-	1.19	1.10	1.59	1.58	0.00	0.00	
Mn	0.02	0.12	0.00	0.00	-	0.00	0.00	-	0.00	0.00	0.01	0.01	0.00	0.00	P=8.60kbar
Mg	0.29	0.66	0.07	0.06	-	0.00	1.85	-	1.22	1.65	0.38	0.42	0.00	0.00	T=598.1°C
Ca	0.30	0.04	0.00	0.00	-	0.03	0.00	-	0.01	0.00	0.00	0.00	0.00	0.00	
Na	0.01	0.00	0.18	0.10	-	0.86	0.01	-	0.04	0.00	0.00	0.00	0.00	0.00	
K	0.00	0.00	0.85	0.90	-	0.11	0.01	-	0.93	1.00	0.00	0.00	0.00	0.00	
Total	8.05	8.00	7.05	7.00	-	7.00	7.85	-	7.85	8.00	14.65	15.00	3.00	3.00	
X_{Mg}	0.10	0.23	0.44	0.33	-	0.00	0.52	-	0.51	0.60	0.19	0.21	0.00	0.00	
Vol %	n/a	n/a	53.9	56.1	28.9	29.5	2.7	0.0	3.9	5.8	5.3	3.8	5.3	4.8	
Mode	n/a	n/a	0.462	0.492	0.265	0.277	0.045	0.000	0.062	0.096	0.093	0.068	0.073	0.067	

Table 8.9: Sample 19: a summary of calculated peak conditions versus observed peak conditions.

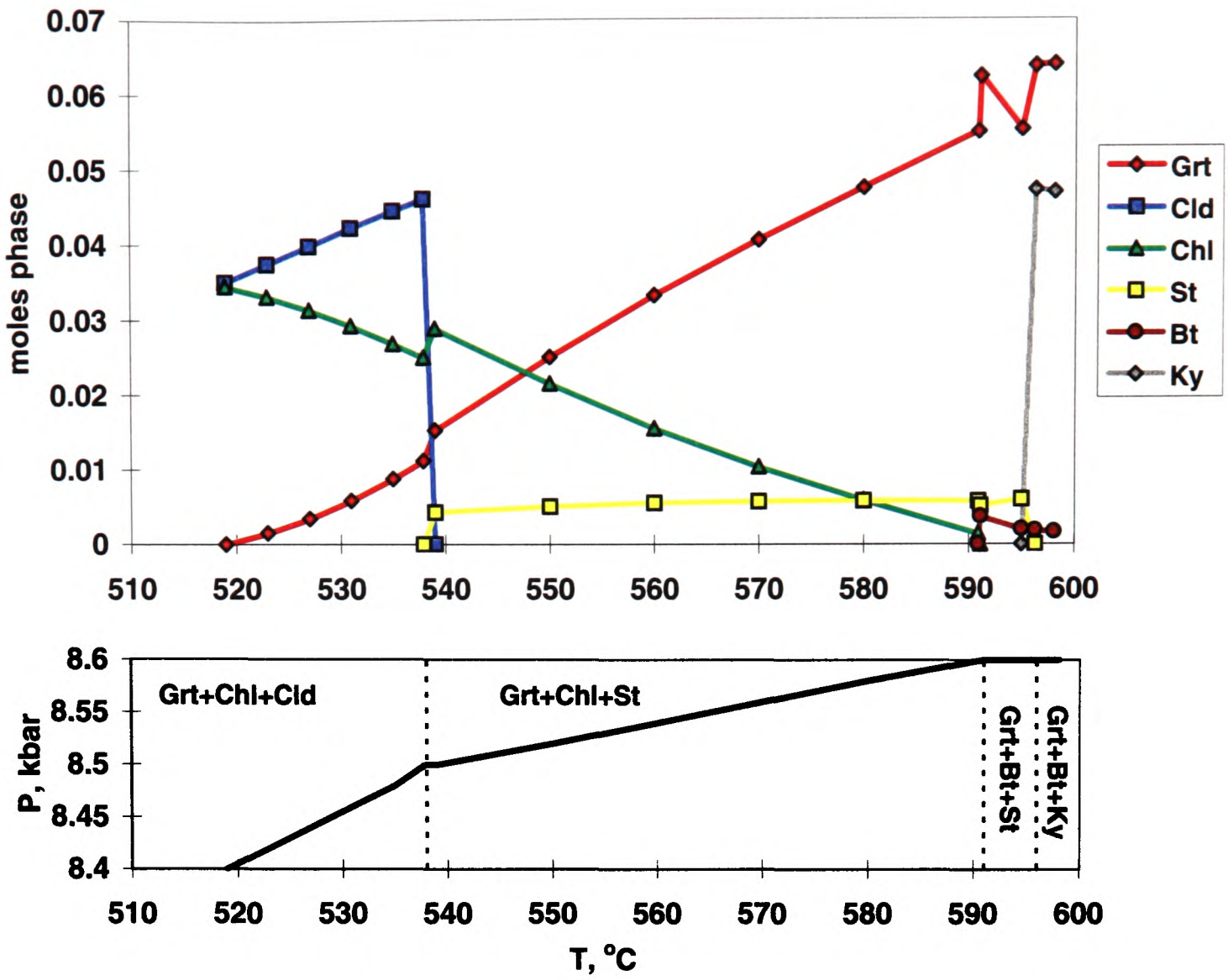


Figure 8.24: A plot showing changes in moles of phases along the plotted P-T procession of sample 19.

8.5.3 Summary of THERMOCALC modelling

THERMOCALC has been used to successfully reconstruct the P-T-X-M conditions of garnet formation, and by using a P-T pseudosection calculated from a fractionated bulk composition, has been able to calculate garnet rim conditions. This gives two points for the evolution of the Hoosac garnets. Initial garnet growth conditions are predicted to lie within Chl+Cld, and final garnet growth conditions within St+Chl, St+Bt or Ky+Bt. These reconstructions fit the petrological model.

Regarding the accuracy of calculation, all metamorphic modelling is subject to a number of assumptions. In the case of THERMOCALC, the way system components are apportioned into phases may be different from observed.

Uncertainties of the estimation of conditions of garnet initiation and growth are shown in figure 8.25. This plots changes in the estimated moles of chlorite and chloritoid as a function of pressure change at the initial point of garnet growth in sample 6, at 8.6kbar ± 1. Chloritoid molar estimation shows a change of 25% over 2kbar.

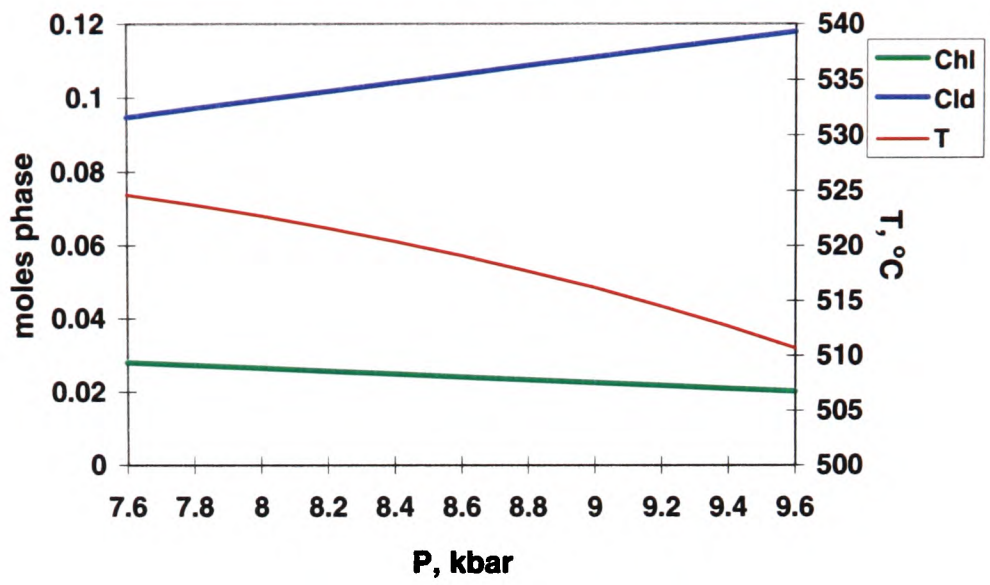


Figure 8.25: Changes in modes of chlorite and chloritoid at the initial point of garnet growth in sample 6, as a function of pressure change. Estimation of 8.6kbar ± 1kbar.

Peak condition calculations give the opportunity to compare the model with what is observed in the rock. A common problem with all three samples was the inability to correctly model the garnet rim mole fractions, with THERMOCALC consistently underestimating grossular, and overestimating pyrope. The former is probably due to the partitioning of Ca into paragonite solid-solution; THERMOCALC commonly assumes over 10% Ca, whilst Hoosac analyses show much less margarite content. In addition, muscovite is calculated to be more iron-rich than is observed, which has some implications given the proportion of muscovite in the rocks.

Sample 6 reproduces the observed phase volumes fairly well, although it calculates twice the volume percent of staurolite than is present (at the expense of paragonite). Samples R76 and 19 suffer from the inability to predict the co-existence of chlorite and biotite over large areas of P-T space. Whilst much of the chlorite in the rocks may be of later, retrograde origin, some of it is original prograde chlorite, and as such represents a metastable phase. This aside, both samples R76 and 19 calculated peak phase volume percent are remarkably close to the observed volume percents.

Polymetamorphism

Petrological examination has shown the existence of two prograde garnet growth events separated by a period of deformation, of unspecified timescale. Garnet rim-rim cation profiles suggest slightly different P-T conditions for rim growth, perhaps higher T and lower P than the core. The spessartine profiles suggest that the second growth of garnet picked up from where the first left off.

However, there is a textural break, a hiatus in garnet growth, and this must be accommodated in the P-T modelling. Speculation on the processes which allow a second prograde metamorphic episode to occur without a period of garnet consumption must invariably focus on an evolving system overstepping until an equilibrium between the matrix and garnet rim (*i.e.* outer core) is reached. At this point garnet growth may recommence. Initial conditions of rim growth appear to be remarkably similar to final conditions of core growth.

While garnet cores grew within a matrix of Chl+Cld, rims are absent of chloritoid and thus imply that matrix chloritoid had been fully consumed before garnet rims started to grow. The relative lack of inclusions in the rims compared to the cores suggests that rim growth was more sluggish than core growth.

In summary, THERMOCALC has reconstructed reasonable garnet core conditions for all three rocks. Given their geographical proximity, it is reasonable that they should experience similar metamorphic conditions, and the fact that all three samples are calculated to commence garnet growth within a Chl+Cld matrix at *circa* 520°C and 8.5 kbar gives a framework within which a differential thermodynamic approach to model rock evolution can be applied.

8.6 PTGRID - modelling isotope fractionation with reaction progress

PTGRID is a computer program written by E.D. Young, Oxford University, and uses a modified Gibbs' method to allow prediction of oxygen isotope shifts as a function of reaction progress.

Using the reconstruction of conditions of garnet formation as calculated by THERMOCALC, PTGRID was employed to model associated oxygen isotope fractionations, using the formalism as set out by Young (1993).

8.6.1 Differential thermodynamics

Differential thermodynamics is a different approach to the one used by THERMOCALC. Spear (1989) describes how a set of linear differential equations can relate changes in the variables pressure, temperature, mineral composition and mineral modes (P-T-X-M). Known changes in one set of variables - for example zonation in a garnet - can be used to predict changes in other variables with the use of these differential relationships.

The following thermodynamic treatment is derived from Spear. This differential thermodynamic method satisfies conditions for homogeneous equilibrium by defining a Gibbs-Duhem equation for each phase k such that:

$$0 = -\hat{S}^{1bar,T}\mathrm{d}T + \hat{V}^{1bar,298}\mathrm{d}P + \sum X_i \mathrm{d}\mu_i \tag{8.8}$$

where i are phase components that describe the chemical variability of phase k, $\hat{S}^{1bar,T}$ is the molar entropy of k at specified conditions, T and P are temperature and pressure respectively, $\hat{V}^{1bar,298}$ is the molar volume of k, X_i is the mole fraction of i, and μ_i is the chemical potential of i in phase k.

For each linearly independent reaction r between components i in a heterogeneous system, equilibrium conditions are satisfied by:

$$0 = \sum_i \nu_{ir}\mu_i \tag{8.9}$$

where ν_{ir} is the stoichiometric coefficient for species i in reaction r. For conditions of heterogeneous equilibrium a complex set of equations relating changes in the chemi-

cal potentials of phase components and system components to changes in composition through the derivatives and second derivatives of the Gibbs' free energy function are required. By augmenting these with mass balance constraints, the number of degrees of freedom is reduced to two.

The differential form of equation 8.9 is then:

$$0 = \sum_i \frac{\partial(\nu_{ir}\mu_i)}{\partial T} \mathrm{d}T + \sum_i \frac{\partial(\nu_{ir}\mu_i)}{\partial P} \mathrm{d}P + \sum_i \frac{\partial(\nu_{ir}\mu_i)}{\partial X_j} \mathrm{d}X_j \tag{8.10}$$

where X_j is the mole fraction of component j. The coefficients are evaluated as follows:

$$\frac{\partial(\nu_{ir}\mu_i)}{\partial T} = \left(-\nu_{ir}\hat{S}_i^{1bar,T*} + \nu_{sr}R\ln a_s + \nu_{\mathrm{H_2O,r}}R\ln f_{\mathrm{H_2O}}^{P,T} + \nu_{\mathrm{H_2O,r}}RT\left(\frac{\partial \Gamma_{\mathrm{H_2O}}^*}{\partial T}\right)\right) \tag{8.11}$$

$$\frac{\partial(\nu_{ir}\mu_i)}{\partial P} = \left(\nu_{sr}\hat{V}_s^{1bar,298*}\right) \tag{8.12}$$

$$\frac{\partial(\nu_{ir}\mu_i)}{\partial X_j} = \sum_i \nu_{ir}\left(\frac{RT}{a_i}\frac{\partial a_i}{\partial X_j}\right) \tag{8.13}$$

where * indicates pure species, a_i is the activity of phase component i, $f_{\mathrm{H_2O}}^{P,T}$ is the fugacity of H_2O, $\Gamma_{\mathrm{H_2O}}^*$ the fugacity coefficient, $\hat{V}_s^{1bar,298*}$ the molar volume of s and R is the ideal gas constant.

The conditions for heterogeneous equilibrium are now satisfied by the simple summing of mole fractions of phase components that is imposed by stoichiometry for each phase k in the system:

$$0 = \sum_j \mathrm{d}X_{jk} \tag{8.14}$$

This equation comprises the relations among intensive variables in the heterogeneous thermodynamic system. Extensive variables, including molar quantities of phases M_k and molar amounts of system components η_l^{sys}, are included by adding one mass balance for each of the C system components of the form:

$$0 = \sum_k \left(\sum_j X_{jk}\epsilon_{jkl}\right) \mathrm{d}M_k + \sum_k \sum_j (M_k\epsilon_{jkl})\mathrm{d}X_{jk} - \mathrm{d}\eta_l^{\mathrm{sys}} \tag{8.15}$$

where ϵ_{jkl} is the number of moles of system component l in phase component j. A special case for this equation is that when there is no change in the moles of system component during reaction progress $\mathrm{d}\eta_l^{\mathrm{sys}}$=0 (*i.e.* a closed system). Equations 8.10, 8.14 and 8.15 represent a system of linear differential equations which can be solved simultaneously for changes in intensive and extensive variables in a heterogeneous thermodynamic system. The total variance of the system of equations is C + 2.

Addition of isotope equations

The following treatment is taken from Young (1993), where full derivation is described. Variations in mineral isotope ratios can be added to the thermodynamic equations above by the addition of equations for the total differentials of $\delta^{18}O$ for each phase i of interest:

$$d\delta^{18}O_i = \left(\frac{\partial\delta^{18}O_i}{\partial T}\right) dT + \sum_k \left(\frac{\partial\delta^{18}O_i}{\partial M_k}\right) dM_k + \sum_f \left(\frac{\partial\delta^{18}O_i}{\partial X_f}\right) dX_f + d\delta^{18}O_{sys} \quad (8.16)$$

where X_f represents the mole fraction of oxygen-bearing fluid species f in the fluid phase. Simultaneous solution of equations 8.10, 8.14, 8.15 and 8.16 allows quantitative assessment of the dependence of $\delta^{18}O$. Equation 8.16 adds one degree of freedom to the system, derived from the distinction between ^{18}O and ^{16}O. This is represented by the variable $\delta^{18}O_{sys}$. However, total variance remains $C + 2$ since ^{18}O is counted among the C system components. Coefficients for equation 8.16 are derived by differentiation of the expression:

$$\delta^{18}O_i = \sum_s \left(\frac{\omega_s M_s}{\tau}\right)\Delta^T_{is} + \sum_f \left(\frac{X_f \omega_f M_{\text{fluid}}}{\tau}\right)\Delta^T_{if} + \delta^{18}O_{sys} \quad (8.17)$$

where ω_s and ω_f are oxygens per mole of solid phase s and fluid species f respectively, τ is the total number of oxygens in the system, and Δ^T_{is} and Δ^T_{if} is the temperature-dependent equilibrium difference in $\delta^{18}O$ between phase i and either phase s or fluid species f (see chapter 1) expressed as:

$$\Delta^T_{is} = \frac{A_{is}}{T^2} + \frac{B_{is}}{T} + C_{is} \quad (8.18)$$

Equation 8.16 closely approximates a mass balance equation for ^{18}O. Note that this is a close approximation since the delta notation does not describe absolute masses, but due to the relative abundancies of the isotopes it is a good enough approximation. The resulting coefficients are:

$$\left(\frac{\partial\delta^{18}O_i}{\partial T}\right) = \sum_{s\neq i}\left(\frac{-2A_{is}\omega_s M_s}{\tau T^3} - \frac{B_{is}\omega_s M_s}{\tau T^2}\right) + \sum_f \left(\frac{-2A_{if}\omega_f X_f M_{\text{fluid}}}{\tau T^3} - \frac{B_{if}\omega_f X_f M_{\text{fluid}}}{\tau T^2}\right) \quad (8.19)$$

$$\left(\frac{\partial\delta^{18}O_i}{\partial M_k}\right) = \frac{\Delta^T_{ik}\omega_k}{\tau} - \frac{\omega_k(\Sigma_s \Delta^T_{is}\omega_s M_s + \Sigma_f \Delta^T_{if}\omega_f X_f M_{\text{fluid}})}{\tau^2} \quad (8.20)$$

$$\left(\frac{\partial\delta^{18}O_i}{\partial X_f}\right) = \frac{\Delta^T_{if}\omega_f M_{\text{fluid}}(\tau - \omega_f X_f M_{\text{fluid}})}{\tau^2} - \omega_f M_{\text{fluid}}\left(\frac{\Sigma_s \Delta_{is}\omega_s M_s + \Sigma_{f_j\neq f}\Delta_{if_j}\omega_{f_j}X_{f_j}M_{\text{fluid}}}{\tau^2}\right) \quad (8.21)$$

Thus simultaneous solutions of equations 8.10, 8.14, 8.15 and 8.16 permit calculation of shifts in mineral $\delta^{18}O$ associated with variations in mode, T, P, phase composition and fluid conditions. This is the approach taken by the program PTGRID.

The advantages to using differential thermodynamics coupled with extensive constraints are:

1. The high variance predicted by Gibbs' phase rule can be reduced to manageable levels. This allows the behaviour of a system with known mineral modes and compositions to be modelled in response to independent changes in only two intensive/extensive variables, P, and T (a principle also used with THERMOCALC).

2. Differential thermodynamics does not require a constant of integration (enthalpy) that is necessary in absolute geobarometry. It deals only with *changes* in entropy and volume, both of which are large changes of small values. Therefore errors in predicted changes of P and T using the differential approach will be smaller than the errors associated with conventional thermobarometry.

3. By dealing with derivatives of activity-composition relationships, the activity coefficient term can be ignored so long as it is independent of composition. This reduces the problems associated with non-ideal mixing; activity modelling in PTGRID is accommodated with the general form $X_j = a_j$.

8.7 PTGRID - application of the theory

PTGRID follows the thermodynamic treatment as set out in Young (1993) for the calculation of oxygen isotope shifts with reaction progress. PTGRID as a program is limited, however it is the only code available to model such oxygen isotope fractionation. Here is described the application of PTGRID to the Hoosac rocks, with some initial conclusions drawn. Although measured core-rim oxygen isotope profiles are indistinct, an attempt is still made to accommodate perceived isotope shifts.

I have taken the original version of PTGRID and modified it to use the thermodynamic dataset of Holland & Powell (1998) to provide continuity with the THERMOCALC mod-

elling. In addition, the isotope fractionation factors of Zheng (1993a,b, 1999) have been incorporated in preference to those of Richter & Hoernes (1988) since the latter does not include fractionation factors for chloritoid.

Finally, the program has been modified to exclude calcium from the modelling. Although calcium is important for correctly modelling garnet stability, when using a forward modelling approach with PTGRID calcium causes a problem with Hoosac rocks. In the Hoosac Schist calcium is found only in garnet, as a margarite component of paragonite solid solution and as minor apatite inclusions. In most grades there is no primary plagioclase, certainly not in the three samples modelled. Since PTGRID treats micas as pure end-members, paragonite is modelled as a sodic mica. Thus, there is no phase to balance calcium against when growing garnet, and as a consequence of this, garnet growth will follow a grossular isopleth which is near-isothermal.

Therefore, following experiments with Ca included, calcium was removed from the system entirely. This renders garnet as a three end-member phase. Furthermore, garnet growth reactions can be accurately modelled within MnFMASH, since using PTGRID paragonite and muscovite play no part in the garnet growth reactions.

An attempt to model the reactions as calculated by THERMOCALC is made here with a view to investigating isotope shifts during growth of the Hoosac garnets. Firstly, a closed system is modelled and then finally the effect of non-equilibrium fluid infiltration is considered.

Isotopic equilibrium

The modelling here has the additional assumption of isotopic equilibrium, as well as chemical equilibrium. This means that as reactions proceed, newly-formed products are in equilibrium with each other - *i.e.* a reacting garnet rim is in equilibrium with the evolving matrix. This supposition of isotopic equilibrium is supported by other stable isotope studies of metamorphic rocks which show this is a valid assumption (*e.g.* Chamberlain & Conrad, 1993; Kohn, 1993).

8.7.1 Modelling results

PTGRID allows calculation of an evolving chemical system with the constraint of Duhem's Theorem. It allows initial P-T-X-M conditions to be stipulated, and then a number of variables to be declared as independent, thus driving the reaction. By default the remainder of the variables are dependent.

The variables that can be defined are:

- $\mathrm{d}T$ and $\mathrm{d}P$ - changes in pressure and temperature
- $\mathrm{d}X_j$ - changes in the mole fractions of system components j
- $\mathrm{d}M_k$ - changes in the moles of phases k
- $\mathrm{d}\eta_i$ - changes in the moles of system components i
- $\mathrm{d}\delta^{18}\mathrm{O}_k$ - changes in $\delta^{18}\mathrm{O}$ of phases k
- $\mathrm{d}\delta^{18}\mathrm{O}_{\mathrm{sys}}$ - changes in the $\delta^{18}\mathrm{O}$ of the system as a whole

For example in the model Hoosac system when growing the garnet core, the phases are Qtz + Grt + Chl + Cld + H_2O. Therefore the variables are:

- $\mathrm{d}T, \mathrm{d}P$
- $\mathrm{d}X^{\mathrm{Grt}}_{\mathrm{Pyp}}, \mathrm{d}X^{\mathrm{Grt}}_{\mathrm{Alm}}, \mathrm{d}X^{\mathrm{Grt}}_{\mathrm{Sps}}, \mathrm{d}X^{\mathrm{Chl}}_{\mathrm{Mg}}, \mathrm{d}X^{\mathrm{Chl}}_{\mathrm{Fe}}, \mathrm{d}X^{\mathrm{Chl}}_{\mathrm{Mn}}, \mathrm{d}X^{\mathrm{Cld}}_{\mathrm{Mg}}, \mathrm{d}X^{\mathrm{Cld}}_{\mathrm{Fe}}, \mathrm{d}X^{\mathrm{Cld}}_{\mathrm{Mn}}$
- $\mathrm{d}M_{\mathrm{Qtz}}, \mathrm{d}M_{\mathrm{Grt}}, \mathrm{d}M_{\mathrm{Chl}}, \mathrm{d}M_{\mathrm{Cld}}, \mathrm{d}M_{\mathrm{H_2O}}$
- $\mathrm{d}\eta_{\mathrm{SiO_2}}, \mathrm{d}\eta_{\mathrm{Al_2O_3}}, \mathrm{d}\eta_{\mathrm{FeO}}, \mathrm{d}\eta_{\mathrm{MgO}}, \mathrm{d}\eta_{\mathrm{MnO}}, \mathrm{d}\eta_{\mathrm{H_2O}}$
- $\mathrm{d}\delta^{18}\mathrm{O}_{\mathrm{Qtz}}, \mathrm{d}\delta^{18}\mathrm{O}_{\mathrm{Grt}}, \mathrm{d}\delta^{18}\mathrm{O}_{\mathrm{Chl}}, \mathrm{d}\delta^{18}\mathrm{O}_{\mathrm{Cld}}, \mathrm{d}\delta^{18}\mathrm{O}_{\mathrm{H_2O}}, \mathrm{d}\delta^{18}\mathrm{O}_{\mathrm{sys}}$

Gibbs' phase rule dictates that the total variance is characterized by three intensive degrees of freedom. The total variance, including both intensive and extensive independent parameters is nine (C + 2, where C refers to the six system components plus $^{18}\mathrm{O}$).

8.7.2 Closed system

Real metamorphic systems are rarely closed systems; in metamorphic study a closed system often refers to a chemical system that is isolated from the outside with the exception of water; a system open to external fluids (Spear, 1993). However, in thermodynamics a closed system refers to a chemical system that is free to evolve but cannot exchange *any* chemical species with the outside world. Additionally, a thermodynamically closed system does allows exchange of energy between the evolving chemical system and the outside. This is the situation that is modelled here, closed to matter but open to energy.

Modelling of this is accomplished by setting the parameters $\mathrm{d}\eta_i = 0$ and $\mathrm{d}\delta^{18}\mathrm{O}_{\mathrm{sys}} = 0$, thus stipulating no change in either moles of system components or of the $\delta^{18}\mathrm{O}$ of the system as a whole. This allows categorization of the evolution of $\delta^{18}\mathrm{O}_{\mathrm{Grt}}$ without reference to external factors.

As described by Young (1993) the functional relation between $\mathrm{d}\delta^{18}\mathrm{O}_i$ for phases i and reaction progress, $\mathrm{d}\xi$ is:

$$\delta^{18}\mathrm{O}_i = \sum_k \nu_k \omega_k \left[\frac{\Delta_{ik}}{\tau} - \sum_j \frac{(\omega_j \Delta_{ij} M_j)}{\tau^2} \right] \mathrm{d}\xi \tag{8.22}$$

Using the conditions of garnet core formation calculated by THERMOCALC, the evolution of garnets in samples 6, R76 and 19 was modelled. Cores are approximately three-quarters of the radius of the garnet, however when this is translated into garnet volume it is approximately 42%. Thus the garnet cores were allowed to grow until 42% of the total garnet moles (as used for bulk rock calculation) were produced. Table 8.10 summarizes how the garnet radius is apportioned.

Sample	Total moles	Core moles	Rim moles
6	0.0678	0.0286	0.0392
R76	0.0783	0.0330	0.0453
19	0.0826	0.0349	0.0477

Table 8.10: Division of moles of garnet between core and rim for the purposes of PTGRID modelling, by sample.

Quartz is taken as excess and a value of 0.4 moles is stipulated, which refers to approximately 10% volume Qtz. Water phase is taken as 0.02 moles, which is approximate to a rock porosity of 0.2%. This value for porosity is similar to the assumptions of Young & Rumble (1993), 0.2%, and Chamberlain & Conrad (1993), 0.1%. The garnet core was grown by the consumption of chlorite and quartz, in the system Qtz + Grt + Chl + Cld + H_2O. This was accomplished until the desired moles of garnet core was grown. The garnet rim was then grown with staurolite at the expense of quartz and chloritoid (in the system Qtz + Grt + Cld + St + H_2O), until all the chloritoid was consumed, and then the remainder of the rim grown from any chlorite left over from the first stage (Qtz + Grt + Chl + St + H_2O). A summary of the starting parameters for this forward-modelling is seen in table 8.11.

Thus for the garnet cores, a total of nine independent variables can be set (see section 8.7.1). Given the stipulation for a closed system that $d\eta_i = 0$ and $d\delta^{18}O_{sys} = 0$, this leaves two other variables. dT was set for an increment of +0.05°C. In addition since the aim was to grow garnet, dM_{Grt} is set to +0.0002 moles.

The results of this forward-modelling is shown in figures 8.26, 8.27, 8.28, and 8.29, for samples 6, 6a, R76 and 19a respectively. Plotted with these are measured cation profiles, which have been normalized without grossular. Sample 6 is a special case. The measured garnet 6a is believed to represent garnet growth during the second stage of garnet production (*i.e.* rim growth). Sample 6a garnet is a small (2mm) garnet by Hoosac standards, and core cation concentrations are similar to that seen in the inner rim in the larger garnets from sample 6. Thus although figure 8.26 shows large garnet measured and modelled core-rim changes for a typical sample 6 garnet, figure 8.27 shows this extrapolated for sample 6a.

The results show strong similarity with measured spessartine profile (especially in the case of R76), however the model enriches in X_{Mg} more rapidly than is observed. These results also show consistent $\delta^{18}O$ enrichment during prograde garnet growth of between 0.6-0.8‰ for all samples. This does not match the measured isotope profiles in samples R76 and 19a; these show a decrease in $\delta^{18}O$ through the core, and then an increase towards the rim. Thus closed-system modelling cannot adequately accommodate the observed shifts.

Sample	**6**			**R76**			**19a**		
	core	*rim 1*	*rim 2*	*core*	*rim 1*	*rim 2*	*core*	*rim 1*	*rim 2*
T°C	519.10	526.20	531.00	514.90	523.10	524.30	519.1	527.80	529.75
P bar	8600	8600	8600	8500	8500	8500	8400	8400	8400
M_{Grt}	0.0001	0.0285	0.0517	0.0001	0.0329	0.0377	0.0001	0.0349	0.0427
X_{Pyp}	0.060	0.127	0.223	0.050	0.106	0.129	0.060	0.144	0.188
X_{Alm}	0.820	0.834	0.752	0.840	0.873	0.853	0.860	0.839	0.798
X_{Sps}	0.120	0.040	0.026	0.110	0.022	0.019	0.080	0.017	0.014
M_{Chl}	0.0244	-	0.0075	0.0426	-	0.0207	0.0345	-	0.0113
X_{Mg}	0.35	-	0.524	0.280	-	0.438	0.300	-	0.509
X_{Fe}	0.64	-	0.474	0.710	-	0.561	0.690	-	0.490
X_{Mn}	0.01	-	0.002	0.010	-	0.001	0.010	-	0.002
M_{Cld}	0.1065	0.1065	-	0.0212	0.0212	-	0.0350	0.0350	-
X_{Mg}	0.18	0.318	-	0.140	0.252	-	0.160	0.320	-
X_{Fe}	0.79	0.674	-	0.840	0.745	-	0.830	0.678	-
X_{Mn}	0.03	0.008	-	0.020	0.003	-	0.010	0.002	-
M_{St}	-	0.0001	0.0094	-	0.001	0.0021	-	0.0001	0.0032
X_{Mg}	-	0.160	0.276	-	0.160	0.192	-	0.150	0.197
X_{Fe}	-	0.830	0.718	-	0.830	0.799	-	0.840	0.795
X_{Mn}	-	0.010	0.006	-	0.010	0.009	-	0.010	0.008
M_{Qtz}	0.4000	0.3621	0.3296	0.4000	0.3563	0.3496	0.4000	0.3536	0.3427
$M_{\mathrm{H_2O}}$	0.0200	0.0957	0.1839	0.0200	0.1075	0.1258	0.0200	0.1128	0.1424
$\mathrm{d}T$	0.05	0.05	0.05	0.05	0.05	0.05	0.05	0.05	0.05
$\mathrm{d}M_{\mathrm{Grt}}$	0.0002	0.0002	0.0002	0.0002	0.0002	0.0002	0.0002	0.0002	0.0002
$\mathrm{d}\delta^{18}\mathrm{O}_{\mathrm{sys}}$	0	0	0	0	0	0	0	0	0
$\mathrm{d}\eta_i$	0	0	0	0	0	0	0	0	0

Table 8.11: Parameters for closed system modelling.

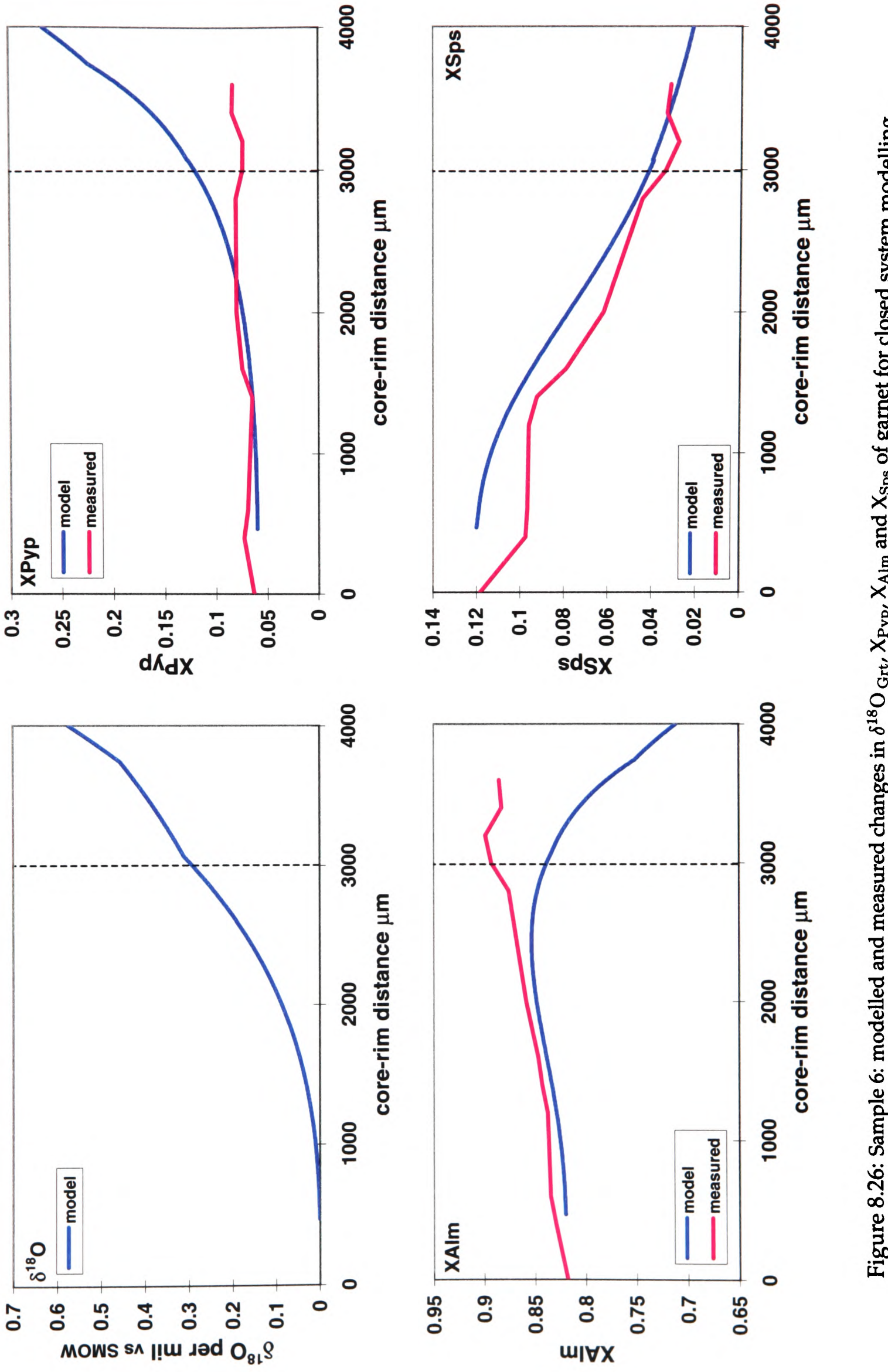
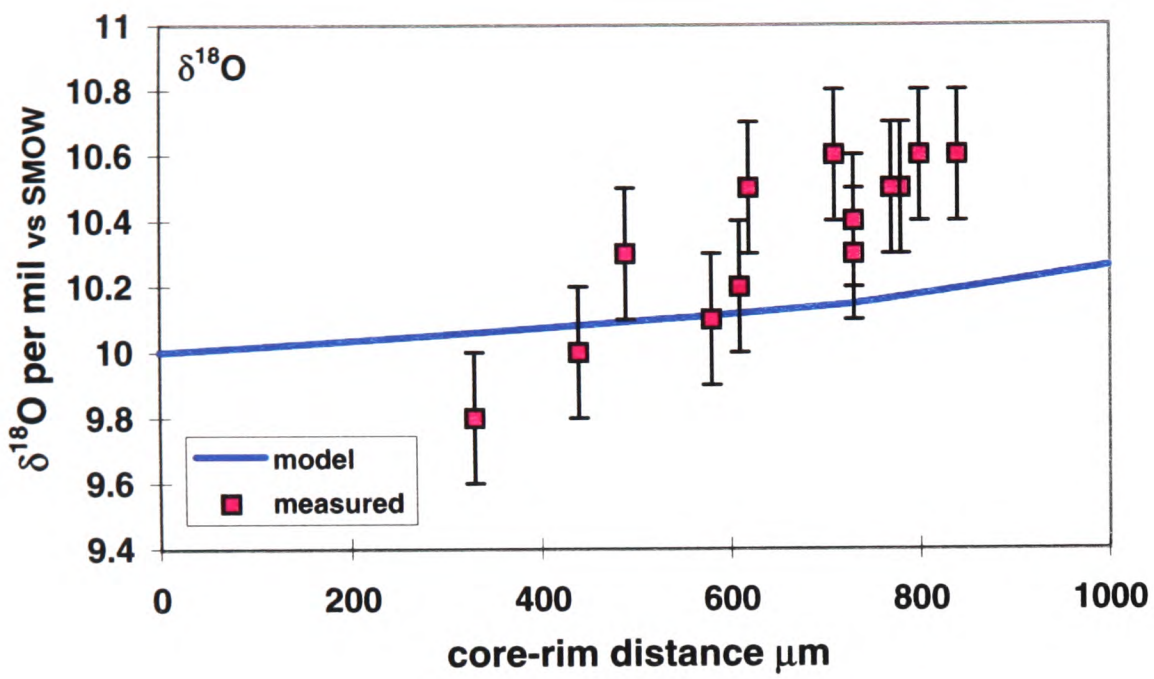
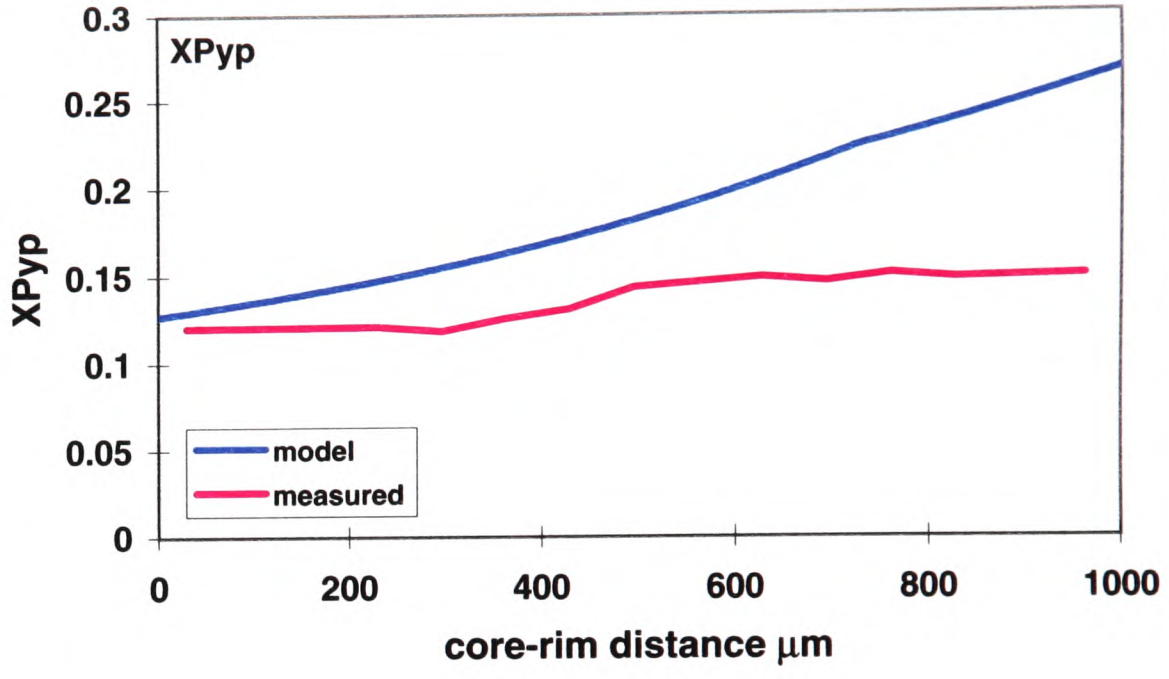
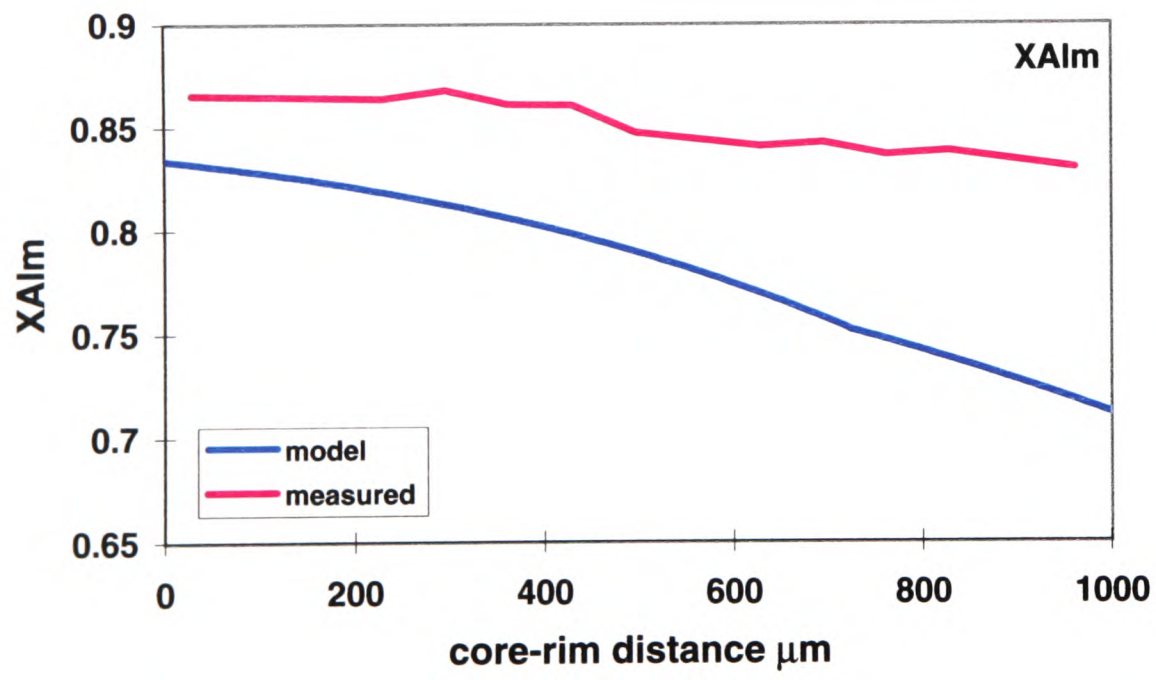


Figure 8.26: Sample 6: modelled and measured changes in $\delta^{18}O$, X_{Grt}, X_{Pyp}, X_{Alm} and X_{Sps} of garnet for closed system modelling.







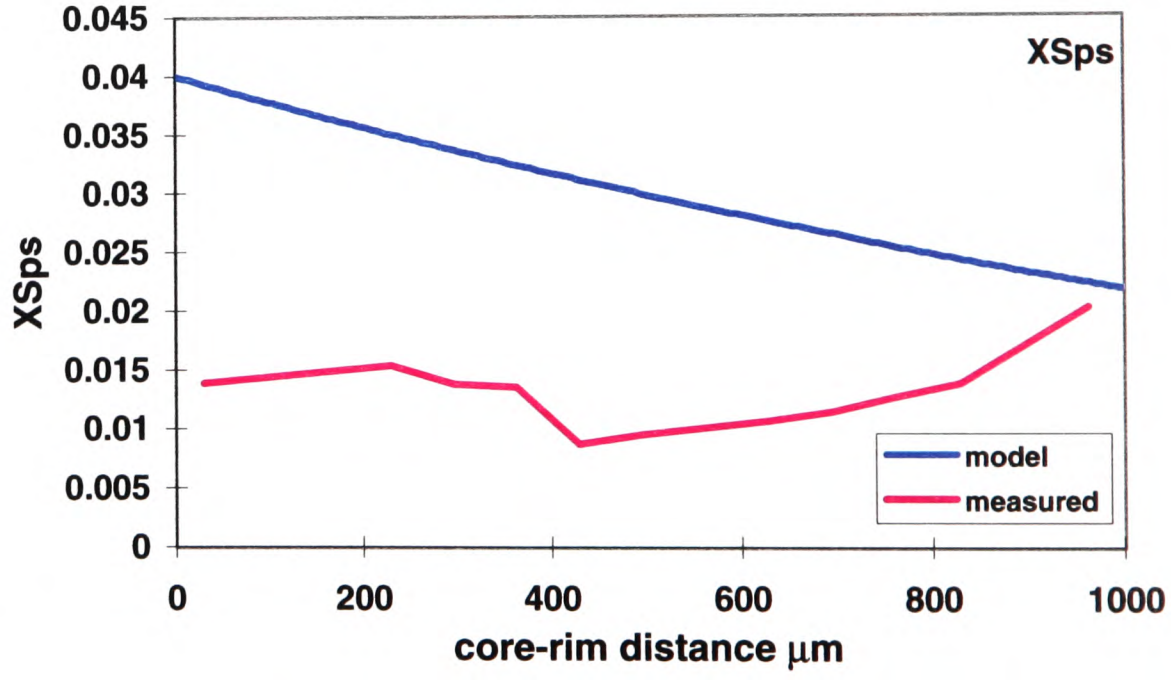
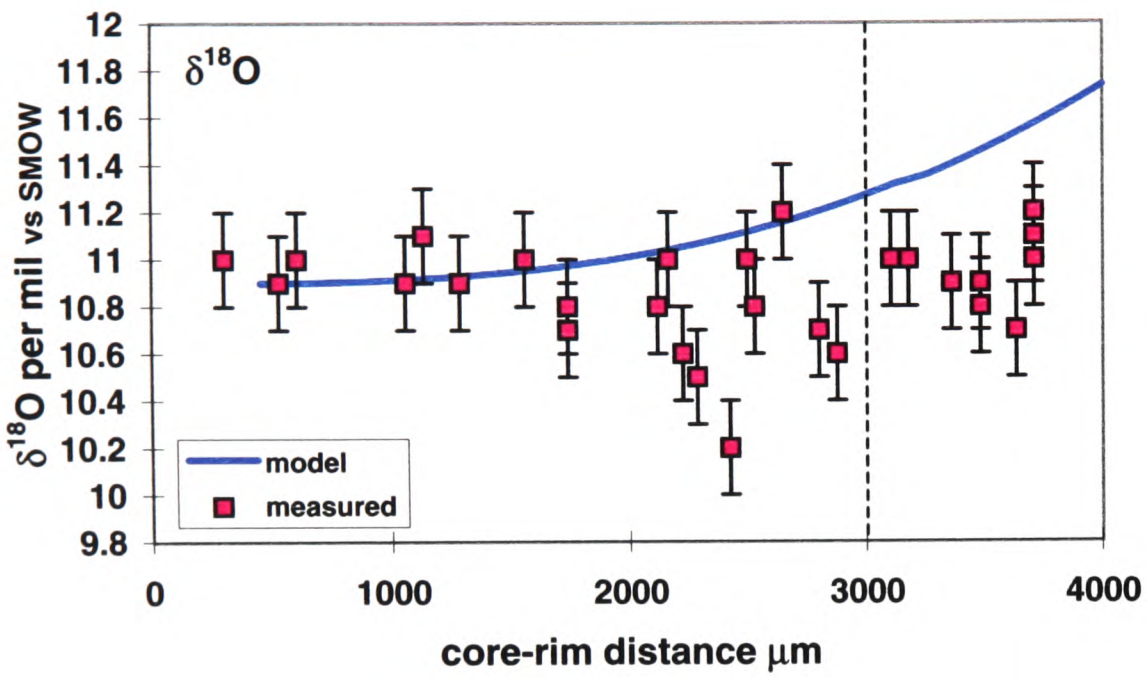


Figure 8.27: Sample 6a: modelled and measured changes in $\delta^{18}O_{Grt}$, X_{Pyp}, X_{Alm} and X_{Sps} of garnet for closed system modelling. Sample 6a is considered to be a product of the second stage of garnet growth; here cation and isotope changes are plotted against the rim part of the model garnet. Sample 6 has been affected by later cation diffusion causing enrichment in X_{Sps} near the rim. Isotope errors are ± 0.2‰ .



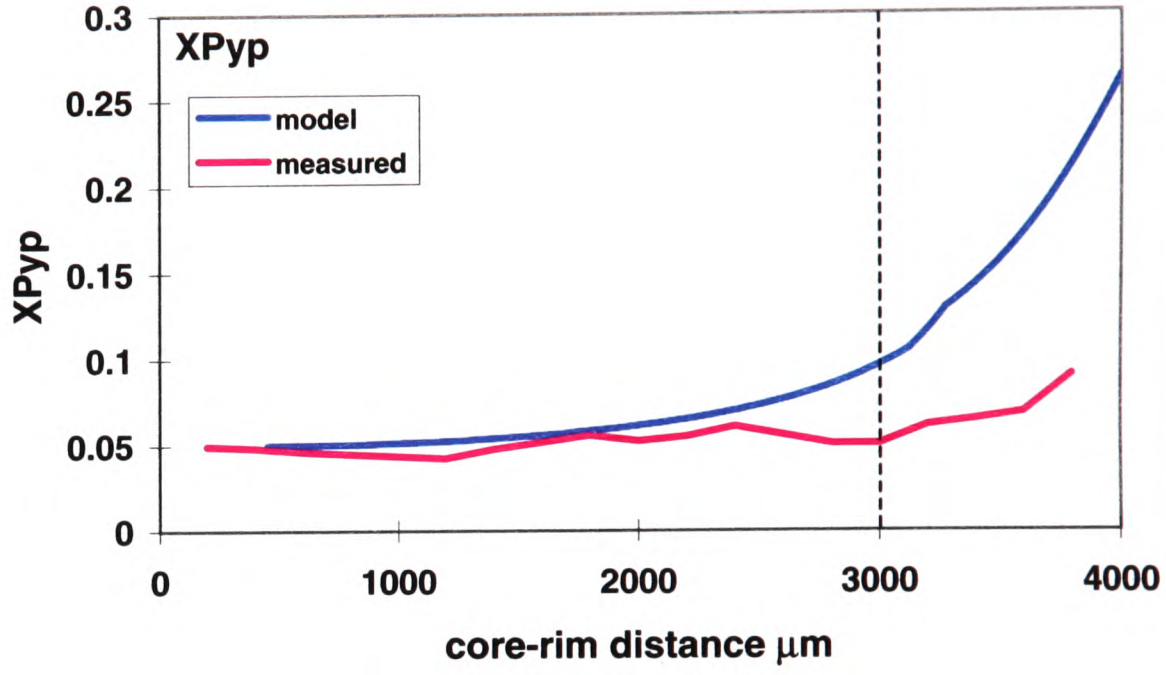
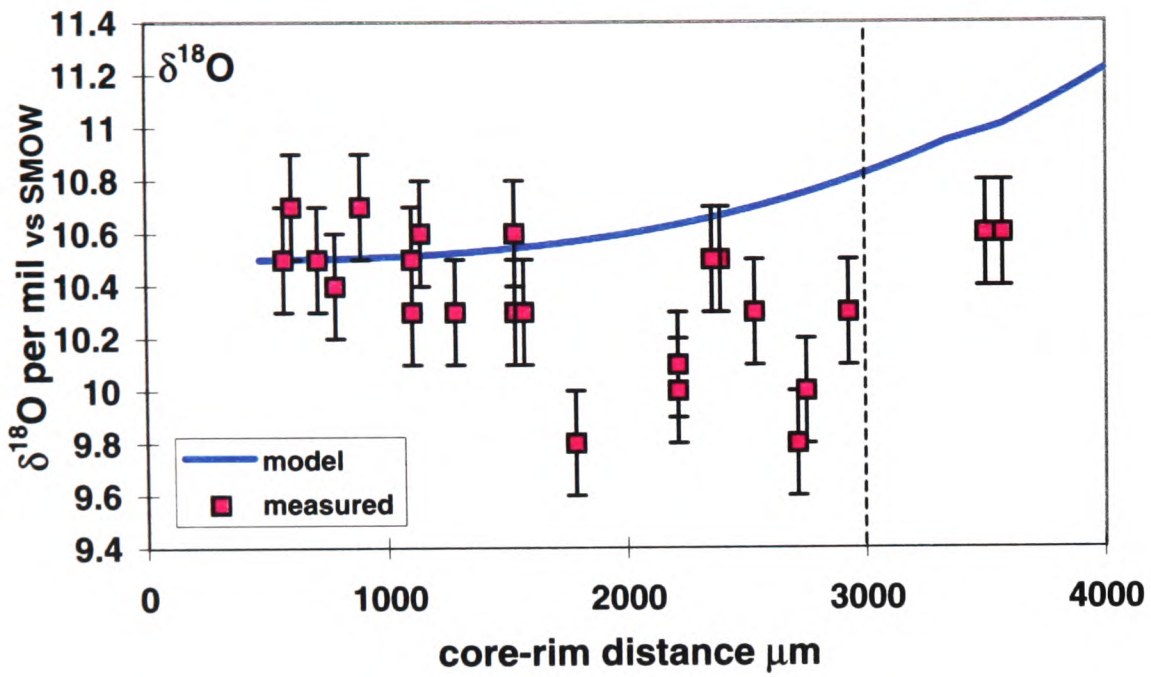
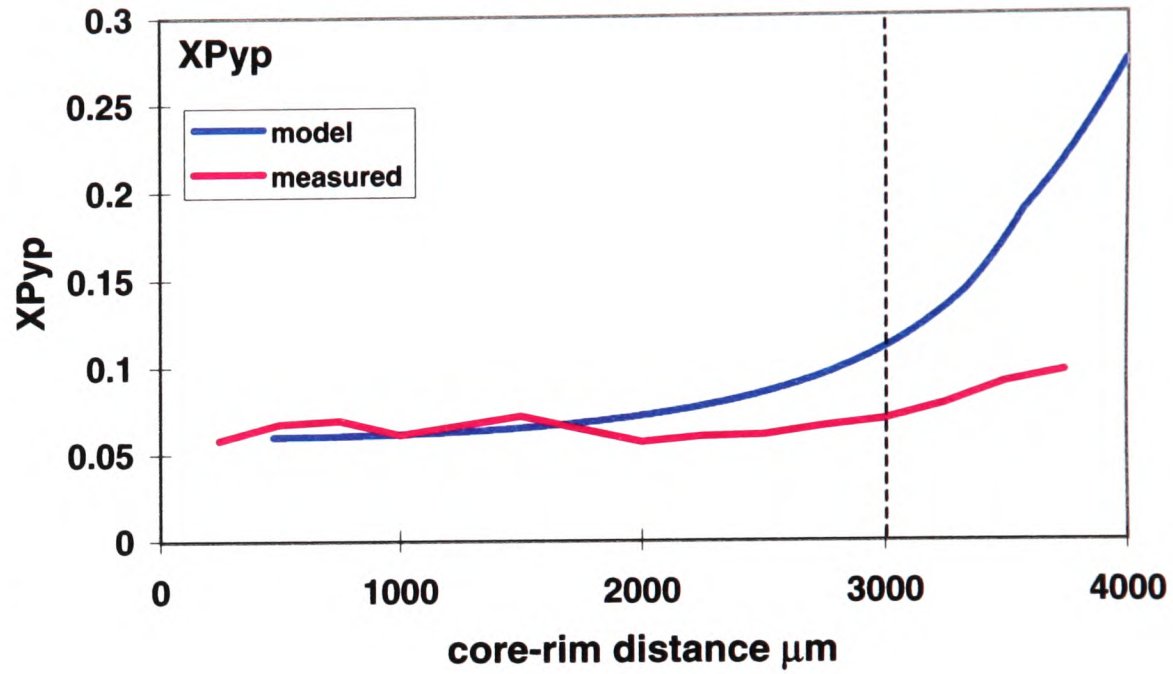
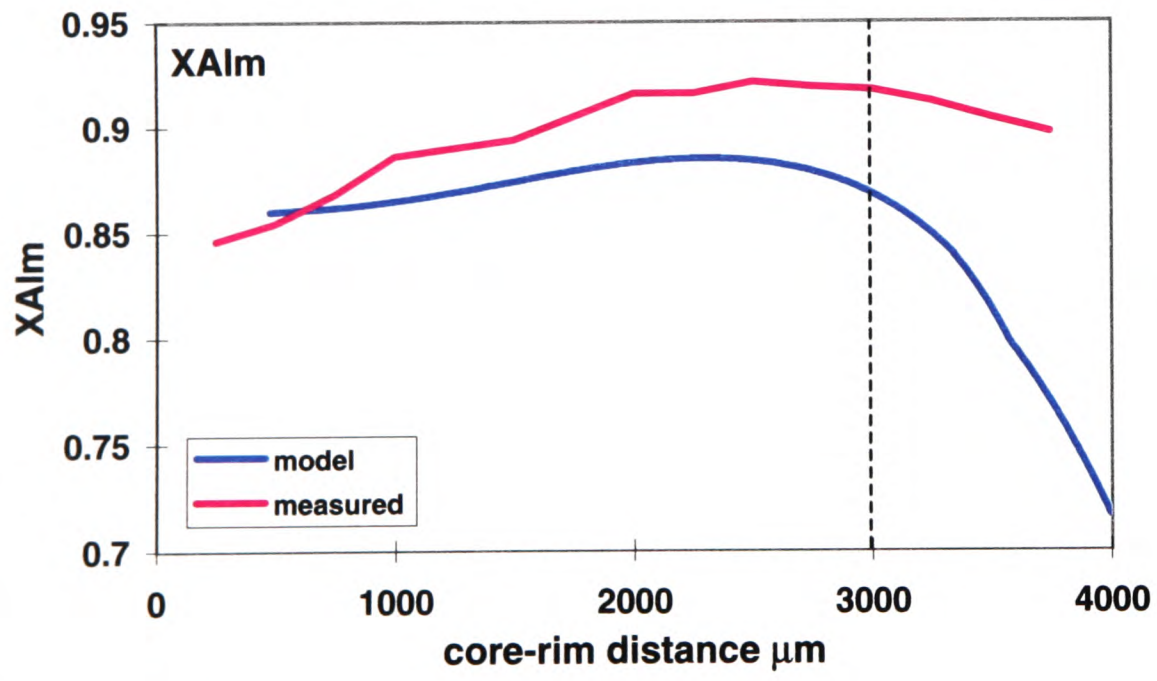


Figure 8.28: Sample R76: modelled and measured changes in $\delta^{18}O_{Grt}$, X_{Pyp}, X_{Alm} and X_{Sps} of garnet for closed system modelling. Dotted line marks transition from core to rim. Isotope errors are ± 0.2‰ .







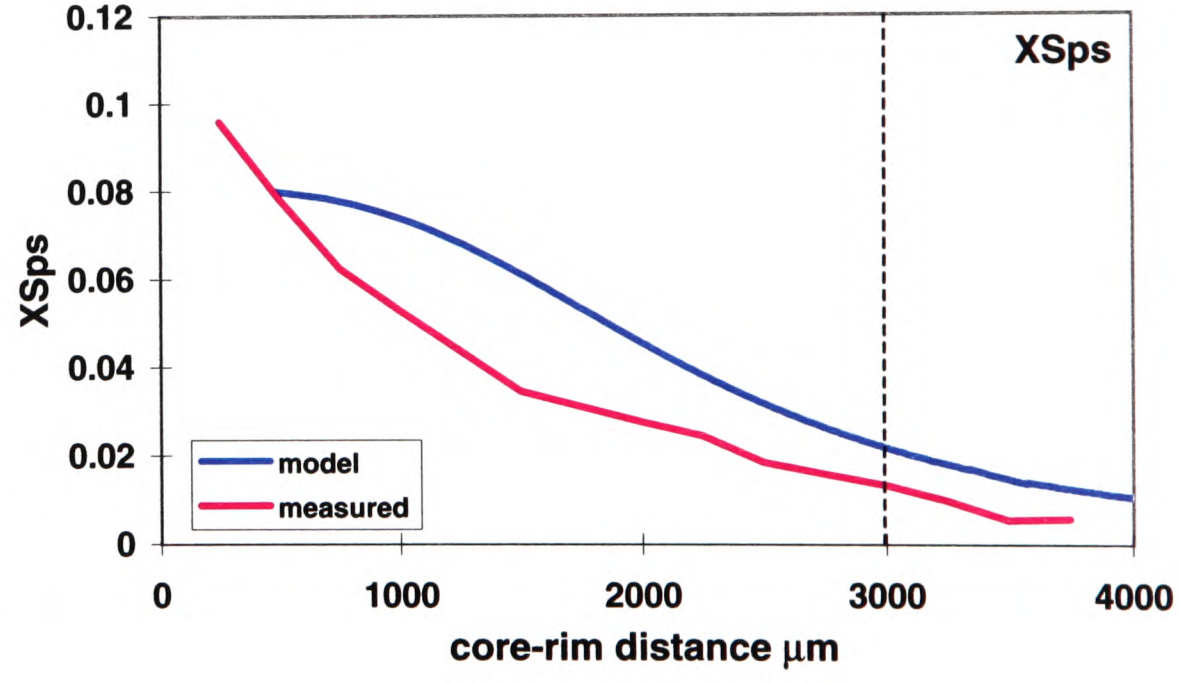


Figure 8.29: Sample 19a: modelled and measured changes in $\delta^{18}O_{Grt}$, X_{Pyp}, X_{Alm} and X_{Sps} of garnet for closed system modelling. Dotted line marks transition from core to rim. Isotope errors are $\pm$ 0.2‰ .

8.7.3 Fluid infiltration modelling

The results seen with the isolated system modelling confirm that prograde garnet growth yields positive core-rim $\delta^{18}O$ zoning, a result confirmed by other studies (*e.g.* Chamberlain & Conrad, 1991; Kohn *et al.*, 1993; Young & Rumble, 1993). However, since metamorphic systems are rarely closed systems and are open to external (non-equilibrium) fluid, an attempt is made here to use PTGRID to calculate infiltration effects.

The first assumption is of a fixed rock porosity. This is accomplished by setting M_{H_2O} as a value determined by porosity, and fixing this such that $dM_{H_2O} = 0$, *i.e.* there is constant moles of water phase. This also assumes the fluid completely occupies an interconnected pore volume. The total M_{H_2O} at any instant includes both *externally*-derived H_2O and that produced *internally* by reaction.

By splitting the component of fluid into H_2O_{int} and H_2O_{ext}, the model can allow internal fluid to be in equilibrium with the evolving chemical system and external fluid to have a fixed isotopic value. Thus modelling fluid infiltration is accomplished by an additional phase. Additionally, $d\delta^{18}O_{sys} = 0$ is replaced by an equation relating $\delta^{18}O_{sys}$ to other parameters in the system and the external fluid:

$$\delta^{18}O_{sys} = \sum_s \frac{\omega_s M_s}{\tau}\delta^{18}O_s + \frac{M^{ext}_{H_2O}}{\tau}\delta^{18}O^{ext}_{H_2O} + \frac{M^{int}_{H_2O}}{\tau}\delta^{18}O^{int}_{H_2O} \tag{8.23}$$

where subscripts 'ext' and 'int' refer to externally derived and internally produced H_2O respectively. The oxygen isotopic composition of internally produced water, $\delta^{18}O^{int}_{H_2O}$ is taken to be the value dictated by equilibrium with solid phases such that only changes in $M^{ext}_{H_2O}$ can affect changes in $\delta^{18}O_{sys}$. Additionally, influx of fluid is represented by:

$$dM^{ext}_{H_2O} = d\eta^{sys}_{H_2O} \tag{8.24}$$

and thus followed by differentiation of 8.23 yields:

$$d\delta^{18}O_{sys} = \frac{1}{\tau^2}\left(\sum_s \omega_s M_s(\delta^{18}O^{ext}_{H_2O} - \delta^{18}O_s)\right) d\eta^{sys}_{H_2O} + \frac{1}{\tau^2}M^{int}_{H_2O}(\delta^{18}O^{ext}_{H_2O} - \delta^{18}O^{int}_{H_2O})d\eta^{sys}_{H_2O} \tag{8.25}$$

Thus with the conditions of $dM_{H_2O} = 0$ and $d\eta^{sys}_{l\neq H_2O} = 0$, calculation of changes in mineral $\delta^{18}O$ with reaction progress as water with a fixed $^{18}O/^{16}O$ flows through the rock at constant porosity is possible.

Solving equation 8.25 for shifts in $\delta^{18}O$ with reaction progress where $d\eta^{sys}_{H_2O} = -d\xi$ (Young, 1993) gives:

$$d\delta^{18}O_i = \sum_s \nu_s \omega_s \left[\frac{\Delta^T_{is}}{\tau} - \frac{\Sigma_j \omega_j \Delta^T_{ij} M_j}{\tau^2} \right] d\xi - \left[\frac{\Sigma_k \omega_k M_k (\delta^{18}O^{ext}_{H_2O} - \delta^{18}O_k)}{\tau^2} \right] d\xi \quad (8.26)$$

In order to cater for external influx and outflow of fluid $d\eta_{H_2O}$ must be set to a value depending on quantity of infiltrating fluid.

Application of fluid infiltration model

Figure 8.30 shows core-rim profiles from samples R76 and 19a with a fitted trendline. Both show a decrease in $\delta^{18}O$ from inner to outer core; this is more apparent in sample 19a. The fitted line shows that projected back to the core sample R76 should decrease from 11.05 → 10.75‰ (-0.3‰), and sample 19a should decrease from 10.67 → 10.07‰ (-0.6‰).

This potential negative $\delta^{18}O$ zoning observed in the cores of samples R76 and 19a implies either garnet growth during temperature decrease *or* equilibrium with an external fluid during garnet growth. The former scenario is considered unlikely here from the results of the THERMOCALC modelling, and so an attempt to quantify possible external fluid effects is made with PTGRID.

Following the rules of fluid infiltration, dM_{Grt} was declared an independent variable, as was dT. These were both increased by an identical amount as with isolated system modelling with each iteration. Thus dT = +0.05°C and dM_{Grt} = +0.0002 moles.

A constant porosity of 0.2% was assumed such that M_{H_2O} = 0.02 moles and $dM_{H_2O} = 0$. In addition, $\delta^{18}O_{sys}$, $d\delta^{18}O_k$, $d\eta_{\neq H_2O}$, dP and X_j were all set as dependent variables. This allows the $\delta^{18}O_{sys}$ to evolve as well. After each reaction step, the model mixes the infiltrating fluid (incremented by $d\eta_{H_2O}$) with internal fluid to calculate $\delta^{18}O_{H_2O}$. Core starting conditions were taken as the same as in the isolated system.

To model the isotope shift with reaction progress at constant porosity leaves two variables: $\delta^{18}O^{ext}_{H_2O}$ and $d\eta^{ext}_{H_2O}$, the isotopic composition of the infiltrating fluid, and the change in moles of infiltrating H_2O respectively. If all else is held constant, these two

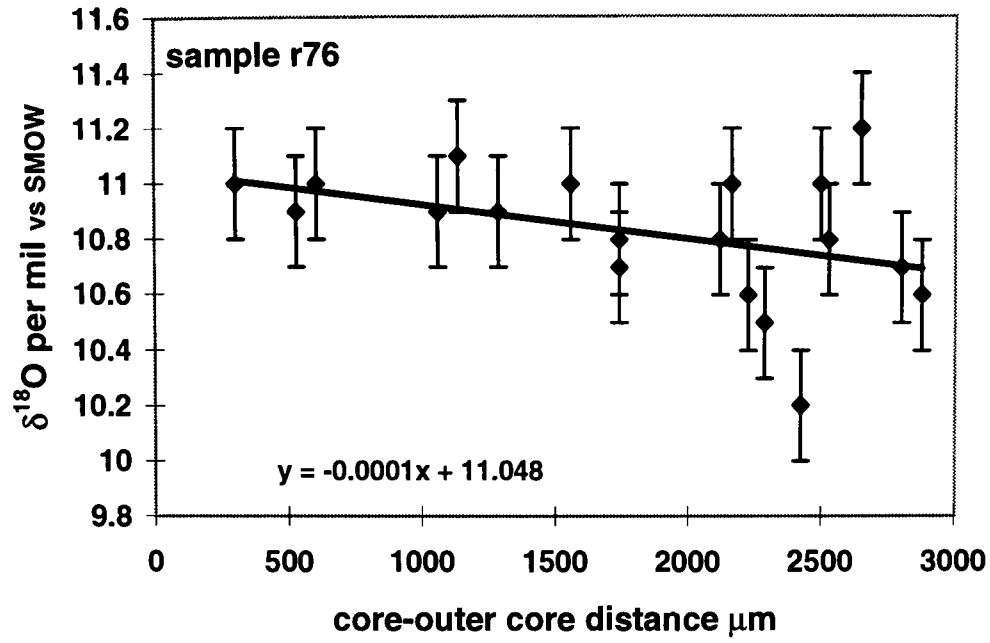


Figure 8.30: Samples R76 (top) and 19a, showing garnet core $\delta^{18}O$ trend from inner to outer core. The equation of the fitted trendline is shown. Errors are $\pm$ 0.2‰ .

variables are dependent upon each other such that the more extreme the fluid $\delta^{18}O$ the less the infiltratant flux required to precipitate a change in growing garnet $\delta^{18}O$.

In order to model the isotope shifts in samples R76 and 19a, a variety of values of $\delta^{18}O^{\ ext}_{H_2O}$ have been used, ranging from a minimum of 1‰ to 10‰ . From equation 8.25 the following approximate relationship can be derived:

$$d\delta^{18}O_{sys} = K(\delta^{18}O^{ext}_{H_2O} - \delta^{18}O_{sys})d\eta^{sys}_{H_2O} \tag{8.27}$$

where K is a constant. Thus the following relationship holds:

$$d\eta^{sys}_{H_2O} \propto \frac{1}{\delta^{18}O_{sys} - \delta^{18}O^{ext}_{H_2O}} \tag{8.28}$$

Figure 8.31 plots required infiltrating moles ($d\eta_{H_2O}$) versus the difference between the

system $\delta^{18}O$ and the infiltrating fluid isotope ratio ($\delta^{18}O_{sys}$ - $\delta^{18}O^{ext}_{H_2O}$) for samples R76 and 19. A fitted curve is shown, that at the extreme value $\delta^{18}O^{ext}_{H_2O} = \delta^{18}O_{sys}$ (*i.e.* the infiltrating fluid has the same isotope ratio as the rock system, 0‰ difference), an infinite quantity of external fluid is required to drive the necessary isotope change.

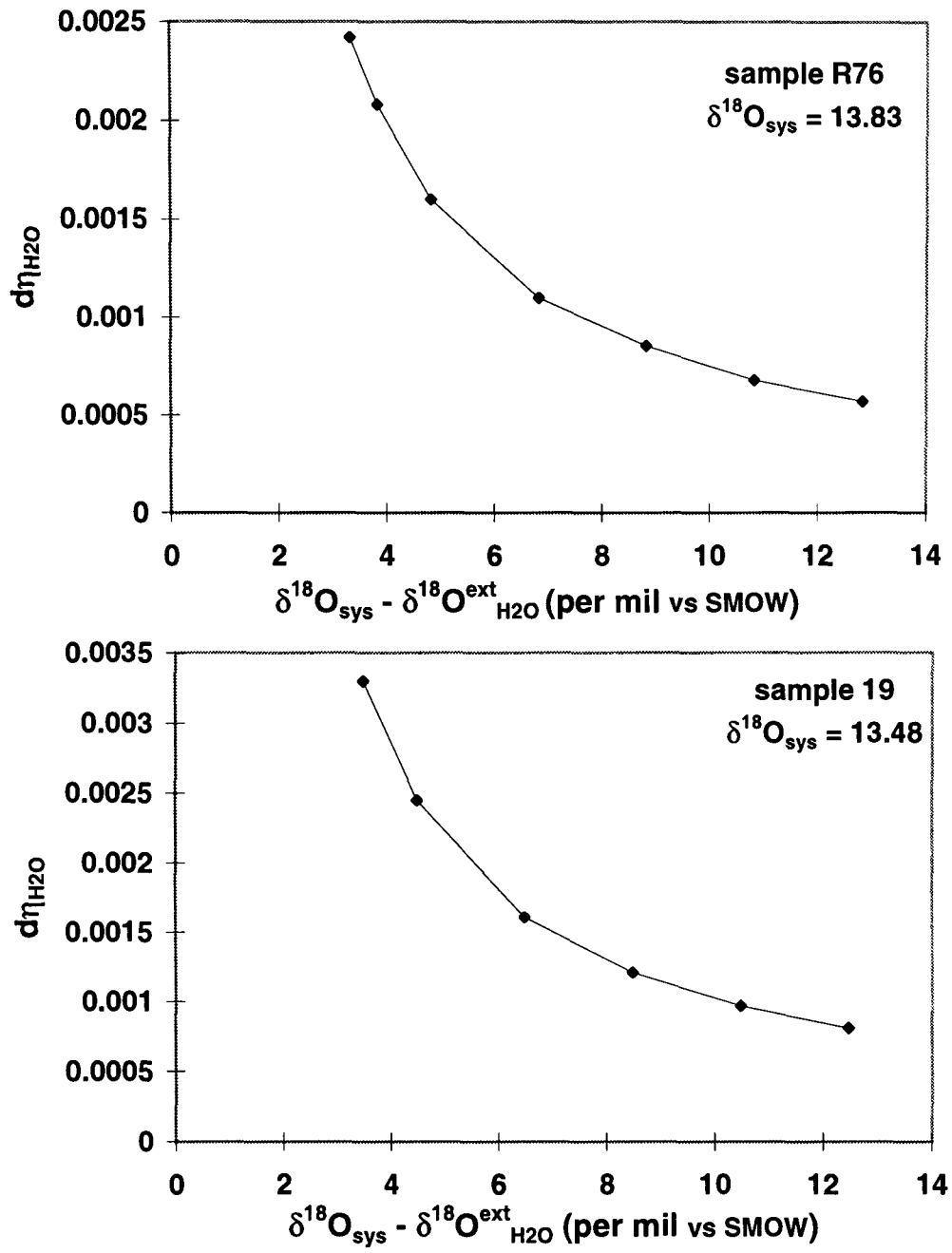


Figure 8.31: Plot of $d\eta_{H_2O}$ versus ($\delta^{18}O_{sys}$ - $\delta^{18}O^{ext}_{H_2O}$) for samples R76 and 19a. This shows the influx of external fluid as a function of external fluid $\delta^{18}O$ necessary to produce the required garnet isotope shifts.

Figure 8.32 shows completed core-rim profiles for both sample R76 and 19a. The core of the garnet shows garnet growth during infiltration of a low $\delta^{18}O$ fluid, and rim growth is taken under normal closed (*i.e.* open to fluid) conditions. This latter is taken as $dM_{H_2O} = 0$, $d\eta_{k \neq H_2O} = 0$, and $d\delta^{18}O_{sys} = 0$.

Since at each iteration both dM_{Grt} and $d\eta^{ext}_{H_2O}$ are fixed it is possible to determine the

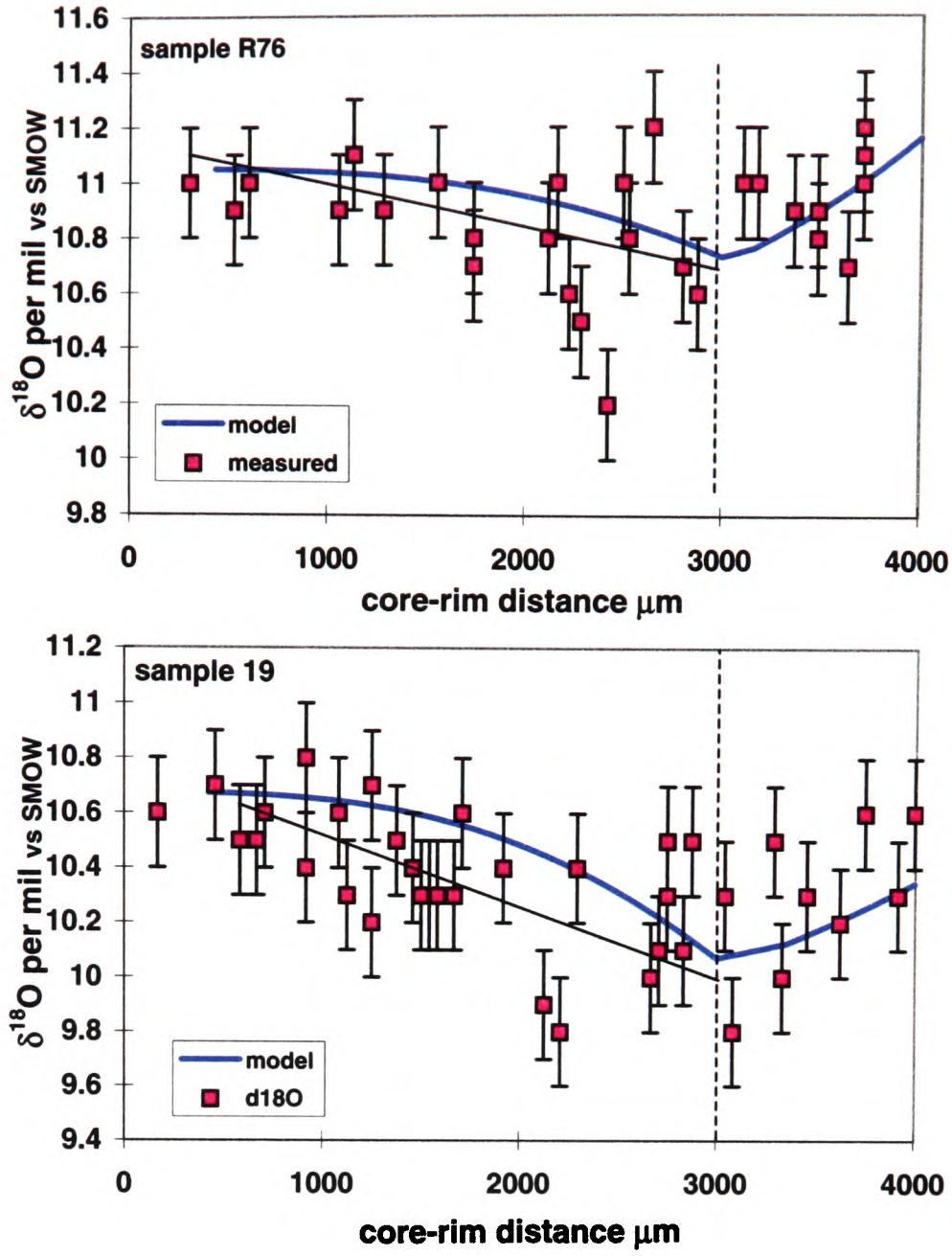


Figure 8.32: Samples R76 (top) and 19a, showing garnet core-rim measured and modelled δ^{18}O zonation. The garnet core profile is modelled as growth during 5‰ fluid infiltration; the rim is modelled as normal prograde growth zoning open to equilibrium fluids. Trendlines have been fitted for the measured core zoning for comparison. The dotted line represents the textural break.

necessary influx of fluid required during garnet core growth to produce the observed isotope shifts.

8.7.4 Calculation of Hoosac fluid fluxes

In order to calculate an estimate for time-integrated fluid flux in the Hoosac rocks several factors need to be quantified. Firstly, the rock porosity has to be estimated, and sec-

ondly, a value for total moles of infiltrating fluid must be assumed. Figure 8.33 shows a schematic of the rock matrix with one-dimensional time-integrated fluid flux J_t.

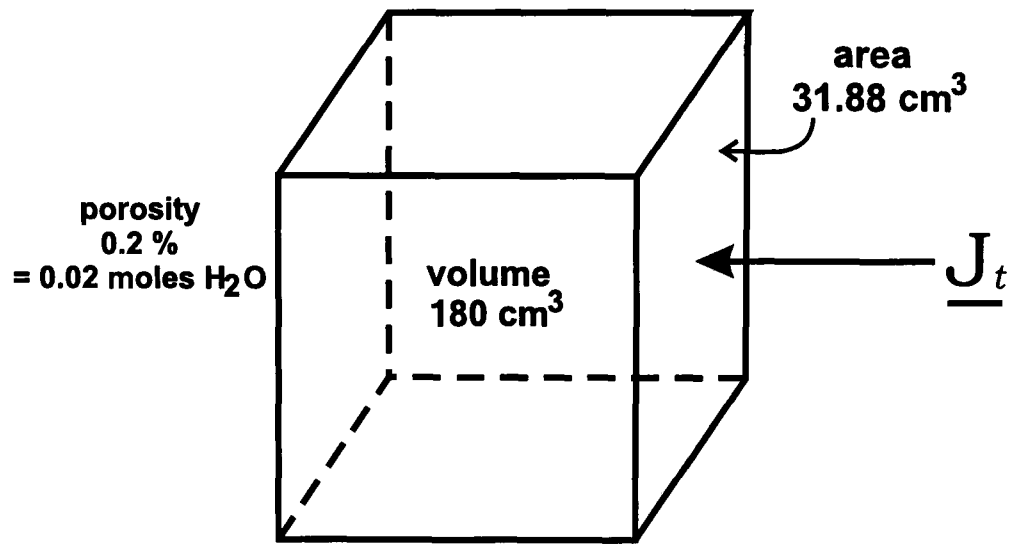


Figure 8.33: Schematic showing rock matrix assumed to be a cube. Given a porosity of 0.2% containing 0.02 moles H_2O, this gives a total volume of 180cm^3. A cube with this volume has sides with an area of 31.88cm^2. One-dimensional time-integrated fluid flux, J_t, flows through this.

If the Hoosac rock system is assumed to have an interconnected rock porosity of 0.2%, and given that this contains 0.02 moles of H_2O, the total rock system can be calculated to have a volume of 180cm^3 (one mole of H_2O has an approximate volume of 18cm^3).

180cm^3 describes a model system that can be represented as a cube with faces of 31.88cm^2 area. Fluxes can be derived by summing the moles of infiltrating water phase during the entire period of garnet core growth. $\eta^{ext}_{H_2O}$ is calculated from the total moles of infiltrated fluid during garnet growth, as calculated from PTGRID modelling. Figure 8.34 shows total moles (defined as $\sum d\eta^{ext}_{H_2O}$) as a function of infiltrating fluid $\delta^{18}O$, plotted as ($\delta^{18}O_{sys}$ - $\delta^{18}O^{ext}_{H_2O}$).

Sample	$\delta^{18}O^{ext}_{H_2O}$ vsSMOW	moles H_2O	vol H_2O, cm^3	J_t
R76	1‰	0.3056	5.508	0.173 cm^3/cm^2
19	10‰	0.7672	13.80	0.433 cm^3/cm^2

Table 8.12: Summary of two extreme calculated parameters for flux calculations.

For estimation of the value of infiltrating fluid $\delta^{18}O$ in the Hoosac rocks, the range of metamorphic fluid compositions can vary widely depending on source; the high-alumina schist is surrounded by quartz-feldspathic schists. If the source of the external

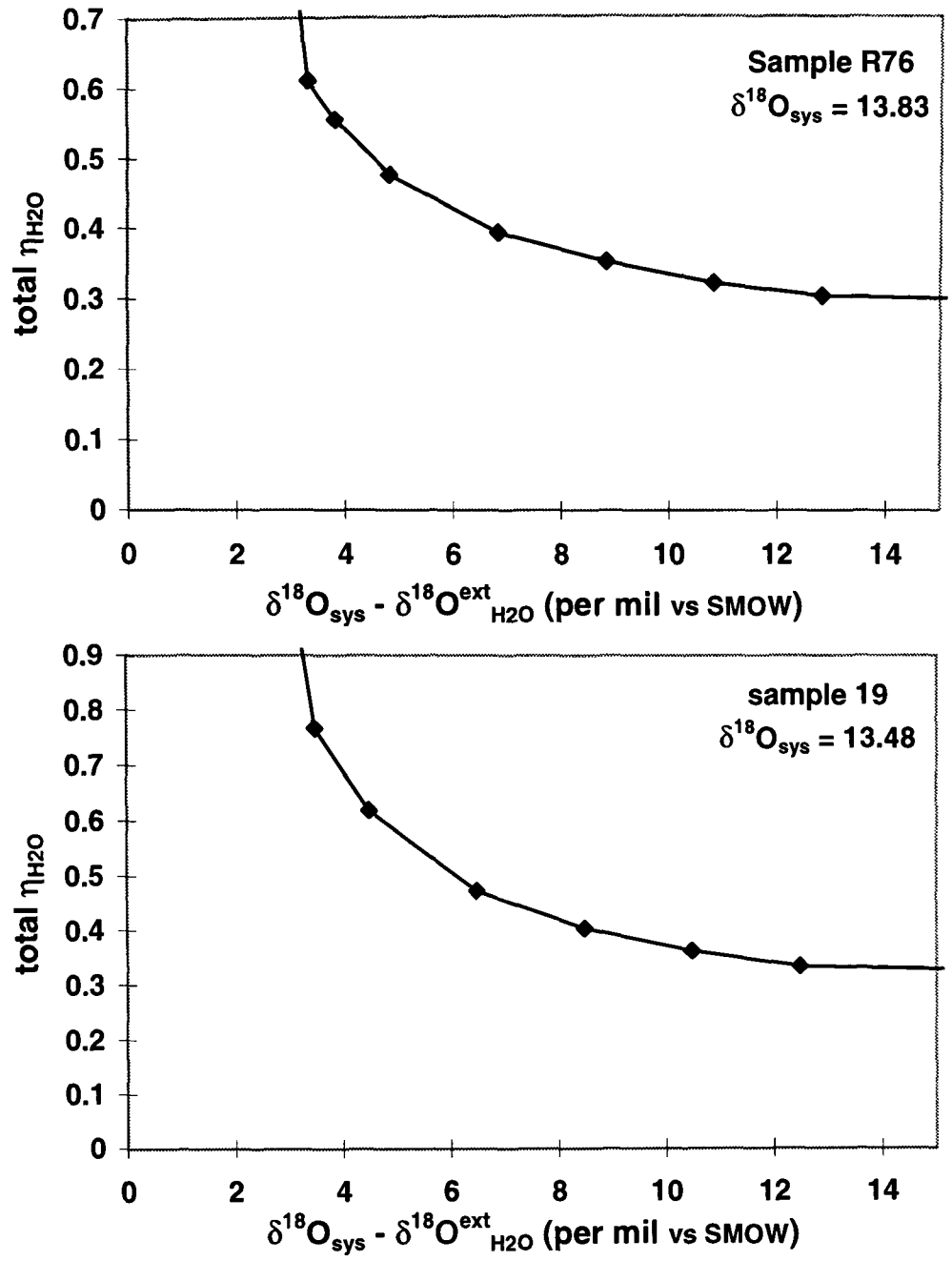


Figure 8.34: Summary of total moles of infiltrating fluid $\sum d\eta^{ext}_{H_2O}$ versus ($\delta^{18}O_{sys}$ - $\delta^{18}O^{ext}_{H_2O}$) by sample required to drive observed garnet $\delta^{18}O$ shifts.

fluids lay in devolatilization reactions occurring in these neighbouring rocks, then estimation of an equilibrium fluid composition requires whole-rock $\delta^{18}O$ data from the Qtz-Ab schist. If, however, the source was either other metamorphic fluids, or meteoric fluids, then a range of values could be predicted.

Modern-day values for meteoric water are measured at -15‰ ; Tertiary estimates are no heavier than -12‰ (*e.g.* Fricke *et al.*, 1992). However, these refer to pristine fluids, and it is unlikely that unaltered meteoric water could percolate down to depths of 25km during the evolution of the garnet cores. Still, a minor component of meteoric water is sufficient to deplete existing crustal fluids to give a low-$\delta^{18}O$ value. Other studies have

given equilibrium $\delta^{18}O_{fluid}$ estimates from New England pelites; 9.5‰ from the Pinney Hollow Formation, and 12.2‰ for the amphibolite-rich Ottauquechee Formation, both in southern Vermont (at 500°C , Chamberlain & Conrad, 1993).

Given two extreme examples of sample R76 with a 1‰ infiltrating fluid ($\eta_{H_2O} = 0.3056$) and 19 with a 10‰ fluid ($\eta_{H_2O} = 0.7672$), these represent volumes of water of 5.508 cm^3 and 13.80 cm^3 respectively. Dividing these figures by the area yields a time-integrated fluid flux during garnet core growth. These are 0.1783 cm^3/cm^2 for sample R76 (1‰) and 0.433 cm^3/cm^2 for sample 19 (10‰). These figures are summarized in table 8.12.

A minimum flux can be inferred from likely minimum values of infiltrating $\delta^{18}O$. Of the possible sources of fluids, meteoric water is perhaps the most depleted in ^{18}O, having a modern-day value of -15‰ . This would, in the case of sample R76, yield a likely minimum value of total moles of 0.3, representing a time-integrated fluid flux of approximately $0.17 cm^3/cm^2$. It is impossible to quantify an upper limit since it would require an infinite quantity of infiltrating fluid with $\delta^{18}O^{ext}_{H_2O} = \delta^{18}O_{sys}$. In this case the fluid would be in equilibrium with the rock system at each stage of rock evolution.

8.7.5 Validity of PTGRID modelling

PTGRID has limitations. One of the major problems with the application of the program is that it predicts a very steep P-T curve for garnet growth, which in turn limits the gradient dM_{Grt}/dT. This constrains the temperature interval within which garnet is grown, as well as implying linear garnet growth with temperature. In terms of predicting oxygen isotope fractionations which are temperature dependent, errors are accrued by incorrectly predicting the appropriate temperature range. However, figure 8.35 shows equilibrium oxygen isotope fractionations between AFM phases of interest over the temperature interval of Hoosac garnet growth (500-600°C). There is very little divergence between the phases, and thus within the temperature range over which PTGRID calculates garnet isotope growth (30-40°C), T estimation errors are not considered to be limiting.

The other main limitation of PTGRID is the inability to model exactly the same reactions as calculated by THERMOCALC. For example, using THERMOCALC, garnet core

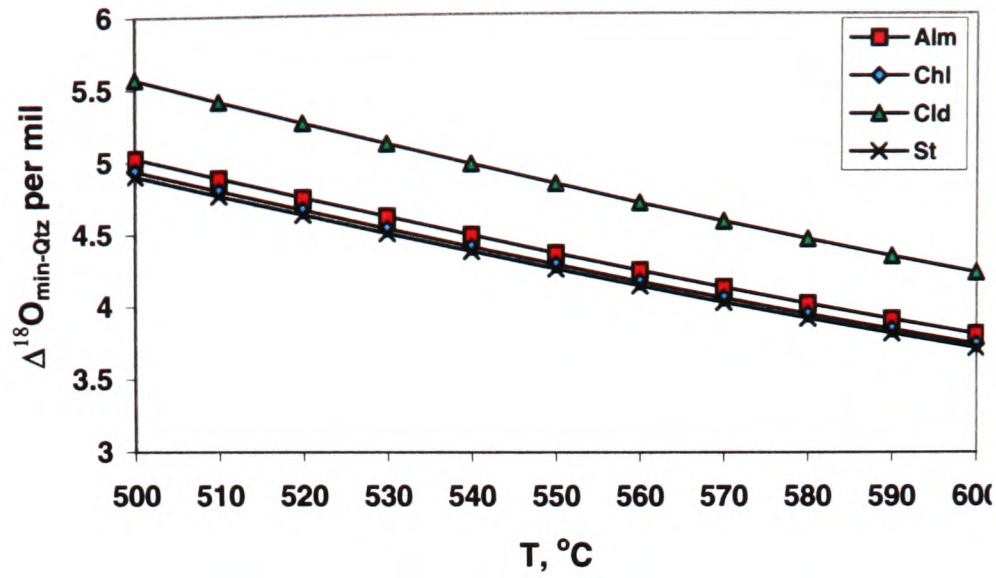


Figure 8.35: Temperature-dependent equilibrium oxygen isotope fractionations between garnet, chlorite, chloritoid and staurolite, calculated using the fractionation factors of Zheng (1993a,b, 1999).

growth is considered to be accompanied by chloritoid growth at the expense of chlorite and quartz. Also calculated are changes in the quantity of white micas present. PTGRID maintains constant moles of chloritoid during core growth, although it does change mole fractions of chloritoid end-members. In addition, muscovite and paragonite play no part in the calculation. Similarly, initial garnet rim growth in PTGRID does not include chlorite in the calculations.

Additionally, water activity has been modelled as unitary here, in contrast to the calculations performed with THERMOCALC. However, despite these problems, PTGRID predicts closed-system observations in line with other studies, and has allowed some quantification of fluid infiltration effects. Results gained from this approach must be applied with these aforementioned provisos in mind.

A final assumption is the continuous infiltration of external fluid during the entire period of garnet core growth, with a fixed isotope ratio and a fixed rock porosity. Also implied is that at each interation complete mixing of internal and external fluids is achieved, and that the rock system equilibrates with the resulting mixture.

Chapter 9

Synthesis

The purpose of this chapter is to bring together the evidence from petrographical examination, isotope analysis and metamorphic modelling, in order to present a hypothesis for the evolution of the Hoosac Schist.

9.1 The Hoosac Schist - a summary

The big garnet schist studied here is a minor member of the high-alumina (garnet-bearing) Hoosac Schist; field study suggests it is at most 30m in thickness. It is characterized by a quartz, muscovite and paragonite-rich matrix within which porphyroblasts of garnet, staurolite and kyanite (at appropriate grades) are found. The high-alumina schist lies within the muscovite-quartz-albite units that dominate the Hoosac Formation, outcropping up to 150m in thickness. Its margin with the albitic schist is abrupt, characterized by fracturing and veining.

Petrological examination of the big garnet schist shows the potential for at least three episodes of deformation and two episodes of prograde metamorphism (with a later retrogressive event). The textural evidence suggests that garnet cores grew within a matrix dominated by quartz and potassic and sodic white micas, with chlorite and chloritoid. Following at least one, and possibly two, deformational events garnet rims are presumed to have grown during a second metamorphic episode, along with second-

generation white micas, staurolite, biotite and kyanite (where appropriate).

9.1.1 Garnet growth models

Two contrasting models for garnet growth with a textural unconformity are those put forward by Thompson *et al.* (1977) and Karabinos (1984). They both describe garnets from Vermont with a marked concentric textural break, and they both describe a characteristic Mn spike at this break. The Hoosac rocks certainly evidence a core-rim discontinuity, as indicated texturally by truncated inclusion trails, a core rich in inclusions (especially of chloritoid) and an inclusion-poor rim. This textural discontinuity also marks the transition from rutile to ilmenite as the dominant Ti phase. However, no Mn peak was observed at this unconformity, with the spessartine trace only showing a slight inflection possibly suggesting slower garnet rim growth compared to the core.

The contrasting models are based on different bulk rock compositions, with the Al-rich schists described by Karabinos more closely linked to the Hoosac Schist from Western Massachusetts. However, there is no direct petrological evidence for simultaneous staurolite and garnet growth, although modelling suggests that this is necessary (see chapter 8). There is also no direct evidence for garnet resorption, with the absence of an observed Mn spike at the textural break (in contrast to that reported by both Karabinos (1984) and Young & Rumble (1993)). The relative absence of inclusions in the garnet rim suggests either slower rim growth or a greater mobility of species.

Garnet growth reactions

The reaction space approach to investigating mineral reactions provides a useful framework to graphically portray reactions (Thompson, 1982; Thompson *et al.*, 1982). A *n*-dimensional framework based about axes defined by linearly independent reactions allows rock reactions to be characterized by a vector moving about this space enclosed by faces defined by moles (or modes) of phases present.

A set of linearly independent reactions (LIRs) are those reactions that either alone, or as a linear combination of two or more, are able to describe any reaction that may occur

within that set of phases. Matrix algebra is used to calculate a set of linearly independent reactions to model garnet growth.

For the system Grt+Chl+Cld+St+Qtz+H_2O there are two linearly independent reactions:

$$\textbf{[Grt]}\ 41\text{Cld} + 6\text{Qtz} \rightarrow 5\text{Chl} + 17\text{H}_2\text{O} + 8\text{St}$$

$$\textbf{[St]}\ \text{Chl} + \text{Cld} + 2\text{Qtz} \rightarrow 2\text{Grt} + 5\text{H}_2\text{O}$$

These two reactions form the axes of the reaction polyhedra; [Grt] and [St] refer to garnet-absent and staurolite-absent reactions respectively.

For the system Grt+Chl+St+Bt+Qtz+Ms+H_2O the two LIRs are:

$$\textbf{[H}_2\textbf{O]}\ 47\text{Ms} + 3\text{Chl} + 58\text{Grt} \rightarrow 12\text{St} + 47\text{Bt} + 87\text{Qtz}$$

$$\textbf{[Qtz]}\ 38\text{Ms} + 45\text{Chl} \rightarrow 6\text{St} + 29\text{Grt} + 38\text{Bt} + 174\text{H}_2\text{O}$$

which represent the water and quartz-absent reactions respectively. The axes scale is represented by reaction progress ($d\xi$), and the origin is the molal composition of the rock at the initiation of reaction. Thus is defined the bounding faces of the reaction space, which represent the various limits of phases present. Reactions are portrayed as vectors within this space, which may lie anywhere within the bounding boxes. A reaction vector progressing towards a face is consuming that phase, and the reaction will cease when it reaches the face as consumption of the phase is complete. Schematic reaction polyhedra charting the possible evolution of the Hoosac rocks are shown in figure 9.1.

Hoosac garnets grew initially in a matrix of Chl+Cld+Ms+Pg+Qtz. Since staurolite is not involved yet, garnet growth must take place along a vector parallel to the [St] reaction, as shown in figure 9.1a. This path represents growth of the garnet core, describing the following reaction:

$$\text{Chl} + \text{Cld} + 2\text{Qtz} \rightarrow 2\text{Grt} + 5\text{H}_2\text{O}$$

Garnet rim growth probably accompanied growth of staurolite, despite the absence of

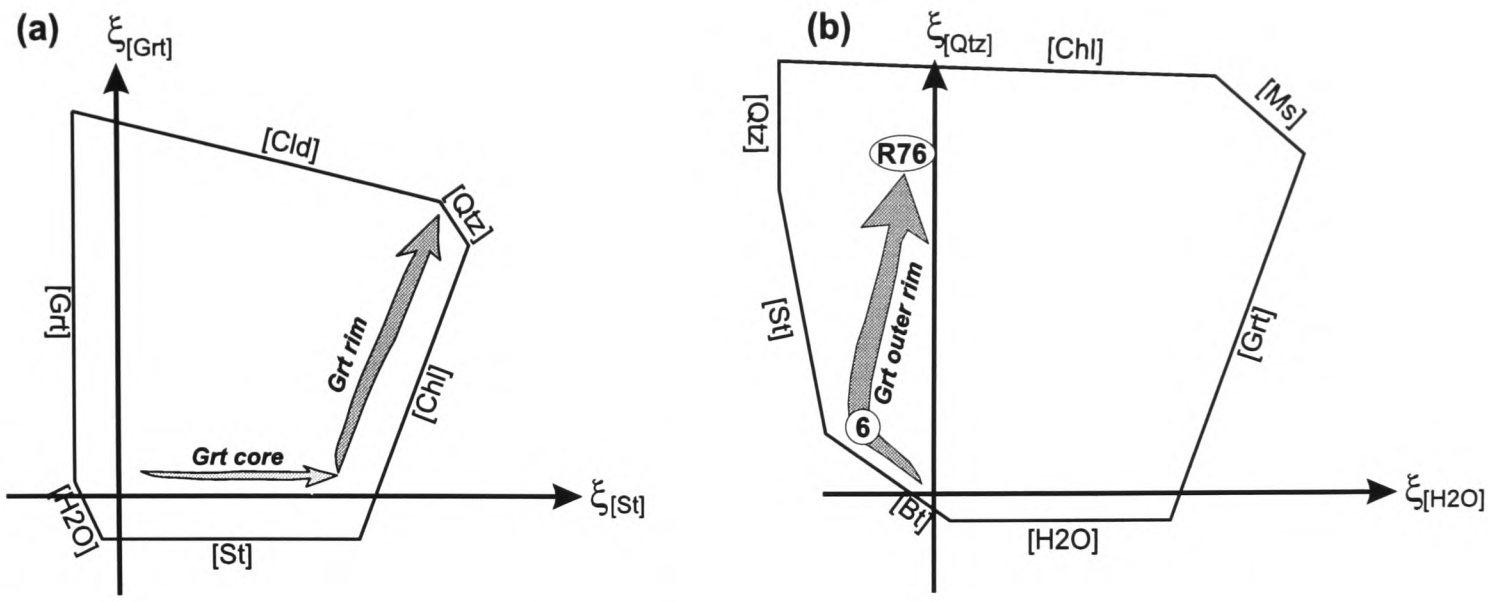


Figure 9.1: Reaction space polyhedra showing evolution of the Hoosac Schist. See text for details.

clear petrological evidence in the form of staurolite inclusions. THERMOCALC predicts initial rim growth at the expense of chloritoid.

Figure 9.1a shows the growth of garnet rim with the simultaneous growth of staurolite, while consuming chloritoid. This vector is shown parallel to the chlorite face, implying the absence of chlorite in the garnet growth equation, although this may not be the case. The reaction is:

$$23\text{Cld} + 8\text{Qtz} \rightarrow 5\text{Grt} + 4\text{St} + 21\text{H}_2\text{O}$$

When all the chloritoid had been consumed, the outer garnet rim then grew at the expense of chlorite. Figure 9.1b shows a new reaction space without chloritoid but with the addition of the potassic phases biotite and muscovite. Within this reaction space the second rim growth must possibly have occurred at the expense of staurolite, and then ultimately growing staurolite again with biotite at the expense of chlorite. The second rim growth equation could be:

$$25\text{Chl} + 38\text{Qtz} + 2\text{St} \rightarrow 41\text{Grt} + 94\text{H}_2\text{O}$$

As suggested by the reaction space, biotite could then grow at the expense of chlorite without any further growth of garnet (*i.e.* a vector parallel to the [Grt] face). In this case the biotite growth reaction would be:

$$41Ms + 31Chl \rightarrow 8St + 41Bt + 29Qtz + 116H_2O$$

Thus simultaneous growth of staurolite and biotite independent of garnet growth or resorption could occur in the upper staurolite zone, for example in sample R76. This also suggests all garnet growth could be catered for before any biotite or kyanite nucleation.

9.2 Fluid infiltration

Ferry (1992) mapped out fluid fluxes derived from petrological observation calculations over a 1500 km^2 area of eastern Vermont. From this data he postulated two large deep-seated (25km) regional metamorphic hydrothermal systems centered on the two major antiforms. These operated during prograde Acadian metamorphic growth, with time-integrated fluid fluxes increasing with metamorphic grade from 1×10^4 to 7×10^5 cm^3/cm^2.

Infiltration of non-equilibrium fluids during prograde metamorphism has been invoked to explain measured oxygen isotope zoning in garnets from New England. Chamberlain & Conrad (1991) reported reverse $\delta^{18}O$ zoning in garnets from the Gassetts Schist, Vermont. This zoning, from a maximum of 10.1‰ in the core to 6.9‰ at the rim, was attributed to inflow of a relatively low $\delta^{18}O$ fluid during the later stages of garnet growth.

Conversely, they reported normal prograde zoning in garnets from the Pinney Hollow Formation, Vermont (Chamberlain & Conrad, 1993), and attributed this to growth during infiltration of heavier $\delta^{18}O$ volatiles during garnet growth. These fluids were presumed to be derived from devolatilization of neighbouring schists. Using a time period of garnet growth of 10Ma, they calculated time-integrated fluid fluxes of 1.5×10^4 cm^3/cm^2.

However, Young & Rumble (1993) proposed a much shorter infiltration episode. Low $\delta^{18}O$ garnet rims from the Gassetts Schist were explained by having grown after a garnet resorption episode when chlorite grew from garnet during infiltration of externally derived fluid. They proposed that the chlorite growing by this hydration reaction acted as a reservoir for the low $^{18}O/^{16}O$ oxygen, and that garnet rims grew later at the expense

of this chlorite, thus exhibiting sympathetic $\delta^{18}O$. Estimates of duration of fluid flow was established by diffusion calculations of muscovite which retained a pre-infiltration oxygen isotope signature. Young & Rumble estimated that the maximum duration of fluid flow was less than 50,000 years. Similarly, Ague (1994a,b) suggested that fracture-controlled fluid flow through similar grade rocks from Connecticut lasted on the order of 10,000 years.

9.2.1 The Hoosac fluid flux results in context

Fluids play a vital role in metamorphic processes, affecting the thermal (their being an effective transport agent of heat); mechanical (they can affect the strength of rock and promote faulting); and chemical properties of the rock. Because of this role, an important goal of metamorphic petrology is to identify the quantity and geometry of fluid flow in metamorphic terranes. Whilst the information gained here from the Hoosac rocks contains no information concerning the large-scale geometry of fluid flow, the quantity of fluids calculated to have passed through the Hoosac Schist during garnet core growth needs to be placed in context.

At its minimum, the flux estimation for the Hoosac rocks (0.17 cm^3/cm^2) is four to five orders of magnitude smaller than those postulated by Ferry (1992) and Chamberlain & Conrad (1993); in addition this study has proved that even at infiltrating fluid values of 10.5‰ this only requires the flux to vary from the minimum by 0.4 cm^3/cm^2. Although the fluxes differ by several orders of magnitude, the methods of estimating a fluid flux differ between these studies.

Chamberlain & Conrad (1993), studying oxygen isotope zonation in garnets, estimated fluid infiltration effects by comparing isotope zoning on two sets of garnets, one more proximal than the other to the considered source of the infiltrating fluids (an adjacent formation undergoing dehydration reaction). Fluid fluxes were calculated by comparing observed $\delta^{18}O$ zoning profiles seen in the two garnet sets with those calculated using an equation describing combined advection-diffusion of a tracer. As such the change in intensity of external fluid effects yielded a time-integrated fluid flux of 1.4×10^4 cm^3/cm^2.

The estimations by Ferry (1992) were based on petrological observations from the Waits

River Formation, Vermont. The Waits River rocks are dominantly impure carbonates. During prograde metamorphism the marls produced a volatile fluid with $X_{CO_2} \geq 0.5$. However, mineral assemblages can record the composition of the fluid that they are in equilibrium with. In the case of the Waits River Formation this was an H_2O-CO_2 fluid with $X_{CO_2} \leq 0.2$. The production of a CO_2-rich volatile mixture in rocks that record equilibrium with an H_2O-rich fluid is common, and is explained by infiltration of the rock by aqueous fluids during metamorphism. This allows an estimation of fluid flux integrated over the duration of flow and reaction.

Ferry estimated a variety of time-integrated fluid fluxes for the different metamorphic grades, from 1×10^4 cm^3/cm^2(ankerite-oligoclase) to 7×10^5 cm^3/cm^2 (diopside). Although Ferry did not specifically stipulate the duration of flow, he postulated that fluid infiltration may have occurred for at least as long as the duration of Acadian garnet porphyroblast growth in southern Vermont ($10 \pm 3 \times 10^6$ years, Christensen *et al.*, 1989).

The Hoosac Schist fluid flux calculations are made with the assumption that the duration of fluid flow lasted throughout the growth of the garnet cores, and that infiltrating fluid $\delta^{18}O$ remained constant. This assumption of continuous fluid infiltration during the entire growth of garnet cores is in contrast to that proposed by Young & Rumble (1993). They postulated a short, punctuated injection of disequilibrium fluid that drove a garnet resorption event.

However, the data presented here suggest that at the very minimum a small, continuous injection of light $\delta^{18}O$ external fluids is necessary to produce the observed oxygen isotope zoning in the Hoosac garnet cores. In contrast, the garnet rims could well have grown by normal prograde dehydration reaction; there is insufficient isotope evidence to suggest otherwise.

9.3 Comparison of this study with other New England Models

Western Massachusetts lies within a zone of overlap between the Ordovician Taconian and the Siluro-Devonian Acadian orogenic events, as shown in figure 9.2. Although the results of this Hoosac Schist study indicate two recorded major metamorphic events

separated by at least one period of deformation, there is little evidence to constrain them temporally, *i.e.* whether they represent a Taconian metamorphic episode with a Acadian overprint, or two episodes within the Acadian orogeny.

Armstrong *et al.* (1992) presented new constraints defining the western and eastern extremes of the Acadian orogenies, and suggested that Acadian metamorphism west of a line defined by the New-Hampshire-Vermont border (where the Hoosac rocks are sited) is of a different age and style to that in the east. Figure 9.3 shows their summary of Taconian, Western Acadian and Eastern Acadian P-T data.

The results from THERMOCALC modelling presented in chapter 8 represent new P-T data from Western Massachusetts. These calculate garnet growth in the Hoosac Schists initiated at temperatures of 520°C and 8.5 kbar pressure, and that garnet rim temperatures were 580-600°C , and at similar pressures of 8-10kbar. However, no constraint on the actual P-T paths taken by each garnet growth event is made.

Figure 9.4 shows a summary of compiled peak P-T data for the Taconian and Western Acadian orogenic events. Given the complexity of New England geology, it is impossible to predict whether the Hoosac garnet core P-T conditions represent growth within the Taconian or Acadian events. Garnet rims, however, are in line with peak estimates for the Western Acadian episode.

It would be reasonable to conclude that, since the two garnet growth events are separated by at least one period of deformation, then the growth of garnet core occurred during the earlier, Taconian orogenic episode, and the rim during the later Acadian episode. This is especially pertinent given the geographical position of the Hoosac rocks, lying in the zone of maximum overlap between the Taconian and Acadian events. Karabinos (1984) came to a similar conclusion with unconformity garnets from the Hoosac Formation of Southern Vermont.

One interesting point to make is the concordancy between the outer core and inner rim cation concentrations. Garnet cores appear to represent growth in fairly constant conditions. When growth of garnet restarted (initiation of rim growth), it appears to have recommenced almost at similar conditions to those experienced by the final core growth.

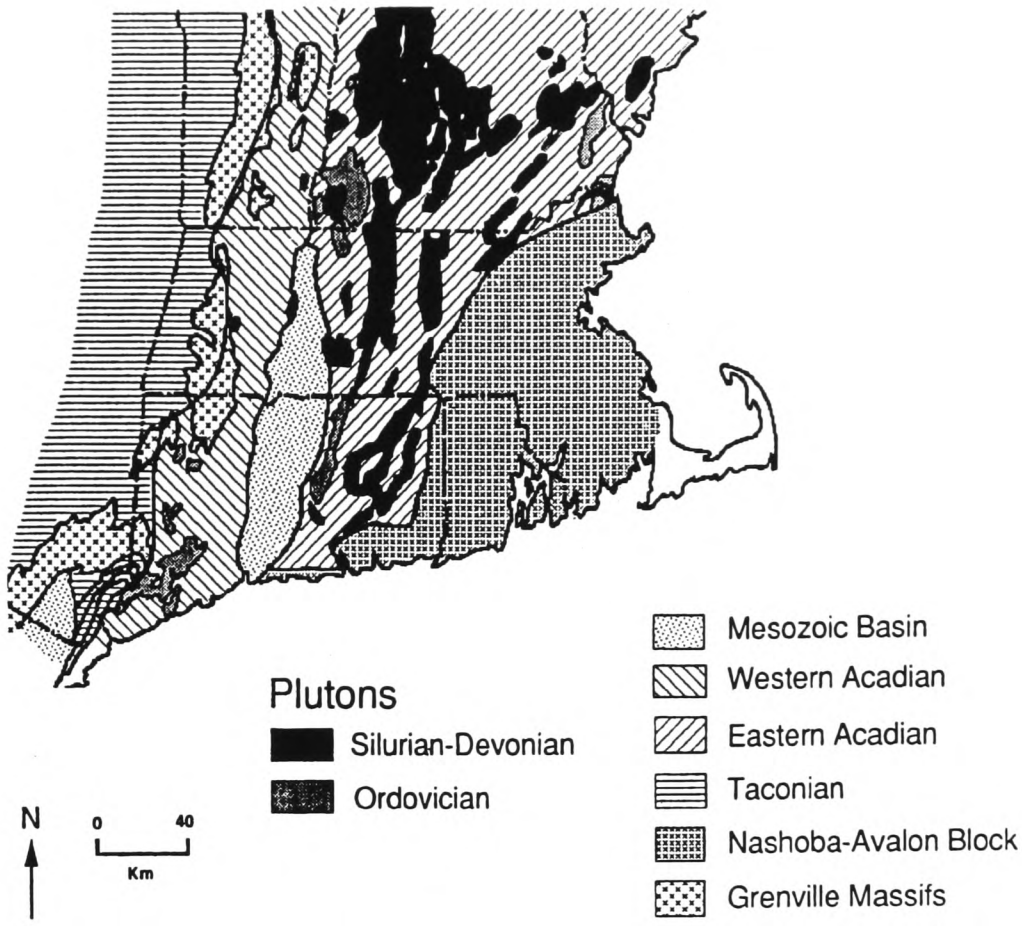


Figure 9.2: Generalized geological map of southern New England showing the geographical distribution of Taconian, Eastern Acadian and Western Acadian metamorphic rocks. After Armstrong *et al.* (1992). Delineated areas for each period of metamorphism indicate where it is the latest and highest-grade event, and has produced the dominant mineral assemblage in the case of overlaps. Also shown are the Grenville massifs of western New England; the Hoosac Schist lies on the eastern flank of the Berkshire Massif.

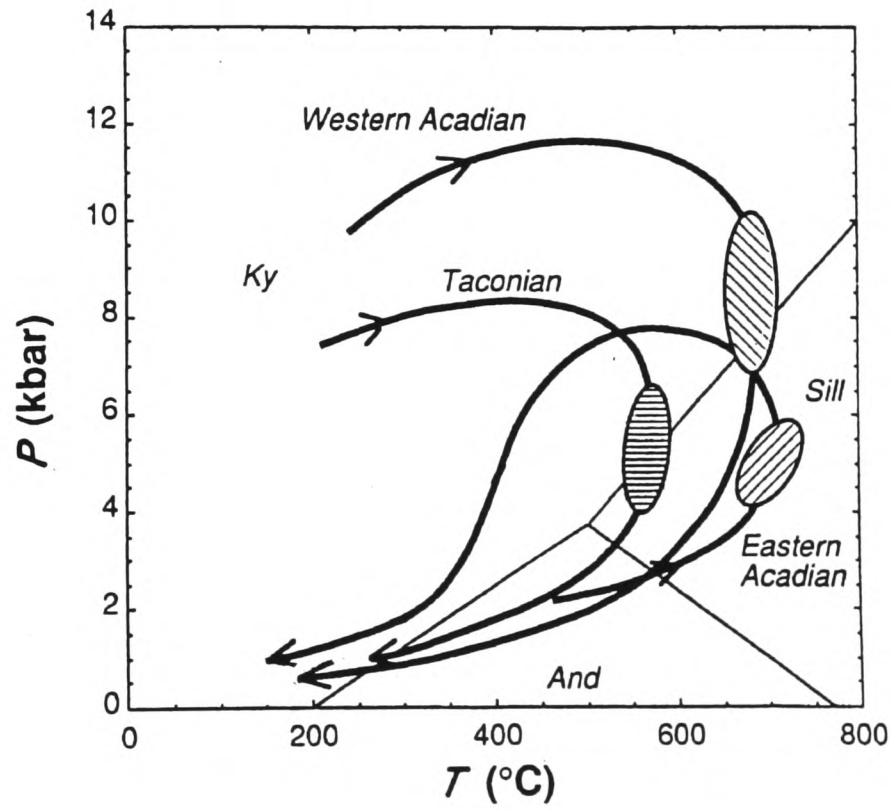


Figure 9.3: P-T diagrams showing schematic P-T trajectories for Taconian, Western and Eastern Acadian orogenies. Hatched ovals represent collated peak P-T data. From Armstrong *et al.* (1992).

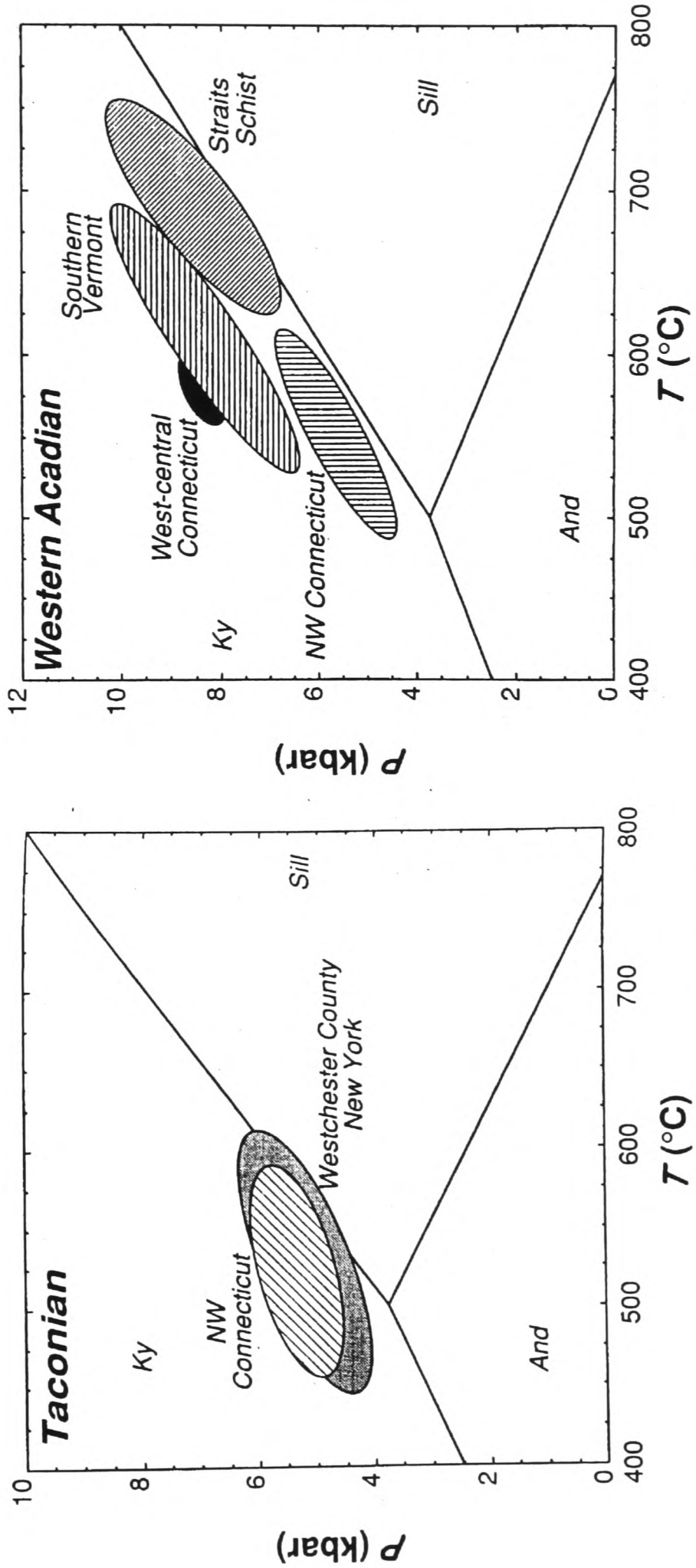


Figure 9.4: P-T diagrams for both Taconian and Western Acadian. Shaded areas show approximate ranges of peak pressures and temperatures for the Taconian and Western Acadian belts, taken from Armstrong *et al.* (1992). Data sources are: Waldron (1986) - Westchester County; Hames *et al.* (1991) - NW Connecticut; Hames *et al.* (1989) - west-central Connecticut; Miller & Tracy (1991) - Straits Schist; Kohn & Spear (1989) and Armstrong & Tracy (1991) - southern Vermont.

9.4 Conclusions

The results presented in this thesis have yielded new P-T data from Western Massachusetts. In addition, they provide a model whereby observed textural breaks in Hoosac Schist garnets are the result of two prograde metamorphic events. Garnet growth initiated at P-T conditions of 8.5kbar and 520°C, and probably represents a Taconian growth episode. Subsequent garnet rim growth probably occurred as an overprint during the Western Acadian event, and garnet rim compositions may reflect peak conditions of 590°C and 8-10kbar.

Development of the Oxford laser system has allowed partially successful oxygen isotope results to be obtained from Hoosac Schist garnets, and isotope fractionation modelling has suggested a required influx of low-$\delta^{18}O$ fluid is necessary to give observed isotope shifts. Based on this modelling, calculations have yielded minimum time integrated fluid fluxes of the order of 0.2-0.5 cm^3/cm^2. These are four to five orders of magnitude less than other reported fluxes, although the methods of calculation differ. In addition, this gives rise to a scenario where infiltration is necessary during the whole period of garnet core formation.

9.5 Further work

Development of the UV laser ablation-GC-*irms* analytical facility has proved the potential for obtaining reasonable results from metamorphic minerals, however there are still a number of problems associated with routine analysis. These generally focus on the nature of gas transfer, and in particular the problems associated with the metal transfer bellows. A separate concern is that results appear to be affected by the slow build-up of the products of the various ablation reactions.

In addition, better modelling and incorporation of oxygen isotope fractionations could be accomplished to allow calculated THERMOCALC reactions to be more faithfully reproduced by PTGRID.

9.6 Epilogue

The development of pioneering analytical facilities is often an evolving process. In April 2000, an excimer UV laser was installed in the Oxford laboratory in place of the Oxford Lasers copper-vapour laser. This promises rapid ablation but at a frequency of the order of 4Hz. An additional advantage is that the beam is steerable; this means the stage can be static and that the metal bellows can be replaced by a piece of fixed tubing.

Early results from meteorite analysis suggest this is a superior set-up, and that it promises to be a more reliable method for routine measurement.

Bibliography

AGUE, J J. 1994a. Mass transfer during Barrovian metamorphism of pelites, south-central Connecticut I: evidence for changes in composition and volume. *American Journal of Science*, **294**, 989–1057.

AGUE, J J. 1994b. Mass transfer during Barrovian metamorphism of pelites, south-central Connecticut II: Channelized fluid-flow and the growth of-staurolite and kyanite. *American Journal of Science*, **294**, 1061–1134.

ARMSTRONG, T R, & TRACY, R J. 1991. Tectonometamorphic evolution of Acadian domes in southern Vermont. *In: Geological Society of America, Abstracts with Programs*, vol. 23.

ARMSTRONG, T R, TRACY, R J, & HAMES, W E. 1992. Contrasting styles of Taconian, Eastern Acadian and Western Acadian metamorphism, central and western New England. *Journal of Metamorphic Geology*, **10**, 415–426.

ASPREY, L B. 1976. The preparation of very pure fluorine gas. *Journal of Fluorine Chemistry*, **7**, 359–361.

ATHERTON, M P. 1968. The variation in garnet, biotite and chlorite composition in medium grade pelitic rocks from the Dalradian, Scotland, with particular reference to zonation in garnet. *Contributions to Mineralogy and Petrology*, **18**, 347–371.

BAERTSCHI, P, & SILVERMAN, S R. 1951. The determination of relative abundancies of the oxygen isotopes. *Geochimica et Cosmochimica Acta*, **1**, 317–361.

BELL, T H, HICKEY, K A, & WANG, J. 1997. Spiral and staircase inclusion trail axes within garnet and staurolite porphyroblasts from schists of the Bolton Syncline, Connecticut: timing of porphyroblast growth and the effects of fold development. *Journal of Metamorphic Geology*, **15**, 467–478.

BELL, T H, HICKEY, K A, & UPTON, G J G. 1998. Distinguishing and correlating multiple phases of metamorphism across a multiply deformed region using the axes of spiral, staircase and sigmoidal inclusion trails in garnet. *Journal of Metamorphic Geology*, **16**, 767–794.

BERMAN, R G. 1988. Internally-consistent thermodynamic data for minerals in the system Na_2O-K_2O-CaO-MgO-FeO-Fe_2O_3-Al_2O_3-SiO_2-TiO_2-H_2O-CO_2. *Journal of Petrology*, **29**, 445–522.

CHAMBERLAIN, C P, & CONRAD, M E. 1991. Oxygen isotope zoning in garnet. *Science*, **254**, 403–406.

CHAMBERLAIN, C P, & CONRAD, M E. 1993. Oxygen-isotope zoning in garnet: A record of volatile transport. *Geochimica at Cosmochimica Acta*, **57**, 2613–2629.

CHENEY, J T, & BRADY, J B. 1992. Petrology of the High-Alumina Hoosac Schist from the chloritoid+garnet through the kyanite+biotite zones in Western Massachusetts. *New England Intercollegiate Geological Conference Field Guide.*

CHENEY, J T, SANDER, M, & BRYAN, D. 1980. Influence of garnet composition on the distribution of metamorphic isograds in the east limb of the Berkshire anticlinorium. *Page 28 of: Geological Society of America Abstracts with Programs*, vol. 12.

CHERNOFF, C B, & CARLSON, W D. 1997. Disequilibrium for Ca during growth of pelitic garnet. *Journal of Metamorphic Geology*, **15**, 421–438.

CHRISTENSEN, J N, ROSENFIELD, J L, & DEPAOLO, D J. 1989. Rates of tectonometamorphic processes from Rubidium and Strontium isotopes in garnet. *Science*, **244**, 1465–1469.

CLAYTON, R N, & MAYEDA, T K. 1963. The use of bromine pentafluoride in the extraction of oxygen from oxides and silicates for isotopic analysis. *Geochimica et Cosmochimica Acta*, **27**, 43–52.

CLAYTON, R N, GOLDSMITH, J R, KAREL, K J, MAYEDA, T K, & NEWTON, R C. 1975. Limits on the effect of pressure on isotopic fractionation. *Geochimica et Cosmochimica Acta*, **39**, 1197–1201.

COUTTS, D W, & BROWN, D J W. 1995. Production of high average power UV by second harmonic and sum-frequency generation from copper-vapour lasers. *IEEE Journal of Quantum Electronics*, **1**, 768–778.

CRAIG, H. 1972. Atmospheric oxygen: Isotopic composition and solubility fractionation. *Science*, **175**, 54–55.

CRANK, J. 1983. *The mathematics of diffusion*. 2nd edn. Oxford University Press.

CROWE, D E, FALLICK, J W, & BAKER, K L. 1990. Microanalysis of sulphur isotope ratios and zonation by laser microprobe. *Geochimica et Cosmochimica Acta*, **54**, 2075–2092.

DEER, W A, HOWIE, R A, & ZUSSMAN, J. 1992. *An introduction to the rock-forming minerals*. 2 edn. Longman.

DROOP, G T R, & HARTE, B. 1995. The effect of Mn in the phase relations of medium-grade pelites: Constraints from natural assemblages in petrogenetic grid topology. *Journal of Petrology*, **36**, 1549–1578.

DUCHÊNE, S, BILCHERT-TOFT, J, LUAIS, B, TÉLOUK, P, LARDEAUX, J-M, & ALBARÈDE, F. 1997. The Lu-Hf dating of garnets and the ages of the Alpine high-pressure metamorphism. *Nature*, **387**, 586–589.

EILER, J M, VALLEY, J W, GRAHAM, C M, & BAUMGARTNER, L P. 1995. Ion microprobe evidence for the mechanisms of stable isotope retrogression in high-grade metamorphic rocks. *Contributions to Mineralogy and Petrology*, **118**, 365–378.

ELSENHEIMER, D, & VALLEY, J W. 1992. In situ oxygen isotope analysis of feldspar and quartz by Nd:YAG laser microprobe. *Chemical Geology*, **101**, 21–41.

FERRY, J M. 1984. A biotite isograd in south-central Maine, USA: Mineral reactions, fluid transfer and heat transfer. *Journal of Petrology*, **25**, 871–893.

FERRY, J M. 1992. Regional metamorphism of the Waits Rover formation, Eastern Vermont: Delineation of a new type of giant metamorphic hydrothermal system. *Journal of Petrology*, **33**, 45–94.

FORTIER, S M, & GILETTI, B J. 1989. An empirical model for predicting diffusion coefficients in silicate minerals. *Science*, **245**, 1481–1484.

FRICKE, H C, WICKHAM, S M, & O'NEIL, J R. 1992. Oxygen and hydrogen isotope evidence for meteoric water infiltration during mylonitization and uplift in the Ruby Mountains-East Humboldt Range core complex, Nevada. *Contributions to Mineralogy and Petrology*, **111**, 203–221.

FRIEDMAN, I, & O'NEIL, J R. 1977. Compilation of stable isotope fractionation factors of geochemical interest. *In:* FLEISCHER, M (ed), *Data of Geochemistry*, 6 edn. US Government Printing Office, Washington D.C.

GARLICK, G D, & EPSTEIN, S. 1967. Oxygen isotope ratios in coexisting minerals of regionally metamorphosed rocks. *Geochimica et Cosmochimica Acta*, **31**, 181–214.

GRAHAM, C M, VALLEY, J W, & WINTER, B L. 1996. Ion microprobe analysis of $^{18}O/^{16}O$ in authigenic and detrital quartz in the St. Peter Sandstone, Michigan Basin and Wisconsin Arch, USA: Contrasting diagenetic histories. *Geochimica et Cosmochimica Acta*, **60**, 5101–5116.

GUIDOTTI, C V. 1984. Micas in metamorphic rocks. *Chap. 10, pages 357–456 of:* BAILEY, S W (ed), *Micas*. Reviews in Mineralogy, vol. 13. Mineralogical Society of America.

GUIDOTTI, C V, & SASSI, F P. 1976. Muscovite as a petrogenetic indicator mineral in pelitic schists. *Pages 97–142 of: Neues Jahrbuch fuer Mineralogie*. E. Schweizerbart'sche Verlagsbuchhandlung, Stuttgart, Federal Republic of Germany.

GUIDOTTI, C V, CHENEY, J T, & GUGGENHEIM, S. 1977. Distribution of titanium between co-existing muscovite and biotite in pelitic schists from northwestern Maine. *American Mineralogist*, **62**, 438–448.

HALL, L M, & ROBINSON, P. 1982. Stratigraphic-tectonic subdivisions of southern New England. *Pages 15–41 of:* ST-JULIEN, P, & BÉLAND, J (eds), *Major structural zones and faults of the northern Appalachians*. Special Paper, no. 24. Geological Association of Canada.

HAMES, W E, TRACY, R J, & BODNAR, R J. 1989. Post-metamorphic unroofing history deduced from petrology, fluid inclusions, thermochronology and thermal modelling: an example from southwestern New England. *Geology*, **17**, 727–730.

HAMES, W E, TRACY, R J, RATCLIFFE, N M, & SUTTER, J F. 1991. Petrologic, structural, and geochronologic characteristics of the Acadian metamorphic overprint on

the Taconide zone in part of southwestern New England. *American Journal of Science*, **291**, 887–913.

HARTE, B, & HENLEY, K J. 1966. Occurrence of compositionally zoned almanditic garnets in regionally metamorphosed rocks. *Nature*, **210**, 689–692.

HATCH, N L, SCHNABEL, R W, & NORTON, S A. 1968. Stratigraphy and correlation of the rocks on the east limb of the Berkshire anticlinorium in Western Massachusetts and north-central Connecticut. *Pages 177–184 of:* ZEN, E, WHITE, W S, HADLEY, J B, & THOMPSON, J B (eds), *Studies of Appalachian geology - Northern and Maritime.* Interscience, New York.

HICKEY, K A, & BELL, T H. 1999. Behaviour of rigid objects during deformation and metamorphism: a test using schists from the Bolton syncline, Connecticut, USA. *Journal of Metamorphic Geology*, **17**, 211–228.

HOLLAND, T J B, & POWELL, R. 1985. An internally consistent thermodynamic dataset with uncertainties and correlations: 2. Data and results. *Journal of Metamorphic Geology*, **3**, 343–370.

HOLLAND, T J B, & POWELL, R. 1990. An enlarged and updated internally consistent thermodynamic dataset with uncertainties and correlations: the system K_2O-Na_2O-CaO-MgO-MnO-FeO-Fe_2O_3-AL_2O_3-TiO_2-SiO_2-C-H_2-O_2. *Journal of Metamorphic Geology*, **8**, 89–124.

HOLLAND, T J B, & POWELL, R. 1998. An internally consistent thermodynamic data set for phases of petrological interest. *Journal of Metamorphic Geology*, **16**, 309–343.

HOLLISTER, L S. 1966. Garnet zoning: An interpretation based on the Rayleigh fractionation model. *Science*, **154**, 1647–1651.

JONES, A M, IACUMIN, P, & YOUNG, E D. 1999. High-resolution $\delta^{18}O$ analysis of tooth enamel phosphate by isotope ratio monitoring gas chromatography mass spectrometry and ultraviolet laser fluorination. *Chemical Geology*, **153**, 241–248.

KARABINOS, P. 1984. Polymetamorphic garnet zoning from Southeastern Vermont. *American Journal of Science*, **284**, 1008–1025.

KARABINOS, P. 1985. Garnet and staurolite producing reactions in a chlorite-chloritoid schist. *Contributions to Mineralogy and Petrology*, **90**, 262–275.

KARABINOS, P, & LAIRD, J. 1988. Structure and metamorphism from Jamaica to the Athens Dome, Vermont. *Pages 281–292 of:* BOTHNER, W A (ed), *Guidebook for Field Trips in Southwestern New Hampshire, Southeastern Vermont, and North-central Massachusetts*. Keene State College, Keene, New Hampshire.

KELLEY, S P, & FALLICK, A E. 1990. High precision spatially resolved analysis of δ^{34}S in sulphides using a laser extraction technique. *Geochimica et Cosmochimica Acta*, **54**, 883–888.

KOHN, M J. 1993. Modeling of prograde mineral δ^{18}O changes in metamorphic systems. *Contributions to Mineralogy and Petrology*, **113**, 249–261.

KOHN, M J, & SPEAR, F S. 1989. Empirical calibration of geobarometers for the assemblage garnet + hornblende + plagioclase + quartz. *American Mineralogist*, **74**, 77–84.

KOHN, M J, VALLEY, J W, ELSENHEIMER, D, & SPICUZZA, M J. 1993. O isotope zoning in garnet and staurolite: Evidence for closed-system mineral growth during regional metamorphism. *American Mineralogist*, **78**, 988–1001.

KRETZ, R. 1973. Kinetics of the crystallization of garnet at two localities near Yellowknife. *Canadian Mineralogist*, **12**, 1–20.

KRETZ, R. 1983. Symbols for rock-forming minerals. *American Mineralogist*, **68**, 277–279.

LAIRD, J, & ABLEE, A L. 1981. Pressure, temperature and time indicators in mafic schists: their application to reconstructing the polymetamorphic history of Vermont. *American Journal of Science*, **281**, 127–175.

LAIRD, J, LANPHERE, M L, & ABLEE, A L. 1984. Distribution of Ordovician and Devonian metamorphism in mafic and pelitic schists from northern Vermont. *American Journal of Science*, **284**, 376–413.

MAHAR, E M, BAKER, J M, POWELL, R, HOLLAND, T J B, & HOWELL, N. 1997. The effect of Mn on mineral stability in metapelites. *Journal of Metamorphic Geology*, **15**, 223–238.

MATTEY, D, & MACPHERSON, C. 1993. High-precision oxygen isotope microanalysis of ferromagnesian minerals by laser-ablation. *Chemical Geology (Isotope Geoscience Section)*, **105**, 305–318.

MILLER, S J, & TRACY, R J. 1991. High-pressure metamorphism of the Straits Schist, northwestern Connecticut. *In: Geological Society of America, Abstracts with Programs*, vol. 23.

NIER, A O. 1950. A redetermination of the relative abundancies of the isotopes of carbon, nitrogen, oxygen, argon and potassium. *Physics Review*, **77**, 789–793.

NORTON, S A. 1976. Hoosac Formation (early Cambrian or older) on the east limb of the Berkshire massif, Western Massachusetts. *Geological Society of America Memoir*, **148**, 357–371.

O'NEIL, J R. 1986. Theoretical and experimental aspects of isotopic fractionation. *Chap. 1, pages 1–40 of:* VALLEY, J W, TAYLOR, H P, & O'NEIL, J R (eds), *Stable isotopes in high-temperature geological processes.* Reviews in Mineralogy, vol. 16. Mineralogical Society of America.

POWELL, R, & HOLLAND, T J B. 1985. An internally consistent thermodynamic dataset with uncertainties and correlations: 1. Methods and a worked example. *Journal of Metamorphic Geology*, **3**, 327–342.

POWELL, R, & HOLLAND, T J B. 1988. An internally consistent dataset with uncertainties and correlations: 3. Applications to geobarometry, worked examples and a computer program. *Journal of Metamorphic Geology*, **6**, 173–204.

POWELL, R, & HOLLAND, T J B. 1990. Calculated mineral equilibria in the pelite system, KFMASH (K_2O-FeO-MgO-Al_2O_3-SiO_2-H_2O). *American Mineralogist*, **75**, 367–380.

POWELL, R, & HOLLAND, T J B. 1994. Optimal geothermometry and geobarometry. *American Mineralogist*, **79**, 120–133.

POWELL, R, HOLLAND, T J B, & WORLEY, B. 1998. Calculating phase diagrams involving solid solutions via non-linear equations, with examples using THERMOCALC. *Journal of Metamorphic Geology*, **16**, 577–588.

RATCLIFFE, N M, BURTON, W C, SUTTER, J F, & MUKASA, S A. 1988. Stratigraphic, structural geology, and thermochronology of the northern Berkshire massif and southern Green Mountains. Part II - Internal structure of the Green Mountain massif and Wilmington Dome. *Pages 126–135 of:* BOTHNER, W A (ed), *Guidebook for Field Trips in Southwestern New Hampshire, Southeastern Vermont, and North-central Massachusetts.* Keene State College, Keene, New Hampshire.

RICHTER, R, & HOERNES, S. 1988. The application of the increment method in comparison with experimentally derived and calculated O-isotope fractionations. *Chemie der Erde*, **48**, 1–18.

ROSENFIELD, J L. 1968. Garnet rotation due to major Palaeozoic deformations in southeastern Vermont. *Pages 185–202 of:* ZEN, E, WHITE, W S, HADLEY, J B, & THOMPSON, J B (eds), *Appalachian Geology, Northern and Maritime.* Interscience, New York.

RUMBLE, D. 1982. Stable isotope fractionation during metamorphic devolatilization reactions. *Chap. 8, pages 327–354 of:* FERRY, J M (ed), *Characterization of metamorphism through mineral equilibria.* Reviews in Mineralogy, vol. 10. Mineralogical Society of America.

RUMBLE, D, & SPEAR, F S. 1983. Oxygen-isotope equilibration and permeability enhancement during regional metamorphism. *Journal of the Geological Society of London*, **140**, 619–618.

RUMBLE, D, FARQUHAR, J, YOUNG, E D, & CHAMBERLAIN, C P. 1997. In situ oxygen isotope analysis with an excimer laser using F_2 and BrF_5 reagents and O_2 gas as analyte. *Geochimica et Cosmochimica Acta*, **61**, 4229–4234.

SANTROCK, J, STUDLEY, S A, & HAYES, J M. 1985. Isotopic analysis based on the mass spectrum of carbon dioxide. *Analytical Chemistry*, **57**, 1444–1448.

SHANNON, R D, & PREWITT, C T. 1969. Effective ionic radii in oxides and fluorides. *Acta Crystallography*, **B25**, 925–946.

SHARP, Z D. 1990. A laser-based microanalytical method for the *in-situ* determination of oxygen isotope ratios of silicates and oxides. *Geochimica et Cosmochimica Acta*, **54**, 1353–1357.

SILVERMAN, S R. 1951. The isotope geology of oxygen. *Geochimica et Cosmochimica Acta*, **2**, 26–42.

SPEAR, F S. 1988. The Gibbs method and Duhem's theorem: The quantitative relationships among P, T, chemical potential, phase composition and reaction progress in igneous and metamorphic systems. *Contributions to Mineralogy and Petrology*, **99**, 249–256.

SPEAR, F S. 1989. Petrologic determination of metamorphic pressure-temperature-time paths. *Page 102 of:* SPEAR, F S, & PEACOCK, S M (eds), *Metamorphic pressure-temperature-time paths*. Short Course, vol. 7. American Geophysics Union.

SPEAR, F S. 1993. *Metamorphic phase equilibria and pressure-temperature-time paths*. Monograph. Mineralogical Society of America, Washington D.C.

SPEAR, F S, & CHENEY, J T. 1989. A petrogenetic grid for pelitic schists in the system SiO_2 - Al_2O_3 - FeO - MgO - K_2O - H_2O. *Contributions to Mineralogy and Petrology*, **101**, 149–164.

SPEAR, F S, & KOHN, M J. 1996. Trace element zoning in garnet as a monitor of crustal melting. *Geology*, **24**, 1099–1102.

SPEAR, F S, & SELVERSTONE, J. 1983. Quantitative P-T paths from zoned minerals: Theory and tectonic applications. *Contributions to Mineralogy and Petrology*, **83**, 348–357.

SPEAR, F S, FERRY, J M, & RUMBLE, D. 1982. Analytical formulation of phase equilibria: The Gibbs method. *Chap. 4, pages 105–152 of:* FERRY, J M (ed), *Characterization of metamorphism through mineral equilibria*. Reviews in Mineralogy, vol. 10. Mineralogical Society of America.

ST-ONGE, M R. 1987. Zoned poikiloblastic garnets: P-T paths and syn-metamorphic uplift through 30km of structural depth, Wopmay Orogen, Canada. *Journal of Petrology*, **28**, 1–21.

STANLEY, R S, & HATCH, N L. 1988. The pre-Silurian geology of the Rowe-Hawley zone. *Pages A1–A39 of:* HATCH, N L (ed), *The bedrock geology of Massachusetts*. US Geological Survey Professional Paper, no. 1366. US Geological Survey.

STANLEY, R S, & RATCLIFFE, N M. 1985. Tectonic synthesis of the Taconian orogeny in western New England. *Geological Society of America Bulletin*, **96**, 1227–1250.

SUTTER, J F, RATCLIFFE, N M, & MUKASA, S B. 1985. $^{40}Ar/^{39}Ar$ and K-Ar dating bearing on the metamorphic and tectonic history of western New England. *Bulletin of the Geological Society of America*, **96**, 123–136.

SYMMES, G H, & FERRY, J M. 1992. The effect of whole-rock MnO content on the stability of garnet in pelitic schists during metamorphism. *Journal of Metamorphic Geology*, **10**, 221–237.

THOMPSON, A B, TRACY, R J, LYTTLE, P T, & THOMPSON, J B. 1977. Prograde reaction histories deducted from compositional zonation and mineral inclusions in garnet from the Gassetts schist, Vermont, USA. *American Journal of Science*, **277**, 1152–1167.

THOMPSON, J B. 1957. The graphical analysis of mineral assemblages in pelitic schists. *American Mineralogist*, **42**, 842–858.

THOMPSON, J B. 1982. Reaction space: An algebraic and geometric approach. *Chap. 2, pages 33–52 of:* FERRY, J M (ed), *Characterization of metamorphism through mineral equilibria*. Reviews in Mineralogy, vol. 10. Mineralogical Society of America.

THOMPSON, J B, LAIRD, J, & THOMPSON, A B. 1982. Reactions in amphibolite, greenschist and blueschist. *Journal of Petrology*, **23**, 1–27.

TRACY, R J. 1982. Compositional zoning and inclusions in metamorphic minerals. *Pages 335–394 of:* FERRY, J M (ed), *Characterization of metamorphism through mineral equilibria*. Reviews in Mineralogy, vol. 10. Mineralogical Society of America.

TRACY, R J, ROBINSON, P, & THOMPSON, A B. 1976. Garnet composition and zoning in the determination of temperature and pressure of metamorphism, central Massachusetts. *American Mineralogist*, **61**, 762–775.

TRCZIENSKI, W R. 1977. Garnet zoning - product of a continuous reaction. *Canadian Mineralogist*, **15**, 250–256.

TUCKER, R D, & ROBINSON, P. 1990. Age and setting of the Bronson hill magmatic arc: a re-evaluation based on U-Pb zircon ages in southern New England. *Bulletin of the Geological Society of America*, **102**, 1404–1419.

VALLEY, J W, & GRAHAM, C M. 1991. Ion microprobe analysis of oxygen isotope ratios in granulite facies magnetites: Diffusive exchange as a guide to cooling history. *Contributions to Mineralogy and Petrology*, **109**, 38–52.

VALLEY, J W, & GRAHAM, C M. 1996. Ion microprobe analysis of oxygen isotope ratios in quartz from Skye granite: healed micro-cracks, fluid flow, and hydrothermal exchange. *Contributions to Mineralogy and Petrology*, **124**, 225–234.

VALLEY, J W, EILER, J M, KOHN, M J, SPICUZZA, M J, BAUMGARTNER, L P, ELSENHEIMER, D, & GRAHAM, C M. 1994. Contrasting styles of oxygen isotope exchange. *Mineralogical magazine*, **58A**, 924–925.

VALLEY, J W, KITCHEN, N, KOHN, M J, NIENDORF, C R, & SPICUZZA, M J. 1995. UWG-2, a garnet for oxygen isotope ratios: Strategies for high precision and accuracy with laser heating. *Geochimica et Cosmochimica Acta*, **59**, 5223–5231.

VANCE, D, & HOLLAND, T J B. 1993. A detailed isotopic and petrological study of a single garnet from the Gassetts schist, Vermont. *Contributions to Mineralogy and Petrology*, **114**, 101–118.

VANCE, D, & MAHAR, E. 1998. Pressure-temperature paths from P-T pseudosections and zoned garnets: potential, pitfalls and examples from the Zanskar Himalaya, NW India. *Contributions to Mineralogy and Petrology*, **132**, 225–245.

VANCE, D, & O'NIONS, R K. 1990. Isotopic chronometry of zoned garnets; growth kinetics and metamorphic histories. *Earth and Planetary Science Letters*, **97**, 227–240.

VANCE, D, & O'NIONS, R K. 1992. Prograde and retrograde thermal histories from the central Swiss Alps. *Earth and Planetary Science Letters*, **114**, 113–129.

WALDRON, K A. 1986. *High pressure contact metamorphism in the aureole of the Cortlandt Complex, southeastern New York.* Ph.D. thesis, Yale University, New Haven.

WALKER, C B. 1999. *The tectonothermal evolution of the high Himalayas in the Suru Valley, NW Zanskar, with constraints from metamorphic modelling*. Ph.D. thesis, University of Oxford, UK.

WIECHERT, U, & HOEFS, J. 1995. An excimer laser-based microanalytical preparation technique for *in-situ* oxygen isotope analysis of silicate and oxide minerals. *Geochimica et Cosmochimica Acta*, **59**, 4093–4101.

WINDLEY, B F. 1995. *The evolving continents*. 3 edn. Wiley.

WINTSCH, R P. 1975. Solid-fluid equilibria in the system $KAlSi_3O_8$-$NaAlSi_3O_8$-Al_2SiO_5-SiO_2-H_2O-HCl. *Journal of Petrology*, **16**, 57–79.

WORLEY, B, & POWELL, R. 1998. Singularities in NCKFMASH (Na_2O-CaO-FeO-MgO-Al_2O_3-SiO_2-H_2O). *Journal of Metamorphic Geology*, **16**, 169–188.

YARDLEY, B W D. 1977. An empirical study of diffusion in garnet. *American Mineralogist*, **62**, 793–800.

YOUNG, E D. 1993. On the $^{18}O/^{16}O$ record of reaction progress in open and closed metamorphic systems. *Earth and Planetary Science Letters*, **117**, 147–167.

YOUNG, E D, & RUMBLE, D. 1993. The origin of correlated variations in *in-situ* $^{18}O/^{16}O$ and elemental concentrations in metamorphic garnets from southeastern Vermont, USA. *Geochimica et Cosmochimica Acta*, **57**, 2585–2597.

YOUNG, E D, & RUSSELL, S S. 1998. Oxygen reservoirs in the early solar nebula inferred from an Allende CAI. *Science*, **282**, 452–455.

YOUNG, E D, FOGEL, M L, RUMBLE, D, & HOERING, T C. 1998a. Isotope-ratio-monitoring of O_2 for microanalysis of $^{18}O/^{16}O$ and $^{17}O/^{16}O$ in geological materials. *Geochimica et Cosmochimica Acta*, **62**, 3087–3094.

YOUNG, E D, COUTTS, D W, & KAPITAN, D. 1998b. UV laser ablation and irm-GCMS microanalysis of $^{18}O/^{16}O$ and $^{17}O/^{16}O$ with application to a calcium-aluminium-rich inclusion from the Allende meteorite. *Geochimica et Cosmochimica Acta*, **62**, 3161–3168.

ZEN, E, GOLDSMITH, R, RATCLIFFE, N M, ROBINSON, P, & STANLEY, R S. 1983. *Bedrock Geological Map of Massachusetts*. U.S. Geological Survey, Reston, and Commonwealth of Massachusetts, Department of Public Works, Boston.

ZHENG, Y F. 1993a. Calculation of oxygen isotope fractionation in anhydrous silicate minerals. *Geochimica et Cosmochimica Acta*, **57**, 1079–1091.

ZHENG, Y F. 1993b. Calculation of oxygen isotope fractionation in hydroxyl-bearing silicates. *Earth and Planetary Science Letters*, **120**, 247–263.

ZHENG, Y F. 1999. On calculations of oxygen isotope fractionation in minerals. *Episodes*, **22**, 99–106.

APPENDICIES

The following appendicies are contained here:

- **Appendix A** - All isotope development data
- **Appendix B** - All Hoosac schist isotope data
- **Appendix C** - USNM Almandine standard data
- **Appendix D** - X-Ray Fluorescence bulk-rock analysis
- **Appendix E** - Microprobe and SEM mineral analysis

Appendix

A: All Development Data

Notes on listings:

- the results are given in chronological order; each table represents either a different sample or a discrete laboratory session
- samples are given as raw, uncorrected values
- a new day is indicated with†
- appropriate blank numbers for correction purposes are described with a superscript
- run conditions (freeze times, chopper status etc) are detailed for the first run listed and all subsequent experiments were performed under the same conditions unless detailed as different

Table A1: Early CO_2 laser runs - using BrF_5

						Refreeze microvolume			
Run No.	BrF_5 mbar	freeze times	V_{32}	$\delta^{18}O$	$\delta^{17}O$	V_{32}	$\delta^{18}O$	$\delta^{17}O$	comment
OQQ Quartz by CO_2 laser - Nov 1996									
2-18	15.2	10/11	1.200			0.967	10.587	6.018	
2-19	15.8	10/11	1.984	9.684	5.771		9.927	5.841	
NCSU Quartz by CO_2 laser - Nov 1996									
2-27	15.2	10/11	1.797	10.176	5.778	1.143	10.416	5.979	
2-28a	15.3	10/11	2.980	10.370	5.870		10.539	6.000	
2-31	15.3	10/11	1.411	10.708	4.445		11.045	4.92	
Wisconsin Gore Mountain Garnet									
2-28b	16.0	10/11	7.945	3.366	2.494				
2-29	18.0	8/15		2.236	1.404				
2-33	20.2	11/11		4.251	11.391		4.251	11.391	
2-34	32.4	11/11		4.081	6.605		4.289	7.113	
2-35	20.2	10/11		3.255	1.963		3.497	2.147	
new U-trap, no more freezing in the chamber									
performed reference gas tests									
2-36	14.9	11/15		4.047	2.322				
2-37	50.4	10/15/15	1.276	3.260	1.925		3.579	2.034	variable temp trap
gold-coated sample holder									
2-39	14.5	5/10	1.512	5.899	3.309		6.153	3.407	
2-41	14.8	5/10	2.460	4.699	2.598		4.866	2.714	
2-42	15.2	8/10	1.130	3.300					
2-43	15.0	5/10	1.400	2.475	1.506		2.850	1.770	
2-45	20.5	5/10	1.322	3.069	1.875				

Table A2: USNM Garnet with UV, microvolume runs and BrF_5

Run No.	BrF_5 mbar	freeze times	V_{32}	$\delta^{18}O$	$\delta^{17}O$	laser mW	comment
repolished chamber; prefluorinated 44.1 mbar BrF_5							
2-46†	24.2	6/10	1.351	10.652	6.771	560	chopper
2-47	15.0	8/11	2.043	8.130	5.528	640	chopper
2-48	15.0	8/10	2.300	9.468	5.597	590	no chopper
2-49	15.6	8/11	3.500	6.769	4.237	603	new chopper
2-50	15.3	8/11	5.000	6.553	4.274	618	refreeze → 6.662 $\delta^{18}O$
2-51†	15.0	8/11	3.960	7.257	4.695	623	chopper
2-52	55.8	8/11	1.500	4.982	4.647	620	no chopper
2-53	56.8	8/11	2.191	5.090	4.755	670	
2-54	73.7	9/11	1.300	4.759	3.838	635	
2-55	35.3	9/11	2.700	5.565	4.506	670	
2-56	23.7	8/11	3.960	5.834	4.132	640	refreeze → 5.949 $\delta^{18}O$
2-57†	23.7	8/11	4.020	4.742	4.267	620	refreeze → 4.901 $\delta^{18}O$
2-58	25.9	7/11	3.191	5.779	4.760	620	refreeze → 5.939 $\delta^{18}O$
2-59	22.9	8/11	2.864	5.940	5.033	620	refreeze → 6.198 $\delta^{18}O$
2-60	23.2	7/11	2.807	7.042	5.444	620	
2-62†	24.0	10/11	4.300	9.384	5.697	670	
2-71†	23.2	9/11	3.337	9.999	5.644	640	
2-72	23.4	9/11	2.469	7.315	4.228	630	no chopper
2-73	23.4	9/11	1.978	7.104	4.104	620	
2-74	24.1	9/11	3.330	8.433	4.870	625	
2-75	40.2	8/11	2.370	6.985	4.047	606	

Table A3: USNM Garnet by GC-irms and BrF_5 - Feb 1997

Run No.	BrF_5 mbar	Area, Vs	$\delta^{18}O$	$\delta^{17}O$	freeze times	laser mV	comment
blank 1†	39.8	7.345	9.38	4.43	8/11/10		
2-96[1]	5.2	9.798	3.94	1.83	8/8/8	30.8	
blank 2	20.9	7.717	9.04	5.00	8/11/10		
2-97[2]	30.5	21.012	-2.60	-1.13		30.5	
2-98[2]	13.0	28.246	4.05	1.93		31.3	
2-99[2]	60.1	25.392	3.40	1.74		32.8	
2-100[2]	51.0	47.750	-	2.54		25.0	too large
blank 1†	55.3	6.488	11.46	6.52	8/11/10		
2-101[1]	49.9	16.093	4.99	2.70		22.8	2 rastors
2-102[1]	19.8	14.220	5.08	2.84		23.4	
2-103[1]	19.8	21.146	3.83	2.16		26.2	
2-104[1]	5.0	56.750	-	2.24		34.8	too large
2-105[1]	5.2	32.786	1.55	1.93		35.7	
2-106[1]	39.7	36.137	5.37	3.08		35.5	
blank 1†	43.0	6.210	8.70	5.00	8/11/10		
2-107[1]	44.9	40.336	-	3.56		34.7	too big
2-108[1]	45.6	31.640	7.86	4.30		36.2	
2-109[1]	45.9	20.435	4.97	2.65		34.3	
2-110[1]	41.0	26.600	6.53	4.00		34.3	
2-111[1]	41.0	36.024	7.60	4.16		34.1	
2-112[1]	40.7	35.648	7.64	4.19		33.0	
put 40.0 mbar BrF_5 in chamber for 3 mins, then cleaned up							
blank 1†	40.0	6.506	10.43	5.58	8/11/10		
2-113[1]	37.6	22.415	5.70	2.88		31.2	
2-115[1]	38.0	27.253	7.35	4.36		31.7	
2-116[1]	39.2	30.188	7.76	4.42		31.2	
blank 1†	40.2	5.346	8.53	4.69	8/11/10		
2-122[1]	38.5	12.891	6.16	3.34		38.5	chopper
2-123[1]	30.6	16.788	4.85	2.87		39.2	

Table A4: USNM Garnet with UV, microvolume runs and F_2

Run No.	F_2 mbar	freeze times	V_{32}	$\delta^{18}O$	$\delta^{17}O$	laser mW	comment
fluorine generator introduced; first samples using fluorine							
first perform blank testing over garnet							
blank 1†	15.2	11/10	0.276				
2-185[1]	16.9	10/10	0.611	7.562	3.164	21.4	
blank 2	15.2	11/10	0.039				
2-186[2]	15.4	11/10	0.608	6.223		21.3	
2-187[2]	15.2	11/10/10	0.903	5.945	-	21.9	took to mol sieve
2-188[2]	15.7	11/10	0.538	5.682	-	20.7	18 rastors

Table A5: USNM Garnet with UV, F_2 and GC-*irms*, June 1997

Run No.	F_2 mbar	Area, Vs	$\delta^{18}O$	$\delta^{17}O$	freeze times	laser mV	comment
first time analysis of mineral with GC-irms and fluorine							
blank 1†	5.0	7.700	5.38	3.10	10/10/10		
2-189[1]	6.2	21.590	5.09	2.80		25.5	
2-190[1]	10.6	35.415	5.42	2.49		22.6	
blank 1†	16.6	28.183	-4.05	-2.30	10/10/10		
blank 2	15.0	8.096	8.39	4.56			
blank 3	14.9	8.603	9.32	4.90			
blank 4	14.5	9.446	9.69	4.95			
blank 1†	13.5	5.682	9.95	4.94	10/10/10		
3-20[1]	14.8	20.941	7.24	4.15		24.5	no chopper, slow
blank 2	13.5	6.256	9.89	5.78			
fluorinated over lunch 14.0 mbar F_2							
blank 3	13.5	7.028	11.42	6.09			
3-21[3]	13.6	20.050	7.24	3.67		23.3	
blank 4	13.7	6.094	9.50	5.33			
3-22[4]	13.7	26.107	7.00	3.70		23.2	pit 150× 80μm
3-23[4]	13.7	19.496	7.29	3.97		23.0	
3-24[4]	13.7	21.254	7.56	4.55		25.1	
3-25[4]	13.0	20.036	6.63	3.74		26.0	

Table A6: USNM Schorl R11871-1, July 1997

Run No.	F_2 mbar	Area, Vs	$\delta^{18}O$	$\delta^{17}O$	freeze times	laser mV	comment
blank s		6.042	10.15	5.44	10,10		Si Gel blank
blank 1†	13.7	6.136	9.53	4.90	10/10/10		
blank 2	13.3	7.252	10.09	5.34			
3-31[2]	13.0	29.539		5.29		22.3	too big
3-32[2]	12.7	19.446	9.04	4.80		21.4	no chopper
3-33[2]	14.1	20.324	8.62	4.58		25.2	chopper
blank 3	14.2	6.348	10.22	5.58			
3-34[3]	14.6	18.706	8.68	4.87		25.7	no chopper
3-35[3]	14.4	16.020	8.97	4.67		21.6	
3-36[3]	13.6	15.361	8.58	4.81		20.4	

Table A7: USNM Forsterite, July 1997

Run No.	F_2 mbar	Area, Vs	$\delta^{18}O$	$\delta^{17}O$	freeze times	laser mV	comment
prefluorinated with 62 mbar F_2							
blank 1†	14.0	7.676	9.81	5.31	10/10/10		
3-37[1]	13.5	29.012	8.18	4.64		23.6	no chopper
blank 2	13.7	7.617	8.78	4.66			
fluorinated with 15.0 mbar F_2 , lazed mineral and cleaned up							
3-38[2]	16.3	20.675	6.70	3.72		22.2	chopper, 2 rastors
3-39[2]	17.2	28.082	8.00	4.61		24.7	
3-40[2]	16.4	21.793	7.76	4.12		22.4	
3-41[2]	21.0	23.900	7.35	3.98		20.8	10% chopper
blank 3	15.7	9.443	10.29	5.92			
3-42[3]	15.3					23.5	sample lost
3-43[3]	15.7	20.412	6.81	3.83		23.2	chopper
3-44[3]	16.2	20.870	7.14	4.40		21.8	no chopper

Table A8: USNM Zircon, August 1997

Run No.	F_2 mbar	Area, Vs	$\delta^{18}O$	$\delta^{17}O$	freeze times	laser mV	comment
attempt to analyse USNM Zircon with the green laser							
blank 1†	16.0	2.007	4.39	2.48	6/10/10		
3-103[1]	15.5						too small
3-104[1]	15.5	2.570	11.20	5.76			
3-105[1]	15.4	3.798	10.38	6.31			shallow, 60× 100μm
3-106[1]	15.9	3.834	20.55	10.67			
3-107[1]	10.6	2.880	14.23	8.08			

Table A9: Gassetts schist garnet, August 1997

Run No.	F_2 mbar	Area, Vs	$\delta^{18}O$	$\delta^{17}O$	freeze times	laser mV	comment
prefluorinated 67 mbar F_2 → 58 mbar, overnight							
blank c		0.450	3.23	2.93	10 mins		cryofocus blank
blank 1†	20.7	2.860	12.81	7.48	6/10/10		
blank 2	10.0	1.064	2.21	1.69			
3-108[2]	20.5	5.519	25.21	13.62		30.0	no chopper
3-109[2]	26.7	4.481	23.55	13.17		26.8	
3-110[2]	10.6	4.213	19.46	10.08	11/10/10	25.0	chopper
3-111[2]	13.1	4.181	14.55	7.95	6/10/10	26.0	
blank 1†	12.0	0.639	5.73	2.91	10/10/10		
3-112[1]	12.8	3.132	19.07	10.97		27.6	chopper
3-113[1]	14.9	12.637	17.20	10.19		23.0	lazed within pit
3-114[1]	13.0	2.554	14.2	7.70		22.0	no chopper

Table A10: USNM Garnet + R94B Garnet, by μvolume, Nov 1997

Run No.	F_2 mbar	$\delta^{18}O$	freeze times	laser mV	comment
Au-coated samples; prefluorinated 25 mbar F_2					
USNM Almandine					
3-208†	6.2	9.70	10/10	25.4	chopper, slow; 750× 500μm
3-209	6.2	9.85	11/10	23.0	chopper, shallow pit
3-211	10.0	8.20	10/10	22.0	
3-210 and 3-212 - too little gas					
3-213†	12.0	7.90		22.5	chopper, went over hole 3-4 times
3-214	11.0	6.60		21.0	went over pit 3 times
3-215	10.6	6.70		20.0	
3-216	14.0	6.10		21.5	
loaded anouther Au-coated USNM garnet					
prefluorinated 23.5 mbar F_2					
3-217†	15.5	8.20	10/10	18.5	fast chopper, 750×500 μm
3-218	13.5	9.20		21.0	
3-219 lost					
line was heated and pumped all night					
3-220†	12.2	5.93	10/10	21.1	larger plume?
3-221	13.0	7.29		21.2	
3-222	12.0	6.57		21.0	
R94B garnet					
3-223	11.8	9.92	10/10	19.0	chopper
3-224	11.8	9.88		20.0	
3-225	11.6	9.32		18.5	
USNM Almandine					
3-226†	13.8	4.40	10/10	18.0	
3-227	11.6	3.80		18.0	
R94B garnet					
3-228	12.2	7.80		19.5	chopper, pit 750×750 μm
3-229	12.0	8.00		18.0	
3-230†	12.6	7.50	10/10	19.0	
3-231	10.6	7.40		19.0	

Table A11a: USNM Almandine, Nov 1997

Run No.	F_2 mbar	Area, Vs	$\delta^{18}O$	$\delta^{17}O$	freeze times	laser mV	comment
loaded USNM Garnet and R96C garnet							
blank 1†	10.4	30.000	-128.0	16.85	10/10/10		
prefluorinated 41 mbar F_2 → 30 mbar overnight							
blank 1†	12.5	9.300	6.11	3.42	10/10/10		
blank 2	11.8	6.280	13.61	7.65			
blank 3	12.4	6.600	15.90	9.10			
USNM Almandine:							
3-262 too small; 3-263 too small - laser low power							
blank 1†	10.0	7.010	9.25	6.05	10/10/10		
blank 2							computer crash
3-264[2]	11.4	28.000	-50.00	8.83		28.0	topped out - too big
blank 3	10.0	2.394	14.56	8.25			
3-265[3]	10.8	18.483	14.42	7.52		28.5	chopper, 100× 50μm
3-266[3]	14.5	4.110	14.18	7.52		23.0	
3.267[3]	12.0	15.919	11.97	6.33		25.5	went over hole again
3-268[3]	10.0	19.600	18.29	10.04		23.0	
3-269[3]	13.2	21.626	13.41	7.37		24.0	no chopper
blank 1†	10.2	2.323	15.81	8.45	10/10/10		
3-270[1]	10.2	25.011	9.73	5.68		25.0	no chopper
3-271[1]	9.2	12.346	14.11	7.53		25.5	slow chopper
maybe surface effect - ablate within hole 3-267							
3-272[1]	10.0	9.232	13.54	7.52		23.0	chopper, bellows hot
3-273[1]	14.8	13.216	15.16	8.25		27.2	increase F_2
3-274[1]	5.8	1.163	11.74	7.13		22.5	all blank
polished and re-loaded USNM garnet, removed sample							
prefluorinated with 18.6 mbar F_2 → 18.0 overnight							
blank 1†	10.0	2.432	7.77	4.53	10/10/10		
blank 2	10.0	1.869	9.72	6.30			
3-275[2]	9.8	9.571	8.58	4.52		24.0	chopper
3-276[2]	10.4	9.009	7.80	3.76		24.0	
3-277[2]	6.8	8.050	6.12	3.14		24.8	
blank 3	8.0	1.200	7.59	3.76			
3-278[3]	8.0	5.565	6.14	3.40		23.5	
3-279[3]	8.7	7.924	5.53	4.03		23.8	
3-280[3]	8.4	8.419	7.16	4.16		22.0	
loaded R96C with USNM Almandine							
blank 1†	8.4	8.175	-10.76	-4.99	10/10/10		
blank 2	8.4	3.679	5.56	3.47			
blank 3	8.2	2.726	6.79	4.19			
USNM Almandine							
3-281[3]	8.4	9.778	15.49	8.81		21.5	chopper
blank 4	8.2	2.64	5.93	3.57			
3-282[4]	8.6	24.272	8.92	4.83		25.2	
removed sample, left USNM Almandine in chamber							

Table A11b: USNM Almandine, Nov 1997 - continued

Run No.	F_2 mbar	Area, Vs	$\delta^{18}O$	$\delta^{17}O$	freeze times	laser mV	comment
blank 1†	8.2	3.223	0.33	-0.14	10/10/10		
blank 2	8.5	1.718	5.04	3.66			
3-283[2]	8.1	3.802	13.70	6.99		24.0	chopper
3-284[2]	8.2	12.680	8.11	4.23		24.2	
3-285[2]	8.4	13.900	7.13	4.22		27.0	
3-286[2]	8.1	11.256	7.16	3.82		25.7	
loaded repolished USNM Garnet, repolished quartered R96							
original sample 2cm in diameter							
prefluorinated 26.5 mbar F_2 → 23.9 mbar overnight							
blank 1†	8.5	4.048	-8.89	-3.61	10/10/10		
blank 2	8.2	2.488	-2.00	-0.39			
blank 3	8.6	2.069	3.94	2.60			
blank 4	8.0	1.870	2.92	3.29			
3-286[4]	8.1	9.537	3.02	2.53		23.6	chopper, slow
blank 5	8.2	2.185	-5.35	-3.41			
3-287[5]	8.4	2.563	11.29	6.38		24.2	

Table A12a: WI Gore Mt Garnet, April 1998

Run No.	F_2 mbar	Area, Vs	$\delta^{18}O$	$\delta^{17}O$	freeze times	laser mV	comment
blank 1†	8.3	7.751	-20.97	-10.71	10/10/10		chamber only
blank 2	7.8	3.544	-11.08	-5.23			chamber only
loaded Wisconsin Gore Mountain Garnet							
blank 1†	8.0	2.108	3.41	0.70	10/10/10		
blank 2	8.4	2.044	4.99	2.08			
4-80[2]	8.4	12.691	13.7	7.8		19.1	no chopper, slow
4-81[2]	8.0	13.150	8.93	5.20		19.0	
blank 3	8.4	2.001	6.72	4.36			
4-82[3]	8.0	12.453	8.34	4.82		27.0	w/o mask, chopped
4-83[3]	8.4	12.491	10.60	5.78		27.0	no chopper
4-84[3]	8.2	6.515	5.56	3.04		17.0	
blank 4	7.8	2.084	8.65	4.10			moving blank
4-85[4]	8.2	6.115	6.11	3.63		27.0	
4-86[4]	7.9	7.387	6.96	3.61		27.0	
blank 1†	8.3	2.004	6.38	4.74	10/10/10		
blank 2	8.6	1.359	6.05	3.42			
4-87[2]	8.1	11.493	8.79	5.13		19.0	with mask, n/chop
4-88[2]	8.0	9.490	5.34	3.13		19.0	
4-89[2]	7.8	8.205	6.09	3.79		19.0	
4-90[2]	8.2	8.526	5.61	3.41		19.0	
4-91[2]	8.7	9.289	4.46	2.80		19.0	
4-92[2]	8.7	5.036	5.06	3.15		19.0	
blank 1†	8.2	1.663	2.74	0.56	10/10/10		
blank 2	8.0	2.306	11.08	5.67			
blank 3	8.0	1.815	10.20	5.40			
4-93[3]	8.2	8.735	7.43	4.31		18.0	no chopper
blank 4	8.0	1.521	8.35	3.43			
4-94[4]	7.8	9.980	4.82	2.36		18.0	
4-95[4]	8.2	8.400	5.70	3.50		18.0	
4-96[4]	8.2	10.983	5.23	343		18.0	
blank 1†	8.2	1.508	4.31	2.33	10/10/10		
blank 2	8.2	2.211	6.29	3.17			
blank 3	9.0	1.771	5.97	3.68			
4-97[3]	7.7	10.851	5.68	3.24		19.0	
4-98[3]	8.0	13.676	4.42	2.68		19.0	
4-99[3]	7.8	7.177	3.98	2.53		19.0	
blank 1†	7.9	1.293	6.34	3.29	10/10/10		
blank 2	8.2	1.725	2.87	2.16			
4-100[2]	8.2	9.130	3.67	2.56		19.0	
heated line bellows to 200° C and pumped							
4-101[2]	8.2	18.187	3.73	2.25		18.0	
loaded new Wisconsin Gore Mountain Garnet, smaller							

Table A12b: WI Gore Mt Garnet - continued

Run No.	F_2 mbar	Area, Vs	$\delta^{18}O$	$\delta^{17}O$	freeze times	laser mV	comment
prefluorinate overnight 9.4 mbar F_2							
blank 1†	7.0	1.659	1.57	1.14	10/10/10		
blank 2	8.3	1.321	4.75	3.70			
blank 3	8.3	1.239	4.48	3.23			
4-102[3]	7.9	10.658	6.22	3.70		17.9	no chopper
4-103[3]	7.9	7.080	2.87	2.18		18.0	
4-104[3]	7.7	12.909	4.71	2.91		17.7	
heated bellows for 1 hour whilst pumping							
4-105[3]	8.0	12.839	4.30	2.16		17.7	
blank 1†	7.7	1.719	1.07	1.15	10/10/13		
blank 2	8.1	1.390	-0.22	0.01	10/10/10		
4-106[2]	4.5	13.553	5.31	3.29		17.7	6-7 rastors
4-107[2]	4.9	16.845	4.96	2.83		17.7	
4-108[2]	5.2	10.990	6.00	3.33		17.7	7 rastors
4-109[2]	4.3	2.400	7.60	4.60		17.7	lost gas

Table A13a: USNM Augite, Sept - Oct 1998

Run No.	F_2 mbar	Area, Vs	$\delta^{18}O$	$\delta^{17}O$	freeze times	laser mV	comment
blank 1†	5.2	3.259	-7.50	-3.56	10/10/10		
blank 2	4.6	2.607	1.92	-0.09			
blank 3	4.8	1.827	2.26	0.21			
4-191[3]	4.6	12.177	4.55	2.57		18.6	no chopper
blank 4	4.4	1.836	1.78	1.37			
4-192[4]	4.6	11.121	4.24	1.88		15.2	4 rastors
4-193[4]	4.5	11.604	5.80	2.57		16.3	
4-194[4]	4.4	10.744	4.72	2.54		15.8	
4-195[4]	5.0	25.041	4.12	2.26		16.9	
blank 1†	4.8	2.173	2.09	1.64	10/10/10		
blank 2	4.8	1.731	1.51	0.20			
4-196[2]	4.5	8.388	8.19	4.15		16.5	
4-197[2]	4.8	10.095	4.50	2.25		14.9	
4-198[2]	4.8	15.493	3.74	1.32		15.7	
4-199[2]	5.6	14.220	3.94	1.94		15.1	
4-200[2]	4.6	10.297	3.13	1.72		14.8	
stopped heating bellows							
4-201[2]	6.2	7.847	4.21	2.09		15.5	stopped heating bellows
4-202[2]	4.2	12.684	5.40	2.52		14.5	
blank 1†	4.3	1.400	2.84	1.20	10/10/10		
blank 2	5.0	1.623	7.60	3.68			
4-203[2]	5.0	13.366	5.81	3.18		13.8	
4-204[2]	4.6	15.778	4.75	2.35		15.3	
4-205[2]	4.8	15.162	4.73	2.61		16.0	
4-206[2]	4.8	13.178	3.70	1.88		15.8	
4-207[2]	4.3	12.057	4.31	1.76		16.5	pumped for longer between
4-208[2]	4.4	11.856	4.03	2.35		16.6	
blank 1†	8.0	2.015	7.12	3.83	10/15/10		try more fluorine,
4-209[1]	8.6	11.278	4.77	2.90		13.8	15 mins to Si Gel
4-210[1]	7.4	14.279	5.22	3.03		14.0	try larger sample
4-211[1]	8.6	14.422	3.93	1.91		14.8	kept traps at minimum
4-212[1]	8.0	19.640	4.88	2.88	10/12/10	14.7	emission at 1A
4-213[1]	5.1	5.138	4.08	2.12	10/10/10	17.7	just 2^{nd} dewer
took GC column to 300° C cycle overnight							
blank 1†	5.0	1.186	6.07	4.37	10/10/10		
4-214[1]	4.8	8.204	2.23	1.23		14.1	
4-215[1]	4.8	10.210	3.52	2.22		15.0	
replaced transfer tube							
blank c		4.437	10.79	4.96	10 min		cryofocus blank
blank 1†	4.8	7.685	10.0	5.51	10/10/10		increased sensitivity
4-216[1]	4.8	42.846	-	-		15.1	too big
4-217[1]	5.4	16.203	7.08	3.61		15.3	
4-218[1]	4.7	16.085	7.44	3.63		15.0	
blank 2	4.8	6.735	8.58	3.92			

Table A13b: USNM Augite - continued

Run No.	F_2 mbar	Area, Vs	$\delta^{18}O$	$\delta^{17}O$	freeze times	laser mV	comment
blank 1†	4.8	7.327	9.09	3.97	10/10/10		
blank 2	5.0	6.590	9.06	4.81			
4-219[2]	4.7	21.589	4.62	2.33		14.8	2 rastors
4-220[2]	5.0	26.993	4.89	2.74		14.5	
4-221[2]	5.0	14.787	7.18	3.47		15.7	
4-222[2]	5.2	12.385	7.65	4.11		16.1	
blank 3	5.1	6.930	9.01	4.03			
4-223[3]	5.0	24.287	5.62	2.96		16.0	
changed cryofocus loop as silica gel may have degraded							
blanks from new cryofocus trap were virtually nil							
test gases run through							
blank 1†	5.2	3.740	-1.21	0.17	10/10/10		
4-224[1]	4.3	30.811	6.24	3.33		14.8	
blank 2	4.8	2.560	7.59	3.33			
4-225[2]	5.6	15.598	3.42	1.22		15.3	
4-226[2]	4.4	15.641	4.10	2.55		15.9	
4-227[2]	4.8	17.955	3.71	2.27		15.0	
blank 3	4.3	2.730	4.66	2.55			
blank 1†	5.0	2.953	4.81	1.17	10/10/10		
blank 2	5.0	2.578	6.57	3.40			
blank 3	5.0	2.558	6.31	2.55			
blank 4	9.6	2.973	3.79	2.68			
4-228[4]	4.8	6.849	3.79	2.68		14.0	
4-229[4]	5.0	40.824	4.09	2.30		16.5	
4-230[4]	4.8	23.080	4.05	2.22	10/4/4/4/10	18.5	
4-231[4]	10.0	24.991	3.27	1.63		16.5	more F_2
blank 1†	5.0	2.236	4.05	1.71	5/10/10		5 mins to Si Gel
4-232[1]	5.0	19.014	1.14	-0.18		15.7	?F_2 attack of Si Gel
4-233[1]	5.0	28.134	3.44	1.83	15/15/10	16.1	longer freeze times
blank 1†	30.5	4.803	-4.53	-1.99	10/10/10		more F_2
4-234[1]	30.0	27.132	1.44	0.69		17.1	
4-235[1]	30.0	20.997	2.71	1.52		17.2	
4-236[1]	29.5	25.430	3.11	1.54		18.0	
blank 1†	26.4	3.304	5.95	4.19	10/10/10		
blank 2	26.4	3.004	6.55	4.21			
4-237[2]	26.5	23.285	4.69	2.48		16.1	
4-238[2]	26.5	24.517	4.85	2.89		16.7	
4-239[2]	26.4	20.893	4.75	2.46		17.1	
blank 1†	5.2	2.740	4.02	2.32	10/10/10		sample from fresh
4-240[1]	5.2	37.438	9.64	4.97		19.1	surface created by lasing
4-241[1]	5.2	16.144	5.19	2.97		20.1	
blank 2	5.1	2.040	9.39	6.62			
4-242[2]	5.2	13.838	5.32	2.99		14.5	

Table A14a: USNM Almandine, Oct 1998

Run No.	F_2 mbar	Area, Vs	$\delta^{18}O$	$\delta^{17}O$	freeze times	laser mV	comment
blank 1†	5.1	2.760	7.83	4.20	10/10/10		
blank 2	4.6	2.244	9.61	4.89			
blank 3	4.5	2.212	9.71	5.26			blanks very steady
4-243[3]	4.8	24.944	6.34	3.29		15.4	3 rastors, n/c
blank 4	4.3	1.895	9.08	6.50	10/10/10		
4-245[4]	4.5	23.839	5.07	2.41		17.1	
4.246[4]	4.8	29.014	5.14	2.53		18.1	
4-247[4]	4.6	19.268	4.84	2.43		18.1	
blank 5	5.0	1.989	9.78	5.39			
4-248[5]	4.9	20.488	5.00	2.18		15.5	
try chopping the laser beam							
blank 1†	7.8	2.085	8.93	3.66	10/10/10		
4-249[1]	7.4	6.660	9.71	4.58	5/12/10	18.4	chopped beam
4-250[1]	7.6	6.965	8.98	5.44		18.2	
4-251[1]	7.6	11.199	7.20	3.93	10/12/10	19.4	
4-252[1]	7.5	9.725	7.71	4.35		20.1	
4-253[1]	7.5	9.857	6.97	3.34		21.0	no chopper
4-254[1]	8.3	7.853	8.09	4.50		18.1	
4.255[1]	7.8	19.471	5.88	3.08		17.8	
blank 1†	10.4	2.299	9.22	4.85	10/12/10		
4-256[1]	10.0	12.985	6.23	2.85		19.1	no chopper
4-258[1]	10.2	20.411	5.32	2.66		20.1	
4-259[1]	10.2	11.275	6.52	3.49		19.5	
4-260[1]	10.3	14.831	5.57	2.90		20.9	
4-261[1]	10.2	7.689	8.21	3.93		21.0	
4-262[1]	10.1	11.343	6.01	3.36		20.5	
blank 1†	10.4	2.507	9.81	4.18	10/15/10		
4-263[1]	10.3	15.828	5.28	2.57		20.1	
4-265[1]	9.8	19.135	5.69	2.82		18.5	
4-266[1]	10.5	20.060	6.45	3.29	10/20/10	19.1	
blank 1†	10.2	3.769	4.28	2.25	10/20/10		
blank 2	9.7	3.044	7.63	5.09			
4-267[2]	10.2	20.061	4.76	2.62		18.2	
4-268[2]	9.9	14.572	5.40	2.90		18.2	
4-269[2]	10.1	9.279	6.01	2.44		19.1	chopper
4-270[2]	9.8	13.168	6.05	2.88		17.6	
blank 1†	10.0	2.493	7.71	5.13	10/15/10		
4-271[1]	10.1	9.751	5.33	2.77		18.1	chopper
blank 2	10.1	2.370	8.26	2.55			
4-272[2]	10.0	10.173	6.20	2.66		17.0	
4-273[2]	10.2	9.313	6.16	3.05		17.5	
4-274[2]	9.8	10.108	5.94	2.81		16.0	
4-275[2]	10.0	14.603	5.63	2.92		16.1	
blank 1	10.0	2.931	7.85	3.64	10/20/10		
4-276[1]	9.8	12.432	4.60	2.30		16.4	chopper
4-277[1]	10.1	11.327	5.36	2.76		15.0	
1st silica gel changed							

Table A14b: USNM Almandine - continued

Run No.	F_2 mbar	Area, Vs	$\delta^{18}O$	$\delta^{17}O$	freeze times	laser mV	comment
blank 1†	7.8	9.758	-20.12	-10.30	10/15/10		
20.0 mbar F_2 over sample for 15 minutes							
blank 2	8.2	3.879	3.38	1.68			
blank 3	7.9	3.554	6.63	2.12			
5-1[3]	8.6	22.418	10.02	4.97		15.1	chopper
blank 4	8.4	3.175	7.94	3.91			
5-2[4]	8.1	10.074	7.51	3.79		14.5	1 hour pumping
5-3[4]	8.1	11.436	6.38	3.24		13.7	
5-4[4]	8.1	9.444	6.16	2.95		13.8	
5-5[4]	8.2	14.464	5.72	2.52		14.2	drifting down
blank 1†	8.1	3.252	6.70	4.38	10/20/10		
bled He thro' line from Si Gel, heated bellows							
blank 2	8.2	4.568	3.21	1.43			
bled He thro' line, heating bellows + traps							
blank 3	8.0	6.142	0.81	0.52			v light
bled He thro' line but did not heat bellows							
blank 4	8.3	4.331	3.16	1.72			$\delta^{18}O$ recovering
blank 5	7.9	3.706	5.00	3.30			
15.2 mb F_2 overnight → 14.2 mbar							
heated bellows 260 °C							
not heating Silica Gel upon release							
blank 1†	7.9	8.242	3.46	1.90	10/20/10		
blank 2	8.4	4.587	8.40	3.70			
5-6[2]	7.9	15.146	7.66	3.92		15.5	chopper, 4 rastors
blank 3	8.1	3.337	9.74	5.09			1 hour between
5-7[3]	8.1	13.784	7.09	3.76		15.7	1 hour pumping
5-8[3]	8.1	13.393	7.08	3.29		15.5	45 min pumping
5-9[3]	8.0	12.919	7.09	3.28		15.4	45 mins
blank 4	7.9	3.127	9.76	5.28			
5-10[4]	7.9	13.781	7.16	3.48		15.3	

Appendix

B: Hoosac Sample Analysis

Notes on listings:

- the results are given in chronological order; each table represents either a different sample or a discrete laboratory session
- samples are given as raw, uncorrected values
- a new day is indicated with†
- superscripts refer to the blank number the analysis should be corrected with
- run conditions (freeze times, chopper status etc) are detailed for the first run listed and all subsequent experiments were performed under the same conditions unless detailed as different

Table B1a: Sample 6A and USNM Almandine, Nov 1998

Run No.	F_2 mbar	Area, Vs	$\delta^{18}O$	$\delta^{17}O$	freeze times	laser mV	comment
30.0 mbar F_2 overnight → 22.5mbar							
heated bellows							
USNM Almandine							
blank 1†	7.4	14.927	8.06	3.08	10/20/10		
blank 2	8.3	6.996	8.42	5.04			
blank 3	8.2	6.037	7.67	4.31			
5-11[3]	8.2	23.236	8.20	4.13		15.5	chopper
blank 4	8.0	5.561	7.86	3.72			pump 1 hour
5-12[4]	8.0	23.566	7.66	4.04		15.5	
blank 5	7.9	5.980	8.21	2.83			
blank 1†	8.0	4.444	10.38	4.75	10/20/10		
blank 2	8.2	4.982	9.54	5.36			
5-13[2]	7.9	17.100	8.29	4.29		16.1	
5-14[2]	7.9	15.687	7.90	4.43		15.5	
5-15[2]	7.9	15.753	8.23	3.98		15.0	
hit specimen 6A to warm up - quartz and mica							
blank 3	8.0	4.708	11.08	5.20			
5-16[3]	8.1	12.944	8.02	4.35		14.6	
5-17[3]	8.0	14.319	8.03	4.31		14.0	
blank 4	8.7	4.228	8.73	4.00			
put 33.2 mbar F_2 over sample overnight →31.5							
heated bellows							
blank 1†	7.9	8.594	6.33	3.31	10/20/10		
5-18[2]	7.5	15.730	7.52	3.78		13.0	
blank 2	8.0	4.053	9.20	5.53	10/15/10		15 mins to Si Gel
5-19[3]	7.7	11.306	7.64	4.21		13.5	
blank 3	8.0	2.678	9.94	5.51			
5-20[3]	7.9	10.889	7.63	4.81		11.5	laser v low
put 20.4 mbar F_2 overnight → 18.8							
heated bellows; laser refilled and adjusted							
blank 1†	8.0	4.822	8.95	5.01	10/15/10		
blank 2	7.8	3.143	10.71	6.49			
5-21[2]	8.0	8.060	9.05	4.82		13.5	
5-22[2]	8.0	12.513	7.28	3.86		13.5	
6A Garnet A							
5-23[2]	8.0	10.464	10.38	5.37		13.8	
5-24[3]	8.0	8.460	10.51	6.37		13.6	
blank 3	8.3	3.072	10.49	5.63			
5-25[3]	8.0	11.602	10.47	5.11		14.4	
5-26[3]	7.8	10.148	10.03	5.10		15.0	
5-27[3]	8.0	11.580	10.38	4.90		14.2	
blank 1†	8.2	2.989	10.82	5.55	10/15/10		
USNM Almandine							
5-28[2]	7.9	15.774	7.18	3.53		15.6	
5-29[2]	8.0	16.465	6.97	4.01		15.5	

Table B1b: Sample 6A and USNM Almandine - continued

Run No.	F_2 mbar	Area, Vs	$\delta^{18}O$	$\delta^{17}O$	freeze times	laser mV	comment
6A Garnet A							
5-30[2]	7.7	14.228	10.08	5.00		14.9	
5-31[2]	8.0	13.471	10.18	5.12		14.8	
blank 2	8.0	2.786	10.47	5.70			
5-32[2]	8.0	12.294	10.39	5.15		14.5	
5-33[2]	8.0	13.224	10.25	5.36		14.7	
5-34[2]	7.8	13.176	10.50	5.44		15.0	
5-35[2]	8.0	13.015	10.57	5.37		15.0	
5-36[2]	8.0	10.666	10.58	5.84		14.0	
new GC Helium							
blank 1†	7.9	2.757	11.13	4.49	10/15/10		
5-37[1]	8.0	11.186	10.49	5.27		14.7	
blank 2	7.8	2.617	10.17	6.57			
6A Garnet D							
5-38[2]	8.0	14.547	10.49	5.30		13.5	
6A Garnet C							
5-39[2]	7.8	14.638	10.38	5.59		14.9	
6A Garnet B							
5-40[2]	7.7	11.030	10.60	5.55		14.9	
5-41[2]	7.7	11.153	10.32	5.27			
6A Garnet A							
5-42[2]	7.8	10.167	10.34	5.41		13.7	
blank 3	7.9	2.624	9.42	6.13			
blank 1†	8.0	2.896	10.31	4.65	10/15/10		
5-43[1]	8.0	9.450	10.46	6.27		13.6	
5-44[1]	8.0	14.060	10.70	5.82		12.5	went over twice
5-45[1]	8.0	10.984	10.52	5.71		13.0	very heavy
Cu buildup at end of laser tube was restricting beam - low power							
took laser apart and cleaned							
beam was mis-aligned; while re-adjusting had to shoot into sample							
blank 1†	8.1	3.808	7.57	3.62	10/15/10		light blank
heated bellows and cleaned out line							
blank 2	7.8	5.148	-0.15	-0.12			big & light
put 20.2 mbar F_2 over sample overnight → 18.4 mbar							
blank 1†	8.1	3.572	7.71	3.65	10/15/10		
blank 2	8.0	3.154	9.27	5.20			
USNM Almandine							
5-46[2]	8.0	14.964	6.34	3.83		18.5	higher laser
blank 3	7.8	2.908	9.90	5.11			
5-47[3]	8.0	16.199	7.81	4.53		19.8	laser too high?
5-48[3]	8.0	12.300	8.29	4.70		13.3	detuned laser
put 40.4 mbar F_2 over sample for 1 hour							
performed 2 dummy blank runs							
5-49*	7.8	15.593	7.66	4.06		17.0	
5-50*	8.0	17.030	7.94	4.11		17.9	
25.7 mbar F_2 overnight→24.3 mbar							

* = hypothetical blank of 2.9Vs, $\delta^{18}O$ =10.5 ‰ , $\delta^{17}O$ =5.4 ‰

Table B1c: Sample 6A and USNM Almandine - continued

Run No.	F_2 mbar	Area, Vs	$\delta^{18}O$	$\delta^{17}O$	freeze times	laser mV	comment
blank 1†	8.0	3.454	8.21	4.76	10/15/10		
5-51*	8.2	17.018	7.78	3.91		17.1	
5-52*	7.9	10.946	8.32	4.05		18.1	
6A Garnet D							
5-53*	7.8	15.867	11.08	6.05		16.6	
USNM Almandine							
5-54*	8.1	11.314	7.87	4.05		16.9	
5-55*	8.2	15.048	7.54	4.30		16.5	
heated bellows briefly and then pumped all night							
blank 1†	8.2	3.669	8.16	3.92	10/15/10		
5-56*	8.0	16.902	7.63	3.56		16.6	
5-57*	8.0	14.754	7.54	4.11		17.1	
5-58*	7.9	14.343	7.59	4.03		17.1	
heated bellows to $\geq$ *300 °C*							
5-59*	7.9	21.801	6.36	3.31		17.0	
5-60*	8.0	12.787	7.37	3.63		17.1	
5-61*	8.0	14.782	7.34	3.93		18.1	
6A Staurolite							
5-62*	7.9	15.969	10.34	5.24		17.0	
6A Garnet A							
5-63*	8.0	14.201	10.92	5.60		17.1	
6A Staurolite							
5-64*	7.8	13.064	10.33	5.00		16.5	
6A Muscovite							
5-65*	8.2	8.990	10.58	5.63		16.5	small plume
6A Chlorite							
5-66*	8.0	15.691	8.86	4.80		16.0	

* = hypothetical blank of 2.9Vs, $\delta^{18}O$ =10.5‰ , $\delta^{17}O$ =5.4‰

Table B2a: Sample 6Xi and USNM Almandine - Feburary 1999

Run No.	F_2 mbar	Area, Vs	$\delta^{18}O$	$\delta^{17}O$	freeze times	laser mV	comment
Heated sample with heat-lamp to get pressure down							
Prefluorinate 45.8mbar→31.4mbar overnight							
fluorinate 40.5mbar→34.9mbar overnight							
heated bellows to 230°C							
blank 1†	5.8	9.604	-7.11	-3.81	10/10/10		
blank 2	5.8	5.575	-4.91	-2.22			
blank 3	5.9	4.021	-8.40	-3.23			
blank 4	5.9	2.830	-2.79	-0.49			
blank 5	5.9	2.521	1.38	0.69			$\delta^{18}O$ increasing
left to pump overnight							
blank 1†	5.8	2.505	2.91	1.92			
blank 2	5.8	2.358	6.84	3.18			
blank 3	6.0	2.133	7.98	4.79			
blank 4	6.1	1.990	8.35	4.00			
blank 1†	6.1	2.263	6.24	3.25			
blank 2	5.8	2.113	8.66	4.92			
USNM Almandine							
5-168[2]	5.8	9.902	12.74	6.50		18.1	chopper
blank 3	5.8	2.030	9.83	4.36			
5-169[3]	5.9	9.264	10.03	4.64		16.1	
5-170[3]	6.0	16.697	8.79	4.64		17.0	
5-171[4]	6.0	12.829	8.44	4.41		15.2	
blank 4	6.0	2.288	9.93	3.40			
fluorinate overnight 36.4mbar F_2 →33.0							
blank 1†	5.8	2.403	10.74	6.49			
5-172[1]	6.3	12.900	8.76	4.45		16.4	
5-173[1]	6.0	10.447	8.76	5.10		15.5	
5-174[1]	5.9	18.298	8.10	3.53		15.1	
5-175[1]	7.8	16.257	8.49	4.66	10/15/10	16.1	
5-176[1]	6.0	17.454	8.26	4.05	10/10/10	16.0	
fluorinate overnight 44.0mbarF_2 →39.4							
blank 1†	6.2	4.091	11.56	5.70			
5-177[1]	5.8	10.563	10.70	5.51		15.4	
blank 3	6.1	2.613	12.83	7.14			
6Xi Garnet							
5-178[3]	6.0	9.987	11.50	5.33		14.7	
blank 4	6.0	2.843	12.24	6.86			
5-179[4]	6.0	11.309	11.72	6.77		14.8	
5-180[4]	6.0	15.525	7.90	4.34		14.0	
blank 5	5.9	2.377	11.99	6.57			
blank 1†	6.0	1.991	11.41	5.37			
6Xi Garnet							
5-181[1]	5.8	9.866	8.20	4.78		15.0	
blank 2	6.1	1.919	11.25	4.33			
USNM Almandine							
5-182[2]	5.8	9.689	8.23	3.67		14.5	

Table B2b: Sample 6Xi and USNM Almandine - continued

Run No.	F_2 mbar	Area, Vs	$\delta^{18}O$	$\delta^{17}O$	freeze times	laser mV	comment
6Xi Garnet							
5-183[2]	6.0	8.730	11.45	6.22			
USNM Almandine							
5-184[2]	6.0	10.779	7.79	3.70		14.1	
5-185[2]	6.0	8.306	8.41	3.86			
5-186[2]	6.0	20.310	7.66	4.12		15.6	
5-187[2]	6.0	12.404	7.89	3.85			
fluorinate overnight 25.5mbar F_2 →24.0							
heated bellows > 300° C							
blank 1†	6.0	4.226	7.35	3.44			
blank 2	6.0	2.968	9.28	4.30			
5-188[2]	6.2	13.767	7.35	4.54		14.5	no chopper,fast
blank 3	6.0	2.358	10.31	4.64			
5-189[3]	6.0	12.400	7.74	3.60		14.5	chopper
blank 4	5.8	2.217	9.77	4.62			
5-190[4]	5.9	14.348	7.47	4.04		14.5	
5-191[4]	5.7	11.203	7.54	3.52		14.5	
5-192[5]	5.8	9.779	7.60	4.09		14.0	
blank 5	6.1	2.055	10.43	4.75			
fluorinate overnight 27.3mbar F_2 →25.6							
but did not heat bellow							
blank 1†	6.1	2.014	10.18	4.85			
5-193[2]	6.0	9.362	8.00	3.78		13.5	
blank 2	6.2	2.092	10.55	5.55			
5-194[2]							sample lost
5-195[2]	6.0	14.088	7.41	3.77		13.0	
5-196[2]	6.0	9.868	7.45	4.14		13.0	
blank 1†	6.2	1.977	10.67	5.86			leave 2-3hrs between
5-197[1]	6.0	9.263	7.88	4.37		13.0	
5-198[1]	6.2	13.853	7.16	3.83		14.0	
5-199[1]	6.0	16.568	7.21	3.24		14.6	
5-200[1]	6.0	13.514	7.51	3.65		14.0	
5-201[1]	6.0	12.167	7.06	3.55			
5-202[1]	6.0	11.971	7.40	3.67			
fluorinate overnight 25.6mbar F_2 →24.1							
heated bellows to 115° C							
blank 1†	6.1	2.396	4.42	1.07			
blank 2	6.1	2.123	8.27	4.98			
5-203[3]	6.1	10.325	7.04	3.39			
blank 3	6.0	1.929	9.23	7.35			
5-204[3]	6.0	14.007	6.89	3.04			
5-205[3]	6.0	11.737	7.40	3.96			
6Xi garnet							
5-206[4]	8.1	9.738	11.03	6.12			

Table B2c: Sample 6Xi and USNM Almandine - continued

Run No.	F_2 mbar	Area, Vs	$\delta^{18}O$	$\delta^{17}O$	freeze times	laser mV	comment
USNM Almandine							
5-207[4]	8.0	11.730	7.05	3.66		14.0	
blank 4	8.0	1.935	9.41	4.98			
5-208[4]	11.764	7.54	3.70				
blank 1[†]	7.8	1.829	11.02	5.74			
5-209[1]	8.0	16.552	7.35	3.96		12.5	
5-210[1]	8.0	18.890	7.21	3.95		15.0	
5-211[1]	8.0	16.563	7.21	3.68		13.5	
5-212[1]	8.0	15.228	7.87	4.17		14.5	
fluorinate overnight 27.3mbar F_2 →25.6NEW KBr - old was tired							
LOADED NEW USNM Almandine - took out old; left in 6Xi							

Table B3: Sample 6Xi and new USNM Almandine - February 1999

Run No.	F_2 mbar	Area, Vs	$\delta^{18}O$	$\delta^{17}O$	freeze times	laser mV	comment
heated traps/bellows > 150° C overnight; pumped overnight							
prefluorinate 39.6mbar for 5 hours → 37.7mbar							
blank 1[†]	8.1						too large
blank 2	8.1	9.743	21.97	11.29			
blank 3	8.0	7.142	17.22	8.08			
heated bellows > 300° C ; pumped overnight							
blank 1[†]	8.0	19.239	23.43	11.29	10/10/10		
blank 2	8.4	5.553	16.63	8.25			
blank 3	8.1	4.597	13.41	6.30			
blank 4	8.1	3.988	12.60	6.55			
blank 5	8.1	3.829	12.05	5.34			
blank 6	8.2	3.622	11.91	6.07			
blank 1[†]	8.0	3.527	12.60	6.81			
blank 2	8.2	3.463	12.68	7.12			
USNM Almandine							
5-213[2]	7.8	16.910	13.78	7.24		13.6	chopper
5-214[2]	8.2	21.658	10.96	5.92		16.1	
blank 3	7.8	3.072	12.79	7.60			
5-215[3]	7.8	14.626	10.36	5.45		14.0	
TOOK OUT sample 6Xi - left USNM Almandine in							

Table B4a: USNM Almandine - March 1999

Run No.	F_2 mbar	Area, Vs	$\delta^{18}O$	$\delta^{17}O$	freeze times	laser mV	comment
Sample left in from previous experiments							
prefluorinated 34.2mbar F_2 for 5 hours → 33.3mbar							
blank 1†	8.0	2.416	8.71	5.63	10/10/10		
blank 2	8.1	2.704	9.00	4.29			
blank 3	8.9	2.495	12.21	6.20			
blank 1†	6.0	1.882	10.67	5.99			
USNM Almandine							
5-216[1]	5.9	18.186	8.85	4.17		14.0	chopper
blank 2	6.1	1.664	11.67	6.49			
5-217[2]	6.0	12.536	7.75	3.12		15.3	
5-218[2]	6.0	10.697	7.46	3.95		14.5	
5-219[2]	6.1	10.006	7.67	3.32		14.2	
5-220[2]	6.0	13.118	6.76	3.01		13.5	
5-221[2]	6.1	10.868	7.19	3.67		14.1	
5-222[2]	6.1	13.332	6.83	3.45		13.5	
blank 1†	6.0	1.691	10.65	3.37			
5-223[1]	6.0	15.559	7.18	3.62		13.1	
blank 2	6.0	1.532	10.03	5.97			
5-224[3]	5.8	12.001	7.26	3.82		13.5	
5-225[3]	6.0	14.245	7.23	3.93		14.0	
blank 3	6.1	1.672	10.21	4.47			
5-226[3]	5.9	13.283	7.59	3.83		15.6	
heated bellows > 300° C , heated traps							
blank 4	6.0	5.336	22.15	11.43			
blank 5	6.0	2.241	19.37	9.99			
blank 1†	6.0	1.784	13.94	6.93			
5-227[1]	6.1	8.430	8.61	4.22		13.3	
blank 2	6.0	1.652	13.49	8.77			
5-228[2]	5.9	8.652	8.25	3.71		14.8	
5-229[2]	6.0	22.955	6.19	3.33		14.0	
5-230[2]	6.0	20.067	6.69	7.28		15.1	
5-231[2]	6.0	18.654	6.48	3.81		15.0	
5-232[2]	6.0	9.358	7.11	3.76		14.1	very small

Table B5: Sample 6Xi and USNM Almandine - March 1999

Run No.	F_2 mbar	Area, Vs	$\delta^{18}O$	$\delta^{17}O$	freeze times	laser mV	comment
loaded piece of 6Xi; heated with heat-lamp							
prefluorinated 39.7mbar F_2 for 5 hours→38.1 mbar							
heated bellows > 300° C; heated traps							
blank 1†	5.8	6.737	12.45	5.81	10/10/10		
blank 2	6.0	3.191	14.36	6.35			
blank 1†	6.5	2.721	11.33	5.57			
blank 2	6.1	2.424	12.46	6.92			
USNM Almandine							
5-233[2]	6.1	21.013	9.85	5.25		13.0	
5-234[2]	6.0	23.716	8.37	4.54		14.0	
5-235[2]	5.8	20.539	7.89	3.64		14.0	
5-236[2]	6.0	21.196	7.63	4.48		15.0	gone over twice
5-237[2]	5.8	28.591	7.25	4.17		13.6	
blank 1†	6.0	2.006	10.58	5.67			
5-238[1]	6.0	7.030	21.73	11.00		13.5	v low yield
5-239[1]	6.1	19.621	7.35	3.83		13.8	
blank 2	6.0	5.373	23.85	12.31	10/15/10		longer to SiGel
blank 3	6.1	1.974	10.73	6.22	10/10/10		
5-240[2]	6.0	27.668	7.22	3.85		13.5	
5-241[2]	6.0	23.025	7.13	3.79	10/15/10	14.5	15 mins
blank 4	6.0	2.454	9.97	4.26	10/10/10		
put 20mbar F_2 in chamber, ablated, cleaned up; heated bellows > 300° C; heated traps							
prefluorinated 49.7mbar F_2 overnight→46.5 mbar							
next day cleaned up & heated bellows > 300° C							
blank 1†	6.1	7.929	15.38	7.96	10/15/10		
blank 2	1.0	1.529	10.37	4.12	5/10/10		less F_2
5-242[2]	1.1	17.208	7.47	3.08		13.8	
5-243[2]	1.1	5.775	21.89	10.75		13.5	
5-244[2]	1.2	20.918	7.27	4.15		13.2	

Table B6a: Sample 19a and USNM Almandine - March 1999

Run No.	F_2 mbar	Area, Vs	$\delta^{18}O$	$\delta^{17}O$	freeze times	laser mV	comment
New KBr; repolished USNM Almandine standard							
heat-lamp and heated bellows > 300° C while pumping; left bellows hot overnight							
prefluorinated 50.1mbar F_2 overnight→37.0 mbar							
heated bellows > 300° C							
blank 1†	6.0	91.610			10/10/10		huge!
blank 2	6.0	17.121	8.70	4.20			
blank 3	6.1	12.605	8.67	4.19			
heated bellows > 300° C and pumped for 2 days							
blank 1†	6.1	27.797	11.00	5.37			
blank 2	6.0	10.129	11.09	5.71			
blank 3	6.0	6.209	9.85	4.70			
blank 4	5.368	8.82	4.03				
blank 5	4.987	8.85	4.57				
blank 1†	6.0	4.648	6.36	3.71			
blank 2	6.0	4.430	7.97	4.28			
blank 3	1.1	2.247	7.26	4.04			1mbar F_2
USNM Almandine							
5-248[3]	1.2	15.512	14.71	7.69		14.0	chopper
5-249[3]	1.2	32.936	9.86	5.15			
5-250[3]	1.2	26.007	8.65	4.21		14.0	
5-251[3]	1.2	20.480	8.04	3.98			
5-252[3]	1.2	28.317	7.77	3.80		13.6	
heated bellows > 300° C and left pump overnight							
blank 1†	6.0	17.080	7.77	3.94			6.0mbar F_2
blank 2	1.0	1.945	10.10	5.03	5/10/10		
blank 3	1.1	2.176	8.56	6.20	5/15/10		
5-253[3]	1.2	25.035	7.26	3.59		13.8	chopper
5-254[3]	1.2	20.164	7.49	4.00		13.8	
5-255[3]	1.2	24.227	7.58	3.90			
5-256[3]	1.4	37.882	7.17	3.65		13.3	
19a garnet							
5-257[3]	1.2	17.069	10.82	5.64		13.0	
USNM Almandine							
5-258[3]	1.2	25.593	6.98	3.51		12.8	
19a garnet							
5-259[3]	1.2	25.922	10.60	5.04		13.0	
USNM Almandine							
5-260[3]	1.2	24.568	6.96	3.27		12.8	
blank 4	1.2	2.590	7.46	3.14			
heated bellows > 300° C							
blank 1†	1.2	2.887	6.36	4.12			
blank 1	1.2	3.463	5.44	1.54			
5-261[3]	1.2	18.407	6.40	3.64		12.8	
blank 3	1.2	2.672	8.37	5.49			

Table B6b: Sample 19a and USNM Almandine - continued

Run No.	F_2 mbar	Area, Vs	$\delta^{18}O$	$\delta^{17}O$	freeze times	laser mV	comment
19a garnet							
5-262[3]	1.2	25.794	10.22	5.49		13.3	
USNM Almandine							
5-263[3]	1.2	21.850	7.04	3.77		13.8	
5-264[4]	1.2	29.110	10.62	5.76		13.0	
blank 4	1.2	2.482	8.58	4.38			
5-265[4]	1.1	21.748	6.59	3.90		13.1	
19a garnet							
5-266[4]	1.2	21.756	10.38	5.11		12.8	
5-267[4]	1.2	22.878	10.31	5.09		13.3	
blank 1†	1.2	2.538	8.20	3.89			
USNM Almandine							
5-268[1]	1.1	24.046	5.64	3.07		12.8	
laser refilled - shot into sample without F_2							
blank 1†	5.0	3.886	3.45	1.50			
blank 2	1.2	2.075	7.97	4.54			
5-269[2]	1.1	18.493	7.21	3.54		19.0	
5-270[2]	1.2	16.457	6.97	3.32		20.2	
19a garnet							
5-271[2]	1.2	25.983	11.08	5.72		19.5	
USNM Almandine							
5-272[2]	1.2	25.017	6.67	3.52		18.0	
19a garnet							
5-273[2]	1.2	21.063	10.41	5.50		17.0	
USNM Almandine							
5-274[2]	1.2	20.984	7.00	3.61		16.5	
blank 1†	1.2	2.420	7.46	3.05			
5-275[1]	1.2	26.832	5.34	2.63		16.8	
5-276[1]	1.2	18.917	6.34	3.65		13.8	
19a garnet							
5-277[1]	1.3	21.868	10.05	4.86		14.0	
5-278[1]	1.2	23.884	10.35	5.09		14.1	
USNM Almandine							
5-279[1]	1.2	17.968	6.92	3.65		14.5	
5-280[1]	1.2	25.509	6.95	3.62		14.0	
5-281[1]	1.1	19.820	6.91	3.12		14.0	
19a garnet							
5-282[1]	1.2	20.044	10.18	5.31		14.0	
blank 1†	1.2	2.436	7.58	3.53			
USNM Almandine							
5-283[1]	1.2	17.672	5.05	2.30		14.0	
5-284[1]	1.2	28.176	6.75	3.35		15.5	
5-285[1]	1.2	21.269	6.70	2.73		14.0	
19a garnet							
5-286[1]	1.2	23.284	10.06	5.09		14.1	

Table B6c: Sample 19a and USNM Almandine - continued

Run No.	F_2 mbar	Area, Vs	$\delta^{18}O$	$\delta^{17}O$	freeze times	laser mV	comment
USNM Almandine							
5-287[1]	1.2	19.651	6.36	3.48		15.5	
19a garnet							
5-288[1]	1.2	23.608	10.27	5.03		15.0	
5-289[1]	1.2	20.856	10.14	5.37		15.5	
USNM Almandine							
5-290[1]	1.1	19.481	6.56	3.46		14.0	
19a garnet							
5-291[1]	1.3	17.640	9.65	4.65		14.0	
blank 1†	1.1	2.218	7.83	4.15			
USNM Almandine							
5-292[1]	1.2	16.348	4.88	2.39		13.5	
5-293[1]	1.2	20.068	6.24	6.04		13.1	
19a garnet							
5-294[1]	1.2	20.700	9.95	4.81		14.5	
5-295[1]	1.2	18.724	9.75	5.26		14.5	
5-296[1]	1.2	22.792	10.09	5.23		14.5	
USNM Almandine							
5-297[1]	1.2	20.742	6.60	3.32		14.0	
blank 2	1.2	2.030	7.57	2.76			
19a garnet							
5-298[2]	1.2	24.900	10.25	5.12		13.1	
5-299[2]	1.2	33.100	10.41	4.98		15.4	
5-300[2]	1.1	19.128	9.82	4.97		14.5	
5-301[2]	1.2	23.505	10.47	5.19		13.2	
USNM Almandine							
5-302†[2]	1.2	26.448	5.09	2.61		13.0	
19a garnet							
5-303[2]	1.2	18.135	9.73	5.05		13.8	
5-304[2]	1.2	21.708	10.01	5.03		12.2	
5-303[2]	1.2	15.022	9.65	5.20		13.5	
USNM Almandine							
5-306[2]	1.2	18.349	6.51	3.34		14.0	
19a garnet							
5-307[2]	1.2	23.714	10.08	5.06		13.2	
5-308[2]	1.2	22.980	9.62	5.30		15.5	
5-309[2]	1.2	19.381	10.23	5.91		13.6	
5-310[2]	1.2	13.683	10.01	5.47		13.0	
5-311[2]	1.2	18.890	10.34	5.17		13.0	
5-312[2]	1.2	32.107	10.63	5.23		12.9	
USNM Almandine							
5-313†[2]	1.2	22.913	4.19	2.48			
19a garnet							
5-314[2]	1.2	23.145	10.19	5.23		15.0	
5-315[2]	1.2	25.215	10.03	5.24		14.0	

Table B6d: Sample 19a and USNM Almandine - continued

Run No.	F_2 mbar	Area, Vs	$\delta^{18}O$	$\delta^{17}O$	freeze times	laser mV	comment
5-316[2]	1.1	29.384	10.14	5.34		13.6	
5-317[2]	1.2	28.330	10.29	5.66		13.0	
5-318[2]	1.2	20.726	9.62	5.07		15.0	
5-319[2]	1.2	27.584	10.39	5.24		14.0	
5-320[2]	1.2	24.590	10.23	5.01		13.5	
5-321[2]	1.2	20.783	10.09	5.33		13.0	
5-322[2]	1.2	22.980	10.11	5.11		13.0	
USNM Almandine							
5-323†[2]	1.2	24.123	5.21	2.79		13.0	
19a garnet							
5-324[2]	1.2	23.621	9.97	5.01		13.5	
5-325[2]	1.2	21.685	9.85	5.12		13.6	
5-326[2]	1.1	22.194	10.04	5.14		13.0	
5-327[2]	1.3	18.770	9.81	5.65		13.5	
USNM Almandine							
5-328[2]	1.2	18.552	6.40	2.93		13.0	
19a garnet							
5-329[2]	1.2	15.090	9.29	4.33		13.0	
5-330[2]	1.2	26.038	9.59	5.08		13.0	
5-331[2]	1.2	21.383	9.61	4.85		14.0	
heated bellows > 300° C							
blank 1†	1.1	3.372	4.65	2.94			
USNM Almandine							
5-332[1]	1.2	22.257	3.68	2.18		13.3	
blank 2	1.3	2.368	8.41	4.70			
19a garnet							
5-333[2]	1.1	20.505	8.99	4.52		13.0	
USNM Almandine							
5-334[2]	1.2	30.978	6.42	3.41			
19a garnet							
6-1[2]	1.1	28.216	9.82	5.33		13.8	
6-2[2]	1.2	25.032	9.60	4.64		13.0	
6-3[2]	1.2	28.731	9.90	4.42		14.0	
6-4[2]	1.2	31.868	9.71	5.24		14.0	
6-5[2]	1.2	25.690	9.85	4.88		14.5	
blank 1†	1.2	2.672	6.03	3.39			
6-6[1]	1.2	23.724	6.86	3.36		13.5	
6-7[2]	1.3	25.360	9.55	5.08		13.0	
blank 2	1.2	2.201	7.35	5.42			
6-8[2]	1.2	25.828	9.26	4.75		13.2	
6-9[2]	1.2	29.502	9.67	5.07		13.0	
6-10[2]	1.2	25.049	9.45	4.71		12.7	

Table B7a: Sample R76 and USNM Almandine - January 2000

Run No.	F_2 mbar	Area, Vs	$\delta^{18}O$	$\delta^{17}O$	freeze times	laser mV	comment
New iris fitted							
30.5mb F_2 over sample for 2hours → 27.5mb							
pumped overnight							
30.9 F_2 over sample for 2hours → 29.6mb							
blank 1†	4.0	39.021	-0.53	-0.86	5/10/10		1min over sample
blank 2	4.3	78.212	-143.43	28.86			
42.0mb F_2 over sample for 3.25hours → 39.8mb							
pumped overnight							
20.2 F_2 over sample for 1.5hours → 19.6mb							
blank 1†	4.0	11.262	2.27	1.24			
blank 2	4.0	8.158	4.54	2.23			
blank 3	3.9	6.531	4.94	2.48			
blank 4	3.9	6.205	5.01	3.09			
blank 1†	4.0	5.584	2.22	1.24			
blank 2	4.0	5.114	4.80	2.54			
blank 3	4.1	5.087	5.19	3.40			
USNM Almandine							
6-355[3]	4.0	34.665	8.56	4.26		12.1	chopper, over pit twice
6-356[3]	4.0	30.490	7.35	4.06		13.5	
6-357[3]	4.0	28.180	7.33	3.65		14.5	
6-358[3]	3.9	27.382	7.26	3.46		12+	
6-359[4]	4.1	38.034	7.00	3.57		12+	
blank 4	4.0	4.091	5.68	2.53			
6-360[4]	4.0	33.687	6.89	3.66		14.0	
14.6mb over for 1 hour → 14.4, run thru as blank							
blank 1†	14.6	32.459	7.65	3.97	10/10/10		
blank 2	4.0	4.190	7.29	3.70	5/10/10		
6-361[2]	4.0	24.924	6.95	3.70		12+	
6-362[2]	4.0	25.929	6.97	3.11		14.0	
15.1mb over for 45mins → 15.0, run thru as blank							
blank 3	15.1	30.822	8.21	3.72	10/10/10		
R76 garnet							
6-363[2]	4.0	20.787	10.39	5.45	5/10/10	9.9	
USNM Almandine							
6-364[2]	4.1	22.951	6.96	3.62		10.5	
blank 4	4.0	3.256	7.50	4.78			
R76 garnet							
6-365[4]	4.0	28.580	10.57	5.01		12+	
blank 1†	3.8	2.719	6.42	3.56			
USNM Almandine							
6-366[1]	4.0	14.716	6.07	3.27		12.5	
6-367[1]	4.0	22.176	6.82	3.20		12.5	
R76 garnet							
6-368[1]	3.9	21.203	10.47	5.28		12.5	
6-369[1]	4.1	25.332	10.49	5.24		12.0	

Table B7b: Sample R76 and USNM Almandine - continued

Run No.	F_2 mbar	Area, Vs	$\delta^{18}O$	$\delta^{17}O$	freeze times	laser mV	comment
6-370[1]	4.2	22.382	10.30	5.18		12.0	
USNM Almandine							
6-371[1]	3.9	24.447	6.79	3.20		11.8	
R76 garnet							
6-372[1]	4.0	25.543	10.42	5.88		12.5	
blank 2	4.0	2.692	8.15	1.97			
6-373[3]	4.2	26.120	10.61	5.76		12.1	
USNM Almandine							
6-374[3]	4.0	23.790	6.58	3.02		12.5	
blank 3	3.8	2.636	8.29	4.63			
6-375†[1]	3.9	26.716	5.61	2.50		14.6	
blank 1	4.0	2.460	7.84	5.17			
6-376[1]	3.9	26.479	6.80	3.57		12.0	
6-377[1]	4.1	22.547	6.44	3.09		12.0	
R76 garnet							
6-378[1]	3.9	20.486	10.22	5.20		12.0	
6-379[1]	4.2	36.631	10.89	5.45		12.0	
6-380[1]	3.9	23.395	10.58	5.50		13.0	
6-381[1]	3.9	28.164	10.85	5.38		13.0	
6-382[1]	3.9	30.316	10.01	5.04		13.0	
6-383[1]	3.9	27.509	10.86	5.74		13.1	
blank 2	4.0	2.472	8.25	3.48			
blank 1†	3.9	2.048	7.29	2.95			
6-384[1]	4.0	25.654	9.80	4.99		12.5	
6-385[1]	4.0	25.721	9.54	4.87		12.8	
6-386[1]	3.9	29.281	10.50	5.39		12.7	
6-387[1]	4.0	33.439	10.44	5.21		12.5	
6-388[1]	4.0	30.436	10.27	5.43		12.4	
6-389[1]	3.9	28.272	10.47	5.32		12.3	
6-390[1]	4.0	28.730	10.74	5.37		12.0	
6-391[1]	4.1	29.848	10.70	5.78		12.8	
6-392[1]	4.0	28.496	10.55	5.36		13.0	
6-393[1]	4.0	34.256	10.64	5.35		13.0	
blank 1†	4.0	2.693	9.48	4.06			
6-394[1]	4.0	30.141	10.10	5.32		12.6	
6-395[2]	3.9	28.948	10.44	5.15		13.0	
6-396[2]	4.0	26.256	10.65	5.25		12.0	
6-397[2]	3.9	33.624	10.82	5.42		13.0	
blank 2	3.9	2.368	8.67	3.27			
6-398[2]	4.0	26.995	10.49	5.67		13.1	
6-399†[1]	4.0	27.781	7.38	3.32		12.8	
blank 1	4.0	2.089	8.48	3.52			
6-400[1]	4.0	27.601	10.22	5.21		13.1	
6-401[1]	4.0	24.806	10.56	5.36		14.0	
6-402[1]	3.9	28.878	11.04	5.90		12.5	

Table B7c: Sample R76 and USNM Almandine - continued

Run No.	F_2 mbar	Area, Vs	$\delta^{18}O$	$\delta^{17}O$	freeze times	laser mV	comment
blank 1†	4.1	2.073	5.66	3.69			
6-403[1]	4.0	31.015	8.75	4.27		12.0	
blank 2	4.1	2.034	9.13	4.79			
6-404[2]	4.1	21.476	9.16	4.62		12.0	
6-405[2]	4.0	25.911	10.03	5.33		13.1	
6-406[2]	4.0	24.507	10.28	5.04		12.5	
14.8mb for 1 hour→14.6, run thru as blank							
blank 1†	14.8	24.550	6.01	2.65	5/10/10		
6-407[1]	3.9	22.886	9.72	4.96	5/10/10		
6-408[1]	4.1	27.180	10.81	5.76		12.2	
6-409[1]	4.0	36.156	10.91	5.57		13.0	
6-410[1]	4.1	24.364	10.67	5.22		12.0	
6-411[1]	4.0	33.159	10.91	5.49		12.7	

Table B8a: R76 matrix and USNM Almandine-feb 2000

Run No.	F_2 mbar	Area, Vs	$\delta^{18}O$	$\delta^{17}O$	freeze times	laser mV	comment
24.6mb for 2.5 hours → 23.0mb							
20.4mb for 1.5 hours → 19.7mb							
pumped overnight							
15.3mb for 1 hour → 14.9mb, run thru as blank1							
blank 1†	15.3	89.897	-175	10.8	10/10/10		
blank 2	4.0	4.431	13.90	6.88	5/10/10		
blank 3	4.0	3.645	13.15	7.05			
blank 4	3.9	3.085	12.68	6.32			
blank 5	3.9	3.083	12.88	6.40			
15.0mb for 0.5 hour → 14.9mb, run thru as blank1							
blank 1†	15.0	21.038	5.98	3.38	10/10/10		
USNM Almandine							
6-412[2]	4.0	42.248	8.77	5.01	5/10/10	13.7	
6-413[2]	3.9	30.618	7.61	3.87		12.0	
6-414[2]	4.1	32.497	6.95	3.40		4.1	
blank 2	4.1	2.473	8.76	2.81			
6-415[2]	4.1	33.294	7.22	3.59		12.0	
14.5mb for 1 hour → 14.4mb, run thru as blank1							
blank 1†	14.5	20.752	2.95	1.34	10/10/10		
6-416[2]	4.0	28.966	6.95	3.22	5/10/10	12.5	
6-417[2]	3.9	31.302	6.99	3.67		14.2	
6-418[2]	4.0	25.696	6.77	3.28		12.5	
blank 2	4.0	2.333	8.21	5.12			
R76 staurolite							
6-419[2]	4.0	20.748	10.38	4.97		13.1	
USNM Almandine							
6-420[2]	4.2	26.725	6.70	3.60		13.1	
R76 staurolite							
6-421[2]	3.9	20.829	10.57	5.66		13.3	
15.3mb for 1 hour → 15.0mb, run thru as blank1							
blank 1†	15.3	19.352	2.28	0.76	10/10/10		
USNM Almandine							
6-422[2]	3.9	27.803	6.97	3.53	5/10/10	12.5	
R76 staurolite							
6-423[2]	4.0	19.203	10.21	4.68		12.7	
USNM Almandine							
6-424[2]	3.9	30.614	6.56	3.49		13.0	
R76 staurolite							
6-425[2]	4.1	28.681	10.48	5.86		13.0	
blank 2	3.9	2.366	8.45	3.58			
6-426[2]	3.9	25.525	10.09	5.48		14.7	
R76 white mica							
6-427[2]	4.1	23.815	10.20	5.24		13.0	
R76 staurolite							
6-428[2]	3.9	25.375	10.43	5.23		12.6	

Appendix

C: Garnet Standard Data

Notes on listings:

- samples are given as corrected values
- superscript number refers to the number of the blank that has been used for correction

Run No.	V_{32}	corrected $\delta^{18}O$
sample 6 and USNM Almandine		
5-17[3]	14.319	6.5
5-19[3]	11.306	6.9
5-20[3]	10.889	6.9
5-28[2]	15.774	6.5
5-29[2]	16.465	6.3
5-54[1]	11.314	6.9
5-55[1]	15.048	6.8
5-57[1]	14.754	6.9
5-58[1]	14.343	6.9
5-60[1]	12.787	6.5
5-61[1]	14.782	6.6
mean		6.7
standard deviation (1σ)		0.2
sample 6x and USNM Almandine		
5-198[1]	13.853	6.6
5-199[1]	16.568	6.7
5-200[1]	13.514	7.0
5-201[1]	12.167	6.4
5-202[1]	11.971	6.8
5-203[3]	10.325	6.5
5-204[3]	14.007	6.5
5-205[3]	11.737	6.8
5-207[4]	11.730	6.6
5-209[1]	16.552	6.9
5-210[1]	18.890	6.8
5-211[1]	16.563	6.7
mean		6.7
standard deviation (1σ)		0.2

Run No.	V_{32}	corrected $\delta^{18}O$
USNM Almandine		
5-218[2]	10.697	6.7
5-219[2]	10.006	6.9
5-220[2]	13.118	6.1
5-221[2]	10.868	6.4
5-222[2]	13.332	6.1
5-223[1]	15.559	6.8
5-224[3]	12.001	6.7
5-225[3]	14.245	6.8
5-230[2]	20.067	6.1
mean		6.5
standard deviation (1σ)		0.3
sample 6xi and USNM Almandine		
5-235[2]	20.539	7.3
5-236[2]	21.196	7.0
5-237[2]	28.591	6.8
5-239[1]	19.621	7.0
5-240[2]	27.668	7.0
5-241[2]	23.025	6.8
5-244[2]	20.918	7.0
mean		7.0
standard deviation (1σ)		0.2

Run No.	V_{32}	corrected $\delta^{18}O$
sample 19a and USNM Almandine		
5-258[3]	25.593	6.8
5-260[3]	24.568	6.8
5-263[3]	21.850	6.8
5-265[4]	21.748	6.3
5-270[2]	16.457	6.8
5-272[2]	25.017	6.6
5-274[2]	20.984	6.9
5-279[1]	17.968	6.8
5-280[1]	25.509	6.9
5-281[1]	19.820	6.8
5-284[1]	28.126	6.7
5-285[1]	21.269	6.6
5-287[1]	19.651	6.2
5-290[1]	19.481	6.4
5-297[1]	20.742	6.5
5-306[2]	18.349	6.4
mean		6.6
standard deviation (1σ)		0.2

Run No.	V_{32}	corrected $\delta^{18}O$
sample r76 and USNM Almandine		
6-362[2]	25.929	6.8
6-364[2]	22.951	6.8
6-367[1]	22.176	6.9
6-371[1]	24.447	6.6
6-374[3]	23.790	6.4
6-376[1]	26.479	6.7
6-377[1]	22.547	6.3
6-414[2]	32.497	6.8
6-417[2]	31.302	6.9
6-418[2]	25.696	6.6
6-420[2]	26.725	6.6
6-422[2]	27.803	6.8
6-424[2]	30.614	6.4
mean		6.7
standard deviation (1σ)		0.2

Appendix

D: X-Ray Fluorescence data

Sample	grade	SiO_2	TiO_2	Al_2O_3	Fe_2O_3	MnO	MgO	CaO	Na_2O	K_2O	P_2O_5	LOI	Total
P21	l grt	46.40	0.98	25.82	15.87	0.62	1.18	2.16	1.39	3.25	0.22	2.13	100.01
P21	l grt	49.42	1.10	25.38	11.61	0.27	1.80	1.37	1.54	3.95	0.24	3.41	100.08
3	l grt	63.24	0.96	13.81	12.55	0.09	2.07	0.55	0.69	4.14	0.18	1.52	99.78
4	u st	50.26	1.22	25.45	10.34	0.21	1.51	0.93	1.05	5.66	0.11	2.94	99.67
22	u grt	56.34	0.98	22.37	9.38	0.18	1.50	1.09	1.26	4.09	0.21	2.73	100.13
R96	u grt	47.11	1.27	26.39	12.13	0.25	1.55	1.82	1.60	5.06	0.18	2.85	100.21
R96	u grt	44.70	1.48	30.63	8.16	0.06	1.65	0.62	1.18	7.55	0.05	3.98	100.05
31	l st	53.09	1.04	23.15	7.28	0.12	2.46	2.95	1.14	5.36	0.30	2.68	99.57
6	l st	55.62	1.02	23.49	8.37	0.13	1.70	0.60	1.44	4.12	0.19	3.03	99.76
6	l st	53.92	1.01	25.45	7.27	0.07	1.77	0.50	1.65	4.60	0.18	3.50	99.76
15	u st	46.53	1.44	30.71	6.83	0.05	1.91	0.97	1.62	6.19	0.27	3.63	100.16
R76	u st	52.44	1.11	28.01	5.93	0.06	1.33	0.58	1.95	5.05	0.24	3.36	100.06
30	l ky	47.92	1.23	28.37	11.59	0.19	1.66	1.38	1.69	3.66	0.17	2.12	99.97
18	l ky	55.84	1.06	24.11	9.03	0.13	1.84	0.78	1.54	3.43	0.19	2.20	100.14
19	l ky	50.39	1.05	25.88	10.04	0.13	1.80	1.14	1.40	5.35	0.18	2.43	99.79
32	u ky	49.68	1.30	25.20	12.24	0.21	1.82	1.70	1.47	4.46	0.08	1.97	100.13
P97	u ky	43.77	1.48	27.96	15.95	0.21	2.44	1.35	0.62	3.71	0.14	2.73	100.35

Recalculation of bulk-rock analysis for the KFMASH, KMnFMASH and CNMnKFMASH systems

XRF results give proportions of major cations in the form of weight % oxides. In the first instance, rock modelling within both the KFMASH and KMnFMASH systems required recalculation to remove the effects of Ca, Na and Ti-bearing phases. For the CNMnKFMASH system, only recalculation for the oxidation states of iron, and remov-

ing the effects of titanium are necessary. Finally, for all systems normalising to 100% yields bulk-rock mode oxides.

In the absence of paragonite and margarite at higher grades, we assume all Ca and Na are taken up by plagioclase. For the KFMASH and KMnFMASH systems, we have to take account of the Al taken up in plagioclase by removing the mole quantities of Na_2O and K_2O in sympathy with their stoichiometry ($CaAlSi_2Si_2O_8$, $NaAlSi_3O_8$). Thus recalculation requires:

$$[Al_2O_3] - ([Na_2O] + [CaO])$$

The problem of the varying oxidation states of iron (Fe^{2+} and Fe^{3+}) needs attention. Fe was reported as weight % Fe_2O_3, and thus conversion to FeO requires equation 9.6 (however a proportion of this will still exist as Fe_2O_3 in the form of iron oxides, such as magnetite).

$$[FeO] = 2\times [Fe_2O_3]$$

The effect of titanium also has to be quantified. If all the Ti exists within ilmenite ($FeTiO_3$) then the effect of ilmenite on molar proportion of FeO is calculated as:

$$[FeO] = [FeO]_{tot} - [TiO_2]$$

Appendix

E: Microprobe data

sample	mineral	SiO_2	TiO_2	Al_2O_3	FeO	MnO	MgO	CaO	Na_2O	K_2O	Total	F.O.	Si	Ti	Al	Fe	Mn	Mg	Ca	Na	K	Total	X_{Mg}
P21	Ms	45.21	0.19	35.43	2.22	0.01	0.51	0.04	1.61	8.88	94.09	22	6.09	0.02	5.63	0.25	0.00	0.10	0.01	0.42	1.53	14.05	0.29
	Pg	44.21	0.08	38.84	0.71	0.02	0.05	0.66	5.79	1.03	91.38	22	5.90	0.01	6.11	0.08	0.00	0.01	0.09	1.50	0.18	13.88	0.09
	Chl	22.93	0.03	21.86	33.90	0.03	8.35	0.01	0.07	0.02	87.20	22	4.02	0.00	4.53	4.98	0.00	2.17	0.00	0.02	0.00	15.74	0.35
	Grt rim	36.27	0.02	20.76	36.42	0.37	1.94	4.53	0.01	0.00	100.95	12	2.94	0.00	1.99	2.47	0.03	0.23	0.39	0.00	0.00	8.06	0.09
	Cld	23.96	0.01	40.37	26.35	0.01	2.61	0.00	0.03	0.00	93.36	14	2.31	0.00	4.59	2.12	0.00	0.37	0.00	0.01	0.00	9.40	0.15
R96	Ms	48.55	0.11	29.08	3.72	0.00	2.25	0.01	0.72	9.50	93.93	22	6.60	0.01	4.66	0.42	0.00	0.46	0.00	0.19	1.65	13.98	0.52
	Pl	61.36	0.01	23.54	0.09	0.00	0.05	4.65	8.46	0.00	98.15	8	2.76	0.00	1.25	0.00	0.00	0.00	0.22	0.74	0.00	4.98	0.00
	Chl	24.28	0.03	22.02	27.92	0.04	12.95	0.03	0.44	0.03	87.75	22	4.08	0.00	4.37	3.93	0.01	3.25	0.01	0.14	0.01	15.80	0.45
	Grt rim	36.33	0.04	20.69	35.40	0.42	1.99	5.59	0.06	0.00	100.52	12	2.88	0.00	1.93	2.34	0.03	0.23	0.47	0.01	0.00	7.90	0.09
Sample 6	Ms	45.54	0.32	35.35	2.15	0.01	0.58	0.01	1.25	8.09	93.30	22	6.14	0.03	5.62	0.24	0.00	0.12	0.00	0.33	1.39	13.87	0.32
	Pg	45.99	0.07	39.46	0.65	0.00	0.10	0.23	5.05	0.75	92.29	22	6.02	0.01	6.09	0.07	0.00	0.02	0.03	1.28	0.13	13.64	0.21
	St	26.45	0.30	51.59	13.25	0.03	1.47	0.01	0.66	0.00	93.76	23	3.84	0.03	8.82	1.61	0.00	0.32	0.00	0.00	0.00	14.81	0.16
	Chl	23.84	0.08	21.91	28.32	0.03	12.33	0.02	0.12	0.02	86.67	22	4.07	0.01	4.41	4.05	0.00	3.14	0.00	0.04	0.00	15.73	0.44
	Grt rim	35.45	0.04	20.38	37.08	1.10	2.05	2.34	0.08	0.01	98.53	12	2.94	0.00	1.99	2.57	0.08	0.25	0.21	0.01	0.00	8.06	0.09
R76	Ms	45.74	0.44	34.91	1.38	0.01	0.87	0.02	1.28	9.18	93.83	22	6.16	0.05	5.54	0.16	0.00	0.17	0.00	0.34	1.58	13.98	0.52
	Pg	45.60	0.07	38.57	0.40	0.02	0.08	0.15	5.82	0.84	91.55	22	6.03	0.01	6.01	0.04	0.00	0.02	0.02	1.49	0.14	13.77	0.23
	Bt	35.66	1.48	18.08	18.70	0.02	10.45	0.02	0.26	9.22	93.88	22	5.49	0.17	3.28	2.41	0.00	2.40	0.00	0.08	1.81	15.64	0.50
	St	27.51	0.55	51.65	13.24	0.06	1.39	0.01	0.06	0.05	94.52	23	3.94	0.06	8.73	1.59	0.01	0.30	0.00	0.02	0.01	14.65	0.16
	Pl	64.60	0.01	20.78	0.22	0.01	0.02	1.88	8.73	0.00	96.24	8	2.93	0.00	1.11	0.01	0.00	0.00	0.09	0.77	0.00	4.90	0.00
	Grt rim	35.92	0.04	20.66	36.53	0.60	2.83	2.60	0.06	0.00	99.25	12	2.94	0.00	1.99	2.50	0.04	0.35	0.23	0.01	0.00	8.06	0.12
	Chl	24.73	0.14	22.35	23.61	0.03	14.22	0.02	0.11	0.27	85.47	22	4.17	0.02	4.44	3.33	0.00	3.58	0.00	0.03	0.06	15.64	0.52
Sample 19	Ms	45.13	0.57	34.85	1.68	0.01	0.79	0.02	1.32	9.87	94.24	22	6.09	0.06	5.55	0.19	0.00	0.16	0.00	0.35	1.70	14.10	0.45
	Chl	24.88	0.02	22.74	23.64	0.01	15.52	0.03	0.03	0.06	86.92	22	4.12	0.00	4.43	3.27	0.00	3.83	0.00	0.01	0.01	15.68	0.54
	Grt rim	36.50	0.05	20.85	36.89	0.24	2.46	3.50	0.05	0.00	100.55	12	2.95	0.00	1.99	2.49	0.02	0.30	0.30	0.01	0.00	8.06	0.11
	Bt	35.44	1.55	18.27	18.85	0.01	10.49	0.04	0.26	9.66	94.57	22	5.44	0.18	3.30	2.42	0.00	2.40	0.01	0.08	1.89	15.71	0.50
	Pl	64.76	0.02	21.16	0.06	0.02	0.01	2.04	9.89	0.02	97.98	8	2.90	0.00	1.12	0.00	0.00	0.00	0.10	0.86	0.00	4.97	0.00
	St	26.30	0.56	52.20	13.23	0.05	1.78	0.01	0.84	0.00	94.97	23	3.77	0.06	8.83	1.59	0.01	0.38	0.00	0.00	0.00	14.87	0.19
P97	Ms	46.71	0.47	34.53	0.95	0.02	0.79	0.07	1.11	9.06	93.71	22	6.26	0.05	5.46	0.11	0.00	0.16	0.01	0.29	1.55	13.88	0.60
	Bt	36.01	1.45	18.44	15.99	0.02	12.28	0.02	0.22	8.98	93.40	22	5.48	0.17	3.31	2.04	0.00	2.79	0.00	0.06	1.75	15.60	0.58
	St	27.81	0.64	52.44	13.79	0.06	1.87	0.01	0.05	0.02	68.69	23	3.91	0.07	8.68	1.62	0.01	0.39	0.00	0.01	0.00	14.69	0.19
	Grt rim	36.20	0.08	20.76	32.55	0.84	3.04	5.39	0.03	0.00	98.90	12	2.95	0.01	1.99	2.22	0.06	0.37	0.47	0.00	0.00	8.06	0.14
	Chl	24.75	0.09	22.59	21.38	0.03	16.76	0.05	0.05	0.09	85.79	22	4.11	0.01	4.42	2.97	0.00	4.15	0.01	0.02	0.02	15.69	0.58
	Pl	58.20	0.02	24.80	0.06	0.01	0.02	6.66	7.17	0.01	96.93	8	2.67	0.00	1.34	0.00	0.00	0.00	0.33	0.64	0.00	4.98	0.00

Table 1: Summary of microprobe data; F.O. - formula oxygens